Using fusion-product spectroscopy to study inertial fusion implosions, stopping power, and astrophysical nucleosynthesis at OMEGA and the NIF

by

Alex B. Zylstra

B.A., Pomona College (2009)

Submitted to the Department of Physics
in partial fulfillment of the requirements for the degree of

Doctor of Philosophy in Physics

at the

MASSACHUSETTS INSTITUTE OF TECHNOLOGY

June 2015

Author .....
Department of Physics
May 1st, 2015

Certified by .....
Richard Petrasso
Division Head, High Energy Density Physics
MIT Plasma Science and Fusion Center
Thesis Supervisor

Certified by .....
Miklos Porkolab
Professor of Physics, Thesis Co-Supervisor
Thesis Reader

Accepted by .....
Nergis Mavalvala
Professor of Physics
Associate Department Head for Education

Using fusion-product spectroscopy to study inertial fusion implosions, stopping power, and astrophysical nucleosynthesis at OMEGA and the NIF

by
Alex B. Zylstra

Submitted to the Department of Physics
on May 1st, 2015, in partial fulfillment of the
requirements for the degree of
Doctor of Philosophy in Physics

Abstract

By measuring energetic charged-particle products from fusion reactions occuring in plasmas, nuclear diagnostics can be used to study the properties of the burning plasma, as a probe of the plasma, or of the fundamental fusion reaction physics. In this thesis, fusion product spectroscopy is used to study ignition-scale inertial fusion implosions, measure charged-particle stopping in dense plasmas to high accuracy, and study reactions relevant to nuclear astrophysics.

'Surrogate' plastic-shell implosions at the National Ignition Facility with D^3He fuel produce 14.7-MeV protons. Spectrometry capability developed for the NIF has been used to study these protons produced at the 'shock' burn in these implosions, which preceeds the main 'compression' burn by several hundred picoseconds (ps). A 1-D implosion model was developed to interpret the spectra of the emitted shock-produced protons. Higher areal densities (ρR) are observed for implosions where the laser is kept on for a longer duration ('no-coast'); combining these data with x-ray radiography reveals that the shock-bang time occurs anomalously late in these implosions relative to hydrodynamic simulations. By using multiple detectors, low-mode (~ 2) implosion asymmetries are measured. When compared to stagnation x-ray self-emission an anomalously-low growth factor is observed relative to models, indicating potential time-dependent asymmetries or that the x-ray shape underestimates the asymmetry amplitude of the surrounding shell.

Charged-particle spectroscopy relies upon untested theory for the stopping power as the particle traverses the dense imploding plasma. These theories are also critical for modeling α-particle self-heating and burn. By using D^3He protons to probe a x-ray isochorically-heated subject plasma in the warm dense matter (WDM) regime, the stopping power has been measured to high accuracy for the first time in a dense plasma. This measurement is also a strong constraint on WDM electron structure models.

Finally, nuclear diagnostics have been used to study several fusion reactions relevant to astrophysics. Unlike prior work using accelerators, these measurements are the first to be done in a hot plasma, like astrophysical plasmas of interest. Cross-section measurements of the reaction $T+{}^3He \rightarrow {}^6Li+\gamma$ show that anomalously-high production of ^6Li during the Big Bang cannot occur via this mechanism. In addition, measurements of the proton spectrum from this reaction, and the solar fusion reaction $^3He+{}^3He$, are used to constrain the R-matrix nuclear theory. Finally, a cross section measurement for the reaction $p+D \rightarrow {}^3He+\gamma$ has been performed; this reaction is relevant to energy generation in brown dwarfs, protostars, and to production of ^3He during the Big Bang.

Thesis Supervisor: Richard Petrasso
Title: Division Head, High Energy Density Physics
MIT Plasma Science and Fusion Center

Thesis Reader: Miklos Porkolab
Title: Professor of Physics, Thesis Co-Supervisor

Acknowledgments

Modern physics is becoming biased towards 'big science'. Inertial fusion and the application of high-energy-density plasmas to fundamental science problems is certainly one such area, and therefore the work in this thesis has been supported by a great number of people, who I will try to acknowledge — hopefully without exception!

First and foremost I thank the other members of the High-Energy-Density Physics Division for their support, encouragement, and advice throughout the years. My advisor, Dr. Richard Petrasso, has been an unwavering source of support and guidance for this work. I also thank the other HEDP Division scientists, Drs Johan Frenje, Chikang Li, Maria Gatu Johnson, and Fredrick Séguin, for contributing to every aspect of my work. For example, Fredrick and Johan helped greatly with the NIF WRF project, Johan and Chikang were very involved in the stopping-power experiments, and Maria and Johan contributed heavily to the nuclear astrophysics experiments.

The other graduate students have been a fantastic source of camaraderie and support throughout the years, in particular my officemates Drs Hans Rinderknecht and Mike Rosenberg. Drs Dan Casey, Mario Manuel, and Nareg Sinenian helped me learn the field and have since moved on in their careers. It has been great to work with Hong Sio and Brandon Lahmann since they joined our group, and we expect great theses from them soon.

I owe a great amount of gratitude to many people who have helped execute these experiments. Jocelyn Schaeffer, Irina Cashen, Bob Frankel, Ernie Doeg, Michelle McCluskey, Michelle Valadez, Mark McKernan, and Minda Cairel have all contributed to the CR-39 processing, which is fundamental to this work. At NIF, Kenn Knittel and Rich Zacharias have been particularly instrumental in implementing the WRF spectrometers. I thank Roger Janezic for implementing the T_2+^{3}He gas fill capability required for the nucleosynthesis experiments. Joe Katz, Dino Mastrosimone, Frank Lopez, Valerie Fatherley, John Oertel, Michelle McCluskey, and Bruce Brannon led the engineering and implementation of several diagnostics used in this work. I thank Michelle Evans for her work on our targets. And as any OMEGA user knows, Chuck Sorce, Steve Stagnitto, Dave Canning, and Sam Morse have been key contributors to the successful implementation of these experiments.

I thank my many scientific collaborators at other institutions. Rip Collins at LLNL motivated and guided much of my work on stopping power and the NIF experiments, and has also been a great mentor over the years. At the NIF, Richard Bionta and Stephan Friedrich were key to getting proton spectroscopy off the ground; Ryan Rygg and Damien Hicks have been heavily involved the experiments; Andy Mackinnon and Nino Landen have been great support for this research. The γ-ray nucleosynthesis experiments were enabled by a huge effort by Los Alamos, particularly Hans Herrmann and Yongho Kim. I thank Craig Sangster, David Meyerhofer, Vladimir Glebov, and Christian Stoeckl for their support in executing my experiments at OMEGA. The nuclear physics work has been supported theoretically by Gerry Hale and Mark Paris from LANL, Andy Bacher from Indiana University, Carl Brune from Ohio University, and Dennis McNabb from LLNL. Paul Grabowski from UC Irvine supported the stopping power experiments with many theoretical

calculations. I also thank many other collaborators from LLNL[*], LANL[†], LLE[‡], SNL[§], GA[¶], SLAC[‖], the University of Michigan[**], and AWE[††].

This work was supported by grants from DOE, NNSA, LLNL, the NLUF program, and LLE. I also personally thank the SSGF and NSF fellowships for financial support.

This thesis itself was greatly improved by a close reading by Johan Frenje and Miklos Porkolab. I also thank my thesis committee, Miklos Porkolab, Rick Temkin, and Ed Bertschinger, for their guidance on this work.

Finally, I thank those people who have supported (and put up with) me outside of physics over the last six years, particularly my close friends Ned Burns, Vadim Spirt, and Jenna Spirt, my sister Ashton, and my parents Kirk and Mariann.

[*]Peter Amendt, Jeff Atherton, Maria Barrios, Perry Bell, Robin Benedetti, Laura Berzak Hopkins, Dave Bradley, Debbie Callahan, Eddie Dewald, Laurent Divol, Sham Dixit, Tilo Doeppner, John Edwards, Steve Glenn, Frank Graziani, Gareth Hall, Steve Hatchett, Omar Hurricane, Warren Hsing, Nico Izumi, Oggie Jones, Shahab Khan, Jeff Koch, Andrea Kritcher, Sebastien Le Pape, John Lindl, Rich London, Tammy Ma, Nathan Meezan, Ed Moses, Sabrina Nagel, Tom Parham, Art Pak, Prav Patel, Jesse Pino, Rahul Prasad, Joe Ralph, Harry Robey, Mordy Rosen, Steve Ross, Marilyn Schneider, Scott Sepke, Brian Spears, Cliff Thomas, Riccardo Tommasini, Richard Town, Steve Weber, and Charles Yeamans

[†]Steve Batha, Gary Grim, Nels Hoffmann, Grisha Kagan, John Kline, George Kyrala, Ray Leeper, Rick Olson, and Doug Wilson

[‡]Radha Bahukutumbi, Riccardo Betti, Suxing Hu, Jim Knauer, Chad Forrest, Dino Mastrosimone, Phil Nilson, Walter Schmayda, and Wolf Seka

[§]Stephanie Hansen

[¶]Paul Fitzsimmons, Abbas Nikroo, and Hannah Reynolds

[‖]Siegfried Glenzer

[**]Paul Keiter

[††]Mike Rubery

Contents

List of Publications

This dissertation is based on several peer-reviewed journal publications:

1. A. B. Zylstra, J. A. Frenje, P. Grabowski *et al.*, "Measurement of charged-particle stopping in warm-dense plasma," accepted by Phys. Rev. Lett. (2015)

2. A. B. Zylstra, J. A. Frenje, F. H. Séguin *et al.*, "In-flight observations of low-mode ρR asymmetries in NIF implosions," Physics of Plasmas, **22**(5), 056301 (2015)

3. A. B. Zylstra, J. A. Frenje, F. H. Séguin *et al.*, "The effect of shock dynamics on compressibility of ignition-scale National Ignition Facility implosions," Physics of Plasmas, **21**(11), 112701 (2014)

4. A. B. Zylstra, M. Gatu Johnson, J. A. Frenje *et al.*, "A compact neutron spectrometer for characterizing inertial confinement fusion implosions at OMEGA and the NIF," Rev. Sci. Instrum., **85**(6), 063502 (2014)

5. A. Zylstra, J. Frenje, F. Séguin *et al.*, "A new model to account for track overlap in CR-39 data," Nuclear Instruments and Methods in Physics Research Section A: Accelerators, Spectrometers, Detectors and Associated Equipment, **681**(0), 84 – 90 (2012)

6. A. B. Zylstra, J. A. Frenje, F. H. Séguin *et al.*, "Charged-particle spectroscopy for diagnosing shock ρR and strength in NIF implosions," Rev. Sci. Instrum., **83**(10), 10D901 (2012)

7. A. B. Zylstra, C. K. Li, F. H. Séguin *et al.*, "Measurements of hohlraum-produced fast ions," Physics of Plasmas, **19**(4), 042707 (2012)

8. A. B. Zylstra, C. K. Li, H. G. Rinderknecht *et al.*, "Using high-intensity laser-generated energetic protons to radiograph directly driven implosions," Rev. Sci. Instrum., **83**(1), 013511 (2012)

9. A. B. Zylstra, H. G. Rinderknecht, N. Sinenian *et al.*, "Increasing the energy dynamic range of solid-state nuclear track detectors using multiple surfaces," Rev. Sci. Instrum., **82**(8), 083301 (2011)

List of Figures

List of Tables

Thesis Overview

This thesis presents original work by the author in the fields of inertial confinement fusion, high-energy-density physics, and nuclear astrophysics. The main body of the work is divided into three parts: studying inertial fusion implosions with proton spectroscopy, measuring charged-particle stopping power in dense plasmas, and studying nuclear astrophysics. The organization of the thesis is described below.

First, a general introduction to the physics of nuclear fusion reactions, and a history of the field of fusion ignition by inertial confinement and high-energy-density physics is given in Chapter 1.

Part I: NIF Proton Spectroscopy

This Part of the thesis discusses in detail the development and use of proton spectroscopy at the NIF. First, the details of proton spectrometry are discussed in Chapter 2, including the details of the NIF spectrometers, necessary corrections for energy loss in the hohlraum wall, and a 1-D implosion model used for interpreting the measured spectra. Chapter 3 uses this capability to study the shock dynamics of 'surrogate' implosions at the NIF, while Chapter 4 uses the multiple detector lines of sight to study low-mode implosion areal-density (ρR) asymmetries.

Part II: Plasma Stopping Power

This Part discusses plasma stopping power experiments. An experiment used a D^{3}He proton source and x-ray isochorically-heated WDM plasmas to measure the stopping power to high precision in dense plasma for the first time, as discussed in Chapter 5. Significant work has been conducted with the aim of developing a platform for similar measurements using the OMEGA EP short-pulse laser facility, which is summarized in Chapter 6.

Part III: Nuclear Astrophysics

This Part of the thesis discusses several experiments, which studied fusion reactions relevant to nuclear astrophysics; a brief overview of this field is given in Chapter 7. Studies of the T+^{3}He reaction are discussed in Chapter 8, in particular the γ branch is focused upon, which is relevant to big-bang nucleosynthesis. The proton spectrum was also used as a constraint on nuclear R-matrix theory. Similarly, the ^{3}He^{3}He proton spectrum was measured in experiments discussed in Chapter 9; this reaction is relevant to solar fusion, and the spectrum at low energies is used as a contraint on nuclear theory. Finally, the p+D γ-producing reaction, relevant to big-bang nucleosynthesis plus energy generation in brown dwarfs and protostars, was measured in experiments discussed in Chapter 10.

Part IV: Conclusion and Appendices

The main results of this thesis are summarized in Chapter 11.

In addition to the material discussed in previous chapters, significant diagnostic development work has been performed by the author over the last few years, and this work is documented in the Appendices. Proton radiography techniques using the short-pulse OMEGA EP laser were developed (Appendix A); a compact recoil spectrometer was developed for DT neutrons (Appendix B); the energy and fluence dynamic ranges of CR-39 detectors were extended by novel techniques utilizing multiple surfaces and statistical analysis, respectively (Appendix C and Appendix D).

Charged-particle spectroscopy was also used to study dynamic charging of hohlraum targets during intense laser irradiation (Appendix E).

Many 1-D hydrodynamics simulations have been performed by the author over the last several years in support of this work and work by other students; these simulations are briefly discussed in Appendix F.

The evaluation and comparison of several common stopping-power models in relevant regimes, and the negligible impact of scattering on this work are discussed in Appendix G.

Additional details on several experiments are documented in the remaining sections: the many NIF shots used in this work (Appendix H) and the T+^{3}He experiments (Appendix I).

Recent experiments on NIF have studied lower-convergence (higher-adiabat) shots, these experiments and preliminary results are discussed in Appendix J.

Finally, fusion reaction product kinematics are discussed in detail in Appendix K.

1

Introduction

In 1905 Albert Einstein developed his theory of special relativity[1], and then further posited a fundamental relation between the inertia (mass) of an object and its energy[2]:

$$E = mc^2, \tag{1.1}$$

which is probably the most famous equation in physics. Since the speed of light (c) is large, this result implies that small differences in mass correspond to large differences in energy. The full implications of this result took a long time to comprehend.

Fifteen years later, spectrographic measurements by Aston[3] revealed that the mass of a ^{4}He ion is slightly less than the sum of the individual nucleons (two neutrons and two protons) by about 0.8%, implying a significant binding energy via Eq. 1.1. Then Arthur Eddington, working on the internal composition of stars[4], suggested that fusion of hydrogen into helium may be the source of energy in stars. Since material in the universe is primarily hydrogen[5], a reaction taking advantage of the mass deficit above could produce helium and copious energy in stellar interiors. Eddington did not know of a mechanism to accomplish this, though it was an attractive way to solve an outstanding conundrum in stellar dynamics: the apparent discrepancy between lifetimes of stars utilizing gravitational Kelvin-Helmholtz contraction as an energy source (of order 10^7 years), and the apparent age of the earth from biological and geologic arguments (of order 10^9 years). The problem was that at central stellar temperatures of order 10^7 K, the energy of ions is much less than the substantial Coulomb potential energy barrier from mutual electrostatic repulsion, which would be necessary to overcome for fusion reactions to occur classically.

The solution came together with the quantum physics revolution. George Gamow was the first to apply the probability for quantum mechanical tunneling to the problem of nuclear reactions, in particular for α particle decays[6], a result which was quickly followed by the application to fusion reactions by Atkinson and Houtermans[7,8]. A major breakthrough in stellar dynamics then came in 1938 from Bethe, who calculated the reaction rate for proton-proton fusion via a weak process[9]. The field of nuclear physics emerged and grew substantially in the 1930s and 40s for both terrestrial applications and stellar physics, as discussed in the following sections.

1.1 Nuclear Reactions

1.1.1 Energetics

The dynamics of nuclear reactions will be driven by the available energy, in particular reactions going from loosely- to tightly-bound systems will be exothermic and release energy equivalent to the

difference in binding energy. It is therefore critical to evaluate the binding energy of the elements using available data[10] or simple models. A semi-empircal relation for the binding energy of nuclei is the Bethe-Weizscker mass formula or the 'liquid drop' nuclear model[11]:

$$\frac{E_B}{A} = a_V - a_S A^{-1/3} - a_C \frac{Z^2}{A^{4/3}} - a_A \frac{(A-2Z)^2}{A^2}, \tag{1.2}$$

which depends on the total number of nucleons (A) and the atomic number (Z). The model has the following components: the nuclear volume term ($a_V = 15.8$), the surface area term ($a_S = 18.3$), the Coulomb term ($a_C = 0.714$), and the asymmetry term ($a_A = 23.2$). Each coefficient is obtained from a fit to available data in units of MeV. The data and liquid-drop model are shown in Fig. 1.1.

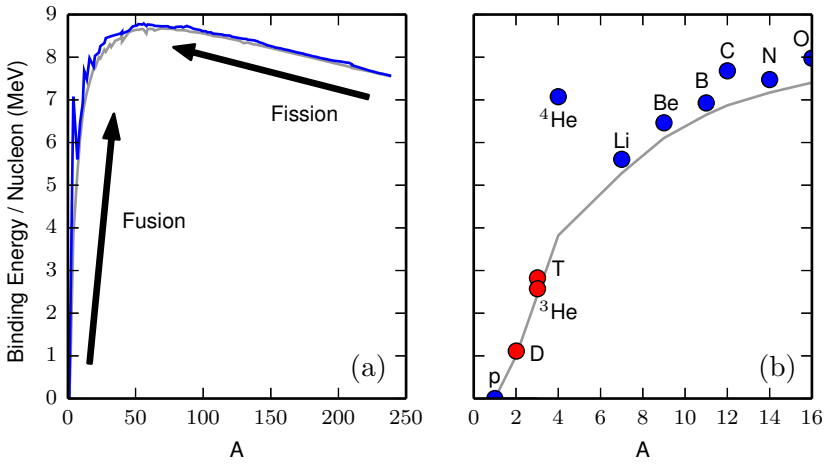

Figure 1.1. Nuclear binding energy per nucleon versus total number of nucleons **(a)** Data (blue) and liquid-drop model (gray) for nuclei up to ^{238}U. The most common or longest-lived isotope of each element is plotted. **(b)** Binding energy for light nuclei up to oxygen.

There is a peak in the binding energy per nucleon around $A = 60$ corresponding to several isotopes of Fe and Ni, with ^{62}Ni the most tightly bound (most binding energy per nucleon) and ^{56}Fe the most efficiently bound (least average mass per nucleon). For lighter nuclei, the binding energy per nucleon generally increases as A increases, meaning that 'fusion' reactions combining light nuclei into a heavier nucleus will generally be exothermic. For heaver nuclei the trend is opposite, meaning that 'fission' reactions splitting a heavy nucleus into multiple lighter nuclei will release energy.

The liquid drop model does a poor job at explaining the binding energy of certain nuclei, which is exceptionally important for fusion reactions. This is shown in Fig. 1.1b. In particular, the nucleons are bound about twice as strongly in ^{4}He as predicted by the model. This is because ^{4}He has a closed nuclear shell; in general, nuclei with proton or neutron numbers corresponding to the 'magic numbers' (2, 8, 20, 28, 50, 82, and 126) are more strongly bound. Some nuclei such as ^{4}He are 'doubly magic' with very high binding energy. Note that ^{12}C and ^{16}O are also tightly bound. This means that light nuclei fusion reactions producing ^{4}He, ^{12}C, or ^{16}O will tend to release large amounts of energy.

The energy released in a reaction is denoted Q and can be calculated from the difference in

reactant-product masses or binding energies:

$$Q = \left(\sum_i m_i - \sum_f m_f \right) c^2 \tag{1.3}$$

$$= \sum_f E_{B,f} - \sum_i E_{B,i}, \tag{1.4}$$

where the index i corresponds to the reactants and f corresponds to the reaction products.

1.1.2 Fusion Reactions

1.1.2.1 Kinematics

The most common fusion reactions have two reactants and two products, which we can denote:

$$A + B \rightarrow C + D. \tag{1.5}$$

Equivalent notation is $A(B,C)D$, both notations will be used interchangeably in this text. The two reactants A, B will have some initial energy, and in the center-of-mass frame the energy of the system is

$$E_{CM} = \frac{1}{2} \frac{m_A m_B}{m_A + m_B} v^2, \tag{1.6}$$

where v is the magnitude of the relative velocity ($v = |\vec{v}_A - \vec{v}_B|$) and m represents the particle masses. The energy E_{CM} is referred to as the 'center-of-mass energy'. The energies of the products C and D are determined from conservation of energy, including the reactant Q (Eq. 1.3), and momentum:

$$E_C = \frac{1}{2} m_C V^2 + \frac{m_D}{m_C + m_D} \left(Q + E_{CM} \right) \tag{1.7}$$

where V is the velocity of the center-of-mass frame $V = m_A v_A / (m_A + m_B)$. The energy of particle D follows similarly. If the reactants have distributions, such as in a thermal plasma, then the product energies can be calculated as functions of distribution-averaged quantities [12].

1.1.2.2 Cross-section and Reactivity

The fusion reaction rate depends on the probability for colliding particles to fuse, the particle number density, and energy distribution. The probability is given by the reaction cross-section σ_{AB} for the reaction $A + B$. In this work we will use the cross-section as a function of E_{CM}. However, the cross-section is commonly determined from accelerator experiments, where a beam of particles A is incident upon a stationary target of particles B. The cross-sections are related by:

$$\sigma_{AB}\left(E_{CM}\right) = \sigma_{AB}^{B-T} \left(E_{CM} \frac{m_A + m_B}{m_B} \right) \tag{1.8}$$

where 'B-T' denotes beam-target fusion.

Generally, the cross-section depends on the geometric probability of 'interaction' (σ_{geom}), the tunneling probability for the reactants to penetrate the barrier of mutual Coulomb repulsion ($\mathcal{T}$), and the probability that two reactants will fuse after tunneling ($\mathcal{R}$):

$$\sigma \approx \sigma_{geom} \times \mathcal{T} \times \mathcal{R}, \tag{1.9}$$

where the geometric factor is approximately the square of the particle's de Broglie wavelength:

$$\sigma_{geom} \sim \lambda_{dB}^2 \propto \frac{1}{E_{CM}}. \tag{1.10}$$

The factors $\mathcal{T}$ and $\mathcal{R}$ depend on the barrier penetration factors for each partial wave and nuclear interactions, which can be approximated by only keeping the S-wave factor as dependent on energy[13]:

$$\mathcal{T} \times \mathcal{R} \propto \exp\left(-\sqrt{E_G/E_{CM}}\right) \tag{1.11}$$

which is known as the 'Gamow factor', where E_G is the 'Gamow energy':

$$E_G = \left(\pi\alpha Z_A Z_B\right)^2 \times 2m_r c^2. \tag{1.12}$$

Here, α is the fine structure constant, m_r is the reduced mass, and Z_A and Z_B are the atomic numbers of the reactants. This result is combined with the geometric factor (Eq. 1.10) and the full cross-section is often written:

$$\sigma(E_{CM}) = S(E_{CM})\frac{\exp\left(-\sqrt{E_G/E_{CM}}\right)}{E_{CM}} \tag{1.13}$$

where S is the 'astrophysical S-factor', a weak function of the energy, while the primary energy dependence is contained in the exponential and inverse dependence on E_{CM}. Typically the S-factor is determined from a combination of experimental data and nuclear theory.

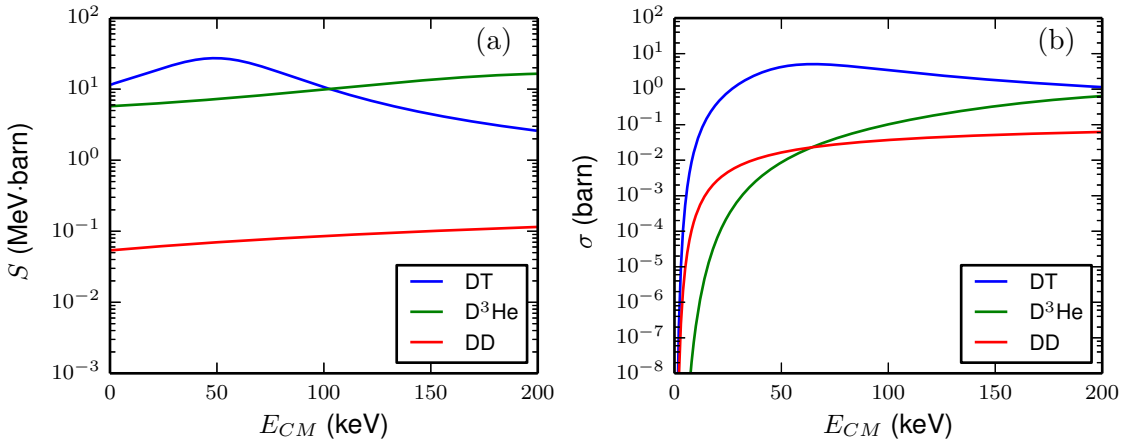

Figure 1.2. **(a)** Astrophysical S-factor and **(b)** resulting cross-section for three fusion reactions of interest.

The S-factors and cross sections for the DT, D^3He, and DD reactions:

$$\mathrm{D} + \mathrm{T} \rightarrow \mathrm{n}\ (14.04\ \mathrm{MeV}) + \alpha\ (3.56\ \mathrm{MeV}) \tag{1.14}$$

$$\mathrm{D} + {}^3\mathrm{He} \rightarrow \mathrm{p}\ (14.65\ \mathrm{MeV}) + \alpha\ (3.72\ \mathrm{MeV}) \tag{1.15}$$

$$\mathrm{D} + \mathrm{D} \rightarrow \mathrm{n}\ (2.45\ \mathrm{MeV}) + {}^3\mathrm{He}\ (0.82\ \mathrm{MeV}) \tag{1.16}$$

$$\rightarrow \mathrm{p}\ (3.03\ \mathrm{MeV}) + \mathrm{T}\ (1.01\ \mathrm{MeV}) \tag{1.17}$$

are shown in Fig. 1.2 using published fits[14]. The cross-section is a very strong function of E_{CM}.

As intended, the astrophysical S-factor is a weak function of E_{CM}, particularly for the D+D and D+^{3}He reactions. The D+T reaction has a resonance at $E_{CM} \sim 65$ keV, which is apparent in both the S-factor and cross-section.

In real systems of interest (both terrestrial and astrophysical), fusion reactants are not monenergetic but will have a distribution of energies, which means that reactions will occur at various center-of-mass energies depending on both the reaction occurring and the reactant distribution. The quantity of interest is the 'averaged reactivity' given by the product $\sigma \times v$, where v is the relative velocity. For a distribution of relative velocities, the reactivity is

$$\langle \sigma v \rangle = \int_0^\infty \sigma(v) v f(v) dv, \tag{1.18}$$

where $f(v)$ is the distribution of relative velocities. Typically, an isotropic Maxwellian distribution is assumed for reactant A:

$$f_A(v) = \left(\frac{m_A}{2\pi k_B T_A}\right)^{3/2} \exp\left(-\frac{m_A v^2}{2 k_B T_A}\right), \tag{1.19}$$

and similarly for reactant B. Then, the reactivity becomes

$$\langle \sigma v \rangle = \iint d\vec{v_A} d\vec{v_B} \sigma_{AB}(v) v f_A(v_A) f_B(v_B), \tag{1.20}$$

where the relative velocity is $v = |\vec{v_A} - \vec{v_B}|$. The velocities can be rewritten in terms of the relative velocity, center-of-mass velocity $V = (m_A \vec{v_A} + m_B \vec{v_B})/(m_A + m_B)$, and reduced mass m_r:

$$\begin{aligned} \langle \sigma v \rangle &= \frac{(m_A m_B)^{3/2}}{(2\pi k_B T)^3} \iint d\vec{v_A} d\vec{v_B} \exp\left(-\frac{(m_A + m_B) V^2}{2 k_B T} - \frac{m_r v^2}{2 k_B T}\right) \sigma(v) v \qquad (1.21) \\ &= \left[\left(\frac{m_A + m_B}{2\pi k_B T}\right)^{3/2} \int d\vec{V} \exp\left(-\frac{(m_A + m_B) V^2}{2 k_B T}\right)\right] \\ &\quad \times \left(\frac{m_r}{2\pi k_B T}\right)^{3/2} \int d\vec{v} \exp\left(-\frac{m_r v^2}{2 k_B T}\right) \sigma(v) v. \qquad (1.22) \end{aligned}$$

The part depending on the center-of-mass quantities (in square brackets) is the integral of a normalized Maxwellian and thus $\equiv 1$. The integral over the relative velocity $\vec{v}$ can be simplified with $d\vec{v} = 4\pi v^2 dv$, and then the integral can be done over E_{CM} with $dE_{CM} = m_r v dv$, so $d\vec{v} = (4\pi v / m_r) dE_{CM}$ and:

$$\langle \sigma v \rangle = \frac{4\pi}{\sqrt{2\pi m_r}(k_B T)^{3/2}} \int \sigma(E_{CM}) E_{CM} e^{-E_{CM}/k_B T} dE_{CM}. \tag{1.23}$$

With a known center-of-mass cross-section, the reactivity is easily calculated. Many parameterizations have also been published for popular reactions[14]; as an example the reactivities corresponding to the reactions in Fig. 1.2 are shown in Fig. 1.3.

In addition to the reactivity, which dictates the total reaction rate, it is important to know the average E_{CM} for reactions occurring in a thermal plasma. The integrand in the reactivity (Eq. 1.23), with the typical form of the cross-section (Eq. 1.13), is the product of a decaying exponential from the distribution function and a rising exponential in the cross-section for the limit $E_{CM} \ll E_G$ (which is the case in this work). The maximum in the integrand of Eq. 1.23 is known as the 'Gamow

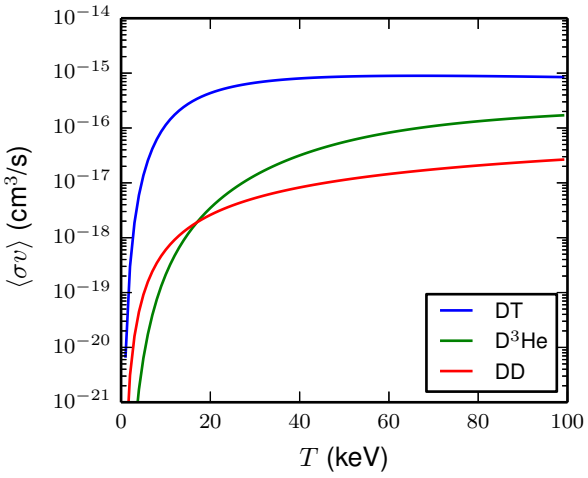

Figure 1.3. Reactivities for three reactions (corresponding to Fig. 1.2).

peak energy':

$$E_{Gp} = \left(\frac{E_G}{4k_BT}\right)^{1/3} k_BT = k_BT \times \left(\frac{(\pi\alpha Z_A Z_B)^2 m_r c^2}{2k_BT}\right)^{1/3}, \tag{1.24}$$

which is the distribution-averaged reaction center-of-mass energy. From here on we will use $E_{CM} = E_{Gp}$ for reactions occurring in a thermal plasma. Additionally, the width (full-width half-max) of the reaction distribution in energy can be obtained from a Taylor expansion of Eq. 1.23 around the E_{Gp} with the result[13]:

$$\Delta = \frac{4}{\sqrt{3}}\left(\frac{(\pi\alpha Z_A Z_B)^2 m_r c^2}{2k_BT}\right)^{1/6} k_BT. \tag{1.25}$$

The Gamow peak is shown schematically in Fig. 1.4.

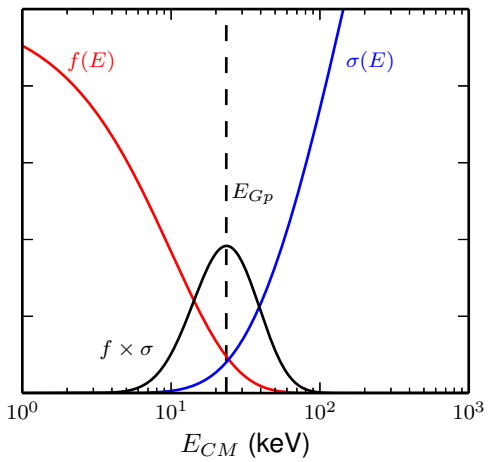

Figure 1.4. Gamow peak resulting from the product of the decaying distribution function ($f(E)$, red) and the cross-section ($\sigma(E)$, blue).

1.2 Terrestrial Fusion Energy

1.2.1 Historical

A number of important discoveries in nuclear physics occurred in the 1930s, starting with Chadwick's discovery of the neutron in 1932[15], Hahn's experimental discovery of fission[16], and Meitner's theoretical explanation of fission[17]. The latter led to the realization by Szilárd that in certain nuclei, neutron-induced fission produces additional neutrons leading to the possibility of chain reactions in 'fissile' elemental isotopes (notably ^{235}U and ^{239}Pu). During the Manhattan project, the first controlled nuclear chain reaction was realized in 1942 by Enrico Fermi and collaborators in the Chicago Pile 1 reactor, which led to the first uncontrolled (explosive) fission chain reaction at the Trinity test in 1945.

During the Manhattan Project several scientists became interested in fusion reactions as a next step beyond fission. Notably Enrico Fermi first proposed to Edward Teller the concept of igniting a nuclear fusion chain reaction, which would be a thermal fusion chain reaction rather than a neutron-induced fission reaction. With significant contributions from Stanislaw Ulam, Teller led US efforts to create the 'super' or thermonuclear (TN) weapon, with the final Tellar-Ulam design based on the following declassified principles[18]:

> "...a fission 'primary' is used to trigger a TN reaction in thermonuclear fuel referred to as a 'secondary'... radiation from a fission explosive can be contained and used to transfer energy to compress and ignite a physically separate component containing thermonuclear fuel."

The first explosive fusion chain reaction was achieved in the 1952 Ivy Mike test.

After the Manhattan Project, research into controlled (i.e. non-explosive) nuclear fusion became prominent. In particular, AEC chairman Lewis Strauss led a substantial increase in research during the 1950s on several proposed schemes of building fusion reactors for power production. Early work focused on magnetic confinement schemes: the 'stellerator' proposed by Spitzer, magnetic mirror machines, and Z-pinch devices. Contemporary efforts by British scientists focused on the Z pinch. Experiments eventually showed that magnetic mirror machines lack sufficient confinement for energy gain, and that Z-pinches studied early produced fusion yield primarily via 'beam-target' reactions, which are fundamentally unable to achieve energy gain. In the Soviet Union, Sakharov and Tamm conceptualized the 'tokamak' in 1950, with experimental work starting in 1956. Significant declassification of fusion research in 1958 spurred developments on both sides of the Cold War. By the 1960s Soviet experimental results showed the promise of tokamak confinement, which remains the primary approach pursued for magnetic confinement.

'Inertial confinement' fusion was developed as an alternative approach to magnetic confinement, and was born out of the weapons program at the Livermore and Los Alamos national laboratories. At Livermore, physicists began exploring 'pure fusion' explosions in the 1950s, though it was not clear what could be used to drive the implosion. In 1960 Theodore Maiman announced the invention of the ruby laser[19]. A year later, John Nuckolls wrote a now-famous memo to the director of LLNL proposing small laser-driven implosions of fusion fuel to produce power[20]. This sparked the development of a laser fusion program at the national labs. By this point it was already apparent that the most promising fuel was a mixture of deuterium and tritium (DT) due to the very high cross-section (and thus reactivity) at low energy (temperature) - see Figs. 1.2 and 1.3.

As of this writing, the two most prominent approaches to fusion energy remain magnetic and inertial confinement, though alternative approaches, such as the hybrid magneto-inertial fusion scheme, are also being explored. For magnetic confinement, the tokamak is the mainline approach

with the next-generation ITER machine under construction in Cadarache, France. The goal of ITER is to produce ∼500 MW of fusion power in a steady-state plasma. Other promising magnetic fusion concepts include, but are not limited to, the stellerator and the spherical torus, with leading candidates including Wendelstein 7-X for the former and the National Spherical Torus Experiment (NSTX) for the latter.

For inertial fusion, laser and pulsed-power drivers are being pursued for ignition and energy gain experiments. The Z-pinch, driven by pulsed power systems, currently being studied at Sandia's Z-machine. Laser-driven experiments are being conducted at the National Ignition Facility in Livermore, CA and soon at the Laser MegaJoule in Bordeaux, Frace, and are discussed in more detail in the subsequent section.

1.2.2 Fusion by Inertial Confinement

The principle of fusion by inertial confinement, first described by Nuckolls in 1972[21], is summarized in this section. Detailed history of experimental efforts and related history, the current understanding of challenges and designs, and summaries of current inertial fusion implosions can be found in several review articles[22–25].

1.2.2.1 Spherical Implosion

For inertial confinement to work, the timescale for fusion burn must be shorter than the mass confinement time, the latter representing the duration of fuel assembly. Considering the simplest possible geometry, a uniform sphere of DT fuel surrounded by vacuum, the mass confinement time will be set by the rarefaction wave which propages into the fuel. The front of a rarefaction propagates at the sound speed, so the confinement time is approximately

$$\tau_{conf} \sim \frac{R}{c_s}, \tag{1.26}$$

where R is the size of the fuel sphere and c_s is the sound speed. The confinement time must be compared to the fusion timescale:

$$\tau_{fus} = \frac{1}{\langle \sigma v \rangle n}, \tag{1.27}$$

where n is the ion number density, so $n = \rho/m_f$ where ρ is the mass density and m_f is the mass of one (average) fuel ion. The ratio of the two timescales is thus

$$\frac{\tau_{conf}}{\tau_{fus}} = \langle \sigma v \rangle n \tau_{conf}, \tag{1.28}$$

which must be greater than some limit for fusion burn. Since the reactivity is set by nature, the main confinement parameter is:

$$n\tau_{conf} = \frac{1}{m_f c_s} \rho R. \tag{1.29}$$

Thus, the inertial confinement of the fusion fuel is primarily set by the 'areal density' ρR. Taking this further, the fraction of fuel burned (Φ) can be related to the ρR by[13]:

$$\Phi \approx \frac{\rho R}{H_B + \rho R}, \tag{1.30}$$

where H_B is a constant parameter depending on the fuel, for DT reactions $H_B \sim 7$ g/cm^2. This means that for a reasonable burn-up fraction of $\sim 20\%$, a fuel areal density of ~ 1.75 g/cm^2 is required. This sets one fundamental requirement for an ICF system.

As cryogenic DT ice has a density ~ 0.225 g/cm^3, a uniform sphere of DT ice with a radius of 7.8 cm would be needed for the given ρR, and thus would have a total mass of 450 g. With volumetric heating of the fuel and with a burn fraction of 20% this system would have a yield of 6×10^{13}J, which is 14kT of energy, roughly equivalent to the yield of the 'Little Boy' fission bomb. Clearly, this is unsuitable for a laboratory experiment or power plant. The solution is spherical compression. Since the density of the fuel in uniform spherical compression is $\propto R^{-3}$, the areal density $\rho R \propto R^{-2}$, implying that a small amount of initial fuel may be compressed by spherical implosion to achieve the required ρR. For reactor-scale systems yield of order 100MJ per implosion would be desirable, corresponding to spherical compression of a fuel mass of order 1mg. This requires compression of the DT fuel to densities of several hundred or 1000 g/cm^3 ($50 - 100\times$ the density of solid lead).

1.2.2.2 Hot-spot Ignition

The previous section considered a uniform sphere of fuel, so-called 'volume ignition'. Unfortunately, the maximum gain of this system is limited by[13]

$$G_{max} = \frac{Q}{4k_BT}\Phi\eta, \tag{1.31}$$

where Φ is the burn fraction, and $4k_BT$ represents thermal energy coupled to the plasma (two ions and two electrons per reaction). η represents the efficiency of coupling driver energy to the fuel, optimistically $\sim 10\%$. With an initial temperature of 5 keV and a burn fraction of 30%, the maximum gain is 20 for the DT reaction. For inertial fusion to be an economically-viable source of energy, the target gain needs to be as high as possible, and simple estimates[13] put the requirement on a gain of at least $30 - 100\times$. This rules out volume ignition.

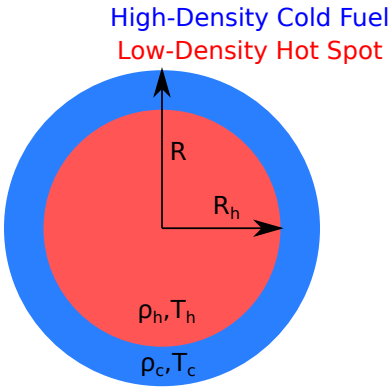

Figure 1.5. Hot-spot ignition geometry.

The solution is to 'volume ignite' a small fraction of the fuel, known as the 'hot spot' and let the subsequent runaway thermonuclear reaction initiate burn in a larger mass of fuel. In this scheme the total energy produced is comparable to volume ignition of the same fuel mass, but the driver energy is significantly reduced since initial thermal energy only needs to be coupled to the low-density hot spot. This scheme is known as hot-spot ignition, and the implosion geometry is

shown schematically in Fig. 1.5.

For thermonuclear burn to initiate in the hot spot and propagate into the cold and dense fuel, the power produced from fusion that 'bootstrap heats' the hot spot must overpower loss mechanisms: decompression (PdV), thermal conduction, and radiation (Bremsstrahlung) losses. Simple analytic expressions for the self-heating condition have been derived[13], with the typical result that the hot-spot $\rho_h R_h$ must be $\gtrsim 0.2 - 0.5$ g/cm^2. The hot-spot temperature is also critical for ignition. If T_h is too low, then radiation losses dominate. If the hot-spot ρR is low, the temperature can also be too high causing conduction losses to dominate. The self-heating condition thus requires that the initial hot spot in ignition designs has a $\rho_h T_h \sim 0.3$ g/cm^2 with $T_h \sim 5 - 8$ keV.

1.2.2.3 Drive

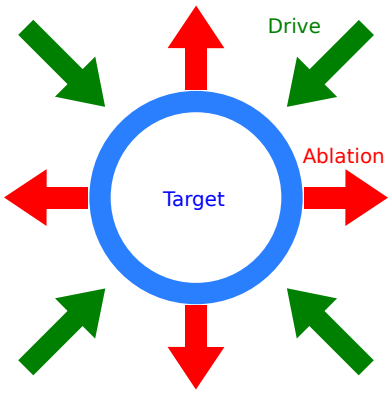

Figure 1.6. Target drive via ablation.

Spherical implosion to hot-spot ignition-relevant conditions must be achieved by suddenly applying a high pressure to the outside of a spherical target containing the fuel. The most efficient mechanism for this is ablation pressure, shown schematically in Fig. 1.6. A radiation source is incident upon the outside of a spherical target. As radiation is absorbed at the outer surface, the target material is rapidly heated to high pressure, causing ablation. Some material is driven rapidly outwards, which forces the remaining target material inwards to conserve momentum. Thus, the outer surface of the capsule is known as the 'ablator'. For ignition at $\sim$ MJ scale, ablation pressures of order 100 MBar are required.

When using lasers as the driver, two main approaches have been proposed (shown in Fig. 1.7). The simplest is the direct-drive approach, in which the laser beams are directly incident upon the outer surface of the target. The laser light is absorbed in the under-dense corona that develops around the target, high temperatures develop around the critical surface and thermal conduction transfers energy to the higher-density ablation front. Alternatively, in an 'indirect-drive' approach, the lasers are incident upon the inner surface of a 'hohlraum', made of high-Z material (typically Au or U). The laser light is converted to x rays, with an approximately black-body distribution of $\sim$ 300 eV temperature. These thermal x rays are absorbed in the target. Unlike direct-drive, the x rays are absorbed directly at the ablation front where a rapid transition in opacity occurs from the high-temperature ionized corona to low-temperature remaining target material.

The two drive schemes have advantages and disadvantages[13]. Direct drive has higher energy coupling efficiency to the target, while indirect drive benefits from ablative stabilization of acceleration-phase Rayleigh-Taylor instability at high mode numbers. The physics of laser-plasma

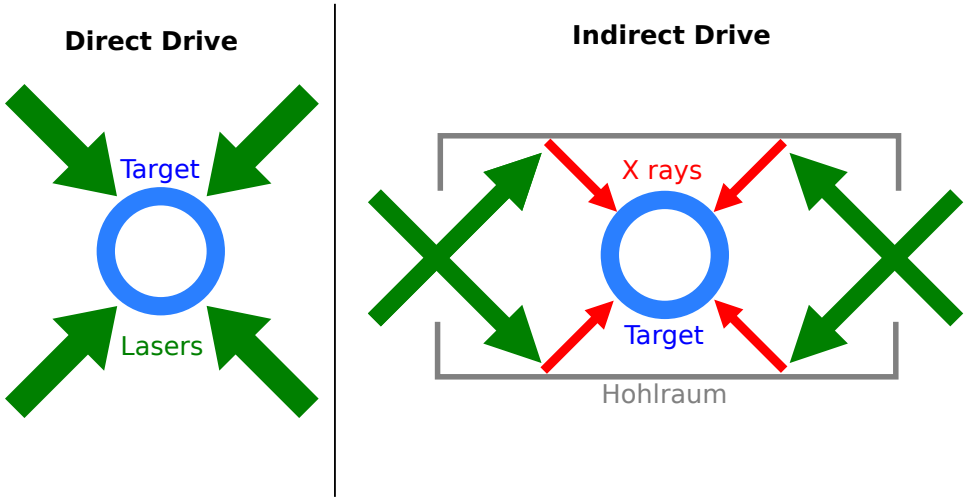

Figure 1.7. Direct- and indirect-drive with lasers.

interaction are also significantly different between the two.

1.2.2.4 NIF Ignition Design

A top-level summary of the main indirect-drive target design used during the National Ignition Campaign at the NIF is shown in Fig. 1.8 (courtesy Ref. 26), including the hohlraum design (left), capsule design (top right), and approximate laser and radiation drive (bottom right).

In addition to the main ignition experiments using the full target with a cryogenic DT-layered capsule, several 'tuning' platforms have been developed. These 'tuning' experiments are designed to either measure key physics variables or adjust parameters to achieve an ignition spec. The main characterization and optimization campaign focuses on four main physics goals: the fuel adiabat, velocity, level of mix, and shape of the stagnated implosion. To address each of these, one or more platforms were developed. Figure 1.9 shows these platforms schematically: at left (a), the physics goals, and at right (b), the experimental platforms to study the adiabat, velocity, mix, and shape.

Fuel adiabat refers to the state of the dense fuel, which is shock-compressed and remains quasi-degenerate during the implosion. A lower adiabat fuel is more compressible. Since it is important to achieve high ρR (high compression) for ignition, the fuel adiabat must be at or below a design value. The adiabat is primarily set by the initial shock compression of the fuel, thus shock-timing measurements are critical to understanding the adiabat[27]. Additionally, hot electrons generated may preheat the fuel, thus increasing the adiabat. The effect of these hot electrons must be characterized[28] and potentially mitigated.

The fuel velocity indicates the level of coupling between incident laser energy and implosion kinetic energy, a key metric for ignition since the PdV hot-spot heating is limited by the kinetic energy in the system. The velocity is measured by in-flight x-ray radiography[29,30].

Mix refers to the amount of high-Z material from the ablator (CH plus dopant - Si or Ge). Any high-Z material introduced into the hot-spot will dramatically increase radiative cooling via bremsstrahlung emission; since the bremsstrahlung power is $\propto n_e n_i Z^2 \sqrt{T_e}$ it is primarily sensitive to Z. Experiments to quantify the level of mix in ignition-relevant implosions have used x-ray spectroscopy of the Ge dopant[31] or an analysis of the total x-ray power radiated[32].

Finally, the shape of the implosion refers to the overall 'low-mode' shape which may develop

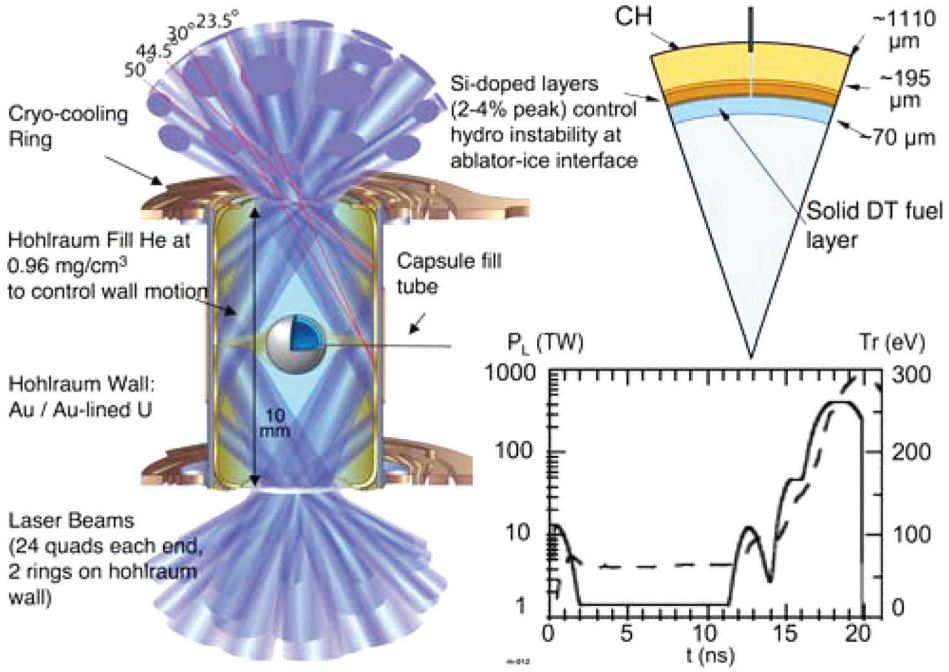

Figure 1.8. NIF Ignition Design, showing the hohlraum target design with laser illumination (left), the capsule design (upper right), and a typical laser pulse with resulting radiation drive (lower right).

perturbations (typically modeled as spherical harmonics) due to the asymmetries in the radiation flux. For example, the hohlraum geometry may induce a P_2 mode if the poles are 'dim' due to the presence of the laser-entrance holes (LEH). Traditionally the shape is diagnosed via x-ray self-emission[33] and in-flight radiography[30].

The performance of an fusion experiment is often described with the Generalized Lawson Criterion[34] (GLC):

$$\mathrm{GLC} = \frac{P\tau}{P\tau_{ign}} \tag{1.32}$$

which is the ICF analogue to the Lawson criterion for magnetically-confined plasmas. The Lawson criterion, the product of the plasma pressure (P) and confinement time (τ), can be compared to a threshold value ($P\tau_{ign}$) required for the fusion self-heating power to overcome loss mechanisms. In this expression, τ is a measure of overall energy confinement and thus more general than the simple hydrodynamic confinement time considered in Eq. 1.26. Since neither P or τ is directly inferred from the data, or is a resulting quantity of one of the four tuning areas, the performance metric for ICF implosions is typically the Ignition Threshold Factor (ITF) or ITF experimental (ITFX). These metrics are derived from suites of radiation-hydrodynamics simulations[23,25]. The ITF is written with quantities normalized to nominal values for an ignition design:

$$ITF = 1.2\left[\frac{M_{DT}}{0.17\mathrm{mg}}\right]\left[\frac{v}{370\mathrm{km/s}}\right]^{8}\left[\frac{\alpha}{1.5}\right]^{-2.6}\left[\frac{1-\Delta R_{HS}/R_{HS}}{0.815}\right]^{3.3} \times \left[\frac{M_{clean}/M_{DT}}{0.7}\right]^{0.5}\left[\frac{1-M_{HS-mix}}{0.9}\right]. \tag{1.33}$$

ITF ≥ 1 corresponds to an implosion with a $\geq 50\%$ chance of igniting with energy gain. The

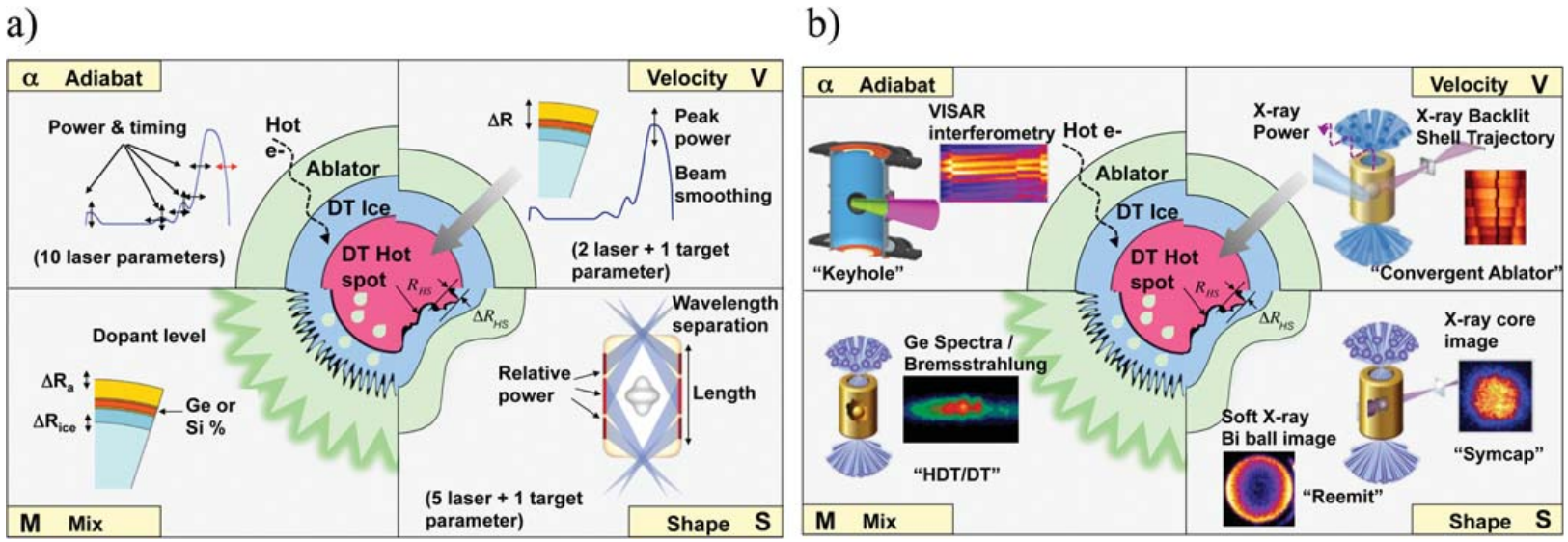

Figure 1.9. NIF tuning campaign platforms for characterizing, controlling, and optimizing adiabat, velocity, mix, and shape. The four physics goals are shown schematically at the left, and the experimental platforms are shown on the right. The campaigns studied the fuel adiabat, set by shock timing, the velocity, measured with x-ray radiography, the mix, measured with x-ray spectroscopy, and the implosion shape, measured by x-ray self-emission imaging.

advantage of the ITF formalism is that it directly relates the implosion performance, relative to ignition (ITF=1), to fundamental ICF design parameters. The first term is the total mass of fuel (M_{DT}), the second term is the peak implosion velocity (v), the third is the fuel adiabat (α), the fourth is the low-mode shape ($\Delta R_{HS}/R_{HS}$), and the final two terms correspond to mix into the cold-fuel and hot-spot. Note the extreme dependence of ITF on velocity $\left[\propto v^8\right]$, low-mode shape $\left[\propto (1-\Delta)^{3.3}\right]$, and adiabat $\left[\propto \alpha^{-2.6}\right]$. Lindl notes[23] that $GLC \approx ITF^{0.45}$. Finally, an 'experimental' expression for ITF (i.e. $ITFX$), which can be calculated from directly-measured experimental values, is expressed as[23]

$$ITFX = \left(\frac{Y_{13-15}}{4\times 10^{15}}\right)\left(\frac{DSR_{10-12}}{0.067}\right)^{2.1}, \tag{1.34}$$

which may be inferred directly from neutron diagnostic results. Y_{13-15} is the primary DT-n yield (between 13 and 15 MeV) without α particle self-heating, and DSR_{10-12} is the 'down-scattered ratio' of neutrons, defined as:

$$DSR_{10-12} \equiv \frac{Y_{10-12}}{Y_{13-15}} \propto \rho R. \tag{1.35}$$

The constant of proportionality is ~ 20 so a DSR of 5% corresponds to approximately 1 g/cm^2 of ρR.

1.3 Experimental Facilities

Four main experimental facilities are used in this work: the MIT Linear Electrostatic Ion Accelerator (LEIA)[35] for development of ICF/HEDP diagnostics, the OMEGA[36] and OMEGA EP[37] laser facilities at the University of Rochester's Laboratory for Laser Energetics, and the National Ignition Facility (NIF) at Lawrence Livermore National Laboratory[38]. These facilities are described in the following sections.

1.3.1 MIT Linear Electrostatic Ion Accelerator (LEIA)

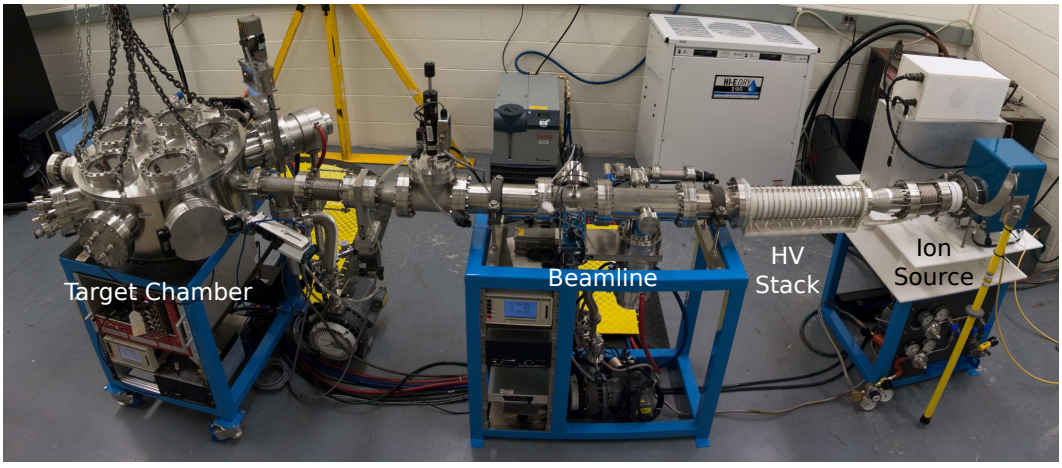

Figure 1.10. The MIT accelerator. D or ^{3}He ions are extracted from a plasma ion source (right) and accelerated onto a ^{3}He-doped ErD_2 target in the target chamber (left).

The LEIA facility is an accelerator fusion product source, shown in Fig. 1.10. D or ^{3}He ions are extracted from a plasma ion source, accelerated to a maximum ion energy of 140 keV. These ions are then incident upon a ^{3}He-doped ErD_2 target, which generates the DD and D^{3}He primary fusion reactions (Eqs. 1.15, 1.16, 1.17). The D+D reactions are generated with typical count rates of 10^6/s into 4π, while a typical D+^{3}He reaction rate is 10^5/s. Diagnostics can be installed in the target chamber at various angles and distances. This lab is primarily used as a development, test, and calibration facility for the diagnostics used at the larger laser facilities. In this thesis, the LEIA facility is used to calibrate the WRF proton spectrometers used in experiments at both NIF and OMEGA (see Chapter 2), to develop the front-vs-back CR-39 counting technique (Appendix C), and to develop a new method to account for track overlap in CR-39 data (Appendix D).

1.3.2 OMEGA

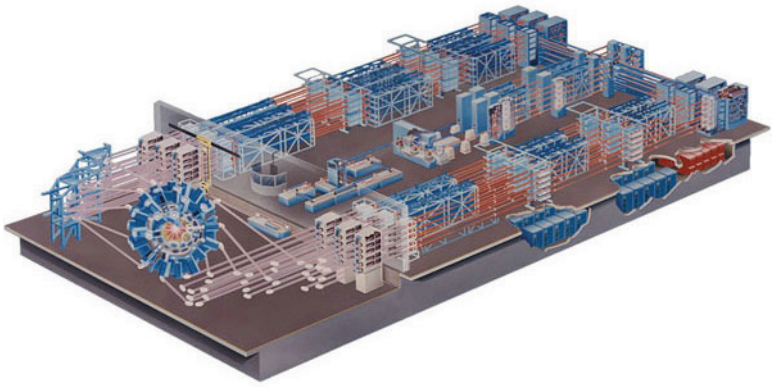

Figure 1.11. The 60-beam OMEGA laser facility. The laser can be operated in either the direct-drive configuration or the indirect-drive configuration (using up to 40 beams).

The OMEGA laser facility (shown schematically in Fig. 1.11) is a 60-beam long-pulse Nd:glass laser system[36], most commonly run at 3ω (351nm). The laser system is capable of up to 30kJ of energy in the 60 beams with extensive pulse-shaping capability. Optional beam smoothing techniques such as distributed phase plates (DPP)[39,40], distributed polarization rotation (DPR)[41], and smoothing by spectral dispersion (SSD)[42] can be used. The final laser light is transported into the experimental target bay, and focused to target chamber center (TCC) inside of the evacuated target chamber. Numerous diagnostic systems are used, either in 'fixed' mode (i.e. permanently attached to the target chamber), or as a modular system inserted using the ten-inch manipulators (TIMs).

The OMEGA facility is used extensively in this thesis: for studies of various astrophysically-relevant nuclear reactions (Chapters 8, 9, and 10), to measure charged-particle stopping powers in WDM plasma (Chapter 5), and for studies of hohlraum-produced fast ions (Appendix E).

1.3.3 OMEGA EP

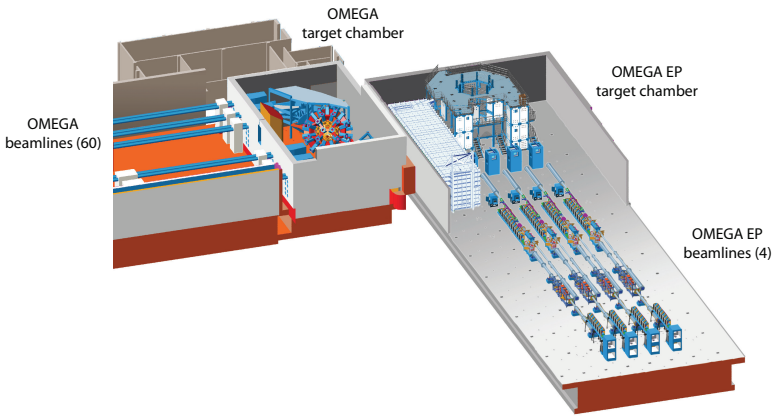

Figure 1.12. The four-beam OMEGA EP facility.

The OMEGA EP laser facility (shown schematically in Fig. 1.12) is a 4-beam Nd:glass laser system[37]. In long-pulse operation, the four beams are typically run at 3ω (351nm) with energies up to several kJ in several ns, with optional beam smoothing by DPP. Similar to OMEGA, the final laser light is transported to a target chamber with many fixed and TIM-based diagnostics. The unique capability of OMEGA EP is that two of the beams (#1 and 2, also known as the sidelighter and backlighter respectively) may be pulse-compressed using the chirped-pulse amplification technique (CPA)[43]. In this mode, energies of several hundred Joules may be delivered to target in a short pulse ($1 - 10$ ps) for resulting powers in the petawatt-class range, and on-target intensities up to several 10^{19} W/cm^2. Additionally, beam #2 may be transported into the OMEGA target chamber for so-called 'joint' shot operations. This allows fundamentally new physics such as ion acceleration to many tens of MeV for backlighting or fundamental physics studies. In this thesis, the OMEGA EP facility was used to develop proton radiography for full-energy 60-beam OMEGA implosions (Appendix A) and in platform-development work for stopping-power measurements (Chapter 6).

1.3.4 NIF

As of this writing, the NIF laser is the largest in the world, with 192 Nd:glass long-pulse laser beams with a maximum capability of 1.9MJ of 3ω light at a peak power of 500TW. The facility is shown schematically in Fig. 1.13. The NIF beams are arranged in a polar-drive configuration, as the primary motivation is to use indirect (hohlraum) drive. As in the OMEGA and OMEGA EP facilities, the lasers are focused to the center of a target chamber. Diagnostics are permanently attached to the chamber, or are inserted into the target chamber by the Diagnostic Instrument Manipulator (DIM). In this thesis, NIF is used to study shock dynamics (Chapter 3) and low-mode ρR asymmetries (Chapter 4) of 'surrogate' ignition-scale implosions.

NIF has not yet achieved ignition. Finding an optimal design in the presence of physics uncertainties in the extreme conditions required for ICF is a challenge. There are direct trade-offs between several quantities in the ITF formalism (Eq. 1.33) that are not apparent in the equation itself. In particular, increasing the velocity is highly beneficial for ITF, but doing so can severely increase the level of mix, which is detrimental. Similarly, the level of mix can be reduced with higher-adiabat designs, at the cost of ρR achieved. The nominal low-adiabat designs[23] have only

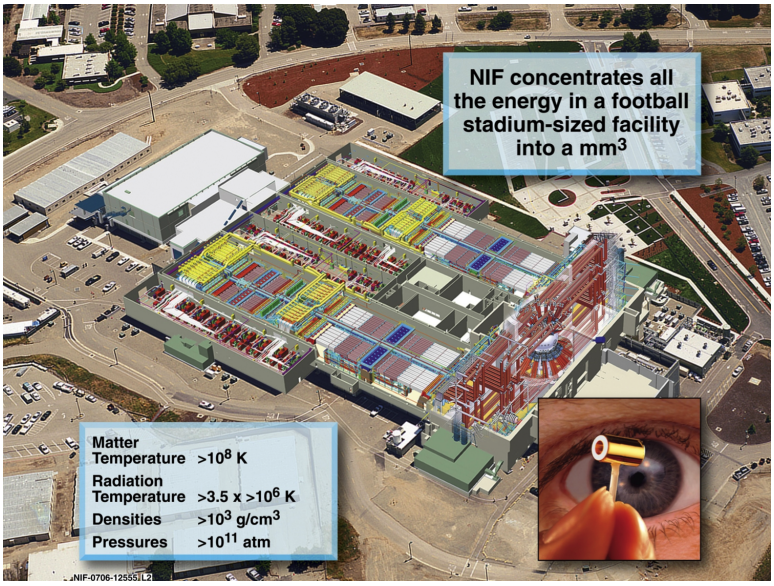

Figure 1.13. The NIF facility.

achieved an ITF ~ 0.1 in the best cases[26]. On the other hand, high-adiabat ('high-foot') experiments have proved very promising, with an achieved GLC of ~ 0.5 and a "fuel gain" exceeding unity[44].

1.4 References

1. A. Einstein, "Zur Elektrodynamik bewegter Körper," Annalen der Physik, **322**(10), 891–921 (1905).
2. A. Einstein, "Ist die Trägheit eines Körpers von seinem Energieinhalt abhängig?" Annalen der Physik, **323**(13), 639–641 (1905).
3. F. Aston, "LIX. The mass-spectra of chemical elements," Philosophical Magazine Series 6, **39**(233), 611–625 (1920).
4. A. S. Eddington, *The Internal Constitution of the Stars* (Cambridge University Press, 1926).
5. C. H. Payne, *Stellar Atmospheres; a Contribution to the Observational Study of High Temperature in the Reversing Layers of Stars.*, Ph.D. thesis, Radcliffe College (1925).
6. G. Gamow, "Zur quantentheorie des atomkernes," Zeitschrift für Physik, **51**, 204–212 (1928).
7. R. d. Atkinson and F. Houtermans, "Transmutation of the lighter elements in stars," Nature, **123**, 567–8 (1929).
8. R. d. Atkinson and F. Houtermans, "Zur frage der aufbaumsglichkeit der elemente in sternen," Zeitschrift für Physik, **54**, 656–7 (1929).
9. H. A. Bethe and C. L. Critchfield, "The Formation of Deuterons by Proton Combination," Phys. Rev., **54**, 248–254 (1938).
10. A. Wapstra, G. Audi and C. Thibault, "The Ame2003 atomic mass evaluation: (I). Evaluation of input data, adjustment procedures," Nucl. Phys. A, **729**, 129 (2003).
11. S. Wong, *Introductory Nuclear Physics* (Wiley, 2004).
12. H. Brysk, "Fusion Neutron Energies and Spectra," Plasma Physics, **15**, 611–617 (1973).
13. S. Atzeni and J. Meyer-Ter-Vehn, *The Physics of Inertial Fusion: Beam Plasma Interaction, Hydrodynamics, Hot Dense Matter*, International Series of Monographs on Physics (Oxford University Press, 2004).
14. H.-S. Bosch and G. Hale, "Improved Formulas for Fusion Cross-Sections and Thermal Reactivities," Nuclear Fusion, **32**, 611–631 (1992).

15. J. Chadwick, "Bakerian Lecture. The Neutron," Proceedings of the Royal Society of London. Series A, **142**(846), 1–25 (1933).
16. O. Hahn and F. Strassmann, "Über den Nachweis und das Verhalten der bei der Bestrahlung des Urans mittels Neutronen entstehenden Erdalkalimetalle," Naturwissenschaften, **27**(1), 11–15 (1939).
17. L. Meitner and O. Frisch, "Disintegration of Uranium by Neutrons: a New Type of Nuclear Reaction," Nature, **143**, 239–240 (1939).
18. US Department of Energy, Office of Declassification, "Restricted Data Declassification Decisions 1946 to the Present," (2001).
19. T. Maiman, "Stimulated Optical Radiation in Ruby," Nature, **187**, 493–494 (1960).
20. Ed: G. Velarde, N. Santamaria, *Inertial Confinement Nuclear Fusion: A Historical Approach by its Pioneers* (Foxwell & Davies (UK), 2007).
21. J. Nuckolls, L. Wood, A. Thiessen *et al.*, "Laser Compression of Matter to Super-High Densities: Thermonuclear (CTR) Applications," Nature, **239**, 139–142 (1972).
22. S. W. Haan *et al.*, "Design and modeling of ignition targets for the National Ignition Facility," Phys. Plasmas, **2**, 2480 (1995).
23. J. Lindl, "Development of the indirect-drive approach to inertial confinement fusion and the target physics basis for ignition and gain," Phys. Plasmas, **2**, 3933–4024 (1995).
24. J. Lindl, P. Amendt, R. Berger *et al.*, "The physics basis for ignition using indirect-drive targets on the National Ignition Facility," Phys. Plasmas, **11**, 339–491 (2004).
25. J. Lindl, O. Landen, J. Edwards *et al.*, "Review of the National Ignition Campaign 2009-2012," Phys. Plasmas, **21**, 020501 (2014).
26. M. Edwards *et al.*, "Progress towards ignition on the National Ignition Facility," Phys. Plasmas, **20**, 070501 (2013).
27. H. Robey *et al.*, "Precision Shock Tuning on the National Ignition Facility," Phys. Rev. Lett., **108**, 215004 (2012).
28. E. Dewald *et al.*, "Hot electron measurements in ignition relevant hohlraums on the National Ignition Facility," Rev. Sci. Instrum., **81**, 10D938 (2010).
29. D. Hicks *et al.*, "Implosion dynamics measurements at the National Ignition Facility," Phys. Plasmas, **19**, 122702 (2012).
30. J. Rygg, O. Jones, J. Field *et al.*, "2D X-Ray Radiography of Imploding Capsules at the National Ignition Facility," Phys. Rev. Lett., **112**, 195001 (2014).
31. S. Regan *et al.*, "Hot-spot mix in ignition-scale implosions on the NIF," Phys. Plasmas, **19**, 056307 (2012).
32. T. Ma *et al.*, "Onset of Hydrodynamic Mix in High-Velocity, Highly Compressed Inertial Confinement Fusion Implosions," Phys. Rev. Lett., **111**, 085004 (2013).
33. G. Kyrala, S. Dixit, S. Glenzer *et al.*, "Measuring symmetry of implosions in cryogenic Hohlraums at the NIF using gated x-ray detectors," Rev. Sci. Instrum., **81**, 10E316 (2010).
34. J. D. Lawson, "Some criteria for a power producing thermonuclear reactor," Proceedings of the Physical Society. Section B, **70**(1), 6 (1957).
35. N. Sinenian, M.-E. Manuel, A. Zylstra *et al.*, "Upgrade of the MIT Linear Electrostatic Ion Accelerator (LEIA) for nuclear diagnostics development for Omega, Z and the NIF," Rev. Sci. Instrum., **83**(4), 043502 (2012).
36. T. Boehly, D. Brown, R. Craxton *et al.*, "Initial performance results of the OMEGA laser system," Optics Communications, **133**(1-6), 495–506 (1997).
37. L. Waxer, D. Maywar, J. Kelly *et al.*, "High-energy petawatt capability for the Omega laser," Optics and photonics news, **16**(7), 30–36 (2005).
38. G. Miller, E. Moses and C. Wuest, "The National Ignition Facility: enabling fusion ignition for the 21st century," Nuclear Fusion, **44**, S228 (2004).
39. Y. Lin, G. N. Lawrence and T. J. Kessler, "Distributed phase plates for super-Gaussian focal-plane irradiance profiles," Opt. Lett., **20**(7), 764–766 (1995).
40. Y. Lin, G. N. Lawrence and T. J. Kessler, "Design of continuous surface-relief phase plates by surface-based simulated annealing to achieve control of focal-plane irradiance," Opt. Lett., **21**(20), 1703–1705 (1996).

41. D. D. Meyerhofer, J. A. Delettrez, R. Epstein *et al.*, "Core performance and mix in direct-drive spherical implosions with high uniformity," Physics of Plasmas, **8**(5), 2251–2256 (2001).

42. S. Skupsky, R. W. Short, T. Kessler *et al.*, "Improved laser-beam uniformity using the angular dispersion of frequency-modulated light," Journal of Applied Physics, **66**(8), 3456–3462 (1989).

43. D. Strickland and G. Mourou, "Compression of amplified chirped optical pulses," Optics Communications, **56**(3), 219 – 221 (1985).

44. O. Hurricane, D. Callahan, D. Casey *et al.*, "Fuel gain exceeding unity in an inertially confined fusion implosion," Nature, **506**, 343 (2014).

Part I

NIF Proton Spectroscopy

2

Proton Spectrometry at the NIF

2.1 WRF Concept

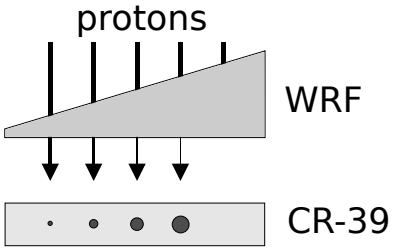

Figure 2.1. A schematic of the Wedge Range Filter (WRF) proton spectrometer concept. Protons are incident on a wedge-shaped filter, protons traversing more material in the filter lose more energy. After the WRF, protons are detected on CR-39; the size of the proton tracks in the CR-39 corresponds to the final particle energy.

The Wedge Range Filter (WRF) is a compact proton spectrometer[1,2]. The basic concept is illustrated in Fig. 2.1. Protons are incident upon the front surface of a wedge-shaped filter made out of aluminum or ceramic. Depending on how much material the proton traverses, it loses a varying amount of energy. This is schematically shown in Fig. 2.1 by the width of the arrows. The protons are detected with CR-39, a solid-state nuclear track detector. Protons create tracks in the CR-39, which are revealed by chemically etching for several hours in a 6 molar solution of NaOH. The rate of material removal is greater for plastic damaged by charged particles, therefore conical 'pits' or 'tracks' are formed. The diameter of a track is related to the incident proton energy[3]. Since the post-filter energy of a proton is known via the track diameter, the incident proton energy is determined from the known thickness profile of the filter, and the proton spectrum is determined by a histogram of individual proton counts. The Linear Electrostatic Ion Accelerator (LEIA) fusion products source at MIT is used to test and calibrate the WRFs[4,5].

The stopping of protons in aluminum, critical physics to the WRF, is shown in Fig. 2.2. The stopping power (dE/dx), range, final energy vs initial energy, and final energy versus thickness are shown. The downshift calculations are performed using the SRIM cold-matter tabulated stopping power[6]. Example images are shown in Fig. 2.3 of a WRF filter itself (a) and a completed WRF diagnostic package (b).

2.2 WRF Calibrations

A robust calibration procedure has been developed for the WRFs using LEIA[1,2,5]. A schematic is shown in Fig. 2.4. The accelerator beam is incident from the right onto a deuterated, ^{3}He-doped target, which produces DD and D^{3}He reactions (see Section 1.3.1). The WRF to be calibrated is placed at a kinematic lab angle of 90°, 15cm away from the target. Simultaneous and real-time

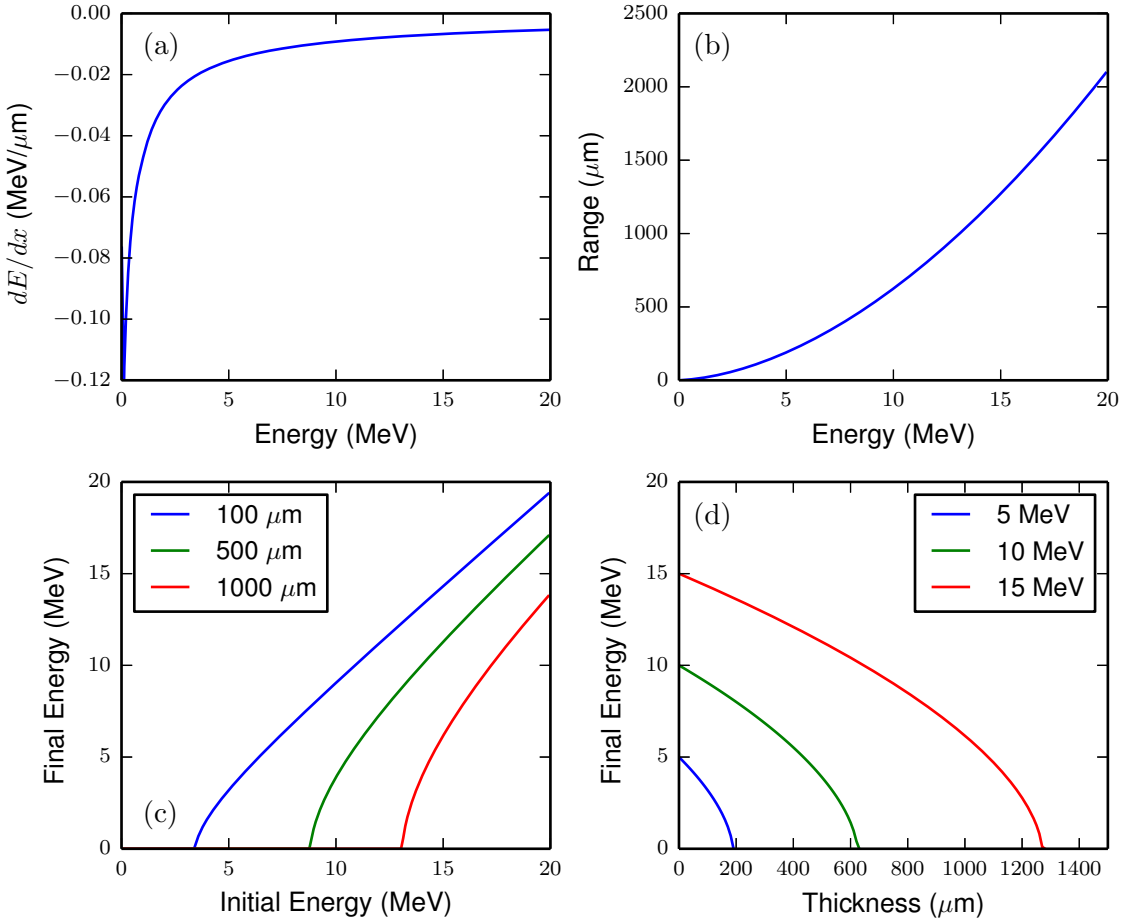

Figure 2.2. Example ranging calculations for protons in aluminum. **(a)** Proton stopping power in Al. **(b)** Proton range in Al versus initial energy. **(c)** Proton final (downshifted) energy versus initial energy for three thicknesses of Al. **(d)** Proton final energy versus Al-filter thickness for three initial energies.

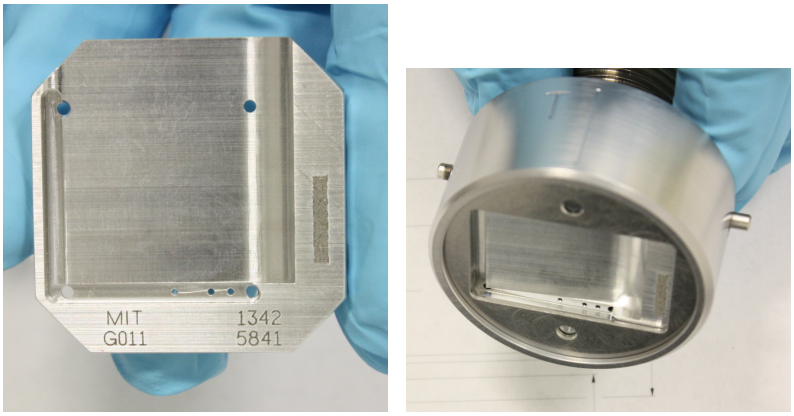

(a) **(b)**

Figure 2.3. WRF detector images. (a) WRF itself, Al Gilbert-series NIF WRF ID 13425841. In the central region the Al thickness is increasing from right to left from $\sim 140\mu$m to $\sim 2000\mu$m. (b) Full WRF assembly. The diagnostic outer diameter is 5cm. Behind the WRF is the spectrometer CR-39 followed by neutron detectors (either CR-39 based or indium activation).

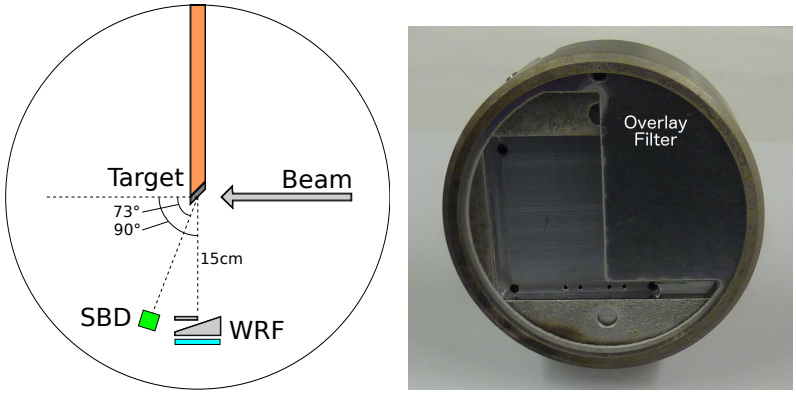

Figure 2.4. The MIT accelerator setup used to calibrate NIF WRFs. (a) Experimental schematic. A D beam at $\sim$ 140 keV is incident from the right onto an ErD_2 target. A WRF is placed at 90° while an SBD is used for real-time proton production measurements at 73°. (b) Image of a calibration setup. An overlay filter is used to create two energy lines on the spectrometer from the incident 14.7 MeV D^3He protons.

proton production information is recorded using a Surface Barrier Detector (SBD), which has 100% detection efficiency for the protons of interest and is energy calibrated to an accuracy of $\pm(50-75)$ keV using a ^{226}Ra α source[5].

The WRF spectrometer assembly for calibration is shown in Fig. 2.4b. Incident D^3He protons create a line at their birth energy $\sim$ 14.7 MeV. To obtain a second calibration point, a lower-energy line is created by placing a flat filter over the thin end of the WRF. The two lines together constrain the total thickness and slope of the aluminum filter itself. Sample data is shown in Fig. 2.5 showing the two lines. In some cases three line filters have been developed and used.

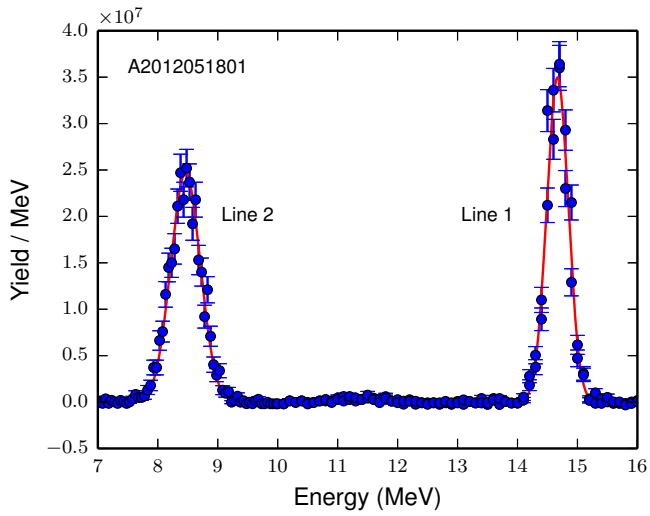

Figure 2.5. Sample calibration data, using the scheme illustrated in Fig. 2.4. The incident unfiltered D^3He protons create Line 1 at $\sim$ 14.7 MeV while the filtered (downshifted) protons are observed in Line 2 at $\sim$ 8.5 MeV. The data shown was obtained with NIF WRF # 13425141 on accelerator shot A2012051801. The red curves are Gaussian fits to the data.

Since LEIA and experimental techniques are being continually upgraded and developed, a number of filter schemes have been used over time for NIF WRF calibrations. These are summarized in Table 2.1. Each filter configuration is identified by a date range of its use, its type (2 or 3 line), and then the provided line energies. In each case, the line energy is measured using the SBD system and ^{226}Ra source cross-calibration[5].

Table 2.1. Filters used for the calibration of WRFs on LEIA.

Start	End	Type	Low E (MeV)	Mid E (MeV)	High E (MeV)
2012-01-30	current	2-line	8.40		14.57
2011-09-19	current	3-line	7.45	11.13	14.57
2011-02-22	2011-09-06	3-line	7.51	9.893	14.638
2010-09-09	2010-11-01	3-line	7.139	9.893	14.638
2009	2010-09-02	2-line	9.893		14.638

2.3 NIF Capability

2.3.1 DIM Cling-on Diagnostics

The NIF has implemented a capability to field several small auxiliary diagnostics on the side of a main x-ray imaging diagnostic in Diagnostic Instrument Manipulators (DIMs)[7] (0,0) and (90,78). These small diagnostics are collectively referred to as 'cling-on' diagnostics.

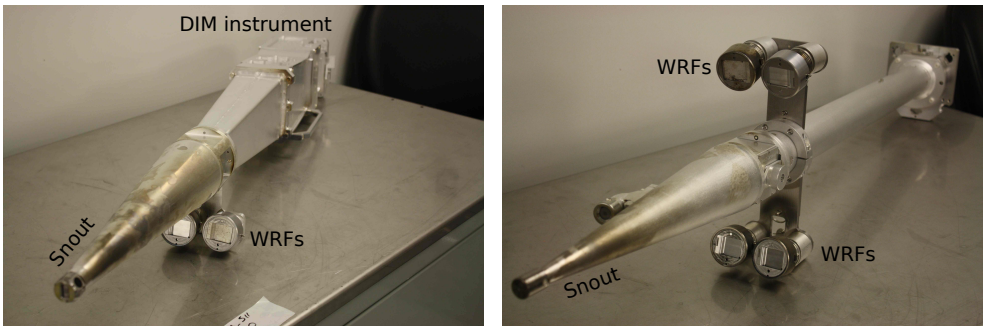

(a) DIM (0,0) **(b)** DIM (90,78)

Figure 2.6. Snout assemblies with cling-on diagnostics, such as WRFs.

The main DIM diagnostic is generally a pinhole-based x-ray imager. A 'snout' is constructed to accurately position the imaging pinholes close to TCC. The cling-on diagnostics are bolted to the outside of this snout assembly. These assemblies are shown in Fig. 2.6. Images of the WRF assembly itself are shown in Fig. 2.3. An image of the DIMs with WRFs cling-on diagnostics in the target chamber on a NIF shot is shown in Fig. 2.7.

A table of snout configurations used on the NIF to acquire WRF data is shown in Table 2.2. For each DIM a list of primary x-ray instruments and snouts (identified by magnifications) is shown. For some configurations x-ray imaging data is not taken simultaneously and the snout is primarily used to hold the WRFs or other cling-on diagnostics. In addition to the WRFs, other diagnostics that can be fielded with this capability include Indium Nuclear Activation Detectors (NAD), particle Time of Flight (pTOF), and Solid RadioChemistry (SRC).

Fig. 2.8 shows a cartoon of the NIF experimental setup. WRFs are fielded on DIMs (0,0) and (90,78) [chamber coordinates (θ,ϕ), where $\theta = 0$ is vertically up]. One to four WRFs are fielded simultaneously on DIMs (0,0) and (90,78). On DIM (0,0) the WRFs have a clear line of sight to the implosion through the laser-entrance hole (LEH). The DIM (90,78) WRFs look through the hohlraum wall, requiring an energy-loss correction in the analysis (see Section 2.4).

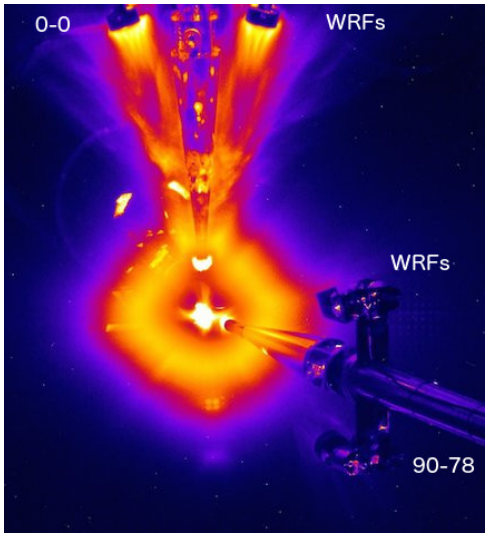

Figure 2.7. False-color photograph of NIF DIM (0,0) [top] and (90,78) [right] with four cling-on diagnostics each inserted into the NIF target chamber for a shot.

Table 2.2. NIF DIM configurations used to field WRFs.

DIM	Primary Instrument	Compatible Snouts
(0,0)	GXD	12x
	HGXI	9x
	DISC	4x
		2.5x
(90,78)	GXD	12x
	HGXI	9x
	DISC	4x
		2.5x
		1x

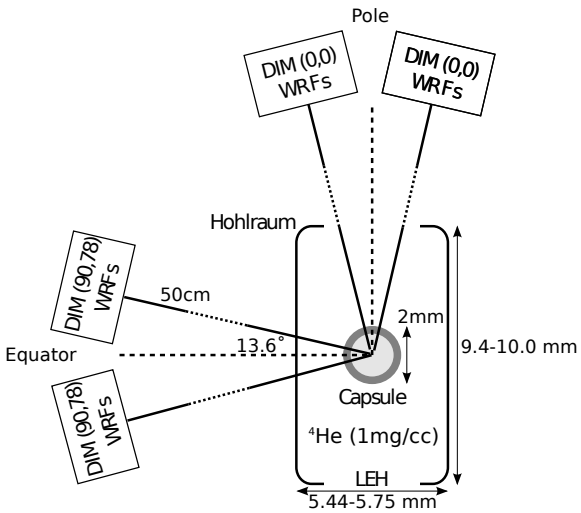

Figure 2.8. WRF setup on the NIF. Compact WRF proton spectrometers are placed at ±13.6° to the DIM axis on both the pole [DIM (0,0)] and equator [DIM (90,78)].

2.3.2 Types of WRF assemblies

Up to three detectors can be fielded within a single WRF module (as shown in Fig. 2.3(b)). In addition to the WRF proton spectrometer, which must be at the front of the module, a number of neutron detectors can be used: CR-39 based recoil detectors, or indium activation samples. In total, up to three detectors are fielded per module in a variety of configurations. An exploded view of a WRF assembly is shown in Fig. 2.9.

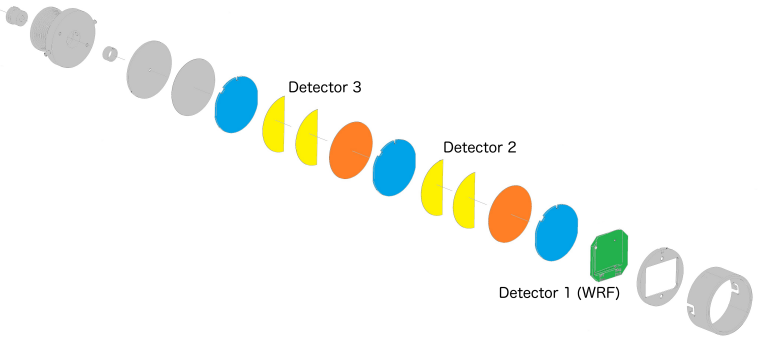

Figure 2.9. Exploded view of a WRF assembly. Housing parts are shown in gray, WRF filters in green, CR-39 in blue, 100μm Al filters in orange, and 100μm polyethylene neutron multipliers in yellow.

Table 2.3. Types of WRF detector assemblies.

Tab #	Detector 1	Detector 2	Detector 3
01	Neutronics	Neutronics	Neutronics
02	Thick WRF	Neutronics	Neutronics
03	Thick WRF		
04	BB WRF	Neutronics	Neutronics
05	BB WRF		
06	Indium		
07	Thin WRF	Neutronics	Neutronics
08	Thin WRF		
09	Indium	Neutronics	Neutronics
10	Thin WRF	Neutronics	Indium
AAA12-119652-AB	10/15/20/25μm SRF		
AAA13-106446-AA	5/10/15/20μm SRF		

A number of different configurations have been created to allow for experimental customization of the detector setup. All WRF assemblies are defined in NIF drawing AAA10-108020 with 'tab numbers' denoting individual module types. For example, subdrawing AAA10-108020-01 is tab-01. All possible defined assembly types are defined in Table 2.3. In the table, 'WRF' refers to the proton spectrometer itself[1] with various types: thick and thin denote Al WRFs with varying low-energy cutoffs[2], broadband (BB) WRFs are made of Zirconia ceramic. 'Neutronics' refers to a CR-39 based neutron detector[8].

A 'step range filter' (SRF) has also been developed and used on NIF[9]. The drawing number for the SRF is separate from the typical WRF configurations, and is given separately in Table 2.3.

2.3.3 CR-39 exposure to vacuum

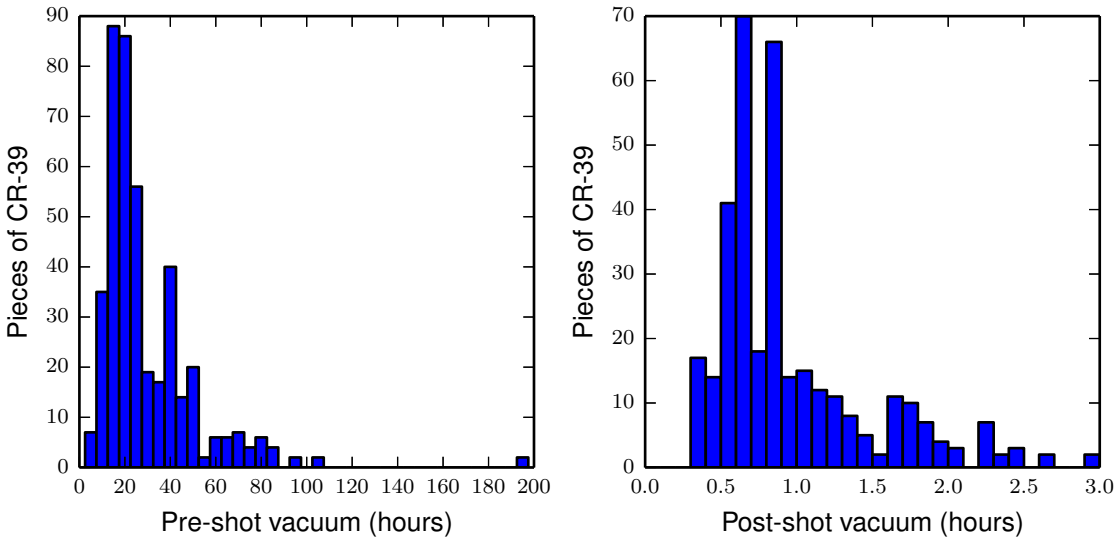

Figure 2.10. WRF CR-39 exposure to vacuum (pre- and post-shot) at the NIF.

The NIF facility records pre- and post-shot vacuum exposure for the WRF CR-39 used on shots. This is because the CR-39 sensitivity changes with prolonged vacuum exposure[10], particularly for pre-shot exposure. Due to the significant operational effort required at NIF for one shot, WRF CR-39 can be exposed to vacuum for very long periods of time relative to other facilities (LEIA, OMEGA). As seen in Fig. 2.10, the NIF WRFs are generally exposed to vacuum for 12-48 hours pre-shot. Post-shot exposure is typically much shorter (1-2h) and less significant.

The time in vacuum is known to affect the CR-39 response to protons[10]. In the WRF analysis, the CR-39 response is primarily described by the maximum observed proton diameter (D_{max}) and the c parameter[2], which describes the shape of the proton diameter versus energy curve. Histograms of these two parameters in the WRF analysis for the NIF dataset are shown in Fig. 2.11. The maximum diameter is observed to average around 15 μm for a 5 hour etch time. The c parameter averages 1.2. These values are plotted against the pre-shot vacuum time in Fig. 2.12. No clear trend is observed, demonstrating that the vacuum exposure is not causing significant shot-to-shot variation in the CR-39 response. Since much of the response change is over the first several hours[10], this is expected. The scatter in the data is likely due to intrinsic variations in CR-39 and other causes of CR-39 response change, such as x-ray exposure[11].

2.4 Hohlraum Correction

The equatorial WRFs on NIF sample the implosion-generated protons after they traverse the hohlraum wall (see Fig. 2.8). This necessitates an after-the-fact correction applied to the proton spectrum, requiring knowledge of the stopping power of protons in the hohlraum wall material, and the thickness of that material. The energy loss in the hohlraum is corrected for using cold-matter stopping powers[6], which are plotted in Fig. 2.13 for the wall materials used at NIF. The inner wall is a high-Z material (Au or DU), while the Thermo-Mechanical Package (TMP), which encircles the hohlraum itself, it made of Al.

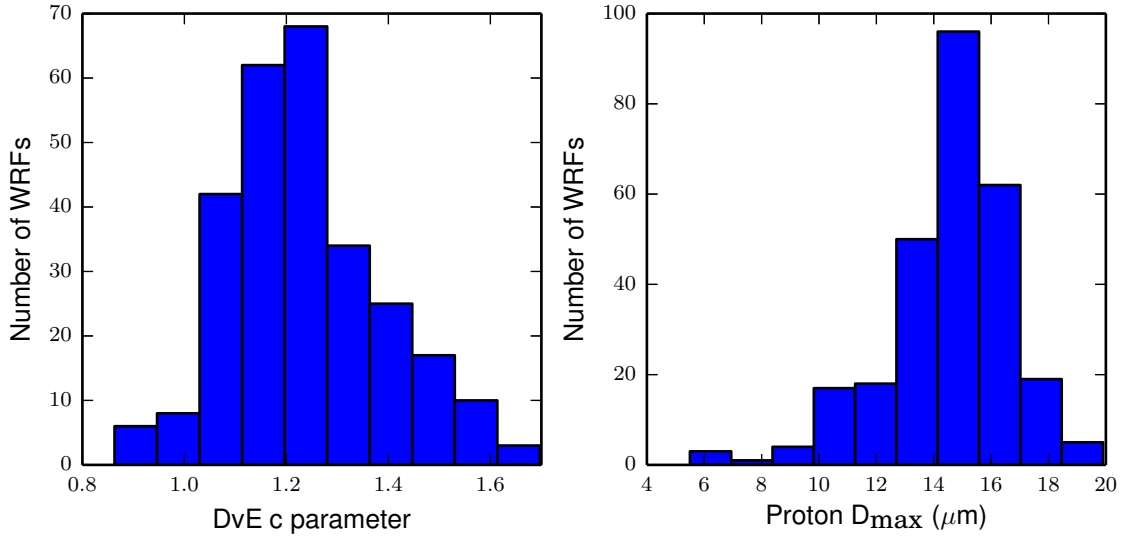

Figure 2.11. CR-39 response is characterized by the DvE c parameter and maximum proton diameter (D_{max}). In the NIF WRF analysis, these are observed to vary around typical values of 1.2 and 15 μm, respectively.

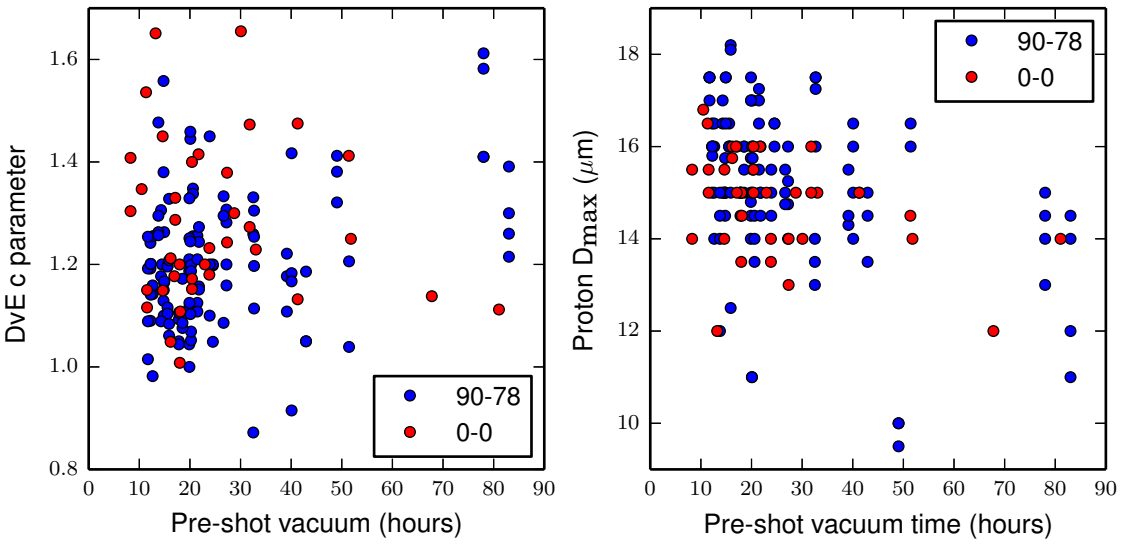

Figure 2.12. Proton DvE parameter c and maximum diameter versus pre-shot vacuum exposure on NIF.

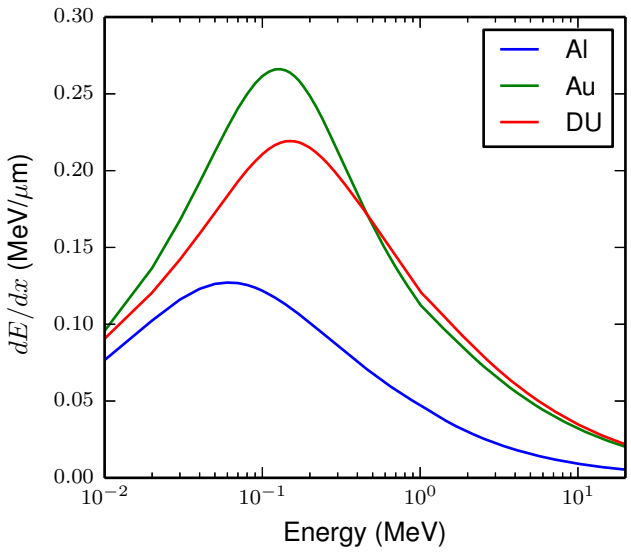

Figure 2.13. Proton stopping power in hohlraum materials: Au, DU, and Al.

The initial hohlraum wall thickness is well known from target fabrication drawings. The high-Z layer, typically Au or depleted Uranium (DU), is known to $\pm 1\mu$m, while the Al thermo-mechanical package (TMP) is known to $\pm 3\mu$m. These uncertainties propagate into an uncertainty in the hohlraum energy-loss correction. Three hohlraum profiles used in this work are shown in Fig. 2.14. The WRF line of sight is marked in blue. The different materials are shown by color. Near the equator ($z = 0$), there is a thick band of Au for assembly purposes, though the WRFs LOS is designed to look through the thin part of the hohlraum wall, plus the Al TMP. An average thickness of material is calculated for each type of hohlraum used, and for each equatorial WRF line of sight.

However, some hohlraum designs have significant 'torus' or 'bump' features (Fig. 2.14 a and b) in the LOS. In these cases, the wall material can move laterally in or out of the WRF LOS as a shock wave propages through the wall during the laser drive. In that case, when the protons probe the wall the thickness may not be the same as the initial profile. This is calculated with 2-D radiation-hydrodynamics simulations, which are shown in Fig. 2.15 as a series of density contour plots as the laser pulse progresses. Near the shock-bang time at $\sim$ 22.5 ns, significant lateral material motion has occurred. All of the wall material also moves outwards several tens of μm because of the interior drive. However, the 1-D motion is negligible, as the wall ρR will drop as $1/r$ and the change in radius is small relative to the initial hohlraum radius.

From the simulations, a thickness of Au is calculated versus polar angle ($\Delta\theta$, defined as displacement from the equatorial DIM). The simulated data is fit with a polynomial, shown in Fig. 2.16. From these fits, an average thickness is calculated over the WRF LOS, shown in Fig. 2.17 versus time. From this calculation, the difference between the thickness at the shock-bang time and the initial thickness is used as a correction factor when analyzing data with the bump or torus features in the hohlraum. This correction factor is -9.5 μm of solid Au for the bump, and -8.3 μm for the torus.

With the known hohlraum thickness, each data point in the measured proton spectrum must be corrected using the stopping power (Fig. 2.13). From the measured energy E, the initial pre-wall energy E' can be calculated as

$$E' = E - \int_0^L \frac{dE}{dx} dx, \tag{2.1}$$

with L as the total hohlraum thickness. In this equation, dE/dx is negative such that E', the

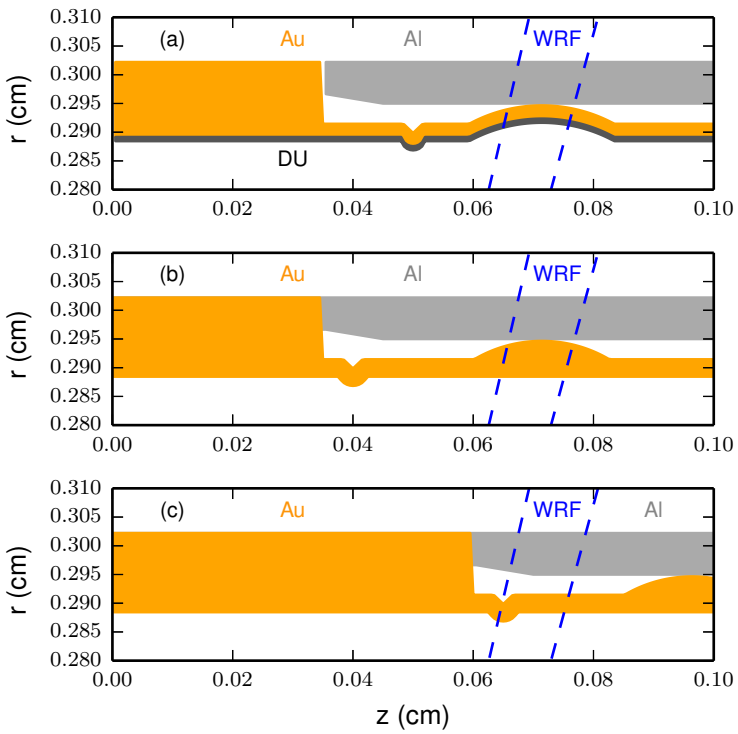

Figure 2.14. Hohlraum profiles in cylindrical coordinates for three designs (from top: AAA11-109089_AA, AAA12-106036_AA, and AAA12-102853_AA). The target chamber's north pole is to the right. The material profiles are taken from hohlraum engineering drawings. The WRF line of sight is marked by the dashed blue lines. In some hohlraums there is a 'torus' (a) or 'bump' (b) obstructing the line of sight.

energy before the wall, is greater than E, the measured energy at the detector. Due to the slope in the stopping power (see Fig. 2.13), a proton spectrum expands due to an 'accordion effect' as it is ranged through material. Fundamentally, this is because higher energies are downshifted less than lower energies, stretching the spectrum. This must also be corrected for: the Yield / MeV in the proton spectrum is given by:

$$Y' = Y \times \frac{\Delta E}{E'(E + \Delta E/2) - E'(E - \Delta E/2)}, \tag{2.2}$$

where ΔE is the spectrum bin width. The denominator is smaller than the numerator due to the 'accordion' effect in reverse when correcting for downshift in the wall. This results in a narrower and higher-amplitude spectrum. The error bars on yield are corrected in a similar fashion.

An example spectral shift is shown in Fig. 2.18. The corrected spectrum is calculated using the hohlraum thickness shown in Fig. 2.14, the stopping power in Fig. 2.13, and Eqs 2.1-2.2.

2.5 ρR Model

In the surrogate implosions studied at NIF in this work, energetic protons are produced via the fusion reaction:

$$\mathrm{D} \ + \ {}^3\mathrm{He} \ \rightarrow \ \alpha \ (3.67 \ \mathrm{MeV}) \ + \ \mathrm{p} \ (14.7 \ \mathrm{MeV}). \tag{2.3}$$

The D^{3}He protons slow down monotonically as they traverse the implosion. The measured proton enery downshift is directly related to the implosion ρR at the time of shock burn. This is illustrated in Fig. 2.19, which shows the birth spectrum plus modeled spectra for several values of the shell center-of-mass radius (R_{cm}) and ρR using the model described in this section, spanning

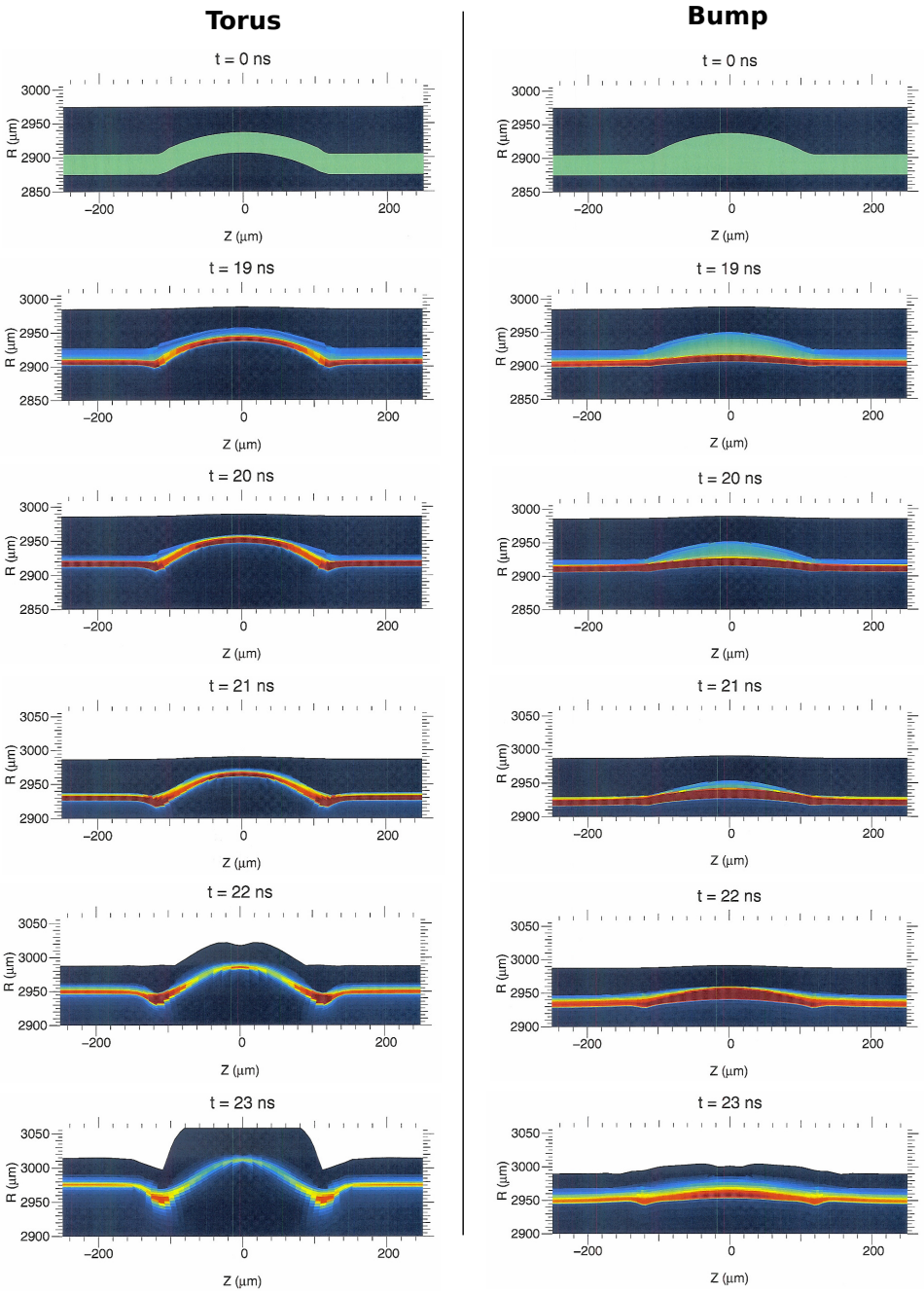

Figure 2.15. Simulated hohlraum density profiles with a torus (left) and bump (right), at various times throughout the pulse. In these implosions, the shock-bang time is around 22.5 ns.

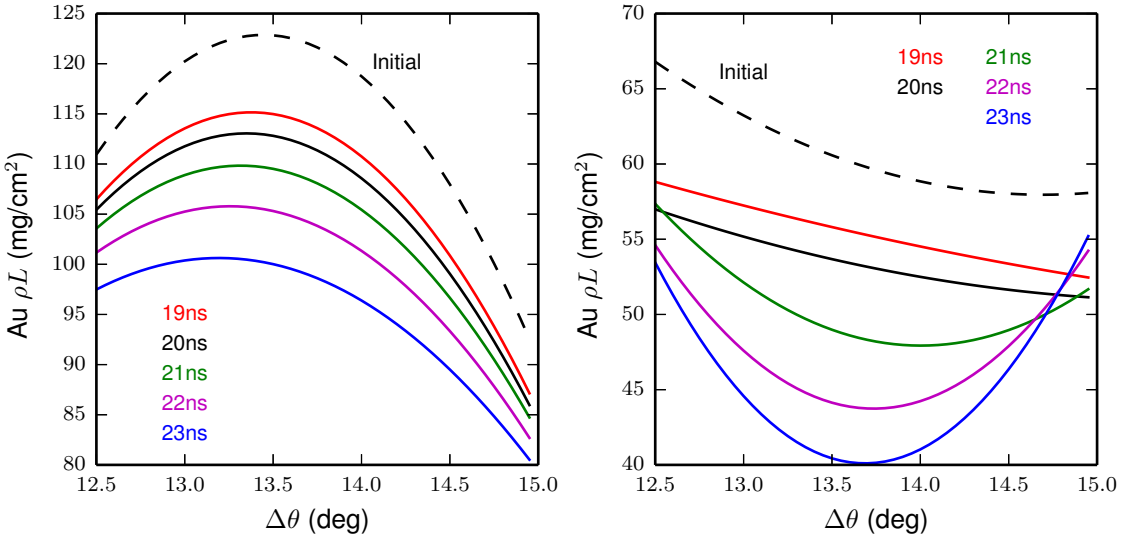

Figure 2.16. Simulated thickness of the Au hohlraum wall (given as ρL) versus polar angle ($\Delta\theta$, the displacement from the equator) for the bump (left) and torus (right) hohlraums.

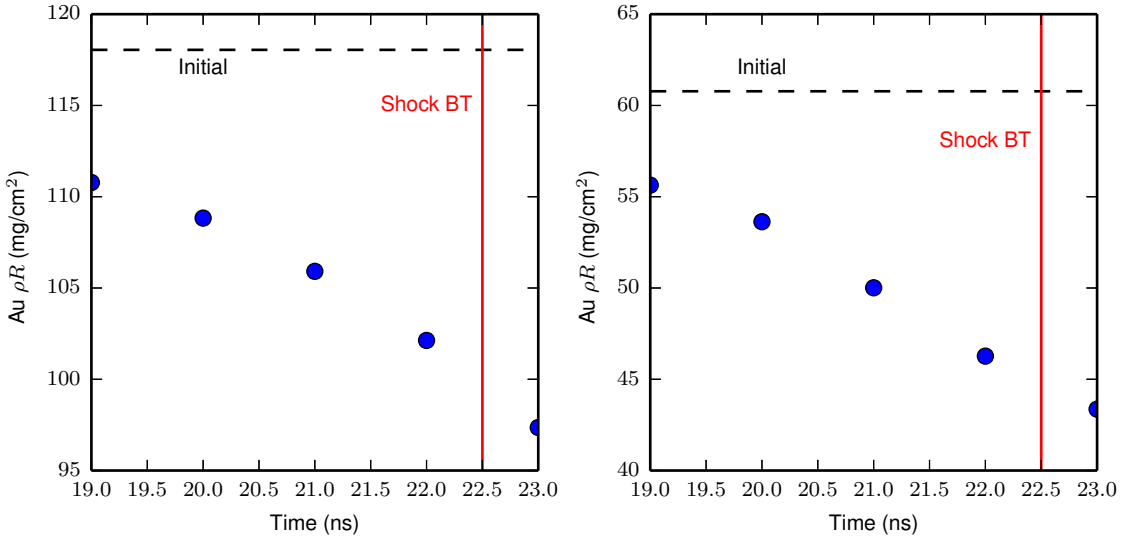

Figure 2.17. Calculated average hohlraum-wall thickness over the WRF LOS versus time for the bump (left) and torus (right) hohlraums.

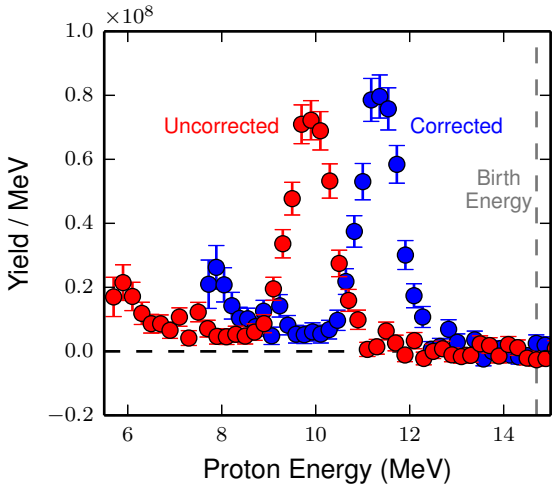

Figure 2.18. Corrected- (blue) and uncorrected- (red) proton spectra for shot N101004. The average birth energy (14.7 MeV) is shown by the dashed line. The ~ 2 MeV shift through the hohlraum wall for this shot is typical.

a typical range of ρR values at shock-bang time in NIF implosions. To relate the measured D^3He-proton spectrum to the implosion conditions, a model involving charged-particle stopping theory [12] is required. The simplest 0-D model is to take a single characteristic plasma composition, density, and electron temperature from a simulation or an estimate, and then use a stopping power theory to calculate dE/dr. This works well for OMEGA implosions where the dense shell dominates slowing [13], but for ignition-scale surrogate implosions being conducted at the NIF, a significant fraction of proton slowing during the shock burn occurs in the fuel and ablated material. These plasmas have much lower density and higher temperature than the dense shell, so a single choice of plasma conditions cannot accurately describe the entire system. This necessitates a 1-D self-consistent model, which is constructed using initial target conditions and assumptions about in-flight plasma conditions to specify the density and temperature profiles of the implosion. As the shell converges, the ρR increases and the energy of emitted protons decreases. The shell center-of-mass radius R_{cm} is taken as a free parameter, and thus is varied to obtain $\rho R(R_{cm})$ with $\rho R \equiv \int_0^\infty \rho(r)dr$. Similarly, the energy of protons escaping the implosion is calculated as a function of R_{cm} by

$$E_p(R_{cm}) = E_0 - \int_0^\infty \frac{dE}{dr}(r, R_{cm})\ dr, \tag{2.4}$$

where E_0 is the average birth energy of the protons. The charged-particle stopping power dE/dr depends on plasma conditions specified by the model and thus on both r and R_{cm}. The Li-Petrasso theory [12] is used in this work.

The initial capsule conditions are used as model inputs: the shell material, inner and outer radii, and gas fill (composition and initial pressure). Figure 2.20 illustrates the typical capsule dimensions and gas fill. The model makes assumptions about the in-flight characteristics of the implosion, informed by data when available or 1-D HYDRA [14] simulations: temperature in the fuel, shell, and ablated mass, thickness* and mass remaining of the shell, and ablated mass profile.

*The thicknesses of the in-flight shell can change depending on the laser drive. In 'short-coast' implosions the laser drive is on for a longer time, whereas 'long-coast' implosions can have shell decompression due to time-truncated drive. However, the modeling reveals that this effect is not significant for interpreting this data, since the shell

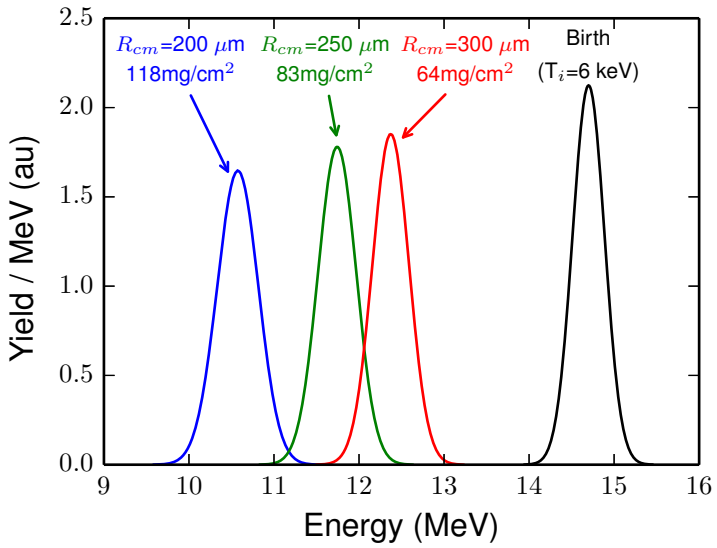

Figure 2.19. For illustration, modeled D^{3}He-proton spectra at birth (black) downshifted through 64 (red), 83 (green), and 118 (blue) mg/cm^2 of ρR are shown. The downshifts are calculated with a 1-D self-consistent model. Values of the shell $R_{\rm cm}$ associated with each spectrum are also shown.

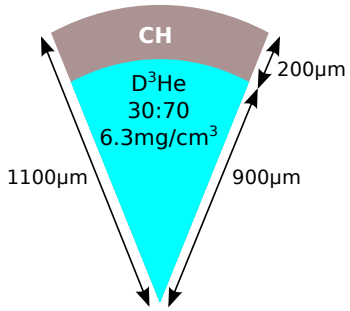

Figure 2.20. Typical NIF surrogate capsule (see Table 2.4 for more information).

With the initial conditions and in-flight assumptions, the gas density and ρR scale with R_{cm} as

$$\rho_{\rm gas} = \rho_{0,\rm gas}\left(\frac{R_i}{R_{cm}-\Delta R_s/2}\right)^3, \tag{2.5}$$

$$\rho R_{\rm gas} = \rho_{\rm gas}(R_{cm}-\Delta R_s/2), \tag{2.6}$$

where $\rho_{0,gas}$ is the initial gas density, R_i is the initial inner shell radius, and ΔR_s is the in-flight shell thickness. Similarly, the shell conditions are given by

$$\rho_{\rm shell} = \frac{M_{rem}\ \rho_{0,\rm shell}\ (R_o^3-R_i^3)}{(R_{cm}+\Delta R_s/2)^3-(R_{cm}-\Delta R_s/2)^3}, \tag{2.7}$$

$$\rho R_{\rm shell} = \rho_{\rm shell}\Delta R_s, \tag{2.8}$$

decompression does not significantly affect the ρR while the shell is at $R_{cm} \sim 250\mu$m.

where $\rho_{0,\text{shell}}$ is the initial shell density, M_{rem} is the remaining mass fraction, and R_o and R_i are the initial outer and inner radii of the shell, respectively.

The ablated mass profile is specified by

$$\rho(r) = \begin{cases} \rho_{\max} \times e^{-(r-r_0)/\lambda} & \text{if } r_0 \le r \le r_1 \\ \rho_{\min} & \text{if } r_1 \le r \le r_2 \end{cases}, \tag{2.9}$$

where $r_0 = R_{cm} + \Delta R_s/2$ is the outer radius of the imploding shell, $\rho_{\max}$ and $\rho_{\min}$ are the maximum and minimum densities of ablated material, and λ is a characteristic scale length of the ablated plasma. The radius r_1 is determined by requiring continuity of the ablated mass density profile as described by Eq. 2.9, and r_2 is determined by conservation of total mass. The values of ρ_{max}, ρ_{min}, and λ are model assumptions. The areal density of ablated material is

$$\begin{aligned} \rho R_{\text{abl}} &= \int_{r_0}^{r_2} \rho(r) dr \\ &= \rho_{\max} \lambda \left[1 - e^{-(r_1 - r_0)/\lambda} \right] \\ &\quad + (r_2 - r_1) \rho_{\min}. \end{aligned} \tag{2.10}$$

An example of the modeled density profile is shown for $R_{\text{cm}} = 250$ μm in Fig. 2.21. The components of ρR, e.g. Eqs 2.6, 2.8, and 2.10, are calculated as functions of R_{cm} both in absolute values of mg/cm^2 and also as fractions of the total ρR (Fig. 2.22). The gas and shell ρR depend strongly on convergence (Eqs 2.6 and 2.8) while the ablated material ρR only increases modestly as R_{cm} decreases. Thus for $R_{cm} \sim 200 - 300\mu$m, the shell ρR will dominate with $60 - 70\%$ of the total ρR.

The final result of the model is the relationships between the three quantities: R_{cm}, ρR, and emitted proton energy (E_p). For the typical parameters, the model produces the curves shown in Fig 2.23. For completeness we show the ρR vs R_{cm}, E_p vs R_{cm}, and finally the ρR vs E_p curves. Thus, the measured quantity (E_p) can be converted directly into ρR and R_{cm} using these relationships.

Each quantity used in the model has an associated error bar, which is used to calculate the uncertainty in the inferred quantities. This is done by an in-line sensitivity analysis to variations in the input quantities. For details of the model inputs and uncertainties, see Table 2.4. As the model uncertainties are assumed to be uncorrelated, they are added in quadrature. Any uncertainties in the proton measurement are propagated in quadrature with the model uncertainties. Uncertainties are shown in Fig. 2.23 by the dashed curves.

This model can be validated against radiation-hydrodynamic simulations using HYDRA. In the simulation, full profiles of hydrodynamic variables (density and temperature) are output at several times. The emitted D^{3}He proton energy is then calculated using the full profiles. The calculated energy is then analyzed with the model, and the model-inferred values for ρR and R_{cm} can be compared to known values directly extracted from the simulation. This is shown in Fig. 2.24 for two different simulations of shot N120408, where six snapshots are used from each simulation corresponding to varying ρR and R_{cm}. The blue points correspond to a nominal simulation, while the red points are a simulation with significant preheat (changing the implosion trajectory and plasma conditions in the shell). Typical model error bars are shown. The chosen ρR values span the typical range of shock ρR and R_{cm} observed. The model's agreement with both simulations of shot N120408, with significantly different plasma conditions between the simulations, shows that the uncertainties used in the model cover the range of expected variation in plasma conditions.

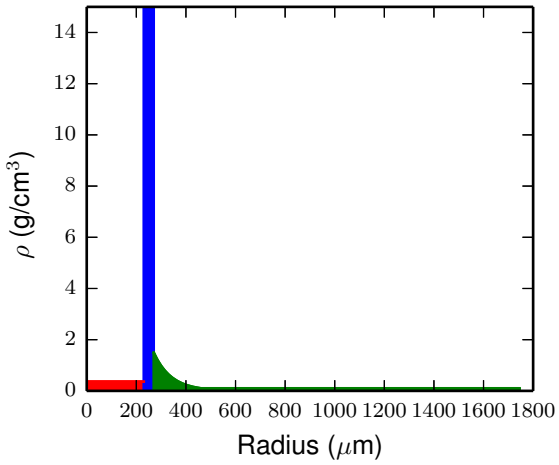

Figure 2.21. Density profile used in the 1-D model at $R_{\rm cm} = 250$ μm. This center-of-mass shell radius is typical for NIF implosions at shock-bang time. The gas material is shown in red (8 mg/cm^2), the shell is shown in blue (53 mg/cm^2), and the ablated mass is in green (23 mg/cm^2).

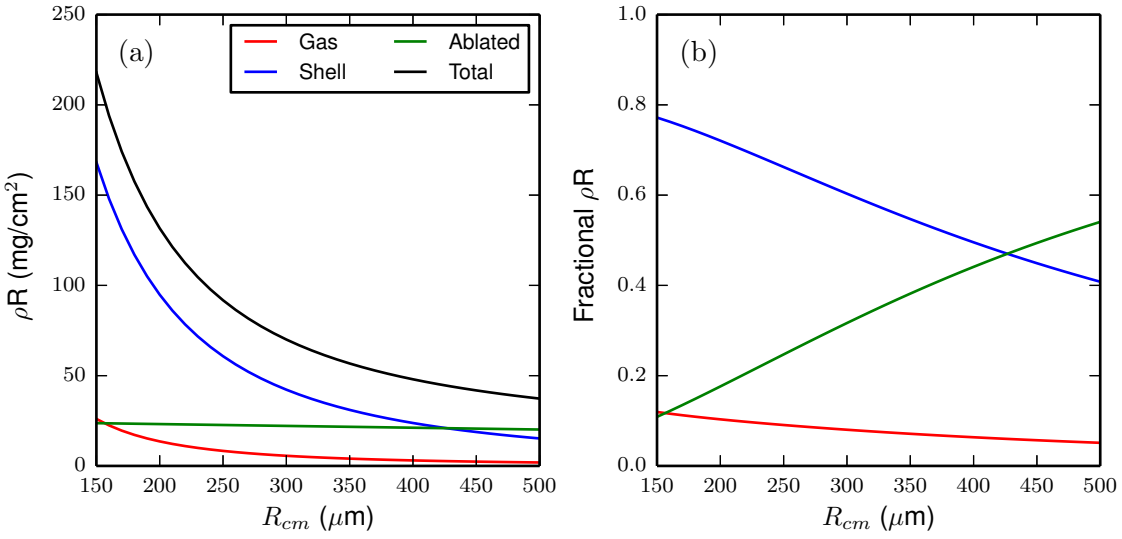

Figure 2.22. ρR components (gas, shell, and ablated material) as a function of R_{cm} for typical model parameters. The results are plotted as absolute ρR **(a)**, and normalized to the total **(b)**.

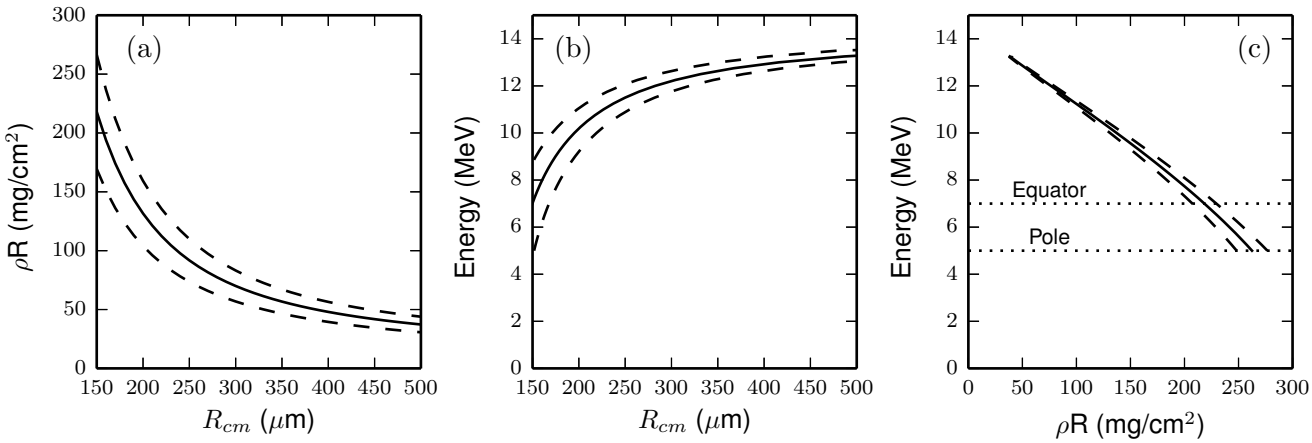

Figure 2.23. **(a)** Modeled ρR vs R_{cm}; **(b)** average energy of emitted protons vs R_{cm}; **(c)** average energy of emitted protons vs ρR. The dashed curves indicate the uncertainties in the modeling. The instrumental lower cutoffs are shown in (c) by the horizontal dotted lines at 5 MeV (pole); depending on the type of hohlraum, the equatorial energy cutoff is typically in the range $7-8$ MeV.

This comparison shows excellent agreement between the simulation and model, demonstrating the model's fidelity as an analysis tool.

Typical parameters and assumptions used in the 1-D implosion model are shown in Table 2.4 with uncertainties. The first six (shell material, inner and outer radius, fuel pressure, and fuel fill) are determined from a database of shot setup parameters. The values shown in the table are typical numbers. For the shell material, the ablator dopant (Ge or Si) is included, though the dopant level ($\sim 1\%$) has negligible effect on the inferred quantities. The plastic is 1.084 g/cc, 57.2% H, 42.3% C, and 0.5% O. The following 10 parameters are treated as assumptions in the model and characterize the in-flight properties of the implosion. The ablated mass density profile (defined by $\rho_{\max}$, $\rho_{\min}$, and λ) is given by Eq. 2.9.

For the assumed in-flight conditions, experimental data is used in the choice of value whenever possible. The shell thickness and mass remaining are measured with x-ray radiography[15] and typical values from that data are used here. The temperature profile and ablated mass density profile are unmeasured, and thus typical values are taken from HYDRA calculations where the implosion trajectory (i.e. bang time) is well matched. Since the simulation may not accurately represent the experimental conditions, large uncertainties are assigned to these values (see Table 2.4). In the table we also give the resulting uncertainties in ρR for shot N101004 (see also Fig. 2.18), which directly result from the uncertainties in the model parameters. The dominant sources are the uncertainty in fuel temperature, ablated mass density profile (collectively from $\rho_{\max}$, $\rho_{\min}$, and λ), in-flight shell thickness, and mass remaining. The other sources of uncertainty are negligible ($\ll 1$ mg/cm^2). The shell thickness has a smaller effect than might be expected. The reason for this is that it only affects the inferred ρR through the stopping power Coulomb logarithm.

A mix model was added to this model to evaluate the potential impact of mix on the proton dE/dx, primarily in the fuel where the electron temperature can be high. In the model, CH is mixed into the fuel uniformly, specified as a fraction of the initial shell mass. Even assuming an implausibly large variation in mix ($0-1\%$ of the initial shell) causes only a 0.3 mg/cm^2 difference in inferred ρR; since 1% mix corresponds to a mix mass of 25μg, about $\sim 10\times$ higher than the worst observed[16], we conclude that mix in unimportant for shock proton spectroscopy.

The primary effect of the different plasma densities and temperatures in the three regions is

Table 2.4. Typical implosion parameters used in the model. Mix fraction is given as a percentage of the initial shell mass, and shell thickness is the in-flight full width.

Parameter	**Value**	±	N101004 ±ρR mg/cm^2
Initial Conditions			
Shell Material	CH	n/a	n/a
Inner Radius (μm)	900	5	0.05
Outer Radius (μm)	1100	5	0.0
Fuel fill (mg/cm^3)	6.3	0.1	0.06
Fuel D Fraction	0.3	0.0	0
Fuel ^{3}He fraction	0.7	0.0	0
In-flight Assumptions			
Gas T (keV)	3	2	4.43
Mix T (keV)	0.5	0.2	0.23
Shell T (keV)	0.2	0.1	0.23
Ablated mass T (keV)	0.3	0.1	0.01
$\rho_{\max}$ (g/cc)	1.5	0.5	1.02
$\rho_{\min}$ (g/cc)	0.1	0.05	1.25
λ (μm)	70	30	1.25
Mix Fraction	0.5%	0.5%	0.16
Shell Thickness (μm)	40	10	1.65
Mass Remaining	17.5%	5%	1.10

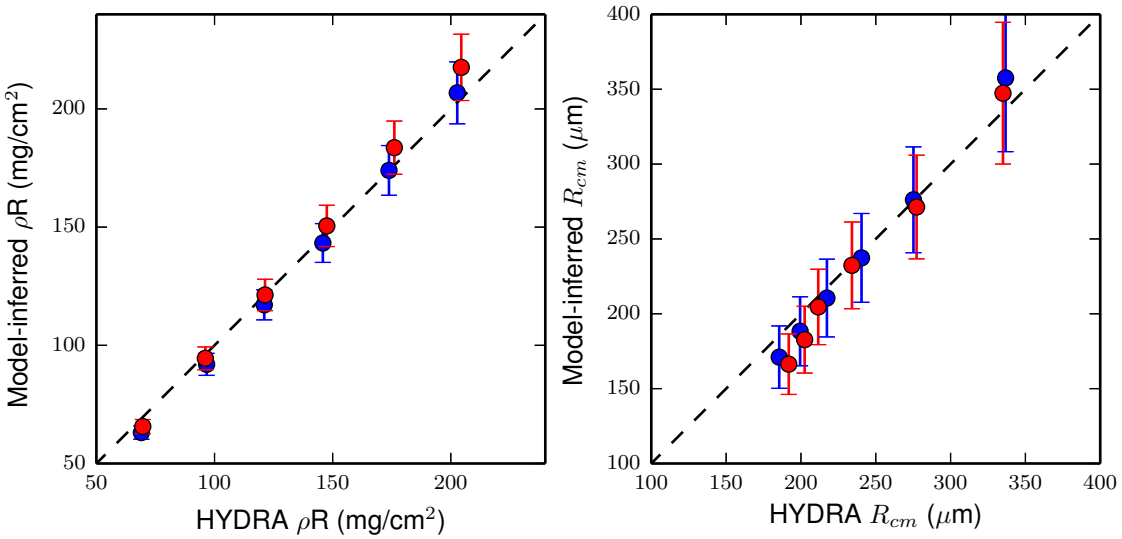

Figure 2.24. Comparison between model-inferred and HYDRA-simulated ρR (top) and R_{cm} (bottom). The data were compared at six time snapshots in two simulations: nominal (blue) and high preheat (red).

variation in the stopping power, which is shown in Fig. 2.25. Higher temperature in the fuel leads to a less pronounced Bragg peak. At high energy, the stopping power in the shell is lower than in the fuel or the ablated mass due to the higher density (leading to a smaller $\log \Lambda$).

A stated choice in this work, which affects the reported ρR values, is the theory used to calculate the charged-particle stopping power. In these dense plasma regimes, no experimental data exists to differentiate between theories. In this work, the Li-Petrasso theory [12] has been used. However, this choice represents a potential quasi-systematic uncertainty in the inferred values. The magnitude of this effect is investigated by evaluating the implosion model at equivalent nominal conditions but with various choices of stopping theory. In particular, we choose Zimmerman's parameterization of the Maynard-Deutsch theory [17,18] and the Brown-Preston-Singleton (BPS) theory [19]. A comparison of the stopping power for the three theories is shown in Fig. 2.26. The magnitude of the BPS and

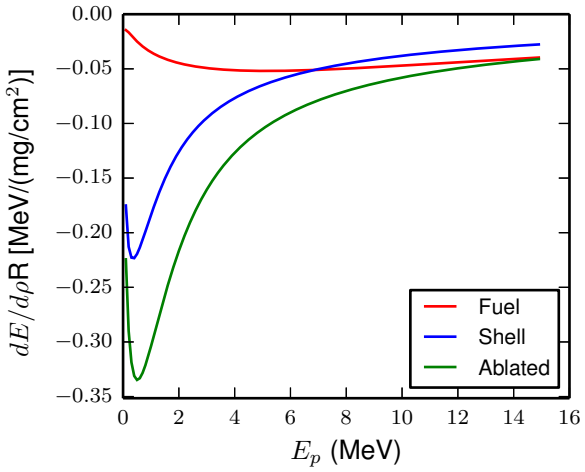

Figure 2.25. Stopping power for the three components of the implosion model: fuel, shell, and ablated mass.

Zimmerman stopping are quite close. In the gas, these other theories have a smaller magnitude of dE/dx than Li-Petrasso, while they are higher in the shell and ablated material. A direct comparison of inferred ρR values using the implosion model and varying only the stopping model is shown in Fig. 2.27. For a wide range of relevant ρR, the Zimmerman and BPS stopping power would lead to an inferred ρR that is lower by $\sim 10\%$ or $\sim 12\%$, respectively. Future experimental data may be able to discriminate these theories from the Li-Petrasso theory in relevant regimes.

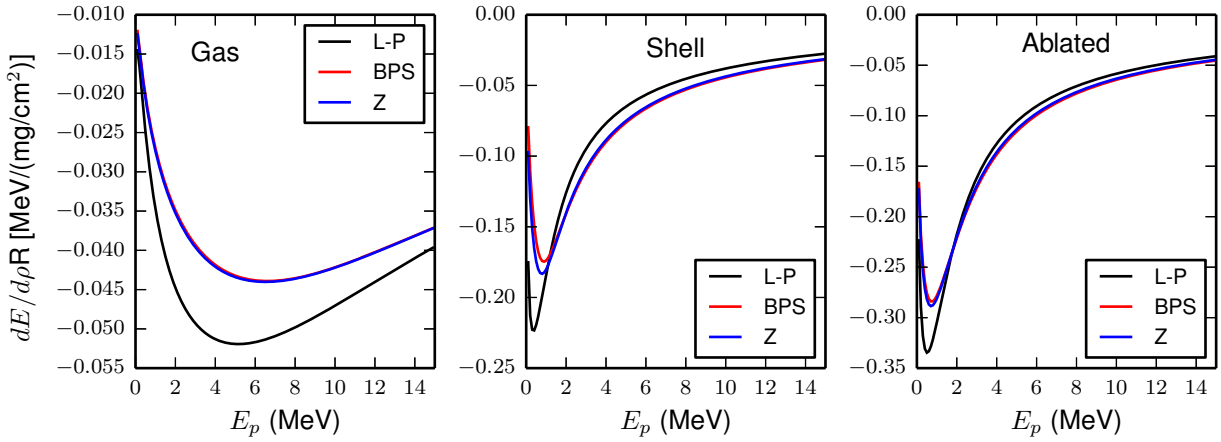

Figure 2.26. Stopping power for the three theories [Li-Petrasso (LP), Brown-Preston-Singleton (BPS), and Zimmerman (Z)] for each region of the implosion model: gas, shell, and ablated material.

2.6 Line Width

For mono-energetic fusion products, the line width can be used as a key diagnostic, for example of the ion temperature[20,21] via the Doppler width[22], or of turbulent or radial residual kinetic energy[23]. Often, these techniques use neutrons from the D+T or D+D reaction; neutrons have the advantage that the primary peak consists of neutrons that do not interact after their birth, and thus closely represent the production spectrum. Protons, the focus of this work, slow down via Coulomb collisions as they exit the implosion (see Section 2.5) and can be affected by electromagnetic fields[†].

For NIF D^{3}He shock-proton spectroscopy, there are four main effects that would significantly complicate any use of the line width as a diagnostic of residual kinetic energy or ion temperature. The implosion ρR evolution over the shock burn is significant, geometric effects broaden the emitted proton spectrum, ρR is high enough for significant straggling, and any high-mode asymmetries from acceleration-phase instabilities could be significant. These effects are discussed in this section, using simple models based upon the ρR model discussed in Section 2.5.

2.6.1 ρR evolution

As the implosion ρR evolves during the finite-duration shock burn, protons born at the beginning of the burn experience a lower ρR than protons born at the end of the burn. The broadening due to

[†]In direct-drive implosions, it is well-known that when the fusion bang time is during the laser pulse the charged particles are affected by electromagnetic fields[24,25,20,26]. For indirect drive, the electric fields decay early in the pulse (see Appendix E) and do not affect the spectrum.

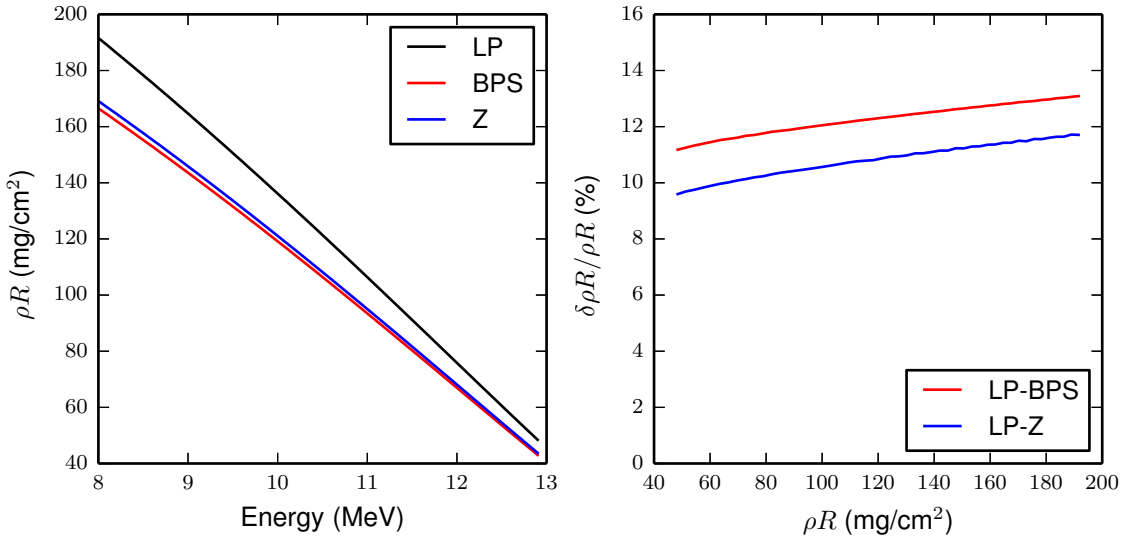

Figure 2.27. Left: Inferred ρR versus final proton energy for three models [Li-Petrasso (LP), Brown-Preston-Singleton (BPS), and Zimmerman (Z)]. Right: Difference (%) between the Zimmerman or BPS models and Li-Petrasso.

this effect depends on the shock-burn duration (Gaussian width σ_{BW}), the implosion velocity (v), and the implosion R_{cm} during the burn. The resulting velocity broadening (σ_v) can be calculated using the ρR model function for proton energy (E_p) as a function of R_{cm} as

$$\sigma_v = \frac{1}{2}\Big[E_p(R_{cm} + v\sigma_{BW}) - E_p(R_{cm} - v\sigma_{BW})\Big]. \tag{2.11}$$

In the following analysis (Section 2.6.5) we assume a velocity $v = 300$ km/s and a burn FWHM of 100 ps ($\sigma_{BW} = \text{FWHM}/2\sqrt{2\ln 2}$), which are nominal for the NIF surrogate D^{3}He implosions. This results in velocity broadening $\sigma_v \sim 200 - 300$ keV.

2.6.2 Geometric broadening

Geometric broadening of the D^{3}He-proton spectrum is caused by the finite size of the burn region, because the proton path lengths through the implosion gas, shell, and ablated mass varies depending on birth location. This is shown in Fig. 2.28.

For a given proton birth location (r and θ in polar coordinates with azimuthal symmetry), the path length in the gas is

$$L_g = \sqrt{r_g^2 - r^2\sin^2\theta} - r\cos\theta, \tag{2.12}$$

where r_g is the radius of the fuel-shell interface in the ρR model. Similarly, the path length in the shell becomes

$$L_s = \sqrt{r_s^2 - r^2\sin^2\theta} - \sqrt{r_g^2 - r^2\sin^2\theta}, \tag{2.13}$$

where r_s is the outer radius of the shell. As the density profile in the ablated mass varies with radius, the proton slowing is a numerical integral along the path depicted in Fig. 2.28. Using the plasma conditions from the ρR model and this geometry the transmitted proton energy is calculated for any initial (r, θ) coordinates.

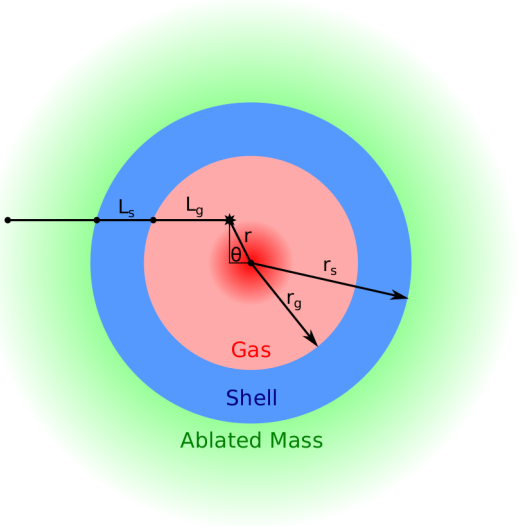

Figure 2.28. Geometric broadening results from different path lengths for protons born in different regions of the fuel. For a given birth location (r and θ in polar coordinates, with azimuthal symmetry) the path length in the gas (L_g) and shell (L_s) vary, as well as the path in the ablated material.

The source profile (S) is assumed to be a radial Gaussian,

$$S(r) = \frac{1}{2\sqrt{2}\pi^{3/2}\sigma_r^3} \exp\left[-\frac{r^2}{2\sigma_r^2}\right], \tag{2.14}$$

where σ_r is the Gaussian width parameter; $S(r)$ is normalized to unity in 3 dimensions.

The geometric broadening (σ_g) can then be calculated by performing a numerical integration over the gas region to calculate a weighted standard deviation of E_p, where the weight is the 3-D spherical polar volume element multiplied by the source function $S(r)$. For the following calculations, a source width of $\sigma = 40$ μm is assumed. This effect typically results in broadening of ~ 100 keV.

2.6.3 Straggling

As the proton slows while transiting the implosion, there is a statistical variation in energy loss due to the random nature of collisions with the plasma particles. This leads to broadening of an originally monoenergetic beam, which is called 'straggling'. To model this effect, we invoke a simple model for plasma straggling[27,28]:

$$\sigma_s^2 = 2k_B T \times \Delta E, \tag{2.15}$$

where σ_s is the amount of straggling (i.e. a Gaussian width), T is the plasma temperature, and ΔE is the total energy lost by the particle. As an extension of the ρR model, the straggling is calculated as the proton traverses each region independently (due to the dependence on T and ΔE) and summed in quadrature to get a total straggling width σ_s.

Additionally, for the equatorial detectors straggling occurs as the protons traverse the hohlraum wall. The amount of straggling in the wall can be easily calculated with the TRIM Monte Carlo package[6]; this effect typically results in broadening ~ 100 keV.

2.6.4 High-mode ρR asymmetries

High-mode asymmetries (mode numbers ~ 100, which are significant[29]) can cause broadening since the protons traverse a shell with a varying ρR. At the shock-bang time, these may be significant due to acceleration-phase Rayleigh-Taylor instabilities at the ablation front. A simple model for

the magnitude of this effect is to assume a normally-distributed fractional variation (f) in the shell radius, $\delta R_{cm} = f \times R_{cm}$, which is convolved with the ρR model to calculate a variation in proton energy:

$$\sigma_{asym} = \frac{1}{2}\left[Ep(R_{cm} + \delta R_{cm}) - Ep(R_{cm} - \delta R_{cm})\right]. \tag{2.16}$$

This requires an assumption on the magnitude of the asymmetries at this time, which are largely unknown and likely vary between shots. In the following analysis, an f of 1 or 2 % is used. Asymmetries at this level result in broadening of $50 - 100$ keV.

2.6.5 Complete broadening model

The broadening from the various sources discussed in the previous sections is plotted in Fig. 2.29 as a function of implosion ρR. Additionally, the thermal width $\sigma_{th} = 0.0767\sqrt{T_i}$ with σ_{th} in MeV and T_i in keV is shown for $T_i = 5, 10, 15$ keV.

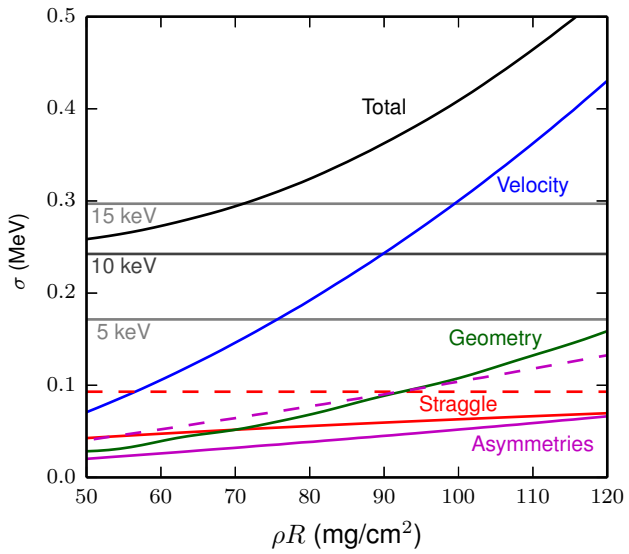

Figure 2.29. Line broadening (σ) for various sources as a function of implosion ρR. The thermal width (σ_{th}) is plotted for $T_i = 5, 10, 15$ keV (gray lines). The velocity (ρR evolution) broadening is shown in the blue curve, geometric broadening is shown in green, straggling is shown in red, and asymmetries in magenta. For straggling, the solid curve is due to the implosion and the dashed curve is due to the hohlraum wall. For asymmetries, the solid curve is due to a 1% high-mode asymmetry amplitude while the dashed curve is for a 2% amplitude.

The total line width according to this model is a quadrature sum of the components. In Fig. 2.29, this is shown assuming $T_i = 10$ keV, straggling only from the shell, and 1% amplitude asymmetries.

Unless the ρR is small ($\lesssim 50$ mg/cm^2), other sources of broadening are a very significant contribution to the total width, in particular the velocity-induced ρR evolution broadening. In order to infer a spectral width due to thermal Doppler broadening, all other effects must be accurately modeled and subtracted in quadrature, which would require significant and high-fidelity models of these sources of broadening, which is an extremely challenging problem.

2.7 References

1. F. H. Séguin, J. A. Frenje, C. K. Li *et al.*, "Spectrometry of charged particles from inertial-confinement-fusion plasmas," Rev. Sci. Instrum., **74**(2), 975–995 (2003).
2. F. H. Séguin, N. Sinenian, M. Rosenberg *et al.*, "Advances in compact proton spectrometers for inertial-confinement fusion and plasma nuclear science," Rev. Sci. Instrum., **83**(10), 10D908 (2012).
3. N. Sinenian, M. Rosenberg, M. Manuel *et al.*, "The response of CR-39 nuclear track detector to 19 MeV protons," Rev. Sci. Instrum., **82**, 103303 (2011).

4. S. McDuffee, J. Frenje, F. Séguin *et al.*, "An accelerator based fusion-product source for development of inertial confinement fusion nuclear diagnostics," Rev. Sci. Instrum., **79**, 043302 (2008).
5. N. Sinenian, M.-E. Manuel, A. Zylstra *et al.*, "Upgrade of the MIT Linear Electrostatic Ion Accelerator (LEIA) for nuclear diagnostics development for Omega, Z and the NIF," Rev. Sci. Instrum., **83**(4), 043502 (2012).
6. J. Ziegler, J. Biersack and U. Littmark, *The stopping and range of ions in matter* (Pergamon, New York, 1985).
7. W. J. Hibbard, M. D. Landon, M. D. Vergino *et al.*, "Design of the National Ignition Facility diagnostic instrument manipulator," Rev. Sci. Instrum., **72**(1), 530–532 (2001).
8. F. Séguin *et al.*, To be submitted to Rev. of Sci. Instrum. (2015).
9. M. J. Rosenberg, F. H. Séguin, C. J. Waugh *et al.*, "Empirical assessment of the detection efficiency of CR-39 at high proton fluence and a compact, proton detector for high-fluence applications," Rev. Sci. Instrum., **85**(4), 043302 (2014).
10. M. Manuel, M. Rosenberg, N. Sinenian *et al.*, "Changes in CR-39 proton sensitivity due to prolonged exposure to high vacuums relevant to the National Ignition Facility and OMEGA," Rev. Sci. Instrum., **82**(9), 095110 (2011).
11. J. Rojas-Herrera, H. G. Rinderknecht, A. B. Zylstra *et al.*, "Impact of x-ray dose on the response of cr-39 to 15.5 mev alphas," Review of Scientific Instruments, **86**(3), 033501 (2015).
12. C. Li and R. Petrasso, "Charged-particle stopping powers in Inertial Confinement Fusion Plasmas," Phys. Rev. Lett., **70**(20), 3059 (1993).
13. J. A. Frenje, C. K. Li, F. H. Seguin *et al.*, "Measuring shock-bang timing and rho R evolution of D^3He implosions at OMEGA," Physics of Plasmas, **11**(5), 2798–2805 (2004).
14. M. Marinak, G. Kerbel, N. Gentile *et al.*, "Three-dimensional HYDRA simulations of National Ignition Facility targets," Physics of Plasmas, **8**, 2275 (2001).
15. D. Hicks *et al.*, "Implosion dynamics measurements at the National Ignition Facility," Phys. Plasmas, **19**, 122702 (2012).
16. T. Ma *et al.*, "Onset of Hydrodynamic Mix in High-Velocity, Highly Compressed Inertial Confinement Fusion Implosions," Phys. Rev. Lett., **111**, 085004 (2013).
17. G. Zimmerman, "Recent Developments in Monte Carlo Techniques," LLNL report, UCRL-JC-105616 (1990).
18. G. Maynard and C. Deutsch, "Energy loss and straggling of ions with any velocity in dense plasmas at any temperature," Phys. Rev. A, **26**, 665 (1982).
19. L. S. Brown, D. L. Preston, and R. L. Singleton Jr., "Charged particle motion in a highly ionized plasma," Physics Reports, **410**(4), 237 – 333 (2005).
20. D. Hicks, *Charged-particle spectroscopy: a new window on inertial confinement fusion*, Ph.D. thesis, Massachusetts Institute of Technology (1999).
21. C. Li, D. Hicks, F. Séguin *et al.*, "D–He proton spectra for diagnosing shell ρR and fuel T of imploded capsules at OMEGA," Physics of Plasmas, **7**, 2578 (2000).
22. H. Brysk, "Fusion Neutron Energies and Spectra," Plasma Physics, **15**, 611–617 (1973).
23. T. Murphy, "The effect of turbulent kinetic energy on inferred ion temperature from neutron spectra," Physics of Plasmas, **21**(7), 072,701 (2014).
24. D. Hicks, C. Li, F. Séguin *et al.*, "Observations of fast protons above 1 MeV produced in direct-drive laser-fusion experiments," Physics of Plasmas, **8**, 606 (2001).
25. N. Sinenian, M. J.-E. Manuel, J. A. Frenje *et al.*, "An empirical target discharging model relevant to hot-electron preheat in direct-drive implosions on OMEGA," Plasma Physics and Controlled Fusion, **55**(4), 045001 (2013).
26. N. Sinenian, *Fast-Ion Spectrometry of ICF Implosions and Laser-Foil Experiments at the Omega and MTW Laser Facilities*, Ph.D. thesis, Massachusetts Institute of Technology (2013).
27. S. T. Butler and M. J. Buckingham, "Energy loss of a fast ion in a plasma," Phys. Rev., **126**, 1–4 (1962).
28. N. R. Arista and W. Brandt, "Energy loss and straggling of charged particles in plasmas of all degeneracies," Phys. Rev. A, **23**, 1898–1905 (1981).
29. D. T. Casey, V. A. Smalyuk, K. S. Raman *et al.*, "Reduced instability growth with high-adiabat high-foot implosions at the national ignition facility," Phys. Rev. E, **90**, 011,102 (2014).

3

Shock dynamics in NIF implosions

3.1 Introduction

While ignition experiments at the NIF use targets with cryogenic layers of DT fuel, numerous surrogate implosions have been conducted where the layer of DT ice is replaced with a surrogate mass of ablator material (CH). The hydrodynamics before deceleration are nearly identical for the cryogenic layered and surrogate implosions,[1] enabling complementary studies and diagnostics of implosion dynamics, such as symmetry[2,3] and velocity.[4,5] One of the main objectives of using these surrogate implosions is to characterize the implosion at various stages to benchmark radiation-hydrodynamics simulations.[6–8,1]

In an implosion, a series of spherically converging shocks are launched with increasing strength. These shocks eventually coalesce at the capsule's inner edge and then converge at the center of the implosion. The final shock 'rebounds' and briefly creates high-ion-temperature conditions at the center of the implosion. In the case of surrogate implosions at NIF with a D^3He gas fill, this ion temperature is high enough to produce energetic protons via the D^3He fusion reaction (Eq. 1.15).

For surrogate implosions at the NIF, this 'shock burn' occurs several hundred ps before the main compression burn, and is approximately concurrent with peak shell implosion velocity. This is shown for a typical surrogate implosion in Fig. 3.1 using the radiation-hydrodynamics code HYDRA[8], where the simulated shock trajectories for the four launched shocks and final merged shock are shown in Fig. 3.1a as contours of the normalized pressure gradient $|(1/P)dP/dr|$. The laser pulse is shown in Fig. 3.1c, a detailed view of the shock dynamics around the shock-bang time and compression-bang time is shown in Fig. 3.1b, and the capsule dimensions are shown in Fig. 3.2.

After the final merged shock rebounds at $\sim$ 22 ns the shock burn occurs over $\sim$ 100 ps, producing energetic D^3He protons (Eq. 1.15). These escaping protons are used to probe the in-flight characteristics of the shell at a radius of $\sim 250\mu$m.

D^3He proton spectroscopy is a well-developed technique for diagnosing inertial fusion implosions[9–13] at the OMEGA laser facility[14] and now at the NIF.[15] As a probe of the implosion shock dynamics, this technique is unique in that it probes the strength of the final merged shock when it hits and rebounds from the center of the implosion. This measurement is complementary to the shock-timing measurements of the shock velocity that use an interferometry technique,[16] which has been highly successful at understanding the shock dynamics in the shell for radii larger than $600-700\mu$m.[17–20] At smaller radii the interferometry measurements 'blank'. As a result, the interferometry measurement would not see any additional shocks launched later in the implosion after the blanking, and does not probe the shock dynamics in the gas, when spherical convergence effects

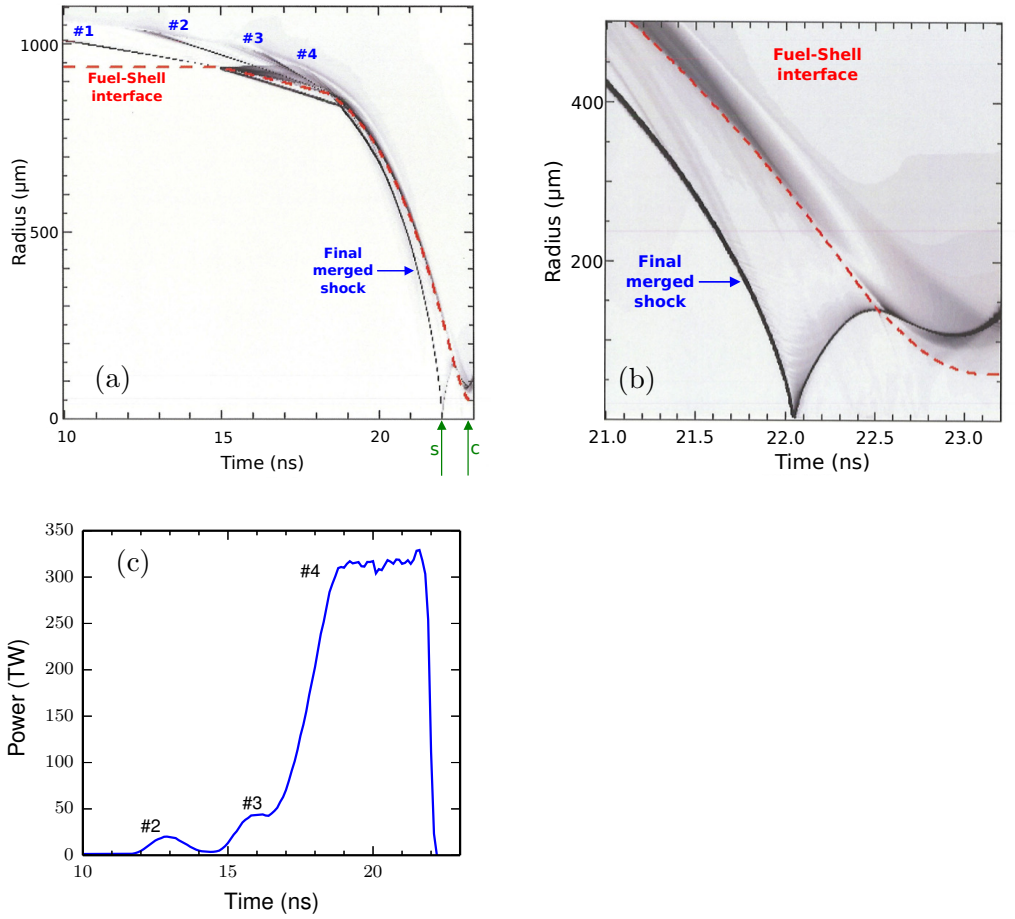

Figure 3.1. NIF surrogate shot N120408-001-999 (CH shell with D^3He gas, see Fig. 3.2). **(a)** Simulated shock trajectory, visualized as the pressure gradient $|(1/P)dP/dr|$ where black indicates a higher value. The shock plot shows the four shocks launched into the shell, which merge to form the final shock that travels to the center where it rebounds, increasing the temperature and density, creating the shock burn at 22.03 ns. The compression bang time is at 22.83ns. Simulated shock (s) and compression (c) bang times are indicated by the arrows. **(b)** zoomed-in Shock trajectory through rebound, shock burn, and compression phases. **(c)** Laser pulse (foot before 10 ns not shown). In the drive, the pickets at ~ 13 and ~ 16 ns launch the 2^{nd} and 3^{rd} shocks respectively, with the 4^{th} launched by the rise to peak power.

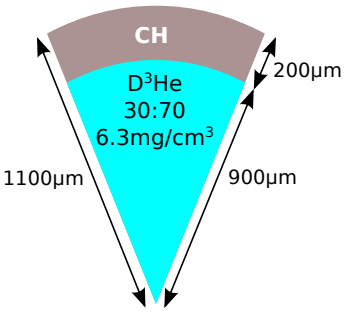

Figure 3.2. Typical NIF surrogate capsule (see Table 2.4 for more information). The plastic shell ($\rho = 1.08$ g/cm^3) is filled with 30:70 atomic D and ^{3}He fuel.

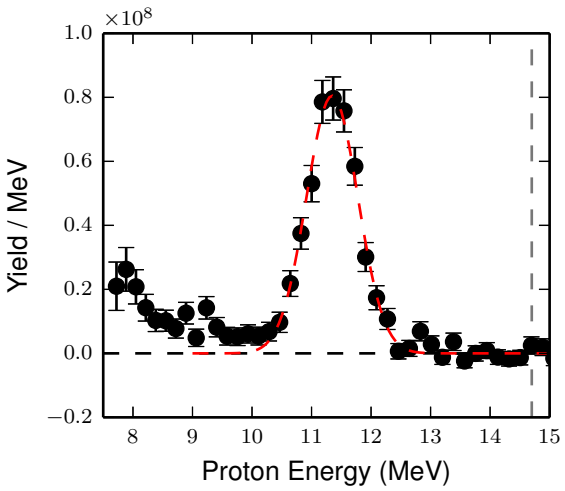

Figure 3.3. Sample D^3He proton spectrum from NIF shot N101004-002-999, measured on the equator (DIM 90-78 Wedge Range Filter (WRF) #1) after hohlraum correction. The D^3He average birth energy of 14.7 MeV is shown by the vertical dashed line. The red dashed line is a Gaussian fit to the spectrum. Surplus protons at low energy, $\sim 8-9$ MeV, are due to the onset of compression burn.

are significant; as the shock strength increases with convergence,[21] non-hydrodynamic behavior may become important.[22,23]

3.2 Sample Analysis

A typical measured D^3He proton spectrum is shown in Fig. 3.3. The protons have been energy downshifted to ~ 11.5 MeV from the birth energy of 14.7 MeV. The downshift is caused by Coulomb collisions with the imploding plasma electrons*, and the observed downshift can be related to the implosion areal density (ρR) using a charged-particle stopping theory[24]. The shock yield observed (8.7×10^7) is related to the final merged shock strength[21,13]. The center-of-mass radius (R_{cm}) of the imploding shell is inferred in addition to ρR using 1-D modeling discussed in Section 2.5.

For the sample spectrum shown in Fig. 3.3, the results of the spectral analysis and subsequent ρR modeling are shown in Table 3.1.

Error bars are 1σ. For the proton energy, the systematic uncertainty primarily comes from the energy calibration of the WRFs[25], and random uncertainty comes from a combination of factors such as the hohlraum, variation in CR-39 properties, and statistical uncertainty. For the yield and line width, there are no systematic uncertainties, and the random uncertainties are primarily variation in CR-39 and statistics.

The energy uncertainties propagate to the modeled quantities ρR and R_{cm}. The systematic uncertainties for these quantities also include, and are dominated by, the modeling uncertainty. The model uncertainty is also listed separately in Table 3.1.

*The proton velocity is high relative to the electron thermal velocity in these regimes, so electron stopping dominates

Table 3.1. Results from the analysis of the D^3He proton spectrum for N101004-002-999 on DIM 90-78.

Quantity	Value	± random	± systematic†	± model
Energy (MeV)	11.34	0.10	0.10	
σ (MeV)	0.43	0.10	n/a	
Yield	8.71×10^7	0.94×10^7	n/a	
ρR (mg/cm^2)	96.0	3.1	6.1	5.3
R_{cm} (μm)	242	5	35	34

3.3 NIF Experiments

The compact WRF proton spectrometers (see Refs. 26,27,15 and Chapter 2) have been used at the NIF since 2009. Between 1 and 4 spectrometers are fielded on the polar (0-0) and equatorial (90-78) diagnostic manipulators (DIMs)[28]. Each WRF provides a complete spectral measurement of the D^3He protons, from which yield, ρR, and R_{cm} are inferred.

WRF proton spectrometers have been used on a total of 85 surrogate D^3He gas-filled indirect-drive implosions on the NIF, forming the basis of this work. For these experiments, the total laser energy varied in the range $0.9 - 1.9$ MJ, and the peak laser power was between $243 - 522$ TW. Gas-filled Au or depleted U (DU) hohlraums were used in these experiments. The hohlraum width was 5.44mm ('544' geometry) or 5.75mm ('575' geometry) with varying lengths in the range of $9 - 10$mm. More details on the spectrometers and NIF geometry are given in Chapter 2.

The capsules were primarily CH with an outer radius varying from 1087 to 1169 μm and thickness from 188 to 231 μm. Si and Ge dopants are used within the shell. The gas fill was typically a 30:70 atomic mixture of D and ^{3}He at an initial gas density of 6.3 mg/cm^3. Each of these parameters is used in the ρR modeling described in the previous section (also see Fig. 3.2).

The complete dataset is shown in Fig. 3.4. Within a DIM, multiple WRFs are averaged when available to reduce random and statistical errors; the weighted mean and resulting uncertainty are shown. The measured ρR is shown in Fig. 3.4a. The random/statistical errors associated with the ρR values are dominated by the larger systematic and model uncertainties (see Sec. 2.5). Many of the shots have asymmetries between the pole and equator: these asymmetries are discussed in Chapter 4. Overall the ρR typically varies between $70 - 110$ mg/cm^2. The most notable set of outliers are the implosions with ρR in the range of $160 - 170$ mg/cm^2 measured on DIM 90-78. The distinguishing feature for these implosions is that they were conducted as part of a series of low-power short-coast implosions.

The proton shock-yield data for the entire dataset is shown in Fig. 3.4b. Only data from the equator (DIM 90-78) is shown. This is because the polar yield data is affected by transverse electromagnetic field structures at the LEH, which can cause deflections and thus a reduction in the apparent yield observed by the WRFs on the pole[29–31]. A significant shot-to-shot yield variation is observed, i.e. $(1 - 35) \times 10^7$. Fundamentally the large variability is due to the extreme temperature sensitivity of the D^3He reaction, which makes the shock-proton yield very sensitive to the final shock strength.[21,13]

Finally, the inferred shell center-of-mass radius (R_{cm}) is shown in Fig. 3.4c. According to this analysis, the shell is typically at a radius of $250 - 300$ μm at the shock-bang time. In the high ρR cases, the inferred R_{cm} is as low as ~ 190 μm. However, the error bars are large, typically $\pm 25 - 30$

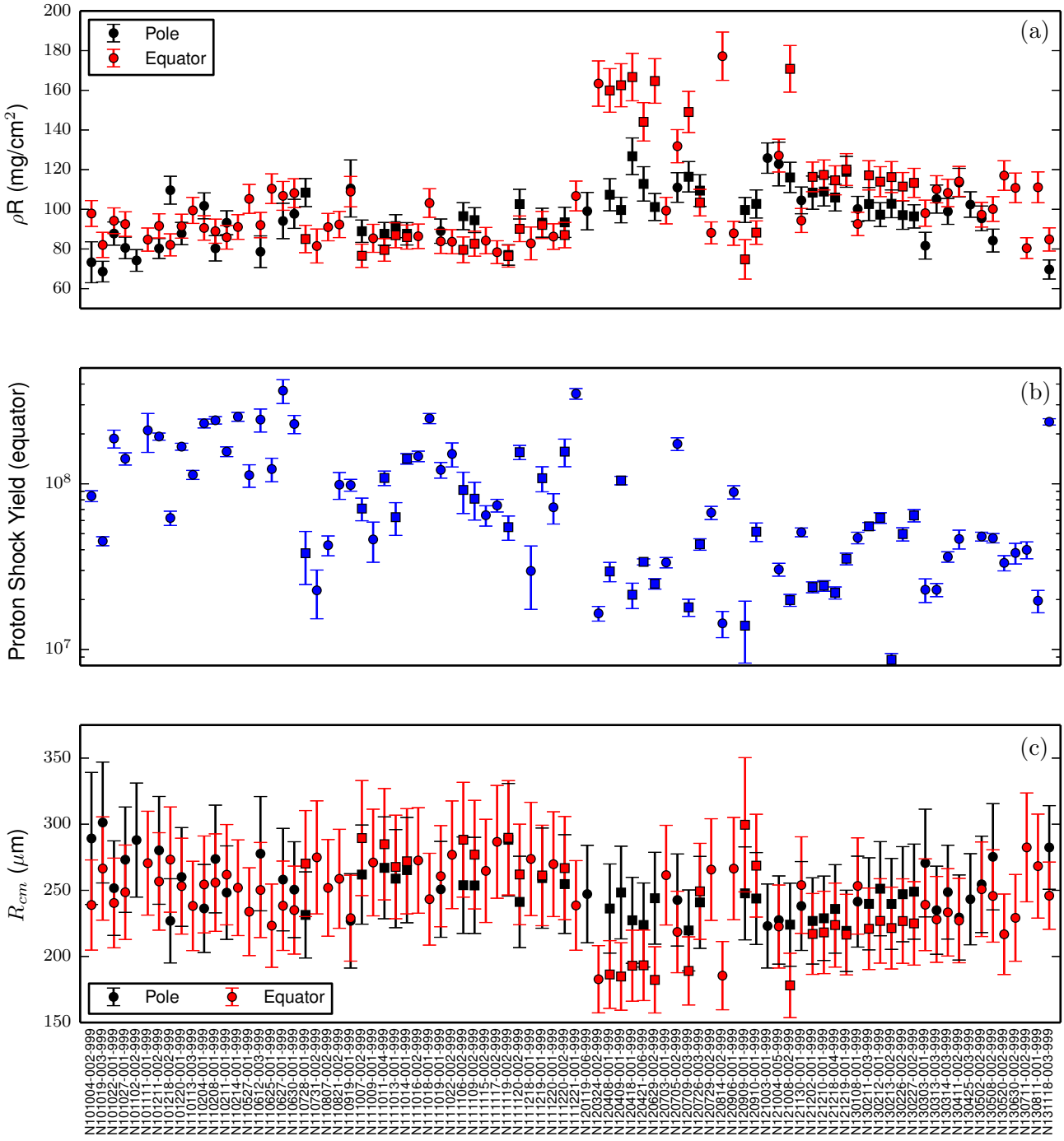

Figure 3.4. WRF data for all surrogate implosions. (a) Shock ρR data. When available both polar (DIM 0-0) and equatorial data (DIM 90-78) are shown. (b) Shock proton yield measured by WRFs on DIM 90-78. (c) Center-of-mass shell radius (R_{cm}) plotted as average values for both pole (DIM 0-0) and equator (DIM 90-78).

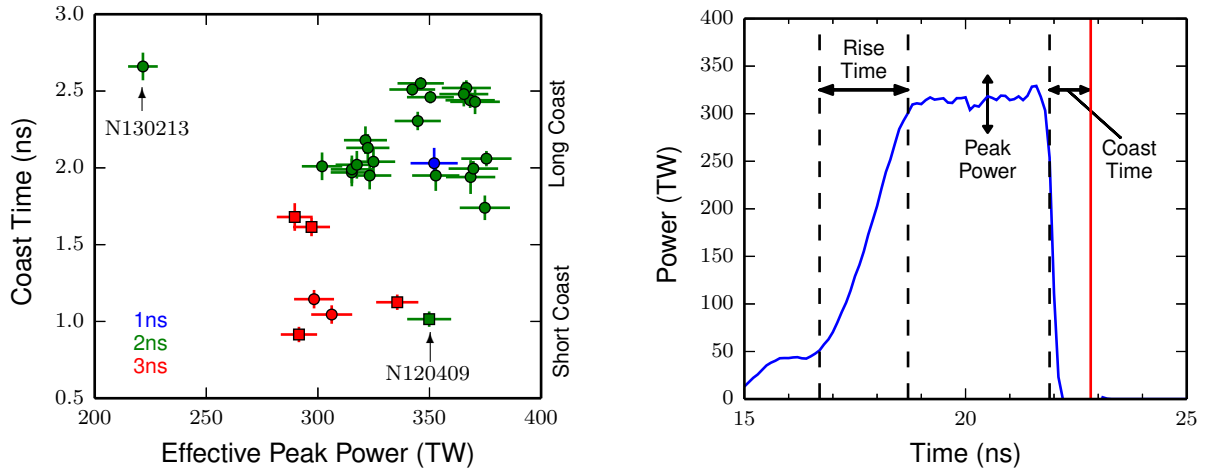

(a) **(b)**

Figure 3.5. **(a)** Coast time and peak power of down-selected experiments. With a few exceptions, implosions have been conducted at low-power, short-coast ($\sim$ 300TW, $\sim$1ns) conditions or high-power, long-coast ($\sim$ 350TW, $\sim$2ns) conditions. **(b)** Relevant variables of the laser pulse: rise time, peak power, and coast time. In this case, the rise time is 2ns, the peak incident power is 300TW, and the coasting time is 0.9ns (short-coast, while long-coast is $\sim$2ns). The bang time is indicated by the red line.

μm, caused by the model uncertainties (described in Section 2.5).

3.4 Data down-selection

Due to the large shot-to-shot parameter variations during the NIF campaigns, it is necessary to select a subset of implosions with similar overall conditions for detailed analysis. We perform this down-selection using the following criteria:

1. Standard capsules (CH with D^{3}He fill, see Fig. 3.2)
2. 5.75mm diameter hohlraums
3. WRF data available on both pole and equator
4. Low-adiabat ('4-shock') pulse shapes

This reduces the number of shots to 30. Criterion #3 is required to allow for modeling of the observed ρR asymmetries (see Fig. 3.4a) and determining of average values for ρR and R_{cm}. Shots selected via these criteria are used in subsequent analysis and are denoted in Fig. 3.4 by square markers.

3.5 Shock Dynamics

The shock dynamics of the down-selected set of 30 implosions can now be explored. The observations indicate that the shock dynamics are most sensitive to the peak power of the laser drive, the coasting time of the implosion, and the rise time of the main laser pulse, see Fig. 3.5b.

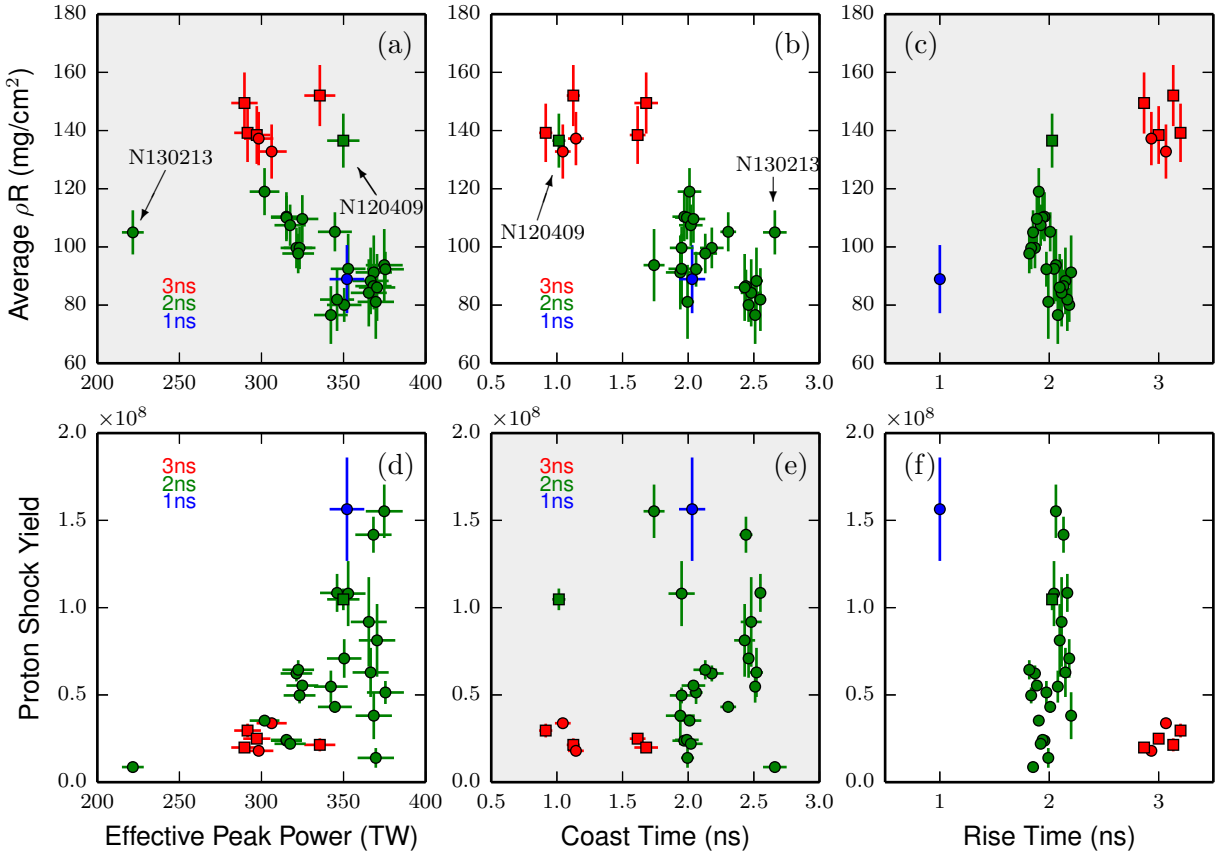

Figure 3.6. Shock ρR and yield data [ρR (a-c) and Y_p (d-f)] versus effective peak power (a,d), coast time (b,e), and rise time (c,f). For the rise time, points are artificially displaced for clarity around the values 1, 2, or 3 ns (see c,f). Rise time is further specified by point color: 1ns (blue), 2ns (green), and 3ns (red) to improve clarity in the power and coast time plots. Additionally, Au-wall hohlraums are denoted by circular markers, and DU-wall hohlraums by square markers.

Since the effective drive experienced by the capsule depends on the absorption of the incident laser light and the effectiveness of conversion to x rays, we add 25TW to the actual laser power for DU hohlraums to account for the latter, and then multiply by the observed absorption fraction to account for the former. The 25TW effective increase in power is based upon measured enhancements in radiation temperature when using DU hohlraums[32]. This gives an 'effective peak power' which is used in this work. The coasting time of an implosion is defined as the difference between the end of the laser drive and the measured compression bang time. The rise times used in these experiments are discrete, with design values of 1, 2, or 3 ns.

With these definitions, the main observables (average ρR and shock yield) are plotted versus the effective peak power, coasting time, and rise time. The data are shown in Fig. 3.6. To eliminate the effect of low-mode asymmetries observed in these implosions, this analysis uses an average ρR obtained from a fit to the polar and equatorial ρR data (see Chapter 4). The different rise times used are differentiated by marker color. Furthermore, the hohlraum material is specified by marker shape: square markers for DU and circular markers for Au hohlraums.

The distribution of implosion parameters used (peak power, coast time, and rise time) is illustrated by Fig. 3.5a. With a few exceptions, the experiments fall into two groups:

1. Low-power ($\sim 275 - 325$ TW), short-coast ($\sim 1 - 1.5$ ns), slow-rise (3ns)

2. High-power ($\sim 325 - 375$ TW), long-coast ($\sim 2 - 2.5$ ns), fast-rise (1 or 2 ns)

Since these two groups are diametrically opposed in all three parameters disentangling their effects requires using a few select implosions that do not fall into these groups. For the rise time a set of three implosions was conducted where only the rise time was varied, significantly aiding this interpretation.

3.5.1 Shock yield interpretation

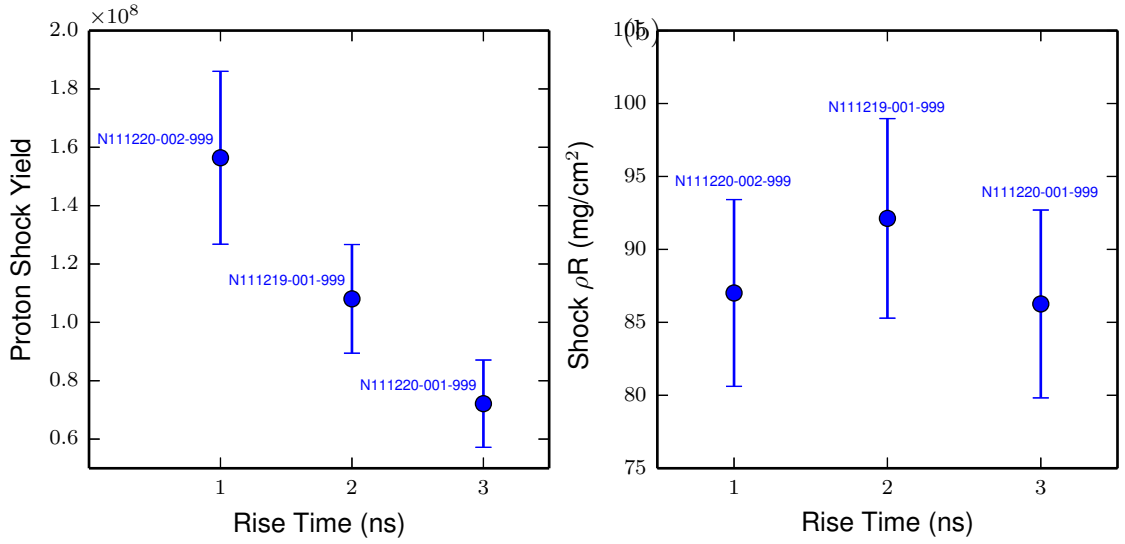

Figure 3.7. Shock yield (a) and ρR (b) versus rise time for a set of three shots where only the rise time was varied.

First, the interpretation of the shock-yield data can be aided by a set of three shots conducted

in which only the rise time was varied. This data is shown in Fig. 3.7a. The faster rise pulse shapes clearly create higher shock yields. This is consistent with the data in Fig. 3.6f.

Conversely, the coast time (Fig. 3.6e) has no clear effect on the shock yield, since short- and long- coast times have data with both high- and low- shock yield.

For the peak power, the data in Fig. 3.6d suggests a trend, where lower peak power creates a weaker shock. This is intuitive and consistent with the fact that all low power ($\lesssim$ 300 TW) shots have low yield, but at higher power the shock yield displays significant variation.

We conclude that the faster-rise pulses create shock yields $2-3\times$ higher (Fig 3.6f and 3.7) with other variables constant, and that increasing the peak power may increase the shock yield. We note that the shock yield varies by approximately $15\times$ over the dataset, indicating substantial variation in shock strength.

3.5.2 ρR interpretation

Two shots that do not fit into the overall implosion parameter grouping are essential to understanding the data: N120409, which was a high-power short-coast shot, and N130213 which was a low-power long-coast shot. These two are specifically annotated in Fig. 3.5a and Fig. 3.6a-b.

Fig. 3.6a plots the shock ρR versus effective peak power. Neglecting the results from shots N120409 and N130213, the data show an anti-correlated trend between ρR and peak power. However, shots N120409 and N130213 clearly suggest that this trend is due to the preponderance of high-power long-coast and low-power short-coast implosions. For the coasting, a clear trend is observed in Fig. 3.6b, including both N120409 and N130213 where large coast times generate significantly lower shock ρR than short-coast implosions.

In Fig. 3.7 the set of three shots with a controlled rise time show no change in shock ρR as the rise time is varied. This demonstrates that the rise time has no effect on the shock ρR; the apparent trend in Fig. 3.6c is due to the low coasting times in the 3ns rise implosions.

3.5.3 Estimated shock-bang time

The dependence between shock ρR and coast time can be further investigated. Fundamentally, the ρR is mainly determined by the shell R_{cm} at the shock-bang time (see Section 2.5).

On many of these shots, simultaneous x-ray radiographs of the implosion trajectory were obtained[4,5,33], and from the x-ray radiographs, $R_{cm}(t)$ is determined near the shock-bang time. Presently the shock-bang time is not directly measured, but the combination of the trajectory measurement and WRF-inferred R_{cm} from shock-produced protons can be used to estimate the shock-bang time. This technique is shown in Fig. 3.8.

From the x-ray data we know the shell velocity at $R_{cm} = 200$ or 300 μm. The absolute timing uncertainty of the x-ray measurement relative to compression bang time is $\pm$50 ps. We know that the compression-bang time uncertainty is typically $\pm$50 ps or better. From this information, combined with the x-ray and proton data, a shock-bang time can be determined relative to compression-bang time: $\Delta_{BT} \equiv t_{shock} - t_{comp}$, to remove any variation in absolute implosion timing. The uncertainty in R_{cm} from this analysis is used to determine the uncertainty in the shock-bang time in addition to the uncertainty in timing of the x-ray measurement and shell velocity.

The shock-bang time is estimated for a set of 14 experiments (a subset of Fig. 3.6) where x-ray radiography is available, and shown in Fig. 3.9. The estimated bang time difference ranges from $\sim 0.4 - 0.8$ ns. The displayed error bars represent random (shot-to-shot) uncertainties, while the larger systematic uncertainty is $\pm$0.11ns.

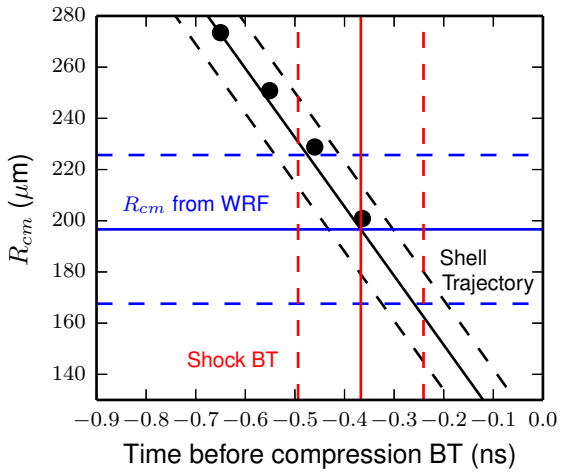

Figure 3.8. R_{cm} versus time before compression-bang time for shot N120408-001-999. As the shell trajectory (black) and R_{cm} (blue) are determined from x-ray radiography and WRF proton spectroscopy, respectively, the shock-bang time (red) can be estimated. Error bars are shown by dashed lines. For this shot, $\Delta_{BT} = 0.34 \pm 0.13$ ns.

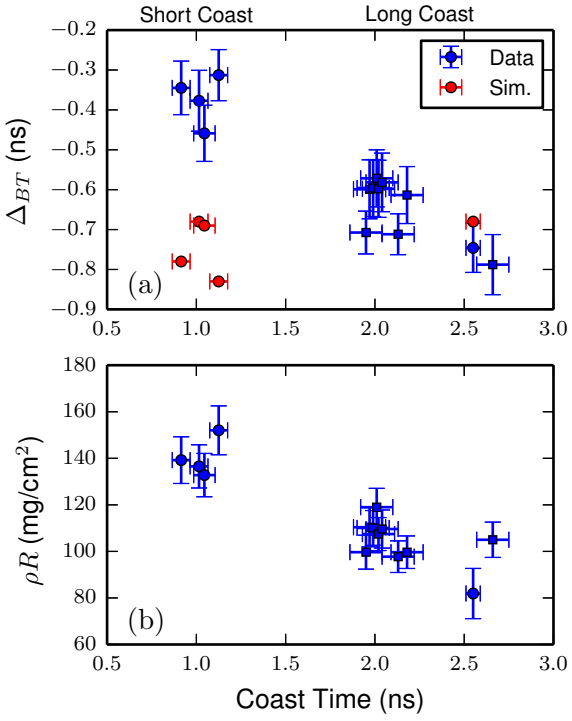

Figure 3.9. **(a)** Estimated difference in time between shock and compression bang, contrasted to simulations, for 2DConA (square) and ConA (round) implosions, which were also probed with in-flight x-ray radiography. The two points at coasting time ~ 2.5ns show good agreement between the two experimental platforms. Uncertainties are random, with an additional ± 0.11ns systematic uncertainty. **(b)** ρR data for the same shots versus coast time. Higher ρR corresponds to higher convergence and thus smaller Δ_{BT}.

For this data, a clear trend is shown where the long-coast implosions have substantially larger differential bang time (more negative Δ_{BT}) than the short-coast shots.

Simulations of Δ_{BT} exist for five of these shots (one of which, N120408-001-999, was simulated and presented earlier in Fig. 3.1; these simulations are also shown in Fig. 3.9. The simulations predict a nearly constant Δ_{BT} of $\sim -(0.7-0.8)$ns while the data show a clear trend where long-coast implosions have a larger differential bang time.

3.6 Interpretation

3.6.1 Coasting

The data indicate that the shock-bang time occurs earlier relative to the main compression burn in long-coast implosions than in short-coast implosions. The interpretation of this observation is that the imploding shell is at a larger radius (R_{cm}) during the shock bang for the long-coast implosions. This means that the final rebounding shock, which creates the shock bang, is either faster relative to the implosion velocity or launched earlier for the long-coast pulses.

The shock transit time in the gas (after break-out from the shell) is $\sim$ 4ns according to HYDRA simulations (see Fig. 3.1a). This can also be estimated using simple models. For example, using the Hugoniot conditions, a shock launched by 100 MBar of pressure at the ablation front propagates through the pre-compressed shell in approximately 450ps. This shock propagates through the density discontinuity at the inner surface of the shell[34] and spherically converges as a Guderley shock[21] through the initial gas, which takes an additional $\sim$ 4.1 ns. However, at the time when the shock is launched into the gas, the sound speed in the shell $c = \sqrt{\gamma P/\rho}$ is quite low. For an ideal gas at 100MBar pressure and density of $\rho = 20$ g/cc, the speed of sound is only ~ 30 μm/ns (in the frame of the imploding shell). But since the inward shell fluid velocity at shock breakout is ~ 60 μm/ns and the shock velocity in the lab frame is ~ 150 μm/ns, the shock is already effectively decoupled from the driving piston of the ablation front. The coasting dynamics happen later in time and thus cannot directly affect the shock strength in this scenario.

The late-time drive will affect the implosion (shell) trajectory. If the implosion comes in late relative to the shock, the bang-time differential will increase. This could occur, for instance, due to in-flight decompression and deceleration of the shell if the ablation pressure decreases while the shell is still at a large radius. Since the data and simulations are discrepant for the short-coast implosions, this suggests that the late-time drive (during the last ns) is not well modeled in the simulation. This could be related to the drive degradation multipliers[‡] not accurately reflecting the late-time drive, an uncertainty in radiation transport through the ablated shell material, or an uncertainty in the compressed ablator equation of state. Another possibility is that severe mix in the coasting implosions may truncate the compression burn, moving the apparent compression bang time earlier and decreasing Δ_{BT}.

One potential significance of an earlier shock-bang time is its implications for the deceleration phase of the implosion. Deceleration begins when the rebounding shock (as a heat wave) encounters the incoming shell. The rebound phase can also be calculated using Guderley's solution[21]. For a constant shock strength, an earlier shock-bang time means that the rebounding shock will hit the incoming shell at an earlier time (larger radius) and thus deceleration will begin earlier. This could reduce the compression and final ρR of the implosion. Interestingly, data in cryogenic implosions

[‡]For simulations of NIF low-adiabat implosions to match the data, in particular the shock timing, implosion trajectory (r vs t), and bang time, multipliers must be applied throughout the pulse to decrease the effective drive on the implosion by a time-varying fraction[35,5].

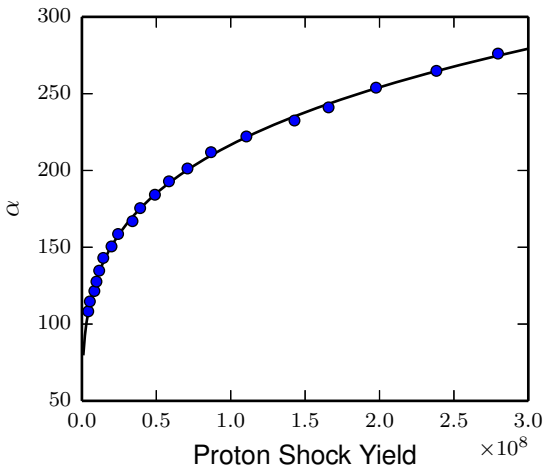

Figure 3.10. Inferred hot-spot adiabat (α) versus proton shock yield using a Guderley model. Points are at values of ξ from $250 - 350$ (at intervals of 5) μm/ns$^{0.688}$. The solid curve is a power-law fit (see Eq. 3.2).

show $25 - 50\%$ higher ρR and higher inferred stagnation pressure for short-coast implosions[36,32]. This is consistent with this work's interpretation of the short-coast implosions where the shock dynamics is more amenable to high compression, i.e. later shock-bang time relative to compression.

3.6.2 Hot-spot adiabat

The significance of large variation in shock proton yield can be interpreted in the context of the shock dynamics and hot-spot adiabat. The initial heating of the low-density material at the center of the implosion is from the imploding and rebounding shock, which sets the incipient hot-spot adiabat prior to the onset of deceleration and subsequent PdV heating of the hot spot. The hot-spot adiabat can be roughly characterized as the ratio of its pressure to the Fermi pressure:

$$\alpha \equiv \frac{P}{P_f} = \frac{n_e k_B T_e + n_i k_B T_i}{\frac{(3\pi^2)^{2/3}\hbar^2}{5m_e} n_e^{5/3}}. \tag{3.1}$$

The shock preferentially heats ions over electrons[13] and in this Guderley model they are assumed to be uncoupled (τ_{ei} long compared to dynamical timescales)[37].

We can interpret the shock proton yield via a simple model based on the Gudelery spherically-imploding shock solution[21,13]. The Guderley model gives hydrodynamic profiles in a self-similar solution as a function of a single shock strength parameter, ξ. For a single choice of ξ, the D^{3}He yield (Y) is calculated from:

$$Y = \int f_D f_{3He} n_i^2 \langle \sigma v \rangle \; d^3 r dt, \tag{3.2}$$

where f_D and f_{3He} are the fuel ion fractions and $\langle \sigma v \rangle$ is the temperature-dependent fusion reactivity. A mass-weighted hot-spot adiabat is also calculated via Eq. 3.1, evaluated when the rebounding shock encounters the incoming shell material. The shock strength ξ is then varied to map out a relationship between the proton shock yield and hot-spot adiabat, and this relationship is well described by a power law:

$$\alpha = 2.10 Y^{0.247} + 16.4, \tag{3.3}$$

where the coefficients are from a fit to the model results. This relation is shown in Fig. 3.10.

Using this model, the adiabat can be determined from the yield and thus rise time (see Fig. 3.11). The hot-spot adiabat increases for faster rise times due to a stronger launched shock.

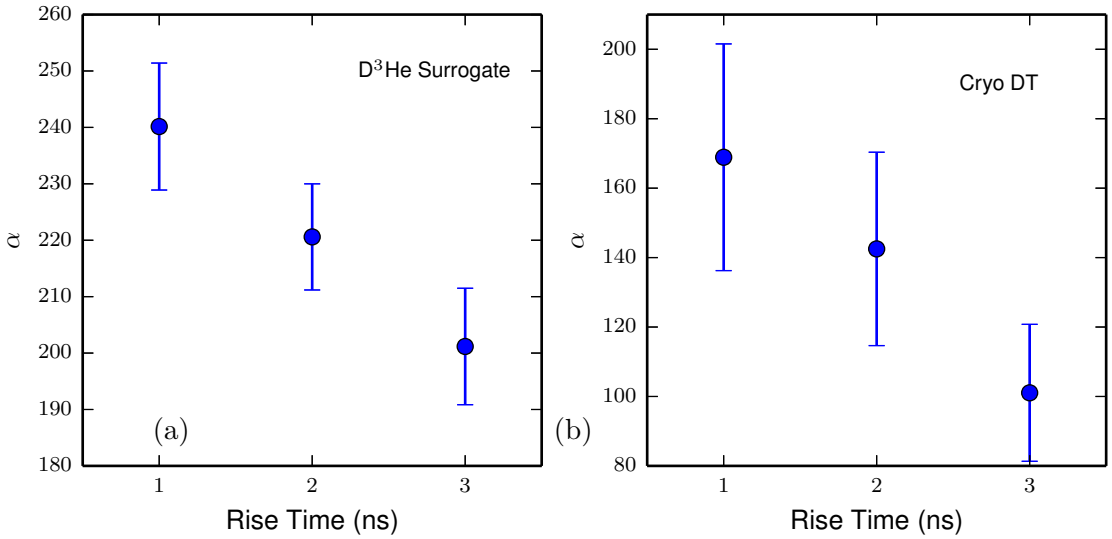

Figure 3.11. (a) Modeled adiabat versus rise time for the same dataset as shown in Fig.**??**. **(b)** Modeled hot-spot adiabat in cryogenic implosions.

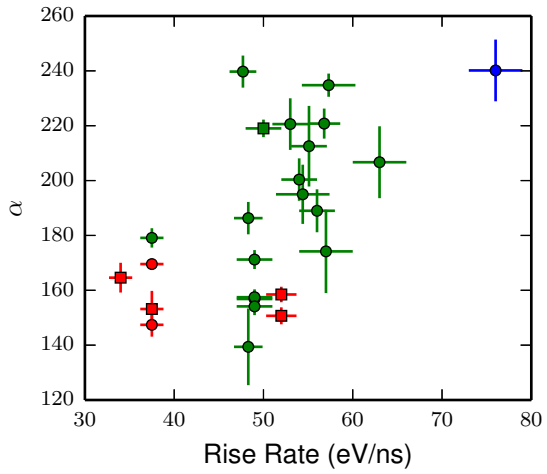

Figure 3.12. Modeled adiabat versus rise rate for the same dataset as Fig.3.6d-f.

This empirical result can be compared qualitatively to modeled hot-spot adiabats[38] for cryogenic implosions[39,32], in which a very similar trend is seen where α increases from ~ 100 to ~ 160 as the rise time decreases from 3 to 1 ns. The absolute values of α inferred for these surrogate implosions are expected to be higher than cryogenic implosions, since ablation of low-adiabat ice material in the latter decreases the hot-spot adiabat. Further modeling is required to directly relate surrogate hot-spot adiabat to cryogenic hot-spot adiabat, but this is motivated by the lack of any other direct measurement of the hot-spot adiabat. Additionally, 3-D effects are expected to alter the inferred hot-spot adiabat in cryogenic experiments, so a better understanding of the incipient adiabat and hot-spot formation process may increase our understanding of these 3-D effects.

Inferred values of α as a function of measured radiation-temperature rise rate are shown for the 30 downselected shots used in Fig. 3.12, analogous to Fig. 59 of Ref. 32. The factor of $10\times$ variation in shock proton yield corresponds to $\sim 75\%$ variation in α, as seen from the power 0.247 in Eq. 3.2. For the entire dataset (Fig. 3.4), a $35\times$ min-max variation in shock yield is observed,

corresponding to a $\sim 2.4\times$ variation in α.

3.6.3 Kinetic Effects

The overall shock dynamics may be significantly affected by kinetic effects. For example, recent OMEGA experiments have shown experimental evidence for long ion-ion mean-free-path effects[22], enhanced diffusive mix[23], and temperature anomalies in shock-heated plasmas[40]. Relative to the OMEGA experiments of Refs 22,23,40, in these experiments the initial gas density is $\sim 2\times$ higher and the shock is weaker; at similar initial density to this work, an indirect-drive exploding pusher on NIF showed excellent agreement with simulation, suggesting a lack of kinetic effects[41]. Further experiments and computational studies are needed to assess whether kinetic effects could be playing a role in these observed anomalies in the NIF low-adiabat implosion shock dynamics.

3.7 Summary

The shock dynamics of surrogate implosions at the NIF have been studied. From proton spectroscopy the shock ρR, proton yield, and shell radius at shock-bang time are determined using a simple self-consistent 1-D implosion model. The shock ρR data show dependence on the coasting time of the implosion, with short-coast implosions having higher shock ρR. The proton shock yield data show a clear dependence on the laser-pulse rise time, and possibly peak power. Using the inferred center-of-mass radius and in-flight x-ray radiography, a shock-bang time is estimated. The short-coast implosions are observed to have significantly smaller differences between the shock- and compression-bang times than the long-coast implosions. This could be due to uncertainties in modeling the late-time drive on the capsule, which is the primary difference between short- and long-coast experiments. An earlier shock-bang time in long-coast implosions could reduce compressibility due to an earlier onset of deceleration; in cryogenic implosions lower compression ρR is measured in long-coast implosions. Further, the large variation in shock yield indicates a variation in post-shock temperature and thus adiabat of the incipient hot-spot material. A model is introduced to relate the proton shock yield to adiabat; this analysis suggests an increase in hot-spot adiabat of up to $2\times$ in fast-rise implosions, potentially reducing compressibility.

Future campaigns could be conducted to more systematically study the effect of coasting time, rise time, and peak power on shock dynamics, or to study the effect of hohlraum material (not addressed in this work). Implementation of a diagnostic for direct measurements of the shock-bang time, which is in progress[42], will be a direct and higher-precision diagnostic of the differential bang time. This new diagnostic will be used to further investigate the discrepancy observed in this work between the model-inferred differential bang time and radiation-hydrodynamics simulations (Fig. 3.9). The potential impact of kinetic effects on these observations should be studied with dedicated experiments (e.g. varying the gas fill density) and kinetic simulations. Accurate modeling of the shock phase in ignition experiments essentially sets the initial conditions for hot-spot formation. The observed inaccuracies in standard hydrodynamic models for the surrogate implosions strongly suggest that the ignition experiments are not being accurately modeled.

3.8 References

1. O. Landen *et al.*, "Capsule performance optimization in the National Ignition Campaign," Physics of Plasmas, **17**, 056,301 (2010).
2. G. Kyrala, S. Dixit, S. Glenzer *et al.*, "Measuring symmetry of implosions in cryogenic Hohlraums at the NIF using gated x-ray detectors," Rev. Sci. Instrum., **81**, 10E316 (2010).
3. G. Kyrala *et al.*, "Symmetry tuning for ignition capsules via the symcap technique," Physics of Plasmas, **18**, 056,307 (2011).

4. D. Hicks, B. Spears, D. Braun *et al.*, "Convergent ablator performance measurements," Physics of Plasmas, **17**, 102,703 (2010).
5. D. Hicks *et al.*, "Implosion dynamics measurements at the National Ignition Facility," Phys. Plasmas, **19**, 122702 (2012).
6. G. Zimmerman and W. Kruer, "Comments plasma phys," Controlled Fusion, **2**(2), 51–61 (1975).
7. S. W. Haan *et al.*, "Design and modeling of ignition targets for the National Ignition Facility," Phys. Plasmas, **2**, 2480 (1995).
8. M. Marinak, G. Kerbel, N. Gentile *et al.*, "Three-dimensional HYDRA simulations of National Ignition Facility targets," Physics of Plasmas, **8**, 2275 (2001).
9. D. Hicks, *Charged-particle spectroscopy: a new window on inertial confinement fusion*, Ph.D. thesis, Massachusetts Institute of Technology (1999).
10. R. Petrasso *et al.*, "Measuring Implosion Dynamics through ρR Evolution in Inertial-Confinement Fusion Experiments," Physical Review Letters, **90**(9), 95,002 (2003).
11. C. K. Li, F. H. Séguin, J. A. Frenje *et al.*, "Capsule-areal-density asymmetries inferred from 14.7-MeV deuterium-helium protons in direct-drive OMEGA implosions," Physics of Plasmas, **10**(5), 1919–1924 (2003).
12. J. A. Frenje, C. K. Li, F. H. Seguin *et al.*, "Measuring shock-bang timing and rho R evolution of D^3He implosions at OMEGA," Physics of Plasmas, **11**(5), 2798–2805 (2004).
13. J. R. Rygg, *Shock Convergence and Mix Dynamics in Inertial Confinement Fusion*, Ph.D. thesis, Massachusetts Institute of Technology (2006).
14. T. Boehly, D. Brown, R. Craxton *et al.*, "Initial performance results of the OMEGA laser system," Optics Communications, **133**(1-6), 495–506 (1997).
15. A. Zylstra, J. Frenje, F. Séguin *et al.*, "A new model to account for track overlap in cr-39 data," Nuclear Instruments and Methods in Physics Research Section A: Accelerators, Spectrometers, Detectors and Associated Equipment, **681**(0), 84 – 90 (2012).
16. P. M. Celliers, D. K. Bradley, G. W. Collins *et al.*, "Line-imaging velocimeter for shock diagnostics at the omega laser facility," Review of Scientific Instruments, **75**(11), 4916–4929 (2004).
17. H. Robey *et al.*, "Precision Shock Tuning on the National Ignition Facility," Phys. Rev. Lett., **108**, 215004 (2012).
18. H. F. Robey, J. D. Moody, P. M. Celliers *et al.*, "Measurement of High-Pressure Shock Waves in Cryogenic Deuterium-Tritium Ice Layered Capsule Implosions on NIF," Phys. Rev. Lett., **111**, 065,003 (2013).
19. J. D. Moody, D. A. Callahan, D. E. Hinkel *et al.*, "Progress in hohlraum physics for the National Ignition Facility," Physics of Plasmas, **21**(5), 056317 (2014).
20. R. P. J. Town, D. K. Bradley, A. Kritcher *et al.*, "Dynamic symmetry of indirectly driven inertial confinement fusion capsules on the national ignition facility," Physics of Plasmas, **21**(5), 056313 (2014).
21. G. Guderley, "Powerful spherical and cylindrical compression shocks in the neighborhood of the center of the sphere and of the cylinder axis," Luftfahrtforsch, **19**, 302–312 (1942).
22. M. Rosenberg, H. Rinderknecht, N. Hoffman *et al.*, "Exploration of the Transition from the Hydrodynamiclike to the Strongly Kinetic Regime in Shock-Driven Implosions," Phys. Rev. Lett., **112**, 185,001 (2014).
23. H. Rinderknecht, H. Sio, C. Li *et al.*, "First Observations of Nonhydrodynamic Mix at the Fuel-Shell Interface in Shock-Driven Inertial Confinement Implosions," Phys. Rev. Lett., **112**, 135,001 (2014).
24. C. Li and R. Petrasso, "Charged-particle stopping powers in Inertial Confinement Fusion Plasmas," Phys. Rev. Lett., **70**(20), 3059 (1993).
25. N. Sinenian, M.-E. Manuel, A. Zylstra *et al.*, "Upgrade of the MIT Linear Electrostatic Ion Accelerator (LEIA) for nuclear diagnostics development for Omega, Z and the NIF," Rev. Sci. Instrum., **83**(4), 043502 (2012).
26. F. H. Séguin, J. A. Frenje, C. K. Li *et al.*, "Spectrometry of charged particles from inertial-confinement-fusion plasmas," Rev. Sci. Instrum., **74**(2), 975–995 (2003).
27. F. H. Séguin, N. Sinenian, M. Rosenberg *et al.*, "Advances in compact proton spectrometers for inertial-confinement fusion and plasma nuclear science," Rev. Sci. Instrum., **83**(10), 10D908 (2012).
28. W. J. Hibbard, M. D. Landon, M. D. Vergino *et al.*, "Design of the National Ignition Facility diagnostic instrument manipulator," Rev. Sci. Instrum., **72**(1), 530–532 (2001).

29. C. Li, F. Séguin, J. Frenje *et al.*, "Observations of electromagnetic fields and plasma flow in hohlraums with proton radiography," Physical review letters, **102**(20), 205001 (2009).
30. C. Li, F. Séguin, J. Frenje *et al.*, "Charged-Particle Probing of X-ray–Driven Inertial-Fusion Implosions," Science, **327**(5970), 1231 (2010).
31. C. K. Li, A. B. Zylstra, J. A. Frenje *et al.*, "Observation of strong electromagnetic fields around laser-entrance holes of ignition-scale hohlraums in inertial-confinement fusion experiments at the National Ignition Facility," New Journal of Physics, **15**(2), 025,040 (2013).
32. J. Lindl, O. Landen, J. Edwards *et al.*, "Review of the National Ignition Campaign 2009-2012," Phys. Plasmas, **21**, 020501 (2014).
33. J. Rygg, O. Jones, J. Field *et al.*, "2D X-Ray Radiography of Imploding Capsules at the National Ignition Facility," Phys. Rev. Lett., **112**, 195001 (2014).
34. R. Drake, *High-Energy-Density Physics* (Springer, 2006).
35. O. S. Jones, C. J. Cerjan, M. M. Marinak *et al.*, "A high-resolution integrated model of the national ignition campaign cryogenic layered experimentsa)," Physics of Plasmas, **19**(5), 056,315 (2012).
36. M. Edwards *et al.*, "Progress towards ignition on the National Ignition Facility," Phys. Plasmas, **20**, 070501 (2013).
37. J. R. Rygg, J. A. Frenje, C. K. Li *et al.*, "Electron-ion thermal equilibration after spherical shock collapse," Phys. Rev. E, **80**, 026,403 (2009).
38. C. Cerjan, P. T. Springer and S. M. Sepke, "Integrated diagnostic analysis of inertial confinement fusion capsule performance," Physics of Plasmas, **20**(5), 056,319 (2013).
39. Springer, P.T., Cerjan, C., Betti, R. *et al.*, "Integrated thermodynamic model for ignition target performance," EPJ Web of Conferences, **59**, 04,001 (2013).
40. H. G. Rinderknecht, J. Rosenberg, M. K. Li, C. *et al.*, "Ion thermal decoupling and species separation in shock-driven implosions," Phys. Rev. Lett., **114**, 025,001 (2015).
41. S. Le Pape, L. Divol, L. Berzak Hopkins *et al.*, "Observation of a reflected shock in an indirectly driven spherical implosion at the national ignition facility," Phys. Rev. Lett., **112**, 225,002 (2014).
42. H. G. Rinderknecht, M. G. Johnson, A. B. Zylstra *et al.*, "A novel particle time of flight diagnostic for measurements of shock- and compression-bang times in d3he and dt implosions at the nifa)," Review of Scientific Instruments, **83**(10), 10D902 (2012).

4

Low-mode ρR asymmetries in NIF implosions

Ignition experiments at NIF must control the cold-fuel symmetry to better than several percent at stagnation[1–3]. In indirect-drive implosions conducted at the NIF, radiation drive non-uniformities can cause detrimental low-mode ($\lesssim 8$) asymmetries[4,5], the focus of this work.

Several techniques are used to study asymmetry at the NIF; in this paper we present the first charged-particle measurements of areal-density (ρR) asymmetries at the shock-bang time in ignition-scale implosions. These measurements are novel in quantifying ρR asymmetries that are present when the implosion is in-flight, at $CR \sim 3-5$, complementing prior methods at different CR. It is comparable to recently-developed in-flight radiography of the imploding shell[6], which can be used simultaneously with the charged-particle diagnostics. Other techniques for diagnosing symmetry include 'Re-Emit' experiments that measure x-ray re-emission from a high-Z capsule to diagnose early-time ($CR \sim 1$) hohlraum drive asymmetries[7,8] and shock-timing experiments that use multiple views to diagnose early-time shock symmetry[9,10]. In addition, x-ray self-emission produced by the implosion at stagnation is imaged to diagnose the final hot-spot symmetry in lower-convergence ($CR \sim 15-20$) surrogate implosions[11]. In cryogenic implosions, the final stagnated hot-spot and cold-fuel shapes are diagnosed by x-ray[12] and neutron[13] imaging techniques.

Charged-particle measurements of ρR asymmetries have previously been used at the OMEGA laser facility[14] for spherically symmetric direct-drive implosions[15,16] and direct-drive implosions with induced asymmetries[17]. Extending this technique to NIF has been discussed[18]. The D^3He reaction (Eq. 1.15) is used. The high-energy proton escapes implosions with $\rho R \lesssim 300$ mg/cm^2. This limit is set by the charged-particle stopping power in plasmas[19]. During an implosion, a strong shock wave runs ahead of the imploding shell and rebounds at the origin several hundred ps before the main compression phase, creating densities and temperatures high enough for a brief period of fusion burn (shock bang)[20,21] that produces protons via Eq. 1.15. Recent work has inferred a shock-compression bang-time differential of $400-800$ ps for these implosions, as discussed in Chapter 3, which will be measured more precisely in the future[22].

For the implosions[11,23] studied at the NIF, surrogate* CH capsules filled with D_2 and ^{3}He gas converge to $R \sim 200-300\mu$m by the shock bang time (compared to an initial inner radius of $\sim 900\mu$m), at which point the total ρR has reached $\sim 60-120$ mg/cm^2. During the main compression burn, ρR $\gg 300$ mg/cm^2, so the D^3He-p are ranged out.

The protons are measured with the WRF spectrometers (see Refs. 24–26 and Chapter 2). Multiple spectrometers are fielded in the (0,0) polar DIM[27] and in an equatorial DIM, (90,78), as shown in Fig. 4.1. Each WRF spectrometer is a 5cm diameter 'can', with an active area

*The cryogenic DT ice layer of an ignition target is replaced with an equivalent mass of ablator material. The implosion dynamics are equivalent until deceleration and stagnation

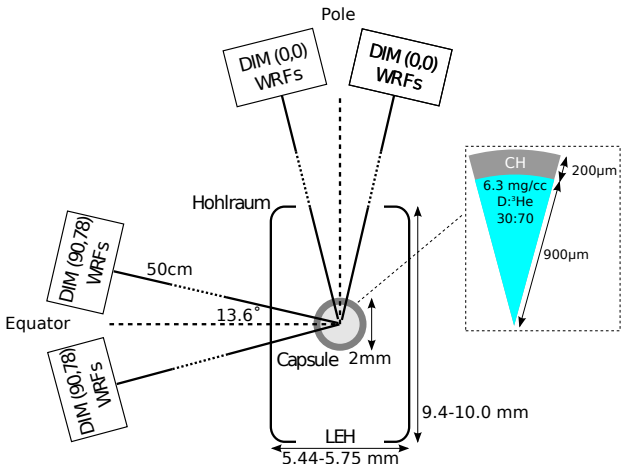

Figure 4.1. WRF proton spectrometer setup for measurements of the D^{3}He-p spectrum in different directions at the NIF. Polar and equatorial WRFs have the same distance (50cm) and displacement from the DIM axis ($\pm 13.6°$). Typical capsule dimensions shown at right, the plastic shell ($\rho = 1.08$ g/cm^3) is filled with a 30:70 atomic mixture of D and ^{3}He fuel.

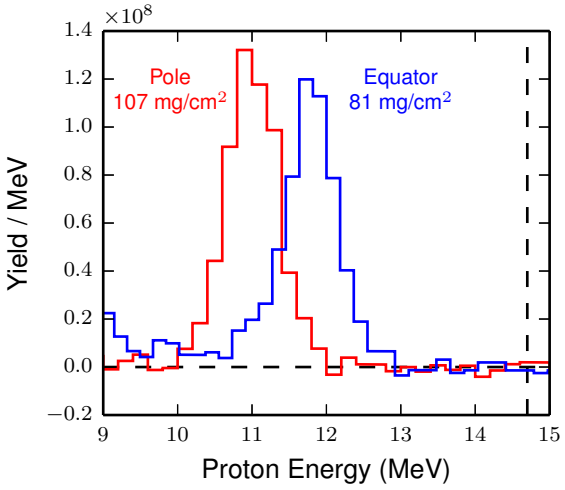

Figure 4.2. Sample WRF proton spectra from NIF shot N101218 on the pole (red) and equator (blue, after hohlraum wall correction). The D^{3}He-p birth energy of 14.7 MeV is also shown (vertical dashed line). From the downshift of the measured spectra, ρR values of $107 \pm 2_{ran} \pm 6_{sys}$ mg/cm^2 (pole) and $81 \pm 2_{ran} \pm 6_{sys}$ mg/cm^2 (equator) were inferred.

approximately 2 × 2 cm, placed 50 cm from target-chamber center (TCC). WRFs in the polar DIM view the implosion through the laser entrance hole (LEH). The equatorial WRFs measure protons through the hohlraum wall which causes additional downshift; the results are corrected for this energy loss in the wall using cold-matter stopping powers[28] and known material thicknesses [†]. Other materials, such as the capsule 'tent' and hohlraum gas fill, are negligible[‡]. One or two spectrometers can be fielded at a displacement of ±13.6° from the axis for both DIMs.

In these surrogate NIF implosions, differences in the mean shock proton energy between the polar and hohlraum-corrected equatorial spectra are routinely observed. Fig. 4.2 shows spectra measured on the pole and equator for shot N101218, which had a large asymmetry induced by a known capsule offset. On this shot the polar WRF measured a lower shock proton energy, thus the polar ρR is higher: 107 mg/cm^2 versus 81 on the equator, for a difference $\Delta\rho R$ of 26 mg/cm^2.

These spectral differences in the polar and equatorial spectrometry data cannot be attributed to electromagnetic fields. First, prior work has demonstrated that electric fields generated in indirect-drive targets decay early within the laser drive(Ref 29 and Appendix E), while this data is obtained after the laser is turned off. Transverse magnetic fields exist near the laser-entrance hole[30] for these implosions; the magnetic fields cause asymmetries in proton flux but do not affect the proton mean energy and thus the inferred ρR and shell R_{cm} are unaffected. The spectral differences must be caused by differences in the energy slowing of the protons exiting the implosion, and thus in the implosion ρR.

4.1 Extension of the Implosion Model to 2- and 3-D

A simple extension of the implosion model (see Chapter 3) to 2- and 3-D is essential for analysis of asymmetries observed between multiple detectors in these implosions. An asymmetry is modeled as Legendre modes in the shape of the imploding shell:

$$R_{cm}(\theta,\phi) = \bar{R}\left[1 + \Delta \times \sqrt{\frac{2\ell+1}{4\pi}\frac{(\ell-m)!}{(\ell+m)!}}e^{im\phi}P_\ell^m(\cos\theta)\right], \tag{4.1}$$

where θ and ϕ are the polar and azimuthal angles, respectively, $\bar{R}$ is the unperturbed shell radius, Δ is the fractional asymmetry amplitude, and P_ℓ^m is an associated Legendre polynomial.

From the 1-D model presented in this paper, we have $\rho R(R_{cm})$. Areal density asymmetries in 2- or 3-D can thus be modeled as the convolution of $R_{cm}(\theta,\phi)$ and $\rho R(R_{cm})$ giving $\rho R(\theta,\phi,\bar{R},\Delta,\ell,m)$. The data points, each with their own coordinates (θ,ϕ), are then be fit using this convolution, where Δ and $\bar{R}$ are free parameters and ℓ, m are chosen.

An example of this analysis is shown in Fig. 4.3 for shot N101218-002-999. In this case a P_2 mode is assumed ($\ell = 2$, $m = 0$). The best fit parameters are $\bar{R} = 250 \pm 2\mu$m and $\Delta = -0.21 \pm 0.02$. The error bars are due to random/statistical errors only, excluding systematic detector calibration uncertainties and model uncertainties.

For the ConA2D implosions (see next section) in-flight 2-D x-ray radiography is used to measure the symmetry. Unfortunately the radiography requires large patches on the hohlraum wall, which induce a known $m = 2$ azimuthal asymmetry. This asymmetry is roughly aligned with the WRF

[†]Total correction is $\sim 1.5 - 2$ MeV. Uncertainty in the material thickness leads to an additional error of ± 50 to 75 keV in the total energy uncertainty.

[‡]The tent material is plastic with a thickness $\lesssim$ 100nm, which the protons traverse nearly normally, so the areal density is $\ll 1$ mg/cm^2. The hohlraum gas material has a density ~ 1 mg/cm^3 with scale lengths of a few mm, so the areal density < 1 mg/cm^2.

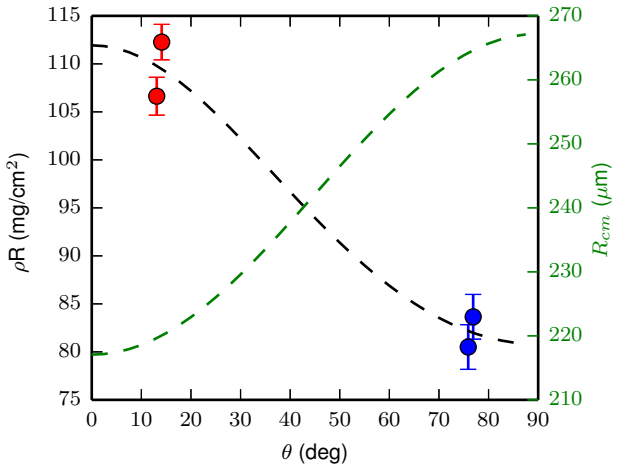

Figure 4.3. ρR asymmetry analysis ($\ell = 2, m = 0$) for shot N101218-002-999, which had an usually large observed asymmetry. The polar (red) and equatorial (blue) data are shown with random/statistical errors only. The fit is shown as $\rho R(\theta)$ and $R_{cm}(\theta)$ (right axis).

equatorial line of sight, leading to an unconstrained problem between the modes $\ell = 2$ and $m = 2$ plus modes such as $\ell = 4$. To address this issue we use the radiography-measured mode amplitudes for the $\ell = 2$ and $\ell = 4$ and fit the amplitude of the $m = 2$ mode:

$$\begin{aligned} R_{cm}(\theta,\phi) &= \bar{R}\left[1 + \Delta_{m=2}\sin\theta\cos(2\phi+\phi_0)\right. \\ &+ \Delta_{\ell=2}\times\sqrt{\frac{5}{4\pi}}P_2^0(\cos\theta) \\ &+ \left.\Delta_{\ell=4}\times\sqrt{\frac{9}{4\pi}}P_4^0(\cos\theta)\right], \end{aligned} \tag{4.2}$$

where $\Delta_{m=2}$ is the free parameter and ϕ_0 is taken as aligned with the equatorial line of sight (78°). The polar amplitudes $\Delta_{\ell=2}$ and $\Delta_{\ell=4}$ are determined from x-ray radiography.

4.2 Low-mode analysis

Multiple proton measurements of R_{cm} at various θ, ϕ are then fit with the functional form for $R_{\rm cm}(\theta,\phi)$ (Eq. 4.1)[§]. Since the asymmetries are manifested as a relative difference between the measurements, only 'random' or statistical uncertainties are retained in this analysis. The polar-equatorial geometry would suggest the assumption of a $\ell = 2, m = 0$ mode asymmetry. However, with limited WRF lines of sight we cannot differentiate between various modes. For instance, in Fig. 4.4 the difference in ρR between the polar and equatorial WRFs for assumed polar ($m = 0$) modes with $\ell = 1, 2, 3, 4$ are plotted. Modes 2 and 4 are known to be prevalent in these NIF implosions[6], and the potential for deleterious mode 1 asymmetries has been recognized[31,32].

[§]For the low modes considered, the variations are much larger than the detector solid angle ($\sim 1°$ subtended) so using a local value of $R_{cm}(\theta,\phi)$ and thus $\rho R(\theta,\phi)$ is a good approximation.

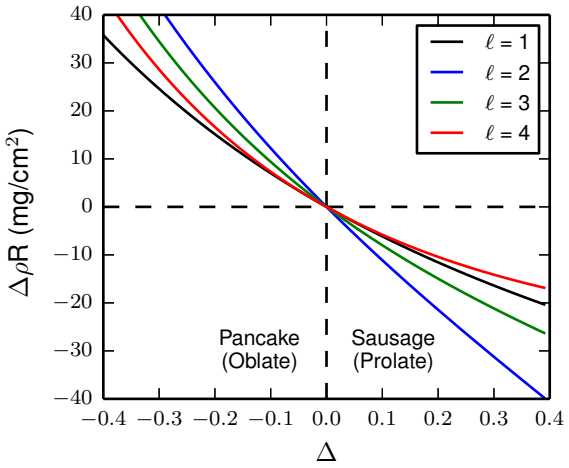

Figure 4.4. Observable ρR asymmetry (pole − equator) versus mode perturbation amplitude Δ for $m = 0$ modes with $\ell = 1, 2, 3, 4$ with the shell average $\bar{R} = 250\mu$m (average $\rho R = 89$ mg/cm^2) corresponding to N101218. For a given perturbation Δ, a $\ell = 2$ mode (blue curve) causes the largest observable asymmetry.

For a given Δ, the observable difference in ρR is maximized if the mode is a P_2 (i.e. $\ell = 2, m = 0$). Fig. 4.4 shows that this technique is half as sensitive to modes $\ell = 1, 3, 4$ with the current detector geometry (Fig. 4.1). While we cannot differentiate between a $\ell = 2$ mode and a $\ell = 1$ mode with twice the perturbation amplitude, due to the limited diagnostic lines of sight[¶], for a difference in ρR between pole and equator this work assumes a $\ell = 2$ mode, which minimizes the inferred Δ. The asymmetry amplitude Δ is plotted for all shots in this work in Fig. 4.5, with 1σ error bars.

The asymmetry amplitude Δ is plotted for all shots in this work in Fig. 4.5, with 1σ error bars. The ρR asymmetries do not have systematic direction, i.e. approximately the same number of shots have a higher polar ρR (negative Δ) as the number of shots with higher equator ρR (positive Δ). Only $20 - 30\%$ of the shots are consistent within error bars with a symmetric ($\Delta = 0$) implosion.

We can compare this work to compression x-ray self-emission imaging[33,11] at $CR \sim 20$. The dataset plotted in Fig. 4.5 is reduced to experiments with very good stagnation azimuthal symmetry as measured by polar-view x-ray imaging ($m_2/m_0 < 10\%$ and $m_4/m_0 < 15\%$) to reduce effects of m modes, and with a small polar mode-4 asymmetry ($P_4/P_0 < 15\%$). For shots satisfying these cuts, the assumption of a P_2-dominated asymmetry in our measurement is valid. In Fig. 4.5, these shots are denoted by the square markers. The ρR P_2 data are compared directly to the stagnation x-ray symmetry measurement in Fig. 4.6. As the x-ray metric is generally referred to in literature as P_2/P_0, we follow that convention here; for the WRF measurement this is equivalent to Δ in Fig. 4.5.

In the data we see a positive correlation between the $\ell = 2$ mode amplitude inferred from the shock ρR and the stagnation x-ray emission shape. A linear fit to the data provides a slope of 0.6 ± 0.1.

To further investigate this, we generate a second dataset using recently-developed in-flight x-ray radiography of the imploding shell, which measures the shape at a similar time in the implosion as the ρR measurements[6]. These shots correspond to a subset of Fig. 4.5 denoted by diamond

[¶]By fielding additional WRFs in key locations around the implosion the in-flight shape could be further constrained, for example at $\theta = 45°$ to measure $\ell = 4$ modes; near the south pole at $\theta \sim 180°$ to measure $\ell = 1$, and at multiple locations around the equator to constrain m modes.

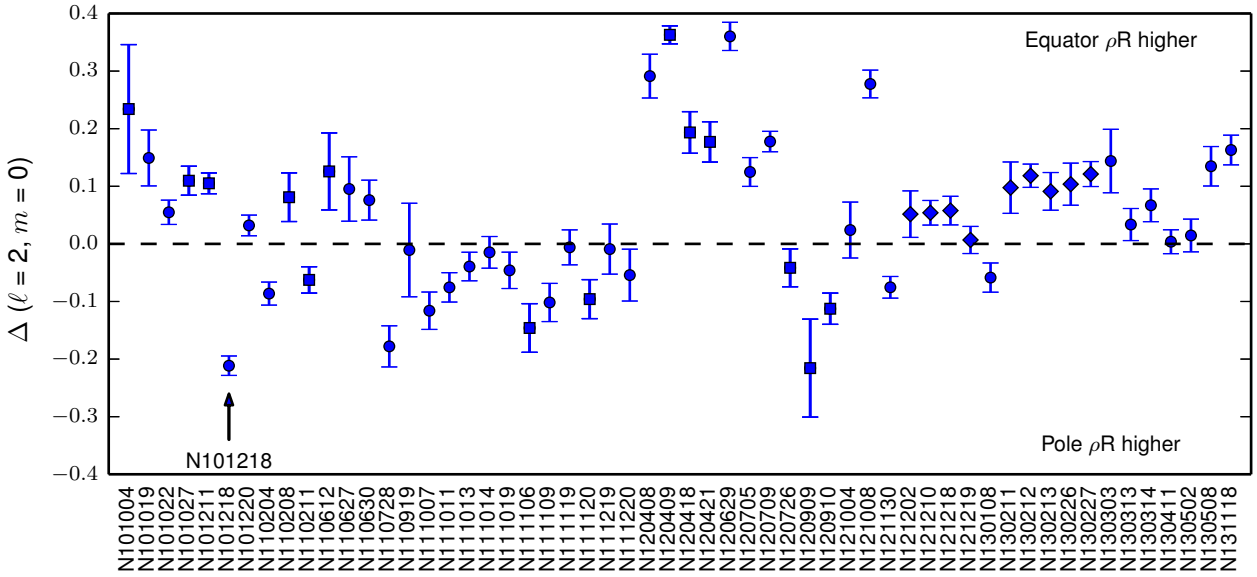

Figure 4.5. Mode amplitude Δ (see Eq. 4.1) for all NIF shots with polar and equatorial WRF data since 2010[‖]. Shot numbers are displayed below. Displayed error bars are 1σ. Positive values represent higher ρR on the equator. Shot N101218 (also shown in Fig. 4.2) is specifically annotated. Shots used in Fig. 4.6 denoted by square markers, and in Fig 4.7 by diamond markers.

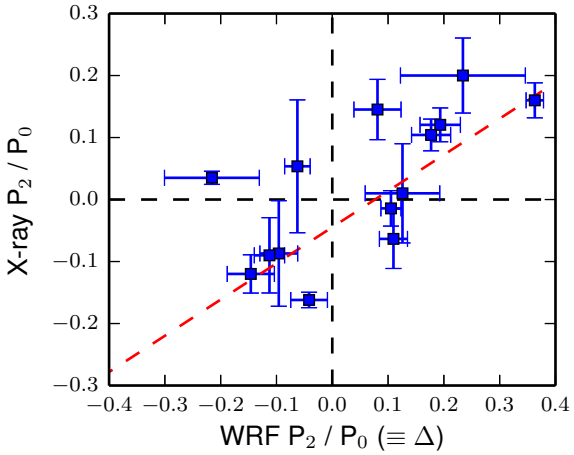

Figure 4.6. Mode $\ell = 2$ amplitude from these measurements (abscissa) versus stagnation x-ray core emission shape. A linear fit (dashed red line) to the data has slope 0.6 ± 0.1 and intercept -0.04 ± 0.02. The data have a weighted Pearson correlation coefficient $p = 0.68$.

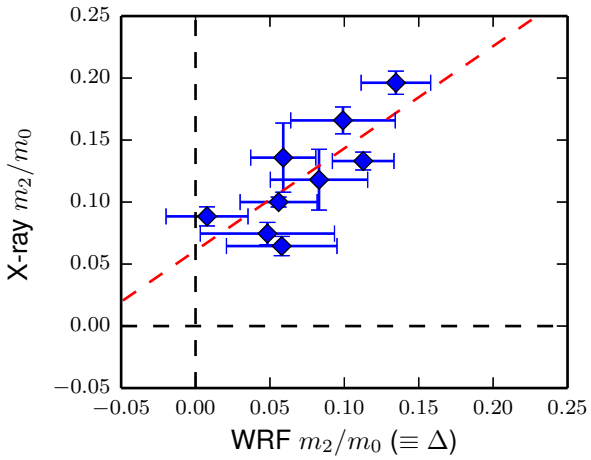

Figure 4.7. Azimuthal mode amplitude inferred for experiments with in-flight x-ray imaging: this work (abscissa) versus stagnation x-ray core shape. A linear fit (dashed red line) to the data has slope 0.82 ± 0.25 and intercept 0.06 ± 0.02. The data have a weighted Pearson correlation coefficient $p = 0.78$.

markers. The radiography data show significant $\ell = 2$ and $\ell = 4$ modes. The radiography requires large oppositely-placed patches on the hohlraum wall, which induces a large $m = 2$ asymmetry roughly aligned with the equatorial WRF line of sight. With limited lines of sight, this generates an unconstrained problem for this analysis. However, if the radiography-measured amplitudes for $\ell = 2$ and $\ell = 4$ modes at $CR \sim 4$ are used with a superimposed azimuthal mode $\Delta \sin(\theta) \cos(m\phi + \phi_0)$ with $m = 2$, ϕ_0 aligned with the WRF equatorial view, and Δ a free parameter, the in-flight azimuthal shape (m_2) is then characterized.

The results of this analysis are shown in Fig. 4.7, compared to the stagnation x-ray emission shape as in Fig. 4.6. Again positive correlation is observed with a slope of approximately unity (0.82 ± 0.25). The positive correlation between the shock and compression asymmetries means that the asymmetry maintains its phase during deceleration (i.e. a prolate in-flight implosions has a prolate stagnated shape).

In Figs. 4.6 and 4.7, as the abscissa is the shock-bang-time asymmetry and the ordinate is the compression-bang-time asymmetry, the slope in the data corresponds directly to the amplitude of the asymmetry at compression relative to shock, i.e. the growth factor between these times. In both data sets (Figs. 4.6 and 4.7), the slope being $\lesssim 1$ indicates a lack of growth in apparent mode amplitude between shock ($CR \sim 4$) and compression ($CR \sim 20$) phases. To explore this further we consider several models for asymmetry growth of a radial $\ell = 2$ perturbation. The simplest is Bell-Plesset, a model for for asymmetric incompressible flows in spherical compression[34], which predicts a simple convergence scaling $\Delta \propto (CR - 1)$. For ICF, modified Bell-Plesset theory for compressible flows[35] is more appropriate. Finally, we also consider typical 2-D radiation hydrodynamics simulations of asymmetrically driven surrogate implosions using HYDRA[36]. The expected growth factors between the shock and compression times using these models are summarized in Table 4.1.

The growth factor corresponds directly to an expected slope in Figs. 4.6 and 4.7, clearly inconsistent with the data for all models. This is in contrast to previous experiments showing that the Bell-Plesset model holds for low-mode asymmetry growth between shock and compression in direct-drive OMEGA implosions[16,17].

The most plausible explanation for this result is that the stagnation x-ray emission shape

Table 4.1. Growth factors from shock to compression for several models.

Model	Growth
Bell-Plesset	$\sim 5\times$
Compressible Bell-Plesset	$\sim 3\times$
2-D HYDRA (picket&trough)**	$\sim -14\times$
2-D HYDRA (peak)††	$\sim 3\times$

asymmetries do not represent (i.e. are smaller than) the ρR asymmetries at that time. A lack of correspondence between stagnation x-ray and ρR asymmetries has been seen in recent computational studies[37,38,9,39,40], in indirect-drive OMEGA experiments[41], and in the 2-D HYDRA simulations used for Table 4.1. This interpretation is consistent with the results of DT-layered cryogenic implosions at NIF, where neutron metrics[42–44] show very large ρR asymmetries, of order $2-3\times$ variation between lines of sight at compression, while the x-ray core shape is much closer to symmetric[45].

The growth models considered in Table 4.1 implicitly assume efficient conversion of the imploding shell's kinetic energy into stagnated thermal energy. If significant residual kinetic energy exists at stagnation, for example through non-radial flows or turbulent motion, then we would not expect the growth models to be valid. Whether a growth factor ~ 1 is consistent with this hypothesis could be investigated with 3-D radiation-hydrodynamics simulations.

Another consideration is scenarios which cause ρR asymmetries but not shape asymmetries, such as variations in shell remaining mass or density in addition to convergence (shape). These scenarios would still cause significant performance degradation, and will be investigated using in-flight x-ray radiography[6] to complement this technique. Finally, the presence of $\ell = 1$ modes could affect the shock ρR but not be apparent in x-ray stagnation imaging; however we note that the asymmetry magnitudes in this work are consistent with in-flight x-ray radiography[6], suggesting that $\ell = 1$ is not dominant. This could be verified with dedicated shots inducing $\ell = 1$ modes in these implosions, similar to recent experiments with DT fuel[31,32]. Finally, the effects of bulk fuel velocity and scattering are small to affect this technique, as discussed in sections 4.4 and 4.5.

4.3 Coasting interpretation

The cause of the large variation in observed asymmetries, both in magnitude and sign, has also been investigated. As in Fig. 4.6, we control for variation in other asymmetry modes by selecting shots with $m_2/m_0 < 10\%$, $m_4/m_0 < 15\%$, and $P_4/P_0 < 15\%$. For this data set, a significant anti-correlation has been found with the implosion coasting time, which is the difference in time between the end of the laser drive and the peak nuclear production. The data are shown in Fig. 4.8. The anti-correlation means that the implosions are more prolate (sausaged) for short-coast (extended drive) pulses. This sensitivity suggests that the asymmetries result from asymmetries in the flux during peak drive. The trend with coasting, and an apparent change in asymmetry sign near a coast time ~ 1.75 ns, means that the peak flux has a time-varying asymmetry. The P_2 flux asymmetry during the peak drive depends on the relative strength of the inner and outer beams (cone fraction), the wavelength separation between beams ($\delta\lambda$), and thus on the cross-beam energy transfer which has an additional complex dependence on the hohlraum plasma conditions.

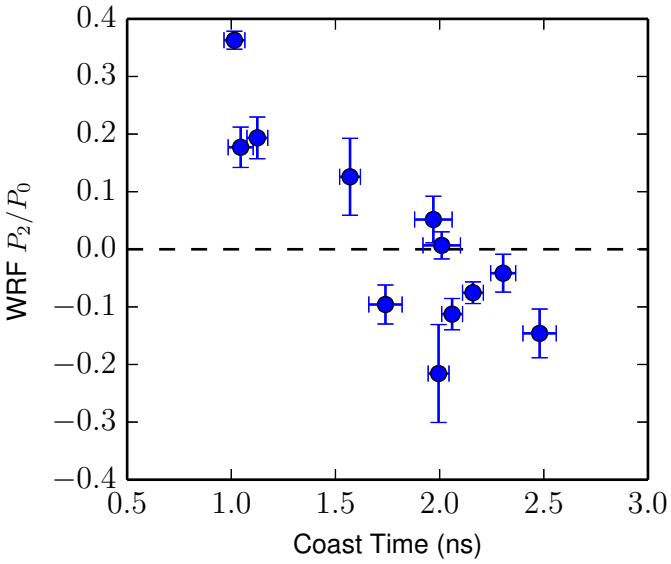

Figure 4.8. WRF-measured P_2/P_0 mode amplitude versus implosion coasting time.

4.4 Bulk velocity effects on asymmetry

Bulk velocity of the fuel creates Doppler shifts in the fusion products due to center-of-mass motion of the reacting ions. The mean D^3He proton birth energy $E_p(T_i)$ is used to calculate the initial velocity in the center-of-mass frame: $\gamma_0 = 1 + E_p/(m_p c^2)$ and $v_0 = c\sqrt{1-\gamma_0^{-2}}$. For a given bulk velocity v_b in the detector direction the velocities add relativistically:

$$v' = \frac{v_0 + v_b}{1 + v_0 v_b/c^2},\ \gamma' = 1/\sqrt{1-(v'/c)^2}, \tag{4.3}$$

with the Doppler shifted energy given by

$$E_p' = (\gamma' - 1)m_p c^2,\ \Delta E_p = E_p' - E_p, \tag{4.4}$$

where ΔE_p is the energy shift due to the bulk velocity. Using relativistic kinematics[46] and the parameterized cross-section[47], ΔE_p is calculated and shown in Fig. 4.9a as a function of the bulk velocity.

If the burning fuel has a bulk velocity in the direction of one of the detectors, the proton spectrum is upshifted in this direction and downshifted in the opposing direction, which results in a lower or higher inferred ρR, respectively. This is shown in Fig. 4.9b. Since the polar and equatorial detectors are approximately orthogonal, a bulk fuel velocity towards one DIM will not cause an energy shift towards the other, meaning that the shift in inferred ρR due to the velocity causes an apparent asymmetry, which is shown in Fig. 4.9c.

As the protons are created by the shock coalescence and burn, any net fuel velocity would be caused by an asymmetry in the converging shock. The most comparable scenario are shock-driven 'exploding pusher' implosions, in which all of the nuclear yield is produced by a single strong shock. The shock strength is much higher in exploding pushers than in the low-adiabat surrogate implosions used in this work, and thus the bulk fuel velocity in exploding pushers can be taken as an upper limit.

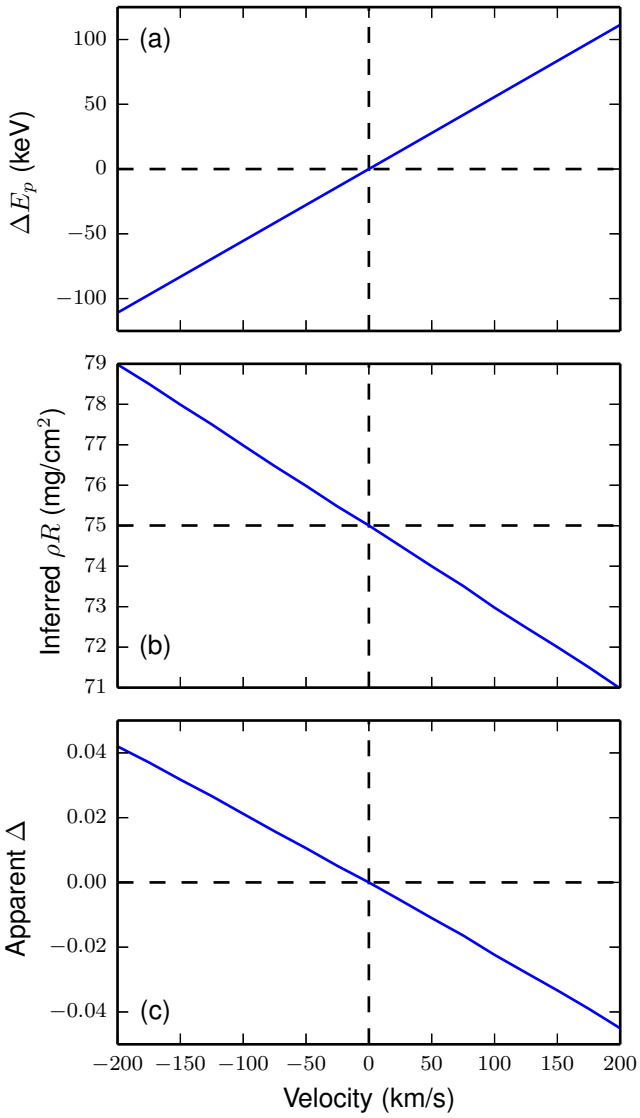

Figure 4.9. **(a)** D^3He proton birth energy shift as a function of bulk fuel velocity. **(b)** For an actual $\rho R = 75$ mg/cm^2, the apparent ρR due to birth energy shift as a function of velocity. **(c)** The apparent asymmetry amplitude (Δ) as a function of bulk velocity.

In a D^3He exploding pusher on NIF, the proton energy uniformity was observed to be ±75 keV between the pole and equator[48], corresponding to $\lesssim 150$ km/s bulk fuel velocity if attributed entirely to Doppler shifts. In DT exploding pushers[49], DT-n Doppler shifts were observed corresponding to fuel velocities up to 200 km/s. For velocities up to ±200 km/s, the apparent asymmetry caused by the proton Doppler shift is ±0.04 in Δ. As this is much smaller than the observed asymmetries, which have $\Delta = 0.1 - 0.2$ routinely, plausible Doppler shifts due to bulk-fuel velocities cannot cause the observed asymmetries, but may be responsible for some of the observed shot-to-shot scatter in Figs 4.6 and 4.7.

4.5 Scattering effects on asymmetry measurements

As the protons traverse material, they undergo collisions. Rutherford scattering off of atomic nuclei can produce large-angle deflections, which could potentially mask asymmetries via scattering in materials surrounding the target. The differential cross section is given by

$$\frac{d\sigma}{d\Omega} = \frac{b_{90}^2}{4} \frac{1}{\sin^4(\theta/2)}, \tag{4.5}$$

with

$$b_{90} = \frac{Z_1 Z_2 e^2}{4\pi\epsilon_0} \frac{1}{m_\mu v_{rel}^2}. \tag{4.6}$$

The protons are energetic, so v_{rel} is relatively high, leading to a suppression of scattering effects as the cross section $\propto v_{rel}^{-4}$. Additionally, large-angle scattering is suppressed by the $\sin^{-4}(\theta/2)$ dependence. This leads to large-angle scattering being a small effect, which can be verified with the TRIM Monte Carlo code[28].

Most of the hohlraum is surrounded by significantly thicker material, such as a diagnostic band, while the equatorial WRFs look through a thinner region of the hohlraum. While protons going through the thicker regions of the wall may undergo large-angle scattering into the detector solid angle, their energies will be much lower than the protons exiting the hohlraum through the thin region, and thus these protons will not be considered in the analysis.

The effect of scattering on protons transiting the nominal hohlraum wall (30μm of Au and 74μm of Al) near the line-of-sight is evaluated with TRIM, and shown in Fig. 4.10. Most of the scattering occurs in the Au wall due to the Z^2 dependence (Eq. 4.5 and 4.6). Fig. 4.10a shows the angular distribution of protons after the wall for a typical initial energy $E_p = 12$ MeV. The distribution peaks $\sim 2°$ scattering angle. Fig. 4.10b shows the distribution as the fraction of protons scattered with angle greater than θ. The TRIM calculation shows that $\sim 90\%$ of protons scatter less than 5° in the wall, and $\sim 98\%$ scatter less than 10°. This means that we expect high-mode asymmetries to potentially be masked by scattering, but low-mode asymmetries, the focus of the previous analysis, are unaffected.

4.6 Higher mode numbers

The previous section's low-mode analysis focused on the observed differences between the polar and equatorial DIM. Within a DIM, the WRFs fielded 'above' and 'below' the DIM axis (see Fig. 4.1) are separated by 26°, providing a potential diagnostic of 'medium' mode number asymmetries. At each polar angle, two WRFs are fielded separated azimuthally by only 7°, which is a potential diagnostic of 'high' mode number asymmetries.

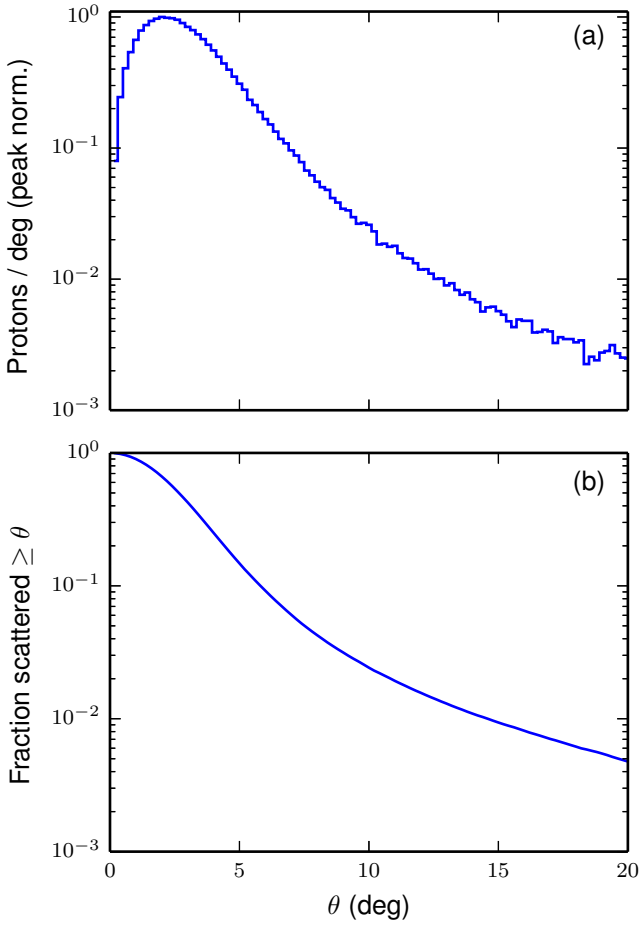

Figure 4.10. Proton scattering in a typical hohlraum wall (30μm of Au and 74μm of Al). **(a)** The proton angular distribution after transiting the wall. **(b)** The fraction of protons scattered more than θ versus θ.

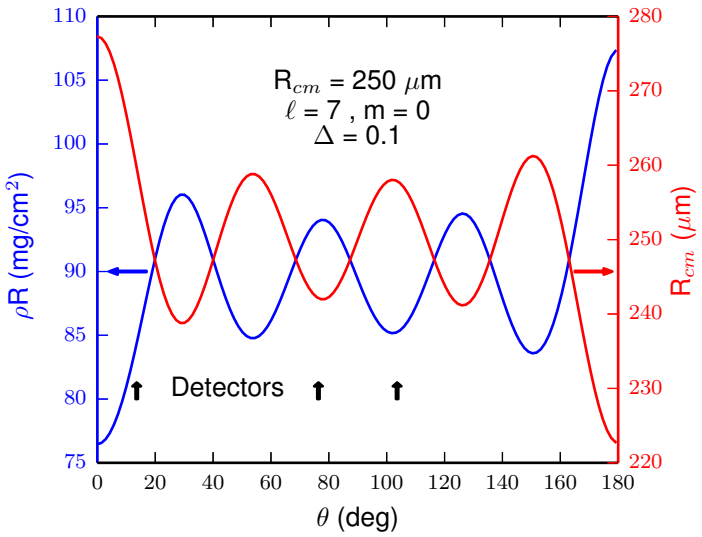

Figure 4.11. Conceptual cartoon for the medium-mode measurement. In this case, a mode-7 asymmetry with a 10% amplitude has been applied to an average shell R_{cm} of 250 μm. The resulting $\rho R(\theta)$ is shown in blue. The detector locations (shown by arrows) above and below the equator are clearly sensitive to the difference in ρR for this asymmetry and geometry.

4.6.1 Medium-mode asymmetries

Sensitivity to the medium-mode asymmetries comes from the detectors separated by 13° above and below the DIM. Focusing on the equatorial DIM, this would correspond to odd polar modes, which create an up-down asymmetry. Schematically, this is shown in Fig. 4.11.

The sensitivity of this technique to various mode numbers can be calculated as the observed difference in ρR ($\Delta\rho R$) between the two views for a fixed mode amplitude and varying mode number. This is shown in Fig. 4.12. As expected from geometry, the peak sensitivity is to modes ~ 7. In the following analysis, a mode number of 7 is assumed. Similar to the low-mode analysis, this corresponds to a 'best-case' scenario in that the inferred mode amplitude is minimized for a given observed difference in ρR.

The available data is shown in Fig. 4.13 using this analysis. The mode amplitude is inferred from a Legendre mode $\ell = 7, m = 0$ fit to the data. Only random error bars are included on the data. The resulting 1σ uncertainty in the fit parameter is calculated from a χ^2 analysis, and shown as the error bar in Fig. 4.13. We observe that many of the data points are close to 1σ away from $\Delta = 0$, i.e. no asymmetry. With the entire dataset, the consistency with zero asymmetry can be evaluated by calculating the value of reduced χ^2, which is 1.76. This suggests more scatter than is consistent with statistical variation, implying that in cases with a large observed asymmetry, the data indicate a physical asymmetry.

4.6.2 High-mode asymmetries

High-mode asymmetries can be studied using the adjacent WRFs (separated by 7°). In this case, the peak sensitivity is expected to be for modes ~ 25. However, at this scale, coherent asymmetries are not expected, and interpreting the data as a Legendre or sinusoidal perturbation is likely incorrect. For this analysis, the data are simply interpreted as a difference in ρR between the two adjacent detectors.

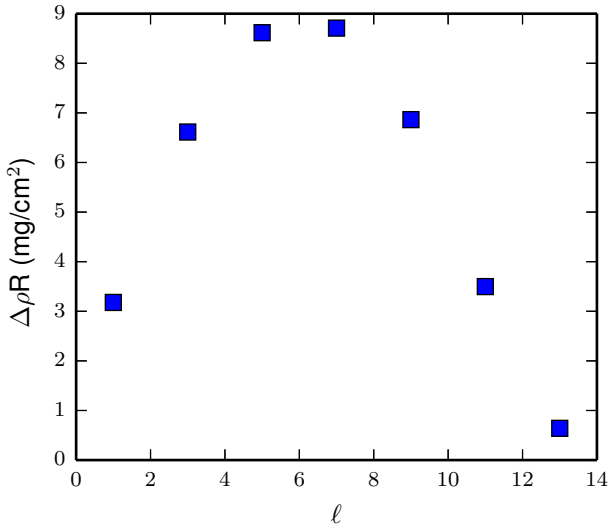

Figure 4.12. WRF sensitivity to medium modes, calculated as the observable difference in ρR between the 90-78 'up' and 'down' WRFs, for a 10% asymmetry and various odd mode numbers. The peak sensitivity is to modes 5 and 7.

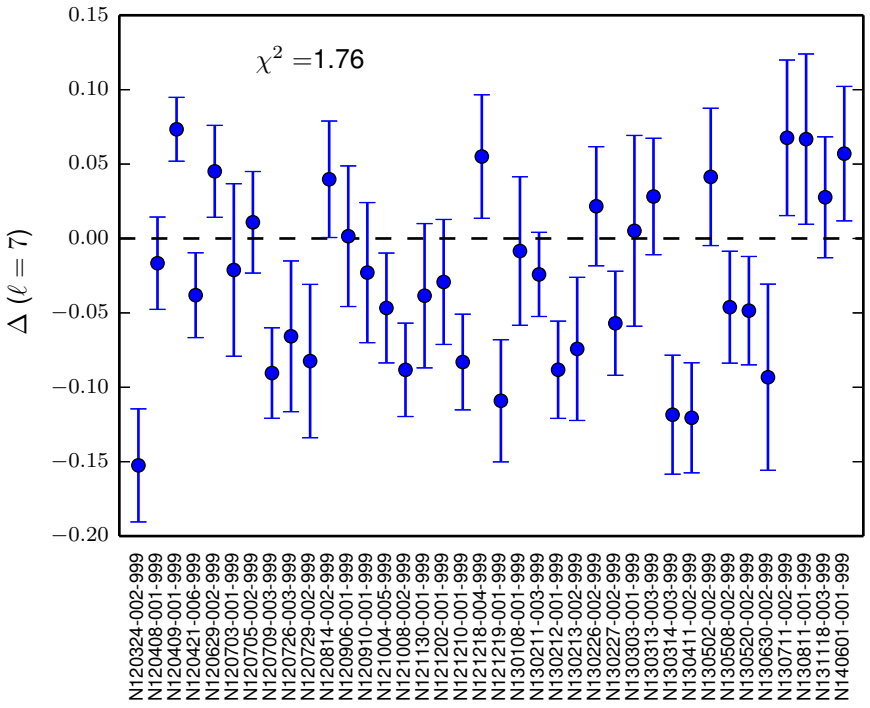

Figure 4.13. Medium-mode asymmetry amplitude (Δ) for various shots at NIF.

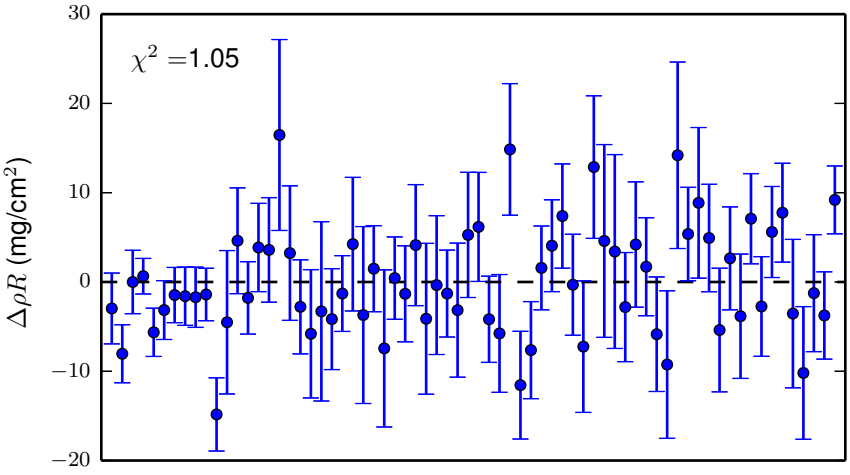

Figure 4.14. High-mode asymmetry data, plotted as a difference in ρR between the two adjacent detectors.

The data are shown in Fig. 4.14. It is immediately apparent that most data are close to 0, i.e. no difference is observed between the adjacent detectors. With the entire dataset, a reduced $\chi^2 = 1.05$ is calculated, which means that the data are statistically consistent with no asymmetries, and the observed scatter between adjacent detectors can be entirely explained by the detector's random uncertainties.

4.7 Summary

In conclusion, implosion low-mode ρR asymmetries are clearly observed at the shock-bang time in D^{3}He surrogate experiments at the NIF. This technique is unique because it uses charged particles to probe ρR asymmetries at the shock bang several hundred ps before implosion stagnation, corresponding to a convergence ratio of $\sim 3-5$ and occurring just before peak implosion velocity, thus isolating acceleration-phase asymmetry growth. The observed low-mode asymmetries are interpreted as a $\ell = 2$ (P_2) asymmetry in shape, with the data routinely showing asymmetry magnitudes $\gtrsim 10\%$ at this time. These asymmetries would degrade performance later in time during stagnation, with growth factors $\gtrsim 3\times$ predicted by several models. However, when comparing these measured asymmetries to the x-ray stagnation emission shape, a lack of growth is observed in apparent asymmetry mode amplitude, in contrast to the expected $\gtrsim 3\times$ growth. This suggests the x-ray stagnation emission shape does not accurately reflect the stagnation shell (ρR) shape, or possibly that significant residual kinetic energy exists. Finally, the observed variations in asymmetry magnitude and sign are partly explained by an anti-correlation with the implosion coasting time, suggesting that a significant time-dependent asymmetry in the peak flux drives the observed implosion asymmetries. Such a time-dependent $\ell = 2$ asymmetry could be caused by the cross-beam energy transfer between the inner and outer beams varying during the main pulse. Importantly, with several techniques now available for measuring the symmetry over the entire implosion from $CR = 1 \rightarrow 20$, these observed asymmetries can be studied and mitigated, as necessary for ignition on the NIF.

Using the WRFs above and below a DIM, or immediately adjacent to each other, medium- and high-mode asymmetries can be diagnosed. For the medium-mode data, primarily sensitive to $\ell = 7$ odd Legendre asymmetries, several shots display statistically significant differences between

the 'up' and 'down' WRFs, while most are consistent with a symmetric implosion in those modes. For the high-mode data, adjacent WRFs are consistent with each other given the measurement asymmetries. This means that high-mode asymmetries are smaller than can be observed with the present technique. WRFs with reduced random uncertainties could provide a better constraint on the size of these modes.

4.8 References

1. S. Atzeni, "Sensitivity of ICF Reactor Targets to Long-Wavelength Drive Nonuniformities," EPL (Europhysics Letters), **11**(7), 639 (1990).
2. J. Lindl, "Development of the indirect-drive approach to inertial confinement fusion and the target physics basis for ignition and gain," Phys. Plasmas, **2**, 3933–4024 (1995).
3. S. W. Haan, J. D. Lindl, D. A. Callahan *et al.*, "Point design targets, specifications, and requirements for the 2010 ignition campaign on the national ignition facility," Physics of Plasmas, **18**(5), 051001 (2011).
4. S. H. Glenzer, B. J. MacGowan, P. Michel *et al.*, "Symmetric inertial confinement fusion implosions at ultra-high laser energies," Science, **327**(5970), 1228–1231 (2010).
5. O. Landen *et al.*, "Capsule performance optimization in the National Ignition Campaign," Physics of Plasmas, **17**, 056,301 (2010).
6. J. Rygg, O. Jones, J. Field *et al.*, "2D X-Ray Radiography of Imploding Capsules at the National Ignition Facility," Phys. Rev. Lett., **112**, 195001 (2014).
7. E. L. Dewald, J. Milovich, C. Thomas *et al.*, "Experimental demonstration of early time, hohlraum radiation symmetry tuning for indirect drive ignition experiments," Phys. Plasmas, **18**(9), 092703 (2011).
8. E. L. Dewald, J. L. Milovich, P. Michel *et al.*, "Early-time symmetry tuning in the presence of cross-beam energy transfer in icf experiments on the national ignition facility," Phys. Rev. Lett., **111**, 235,001 (2013).
9. R. P. J. Town, D. K. Bradley, A. Kritcher *et al.*, "Dynamic symmetry of indirectly driven inertial confinement fusion capsules on the national ignition facility," Physics of Plasmas, **21**(5), 056313 (2014).
10. J. D. Moody, D. A. Callahan, D. E. Hinkel *et al.*, "Progress in hohlraum physics for the National Ignition Facility," Physics of Plasmas, **21**(5), 056317 (2014).
11. G. Kyrala, S. Dixit, S. Glenzer *et al.*, "Measuring symmetry of implosions in cryogenic Hohlraums at the NIF using gated x-ray detectors," Rev. Sci. Instrum., **81**, 10E316 (2010).
12. S. H. Glenzer, B. K. Spears, M. J. Edwards *et al.*, "First implosion experiments with cryogenic thermonuclear fuel on the national ignition facility," Plasma Physics and Controlled Fusion, **54**(4), 045,013 (2012).
13. G. P. Grim, N. Guler, F. E. Merrill *et al.*, "Nuclear imaging of the fuel assembly in ignition experimentsa)," Physics of Plasmas, **20**(5), 056320 (2013).
14. T. Boehly, D. Brown, R. Craxton *et al.*, "Initial performance results of the OMEGA laser system," Optics Communications, **133**(1-6), 495–506 (1997).
15. C. K. Li, F. H. Séguin, J. A. Frenje *et al.*, "Capsule-areal-density asymmetries inferred from 14.7-MeV deuterium-helium protons in direct-drive OMEGA implosions," Physics of Plasmas, **10**(5), 1919–1924 (2003).
16. J. A. Frenje, C. K. Li, F. H. Seguin *et al.*, "Measuring shock-bang timing and rho R evolution of D^3He implosions at OMEGA," Physics of Plasmas, **11**(5), 2798–2805 (2004).
17. C. K. Li, F. H. Séguin, J. A. Frenje *et al.*, "Effects of nonuniform illumination on implosion asymmetry in direct-drive inertial confinement fusion," Phys. Rev. Lett., **92**, 205,001 (2004).
18. R. Petrasso *et al.*, "Measuring Implosion Dynamics through ρR Evolution in Inertial-Confinement Fusion Experiments," Physical Review Letters, **90**(9), 95,002 (2003).
19. C. Li and R. Petrasso, "Charged-particle stopping powers in Inertial Confinement Fusion Plasmas," Phys. Rev. Lett., **70**(20), 3059 (1993).
20. G. Guderley, "Powerful spherical and cylindrical compression shocks in the neighborhood of the center of the sphere and of the cylinder axis," Luftfahrtforsch, **19**, 302–312 (1942).
21. J. R. Rygg, *Shock Convergence and Mix Dynamics in Inertial Confinement Fusion*, Ph.D. thesis, Massachusetts Institute of Technology (2006).

22. H. G. Rinderknecht, M. G. Johnson, A. B. Zylstra *et al.*, "A novel particle time of flight diagnostic for measurements of shock- and compression-bang times in d3he and dt implosions at the nifa)," Review of Scientific Instruments, **83**(10), 10D902 (2012).
23. D. Hicks, B. Spears, D. Braun *et al.*, "Convergent ablator performance measurements," Physics of Plasmas, **17**, 102,703 (2010).
24. F. H. Séguin, J. A. Frenje, C. K. Li *et al.*, "Spectrometry of charged particles from inertial-confinement-fusion plasmas," Rev. Sci. Instrum., **74**(2), 975–995 (2003).
25. F. H. Séguin, N. Sinenian, M. Rosenberg *et al.*, "Advances in compact proton spectrometers for inertial-confinement fusion and plasma nuclear science," Rev. Sci. Instrum., **83**(10), 10D908 (2012).
26. A. Zylstra, J. Frenje, F. Séguin *et al.*, "A new model to account for track overlap in cr-39 data," Nuclear Instruments and Methods in Physics Research Section A: Accelerators, Spectrometers, Detectors and Associated Equipment, **681**(0), 84 – 90 (2012).
27. W. J. Hibbard, M. D. Landon, M. D. Vergino *et al.*, "Design of the National Ignition Facility diagnostic instrument manipulator," Rev. Sci. Instrum., **72**(1), 530–532 (2001).
28. J. Ziegler, J. Biersack and U. Littmark, *The stopping and range of ions in matter* (Pergamon, New York, 1985).
29. C. Li, F. Séguin, J. Frenje *et al.*, "Observations of electromagnetic fields and plasma flow in hohlraums with proton radiography," Physical review letters, **102**(20), 205001 (2009).
30. C. K. Li, A. B. Zylstra, J. A. Frenje *et al.*, "Observation of strong electromagnetic fields around laser-entrance holes of ignition-scale hohlraums in inertial-confinement fusion experiments at the National Ignition Facility," New Journal of Physics, **15**(2), 025,040 (2013).
31. J. Kilkenny *et al.*, submitted to EPJ Conf. Series (2013).
32. B. K. Spears, M. J. Edwards, S. Hatchett *et al.*, "Mode 1 drive asymmetry in inertial confinement fusion implosions on the national ignition facility," Physics of Plasmas, **21**(4), 042702 (2014).
33. D. K. Bradley, P. M. Bell, J. D. Kilkenny *et al.*, "High-speed gated x-ray imaging for ICF target experiments (invited)," Rev. of Sci. Instrum., **63**(10), 4813 (1992).
34. M. S. Plesset, "On the stability of fluid flows with spherical symmetry," Journal of Applied Physics, **25**(1), 96 (1954).
35. P. Amendt, J. D. Colvin, J. D. Ramshaw *et al.*, "Modified bell-plesset effect with compressibility: Application to double-shell ignition target designs," Phys. Plasmas, **10**(3), 820–829 (2003).
36. M. Marinak, G. Kerbel, N. Gentile *et al.*, "Three-dimensional HYDRA simulations of National Ignition Facility targets," Physics of Plasmas, **8**, 2275 (2001).
37. R. H. H. Scott, D. S. Clark, D. K. Bradley *et al.*, "Numerical modeling of the sensitivity of x-ray driven implosions to low-mode flux asymmetries," Phys. Rev. Lett., **110**, 075,001 (2013).
38. A. Kritcher *et al.*, APS DPP Bulletin, page NO4.00004 (2013).
39. J. Gu, Z. Dai, Z. Fan *et al.*, "A new metric of the low-mode asymmetry for ignition target designs," Phys. Plasmas, **21**(1), 012,704 (2014).
40. A. L. Kritcher, R. Town, D. Bradley *et al.*, "Metrics for long wavelength asymmetries in inertial confinement fusion implosions on the national ignition facility," Physics of Plasmas, **21**(4), 042708 (2014).
41. N. Izumi *et al.*, APS DPP Bulletin, page BO1.010 (2004).
42. D. L. Bleuel, C. B. Yeamans, L. A. Bernstein *et al.*, "Neutron activation diagnostics at the National Ignition Facility (invited)," Rev. of Sci. Instrum., **83**(10), 10D313 (2012).
43. C. B. Yeamans, D. L. Bleuel and L. A. Bernstein, "Enhanced NIF neutron activation diagnosticsa)," Rev. of Sci. Instrum., **83**(10), 10D315 (2012).
44. J. Frenje, R. Bionta, E. Bond *et al.*, "Diagnosing implosion performance at the National Ignition Facility (NIF) by means of neutron spectrometry," Nuclear Fusion, **53**(4), 043014 (2013).
45. M. Edwards *et al.*, "Progress towards ignition on the National Ignition Facility," Phys. Plasmas, **20**, 070501 (2013).
46. L. Ballabio, J. Källne and G. Gorini, "Relativistic calculation of fusion product spectra for thermonuclear plasmas," Nuclear Fusion, **38**(11), 1723 (1998).
47. H.-S. Bosch and G. Hale, "Improved Formulas for Fusion Cross-Sections and Thermal Reactivities," Nuclear Fusion, **32**, 611–631 (1992).

48. M. Rosenberg *et al.*, "A direct-drive exploding-pusher implosion for development of a monoenergetic proton, alpha, and triton backlighting platform at the national ignition facility," to be submitted to Rev. Sci. Instrum. (2015).

49. M. Gatu Johnson, D. T. Casey, J. A. Frenje *et al.*, "Measurements of collective fuel velocities in deuterium-tritium exploding pusher and cryogenically layered deuterium-tritium implosions on the NIF," Physics of Plasmas, **20**(4), 042707 (2013).

Part II

Plasma Stopping Power

5

Probing charged-particle stopping in WDM plasma

5.1 Introduction

Fusion reactions of interest to terrestrial energy production and laboratory nuclear astrophysics commonly produce energetic charged particles. As these products traverse any ambient material, they lose momentum via Coulomb collisions with ions and electrons in that material. This problem was first treated by Bohr, who was interested in energetic α particles traversing material[1]. The rate of energy loss per path length traversed (dE/dx) is called the 'stopping power'.

For nomenclature, the particle of interest (traversing the ambient material and losing energy) is typically referred to as the 'test particle' (subscript t) or 'projectile'. The ambient material is composed of 'field' (subscript f), 'plasma', or 'background' particles.

A simple expression for the stopping power can be derived (following Ref. 2). In a collision with an ambient particle, the energy transferred is

$$\Delta E = \frac{(\Delta p)^2}{2m_f}. \tag{5.1}$$

Note the inverse dependence on the field particle mass - in most cases, the field electrons will dominate the stopping power. The momentum transferred in a Coulomb collision is[2]:

$$\Delta p = \frac{2m_f v_t}{\sqrt{1+(b/r_0)^2}}, \tag{5.2}$$

where b is the impact parameter, v_t is the test particle velocity, and

$$r_0 = \frac{Z_f Z_t e^2}{m_f v_t^2} \tag{5.3}$$

is referred to as the 'Landau length', also referred to as b_{90} or the impact parameter corresponding to a 90° collision. Z refers to the charge of the particles in atomic units, and e is the fundamental charge. The energy exchanged is thus

$$\Delta E = \frac{2(Z_t Z_f e^2)^2}{m_f v_t^2}\frac{1}{b^2+r_0^2}. \tag{5.4}$$

Combining these results, the stopping power can be written:

$$\frac{dE}{dx} = -\frac{4\pi(Z_t Z_f e^2)^2}{m_f v_t^2} n_f \log\Lambda, \tag{5.5}$$

where n_f is the field-particle number density; this expression is often simplified with the field plasma frequency $\omega_{pf}^2 \equiv 4\pi Z_f^2 e^2 n_f / m_f$ to:

$$\frac{dE}{dx} = -\left(\frac{Z_t e}{v_t}\right)^2 \omega_{pf}^2 \log\Lambda. \tag{5.6}$$

The quantity $\log\Lambda$ is the 'Coulomb Logarithm' (sometimes referred to as the 'Stopping Number' L). In this simple derivation, it is given by an integral over possible impact parameters:

$$\log\Lambda = \int_0^{b_{max}} \frac{bdb}{b^2 + r_0^2} = \frac{1}{2}\log\left(1 + \frac{b_{max}^2}{r_0^2}\right), \tag{5.7}$$

where b_{max} is a quasi-arbitrary cutoff, necessary to prevent a logarithmic divergence, but physically motivated. The last expression is often approximated as $\log\Lambda \approx \log(b_{max}/r_0)$ in the limit $b_{max} \gg r_0$.

The preceding derivation treated classical binary collisions with free field particles. In general, stopping theories can be grouped into a categories such as bound-electron stopping, binary collisions with free field particles, and plasma dielectric response theories. More generally a mixture of the three may be appropriate, depending on the the ambient material. Brief summaries of the stopping power in these regimes is given in the following sections.

5.1.1 Bound-electron stopping theory

The physics of stopping on bound electrons was first treated in detail by Bethe[3] and Bloch[4]. The stopping power is taken in the form of Eq. 5.5 with the Coulomb logarithm given as the ratio of the maximum to minimum momentum transfer in a collision with an electron. The latter is taken as the electron's ionization energy, and the former is taken as $2m_e v_t^2$, so that:

$$\log\Lambda = \log\left(\frac{2m_e v_t^2}{I}\right). \tag{5.8}$$

In systems with multiple electron energy levels, an average-ionization potential is used ($I \to \bar{I}$), which is typically defined as

$$Z_b \log\bar{I} \sum_n f_n \log E_n, \tag{5.9}$$

where for each electron state n, f_n is the oscillator strength and E_n is the binding energy[2]. In practice, effective ionization potentials are often determined from experimental data[5].

5.1.2 Binary collision stopping theory

In plasmas, the binary collision stopping theory is typically approached through the kinetic equations[6]. More recently and of relevance to ICF, the Li-Petrasso theory[7,8] is commonly used. The result is close to Eq. 5.5, except a correction is added for low particle energies in the form of the

'Chandrashekar function' G:

$$\frac{dE}{dx} = -\left(\frac{Z_t e}{v_t}\right)^2 \omega_{pf}^2 G(x) \log\Lambda. \tag{5.10}$$

with $x = v_t/v_f$. For low-density plasmas, the Coulomb logarithm is often taken as $\log\Lambda = \log(\lambda_D/p_{min})$ with $p_{min} = Z_t Z_f e^2/m_r u^2$ where m_r is the reduced mass and u is the relative velocity between field and test particle. The function G averages momentum transfer over the field-particle distribution; in the low-density limit [6] it is

$$G(x) = \mu(x) - \frac{m_f}{m_t}\frac{d\mu}{dx}, \quad \mu(x) = \frac{2}{\sqrt{\pi}}\int_0^x d\xi e^{-\xi}\sqrt{\xi}. \tag{5.11}$$

As large-angle scattering becomes important, additional terms must be retained in G. Li and Petrasso derived the expression [7]

$$G(x) = \mu(x) - \frac{m_f}{m_t}\left\{\frac{d\mu(x)}{dx} - \frac{1}{\log\Lambda}\left[\mu(x) + \frac{d\mu(x)}{dx}\right]\right\}, \tag{5.12}$$

which is valid for $\log\Lambda \gtrsim 2$. As large-angle scattering becomes even more signicant, T-matrix scattering theory [9] should be used.

5.1.3 Plasma dielectric response theory

An energetic charged particle moving through a plasma also triggers a dielectric response of the plasma. Waves (oscillatory motions) are excited in the dielectric medium by the projectile. Generally, the stopping power associated with the dielectric response can be written in the form [2]

$$\frac{dE}{dx} = -Z_t e \int \frac{d^3k}{(2\pi)^3}\frac{i\vec{k}\cdot\vec{v_t}}{v_t}\frac{4\pi Z_t e}{k^2\epsilon(k,\vec{k}\cdot\vec{v_t})}, \tag{5.13}$$

which is an integral over wavenumber k, where ϵ is the plasma dielectric function.

5.1.4 Complications in dense plasma and current theory

Several complications arise in plasmas of relevance to inertial confinement fusion and laboratory nuclear astrophysics experiments. First, in dense plasmas, the Coulomb logarithm is often small (i.e. of order 1), and most binary collision theories are derived in the limit $\log\Lambda \gg 1$. They must be modified to retain terms of order $1/\log\Lambda$, which was first treated by Li and Petrasso [7,8].

Similarly, the momentum transfer between the test and field particle must be modified for quantum mechanical effects, since in regimes of interest the classical minimum impact parameter may be smaller than the particle de Broglie wavelength.

The ambient plasma itself is often in a complex state: the electrons may be degenerate, which invalidates the typical assumption of a Maxwellian distribution. In very high density plasmas, ion-ion correlations become important (a strongly-coupled plasma), which limits the applicability of the binary collision scheme. And finally, some plasmas of interest are partially ionized, which requires simultaneously treating collisions with a combination of bound and free electrons.

A variety of plasma stopping theories are used in this work. The Li-Petrasso theory [7,8] is used, which is fundamentally a binary-collision theory retaining terms of order $1/\log\Lambda$, an *ad-hoc* quantum correction, and a correction for collective plasma effects. The Brown-Preston-Singleton theory [10] is also used, which combines both binary-collision and dielectric-response treatments with

a rigorous quantum correction. Finally, the Maynard-Deutsch[11,12] dielectric-response theory for arbitrary-degeneracy electrons is also used. Treatment of partial ionization is done with the formalisms of Mehlhorn[13] and Zimmerman[14].

5.1.5 Experimental motivation

Studying charged-particle stopping in dense plasmas is relevant to fundamental plasma physics and to the potential realization of laboratory-scale thermonuclear fusion. Dense plasmas in the warm-dense-matter (WDM) regime, approximately solid density and tens of eV temperature, are of great interest as a probe of stopping-power theories, with broader physics relevance to non-equilibrium statistical mechanics[15], dense plasma transport properties[16–18], and bound-free transitions in WDM plasmas[19]. Accurate theory for bound-free transitions is required to interpret data obtained with common laser-plasma diagnostics including Thomson scattering[20] and opacity-based areal density techniques[21].

In ICF hot-spot ignition (see Section 1.2.2), the burn wave propagates via fusion-produced energetic α particle self-heating. Understanding the transport of these αs in plasmas at extreme conditions is required to accurately model ignition experiments. Charged-particle transport in and heating of dense plasmas is also highly relevant to alternative particle-beam-driven inertial fusion designs such as heavy-ion fusion[22] and proton fast ignition[23,24].

This chapter describes the first high-precision measurement of charged-particle energy loss in a dense moderately-degenerate and moderately-coupled plasma. The results are compared to theories in common use by simulation codes. For testing theory in this regime, these results are a significant improvement on previous experiments, which utilized simpler low-density non-degenerate plasmas[25–30] or had significantly less precision[31].

5.2 Experimental platform design

The OMEGA laser facility[32] was used to create a pulsed mono-energetic source of protons that probe a subject plasma isochorically heated to WDM conditions. Fig. 5.1 shows the experimental platform used for these experiments. A shock-driven 'exploding pusher' implosion[33] filled with D^3He fuel is used to produce the probing protons via the D^3He fusion reaction (Eq. 1.15). The implosion is driven by 20 of the OMEGA laser beams at 3ω (351nm), delivering 10kJ of energy in a 1ns duration square pulse. These protons, produced over a $\sim$ 100ps burst, then traverse the x-ray isochorically-heated subject plasma. The subject target consists of a plastic (CH) tube coated with $1-2$ μm of Ag, with an inner diameter of 870μm, a wall thickness of 24 μm, and 800 μm in length. A cylindrical Be plug is inserted into the tube, with total $\rho L = 94.2 \pm 0.6$ mg/cm^2, which serves as the subject material for the experiment*. 30 of the OMEGA beams are incident upon the outer surface of the tube, arranged in 3 rings positioned along the axis of the cylinder. The lasers are defocused to create $\sim$ 100 μm diameter illumination spots on the cylinder. The total drive energy on the subject target was 15kJ, delivered in a 1ns square pulse. The resulting intensity in each spot is $\sim 10^{15}$ W/cm^2. This laser intensity generates Ag L-shell emission at 3-4keV in the corona surrounding the cylindrical target, which volumetrically heats the Be plug as the attenuation length in solid Be is $300-500$ μm, comparable to the cylinder's dimensions. The heating occurs over 1ns, and the temperature is quiescent for another ns after the drive turns off[34]. The implosion proton

*The Be used was 99.8% atomic purity, purchased from Goodfellow, with measured mass density 1.77 ± 0.01 g/cm^3. Each target plug was laser-machined from a single sheet with average thickness 532.1 μm and 1σ variation of 1.2 μm, so that each target had to the same total ρL within 0.2%.

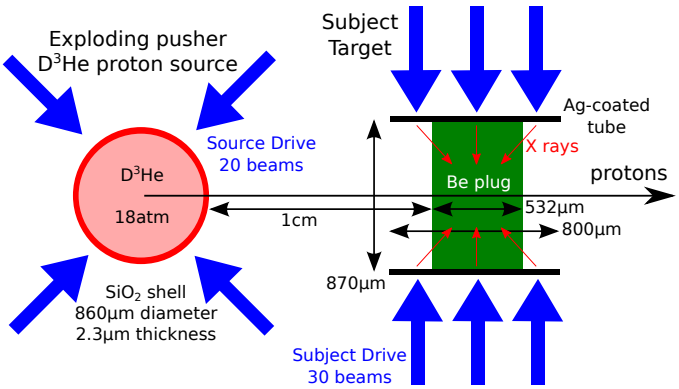

(a) Cartoon

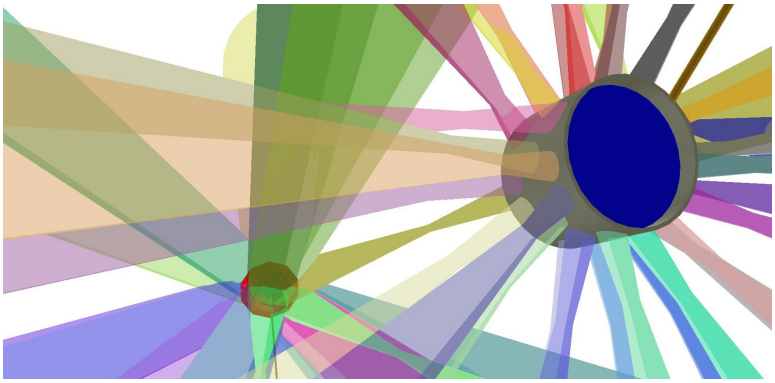

(b) Visrad

Figure 5.1. Experimental geometry. A thin-glass exploding-pusher proton source (left) imploded by 20 laser beams creates energetic D^3He protons to probe a subject plasma, which is created by isochorically heating a solid Be plug with x rays (right). These x rays are created by the 30 laser beams irradiating the Ag-coated CH tube. The subject target is at TCC.

source was timed so that the proton probing occurs at 1.4 ns after the onset of the heating beams, at which time electrostatic charging[28,35] of the subject target is negligible (see Section 5.4).

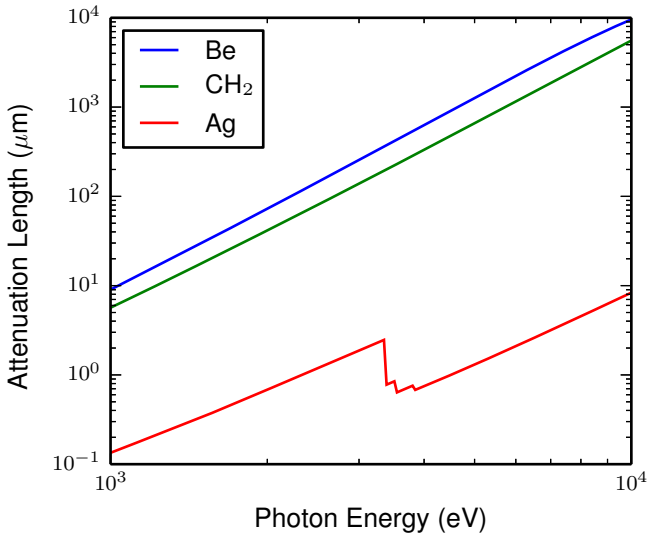

Figure 5.2. Photon attenuation length in materials used: Be, plastic, and Ag.

On each shot, several WRF proton spectrometers[36] are used. Each spectrometer is individually calibrated using an accelerator fusion product source (see Ref. 37 and Section 1.3.1). Three WRFs measured the spectrum emitted from the source, while one measures the downshifted protons traversing the subject plasma. The WRF line-of-sight is small due to its compact nature, and the downshifted spectrum is measured through a ~ 400 μm diameter region in the center of the subject plasma.

5.2.1 Cylinder drive

The arrangement of drive beams on the cylinder target (see Fig. 5.1) must be chosen to optimally distribute the laser energy in the cylinder's azimuthal and axial directions. In this experiment, 30 OMEGA beams are available to heat the subject target. The chosen design arranges these beams into three rings of 10 beams each, which are pointed to achieve azimuthal symmetry. The three rings are displaced for axial symmetry. The chosen design is shown in Fig. 5.3, plotting the incident laser intensity versus z and ϕ in the cylinder target's coordinate system.

The beams are run without phase plates. The best focus conditions for OMEGA beams achieve radii of 50 μm. The beams were defocused so that the spot size is ~ 100 μm. The three rings are clearly visible at $z \sim -250$, 0, and 250 μm. The axial displacement for the first and last rings were chosen to match the Be plug dimensions (500 μm nominal total thickness). The final laser intensity in the spots is very high ($2 - 4 \times 10^{15}$ W/cm^2), which is desirable for generation of the Ag L-shell photons.

The power balance in z and ϕ is obtained by summation of the illumination data over the other coordinate. This is shown in Fig. 5.4. Good power balance is obtained in both directions. The laser configuration used for the cylinder heating in this experiment is summarized in Table 5.1.

5.2.2 X-ray diagnostics

Several instruments were used to diagnose the cylinder's x-ray emission. In particular, framing camera (XRFC) data and streaked spectrometer (SSCA) data were taken to qualitatively diagnose

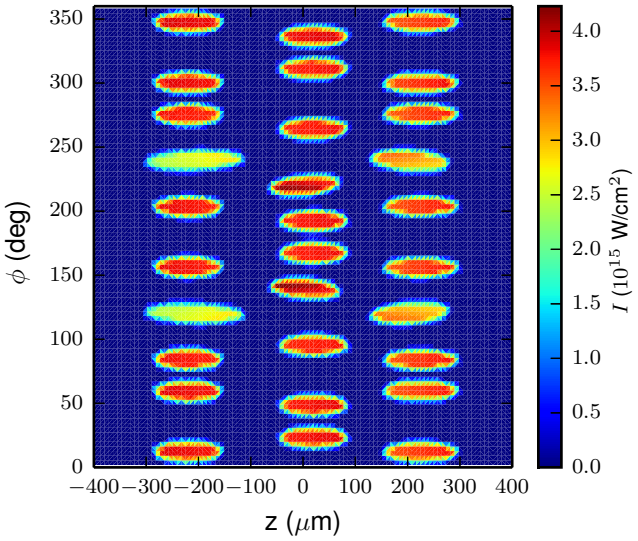

Figure 5.3. Laser intensity on the Ag-coated cylinder.

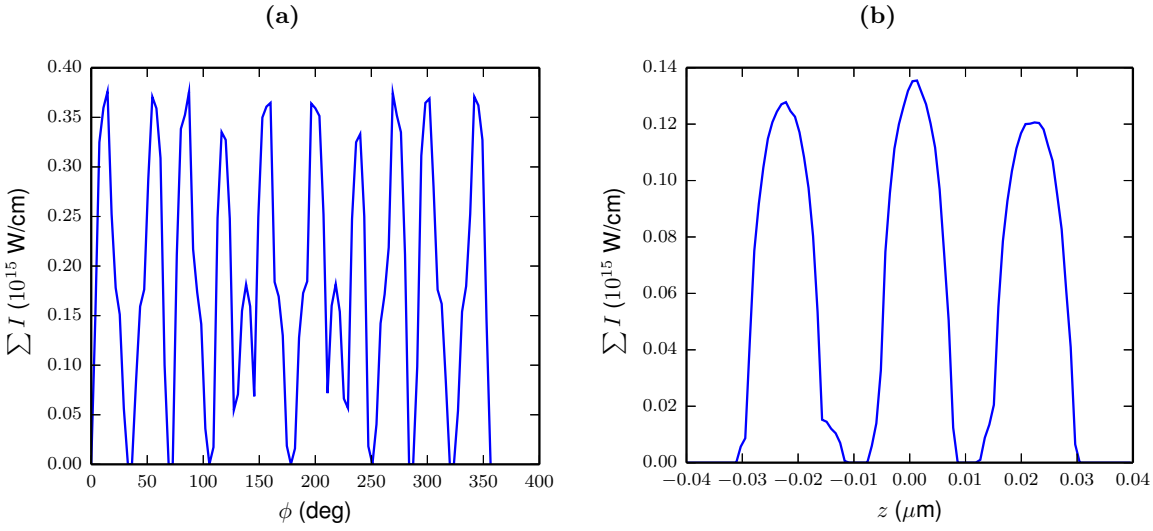

Figure 5.4. Laser intensity on the cylinder versus ϕ (a) and z (b).

Table 5.1. Beam pointing configuration for the cylinder drive. The target is centered at TCC. All spatial units in mm. Pointing expressed as mm towards a port, or (r, θ, ϕ) in target chamber coordinates.

Beams	Pointing	Focus Offset
14, 18, 19, 30, 43, 49, 55, 68	0.15 / P7	-1.0
12, 23, 24, 29, 38, 41, 56, 61	0.05 / P7	-1.0
21, 22, 27, 32, 34, 36, 39, 46	0.05 / P7	-1.0
20	(0.502, 76.6°, 107.3°)	-0.5
30	(0.502, 76.6°, 216.7°)	-0.5
58	(0.46, 46.7°, 100.1°)	-0.3
63	(0.502, 54.0°, 262.8°)	-0.5
65	(0.46, 46.7°, 223.9°)	-0.3
67	(0.502, 54.0°, 61.2°)	-0.5

the spatial and temporal emission. The XRFC data is shown in Fig. 5.5a. The emission in time clearly lasts approximately 1ns, as expected from the laser drive. Early in time (top strip) the emission is dominated by the laser spots on the cylinder's surface. Later in time (strips 2 and 3) the emission region clearly increases, as the emission becomes more dominated by the hot coronal plasma surrounding the cylinder.

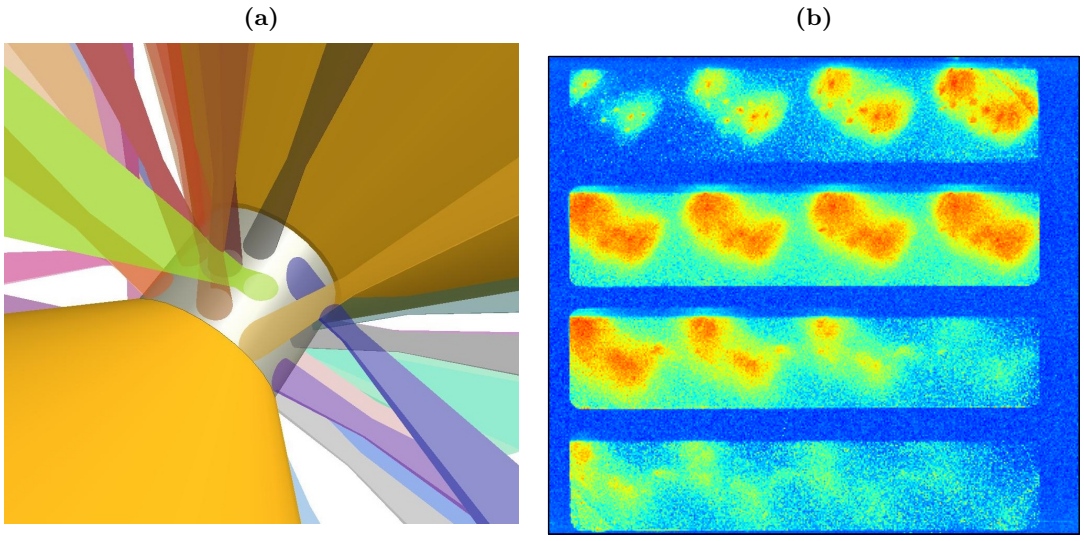

Figure 5.5. **(a)** XRFC view from TIM 1. **(b)** XRFC data as $\log I$ from shot 72016. A four-strip camera was used with 12× magnification. Time increases left to right and top to bottom. The time spanned by a single strip is 200ps, and the timing between strips is 400ps.

The raw SSCA data is shown in Fig. 5.6. The energy dispersion direction is vertical, while time increases to the right (streak direction). This data can be qualitatively analyzed by looking at the emission profile in time of one of the bright lines (Fig. 5.7a), and looking at the spectrum for a single time in the middle of the pulse (Fig. 5.7b).

The emission time history clearly shows that most of the Ag L-shell emission occurs early in the laser pulse. 1-D HYADES simulations indicate that the $1-2$ μm thick Ag layer burns through at around 0.5ns, corresponding to the rapid decrease in L-shell emission. It was expected that the coronal plasma would be hot enough to continue L-shell line emission, but the HYADES simulations suggest that the corona may be too hot - simulated electron temperatures reach $6-10$ keV towards the end of the pulse, which would mean that the Ag will be ionized to a He-like state. Future experiments could use a thicker Ag layer or a shorter laser pulse. The rough inferred x-ray spectrum (Fig. 5.7), using a rough calibration, suggests that the emission is dominated by the Ag L_α at 2.9-3.0 keV and the $L_{\beta 1}$ line at 3.1 keV.

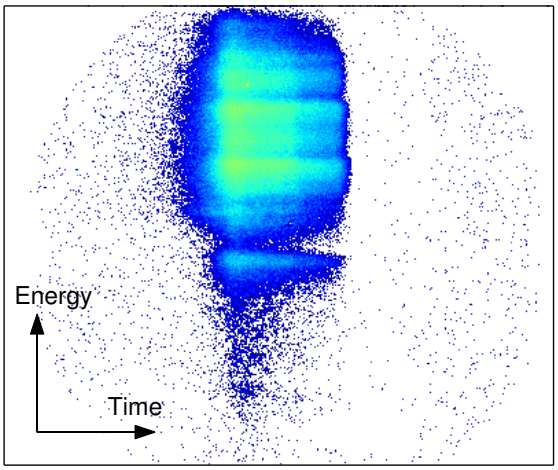

Figure 5.6. Streaked spectrometer (SSCA) data from shot 72028 as background-subtracted $\log I$. The energy dispersion direction is vertical, while the temporal streak is horizontal. A RbAP crystal was used with an energy range of approximately $2.7-3.8$ keV, and the streak time is 4ns.

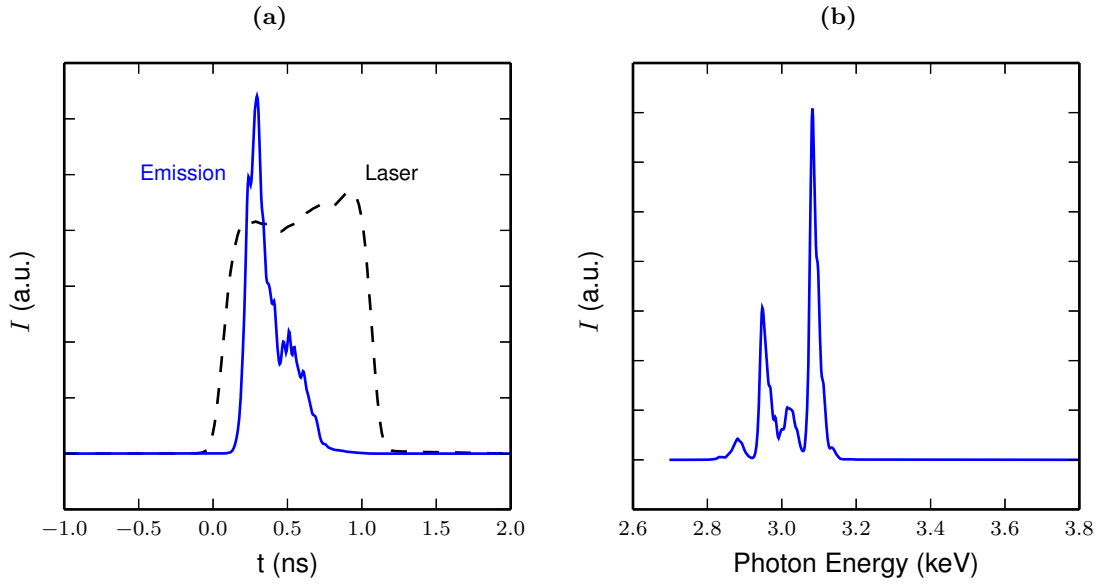

Figure 5.7. Temporal emission profile (a) and time-snapshot spectrum (b) from the SSCA data on shot 72028. The time and energy axes are only approximately calibrated, due to a lack of absolute calibration for this instrument.

5.2.3 Plasma conditions

The x-ray isochoric-heating technique used in this work has been used extensively at OMEGA for dense plasma physics studies[38,34,39,40]. The subject target used here mimics the previous experiments[†]. This technique is uniquely appropriate for stopping-power measurements. Relative to other techniques such as shock compression and proton isochoric heating, the x-ray isochoric heating technique is advantageous in that it produces a large, quiescent, and homogenous plasma.

The isochoric and homogenous nature of the heated plasma comes from several effects. First, the sound speed in solid-density Be is $c_s = \sqrt{\gamma \bar{Z} k_B T_e / m_i} \approx 4 \times \sqrt{\bar{Z} T_e}$ μm/ns, where T_e is the electron temperature in eV, $\bar{Z}$ is the ionization state, and γ is the adiabatic index. The sound speed for these conditions is of order tens of μm/ns; since scale lengths are hundreds of μm and timescales are of order of ns, significant hydrodynamic motion of the Be cannot occur. Secondly, the laser interaction on the outside of the cylinder does not interact hydrodynamically with the Be sample, since the inward-propagating shock wave does not reach the inner material region probed by the protons at the sampling time. This was verified with radiation-hydrodynamics simulations.

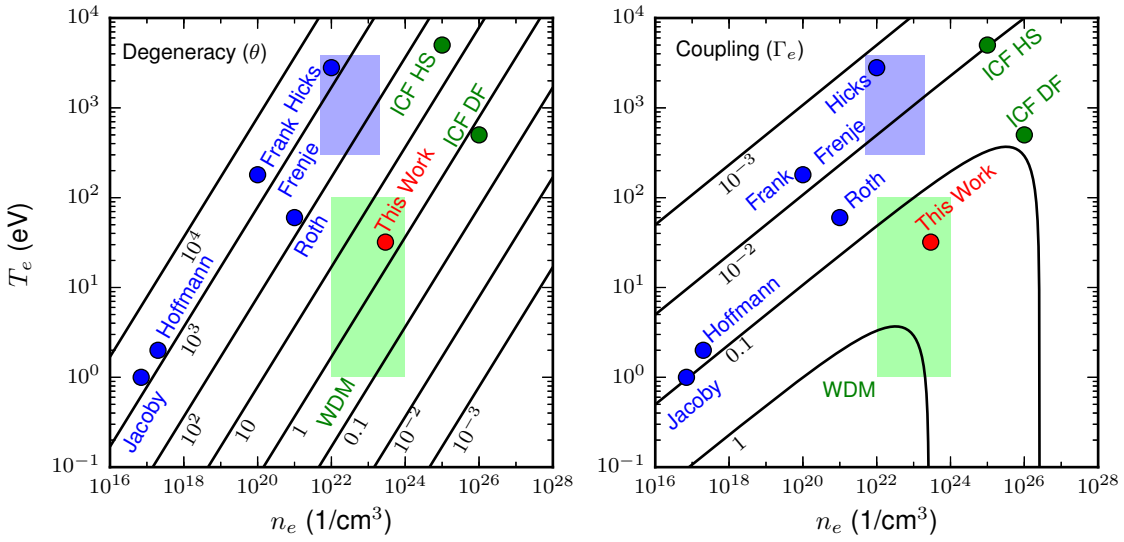

Figure 5.8. Parameter space, showing contours of constant degeneracy (θ, left) and coupling (Γ_e, right) as functions of electron density and temperature. Previous experiments[25–30] are shown in the blue points (blue shaded region for Ref. 30), and this work is shown by the red points. A typical range for WDM ($n_e = 10^{22} - 10^{24}$ 1/cm^3, $T_e = 1 - 100$ eV) is shown by the green shaded box, while typical parameters for the ICF hot spot (HS) and dense fuel (DF) are shown by green points.

Since the mass density is constant, the heated plasma conditions are characterized by the electron temperature (T_e) and the ionization state of the Be ($\bar{Z}$). These are inferred from very similar experiments (Fig. 9 of Ref. 34). The electron temperature, which defines the ionization state (or free-electron density), is set by the x-ray heating. As the drive energy was the same as in previous experiments (15kJ/1ns), we assumed that the conversion of laser energy to L-shell emission is comparable in these experiments, corrected for attenuation in the plastic tube used (12%) and a larger volume of Be (45%). Using this information, the temperature is estimated to

[†]X-ray Thomson scattering to diagnose the Be-plasma conditions simultaneously with the stopping-power measurement was unsuccessful, so we use results previously reported for the determination of T_e and n_e.

be $T_e = 32$ eV. The T_e data in previous experiments had an uncertainty of ±5.5eV; in the following analysis, this is increased to ±15 eV to include any uncertainty in the scaling. The ionization state[‡] using the Glenzer data is then $\bar{Z} = 2.46 \pm 0.15$, corresponding to a free-electron density of $n_e = (2.91 \pm 0.18) \times 10^{23}$ 1/cm^3. This plasma can be understood by the dimensionless parameters for degeneracy (θ) and coupling (Γ_e),

$$\theta \equiv \frac{k_B T_e}{E_F}, \quad \Gamma_e \equiv \frac{e^2}{a(k_B T_e + E_F)}, \tag{5.14}$$

where θ is the ratio of the thermal to Fermi energy (E_F), and Γ_e is the ratio of the electron inter-particle Coulomb potential energy to average kinetic energy ($k_B T_e + E_F$), where $a = [3/(4\pi n_e)]^{1/3}$ is the Wigner-Seitz radius. At these conditions, $\theta \approx 2$ and $\Gamma_e \approx 0.3$, indicating moderate degeneracy and coupling. The parameter space for the degeneracy and coupling versus electron density and temperature is shown in Fig. 5.8, with this work and prior experiments marked. We note that the Graziani et al. (Ref 31) experiments are close to this work in parameter space, but the uncertainty in their stopping-power data is significantly larger, and they were unable to differentiate any stopping models. In Ref. 31, the stopping-power uncertainty reported was ∼ 24%. In this work, the use of mono-energetic D^{3}He protons, WRF proton spectrometers[36,41] with intrinsic energy uncertainty ∼ 40 keV[§], and a large subject plasma with $\rho L \sim 100$ mg/cm^2 enable stopping-power measurements with precision of ∼ 1.5%. On each shot, several WRFs were used: three WRFs measured the spectrum emitted from the source, while one measures the downshifted protons traversing the Be plasma. For the protons traversing the Be plasma, the small WRF solid angle corresponds to measuring protons traversing a ∼ 400 μm diameter cross-section in the center of the Be plasma.

5.3 X-ray Thomson scattering

Ideally the plasma conditions would be measured directly with a surrogate stopping power target. This was attempted with imaging x-ray Thomson scattering using the IXTS diagnostic[42], with the setup shown in Fig. 5.9. Eight additional beams are used to drive a Ni foil, which is radially displaced from the cylinder. The high-intensity illumination of this foil generates Ni K-shell emission at 7.8 keV. These photons can Thomson scatter in the Be sample. Two large conical Au shields are attached to either end of the tube to prevent unscattered radiation from entering the diagnostic line of sight. Additional collimation is provided by a collimator placed between the Ni foil and the tube assembly, and a window in the IXTS-facing conical shield (as depicted in Fig. 5.9). The two collimators were designed so that the photons sampled scatter in a ∼ (200 × 200 × 500) μm volume in the center of the cylinder, with the long dimension oriented radially (i.e. spanning ±250 μm) corresponds to the IXTS spatial imaging axis.

The IXTS data taken is shown in Fig. 5.10. One shot's raw CCD data is shown on the left, and lineouts of the data from all four shots taken are shown on the right. In the CCD image, the main data appears as a streak slightly to the lower left of the center. Some emission is observed around the target shield cone (see Fig. 5.9) above and below the signal region. In the lineout, the Ni K lines appear around pixel 900. The Thomson scattered photons are at a lower pixel number (lower energy). On one shot with a cold subject target (72015, red spectrum), the scattering signal from cold Be is clearly recorded. Two shots were then taken with a heated target (72014 and 72017, blue and purple spectra). Finally, a shot was taken where the Ni K photon source was turned off, so that

[‡] Alternatively, using $T_e = 32 \pm 15$eV and the Muze LDA model gives $Z = 2.28^{+0.42}_{-0.27}$.

[§] The spectrometers employ a single-particle-counting technique using CR-39, with resulting signal-to-noise ratio ∼ 100. The ∼ 40keV energy uncertainty is dominated by the CR-39 proton response (see Ref. 41)

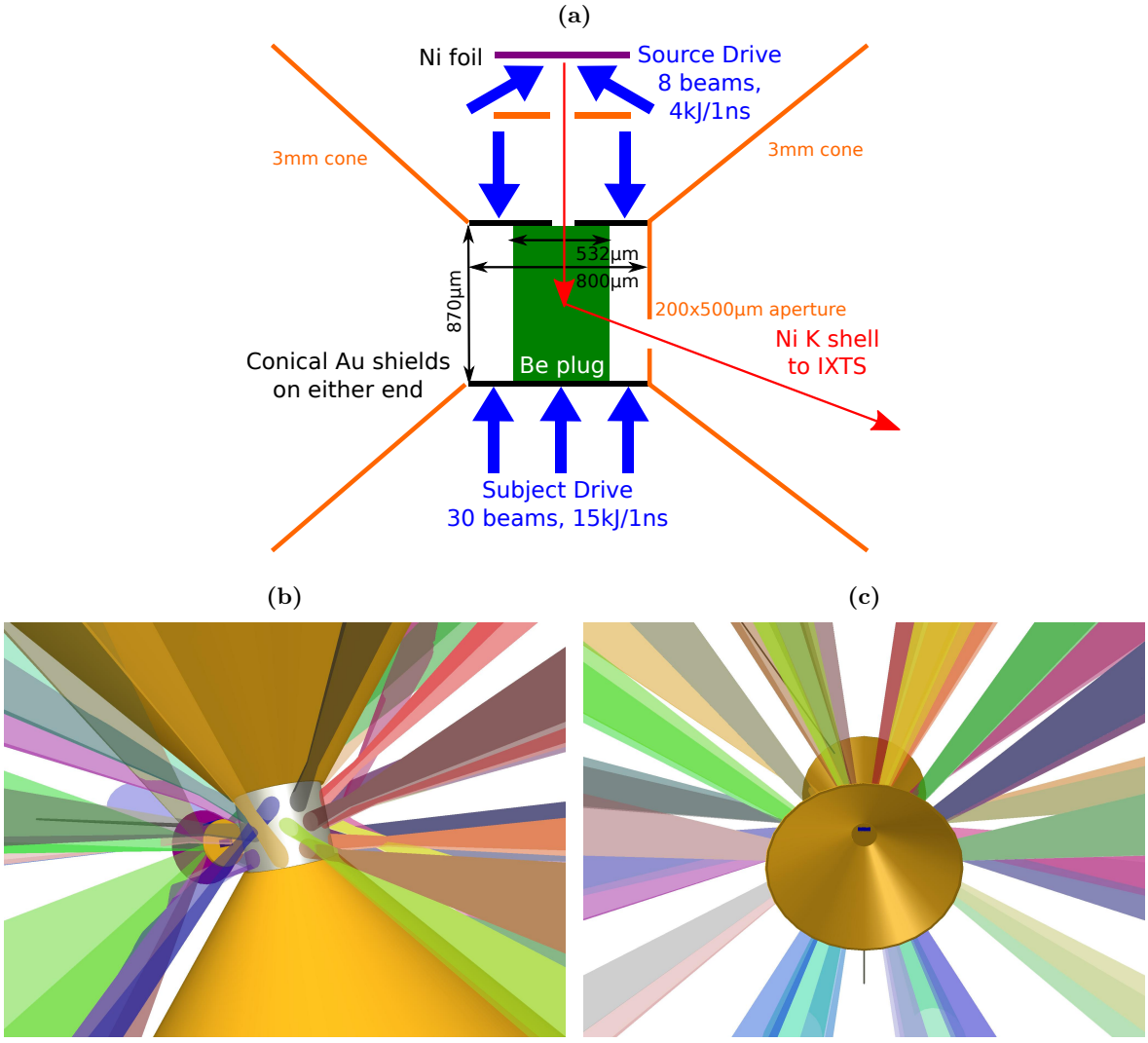

Figure 5.9. Configuration for the IXTS measurement. A Ni foil generates K-shell radiation which scatters in the center of the Be into the IXTS line of sight. Thick conical Au shields (3mm height and maximum radius) are added to either end of the cylinder to shield the diagnostic from unscattered signal. A $100\times200\mu$m collimator is placed between the Ni foil and Be. Additional collimation is provided by a $200\times500\mu$m window in the IXTS-facing conical shield. Shown: **(a)** experimental cartoon, **(b)** Visrad model, **(c)** view from IXTS.

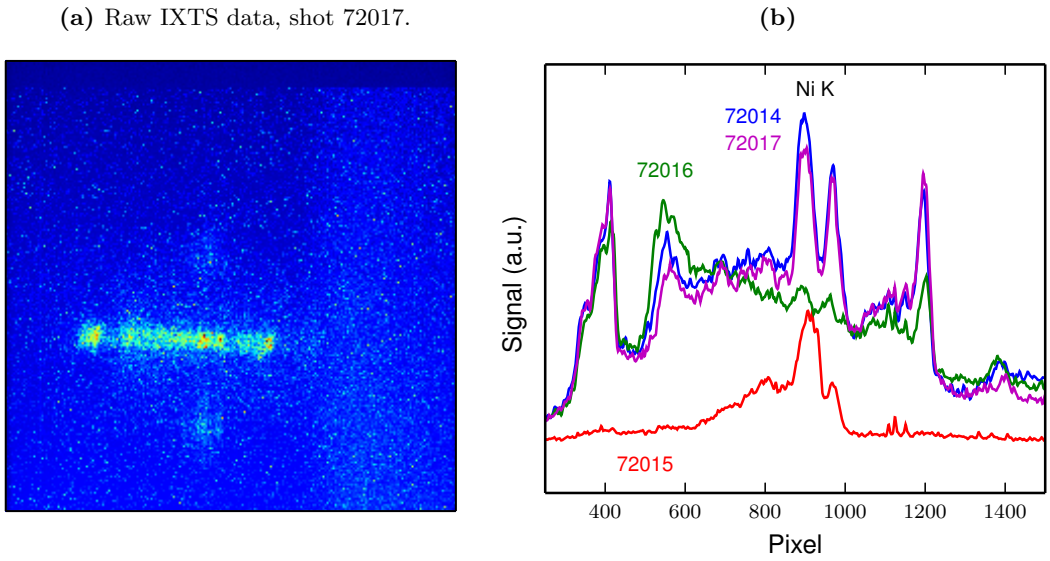

Figure 5.10. **(a)** Raw CCD image from IXTS on shot 72017. The imaging axis is vertical, and the energy dispersion direction is horizontal. **(b)** Lineout data from four IXTS measurements with nominal conditions (72014, 72017), cylinder heating only (72016), and Ni x-ray source only (72015). The cylinder heating (shot 72015) is an unexpectedly large background source.

only signal originating from the cylinder heating is recorded (72016, green spectrum). We observe an unexpectedly high background originating from the cylinder heating. Particularly problematic is the very low signal-to-background in the scattering region, which precludes any high-quality interpretation of this data.

5.4 Proton radiography

The heating occurs over 1ns, and the temperature is quiescent for another ns after the drive turns off[34]. The implosion proton source was timed so that the proton probing occurs at 1.4 ns, which prevents target electrostatic charging effects[28,35] while preserving the temperature. The absence of target charging at the proton probing time was verified using proton radiography[33] on a single shot, using the same experimental configuration as the stopping power measurement.

The radiography data is shown in Fig. 5.11. The expected view (left) is generated from a Visrad model of the experiment. Due to the use of larger implosion targets (see Fig. 5.1), the spatial resolution is degraded relative to standard D^3He proton backlighting[33]. However, the cylinder target with large ρL generates a central region without proton fluence, since protons transiting the cylinder are ranged out in the detector filtering. The expected cylinder size from geometric magnification is shown by the red dashed circle superimposed on the radiograph. The diameter of the image is consistent with the geometric magnification, demonstrating that field effects are not present.

In the corona surrounding the driven cylinder, magnetic fields generated by the Biermann battery ($\nabla n \times \nabla T$) or laser-plasma interaction instabilities are present. While the electric charging of the target decays rapidly after the laser turns off[28,35], these magnetic fields can persist in the low-density coronal plasma, and show up in the radiograph as quasi-filamentary structures around

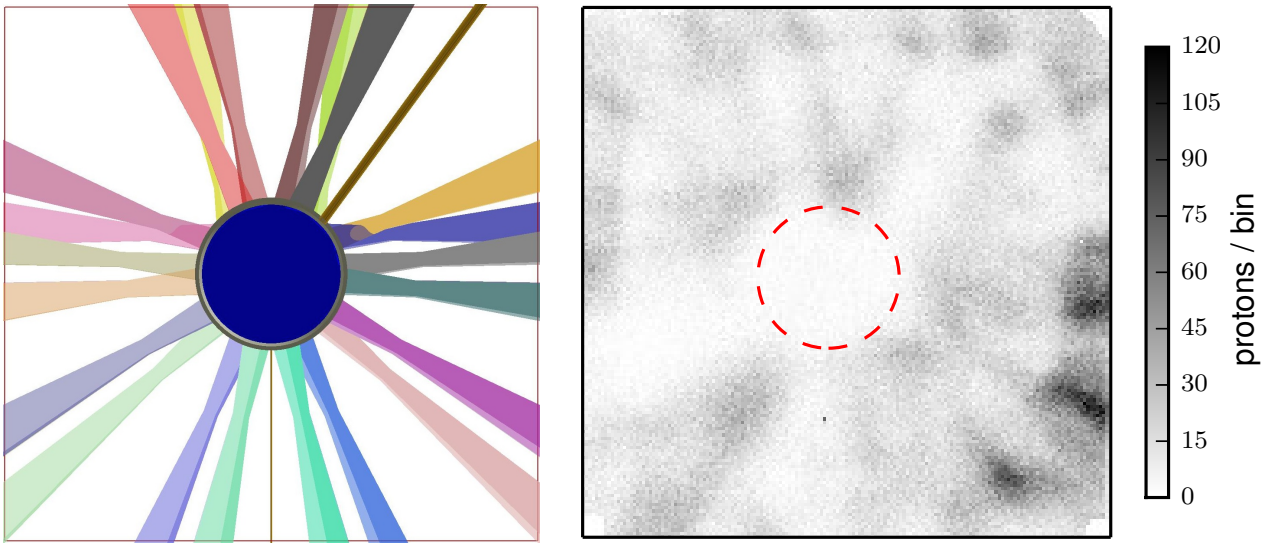

(a) **(b)**

Figure 5.11. Proton radiography from shot 72028. **(a)** Radiography field of view from Visrad model. **(b)** Measured D^3He-p radiograph. The expected geometric size of the cylinder is shown by the red dashed circle.

the periphery of the image. These fields will not affect the stopping power measurement.

5.5 Stopping-power data and downshift analysis

Shots were taken with both undriven (i.e. cold) and heated (warm) Be targets. Data from each type of shot are shown in Fig. 5.12. Three WRFs measured the source spectrum; each is fit with a Gaussian to determine the mean energy. The weighted mean of the three measurements represents the initial proton energy, where the primary source of uncertainty is the WRF response and only relative (random or statistical) uncertainties are retained. Systematic calibration uncertainty is correlated between the WRFs since they are calibrated against the same proton source [37]. The D^3He proton spectra are Doppler-broadened due to the plasma temperature and upshifted slightly from their birth energy (Eq. 1.15) due to radial electric fields around the exploding-pusher implosion [28]. The initial (E_i) and final (E_f) proton energies are determined from a Gaussian fit; the downshift, or total energy loss, is $\Delta E \equiv E_i - E_f$. The measured quantities for each shot are given in Table 5.2. The data clearly show a larger ΔE in the plasma case than in the cold (undriven) case, which means that the stopping power increases in the WDM plasma.

The measured quantities for each shot are given in Table 5.2. The data clearly show a larger ΔE in the plasma case than in the cold (undriven) case, which means that the stopping power increases in the warm-dense-matter plasma.

For comparison, the energy loss can be obtained from theory by integrating the stopping power

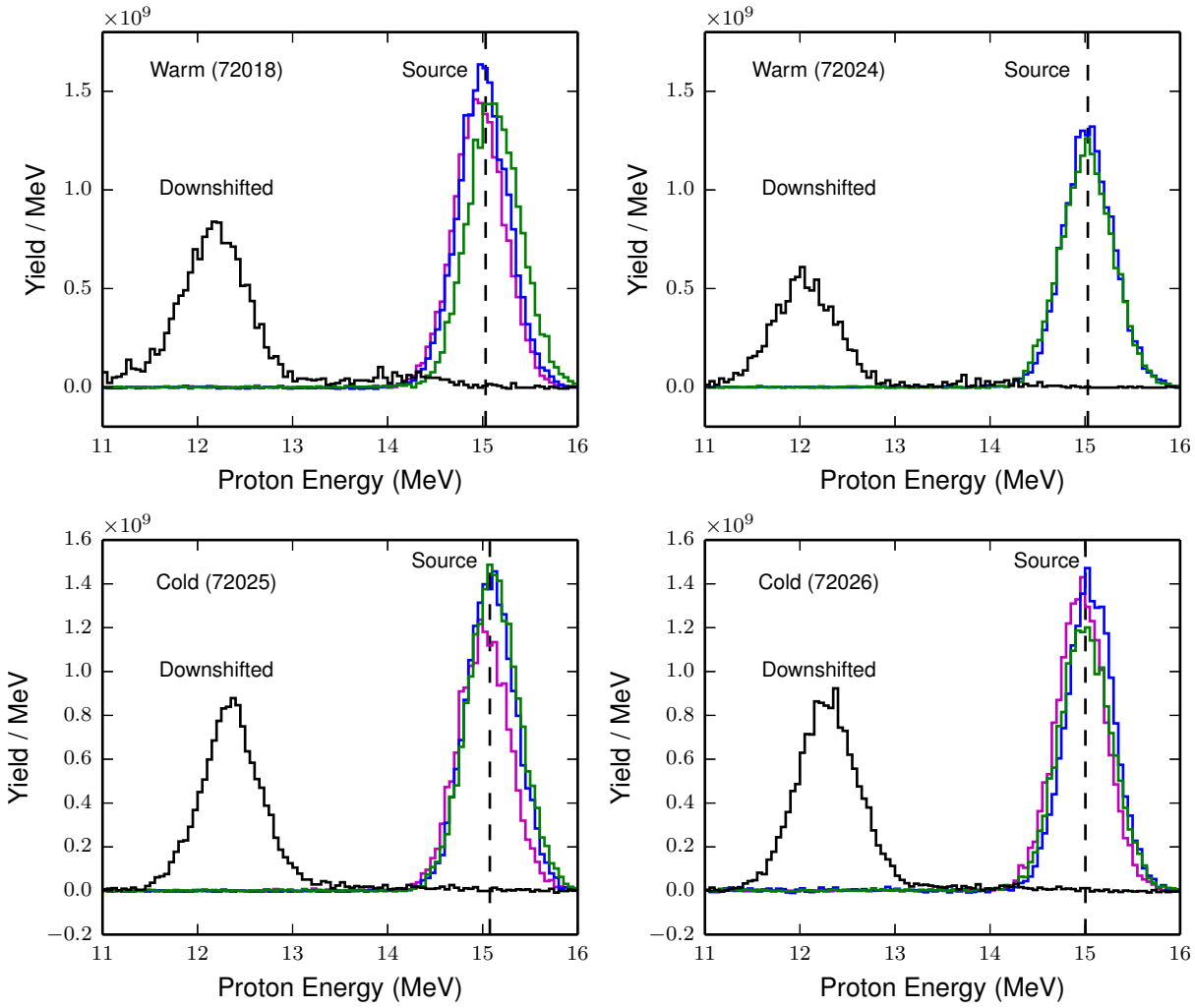

Figure 5.12. Proton spectral data for four shots: with warm subject target (top row) and with a cold subject target (bottom row). The source spectrum is measured directly by several WRFs, while a single WRF measures the downshifted spectrum.

Table 5.2. Data summary: initial (E_i) and final (E_f) energies, and downshift (ΔE) for each shot.

Shot	E_i **(MeV)**	E_f **(MeV)**	ΔE **(MeV)**
72018 (Warm)	15.019 ± 0.020	12.167 ± 0.039	2.851 ± 0.044
72024 (Warm)	15.025 ± 0.029	12.043 ± 0.037	2.981 ± 0.047
72025 (Cold)	15.075 ± 0.018	12.355 ± 0.036	2.720 ± 0.040
72026 (Cold)	15.004 ± 0.017	12.296 ± 0.040	2.708 ± 0.044

over the path-length traversed[¶],

$$\Delta E = -\int_0^L \frac{dE}{dx} dx, \tag{5.15}$$

where dE/dx depends on the particle energy and plasma conditions. A comparison of our data to several theories is shown in Fig. 5.13. The measurement uncertainty is due to the proton spectroscopy uncertainties. In the cold-matter theory calculations the primary uncertainty is the areal density uncertainty and initial energy variations, while the plasma theory uncertainties are dominated by the uncertainty in plasma conditions (n_e, T_e, and $\bar{Z}$ where applicable).

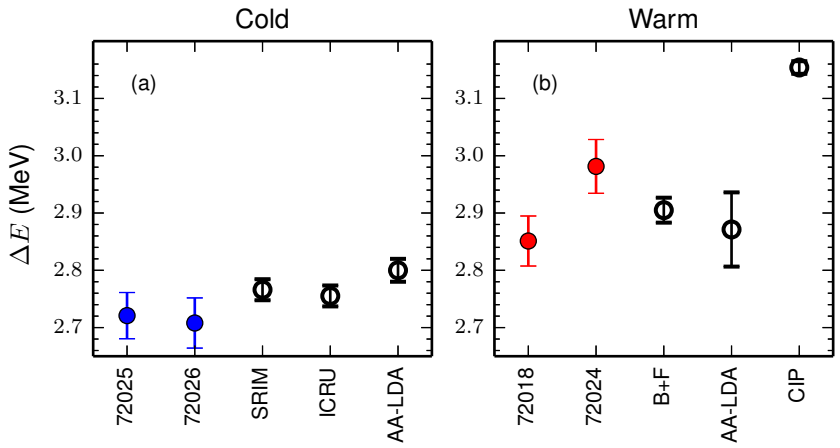

Figure 5.13. Downshift (ΔE) for cold (left) and warm (right) shots compared to theory. The solid points are data (denoted by shot number), and theories are hollow points. The cold data show excellent agreement with SRIM. In the heated plasma experiments, discrepancies with theory are observed. The uncertainties in theoretical calculations are due to uncertainties in ρL and plasma conditions.

First, we compare our cold data to the well-established SRIM[5] and ICRU[43] stopping powers, derived from fits to prior data, which show good agreement given our measurement uncertainty and an expected $\sim 1\%$ uncertainty in the SRIM/ICRU databases (not included in Fig. 5.13 error bars).

The warm data (shots 72018 and 72024) show a clear enhancement in stopping power (downshift) relative to the cold material. dE/dx is enhanced by the long-range nature of stopping on the

[¶]For these conditions the path- and linear-distance energy losses are equivalent to better than 0.1%, since large-angle Coulomb scattering is negligible

plasma (free) electrons relative to the atomic (bound) electrons. There are three common theoretical techniques for treating the partially-ionized material in the warm subject plasma: either an *ad-hoc* combination of independent bound- and free-electron components, or using an inhomogeneous WDM theory such as the average-atom local-density approximation (AA-LDA) model[44,45], or with a Bethe-style effective ionization potential.

In the first case, the partially-ionized plasma is approximated by treating free and bound electrons entirely separately; we use Zimmerman's model[14] for the bound electrons, where a Bethe-Bloch style Coulomb logarithm term is used with an mean ionization potential. For the free electrons, any plasma stopping model which properly reduces to the quantum RPA limit at high particle velocity can be used, such as the Maynard-Deutsch[11] or Brown-Preston-Singleton[10] which give nearly identical results. This *ad hoc* bound+free model is shown in Fig. 5.13 as 'B+F'. In this regime, the approximation agrees with the experimental results. The uncertainty in the theoretical value results from the experimental uncertainties in T_e and $\bar{Z}$.

Secondly, the partially-ionized material can be treated with the AA-LDA model[46], which allows for a self-consistent first-principles treatment of the inhomogeneous electron distribution around an ion ('local'). The inhomogeneities in the electron distribution are, in essence, the system's partial ionization. The AA-LDA stopping-power result is shown in Fig. 5.13, also showing agreement with the experimental data. The uncertainty in the calculated downshift results from the experimental uncertainty in T_e.

Finally, we compare to a 'classical ideal plasma' (CIP) in Fig. 5.13b, which is calculated using a non-degenerate BPS stopping power with an assumed fully-ionized homogenous plasma, i.e. neglecting the partial ionization of this system. This model clearly disagrees with the data, demonstrating the importance of the partial ionization for stopping in this regime.

In calculating the total stopping power, the electron temperature and degeneracy have little direct effect ($\ll 1\%$). This is because the D^3He proton velocity is very high relative to the plasma electron thermal velocity, so this experiment is in the high-energy Bethe stopping limit. However, the heating affects the ionization state and thus the stopping power. The data thus serve as a sensitive probe of the relative importance of bound-free and free-free collisions in each case (cold vs warm), as the electron 'configuration' causes the increased stopping in the WDM plasma through an increase in the average energy transferred to a plasma electron during a collision. This can be modeled using a Bethe-style stopping-power equation[5],

$$\frac{dE}{dx} = -\frac{4\pi Z_t^2 e^4}{m_e v_t^2} n_e \ln\left[\frac{2m_e v_t^2}{\bar{I}}\right], \tag{5.16}$$

where physically, in the Coulomb logarithm, $2m_e v_t^2$ represents the maximum energy transfer to an electron (a head-on collision), and $\bar{I}$ is the 'mean ionization potential' representing the minimum energy transfer, which is sensitive to the electron configuration (bound vs free). This is a simple form of the Coulomb logarithm, neglecting quantum diffraction, dynamical screening, and strong collisions[47,48], but this form can be used to further understand the experimental data. We fit the downshift data using the known target areal density and Eq. 5.16 to infer $\bar{I}$. The best-fit values are shown in Fig. 5.14. The data clearly show a higher $\bar{I}$ in the cold case than in the warm, which corresponds to the observed increase in stopping power (Fig. 5.13). The inferred values of $\bar{I}$ show good agreement with the Andersen-Ziegler value[49] in the cold-matter stopping case. The ideal high-energy-projectile plasma limit, $\bar{I} = \hbar\omega_{pe}$, represents a lower bound on $\bar{I}$, shown by the shaded region in Fig. 5.14. As expected, the WDM case falls between the cold-matter and ideal-plasma limits.

These measurements of the mean ionization potential in a WDM plasma are a strong constraint

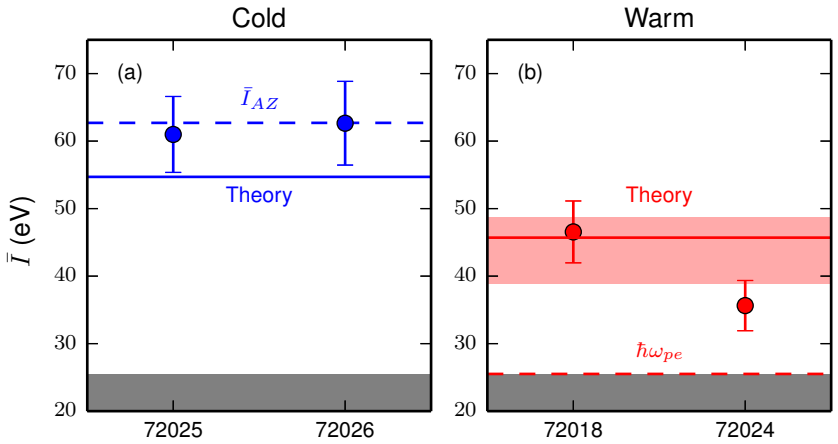

Figure 5.14. Mean ionization potential ($\bar{I}$) inferred from the stopping-power data in the cold (a) and warm (b) cases compared to the Andersen-Ziegler empirical fits ($\bar{I}_{AZ}$), the ideal plasma case ($\hbar\omega_{pe}$), and electronic structure theory.

on modeling of atomic physics and transport phenomena[50], as $\bar{I}$ can be straightforwardly calculated from any electronic structure model. Theoretical values of $\bar{I}$ are calculated in the cold ($\bar{I} = 54.7$ eV) and WDM ($\bar{I} = 45.7^{+3.1}_{-6.8}$ eV) cases using a Kohn-Sham density-functional theory and shown in Fig. 5.14. While this theory slightly underpredicts the data and Andersen-Ziegler values in the cold-matter case, it is in good agreement with the data in the WDM case. Additional tests of such electronic structure models or density functional theory predictions[51] are valuable as these models are applicable to a wide range of transport properties in dense plasmas, for example the phenomena of ionization potential depression[52,53], which is the subject of intensive recent study[54,55], is connected to the mean ionization potential as studied in this work. Other WDM collisional transport rates, such as resistivity and thermal conductivity, cannot be directly tested using this technique, but can be separately calculated using models like the AA-LDA in this work.

5.6 Conclusions

In conclusion, we report the first high-precision energy-loss measurements for energetic D^3He protons traversing an isochorically-heated WDM Be plasma, which show an enhanced stopping power relative to cold matter. By using high-energy protons, the measurement is insensitive to temperature and degeneracy effects, and we thus probe the relative importance of the inhomogeneous electron distribution (bound states) on the stopping power. The partially-ionized material may be treated by an *ad-hoc* combination of independent bound and free components, using the AA-LDA model, or by using a Bethe-style mean ionization potential. The first two models from previous theoretical work are found to be in good agreement with our experimental results. We also use the stopping data to infer $\bar{I}$ in this WDM plasma and compare to results from density functional theory, showing good agreement; this technique is an effective constraint on electronic structure models in WDM. In addition to the basic physics, accurate treatment of stopping in partially-ionized material is particularly relevant to heavy-ion fusion, proton fast ignition, and hot-spot ignition with ablator materials mixed into the fuel.

Accurate theory of charged-particle stopping in dense, degenerate, strongly-coupled and/or

partially-ionized plasmas is a fundamental challenge. We anticipate that this technique will be a robust platform for further stopping-power studies, such as probing at various electron degeneracies, plasma couplings, degrees of ionization, and with other materials to further constrain modeling of WDM plasma physics and stopping in partially-ionized material. Finally, lower-energy particles such as DD-p, DD-T, and D^3He-α will be used to increase the experimental sensitivity to temperature and degeneracy effects.

5.7 References

1. N. Bohr, "On the decrease of velocity of swiftly moving electrified particles in passing through matter," Philosophical Magazine, **30**, 581–612 (1915).
2. S. Atzeni and J. Meyer-Ter-Vehn, *The Physics of Inertial Fusion: Beam Plasma Interaction, Hydrodynamics, Hot Dense Matter*, International Series of Monographs on Physics (Oxford University Press, 2004).
3. H. Bethe, "Zur Theorie des Durchgangs schneller Korpuskularstrahlen durch Materie," Annalen der Physik, **5**, 325–400 (1930).
4. F. Bloch, "Zur Bremsung rash bewegter Teilchen beim Durchgang durch Materie," Annalen der Physik, **16**, 285–320 (1933).
5. J. Ziegler, J. Biersack and U. Littmark, *The stopping and range of ions in matter* (Pergamon, New York, 1985).
6. B. Trubnikov, *Particle Interactions in a Fully Ionized Plasma* (Consultant's Bureau, 1965).
7. C. Li and R. Petrasso, "Charged-particle stopping powers in Inertial Confinement Fusion Plasmas," Phys. Rev. Lett., **70**(20), 3059 (1993).
8. C. Li and R. Petrasso, "Erratum: Charged-particle stopping powers in Inertial Confinement Fusion Plasmas," Phys. Rev. Lett. (2015).
9. H. A. Gould and H. E. DeWitt, "Convergent kinetic equation for a classical plasma," Phys. Rev., **155**, 68–74 (1967).
10. L. S. Brown, D. L. Preston, and R. L. Singleton Jr., "Charged particle motion in a highly ionized plasma," Physics Reports, **410**(4), 237 – 333 (2005).
11. G. Maynard and C. Deutsch, "Energy loss and straggling of ions with any velocity in dense plasmas at any temperature," Phys. Rev. A, **26**, 665 (1982).
12. G. Maynard and C. Deutsch, "Born random phase approximation for ion stopping in an arbitrary degenerate electron fluid," J. Physique, **46**, 1113–1122 (1985).
13. T. A. Mehlhorn, "A finite material temperature model for ion energy deposition in iondriven inertial confinement fusion targets," Journal of Applied Physics, **52**(11), 6522–6532 (1981).
14. G. Zimmerman, "Recent Developments in Monte Carlo Techniques," LLNL report, UCRL-JC-105616 (1990).
15. R. Zwanzig, *Nonequilibrium statistical mechanics* (Oxford University Press, 2001).
16. Z. Donkó and B. Nyíri, "Molecular dynamics calculation of the thermal conductivity and shear viscosity of the classical one-component plasma," Phys. Plasmas, **7**(1), 45–50 (2000).
17. J. Daligault and G. Dimonte, "Correlation effects on the temperature-relaxation rates in dense plasmas," Phys. Rev. E, **79**, 056,403 (2009).
18. L. X. Benedict *et al.*, "Molecular dynamics simulations and generalized lenard-balescu calculations of electron-ion temperature equilibration in plasmas," Phys. Rev. E, **86**, 046,406 (2012).
19. S. Vinko, O. Ciricosta and J. Wark, "Density functional theory calculations of continuum lowering in strongly coupled plasmas," Nature communications, **5** (2014).
20. G. Gregori, S. H. Glenzer, W. Rozmus *et al.*, "Theoretical model of x-ray scattering as a dense matter probe," Phys. Rev. E, **67**, 026,412 (2003).
21. S. J. Rose, "Calculations of the radiative opacity of laser-produced plasmas," Journal of Physics B: Atomic, Molecular and Optical Physics, **25**(7), 1667 (1992).
22. S. Humphries Jr., "Intense pulsed ion beams for fusion applications," Nuclear Fusion, **20**(12), 1549 (1980).
23. M. Tabak, J. Hammer, M. E. Glinsky *et al.*, "Ignition and high gain with ultrapowerful lasers*," Phys. Plasmas, **1**(5), 1626–1634 (1994).

24. M. Roth *et al.*, "Fast ignition by intense laser-accelerated proton beams," Phys. Rev. Lett., **86**, 436–439 (2001).
25. D. H. H. Hoffmann, K. Weyrich, H. Wahl *et al.*, "Energy loss of heavy ions in a plasma target," Phys. Rev. A, **42**, 2313–2321 (1990).
26. J. Jacoby, D. H. H. Hoffmann, W. Laux *et al.*, "Stopping of Heavy Ions in a Hydrogen Plasma," Phys. Rev. Lett., **74**, 1550–1553 (1995).
27. M. Roth, C. Stöckl, W. Süß *et al.*, "Energy loss of heavy ions in laser-produced plasmas," EPL (Europhysics Letters), **50**(1), 28 (2000).
28. D. G. Hicks *et al.*, "Charged-particle acceleration and energy loss in laser-produced plasmas," Phys. Plasmas, **7**(12), 5106–5117 (2000).
29. A. Frank, A. Blažević, V. Bagnoud *et al.*, "Energy loss and charge transfer of argon in a laser-generated carbon plasma," Phys. Rev. Lett., **110**, 115,001 (2013).
30. J. Frenje *et al.*, to be submitted to Phys. Rev. Lett. (2015).
31. F. Graziani *et al.*, "Large-scale molecular dynamics simulations of dense plasmas: The cimarron project," High Energy Density Physics, **8**, 105–131 (2012).
32. T. Boehly, D. Brown, R. Craxton *et al.*, "Initial performance results of the OMEGA laser system," Optics Communications, **133**(1-6), 495–506 (1997).
33. C. K. Li, F. H. Séguin, J. A. Frenje *et al.*, "Monoenergetic proton backlighter for measuring E and B fields and for radiographing implosions and high-energy density plasmas (invited)," Rev. Sci. Instrum., **77**(10), 10E725 (2006).
34. S. H. Glenzer, G. Gregori, F. J. Rogers *et al.*, "X-ray scattering from solid density plasmas," Phys. Plasmas, **10**(6), 2433–2441 (2003).
35. N. Sinenian, M. J.-E. Manuel, J. A. Frenje *et al.*, "An empirical target discharging model relevant to hot-electron preheat in direct-drive implosions on OMEGA," Plasma Physics and Controlled Fusion, **55**(4), 045001 (2013).
36. F. H. Séguin, J. A. Frenje, C. K. Li *et al.*, "Spectrometry of charged particles from inertial-confinement-fusion plasmas," Rev. Sci. Instrum., **74**(2), 975–995 (2003).
37. N. Sinenian, M.-E. Manuel, A. Zylstra *et al.*, "Upgrade of the MIT Linear Electrostatic Ion Accelerator (LEIA) for nuclear diagnostics development for Omega, Z and the NIF," Rev. Sci. Instrum., **83**(4), 043502 (2012).
38. S. H. Glenzer, G. Gregori, R. W. Lee *et al.*, "Demonstration of Spectrally Resolved X-Ray Scattering in Dense Plasmas," Phys. Rev. Lett., **90**, 175002 (2003).
39. S. H. Glenzer, O. L. Landen, P. Neumayer *et al.*, "Observations of plasmons in warm dense matter," Phys. Rev. Lett., **98**, 065,002 (2007).
40. S. H. Glenzer and R. Redmer, "X-ray Thomson scattering in high energy density plasmas," Rev. Mod. Phys., **81**, 1625–1663 (2009).
41. F. H. Séguin, N. Sinenian, M. Rosenberg *et al.*, "Advances in compact proton spectrometers for inertial-confinement fusion and plasma nuclear science," Rev. Sci. Instrum., **83**(10), 10D908 (2012).
42. E. J. Gamboa, C. M. Huntington, M. R. Trantham *et al.*, "Imaging x-ray Thomson scattering spectrometer design and demonstration (invited)," Rev. Sci. Instrum., **83**(10), 10E108 (2012).
43. International Commission on Radiation Units and Measurements, *ICRU Report 49, Stopping Powers and Ranges for Protons and Alpha Particles* (1993).
44. I. Nagy and B. Apagyi, "Scattering-theory formulation of stopping powers of a solid target for protons and antiprotons with velocity-dependent screening," Phys. Rev. A, **58**, R1653–R1656 (1998).
45. G. Faussurier, C. Blancard, P. Cossé *et al.*, "Equation of state, transport coefficients, and stopping power of dense plasmas from the average-atom model self-consistent approach for astrophysical and laboratory plasmas," Phys. Plasmas, **17**(5), 052707 (2010).
46. S. B. Hansen, A. Y. Faenov, T. A. Pikuz *et al.*, "Temperature determination using $k\alpha$ spectra from m-shell ti ions," Phys. Rev. E, **72**, 036,408 (2005).
47. D. Gericke, M. Schlanges and W. Kraeft, "Stopping power of a quantum plasma t-matrix approximation and dynamical screening," Physics Letters A, **222**(4), 241 – 245 (1996).
48. G. Röpke, R. Redmer, A. Wierling *et al.*, "Strong collisions and response function for two-component plasmas," Physics of Plasmas, **7**(1), 39–44 (2000).

49. H. Andersen and J. Ziegler, *Hydrogen Stopping Powers and Ranges in All Elements* (Pergamon, New York, 1979).
50. D. Ballester and I. M. Tkachenko, "Fast-projectile stopping power of quantal multicomponent strongly coupled plasmas," Phys. Rev. Lett., **101**, 075,002 (2008).
51. M. S. Murillo, J. Weisheit, S. B. Hansen *et al.*, "Partial ionization in dense plasmas: Comparisons among average-atom density functional models," Phys. Rev. E, **87**, 063,113 (2013).
52. G. Ecker and W. Kröll, "Lowering of the ionization energy for a plasma in thermodynamic equilibrium," Physics of Fluids (1958-1988), **6**(1), 62–69 (1963).
53. J. C. Stewart and K. D. Pyatt, Jr., "Lowering of Ionization Potentials in Plasmas," Astrophysical Journal, **144**, 1203 (1966).
54. O. Ciricosta *et al.*, "Direct measurements of the ionization potential depression in a dense plasma," Phys. Rev. Lett., **109**, 065,002 (2012).
55. D. J. Hoarty, P. Allan, S. F. James *et al.*, "Observations of the effect of ionization-potential depression in hot dense plasma," Phys. Rev. Lett., **110**, 265,003 (2013).

6

Development of platforms for plasma-stopping-power experiments on OMEGA EP

6.1 Introduction

The Target-Normal Sheath Acceleration (TNSA)[1] mechanism is a well-known technique for producing high fluences of energetic ions, mainly in a forward-directed beam. These ion beams have many potential applications including proton radiography (see Appendix A), proton probing, and proton isochoric heating[2]. Typically mid- or high-Z flat foils are used as source targets for these experiments. In this work, several advanced target types were tested on the OMEGA EP laser[3]. In Section 6.2.1, several types of substrate material were used to study the material's effect on proton beam uniformity, which is also critical for proton radiography applications. In Section 6.2.2, microstructured plastic-coated targets were used in a replication experiment of previously-published results showing quasi-monoenergetic peaks in the TNSA spectrum[4]. TNSA protons were also studied for use in proton isochoric heating (Section 6.3). Lastly, a EP platform using halfraum-heated foams as a subject plasma were recently attempted (Section 6.4).

6.2 TNSA Proton Sources

The geometry for TNSA proton source experiments is shown schematically in Fig. 6.1. The target is a planar source foil with the short-pulse beam incident upon the front surface. The primary diagnostics are radiochromic film (RCF)[5] and a Thomson-Parabola Ion Energy analyzer (TPIE)[6–8]. To support several experiments, including this work, a smaller-field 1.6kG permanent dipole magnet was purchased for the TPIE system[6]. The calibrati on of this magnet is described in Sec. 6.2.3.

6.2.1 Proton Source Foils

Non-uniform proton emission from TNSA foils is commonly observed at OMEGA EP, where 10μm-thick Au foils are typically used[9]. It is known that the surface quality of these targets is not good, with thickness variation up to 10% expected. Since the TNSA mechanism is highly sensitive to the conditions on both target surfaces, it has been expected that these targets may have degraded performance due to the poor surface quality. Previous experiments on the TITAN laser facility found improved uniformity with improved target surface quality[10], motivating similar experiments at OMEGA EP.

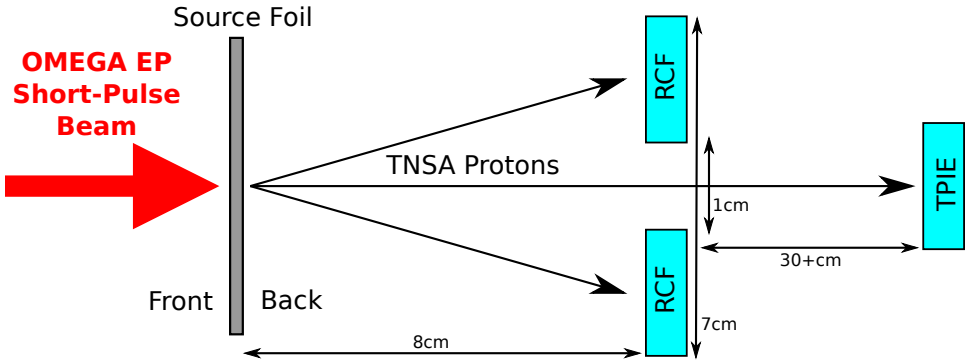

Figure 6.1. Experimental geometry for the TNSA proton source experiments. The short-pulse laser is incident upon the front surface of a source foil. Ions accelerated from the rear surface are detected by RCF and the TPIE spectrometer.

Table 6.1. Types of target foils used, and their RMS surface roughness (δT).

Foil type and thickness	RMS δT (nm)
Goodfellow 10μm Au	$800 - 900$
GA-machined 10μm Au	30
50μm Si Wafer with 1μm Au coating	4
50μm CVD Wafer with 1μm Au coating	≤ 10

Four different types of planar foils were made and tested. The foils types and their RMS surface roughness are summarized in Table 6.1. The Goodfellow[11] and GA-machined Au foils are 10 μm total thickness. The wafer targets have a 50 μm substrate thickness, with 1 μm of Au coating on either side. The advanced targets have a $10 - 100\times$ improvement in surface roughness over the standard Goodfellow foils.

The foils were all driven by one short-pulse beam of OMEGA EP using 'best compression' (1ps pulse). The uniformity is diagnosed with RCF. Three shots with identical high-intensity drive and various foil types are shown in Fig. 6.2. The wafer foils, with much less surface roughness, still exhibit significant spatial non-uniformities in the emitted proton beam. Similarly, a comparison of Goodfellow and GA-machined Au foils is shown in Fig. 6.3.

The images clearly show that the foils with very poor surface uniformity (the Goodfellow Au) have significant high-mode quasi-filamentary structures in the emitted proton beam, which are not observed in the beams from smoother foils. However, the advanced foils have very significant lower-mode structure in the emitted beams, which would be extremely problematic for radiography applications.

One common factor is the laser spot uniformity on a foil, which is shown in Fig. 6.4. The extremely non-uniform laser illumination is typical for experiments at EP, and may seed instabilities. In particular, prior experiments and simulation work have shown that resistive filamentation instabilities can develop as the laser-accelerated electrons propagate through the solid source target[12,13]. The non-uniform laser irradiation may seed an initial non-uniformity in electron flux, which will accentuate through the filamentation instability. The prior literature predicts a stabilization of the resistive filamentation instability in diamond wafer targets at lower intensity due to the low-temperature resistivity behavior of diamond[12].

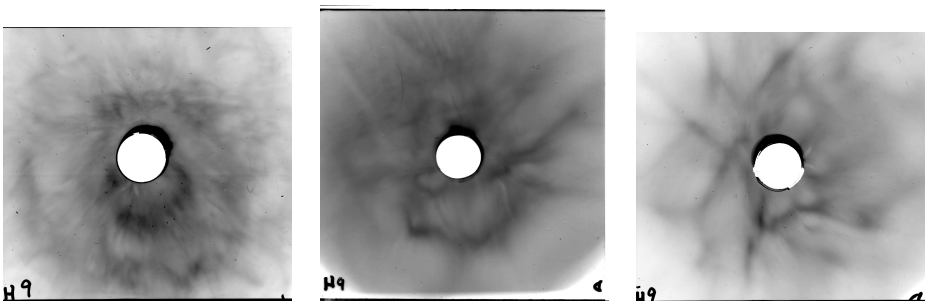

(a) Goodfellow Au (13965) **(b)** Si wafer (15305) **(c)** CVD wafer (17420)

Figure 6.2. Proton beam images using 400J/1ps drive with three target types. RCF filtering corresponds to a peak sensitivity to 35 MeV protons. All target types display significant non-uniformities. Shot numbers are given for each experiment in parentheses. The hole in the middle of the film is for the TPIE spectrometer LOS (see Fig. 6.10). Each film is 7cm square (see Fig. 6.1).

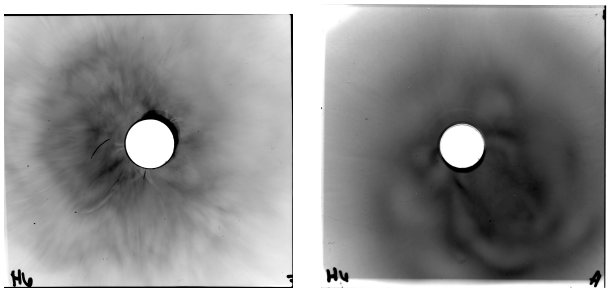

(a) Goodfellow Au (13971) **(b)** GA Au (15296)

Figure 6.3. Proton beams produced by using 200J/1ps laser pulses incident upon the two types of Au target. RCF filtering corresponds to a peak sensitivity to 18 MeV protons (lower than Fig. 6.2 due to the lower drive energy). Both target types display significant non-uniformities.

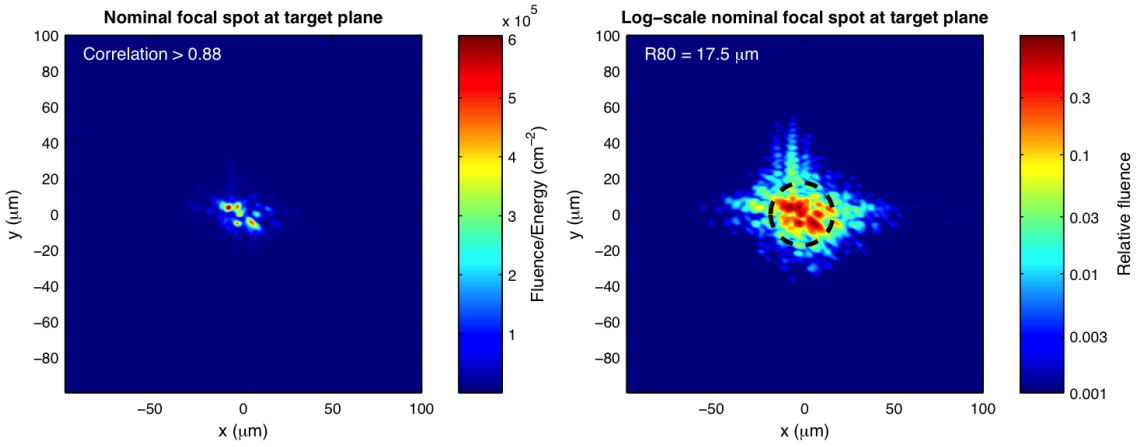

Figure 6.4. Laser focal spot shape for shot 15301. Significant non-uniformity in the laser illumination on the foil is routinely seen at EP.

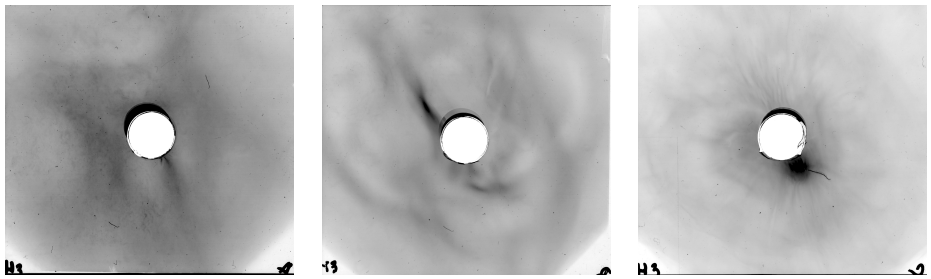

(a) CVD wafer (17414) **(b)** Si wafer (17416) **(c)** Goodfellow Au (17418)

Figure 6.5. Images of proton beams using 40J/1ps laser pulses incident upon three target types. RCF filtering corresponds to a peak sensitivity to 9 MeV protons.

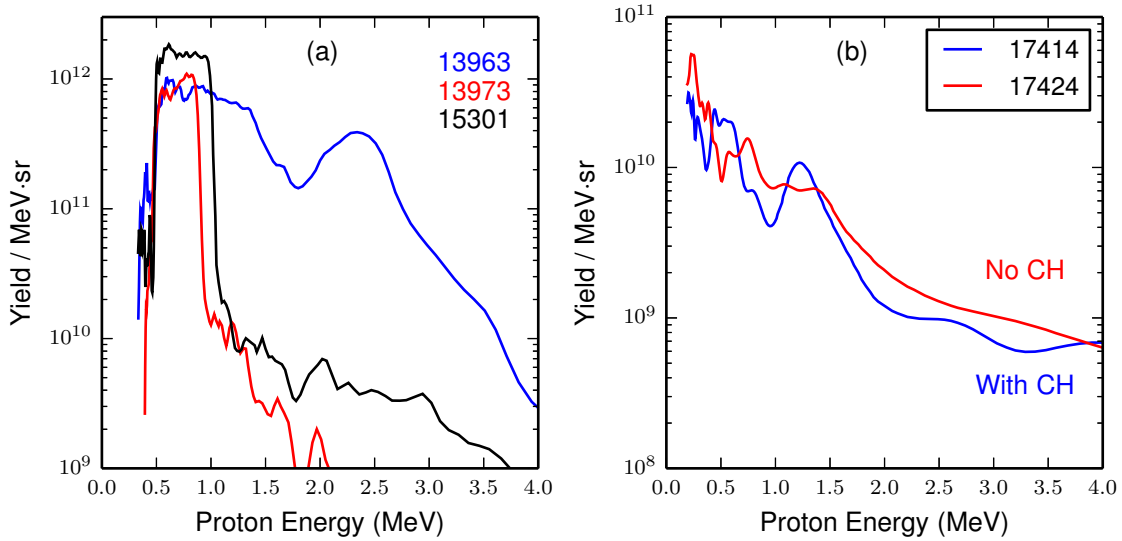

Figure 6.6. Proton spectra measured with TPIE. These protons were produced using high-intensity drive (400J/1ps, a) or low-intensity drive (40J/1ps, b) onto microstructured foils.

To test this, the same targets were shot with a factor of 10× less energy (40J/1ps). The results are shown in Fig. 6.5. While non-uniformities are still apparent in all experiments, the CVD wafer qualitatively appears to have the best uniformity, which may support prior results, and the hypothesis that the focal spot non-uniformity is causing the observed variation at higher intensity.

6.2.2 CH-coated foils

Shots with CH-coated foils were also conducted. The motivation for these experiments was to repeat prior experiments[4], which showed quasi-monoenergetic peak structures in the spectra of TNSA protons when using microstructured foils. A large dot (500μm square) of CH was deposited onto the rear surface of a TNSA planar foil. The size of the coating is much larger than the laser spot size ($\sim 20\mu$m). The data taken at EP using microstructured targets is shown in Fig. 6.6.

When driven at high intensity, one shot of data (13963) does display a clear peak at $E_p \sim 2.5$ MeV, similar to the Schwoerer results (Ref. 4). However, attempts to repeat the experiment (shots 13973, 15301) result in very different proton spectra. The sharp cutoffs ~ 1 MeV in these spectra

Table 6.2. Configuration of TPIE for the calibration shots.

Pinhole	250 μm
E Field	9 kV/cm
Detector Position	P1 (10cm)
Pinhole-TCC	40 cm
Detector	CR-39 + BAS-TR IP
Magnet	1.6 kG

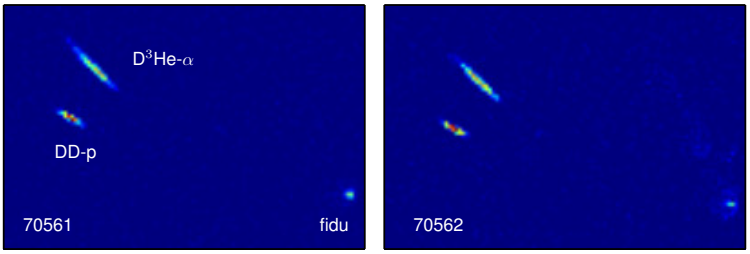

Figure 6.7. Raw data from two TPIE calibration shots (70561 and 70562). Red=more signal. The fiducial, DD-p, and D^3He-α are clearly visible. Here the electric deflection is vertical, and the magnetic deflection is horizontal. The TPIE CR-39 is 5×10 cm.

are not typical of TNSA. We hypothesize that the cutoff results from non-uniformities in the proton emission (see Sec. 6.2).

At low intensity (17414), a similar result is seen, with a peak at ~ 1 MeV. In this case we have a direct comparison to an identical shot without plastic coating (17424). However the repeatability or reliability of this peak generation has not yet been tested.

6.2.3 TPIE 1.6kG magnet calibration

A Thomson parabola consists of parallel electric and magnetic fields. In TPIE, these are provided by parallel electrically-biased plates and a permanent dipole magnet, respectively. The magnetic deflection can be calibrated by using particles of known species and energy. In this work, D^3He-gas-filled 'exploding pusher' implosions were conducted on the OMEGA laser to calibrate TPIE. The targets were 860 μm OD SiO_2 shells of 2.3 μm thickness filled with 15 atm of equimolar fuel, driven by 60 beams with 14kJ of total energy in a 600ps pulse shape with SSD, DPR, and SG4 DPP. The D^3He and DD nuclear reactions (Eqs. 1.15 and 1.17) were used to generate 3.7 MeV αs and 3.0 MeV protons, respectively, which are used for the calibration. The TPIE configuration for the calibration experiment is shown in Table 6.2. The raw data are shown in Fig. 6.7. The fiducial is visible at lower right. The DD-p and D^3He-α are clearly visible as peaks in particle fluence. In these images, the magnetic deflection is horizontal and the electric deflection is vertical. Both are measured relative to the fiducial. The data are analyzed by generating lineouts in x and y (magnetic and electric deflection, respectively) for each peak. The lineouts for shot 70561 are shown in Fig. 6.8. Gaussian fits to each peak in x and y (shown by the red dashed curves) are used to determine the peak position.

The energies of these particles were also measured with both Charged-Particle Spectrometers (CPS)[14], which are used for a cross-calibration, and are shown in Table 6.3. Agreement between the

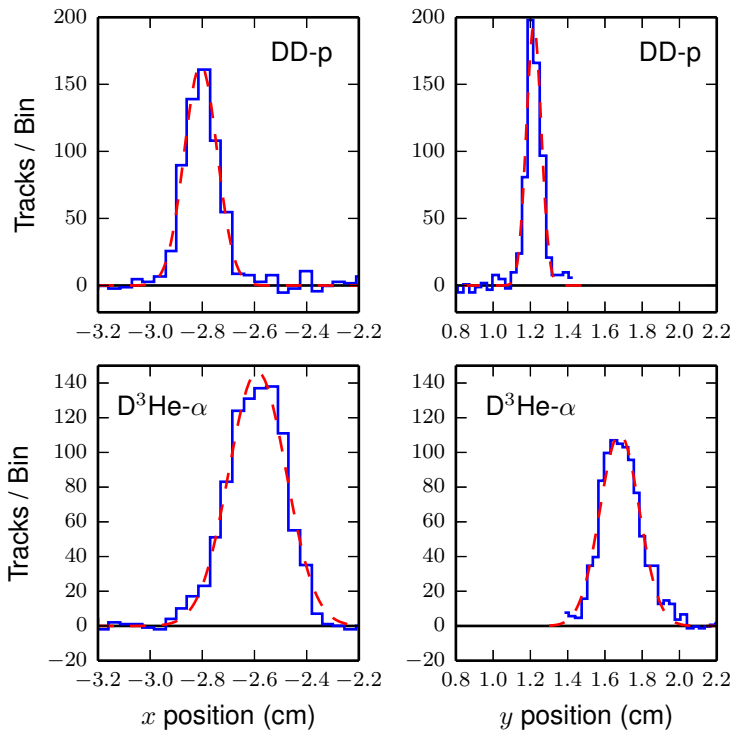

Figure 6.8. TPIE analysis: peak lineouts and fits for the DD-p (top) and D^{3}He-α (bottom) calibration data from shot 70561.

Table 6.3. Particle energies measured by CPS 1 and 2, which are used for the energy calibration of TPIE.

	CPS 1		**CPS 2**	
Shot	DD-p E (MeV)	D^{3}He-α E (MeV)	DD-p E (MeV)	D^{3}He-α E (MeV)
70561	3.08	3.69	3.11	3.74
70562	3.12	3.82	3.17	3.74

two diagnostics is observed, demonstrating good spatial uniformity in the emitted particle energy. The TPIE results are shown in Table 6.4. First, the electric deflection of each peak is used to infer a droop in the electric field, which is a known effect caused by implosion-generated hot electrons reducing the applied potential[6]. Good agreement in the inferred post-droop electric field is found between the two particles as well as between the two shots, demonstrating consistency.

The calibration of the magnet itself in the analysis[6] is based upon a fit to the data, with the functional form

$$x = \frac{m}{\sqrt{E}} + b, \tag{6.1}$$

where x is the magnetic deflection, E is the particle energy, and m and b are calibration coefficients. A preliminary calculated calibration[6] had given $m = 4.24$ and $b = -0.12$. The data are given in Table 6.4. Average values $m = 4.47$ and $b = -0.005$ are used. The fact that b is found to be close to 0 is reassuring, since in the limit $E \to \infty$ the magnetic deflection is expected to go to 0.

The particle yield inferred from TPIE is also compared to the well-understood CPS 1 and 2

Table 6.4. TPIE 1.6kG magnet calibration results

Shot	DD-p $\|E\|$ (kV/cm)	D^3He-α $\|E\|$ (kV/cm)	m	b
70561	6.01	6.04	4.38	.05
70562	6.05	6.08	4.56	-0.06

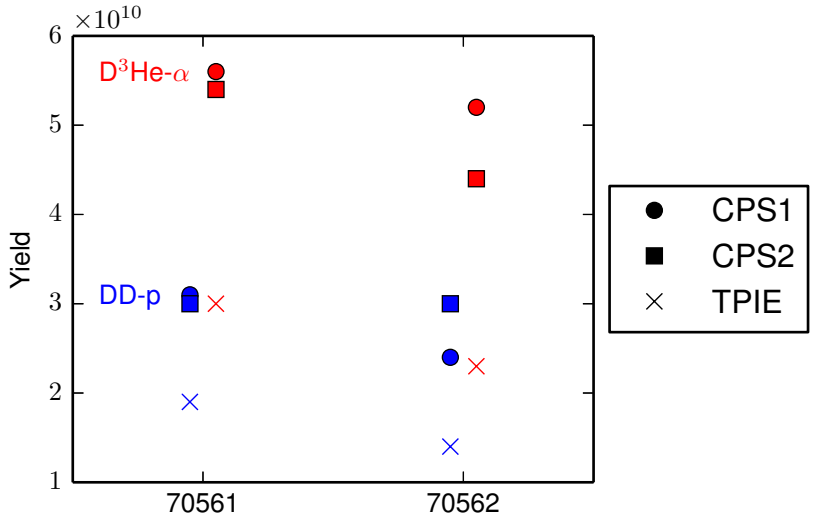

Figure 6.9. Yield inferred from TPIE (×) compared to CPS 1 (●) and CPS 2 (■) for both shots, for DD-p (blue) and D^3He-α (red), indicating that the TPIE yield is low $\sim 2\times$.

systems. The results are shown in Fig. 6.9. CPS 1 and 2 are consistent with each other, but the TPIE yield measurements are low by $\sim 2\times$. This is explained by the high aspect ratio of the TPIE pinhole, which is formed by two crossed slits. Each slit substrate is 0.8 cm thick, so the total pinhole substrate thickness is 1.6cm for a 250 μm diameter pinhole*. The system is thus very sensitive to misalignment, which reduces the effective pinhole area.

6.3 Proton Isochoric Heating

Proton isochoric heating using petawatt lasers[2] is potentially an interesting technique for stopping power experiments, which require a 'subject' plasma be generated in an interesting state to probe. Fast proton beams generated by the TNSA mechanism can be used to rapidly and quasi-volumetrically heat a sample of solid-density material to Warm Dense Matter (WDM) conditions. In this work, experiments were conducted at EP[3] using TNSA-generated protons to heat a sample, which is diagnosed with self-radiography and orthogonal x-ray radiography.

The experimental configuration is shown in Fig. 6.10. One of the EP short-pulse laser beams was incident upon a planar foil, which was typically a 10μm-thick Au foil. The generated protons traverse a slab of plastic (dimensions 200 × 200 × 50 μm), heating the slab by energy deposition. The stopping power of protons in the slab is shown in Fig. 6.11.

*See LANL Drawing 78Y-1765705

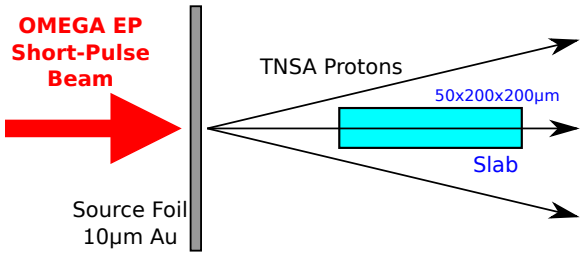

Figure 6.10. Experimental configuration for studying proton isochoric heating. Protons generated by TNSA traverse and heat a plastic (CH) slab (blue). Broadband area-backlit x-ray radiography (not shown) is conducted perpendicular to the page.

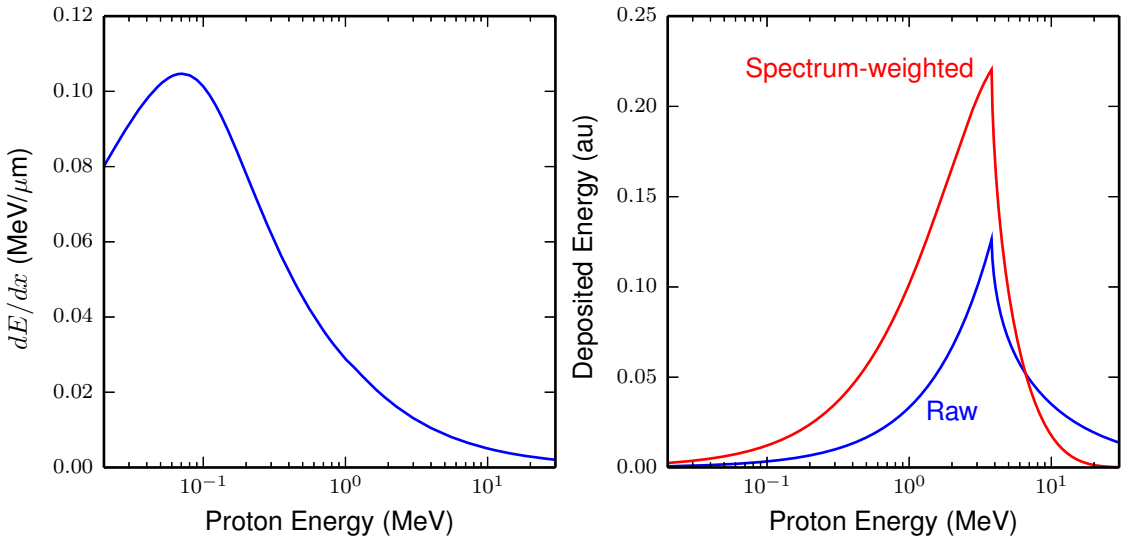

Figure 6.11. Left: proton stopping power in the plastic slab. Right: Energy deposited versus proton energy, area normalized. The blue curve does not take the proton spectrum into account, while the red curve is weighted by a typical TNSA exponentially-decaying spectrum.

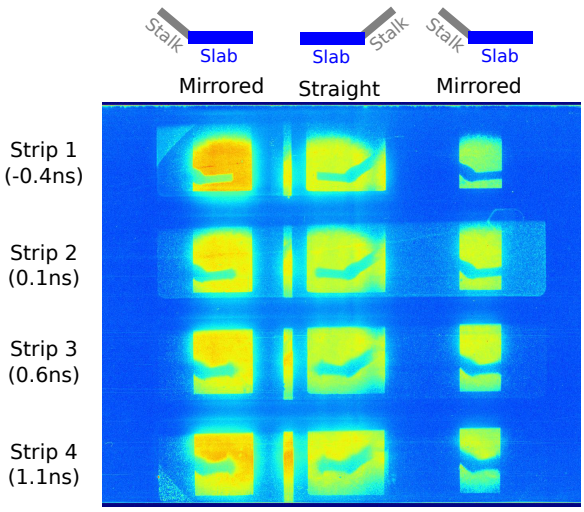

Figure 6.12. The raw XRFC data from shot 15308. The x rays image the slab and part of its stalk. The protons are incident upon the tip of the slab opposite the stalk. With the snout used, the center channel is straight through while the two side channels are mirror images.

The slab is 200μm thick along the proton's path, corresponding to the total range of a 3.8 MeV proton, which is apparent as the peak in the energy deposition profile in Fig. 6.11. Most of the proton heating comes from particles around this energy. When the exponentially-decaying spectrum (see Appendix A and Fig. A.11 for more information) is taken into account, more of the heating comes from lower-energy protons. Since the low-energy particles will be ranged out in the slab, this may cause non-uniform heating.

6.3.1 X-ray radiography to characterize slab heating

X-ray radiography was used to characterize the expansion of the plasma slab after proton heating. The radiography is perpendicular to the proton heating beam, and views the slab 'edge-on', as it appears in Fig. 6.10. A depleted-uranium foil is driven by two long-pulse OMEGA EP beams (#3 and #4) with a 2ns square pulse, up to 2kJ/beam, and with SG8 DPP. The resulting x-ray emission area is large enough for area backlighting. A 3μm-thick Al foil is placed between the backlighter foil and the proton heating target to reduce x-ray preheat.

A standard X-Ray Framing Camera (XRFC) was used to record the radiographs. The XRFC was configured with 4 strips and a 12-pinhole array. The soft x-ray snout (SXS) was used, which consists of a straight-through central channel and two mirror-reflected channels on each strip. The mirror channels are only sensitive to soft x rays, thus reducing hard-photon background in the images. Al filtering was used to optimize the signal strength, and the strips were timed with 500ps between them, starting 400ps before the heating, and with a 200ps pulse-forming module (PFM). The data are recorded on Biomax film.

The data from shot 15308 is shown in Fig. 6.12. On this shot, the proton heating drive was 500J/10ps. The slab is roughly centered in each image. The feature extending up and to the right (left) is the stalk in the central (mirrored) channels. The proton heating beam goes left-to-right (right-to-left) in the central (mirrored) images. The first strip is taken before the heating, with subsequent strip delays of 0.1, 0.6, and 1.1 ns relative to the proton heating.

In the 4$^{\text{th}}$ strip (bottom of the image), the slab has clearly expanded. The tip of the slab is also observed to expand farther in a 'mushroom' shape, which suggests non-uniform heating along the

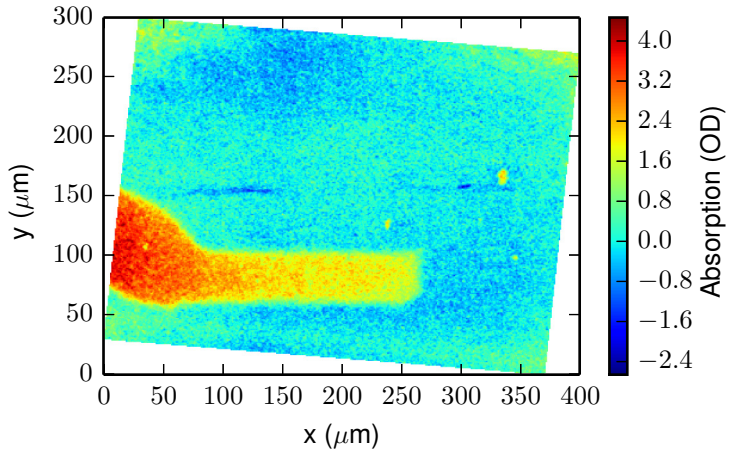

Figure 6.13. Reduced third image of first strip (Fig. 6.12), showing the stalk entering from left and the slab. The protons are incident upon the slab opposite the stalk (at right of the image).

proton beam direction.

The radiography data are first converted into x-ray flux using the step wedge calibration. Each frame is background-subtracted using regions between the frames. Within a given frame, a 2-D polynomial fit to the backlighter profile is subtracted from the image to obtain the target opacity image. Supergaussian fits across the slab at two locations are used to correct for the image's rotation. The image is also converted to image-plane-distance units using the known magnification. The final result of this analysis for an example from (strip 1, 3$^{\text{rd}}$ frame) is shown in Fig. 6.13.

Profiles of the slab absorption from this image analysis are used to infer the heating dynamics. For example, profiles at various depths from 10 to 90 μm into the slab, along the proton propagation direction, are shown in Fig. 6.14. The profile near to the tip of the slab (10 μm) is clearly different from the more recessed lineouts.

A straightforward analysis technique is to fit the data and infer the increase in FWHM due to the slab expansion, which can be directly compared to simulations. The images from frame 3 of each strip are analyzed at a depth of 30μm into the slab. The profile is fit with a supergaussian:

$$f(y) = A \times \left(\frac{1}{2^{1+1/N}\sigma} \frac{1}{2\Gamma(1+1/N)} \right) \exp\left[\frac{(y-\mu)^n}{2\sigma^N} \right] + B, \tag{6.2}$$

where y is the coordinate perpendicular to the proton direction. The fit parameters are the amplitude A, an offset B, the supergaussian width σ, mean position μm, and order N. Fits to three profiles are shown in Fig. 6.15.

The FWHM from the fits in Fig. 6.15 is used to compare to simulations. The expansion into vacuum of a CH slab artificially preheated[†] to various temperatures was modeled with the HYADES radiation-hydrodynamics code[15]. The simulated density (OD) profile is motion- and resolution-blurred to calculate an inferred simulation FWHM of the profile.

The time axis is normalized so that the proton heating occurs at $t = 0$. One radiograph was taken before the heating occurs, resulting in a FWHM= 50 μm, the initial slab width, as expected. After the heating, the slab is observed to rapidly puff up to a 75 μm thickness in $\sim$ 0.3 ns, and then to 80 μm thickness in 0.8ns.

[†]Since the proton heating occurs rapidly ($\sim$ps) compared to dynamical timescales ($\sim$ 100s of ps), the HYADES simulations are configured using an initial temperature to approximate the heating process.

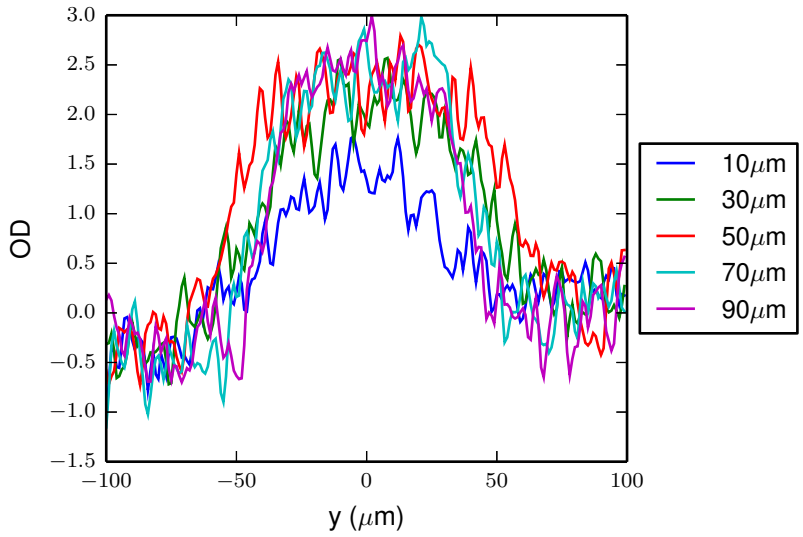

Figure 6.14. Optical density of the slab at several depths (corresponding to distance along the proton heating path)

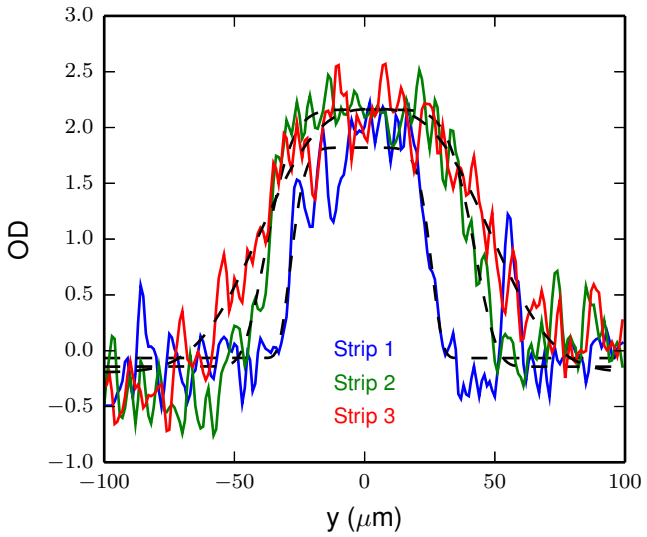

Figure 6.15. Supergaussian fits to optical density profiles at a depth of 30 μm, obtained from frame 3 images using strips 1, 2, and 3.

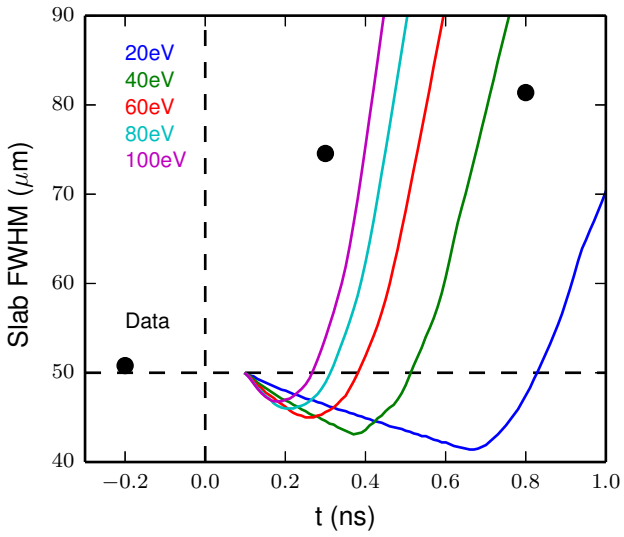

Figure 6.16. Comparison of experimental and simulated FWHM vs time for the slab expansion. Simulated curves are shown for various initial temperatures.

This behavior clearly contradicts the hydrodynamic result, as illustrated by the curves. In the simulation, FWHM initially decreases as the rarefaction wave propagates into the solid slab. After the two-sided rarefaction meets in the middle, the material is all expanding and the calculated FWHM increases rapidly.

The temporal history of the slab expansion is not driven by hydrodynamic rarefaction. Another possibility is that the slab motion is driven by the Lorentz force. The petawatt laser interaction generates an extreme flux of energetic electrons, which pass through the slab, followed by the ion beam. This has the potential to induce electromagnetic fields in and around the slab target. Evidence for this is explored in Sec. 6.3.2. If the slab is charged (either positively or negatively) by the TNSA particle flux, then electrostatic self-repulsion will lead to a rapid expansion in a 'Coulomb explosion'. Neutralization of the charge will occur over several hundred ps via a stalk return current [16,17], which could explain the rapid expansion and subsequent apparent deceleration observed. Unfortunately, this effect means that inferring a temperature from the slab expansion is not possible.

6.3.2 Electromagnetic fields around the slab

In these experiments, the proton beam is recorded on RCF after passing through the slab target. This data is useful to diagnose potential electromagnetic fields that might develop around the slab. Three radiographs from the experiments are shown in Fig. 6.17. All experiments used identical laser conditions (500J/10ps short-pulse drive) and targets (10μm Au source foils, 200 × 200 × 50 μm CH slabs). The difference between 13964 (left) and 15310 (center) is how the slab is attached: via stalk to the source foil (13964) or by an independent stalk (15310). The difference between 15310 and 15306 is that the orthogonal x-ray backlighter was turned on for 15306.

Shot 13964 has an obvious qualitative difference in the image than the other two, in that the slab is substantially magnified relative to the expected geometric magnification. This indicates an

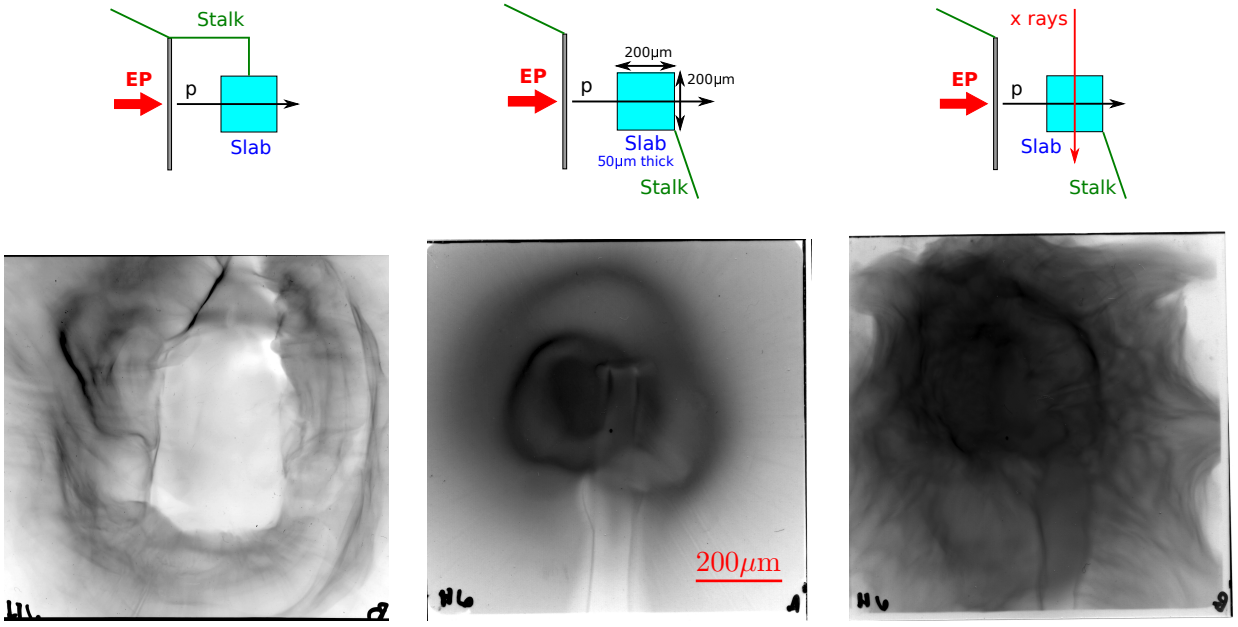

(a) 13964 **(b)** 15310 **(c)** 15306

Figure 6.17. Self-radiography of proton heating slab target. The proton heating beam, after passing through the slab, is recorded on RCF. These films correspond to 18 MeV protons. The short-pulse drive is 500J/10ps in all cases. For shot 13964 (left), the slab was attached to the proton source target via stalk. For shot 15310, the slab was independently positioned. Shot 15306 is like 15310, but with the x-ray backlighter turned on 500 ps before the proton heating occurs. Cartoons above each RCF image depict the geometry. The image magnification is 80×; a 200μm scale bar is shown in the center. In this view, the slab is initially 200μm vertical by 50μm horizontal.

electric or magnetic field:

$$\begin{aligned} \theta_B &= \frac{q}{\sqrt{2m_p E_p}} \int B_\perp d\ell, \\ \theta_E &= \frac{q}{2E_p} \int E_\perp d\ell. \end{aligned} \tag{6.3}$$

The deflection (θ) depends on the path-integrated perpendicular electric or magnetic field, and the proton energy (E_p). Typically E and B would be discriminated by using multiple proton energies. Unfortunately in this experiment, the other film images are low quality. It is clear, however, that the slab image is uniformly magnified, which is highly suggestive of an electric field.

In this image, the maximum deflection is $\theta_E \sim 17^\circ$ for $E_p = 18$ MeV. This corresponds to a value of $\int E_\perp d\ell \sim 10^7$ V. For a scale length of hundreds of μm, that is an electric field of tens of GV/m. If the drop to zero potential occurs over mm scale, then the slab charging is of order tens of MV, which is comparable to the petawatt-induced charging of the foil target, which accelerates the TNSA ions. Since the slab is small and mounted close to the foil (1mm away) compared to the foil lateral dimensions (2mm), the entire target must charge and discharge. Unfortunately this significantly complicates the proton heating dynamics. The lack of significant charging effects[‡] in shot 15310 clearly suggests that an independent stalk mount is desirable for proton isochoric heating experiments.

The other clear observation is that the presence of the x-ray backlighter induces significant chaotic structure in the self-radiograph (shot 15306). Since the drive beams for the backlighter are turned on 500ps before the proton heating occurs, the x-ray flux may affect the proton heating targets. The x-ray flux from the backlighter is not sufficiently intense to bulk heat and drive the targets, but could potentially create a small amount of tenuous plasma surrounding the proton source targets. This could have an effect on the TNSA proton generation (see Appendix A), or the electromagnetic fields surrounding the two targets, plausibly explaining the observed self-radiograph.

6.3.3 Cross-talk effects on proton probing

Combining the proton source and proton heating techniques raises the issue of crosstalk between them. Preliminary integrated experiments have been conducted to assess this possibility, where proton heating is used to create a subject plasma, and a proton source (Sec. 6.2) is generated after the heating, with the probing protons passing through the subject plasma orthogonal to the original heating protons. This experimental geometry is shown in Fig. 6.18. The resulting RCF images of the probing proton beam (see Fig. 6.18) are shown in Fig. 6.19. Based on the experimental geometry, the projected image of the slab was expected to be centered on the TPIE spectrometer line of sight, which is the white circle in the RCF images. Instead, protons going through the slab are displaced by ~ 1 cm in the image plane. In the experiment, no target or diagnostic misalignment can explain this much offset. In addition, the offset is repeatable, and observed on both shots with and without proton heating (left and right of Fig. 6.19).

The deflection angle of the protons is inferred from the slab's centroid location as a function of proton energy, and plotted in Fig. 6.20. The deflection angle is found to be $\sim 8-9$ degrees for a wide range of proton energies ($15-35$ MeV). This is inconsistent with a constant electric or magnetic field deflection (see Eq. 6.3) - the expected $1/E_p$ or $1/\sqrt{E_p}$ scaling is shown in Fig. 6.20

[‡]Non-uniformities in the observed radiograph may result from field structures around the slab, but it is also very likely that they result from non-uniformities in the proton beam emission (see Sec. 6.2).

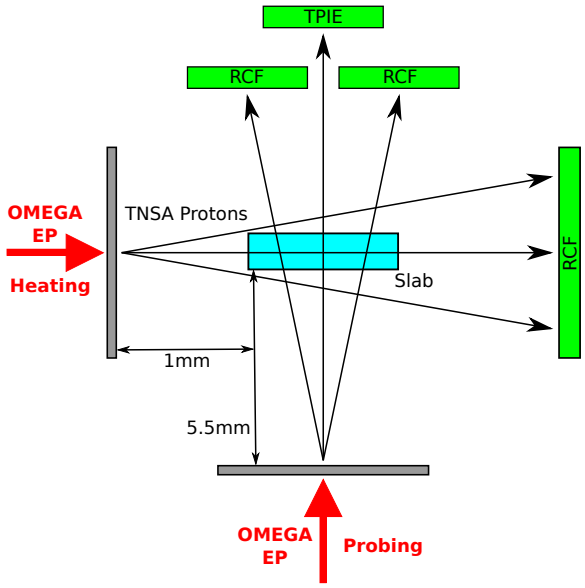

Figure 6.18. Experimental geometry with both proton heating (horizontal) and proton probing (vertical). The proton heating beam self-radiograph is recorded on RCF (8cm from TCC). The proton source beam is recorded on RCF (8cm) and the TPIE spectrometer (40+ cm from TCC).

(a) 15307 **(b)** 15310

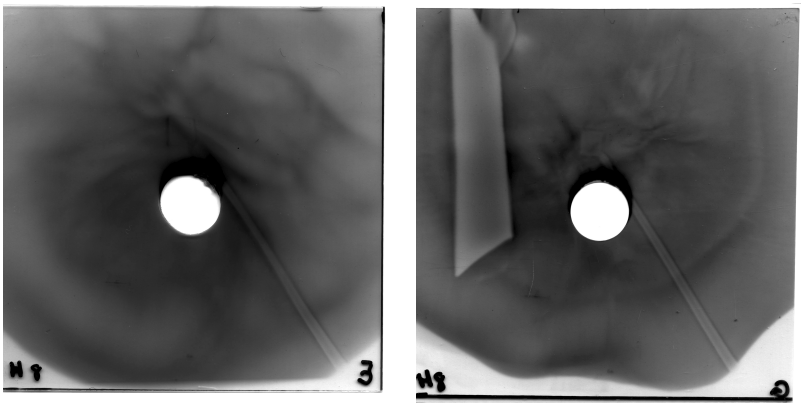

Figure 6.19. RCF image of the probing protons (see Fig. 6.18) from two integrated shots: 15307 without proton heating (slab only), and 15310 with a heated slab. The film is 7cm square.

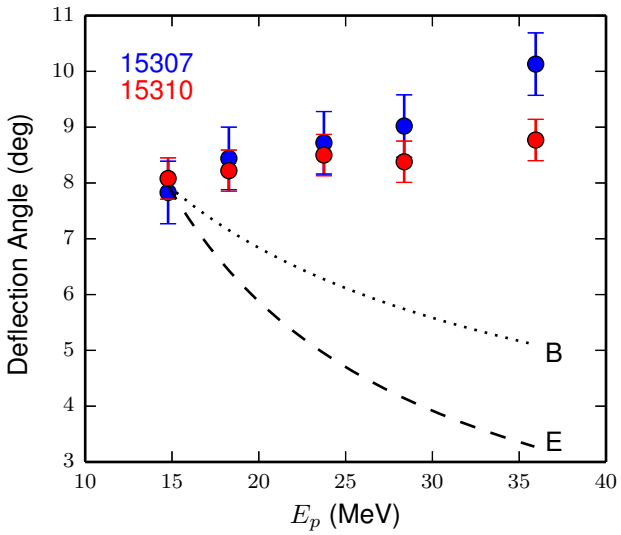

Figure 6.20. Proton deflection angle versus energy inferred via slab image location. In comparison to the expected $1/E_p$ and $1/\sqrt{E_p}$ scaling for E and B field deflections, no change with energy is observed.

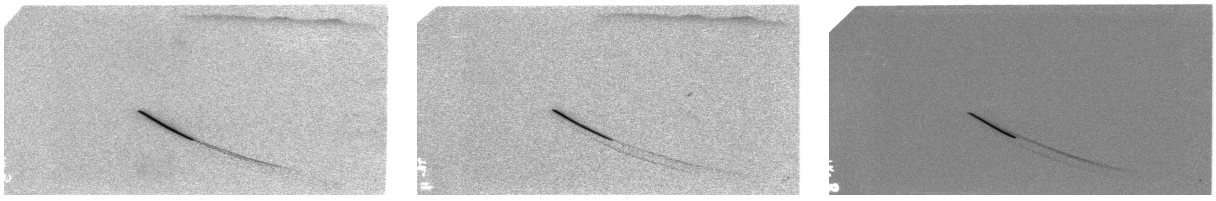

Figure 6.21. Raw TPIE signals from proton source experiments, where multiple proton parabolas are clearly visible. The fiducial is at the lower right, and magnetic (electric) displacement is horizontal (vertical). From left to right, data are from shots 17414, 17416, and 17418. The TPIE CR-39 is 5 × 10cm.

normalized to the lowest-energy data point.

Two possible explanations for this effect are rapid field evolution and virtual or multiple proton sources. Since the TNSA protons have time-of-flight spreading of order 50ps, a rapidly-decaying electromagnetic field could explain the data, as the higher-energy protons would be deflected by a stronger path-integrated field than the lower-energy protons.

Another possibility is that the protons creating the image in Fig. 6.19 are not born at the expected location (i.e. where the short-pulse laser hits the target foil). Evidence for multiple proton sources in these types of experiments has been observed in the TPIE data, illustrated by Fig. 6.21. Multiple sources of protons are also problematic for potential stopping-power experiments, as the path length traversed by protons in the subject plasma depends on where the protons are born.

Finally, another crosstalk concern is that the proton-heating interaction may generate protons that would be detected on the spectrometer, even with the orthogonal line-of-sight (see Fig. 6.18). For example, this could happen if the slab charges to an electric potential of several MV. This was tested with two shots: 17414, with only the proton probing source, and shot 17422, using an identical proton source but with a proton-heated slab. These spectra are shown in Fig. 6.22 (shot 17414 also in Fig. 6.6). The shot with the proton heating displays considerably higher proton flux across the entire energy range. This data suggests that $\sim 5\times$ more protons from the heating than the probing are detected in the spectrometer. This would represent a very small S/B for any potential stopping-power measurement, and it is not clear if this effect can be mitigated.

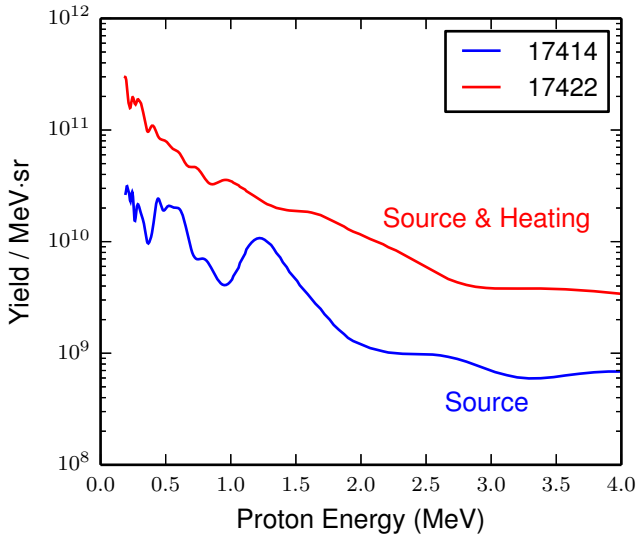

Figure 6.22. Spectra from proton source only (17414) and proton source with a proton-heated slab (17422). The proton source was a CVD wafer with CH overcoating driven by 40J/1ps pulse. The proton heating drive was 150J/10ps.

6.4 Hohlraum-heated subject plasma

Experiments were conducted at OMEGA EP to test the feasibility of using radiatively-heated foams as a subject target for stopping-power experiments. The experimental geometry is shown in Fig. 6.23. The concept is to use a halfraum (right) to launch a supersonic heat wave into a low-density foam (left, blue), which would be quasi-isochorically heated to warm (∼10s-100 eV) conditions.

The detailed target design is also shown in Fig. 6.23. Three of the OMEGA EP beams (#2,3,4) were used in long-pulse mode to drive the hohlraum with a 2ns long pulse shape and 2kJ of energy per beam. The heat wave propagated through the low-density (50 mg/cm^3) CH foam. A 300μm thick region of the foam was inserted into the halfraum, providing a 'tamp' so that hydrodynamic motion is minimized in the sampling region. At the end of the halfraum, a 600μm cube of foam was the subject plasma for the experiment, presenting a uniform thickness of material along the

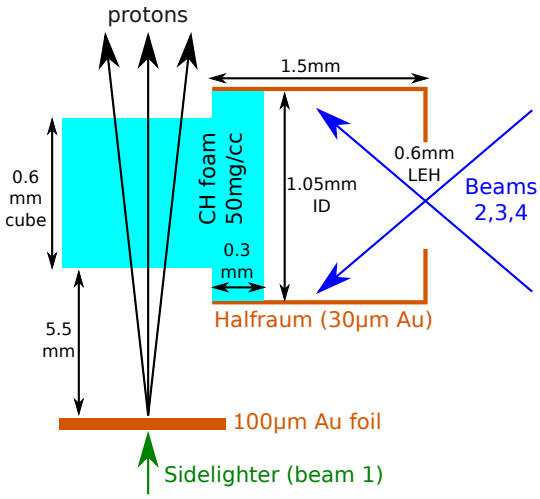

Figure 6.23. Experimental geometry for the halfraum-heated foam experiment. A halfraum (right) drives a heat wave in a low-density foam, which is probed by TNSA-generated energetic protons.

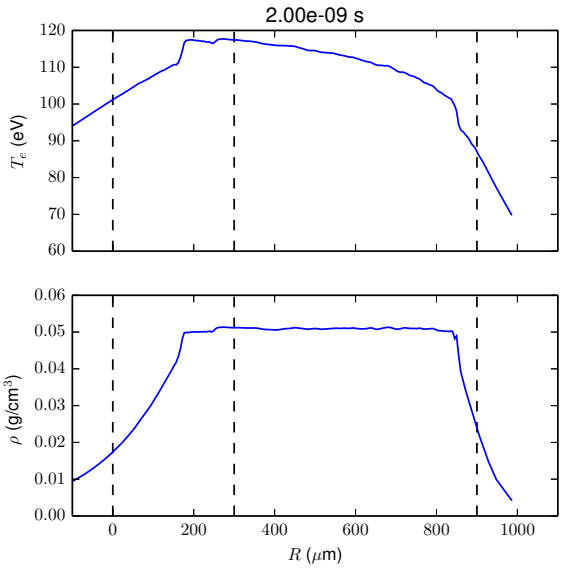

Figure 6.24. HYADES-simulated T_e adn ρ for the foam after heating by a 150eV black-body source. The bulk of the foam is close to the initial density (50mg/cm^3) and has been heated to $\sim$ 100eV.

proton propagation direction. The probing protons were generated with the sidelighter beam, using a 40J/1ps pulse incident upon a 100μm-thick Au foil.

A radiation temperature of up to 150 eV was expected based on scaling relations and prior work[18]. A HYADES simulation of the foam 2ns after the start of the drive, well after the heat wave has propagated through, is shown in Fig. 6.24.

This experiment was diagnosed with radiochromic film (RCF) and the Electron-Proton-Positron Spectrometer (EPPS)[19§] The RCF was used to diagnose the spatial distribution of the proton beam. A selection of low-energy films is shown in Fig. 6.25.

In the proton images, the halfraum and foam outline are clearly apparent in the cold foam (undriven hohlraum) experiment, shot 18860 (upper left). When the hohlraum drive and heating starts 2ns before the proton probing, shot 18861, significant distortion of the proton image is observed due to electromagnetic fields. The last two shots (18864 and 18866) probed the foam earlier (1ns after the start of the heating), and show significantly less distortion. However, a filamentary field structure around the subject target is still apparent. Unlike the proton isochoric heating experiment, no anomalous deflection of the entire proton beam is observed in this configuration.

EPPS was used to measure the proton spectrum transmitted through the foam (through the hole in the center of the RCF). The spectra are shown in Fig. 6.26. Shot 18857 (black curve) had the proton source only, shot 18860 (red) had an unheated foam, and the remaining shots all had heated foams. On shot 18861, the proton probing occurred 2ns after the start of the hohlraum heating, while the other three shots were probed 1ns after the start of heating.

The proton spectrum in the 2ns probing case is clearly suppressed relative to the other shots, corroborating the RCF image (Fig. 6.25). Likely this is caused by suppression of the proton generation: the hohlraum may preheat the proton source foil. Oddly, the shot with a cold foam is seen to have a higher intensity and energy proton spectrum than the source-only shot, opposite to what we would expect. The three nominally-identical shots, 18863-6, also show significant variation. This suggests that the shot-to-shot repeatibility of the TNSA proton souce in this configuration is still not adequate for a stopping power measurement.

On a separate halfraum-only shot, the EPPS detector recorded no energetic proton signal,

[§]Unlike the prior shots, EPPS was used due to its higher solid angle relative to TPIE, which was expected to be improve the data quality with the thicker Au targets and lower laser energy.

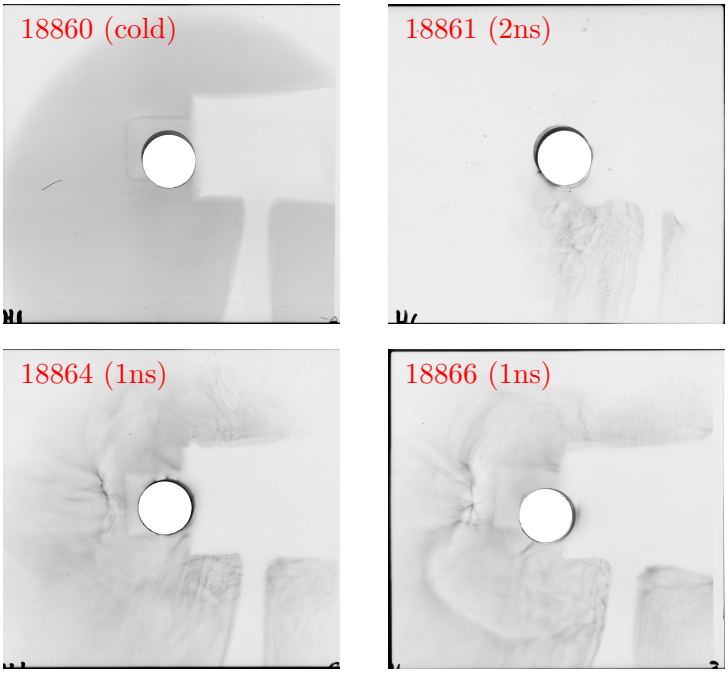

Figure 6.25. 5 MeV proton images from RCF for four halfram shots. **18860:** Cold foam (undriven halfraum), **18861:** heated foam (2ns after start of the hohlraum drive), **18864 & 18866:** heated foam (1ns after start of the hohlraum drive).

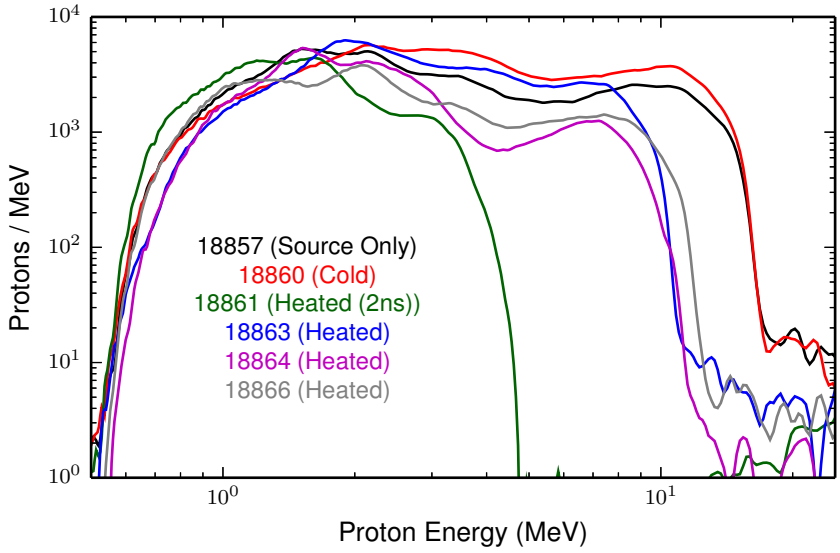

Figure 6.26. EPPS proton spectra measured on all shots.

indicating that the halfraum scheme eliminates direct 'crosstalk', i.e. the hohlraum target does not generate protons (no background for the stopping measurement).

6.5 Conclusions and future work

Platform test and development experiments have been conducted, where the goal was to study charged-particle stopping power using petawatt lasers, which would potentially have several potential advantages over long-pulse experiments (Chapter 5). Fundamentally, such an experiment requires well-understood heating of a subject target, and an independent source of well-characterized probing protons that would traverse the subject plasma.

The proton sources considered are planar foils driven by a short-pulse petawatt laser, generating energetic charged particles via the TNSA mechanism. In plain foils, smoother foil substrates (smoother Au, Si wafers, and CVD wafers) were used in an attempt to improve proton beam uniformity. At high intensity, laser-seeded filamenetation instabilities appear to dominate the beam non-uniformities. These non-uniformities persist at lower intensity; a potential advantage to using CVD[12] is suggested by the data. Plastic-coated targets were tried in an attempt to replicate prior work[4]. Quasi-monoenergetic peaks in the proton spectrum are sometimes observed using this technique, but are not repeatable. The lack of repeatibility may be related to the uniformity issues.

Proton isochoric heating has been studied as a method of generating the subject plasma. TNSA-generated fast protons traverse a subject 'slab' target, depositing energy quasi-volumetrically. The slab expansion is studied using x-ray radiography, which shows significant non-uniformities along the proton heating axis. Comparison to simulations suggest that the expansion is not governed by hydrodynamic rarefaction, but that an electrostatic 'Coulomb explosion' may be responsible for much of the slab motion. Furthermore, the proton heating targets appear to interfere with the probing proton propagation, and the proton heating generates signal in the proton spectrometer at much higher levels than the probe itself.

In the last set of shots, a halfraum-driven radiatively-heated foam configuration was explored. In this case, the cross-talk issues between the two targets appear less severe. However, the shot-to-shot repeatibility in the proton source or proton probing is not adequate for a stopping power measurement.

This variety of effects presents a severe challenge to realizing a stopping power experiment on OMEGA EP. For the proton source, using a substantially thicker Au target and low intensity may generate a well-understood exponential spectrum, which could be used for the proton probing. Based on this data, proton isochoric heating does not seem to be a suitable technique for this type of experiment. Using the long-pulse beams on OMEGA EP to generate a radiatively- or shock-heated subject plasma may be feasible, but would need to be coupled with a reliable proton probing technique.

6.6 References

1. S. Hatchett, C. Brown, T. Cowan *et al.*, "Electron, photon, and ion beams from the relativistic interaction of Petawatt laser pulses with solid targets," Physics of Plasmas, **7**, 2076 (2000).
2. P. K. Patel, A. J. Mackinnon, M. H. Key *et al.*, "Isochoric Heating of Solid-Density Matter with an Ultrafast Proton Beam," Phys. Rev. Lett., **91**, 125,004 (2003).
3. L. Waxer, D. Maywar, J. Kelly *et al.*, "High-energy petawatt capability for the Omega laser," Optics and photonics news, **16**(7), 30–36 (2005).
4. H. Schwoerer, S. Pfotenhauer, O. Jäckel *et al.*, "Laser-plasma acceleration of quasi-monoenergetic protons from microstructured targets," Nature, **439**, 445–448 (2006).

5. D. Hey, M. Key, A. Mackinnon *et al.*, "Use of GafChromic film to diagnose laser generated proton beams," Rev. Sci. Instrum., **79**, 053501 (2008).
6. N. Sinenian, *Fast-Ion Spectrometry of ICF Implosions and Laser-Foil Experiments at the Omega and MTW Laser Facilities*, Ph.D. thesis, Massachusetts Institute of Technology (2013).
7. J. A. Cobble, K. A. Flippo, D. T. Offermann *et al.*, "High-resolution Thomson parabola for ion analysis," Rev. Sci. Instrum., **82**(11), 113504 (2011).
8. C. G. Freeman, G. Fiksel, C. Stoeckl *et al.*, "Calibration of a Thomson parabola ion spectrometer and Fujifilm imaging plate detectors for protons, deuterons, and alpha particles," Rev. Sci. Instrum., **82**(7), 073301 (2011).
9. A. B. Zylstra, C. K. Li, H. G. Rinderknecht *et al.*, "Using high-intensity laser-generated energetic protons to radiograph directly driven implosions," Rev. Sci. Instrum., **83**(1), 013511 (2012).
10. A. Hazi and R. Shepherd, private communication (2012).
11. "Goodfellow corp." `http://www.goodfellow.com/` (2012).
12. P. McKenna, A. P. L. Robinson, D. Neely *et al.*, "Effect of Lattice Structure on Energetic Electron Transport in Solids Irradiated by Ultraintense Laser Pulses," Phys. Rev. Lett., **106**, 185004 (2011).
13. D. A. MacLellan, D. C. Carroll, R. J. Gray *et al.*, "Annular Fast Electron Transport in Silicon Arising from Low-Temperature Resistivity," Phys. Rev. Lett., **111**, 095001 (2013).
14. D. Hicks, *Charged-particle spectroscopy: a new window on inertial confinement fusion*, Ph.D. thesis, Massachusetts Institute of Technology (1999).
15. J. T. Larsen and S. M. Lane, "HYADES-A plasma hydrodynamics code for dense plasma studies," Journal of Quantitative Spectroscopy and Radiative Transfer, **51**(1-2), 179 – 186 (1994), special Issue Radiative Properties of Hot Dense Matter.
16. M. J.-E. Manuel, N. Sinenian, F. H. Séguin *et al.*, "Mapping return currents in laser-generated Z-pinch plasmas using proton deflectometry," Applied Physics Letters, **100**(20), 203505 (2012).
17. N. Sinenian, M. J.-E. Manuel, J. A. Frenje *et al.*, "An empirical target discharging model relevant to hot-electron preheat in direct-drive implosions on OMEGA," Plasma Physics and Controlled Fusion, **55**(4), 045001 (2013).
18. D. Hinkel, Private Communication (2014).
19. H. Chen, A. J. Link, R. van Maren *et al.*, "High performance compact magnetic spectrometers for energetic ion and electron measurement in ultraintense short pulse laser solid interactionsa)," Review of Scientific Instruments, **79**(10), 10E533 (2008).

Part III

Nuclear Astrophysics

7

An overview of big-bang and stellar nucleosynthesis

Nuclear reactions in the cosmos are responsible for the creation of the elements present today. Astrophysical nucleosynthesis can be broken down into three general categories:

1. **Big-bang nucleosynthesis**
   As the universe expanded during the big bang, the temperature decreased, passing through temperatures relevant to fusion; fusion reactions in this epoch created nuclei from primordial nucleons (protons and neutrons).

2. **Stellar fusion nucleosynthesis**
   In stars, a variety of reactions work to burn hydrogen into helium; in larger stars helium may be converted into heavier elements. Stellar processes cannot produce elements heavier than Fe (see Fig. 1.1).

3. **Neutron-capture processes**
   Elements heavier than Fe are created by neutron capture and β-decay processes[1]. In particular, the 'slow process' (s-process) occurs in asymptotic giant branch stars and the 'rapid process' (r-process) occurs in supernovae.

This work will include studies directly relevant to big-bang and stellar nucleosynthesis, which are described in detail in the following sections.

7.1 Big-bang nucleosynthesis

Synthesis of heavy elements during the big bang was first proposed by Alpher and Gamow[2]. Following the big bang, matter existed at first as a quark-gluon plasma, but as the universe expanded and cooled the quarks combined to form bound states - protons and neutrons. At first any heavier nuclei, such as deuterium, would be quickly destroyed via photo-disintegration. But when the temperature of the universe was below a few MeV (several tenths of seconds after the big bang), heavier nuclei were formed and persisted.

The temperature of the universe during the big bang can be approximated by[3]:

$$T^2 = 0.74\sqrt{\frac{10.75}{g_*}}\frac{1}{t}, \tag{7.1}$$

where T is the temperature in MeV, t is the time in seconds, and g_* is the effective number of particle species (in the standard model, $g_* = 10.75$).

Big-bang nucleosynthesis forms a reaction chain starting from protons and neutrons. The first step is

$$p + n \rightarrow D + \gamma, \tag{7.2}$$

which is critical since the subsequent reactions all rely on synthesis of deuterium. For example, mass $A = 3$ nuclei ^{3}He and tritium (T) are then produced via:

$$p + D \rightarrow {}^3He + \gamma, \tag{7.3}$$
$$n + D \rightarrow T + \gamma. \tag{7.4}$$

From T and ^{3}He, the reaction network[4] can produce ^{4}He plus several stable and unstable isotopes of Li, Be, and B; for example via:

$$T + {}^3He \rightarrow {}^6Li + \gamma, \tag{7.5}$$
$$T + {}^4He \rightarrow {}^7Li + \gamma, \tag{7.6}$$
$${}^3He + {}^4He \rightarrow {}^7Be + \gamma. \tag{7.7}$$

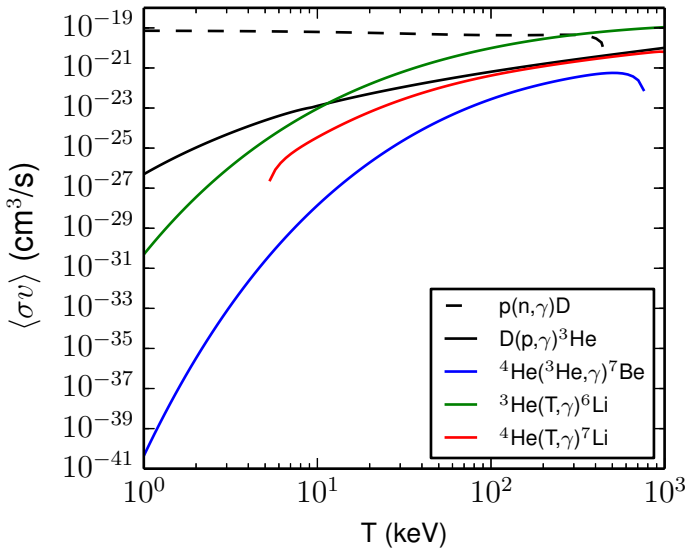

Figure 7.1. Reactivities of some reactions relevant to big-bang nucleosynthesis.

Reactivities for relevant astrophysical reactions are commonly reported as fits to calculations or experiments[5,6,4]. The reactivities for reactions 7.2, 7.3, 7.5, 7.6, and 7.7 are shown in Fig. 7.1. The reaction D(n,γ)T is strongly dependent on the population of non-thermal neutrons.

A 'mass gap' exists at $A = 8$ where no stable nuclei exist. This leads to an inability of big-bang nucleosynthesis to produce any heavier elements such as C. Because the abundance of heavy nuclei during the big bang remains extremely low, a triple-α process cannot occur to produce ^{12}C. At the same time, any produced ^{9}Be (which could proceed to higher masses) is quickly destroyed via the reaction $^9Be(p,\alpha)^6Li$. Therefore big-bang nucleosynthesis 'stops' at $A = 7$. Recent modeling predicts[4] that the most common stable isotopes produced via this process are, in order of decreasing number abundance: ^{4}He, D, ^{3}He, ^{7}Be, ^{7}Li, and ^{6}Li.

It is interesting to note that processes producing D or ^{3}He later in time (e.g. in stellar nucleosynthesis, next section) lead to their immediate consumption in stellar interiors. Therefore, all D

and ^{3}He available to us today was produced in the big bang.

7.2 Stellar nucleosynthesis

7.2.1 Main-sequence stars

The main source of energy in stars similar in mass to our sun is direct burning of hydrogen into helium, the 'proton-proton' chain, the existance of which was first realized by Hans Bethe[7,1]. His critical contribution was the realization that two protons can form deuterium via the process:

$$\begin{aligned} p \ + \ p \rightarrow \ & {}^2He \ + \gamma \\ & {}^2He \ \rightarrow D + e^+ + \nu_e \quad \text{(Q=1.44 MeV)}. \end{aligned} \tag{7.8}$$

The two protons initially form a 'diproton' (^{2}He). During the lifetime of the diproton, one proton must undergo β^+ decay, which forms deuterium. Since this is a weak process, the reaction goes extremely slowly. The energy produced (Q) includes that from subsequent annihilation of the positron. The produced deuteron reacts quickly via:

$$D \ + \ p \ \rightarrow \ {}^3He \ + \ \gamma \quad \text{(Q=5.5 MeV)}. \tag{7.9}$$

Once ^{3}He is produced, the proton-proton chain can proceed via one of three main branches[1] discussed subsequently.

pp-1 branch

The first possible branch proceeds via direct reaction of the ^{3}He with another ^{3}He:

$${}^3He \ + \ {}^3He \ \rightarrow \ {}^4He + 2p \quad \text{(Q=12.86 MeV)}. \tag{7.10}$$

In total the pp-1 chain produces 26.22 MeV of energy, with almost half produced in the ^{3}He+^{3}He reaction. This branch is dominant in low-mass stars, with central temperatures of $(10 - 14) \times 10^6$ K. In the sun, this branch is responsible for $\sim 86\%$ of the reactions.

pp-2 branch

The second possible branch involves the reaction of ^{3}He produced by the first two steps with a ^{4}He:

$$\begin{aligned} {}^3He \ + \ {}^4He \ \rightarrow \quad & {}^7Be \ + \gamma \\ & {}^7Be \ + e^- \ \rightarrow \ {}^7Li \ + \ \nu_e \\ & {}^7Li \ + \ p \ \rightarrow \ 2{}^4He. \end{aligned} \tag{7.11}$$

The energetics depends on whether the ^{7}Li is formed in the ground or excited state. The pp-2 branch is dominant in stars with core temperatures between $(14 - 23) \times 10^6$ K. In the sun, this branch is responsible for 14% of reactions.

pp-3 branch

The pp-3 branch also begins by forming ^{7}Be that subsequently reacts with another proton:

$$\begin{aligned} {}^3He \ + \ {}^4He \ \rightarrow \quad & {}^7Be \ + \gamma \\ & {}^7Be \ + p \ \rightarrow \ {}^8B \ + \ \gamma \\ & {}^8B \ \rightarrow \ {}^8Be + e^+ + \nu_e \\ & {}^8Be \ \rightarrow \ 2{}^4He. \end{aligned} \tag{7.12}$$

This branch is only dominant at central temperatures exceeding 23×10^6 and is negligible in terms of solar energetics, though the ν_e produced is energetic and was very important in the solar neutrino problem[8].

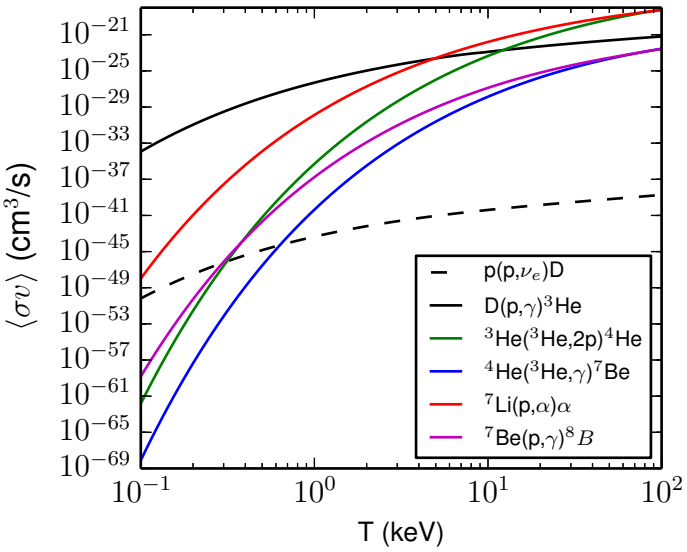

Figure 7.2. Reactivities as a function of temperature (T) for reactions in the proton-proton chain, taking place in hydrogen-burning stars.

Reactions relevant to the three proton-proton chains are shown in Fig. 7.2. Note that for conditions relevant to stellar interiors ($\gtrsim$ 1 keV) the first step p(p,ν_e)D is the slowest by several orders of magnitude, thus becoming the rate-limiting step for energy production in stars burning hydrogen via the p-p chains. For reactions where both reactants are minority species, such as ^{3}He(^{3}He,2p)^{4}He, the reactivity primarily sets the concentration of the minority species (^{3}He) to obtain an equilibrium balance between production and destruction.

7.2.2 CNO cycle

In heavier stars with finite metallicity, hydrogen burning may also proceed via a catalyzed 'CNO process' proposed by Bethe[9]. If ^{12}C is present, then the following cycle can proceed:

$$^{12}C + p \rightarrow {}^{13}N + \gamma \tag{7.13}$$
$$^{13}N \rightarrow {}^{13}C + e^+ + \nu_e \tag{7.14}$$
$$^{13}C + p \rightarrow {}^{14}N + \gamma \tag{7.15}$$
$$^{14}N + p \rightarrow {}^{15}O + \gamma \tag{7.16}$$
$$^{15}O \rightarrow {}^{15}N + e^+ + \nu_e \tag{7.17}$$
$$^{15}N + p \rightarrow {}^{12}C + {}^4He. \tag{7.18}$$

Since the original ^{12}C is reproduced, this is clearly a catalyzed cycle, and can proceed and dominate hydrogen burning even for small concentrations of the catalyst ^{12}C. However, these reactions are more strongly dependent on temperature than the pp cycle reactions, and thus the CNO cycle dominates only in massive stars. In the sun, the CNO cycle is responsible for approximately 2% of energy generation. Reactivities for the proton-capture reactions in the CNO cycle are shown in Fig. 7.3.

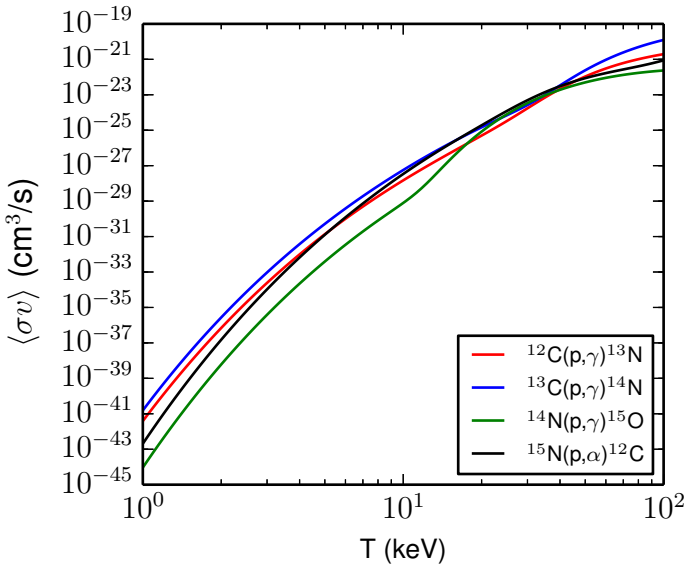

Figure 7.3. Reactivities of reactions relevant to CNO-catalyzed hydrogen burning.

7.2.3 Heavy helium-burning stars

Once a star has burnt its hydrogen into helium, the helium-rich core of a massive star begins to collapse due to Kelvin-Helmholtz contraction since the hydrogen-burning energy production has decreased. When the helium core reaches temperatures around 10^8 K (8.6 keV), a star can directly burn helium via the 'triple-α process'[1]:

$$^4He + {}^4He \rightarrow {}^8Be \tag{7.19}$$

$$^8Be + {}^4He \rightarrow {}^{12}C. \tag{7.20}$$

The triple-α process is strongly dependent on density; since the ^{8}Be nucleus is unstable it must rapidly react with another ^{4}He in the second step. Once carbon is produced in abundance, the star can continue to burn and produce heavier elements, for example oxygen is produced via:

$$^{12}C + {}^4He \rightarrow {}^{16}O. \tag{7.21}$$

Large stars can continue to burn and produce elements up to $A = 56$ via C-, O-, Ne-, and Si-burning in addition to the 'α ladder'; afterwards neutron-capture processes are required to produce heavier elements.

7.2.4 Deuterium burning

In sub-stellar objects, the central temperature is not high enough for the pp chain to proceed. However, energy can be produced by burning primordial D (produced in the big bang) via the D(p,γ)^{3}He reaction (see Eq. 7.3 and Fig. 7.2). There are two classes of astrophysical objects where this is particularly interesting.

During the star formation process, a cloud of gas collapses, a process described by the 'Jeans instability'[10]. During the gravitational collapse, the central temperature rises as described by Kelvin-Helmholtz contraction. These collapsing pre-stellar objects are commonly referred to as protostars[11]. Since the material typically contains a small amount of D, produced during the big bang, eventually the core temperature of the protostar reaches $\sim 10^6$ K, at which point the energy

produced via deuterium burning is sufficient to halt the contraction temporarily. Once the D is exhausted, contraction resumes. The length of the deuterium-burning phase of a protostar is critical for understanding star formation; in particular the mass of stars formed depends sensitively on this process[11].

A second class of astrophysical objects where deuterium burning is important are brown dwarfs[12], typically $13 - 80\times$ the mass of Jupiter, which are massive enough to burn deuterium but not massive enough for the pp chain to proceed. The lifetime and luminosity of brown dwarfs are set by the deuterium burning process.

7.3 References

1. E. M. Burbidge, G. R. Burbidge, W. A. Fowler *et al.*, "Synthesis of the Elements in Stars," Rev. Mod. Phys., **29**, 547–650 (1957).
2. R. A. Alpher, H. Bethe and G. Gamow, "The Origin of Chemical Elements," Phys. Rev., **73**, 803–804 (1948).
3. C. Grupen, *Big Bang Nucleosynthesis* (Astroparticle Physics, Springer, 2005).
4. R. N. Boyd, C. R. Brune, G. M. Fuller *et al.*, "New nuclear physics for big bang nucleosynthesis," Phys. Rev. D, **82**, 105005 (2010).
5. C. Angulo, M. Arnould, M. Rayet *et al.*, "A compilation of charged-particle induced thermonuclear reaction rates," Nuclear Physics A, **656**(1), 3 – 183 (1999).
6. P. D. Serpico, S. Esposito, F. Iocco *et al.*, "Nuclear reaction network for primordial nucleosynthesis: a detailed analysis of rates, uncertainties and light nuclei yields," Journal of Cosmology and Astroparticle Physics, **2004**(12), 010 (2004).
7. H. A. Bethe and C. L. Critchfield, "The Formation of Deuterons by Proton Combination," Phys. Rev., **54**, 248–254 (1938).
8. Q. Ahmad *et al.*, "Measurement of the rate of interactions produced by ^{8}B solar neutrinos at the Sudbury Neutrino Observatory," Phys. Rev. Lett, **87**, 071,301 (2001).
9. H. A. Bethe, "Energy Production in Stars," Phys. Rev., **55**, 434–456 (1939).
10. J. H. Jeans, "The Stability of a Spherical Nebula," Philosophical Transactions of the Royal Society of London. Series A, Containing Papers of a Mathematical or Physical Character, **199**, pp. 1–53 (1902).
11. F. Palla and H. Zinnecker, *Physics of Star Formation in Galaxies* (Springer-Verlag, 2002).
12. F. LeBlanc, *An Introduction to Stellar Astrophysics* (John Wiley & Sons, 2010).

8

The T^3He reaction

8.1 Introduction

Studying the T^3He fusion reaction is motivated by both nuclear astrophysics (see Chapter 7) and basic nuclear physics. While abundances of many light nuclei in primordial material are explained well by the BBN theory[1–3], observations of high levels of ^6Li in low-metallicity stars[4,5] is in contradiction to BBN-modeled levels of ^6Li by three orders of magnitude. Recent work has ruled out the $D(\alpha,\gamma)^6Li$ reaction as a solution[6]. The potential role of the $T(^3He,\gamma)^6Li$ reaction (Q=15.8 MeV) in BBN has been hypothesized as a solution to this problem[7] if the rate is much higher than expected. The nuclear physics of this hypothesis is contentious[8] yet still an open question[3]. This is primarily due to the lack of high-quality data for this reaction, with previous experiments being conducted primarily at high energies and with large inconsistencies between the reported data sets[9]. Furthermore, only one dataset exists at low energy ($E_{cm} \leq 1$ MeV), which is in the range where BBN reactions occurred. This strongly motivates additional experiments to determine if this reaction could explain the high levels of ^6Li observed in low-metallicity stars.

For basic nuclear physics, the T^3He reaction provides stringent constraints on first-principle theory or R-matrix modeling of six-nucleon systems, similar to the TT and $^3He^3He$ reactions. In particular, the final-state interactions of the reaction products may be studied via spectroscopy of the products. As with the γ branch, the existing charged-particle data is taken at high energy and with poor precision and spectral resolution[10–12]. High-quality spectra obtained at lower energy will be of high value as it will put a strong constraint on nuclear theory.

8.2 Experimental Overview

The T^3He reaction was studied at the OMEGA laser facility[13] using spherical thin-glass 'exploding pusher' implosions; the targets are shown in Fig. 8.1. A 2.5μm thick SiO_2 shell with an outer diameter of 960 μm was filled with various gas mixtures. The outer surface of the spherical shell was illumined with the OMEGA laser at 3ω (351nm) using SG4 DPP and DPR smoothing, but without SSD to maximize on-target energy delivered. A 600ps duration square pulse was used with 17kJ of total energy. The short square pulse was chosen so that nuclear production occurs after the laser turns off, by which time the target self-charging is neutralized[14,15] and the charged-particle spectra are undistorted.

The targets were filled with T_2, T_2 and ^3He, or ^3He gas. The T_2 gas supply used was con-

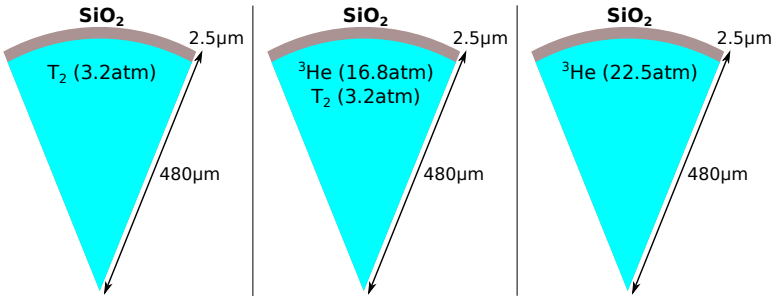

Figure 8.1. Targets used were 2.5μm-thick glass shells with an outer diameter of approximately 960 μm. These shells were filled with 3.2atm of T_2 gas, 3.2atm of T_2 gas plus 16.8atm of ^{3}He gas, or 22.5atm of pure ^{3}He gas.

taminated with approximately 1.5% atomic D*. Similarly, the ^{3}He supply is contaminated with approximately 0.01% D. The primary experimental data was obtained from the implosions with a mixture of T and ^{3}He. The ^{3}He-rich mixture (72% atomic ^{3}He) was chosen to increase the S/B for the γ measurement, as the primary source of background comes from the T(D,γ)^{5}He reaction. Even with the lower D content, the higher cross-section for D+T fusion results in a large number of reactions. The targets filled with only T_2 gas are used to provide a background calibration for the D+T contribution to the γ measurement. Similarly, the ^{3}He targets provide a characterization of the background in the γ-ray measurement arising from either the ^{3}He+^{3}He reaction or a plasma process. The shots taken in the experiment are summarized in Table 8.1.

Table 8.1. Gas fills used in the T^{3}He experimental campaign.

Shot #s	Type	T_2 (atm)	^{3}He (atm)
70401 - 70403	T_2	3.2	0
70404 - 70410	T^{3}He	3.2	16.8
70411 - 70412	^{3}He	0	22.5

In the primary targets, the following nuclear reactions occured:

$$\begin{aligned}
\mathrm{T} + {}^3\mathrm{He} &\rightarrow {}^4\mathrm{He}\ (4.8\ \mathrm{MeV}) + \mathrm{D}\ (9.5\ \mathrm{MeV}) && (8.1)\\
&\rightarrow {}^4\mathrm{He} + \mathrm{n} + \mathrm{p}\ \ (Q = 12.1\ \mathrm{MeV}) && (8.2)\\
&\rightarrow {}^5\mathrm{He}\ (1.9\ \mathrm{MeV}) + \mathrm{p}\ (9.5\ \mathrm{MeV}) && (8.3)\\
&\rightarrow {}^6\mathrm{Li} + \gamma\ (Q = 15.8\ \mathrm{MeV}) && (8.4)\\
\mathrm{T} + \mathrm{T} &\rightarrow {}^4\mathrm{He} + 2\mathrm{n}\ (Q = 11.3\ \mathrm{MeV}) && (8.5)\\
\mathrm{D} + \mathrm{T} &\rightarrow {}^4\mathrm{He}\ (3.5\ \mathrm{MeV}) + \mathrm{n}\ (14.1\ \mathrm{MeV}) && (8.6)\\
\mathrm{D} + {}^3\mathrm{He} &\rightarrow {}^4\mathrm{He}\ (3.6\ \mathrm{MeV}) + \mathrm{p}\ (14.7\ \mathrm{MeV}). && (8.7)
\end{aligned}$$

Yields and spectra for the products marked in blue above were measured with various diagnostics. WRF spectrometers[16] measured the D^{3}He-p spectrum and part of the T^{3}He-p spectrum. Flat-filtered ('range filter', RF) CR-39 measured the T^{3}He-d reaction yield. Neutron time-of-flight (nTOF) detectors[17] measured the DT yield and the TT-n spectrum. The T^{3}He-d and -p were measured with the charged-particle spectrometers (CPS)[18] and the Magnetic Recoil Spectrometer (MRS)[19]. Finally, the γ signal was recorded using a gas Cherenkov detector (GCD)[20].

*In the future, a planned isotope separator at LLE will enable fills with higher purity tritium.

8.3 Diagnostic development

8.3.1 T^3He-d measurement with RF

The measurement of the T^3He-produced deuterons (from reaction 8.1) with a simple ranging filter requires selection of the filter thickness. Using an aluminum filter, the final energy of the T^3He-d is plotted versus the filter thickness in Fig. 8.2. Filter thicknesses of 200 and 275 μm were chosen, so the final deuteron energies were $\sim$ 4 and 6 MeV, respectively. Because the implosions also produced protons via the reaction 8.2, those protons were detected behind the Al filters. For the chosen filter thickness, protons between $5 - 10$ MeV were detected (see Fig. 8.2).

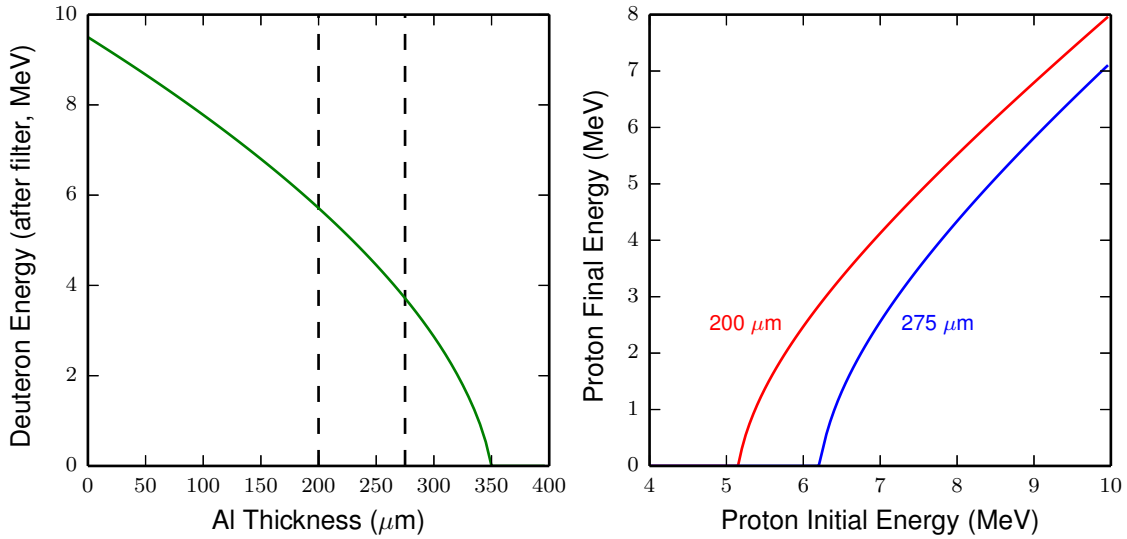

Figure 8.2. Particle ranging in an aluminum filter. Left: deuterons with an initial energy of 9.5 MeV through various thicknesses of aluminum. Filter thicknesses of 200 and 275 μm (dashed lines) were chosen for these experiments. For these thicknesses, T^3He protons in the range 5-10 MeV were also detected behind the filter (right).

The deuteron ranging filters were fielded in two of the windows (1 and 4) within the broadband (BB) WRF diagnostic package, as shown in Fig. 8.3. Raw data for particle fluence is also shown in Fig. 8.3. Example data is shown in Fig. 8.4, plotted versus track diameter. The monoenergetic deuterons appear as a line with diameter $\sim$ 5 μm in this case. The protons appear as a background, which must be corrected for to obtain an accurate value of the area under the peak (for a deuteron yield determination). The data is fit with a Gaussian plus power-law function for the background, as shown in Fig. 8.4, and the deuteron yield is obtained from this fit. Agreement between the two windows with different filtering demonstrates the fidelity of the yield measurement.

8.3.2 CPS filtering for T^3He reaction products

In the CPS diagnostic[18], ranging filters must be designed for each window to downshift the detected fusion products into an appropriate energy range for detection on the CR-39. For this experiment, CPS filtering was designed to detect the charged products from the T^3He reaction (see Eqs 8.1 and 8.2). The filter is designed by taking the incident particle energy as a function of position for each window, and by choosing a filter thickness profile so that the particles of interest have an energy

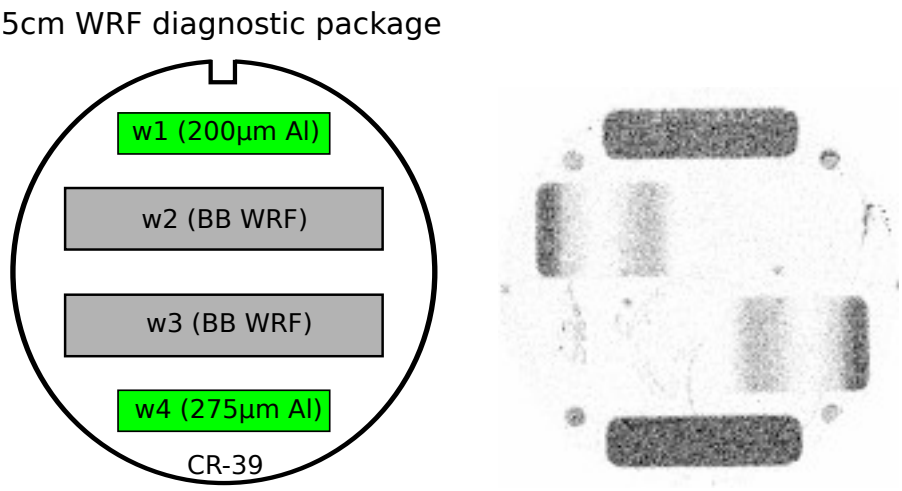

Figure 8.3. Range-filter setup for T^3He-D yield measurement. **(a)** diagnostic schematic. The broadband (BB) WRF package's w1 and w4 were used with 200 and 275 μm Al filters. **(b)** Raw data, black corresponds to more particle fluence. The middle two window images show WRF data. The top (w1) and bottom (w4) windows measured the d fluence.

Figure 8.4. Data for shot 70404 obtained from w1 (200 μm Al filter). The data is displayed as particle fluence versus track diameter. The T^3He-d are monoenergetic and appear as a peak at diameter $\sim$ 5 μm. The T^3He protons are also observed and consitute the background. A fit to the data + background (blue) is used to calculate the yield under the d peak.

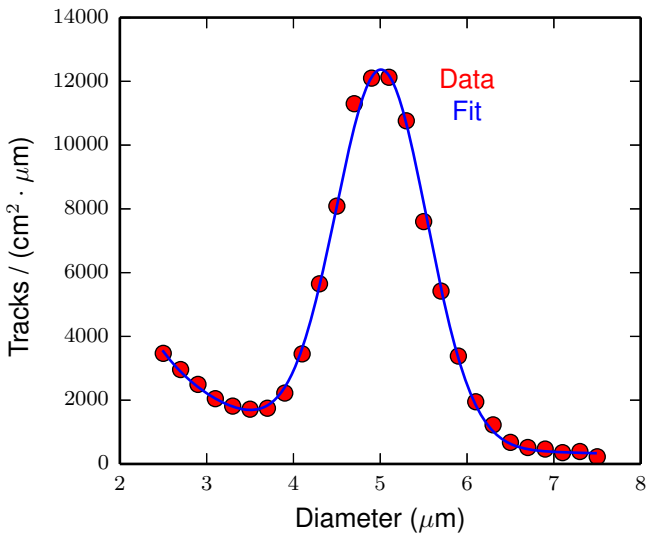

optimal for CR-39 detection. The pre- and post-filter particle energies are shown in Fig. 8.5, while drawings of each filter are shown in Fig. 8.6.

In these experiments, three windows were selected for each CPS: C7W, D4W, and D8W on CPS 1; C8W, D4W, and D8W on CPS 2. These windows span proton energies of interest above 1 MeV. Additionally, the T^3He-d can be detected on the higher windows (D8W). For the two lower-energy windows on each diagnostic, the stepped-aluminum filters are designed to admit protons only, which result from the T^3He reaction (Eq. 8.2).

The design of the highest-energy window is more complex. The D^3He-p (Eq. 8.7), T^3He-d (Eq. 8.1), and the high-energy part of the T^3He-p spectrum all land on this single window. At the low-energy side (left of Fig. 8.6), a series of stepped aluminum filters is used to detect the T^3He protons. At the high-energy side, a vertical split filter is introduced to detect D^3He-p and T^3He-d simultaneously, as these particles require substantially different thicknesses of filtering.

8.4 Yield and T_i measurements

8.4.1 DT reaction

The measured DT-n yield and ion temperature (inferred from Doppler broadening) are shown in Fig. 8.7. On the left of each plot are the T_2-filled implosions, which have higher DT-n yield and higher T_i. In the T^3He case, the DT-n measurement is still of high quality. Since the DT fusion γ is the primary background source for the T^3He-γ measurement, the total DT yield, as measured by nTOF, is used to do a background subtraction.

8.4.2 D^3He reaction

The D^3He-p data is shown in Fig. 8.8. The yield (left) is measured simultaneously by several diagnostics: CPS2, MRS, RF, and WRFs. The four measurements are in good agreement with each other given the uncertainties in each measurement, which indicate minimal yield variation around the implosion.

From the WRF spectral measurement, a Doppler ion temperature is inferred from the width of the line, and shown in the right-hand plot of Fig. 8.8. The six shots have very similar measured T_i. Compared to the DT-n ion temperature measured on the same shots (see Fig. 8.7), the D^3He Doppler temperature is systematically higher by ~ 7 keV. This is expected from calculations; since the D^3He reaction rate is more strongly temperature dependent, the reactions occur closer to the center of the implosion, and thus the burn-weighted temperature is higher.

Since the D^3He and T^3He reactivities have a very similar temperature dependence (which mostly results from the atomic charge of the reactants), the D^3He Doppler temperature is used as a surrogate for the T^3He reaction-weighted temperature and thus center-of-mass reactant energy. Simulations show that the two burn-weighted temperatures for those two reactions are within 1 keV of each other.

8.4.3 T^3He-d reaction branch

The T^3He-d yield is simultaneously measured with CPS 2, MRS, and flat-filtered CR-39 (RF). In the latter, the deuterons are discriminated from protons by track diameter, as described in Section 8.3.1. The filter setup for CPS 2 was described in Section 8.3.2. The data are shown in Fig. 8.9 for the six T^3He shots. The three diagnostics are in good agreement.

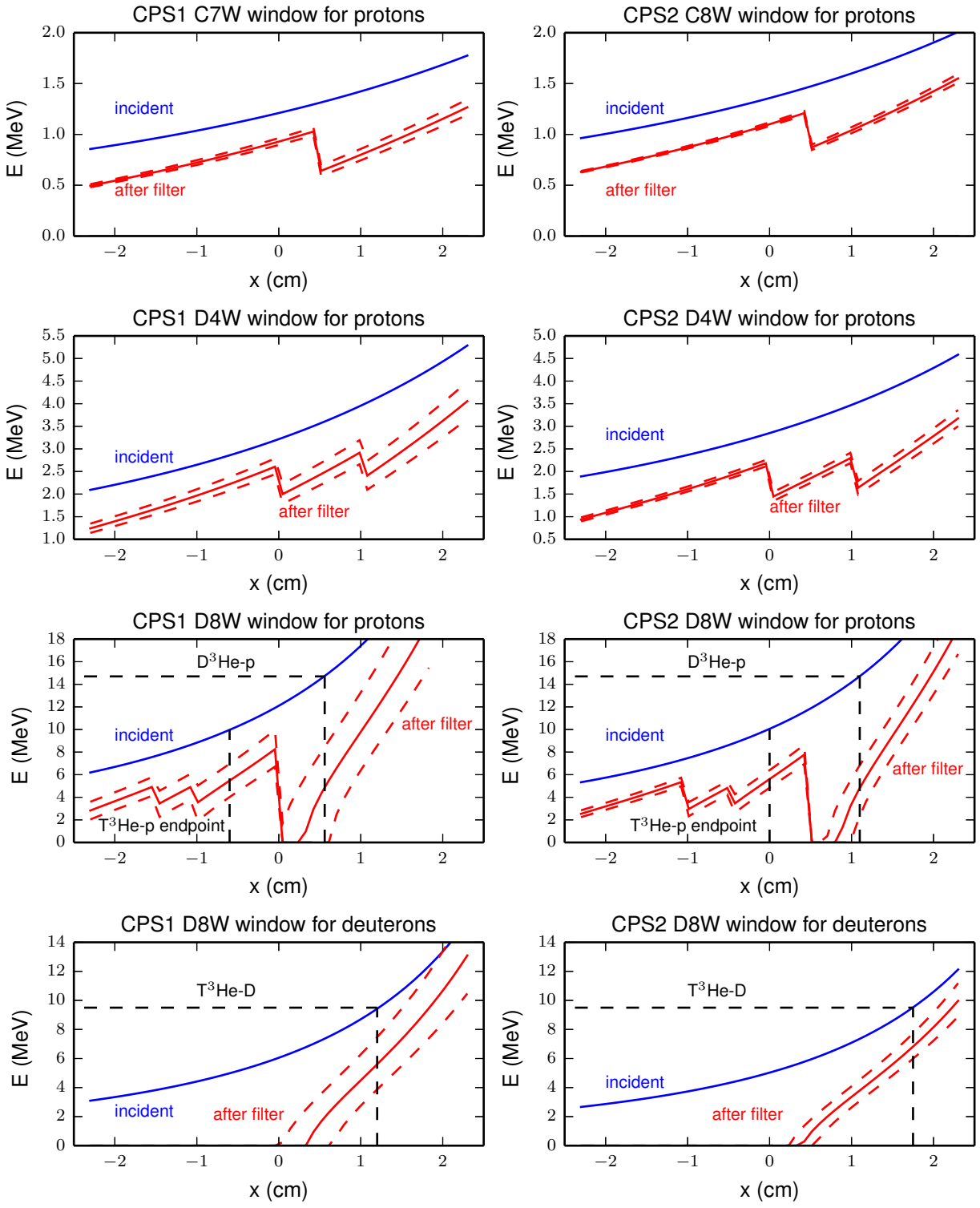

Figure 8.5. Pre- and post-filter particle energies for protons and deuterons on all windows used for CPS 1 and 2.

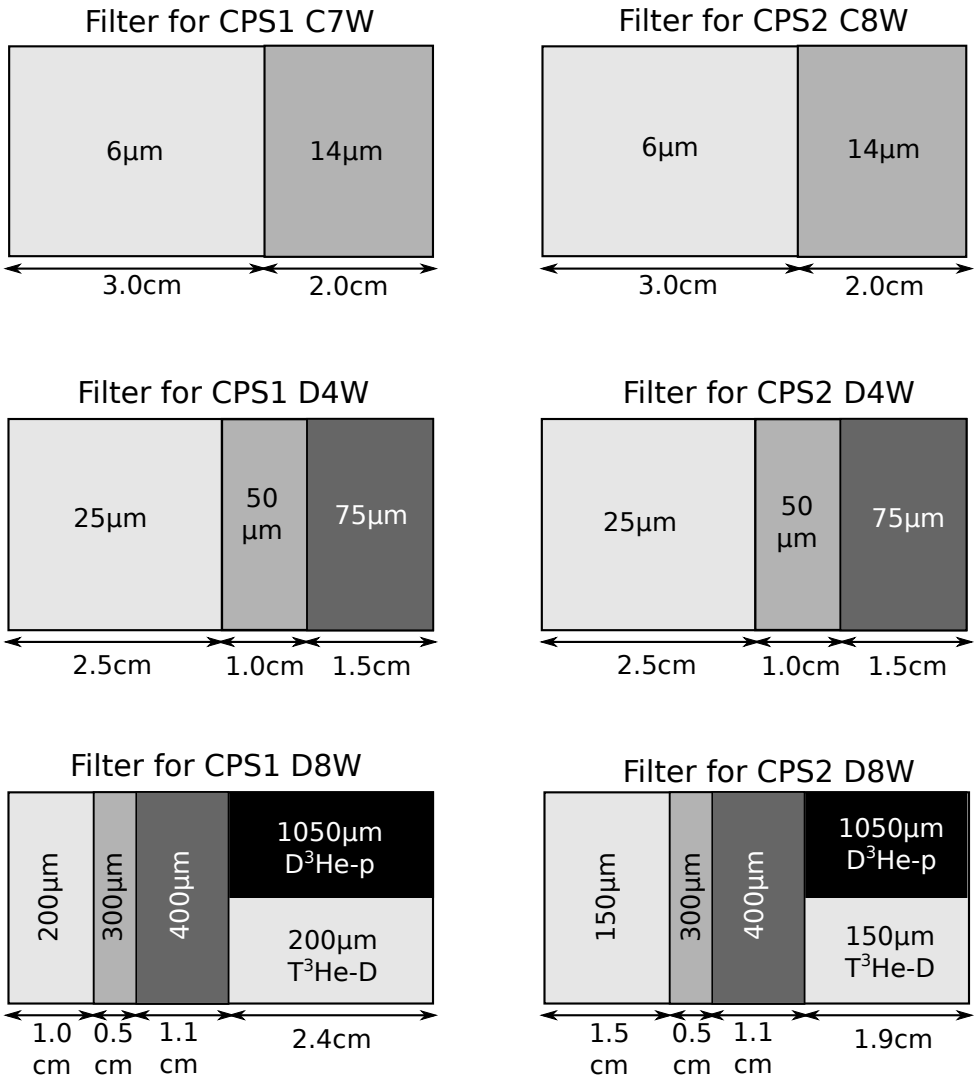

Figure 8.6. Filter drawings used for each of three windows for CPS 1 and 2. The energy dispersion direction is horizontal, displayed with higher energies to the right of each drawing (i.e. in CR-39 coordinates).

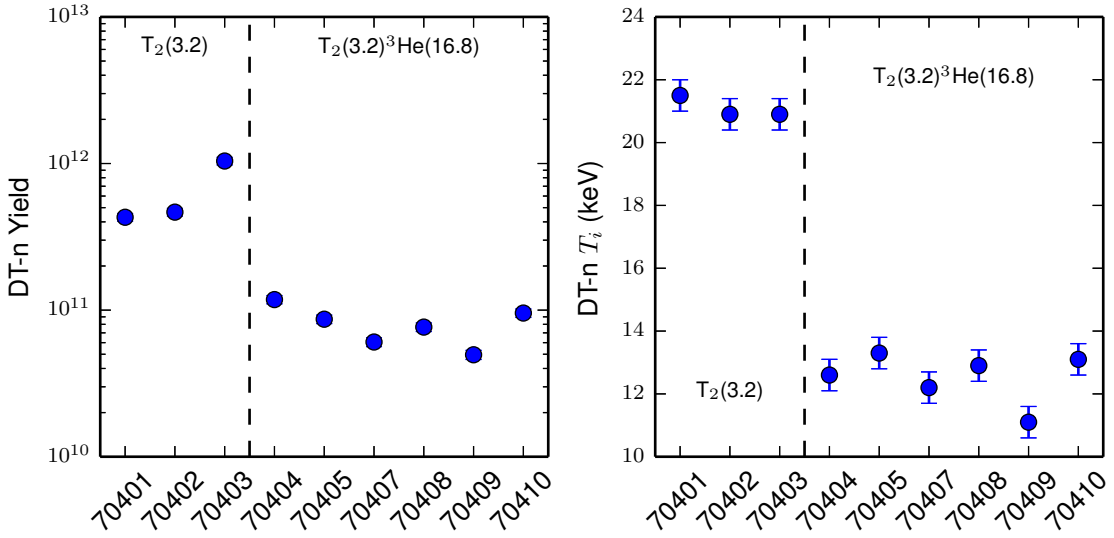

Figure 8.7. Measured DT-n yield (left) and ion temperature (right) for shots containing T_2 or T^3He gas (with trace D contamination).

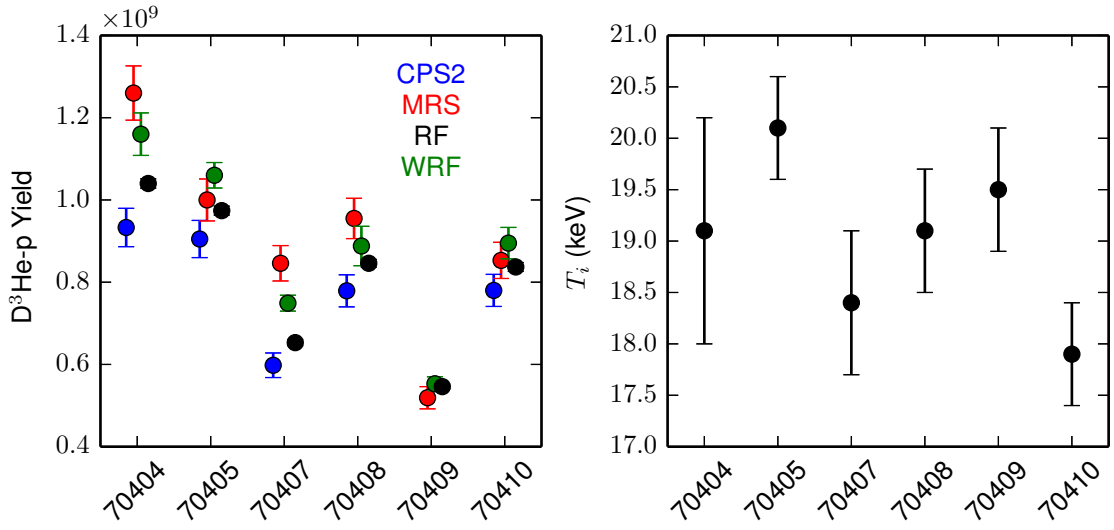

Figure 8.8. Measured D^3He-p yield (left) and ion temperature (right) for the T^3He-gas-filled shots.

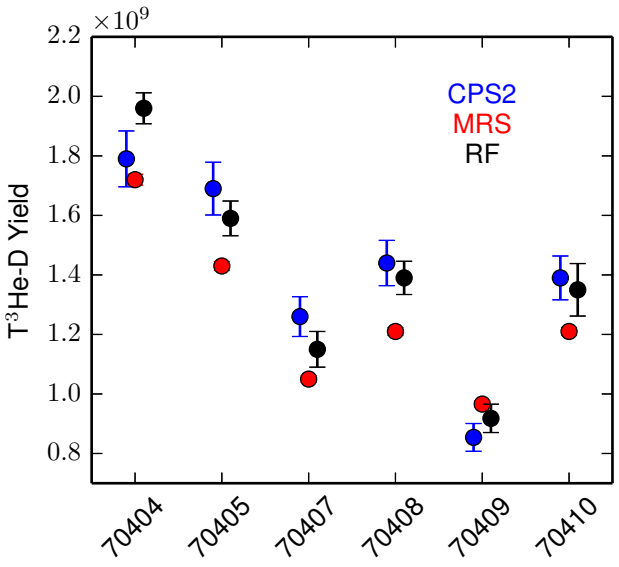

Figure 8.9. Measured T^{3}He-d yield from three diagnostics: CPS2, MRS, and flat-filtered CR-39 (RF).

8.5 T(^{3}He,γ)^{6}Li S-factor

The T+^{3}He reaction also produces an energetic γ ray at 15.8 MeV, which was measured with the Gas Cherenkov Detector (GCD)[20]. In this system, the incident γ rays Compton scatter electrons into a CO_2 gas-filled pressure cell, where the electrons exceed the local speed of light, producing Cherenkov radiation that is detected with a photomultiplier tube[20,21]. The number of detected Cherenkov photons depends on the system response, energy of the initial γ ray, and total number of γ rays produced in the implosion.

The Cherenkov detector data are shown in Fig. 8.10. Each curve corresponds to a single implosion. The signal amplitude represents the peak γ production, and each curve is shifted so that $t = 0$ corresponds to peak burn. The signal width corresponds to a combination of the instrument temporal response and burn duration of the implosion. Signal later in time at ~ 0.5 ns is a photomultiplier tube ring, which is excluded in the analysis. The data from the T^{3}He gas-filled implosions are shown by the blue curves. There are two sources of background for this measurement, which were measured with pure T_2 or ^{3}He filled implosions (red and green curves, respectively).

T^{3}He data from two shots are eliminated in this analysis. These shots (70404 and 70410, which are not shown in Fig. 8.10 are plotted in Fig. 8.11. As shown by the figure, shot 70404 had a high DT neutron yield (see Fig. 8.7), which results in a low S/B for the measurement; the yield-normalized peak is barely above the expected DT contribution. Shot 70410 has an anomalous background subtraction, which is demonstrated by the negative signal level after the peak (around 0.6ns).

The primary source of background is due to a $\sim 1.5\%$ deuterium (D) impurity in the T_2 gas used for these experiments, resulting in D+T reactions that generate γ rays at 16.75 MeV with a branching ratio of $\sim 4 \times 10^{-5}$ (fraction of total DT reactions)[21]. Since the D+T cross section is much higher than the T+^{3}He cross section, this is the dominant source of background. T_2-filled implosions, including the D contamination, were used to measure the background level, shown in Fig. 8.10. On the T_2 shots, the total Cherenkov signal and DT neutron yield are measured, the latter with standard time-of-flight diagnostics[22], giving the Cherenkov signal produced per DT neutron. Since the γ/n ratio is constant, the γ/n factor is used with the measured DT neutron

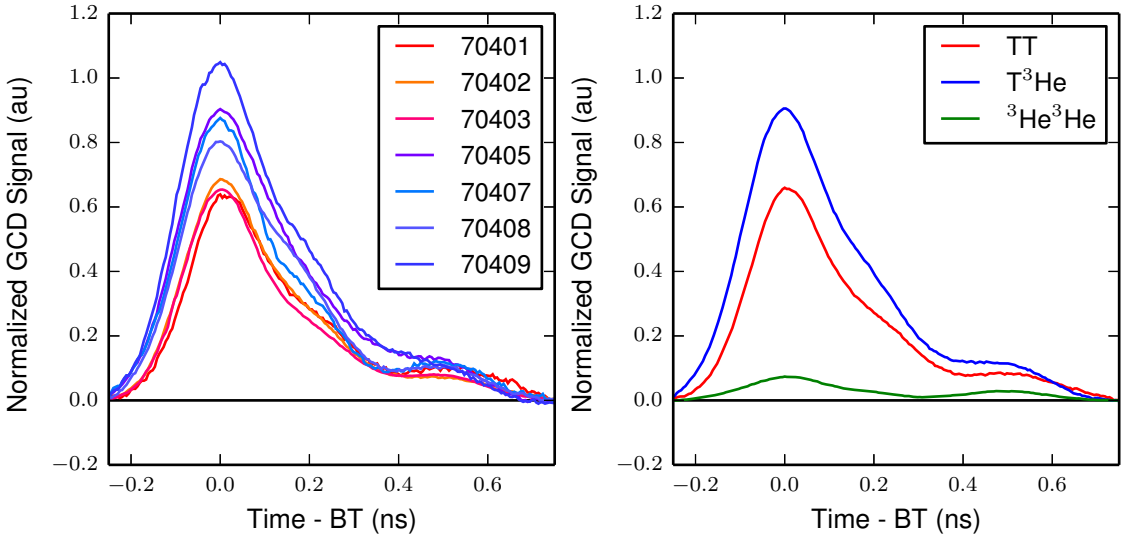

Figure 8.10. Left: Cherenkov data from seven individual implosions. $t = 0$ has been set at the signal peak. In addition to the T^3He gas-filled implosions (blue), sources of background are measured with T_2 (red) implosions. Right: average signal level for the T^3He (blue) and T_2 (red) shots, plus an additional source of background characterized by ^3He gas-filled implosions.

Figure 8.11. Two shots (70404 and 70410) with high γ-ray background levesl; as a result, these shots are excluded from the analysis. Shot 70404 has very low S/B due to a high DT yield, while a poor background subtraction was obtained for 70410.

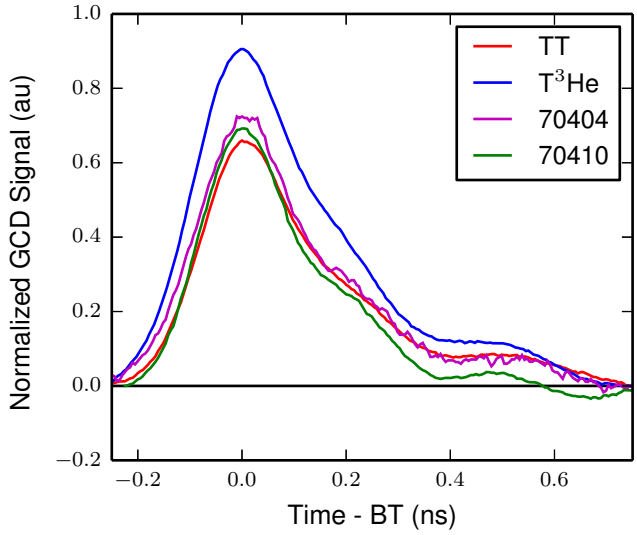

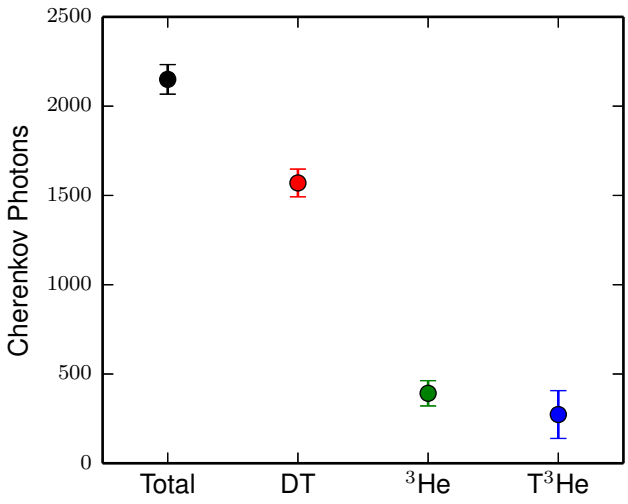

Figure 8.12. From left to right: total Cherenkov signal in a T^{3}He-gas-filled implosion, signal due to the DT γ rays, signal from the 'plasma' or ^{3}He background, and the signal due to T^{3}He-γs.

yield to calculate the Cherenkov signal due to DT reactions in the T^{3}He implosions. The second and smaller source of background was measured in an implosion with only ^{3}He gas, shown in Fig. 8.10, where Cherenkov signal is generated from either a plasma process or ^{3}He+^{3}He reactions[21].

The signal levels (i.e. number of photons) due to the data and background sources are shown in Fig. 8.12. For each T^{3}He-gas-filled implosion, the number of photons recorded is the total signal. The contribution from the two background sources (denoted 'DT', $\sim$ 70% of the total, and '^{3}He', $\sim$ 15% of the total) are calculated using the D-contaminated T_2 and pure ^{3}He gas-filled reference shots. The contribution of the T^{3}He γs to the total signal is determined by subtracting the signal from the two background sources from the total signal. For the following analysis, all quantities are weighted mean values from the individual T^{3}He data. In Fig. 8.12, the statistical uncertainties are shown for each quantity. The statistical limitation of this detection technique is set by the number of Compton-scattered electrons in the γ-to-e converter, with $\sim$ 14 Cherenkov photons detected per electron. The fractional statistical uncertainty in each measurement is thus $1/\sqrt{n_e}$ where n_e is the number of Compton electrons. In addition, the DT-γ background subtraction depends on the DT-neutron yield measurement, which has an associated statistical uncertainty. A source of systematic uncertainty in the number of Cherenkov photons is due to the subtraction of the background observed on ^{3}He shots, which is either a plasma process or ^{3}He-fusion-γ background. The former is expected to be constant between the implosion types, while the latter scales with the square of the ^{3}He ion fraction. Since the nature of this background is still unknown, these two possibilities are taken as an upper and lower bound on this background contribution with the difference as a systematic uncertainty.

The number of Cherenkov photons from the T^{3}He-γ signal is thus $273 \pm 134_{\text{stat}} \pm 84_{\text{sys}}$. This is converted to a total yield of T^{3}He-γ using the absolute detector response[23] and the expected γ-ray spectrum, which are shown in Fig. 8.13. The calculated γ-ray spectrum, in blue, is derived from a R-matrix calculation[24] showing the ^{6}Li ground state at $E_\gamma \sim 15.8$ MeV and excited states of ^{6}Li at lower γ energies. For example, the first two excited states of ^{6}Li have excitation energies $\Delta E = 2.184$ and 3.562 MeV, respectively. The R-matrix calculation gives the γ spectrum, which results from a combination of the ground state and excited states of ^{6}Li. In a finite temperature plasma, the ground-state emission is upshifted and broadened by reaction kinematics. In the case

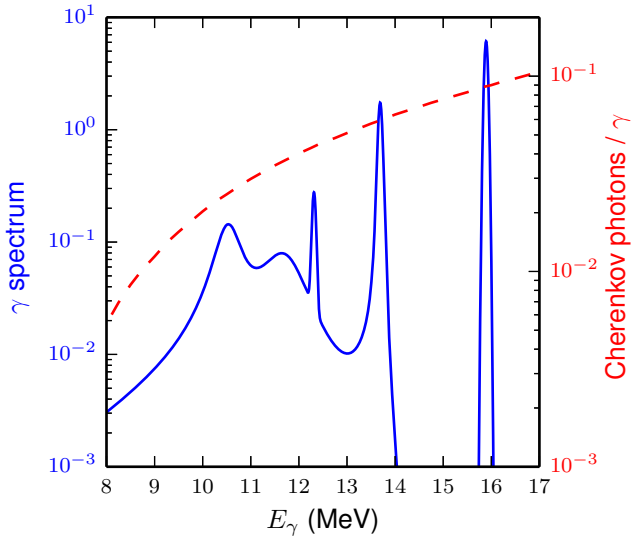

Figure 8.13. R-matrix calculated γ-ray spectrum for the T^3He reaction (blue curve, left abscissa, normalized) and the GCD-1 response curve as Cherenkov photons detected per incident γ (red dashed curve, right abscissa).

of a γ-emitting reaction the mean γ energy is given by

$$\langle E_\gamma \rangle = Q + \langle K \rangle, \tag{8.8}$$

from Eq. 5 of Ref. 25, while the thermal broadening is given by

$$\sigma_{th}^2 = \langle K^2 \rangle - \langle K \rangle^2, \tag{8.9}$$

from simplifying Eq. 12 of Ref. 25. In Eqs. 8.8 and 8.9 K is measure of the kinetic energy in the center-of-mass frame, with its averages given by

$$\langle K^n \rangle = \frac{\int_0^\infty dk\ k^{n+1}\sigma(k)\exp\left[-\frac{k}{T_i}\right]}{\int_0^\infty dk\ k\sigma(k)\exp\left[-\frac{k}{T_i}\right]}, \tag{8.10}$$

from Eq. 35 of Ref. 25, where T_i is the thermal temperature in energy units and σ is the reaction cross section. If the S-factor for the reaction is approximately constant over the range of center-of-mass energies probed by the thermal plasma, typically a reasonable assumption, this expression can be simplified to

$$\langle K^n \rangle = \frac{\int_0^\infty dk\ k^n \exp\left[-\frac{k}{T_i} - \sqrt{\frac{E_G}{k}}\right]}{\int_0^\infty dk\ \exp\left[-\frac{k}{T_i} - \sqrt{\frac{E_G}{k}}\right]}, \tag{8.11}$$

which is numerically evaluated to calculate the thermal broadening for this reaction. The effective GCD response is then calculated by folding the thermally-broadening γ-ray spectrum[†] with the

[†]Alternatively, using the γ_0, γ_1, and γ_2 cross sections from Blatt[9] gives a response of 7.65×10^{-2} Cherenkov photons per incident γ

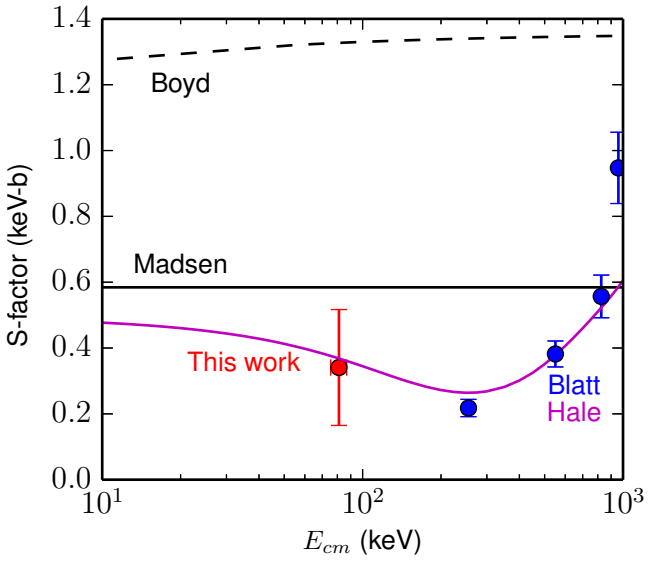

Figure 8.14. S-factor for the reaction T(^{3}He,γ)^{6}Li measured in this work, compared to previous data (Blatt, Ref. 9) and values used in BBN theory (Madsen and Boyd, Refs. 7 and 3). The purple curve is a R-matrix calculation.

response curve, shown in Fig. 8.13. This gives 6.91×10^{-2} Cherenkov photons per incident γ, a reduction of 21% from a naïve calculation assuming all reactions go to the ^{6}Li ground state. Using this response factor with the GCD solid angle and the measured number of detected Cherenkov photons gives a total γ yield of $Y_\gamma = (2.8 \pm 1.4_{\text{stat}} \pm 1.3_{\text{sys}}) \times 10^5$. An additional 34% systematic uncertainty is included in the absolute γ yield to account for the calibration uncertainty in the absolute detector response[21].

The quantity of interest in these experiments is the astrophysical S-factor (S) for the T(^{3}He,γ)^{6}Li reaction, which is related to the cross section (σ) by Eq. 1.13. To determine the S-factor from the γ yield in this experiment, a better-known T^{3}He reaction branch can be used as a reference, such as the T^{3}He-d reaction (Eq. 8.1). The absolute yield of the 9.5 MeV deuterons was measured to be $Y_d = (1.17 \pm 0.01) \times 10^9$ with six independent detectors using two different techniques (see Section 8.4.3). The S-factor for the T(^{3}He,γ)^{6}Li branch is thus

$$S_\gamma = S_d \times \frac{Y_\gamma}{Y_d} = 0.14 \pm 0.09 \ \ \text{keV-b}, \tag{8.12}$$

where the deuteron branch S-factor (S_d) was taken from ENDF[26], and the error bar is a root-mean-square sum of the statistical and systematic uncertainties.

In these experiments, the reactant E_{cm} was determined from proton spectroscopy[27] of the D^{3}He reaction (Eq. 1.15). From the line width of the D^{3}He-proton spectrum, a thermal Maxwellian temperature of 19 ± 1 keV was determined[28]. Radiation-hydrodynamic simulations demonstrate that the T^{3}He and D^{3}He reactions have burn-averaged temperatures well within 1 keV due to the similar reactivity energy dependence, suggesting a similar T_i for the T^{3}He reaction. To account for the reliance on simulation, we increase the uncertainty to $T_i = 19 \pm 2$ keV for the T^{3}He reaction, which corresponds to $E_{cm} = 81 \pm 6$ keV.

The S-factor determined in this work is shown in Fig. 8.14, and contrasted to higher-energy data obtained in previous experimental work[9]. Values used in BBN reaction theories[7,3] are also shown

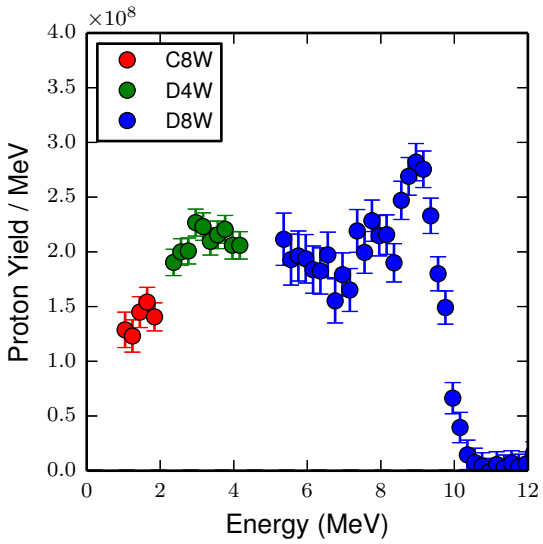

Figure 8.15. Proton spectrum measured with CPS 2. The weighted mean of six shots is shown.

for comparison. We find that the S-factor at lower energy is consistent with the lowest-energy Blatt data and a R-matrix calculation by Hale[24], which is fit to the Blatt data. The R-matrix calculations suggests competition between a high-energy resonance (known to be at $2 - 3$ MeV) and unexpected behavior at low energy, which causes the 'dip' ~ 250 keV. Furthermore, our data is clearly inconsistent with the higher S-factors assumed by BBN theory[7,3], meaning that the theories already overpredict the production of ^{6}Li via this reaction.

8.6 T+^{3}He proton spectrum

The T^3He-p spectrum was measured with two instruments: CPS 2 (see Sec. 8.3.2), and MRS.

The proton spectrum measured by CPS 2 is shown in Fig. 8.15. The number of counts per bin are low for an individual shot, resulting in significant statistical scatter in the spectra. An average proton spectrum is therefore calculated from the six shots, as shown in Fig. 8.15. The error bars are significantly reduced from a single-shot measurement due to improved statistics per bin. The three windows used are denoted by different colors.

The MRS-measured proton spectrum is shown in Fig. 8.16. Similarly, the individual spectra are summed over the individual shots to calculate an average spectrum. In the MRS analysis, shot 70404 is excluded due to a background issue in the data. The MRS system has a higher collection efficiency than CPS due to focusing properties in the dipole magnet over this energy range, but the low-energy cutoff in the MRS data is ~ 5 MeV.

The two diagnostics are directly compared in Fig. 8.17. The MRS data is only comparable with the highest-energy CPS 2 window (D8W). In this energy range, excellent agreement is found between the two diagnostics both in the spectral shape, and the absolute average yield over the six shots. The resolution of CPS 2 is worse than MRS with this configuration (See Appendix I), leading to the broader peak. The MRS data also has better statistics and thus smaller error bars. Because of this, a final spectrum using the MRS data at high energy and the CPS 2 data at lower energy is used as the final measured spectrum, shown in Fig. 8.18.

The final spectrum exhibits several notable features. First, the clear peak at 9.5 MeV results

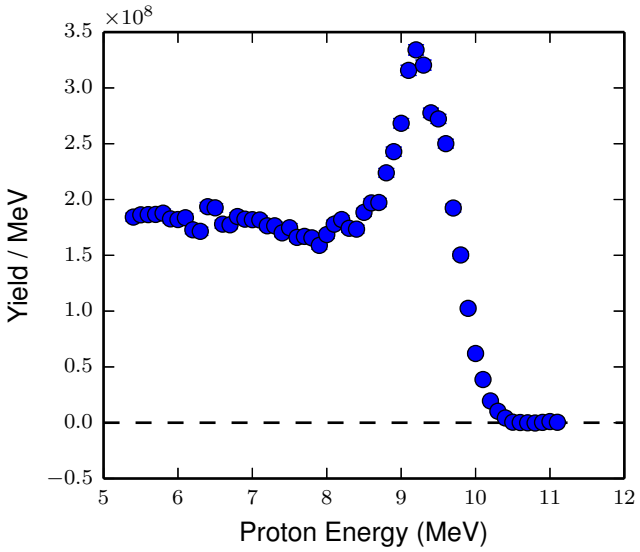

Figure 8.16. Proton spectra measured with MRS.

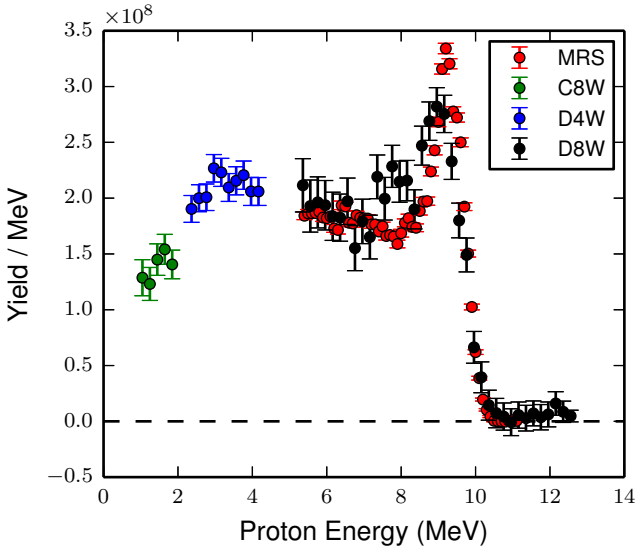

Figure 8.17. Comparison of MRS- and CPS-measured proton spectra.

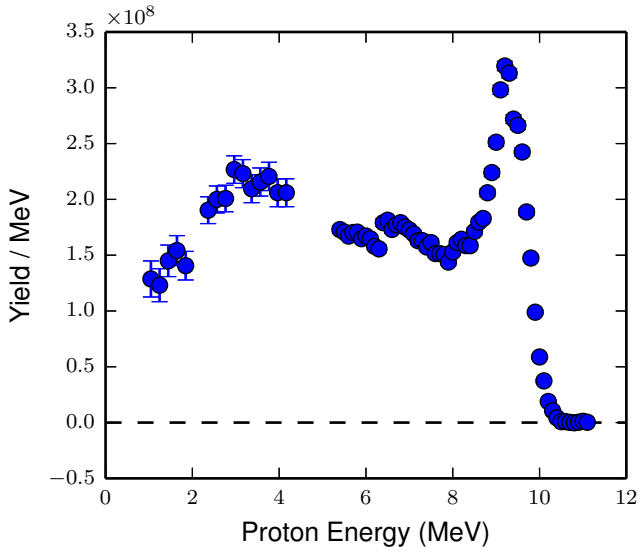

Figure 8.18. Final T^3He-p spectrum from a combination of the two instruments.

from the ^5He branch of the reaction, Eq. 8.3. The cutoff in the proton spectrum occurs ~ 10 MeV as expected from the kinematics. The shape of the proton spectrum at lower energy is a sensitive probe of the nuclear physics of the reaction.

8.7 $T(^3He,d)^4He$ / $T(^3He,np)^4He$ branching ratio

With the proton spectrum (Sec. 8.6) and deuteron yield (Sec. 8.4.3), the cross-section ratio between those two reaction branches can be calculated. In this experiment, the center-of-mass energy (Gamow peak energy) $E_{cm} = 81 \pm 6$ keV (see Sec. 8.5) is significantly lower than any previous nuclear data obtained for this branching ratio[11]. Due to its monoenergetic spectrum, the d yield is readily determined. However, the total proton yield must be determined from a fit or interpolation of the spectrum. In this analysis, an interpolated spectrum is integrated to obtain the total yield, as shown in Fig. 8.19. The two yields are $Y_p = (1.80 \pm 0.18) \times 10^9$ and $Y_D = (1.28 \pm 0.02) \times 10^9$, resulting in a branching ratio

$$\frac{T(^3He,d)^4He}{T(^3He,np)^4He} = 0.71 \pm 0.07. \tag{8.13}$$

As shown in Fig. 8.20 this result agrees with previous data obtained by Kuhn at higher energies[11]. A constant branching ratio is intuitively understandable. The primary difference between the two branches is if the neutron and proton emerge independently, or in the deuteron bound state. The deuteron binding energy is 2.2 MeV, and since all center-of-mass energies considered here are much less than the deuteron binding energy, the center-of-mass energy is not expected to affect the reaction dynamics. However, this contradicts the result from ENDF[26], which is shown as the solid black curve in Fig. 8.20. From $0 \rightarrow 600$ keV, the ENDF cross-sections predict a $2\times$ decrease in the deuteron yield relative to the proton yield, which is clearly inconsistent with the data. Since this measurement is a probe of the final-state interactions of the nuclear products, this data will be used to further constrain nuclear modeling of six-nucleon systems.

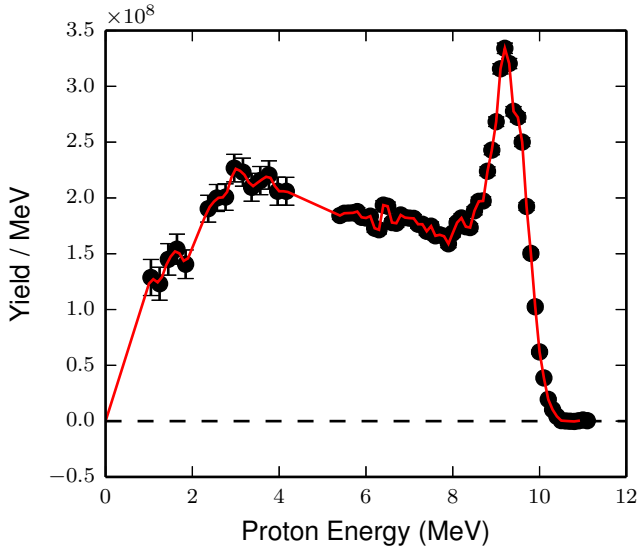

Figure 8.19. The total T^{3}He proton yield is estimated from an interpolation of the data (red curve), which is integrated to obtain a total yield $Y_p = 1.80 \times 10^9$. An uncertainty in the total yield of 10% is used to account for errors resulting from this interpolation.

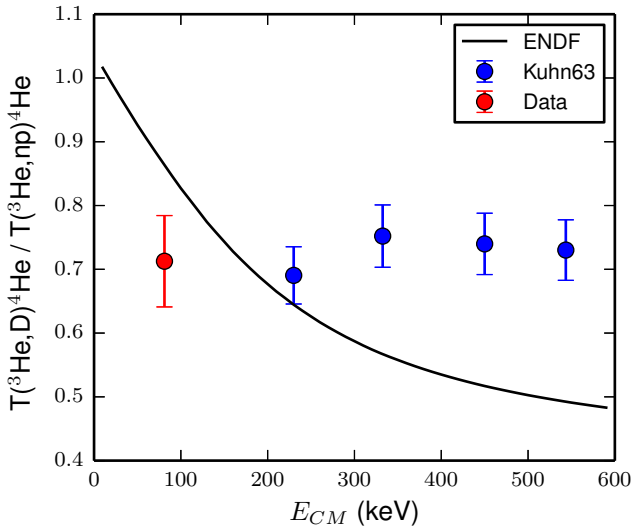

Figure 8.20. The branching ratio for the reaction channels T(^{3}He,D)^{4}He / T(^{3}He,np)^{4}He, compared to data from Kuhn[11].

8.8 Proton spectrum R-matrix analysis

The charged-particle data from Sections 8.6 and 8.4.3 can be used to constrain R-matrix nuclear theory[29,30], which is a phenomenological model based on several 'feeding factors', which describe the relative scattering amplitudes, to calculate the spectral components for these nuclear reactions. An initial calculation with feeding factors derived from higher-energy T-T reaction data[31] is shown in Fig. 8.21.

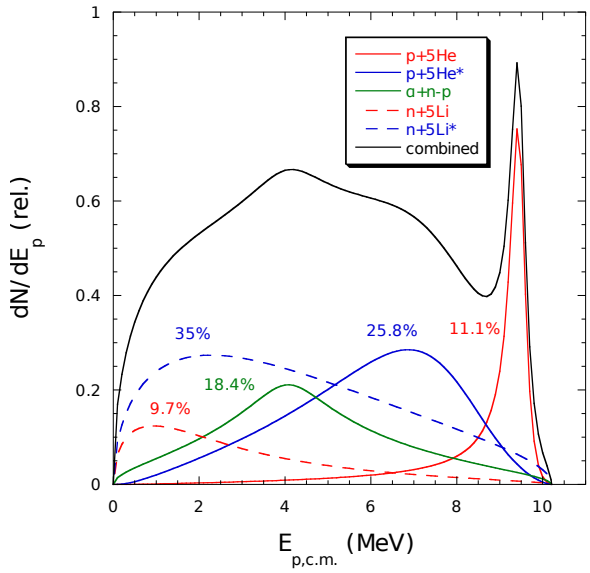

Figure 8.21. The R-matrix modeled proton spectrum including several branches. The %s are the fraction of the total reactions for each of the different branches.

The combined proton spectrum from the R-matrix calculation is convolved with the thermal broadening and the instrument response functions for MRS and CPS to compare to the data; the comparison is shown in Fig. 8.22 with the total yield adjusted to minimize χ^2. The comparison clearly shows that this initial R-matrix calculation is underestimating the spectral contribution from the ^{5}He ground state, which corresponds to the peak at $E \sim 9$ MeV.

Future R-matrix calculations will fit the data using the feeding factors as free parameters to infer the relative strength of the reaction branches. These results will be valuable in understanding these light-nuclei reactions, in particular the $A = 6$ systems (T+T, T+^{3}He, and ^{3}He+^{3}He).

8.9 Conclusion

As HED plasmas better mimic conditions in stellar interiors and the universe during BBN than accelerator experiments, a rich set of nuclear-astrophysics research can be uniquely conducted at the OMEGA[13] and NIF[32] lasers. The present work is significant in that it represents the first use of HEDP to directly address an open problem in nuclear astrophysics. In a broader context, this effort is part of a program where HEDP are used to probe basic nuclear science[33–36].

Based on these results, we conclude that the reaction T(^{3}He,γ)^{6}Li cannot produce sufficient ^{6}Li to explain the observed levels of ^{6}Li in primordial material. While the levels of ^{6}Li detected in some stars is debated[37], the excess has been confirmed for a few low-metallicity stars[5,38]. This work, and a recent study of the D(α,γ)^{6}Li reaction[6], suggest that a nuclear physics solution to the

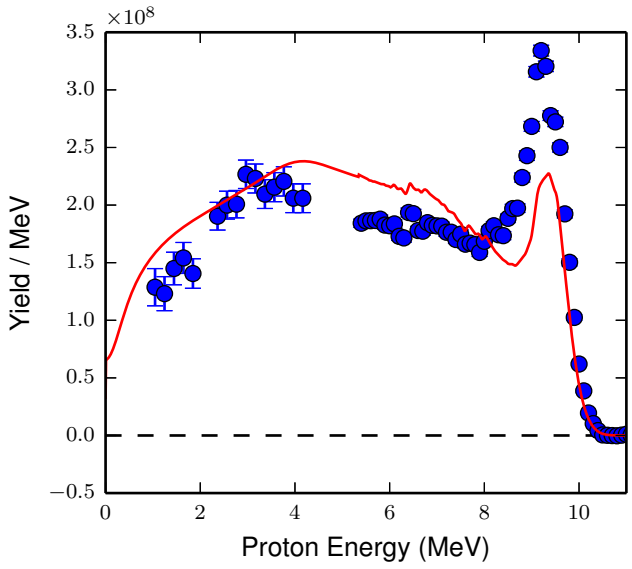

Figure 8.22. Comparison of the R-matrix modeled spectral shape (Fig. 8.21), after thermal broadening and IRF convolution (red curve), to the measured data (blue points).

^{6}Li problem is unlikely, lending weight to alternative theories such as in-situ stellar production[39] or non-Standard-Model physics[40–42].

The S-factor for the T(^{3}He,γ)^{6}Li reaction is found to be in good agreement with previous data at ~ 250 keV and a R-matrix calculation. Future experiments with higher precision could explore the nuclear physics of this reaction at low energy. Finally, the data clearly show that current Big-Bang nucleosynthesis models (such as Ref. 3) overestimate the rate for this reaction.

In addition to the γ data, the charged-particle data are used to enhance our understanding of the underlying nuclear physics. Specifically, the measured proton spectrum has been compared to an R-matrix calculation based on higher-energy T-T reaction data and first order corrections, which clearly underestimates the contribution of the ^{5}He ground state.

8.10 References

1. R. A. Alpher, H. Bethe and G. Gamow, "The Origin of Chemical Elements," Phys. Rev., **73**, 803–804 (1948).
2. P. D. Serpico, S. Esposito, F. Iocco *et al.*, "Nuclear reaction network for primordial nucleosynthesis: a detailed analysis of rates, uncertainties and light nuclei yields," Journal of Cosmology and Astroparticle Physics, **2004**(12), 010 (2004).
3. R. N. Boyd, C. R. Brune, G. M. Fuller *et al.*, "New nuclear physics for big bang nucleosynthesis," Phys. Rev. D, **82**, 105005 (2010).
4. M. Asplund, D. L. Lambert, P. E. Nissen *et al.*, "Lithium Isotopic Abundances in Metal-poor Halo Stars," The Astrophysical Journal, **644**(1), 229 (2006).
5. B. D. Fields, "The primordial lithium problem," Annual Review of Nuclear and Particle Science, **61**(1), 47–68 (2011).
6. M. Anders, D. Trezzi, R. Menegazzo *et al.*, "First Direct Measurement of the ^{2}H(α,γ)^{6}Li Cross Section at Big Bang Energies and the Primordial Lithium Problem," Phys. Rev. Lett., **113**, 042,501 (2014).
7. J. Madsen, "CNO and Li^6 from big-bang nucleosynthesis¯Impact of unmeasured reaction rates," Phys. Rev. D, **41**, 2472–2478 (1990).
8. M. Fukugita and T. Kajino, "Contribution of the He^3(t,γ)Li^6 reaction to Li^6 production in primordial nucleosynthesis," Phys. Rev. D, **42**, 4251–4253 (1990).

9. S. L. Blatt, A. M. Young, S. C. Ling *et al.*, "Reaction T(He^3, γ)Li^6 in the Energy Range 0.5-11 MeV," Phys. Rev., **176**, 1147–1153 (1968).
10. Li Ga Youn, G.M. Osetinski, N. Sodnom *et al.*, "Research of He-3 + H-3 Reaction," Journal of Experimental and Theoretical Physics, **39**, 225 (1960).
11. B. Kühn and B. Schlenk, "Winkelverteilungen Für Die Reaktion He^3 + T," Nuclear Physics, **48**, 353–360 (1963).
12. J. Beveridge and R. Johnson, "Final State Interactions in the Reaction T(^{3}He,^{4}He)np," Can. J. Phys., **49**, 1374–1383 (1971).
13. T. Boehly, D. Brown, R. Craxton *et al.*, "Initial performance results of the OMEGA laser system," Optics Communications, **133**(1-6), 495–506 (1997).
14. D. G. Hicks *et al.*, "Charged-particle acceleration and energy loss in laser-produced plasmas," Phys. Plasmas, **7**(12), 5106–5117 (2000).
15. N. Sinenian, M. J.-E. Manuel, J. A. Frenje *et al.*, "An empirical target discharging model relevant to hot-electron preheat in direct-drive implosions on OMEGA," Plasma Physics and Controlled Fusion, **55**(4), 045001 (2013).
16. F. H. Séguin, J. A. Frenje, C. K. Li *et al.*, "Spectrometry of charged particles from inertial-confinement-fusion plasmas," Rev. Sci. Instrum., **74**(2), 975–995 (2003).
17. C. J. Forrest, P. B. Radha, V. Y. Glebov *et al.*, "High-resolution spectroscopy used to measure inertial confinement fusion neutron spectra on Omega (invited)," Rev. Sci. Instrum., **83**(10), 10D919 (2012).
18. D. Hicks, *Charged-particle spectroscopy: a new window on inertial confinement fusion*, Ph.D. thesis, Massachusetts Institute of Technology (1999).
19. D. Casey, *Diagnosing Inertial Confinement Fusion Implosions at OMEGA and the NIF Using Novel Neutron Spectrometry*, Ph.D. thesis, Massachusetts Institute of Technology (2012).
20. J. Mack, R. Berggren, S. Caldwell *et al.*, "Observation of high-energy deuterium-tritium fusion gamma rays using gas Cherenkov detectors," Nuclear Instruments and Methods in Physics Research Section A: Accelerators, Spectrometers, Detectors and Associated Equipment, **513**(3), 566 – 572 (2003).
21. Y. Kim, J. Mack, H. Herrmann *et al.*, "D-T gamma-to-neutron branching ratio determined from inertial confinement fusion plasmas," Phys. Plasmas, **19**, 056313 (2012).
22. V. Y. Glebov, D. D. Meyerhofer, T. C. Sangster *et al.*, "Development of nuclear diagnostics for the National Ignition Facility (invited)," Rev. Sci. Instrum., **77**(10), 10E715 (2006).
23. M. S. Rubery, C. J. Horsfield, H. Herrmann *et al.*, "Monte carlo validation experiments for the gas cherenkov detectors at the national ignition facility and omega," Review of Scientific Instruments, **84**(7), 073504 (2013).
24. G. Hale, private communication (2015).
25. L. Ballabio, J. Källne and G. Gorini, "Relativistic calculation of fusion product spectra for thermonuclear plasmas," Nuclear Fusion, **38**(11), 1723 (1998).
26. M. Chadwick, P. Oblozinsky, M. Herman *et al.*, "ENDF/B-VII.0: Next Generation Evaluated Nuclear Data Library for Nuclear Science and Technology," Nuclear Data Sheets, **107**(12), 2931 – 3060 (2006), evaluated Nuclear Data File ENDF/B-VII.0.
27. F. H. Séguin, N. Sinenian, M. Rosenberg *et al.*, "Advances in compact proton spectrometers for inertial-confinement fusion and plasma nuclear science," Rev. Sci. Instrum., **83**(10), 10D908 (2012).
28. H. Brysk, "Fusion Neutron Energies and Spectra," Plasma Physics, **15**, 611–617 (1973).
29. A. M. Lane and R. G. Thomas, "R-matrix theory of nuclear reactions," Rev. Mod. Phys., **30**, 257–353 (1958).
30. F. Barker, "Consistent description of unbound states observed in scattering and reactions," Australian Journal of Physics, **41**, 743–764 (1988).
31. C. Wong, J. Anderson and J. McClure, "Neutron spectrum from the t+t reaction," Nuclear Physics, **71**, 106–112 (1965).
32. G. Miller, E. Moses and C. Wuest, "The National Ignition Facility: enabling fusion ignition for the 21st century," Nuclear Fusion, **44**, S228 (2004).
33. J. A. Frenje, C. K. Li, F. H. Seguin *et al.*, "Measurements of the differential cross sections for the elastic n-^{3}H and n-^{2}H scattering at 14.1 mev by using an inertial confinement fusion facility," Phys. Rev. Lett., **107**, 122,502 (2011).
34. D. T. Casey, J. A. Frenje, M. Gatu Johnson *et al.*, "Measurements of the $\mathbf{T}(t, 2n)^4$He neutron spectrum at low reactant energies from inertial confinement implosions," Phys. Rev. Lett., **109**, 025,003 (2012).

35. D. B. Sayre, C. R. Brune, J. A. Caggiano *et al.*, "Measurement of the $t + t$ neutron spectrum using the national ignition facility," Phys. Rev. Lett., **111**, 052,501 (2013).

36. M. Barbui, W. Bang, A. Bonasera *et al.*, "Measurement of the plasma astrophysical s factor for the ^{3}He$(d,p)^4$He reaction in exploding molecular clusters," Phys. Rev. Lett., **111**, 082,502 (2013).

37. Lind, K., Melendez, J., Asplund, M. *et al.*, "The lithium isotopic ratio in very metal-poor stars," A&A, **554**, A96 (2013).

38. M. Steffen, R. Cayrel, E. Caffau *et al.*, "^{6}li detection in metal-poor stars: can 3d model atmospheres solve the second lithium problem?" arXiv, pages arXiv:1206.2239 [astro–ph.SR] (2012).

39. Prantzos, N., "Production and evolution of li, be, and b isotopes in the galaxy," A&A, **542**, A67 (2012).

40. M. Kusakabe, T. Kajino, R. N. Boyd *et al.*, "Simultaneous solution to the ^{6}Li and ^{7}Li big bang nucleosynthesis problems from a long-lived negatively charged leptonic particle," Phys. Rev. D, **76**, 121,302 (2007).

41. K. Jedamzik and M. Pospelov, "Big bang nucleosynthesis and particle dark matter," New Journal of Physics, **11**(10), 105,028 (2009).

42. M. Pospelov and J. Pradler, "Big bang nucleosynthesis as a probe of new physics," Annual Review of Nuclear and Particle Science, **60**(1), 539–568 (2010).

9

The ^{3}He^{3}He proton spectrum

9.1 Introduction

The proton-proton I chain (pp-I), shown schematically in Fig. 9.1, accounts for $\sim$ 86% of ^{4}He produced via nuclear fusion in the sun (see Section 7.2). The final step of this process is the fusion of two ^{3}He nuclei, which generates most of the energy produced in the pp-I chain, and is the focus of this chapter.

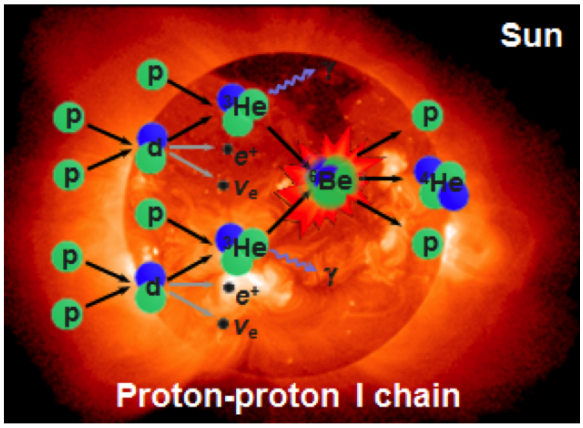

Figure 9.1. Schematic of the proton-proton I (pp-I) chain, which burns hydrogen into helium in the Sun.

An accurate understanding of thermonuclear reaction rates for this and other reactions are required for high-fidelity modeling of nucleosynthesis and energy production in low-mass stars like our sun[1]. Conventionally, beam-target fusion reactions in accelerator experiments are used to measure astrophysically-relevant nuclear reaction rates[2,3]. Significant efforts have been taken to measure the cross section for the ^{3}He^{3}He reaction at low energies relevant to solar fusion[4–8], but some issues and uncertainties in this data set still need to be addressed. First, the accelerator data must be corrected for bound-electron screening effects on the cross section. Secondly, the accelerator experiments at low energy have poor spectral resolution due to an extremely low count rate, background radiation, and intrinsic instrument resolution. As a result, the data analysis must assume a spectral shape for the resulting proton spectrum, which considerably increases the uncertainty in the cross section measurement.

The ^{3}He^{3}He reaction can proceed via two branches:

$$^3\text{He} + {}^3\text{He} \rightarrow 2\text{p} \ (< 10.8 \text{ MeV}) + {}^4\text{He} \ (< 4.3 \text{ MeV}), \quad (9.1)$$

$$\rightarrow p \ (9.1 \text{ MeV}) + {}^5\text{Li} \ (1.8 \text{ MeV}). \quad (9.2)$$

The energy produced in this reaction is $Q = 12.86$ MeV. In the first branch, the three products (two protons and a ^{4}He) have a wide range of energies, with their spectra determined by conservation of energy and momentum. The maximum proton energy is 10.8 MeV. Alternatively, a short-lived ^{5}Li nucleus may be produced; in this case the two products are monoenergetic, determined by the reaction kinematics.

Current nuclear theory for this reaction at low energy needs to be benchmarked against data. Recently, experiments using inertially-confined plasmas have measured the neutron spectrum from the mirror reaction T(T,2n)^{4}He for the first time[9,10]. Sayre *et al* utilize a R-matrix analysis[11,12] to show that the TT reaction is dominated by the ^{5}He $1/2^-$ partial wave, in contradiction to prior work. This strongly motivates studies of the shape of the ^{3}He^{3}He proton spectrum, as a probe of the fundamental nuclear physics of that reaction, and for improved data analysis of accelerator reaction-rate measurements relevant to solar fusion.

9.2 OMEGA Experiments

For the first time, the ^{3}He^{3}He reaction was studied using inertially-confined laboratory plasmas. The OMEGA laser[13] imploded thin-glass 'exploding-pusher' targets, which are shown in Fig. 9.2. $2-3$ μm thick SiO_2 shells with outer diameters of $860-1000$ μm were filled with ^{3}He gas. The gas is typically contaminated with $(1-10)\times10^{-4}$ parts D. The outer surface of the spherical shell was illuminated with the OMEGA laser at 3ω (351nm) using SG4 DPP and DPR smoothing, but without SSD to maximize on-target energy delivered. Either a 600ps or 1ns duration square pulse was used with 17kJ (600ps) or 30kJ (1ns) of total energy.

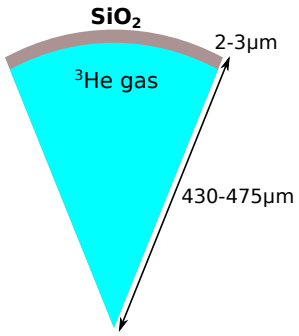

Figure 9.2. Thin-glass exploding pusher targets.

On each shot, several Wedge Range Filter (WRF) proton spectrometers[14,15] were fielded around the implosion at a distance of 10.5cm, maximizing detection efficiency. From the available data, four shots with high-quality WRFs fielded* are used in this analysis. The shots are summarized in Table 9.1. For a listing of all experiments, see Table 9.4 at the end of this chapter.

*After the ^{3}He-^{3}He experiments, calibration issues with some batches of WRF were discovered (F. Séguin, private communication).

Table 9.1. Shots used in the ^{3}He^{3}He analysis

		Laser				Target		
Shot	Date	Energy (kJ)	Pulse	DPP	SSD	Dia (μm)	Wall (μm)	^{3}He (atm)
61241	Feb 22, 2011	28.9	1ns	SG4	Off	854.8	2.4	11.5
61252	Feb 22, 2011	29.1	1ns	SG4	Off	893.6	2.3	11.5
63038	July 29, 2011	28.5	1ns	SG4	Off	892.6	3.3	14.3
70411	July 17, 2013	16.8	600ps	SG4	Off	958	2.1	22.4

9.3 Proton spectrometry

Since the proton statistics for individual spectra are poor, a single spectrum per shot can be obtained by averaging several detectors to reduce these statistical uncertainties. For each spectral bin i, a weighed mean is computed:

$$\langle Y_i \rangle = \frac{\sum_j Y_{i,j}\sigma_{i,j}^{-2}}{\sum_j \sigma_{i,j}^{-2}}, \tag{9.3}$$

where the sum j is over all available WRF detectors, and $\sigma_{i,j}$ is the standard uncertainty in each measurement. The uncertainty in the summed spectrum is then

$$\langle \sigma_i \rangle = \frac{1}{\sqrt{\sum_j \sigma_{i,j}^{-2}}}. \tag{9.4}$$

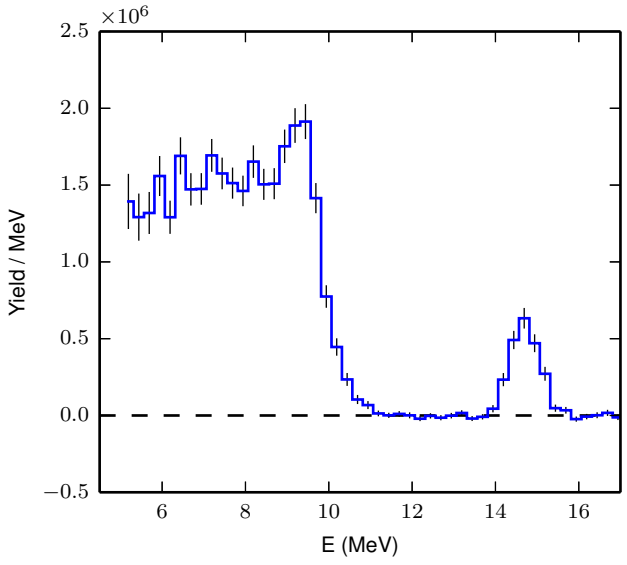

Figure 9.3. Combined proton spectrum from shot 61241, including uncertainties.

The summed proton spectrum for shot 61241 is shown in Fig. 9.3. The spectrum shows the

^{3}He^{3}He-p spectrum at proton energies lower than $\sim$ 10 MeV. A small D^{3}He-p peak is visible at $\sim$ 15 MeV from the D contamination in the fuel. At the lowest energies, fewer detectors are available[†] resulting in increased statistical uncertainties, even after the weighted averaging. For this reason, only energies above 5 MeV are plotted. In the combined spectrum, the D^{3}He proton line (at a known energy of 14.7 MeV) is used to correct the energy for known electrostatic upshifts [16,17]. The same analysis procedure was used for the other three shots. The average spectra for all four shots are shown in Fig. 9.4. In shot 70411 (lower right), a much higher level of D contamination is observed.

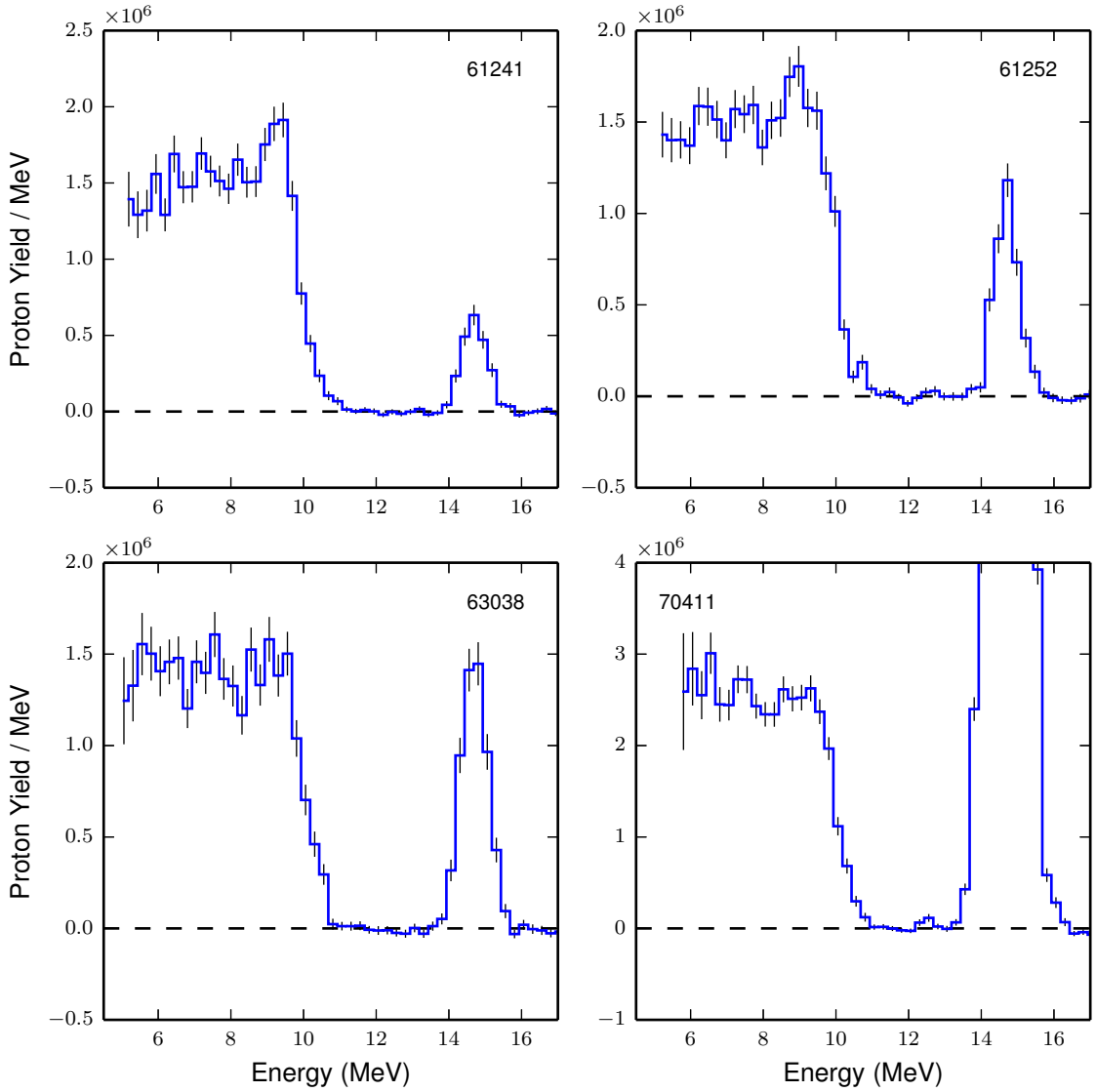

Figure 9.4. Proton spectra from all four shots. Shot 70411 (lower right) had a higher level of D contamination in the ^{3}He gas used.

[†]The low-energy cutoff of the WRF detector depends on the minimum thickness, which varies due to the machining process.

9.4 Inference of E_{cm}

The average center-of-mass energy (E_{cm}) for the ^{3}He^{3}He reactions must be determined to compare the result to theory and accelerator experiments. Typically ICF plasma temperatures are diagnosed via Doppler broadening of product lines (i.e. the DT-n or D^{3}He-p). For the ^{3}He^{3}He reaction, there is no suitable monoenergetic product line[‡]. An estimate of the plasma temperature can be obtained using the small D impurity, which produces D^{3}He protons at 14.7 MeV (see Fig. 9.4). This spectral line is fit with a Gaussian, the spectral width (σ) is related to a Maxwellian thermal temperature by the reaction kinematics (see Appendix K):

$$T_i = \frac{\left(\sigma_{th} \times 10^3\right)^2}{5898}, \tag{9.5}$$

where both σ and T_i are in keV. The thermal width (σ_{th}) is determined from the fit to the measured spectral width including the known instrument response

$$\sigma_{th} = \sqrt{\sigma^2 - \sigma_{inst}^2}. \tag{9.6}$$

For the WRFs used[§], $\sigma_{inst} = 180 \pm 20$ keV. A single temperature is calculated as weighted mean of the individual WRF measurements, with an uncertainty derived from the weighted mean uncertainty and the instrument response uncertainty. The temperatures determined from this procedure for the four shots are shown in Fig. 9.5.

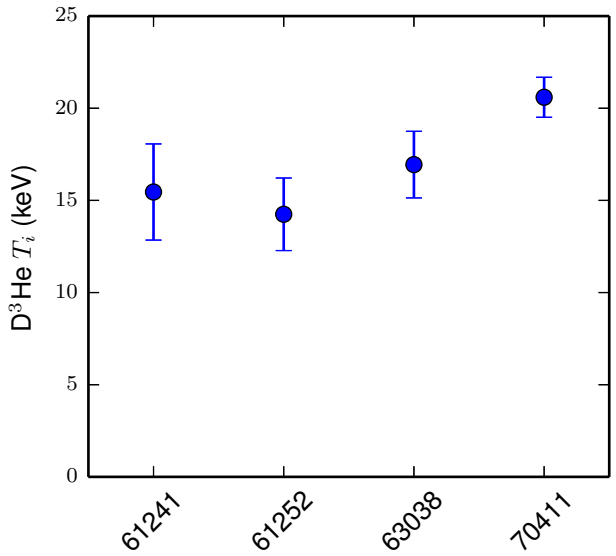

Figure 9.5. Temperature determined from the D^{3}He-p line using fusion-product kinematics.

For these temperatures, an equivalent E_{cm} for the ^{3}He^{3}He reaction can be calculated from

[‡]The proton produced in the ^{5}Li resonance channel is broadened due to the short lifetime of the ^{5}Li state, corresponding to an intrinsic FWHM of 1.23 MeV, significantly larger than the Doppler broadening.

[§]The instrumental WRF broadening is determined from accelerator calibrations[18], where the incident spectral width is well known from SBD measurements.

Gamow's formula

$$E_{cm} = \left[\frac{(\pi\alpha Z_1 Z_2)^2 m_r c^2}{2}\right]^{1/3} (k_B T_i)^{2/3} = 122\left[A(Z_1 Z_2)^2\right]^{1/3} (0.0116 \times T_i)^{2/3}, \tag{9.7}$$

where Z_1 and Z_2 are the reactant charges in fundamental units, A is the reactant reduced mass in AMU, and in the simplification E_{cm} and T_i are both in keV. For $T_i = 16 - 20$ keV, this indicates $E_{cm} = 115 - 133$ keV.

However, this estimate is potentially an underestimate of the effective burn-averaged ^{3}He^{3}He E_{cm}. Significant temperature gradients exist in the imploded plasma, such that burn-weighted temperatures for the ^{3}He^{3}He reaction should be higher than the D^{3}He reaction, since it is more strongly weighted towards the hotter region. Thus the D^{3}He-determined E_{cm} is taken as a lower bound on the actual ^{3}He^{3}He E_{cm}. For an upper bound, we use 1-D radiation-hydrodynamics simulations. These simulations over-predict the ^{3}He^{3}He yield by an order of magnitude, meaning that the simulated T_i and thus E_{cm} must be an upper bound. The difference between these two limits is taken as a systematic uncertainty in E_{cm}, and the data are shown in Fig. 9.6.

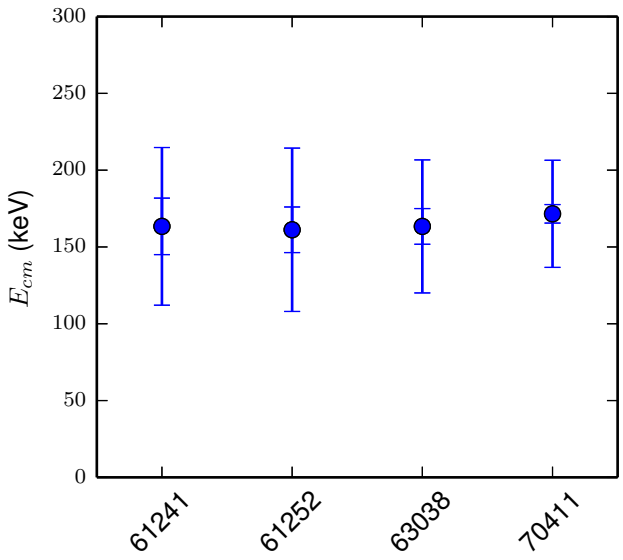

Figure 9.6. Center-of-mass energy (E_{cm}) determined for the four shots. The smaller error bars are statistical uncertainties, while the larger include a systematic uncertainty in the method used to determine E_{cm}.

The shape of the spectrum can be used to constrain nuclear theory, which is discussed in the following sections. This can be done either using simple models to examine the relative importance of the ^{5}Li resonance (Sec. 9.5), or by using the data to validate phenomenological R-matrix nuclear theory (Sec. 9.6).

9.5 Basic Elliptic + Gaussian spectral analysis

A simple model of the spectral shape for the ^{3}He^{3}He protons from the three-body breakup (Eq. 9.1) and the two-body ^{5}Li resonance (Eq. 9.2) is used to fit the data. When only considering

kinematic partition of the energy and momentum available to the particles, the three-body proton spectrum is simply described by an elliptical continuum:

$$\frac{dY_3}{dE_p} = \frac{8}{\pi}\left(\frac{6}{5Q}\right)^2 \sqrt{E_p\left(\frac{5Q}{6} - E_p\right)}, \tag{9.8}$$

where E_p is the proton energy, $Q = 12.86$ MeV, and Y_3 is the spectral amplitude. The three-body elliptical spectrum is normalized so that $\int (dY_3/dE_p)dE_p = 1$. In this analysis, the two-body spectrum is approximated by a Gaussian:

$$\frac{dY_2}{dE_p} = \frac{1}{\sigma_{Li}\sqrt{2\pi}} \exp\left[-\frac{(E_p - E_{Li})^2}{2\sigma_{Li}^2}\right], \tag{9.9}$$

where $E_{Li} = 9.1$ MeV is the mean energy of the protons (see Eq. 9.2), and $\sigma_{Li} = 0.52$ MeV is the width of the resonance dictated by the lifetime of ^{5}Li. The total spectrum is a combination of the two branches:

$$\frac{dY}{dE_p} = A\left[BR\frac{dY_2}{dE_p} + 2(1 - BR)\frac{dY_3}{dE_p}\right], \tag{9.10}$$

where BR is the branching ratio of the two-body ^{5}Li branch to the three-body branch, A is the total proton yield, and a factor of 2 is included to account for the double proton production in Eq. 9.1. This model is used to fit the data with A and BR as the two free parameters. The fits are shown in Fig. 9.7.

The fit parameters, summarized in Table 9.2, are reasonably self-consistent. The large values of reduced χ^2, evaluated only in the ^{3}He^{3}He proton spectral region, indicate that this assumed spectrum is not a good model for the data. Nuclear models are required to explain the spectral shape. This is expected, as the elliptical + Gaussian model neglects any final-state interactions (i.e. the di-proton), excited states of ^{5}Li, and interference effects between the branches.

Table 9.2. Fit parameters using the elliptical + Gaussian spectral model.

Shot	A	BR	χ^2 / dof	E_{cm} (keV)
61241	$(7.15 \pm 0.12) \times 10^6$	0.14 ± 0.01	5.1	$163 \pm 18_{\text{ran}} \pm 48_{\text{sys}}$
61252	$(6.96 \pm 0.11) \times 10^6$	0.13 ± 0.01	7.5	$161 \pm 15_{\text{ran}} \pm 51_{\text{sys}}$
63038	$(6.69 \pm 0.13) \times 10^6$	0.09 ± 0.01	1.2	$163 \pm 12_{\text{ran}} \pm 42_{\text{sys}}$
74011	$(1.18 \pm 0.02) \times 10^7$	0.09 ± 0.01	4.3	$172 \pm 6_{\text{ran}} \pm 34_{\text{sys}}$

9.6 R-matrix analysis

The proton spectrum can be used to constrain R-matrix modeling[11,12], which is a phenomenological treatment based on several 'feeding factors', which are related to scattering amplitudes and the relative abundance of reaction branches, to calculate the spectral components for these nuclear reactions. Two calculations are shown in Fig. 9.8. The first, by Gerry Hale, uses feeding factors from higher-energy accelerator T-T data[19] while the second, by Carl Brune, uses lower-energy NIF T-T data[10] and includes angular interference effects. Both account for the difference between

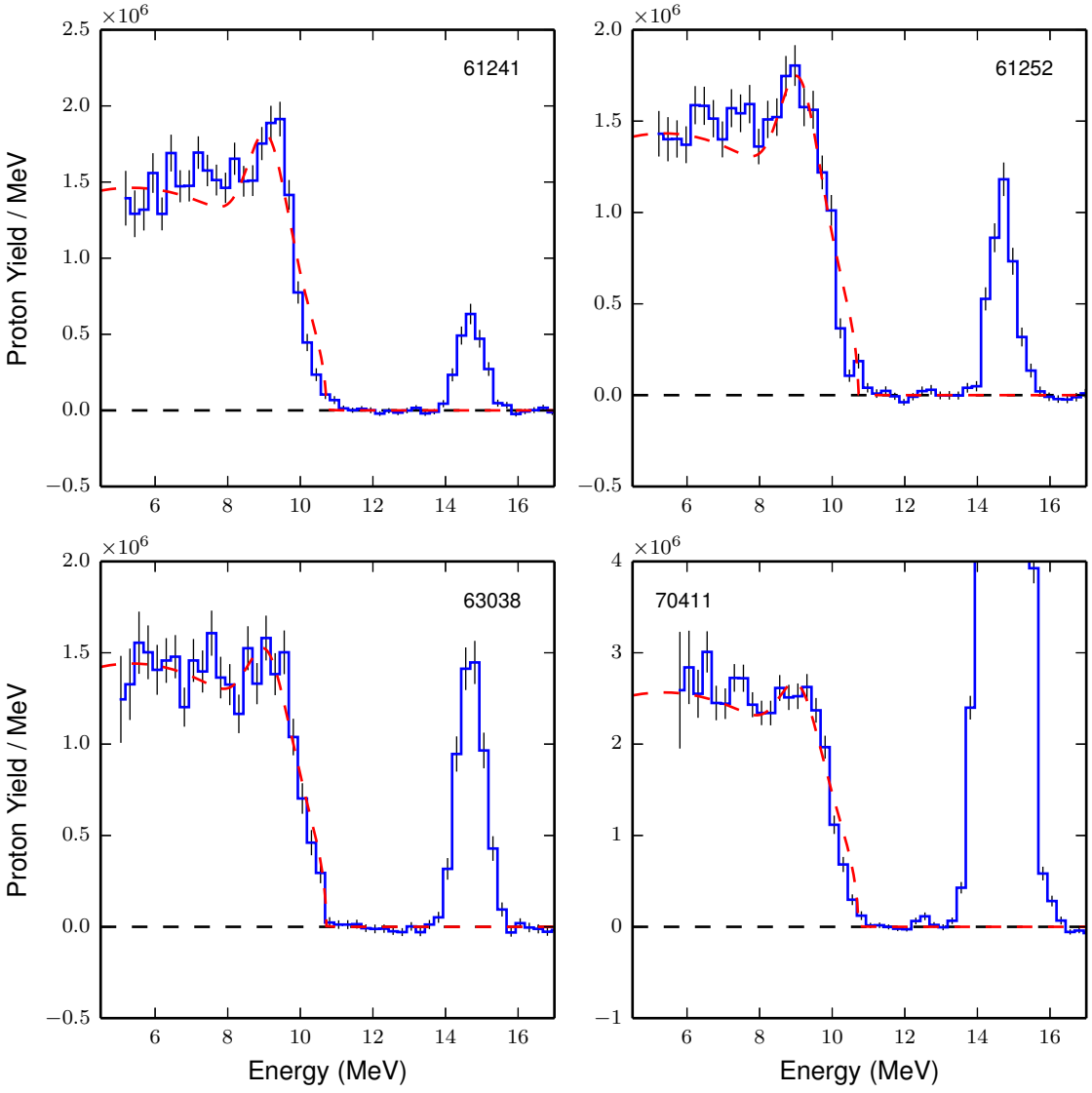

Figure 9.7. ^{3}He^{3}He proton spectra from four shots of data including fits (red dashed curves) using the simple elliptical + Gaussian model.

^{3}He-^{3}He and T-T by the basic mirror symmetry assumption.

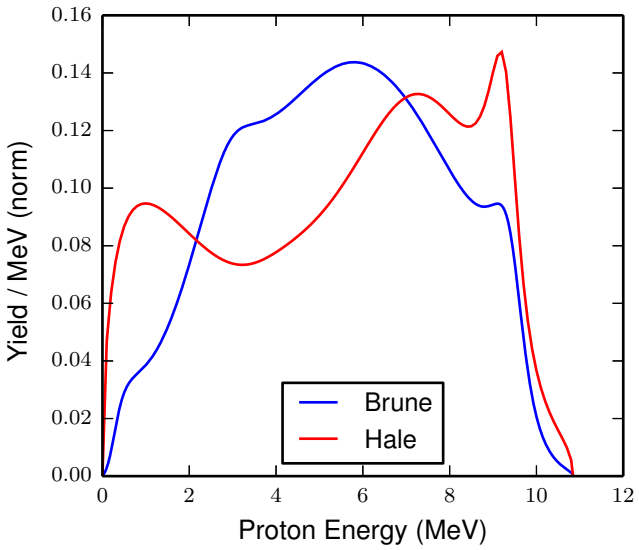

Figure 9.8. R-matrix calculations of the ^{3}He-^{3}He proton spectrum.

For comparison to the data, the calculated spectra must account for the uncertainty in center-of-mass energy (see Section 9.4), the thermal broadening of the spectrum, and the WRF instrument response. In the left plot of Fig. 9.9, calculations by Brune show minimal sensitivity to the center-of-mass energy within the uncertainty range. On the right, the Hale spectrum is convolved with the thermal broadening and instrument response. The biggest effect is the reduction in the prominance of the ^{5}Li ground state peak at 9.1 MeV.

The thermal- and instrument-broadened R-matrix calculated spectrum can be compared directly to the data by adjusting the amplitude (yield) to minimize χ^2. These comparisons are shown in Figs. 9.10 (Brune calculation) and 9.11 (Hale calculation).

The three models discussed herein can be compared by using the reduced χ^2 of the fits to the data. This is summarized in Table 9.3. It is clear that the Brune calculation differs significantly from the data. The Hale spectrum shows best agreement with the observed spectral shape, yet the reduced $\chi^2 \sim 3$ means that a statistically-significant difference in shape still exists.

Table 9.3. Minimum reduced χ^2 from fits to the data using the three models considered.

	χ^2 / dof		
Shot	Simple	Brune	Hale
61241	5.1	14.5	3.4
61252	7.5	13.4	3.4
63038	1.2	8.3	3.0
74011	4.3	11.3	3.2

The components of the Hale R-matrix calculated spectrum are shown in Fig. 9.12. Qualitatively, it can be seen in the comparison to the data (Fig. 9.11) that the R-matrix calculation

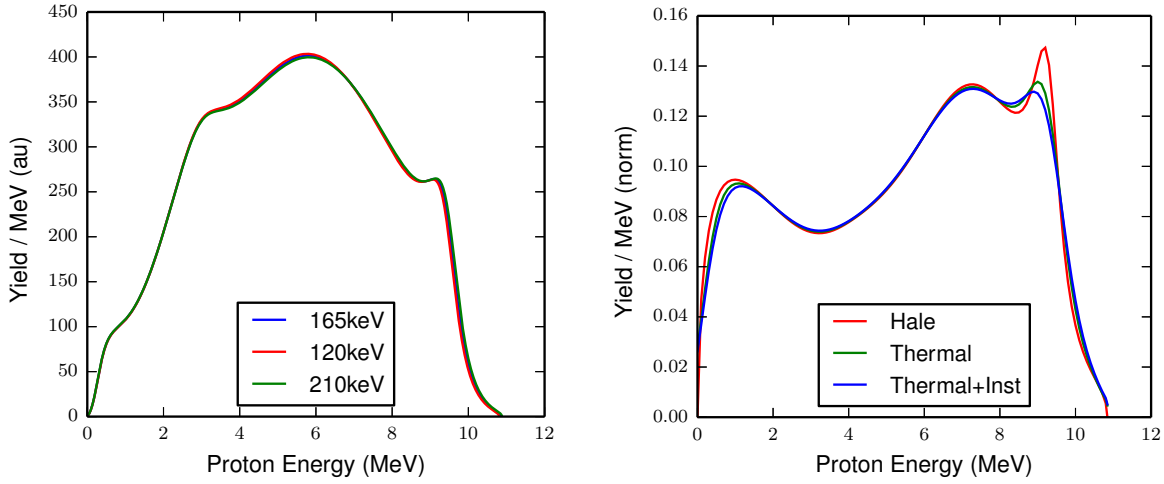

Figure 9.9. Left: R-matrix calculations by Brune show minimal sensitivity to the center-of-mass energy. Right: R-matrix spectrum calculated by Hale convolved with thermal broadening and instrument resolution.

underestimates the experimental spectral amplitude around the ^{5}Li ground state and at the low-energy range of the data, and overestimates at $\sim$ 7 MeV. By looking at the components in Fig. 9.12, it is clear that the R-matrix calculation overestimates the contribution of the ^{5}Li excited state while understimating the other two components.

9.7 Conclusions

In summary, the first high-quality proton spectra from the ^{3}He(^{3}He,2p)^{4}He reaction have been measured at low reactant center-of-mass energies. This is also the first study of this reaction in a plasma environment. Thin-glass shells filled with ^{3}He gas (shock-driven 'exploding pushers') imploded by the OMEGA laser generate proton yields $\sim 10^7$, which can be diagnosed with WRF proton spectrometers. The data show best agreement with R-matrix calculations by Hale, who used higher-energy T-T accelerator data as input for the modeling. However, the spectral shape indicates that this calculation overestimates the ^{5}Li excited state branch while underestimating the ^{5}Li ground state and 3-body breakup. In contrast, a significant discrepancy is found when the data are compared to calculations by Brune, who used low-energy TT-n data from NIF [10]. This could suggest an energy dependence in the branching ratios, or that using the TT data to infer ^{3}He^{3}He feeding factors may not be accurate.

This reaction is the final step of the solar proton-proton I chain, responsible for approximately half of the energy generated in the sun. This unique data can be used to enhance our understanding of the proton spectral shape, which is indicative of the underlying nuclear physics for this reaction. Furthermore, accelerator experiments typically assume a spectral shape, so enhanced understanding of the shape will impact the inferred cross section and thus reaction rates relevant to main-sequence stars.

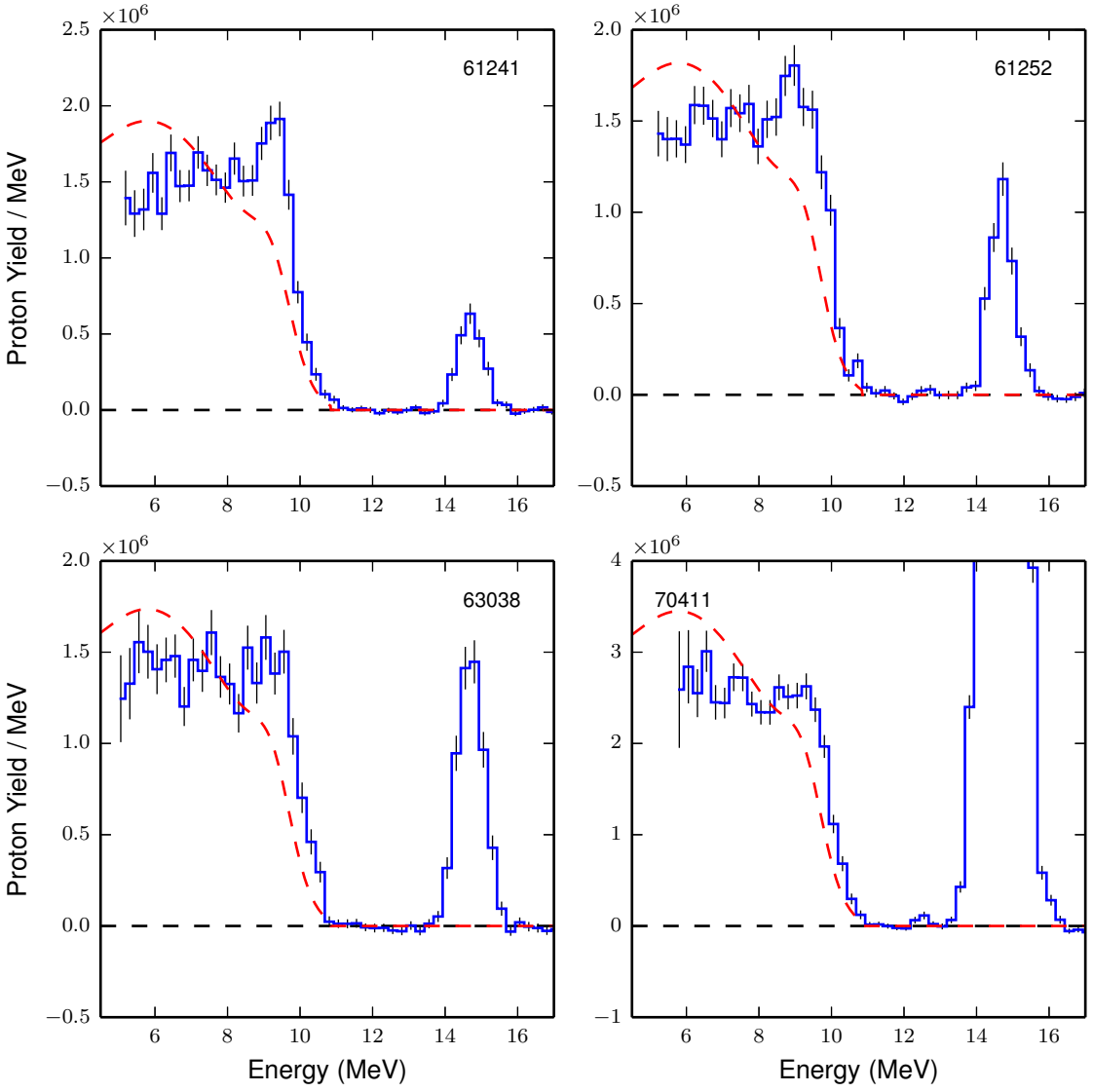

Figure 9.10. ^{3}He^{3}He proton spectra from four shots of data (blue) compared to the Brune R-matrix calculations (red).

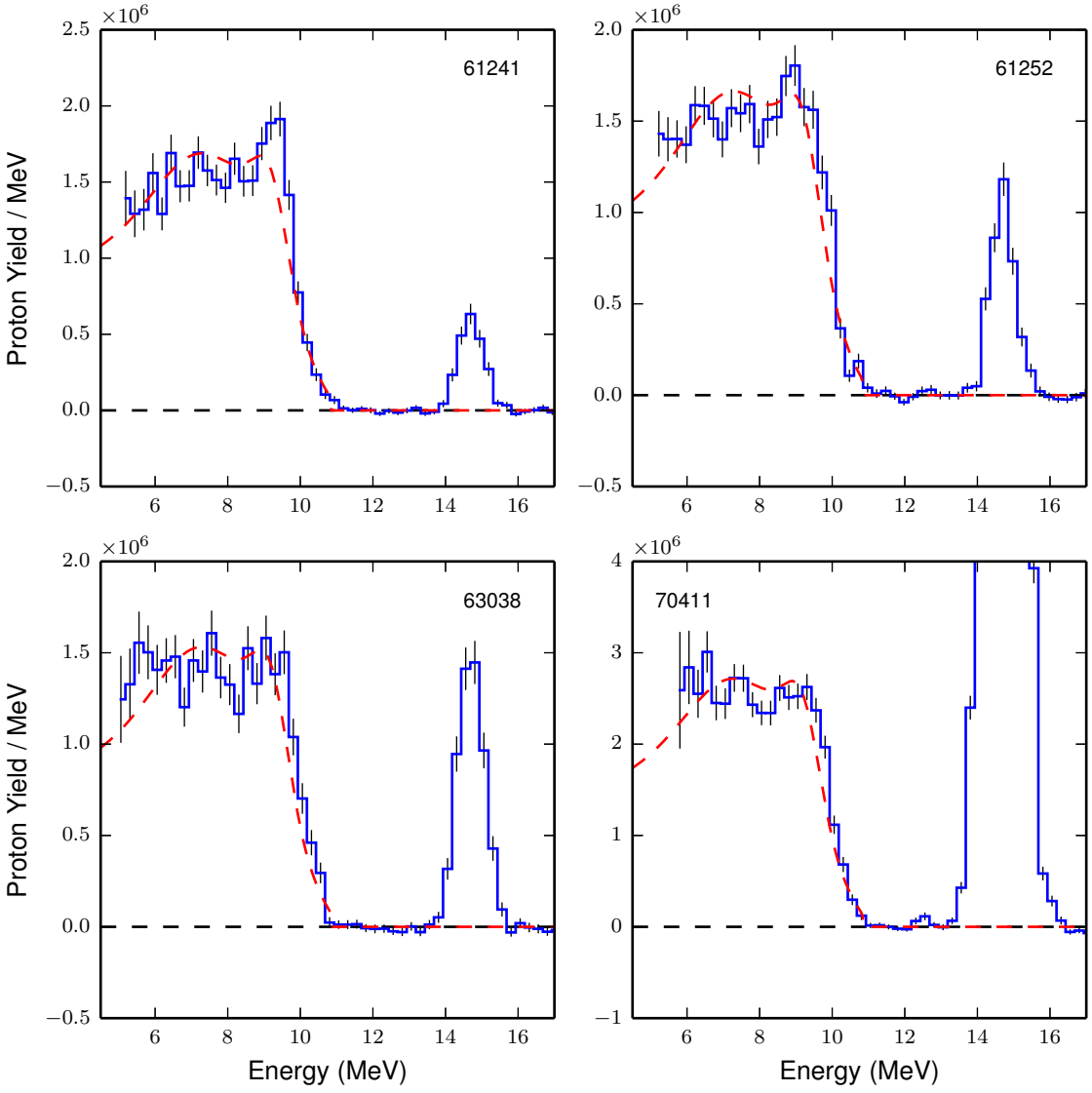

Figure 9.11. ^{3}He^{3}He proton spectra from four shots of data (blue) compared to the Hale R-matrix calculations (red).

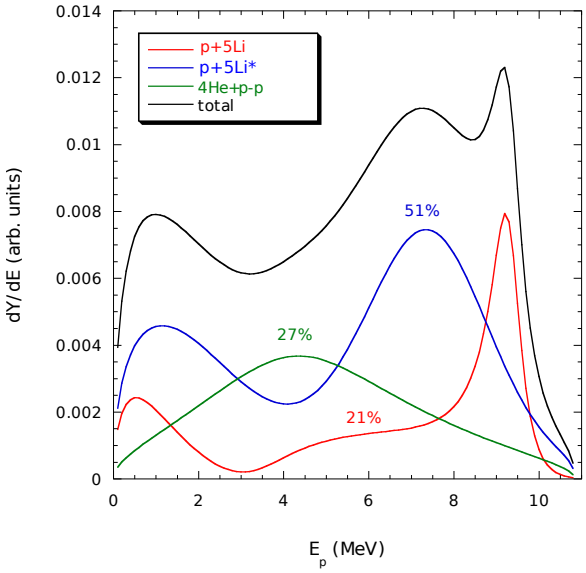

Figure 9.12. Individual components (branches) in the Hale R-matrix calculation of the ^{3}He-^{3}He proton spectrum.

9.8 Shot Summary

A summary of all pure ^{3}He-filled implosions conducted at OMEGA is shown in Table 9.4.

Table 9.4. Summary of all ^{3}He^{3}He experiments conducted

		Laser				Target		
Date	Shot	Energy (J)	Pulse	DPP	SSD	Dia (μm)	Wall (μm)	^{3}He (atm)
8-Feb-11	61094	29417.8	SG1018	SG4	No	871.8	2.4	11.8
8-Feb-11	61095	29324.1	SG1018	SG4	No	858.8	2.4	11.8
22-Feb-11	61241	28923.1	SG1018	SG4	No	854.8	2.4	11.5
22-Feb-11	61251	28629.5	SG1018	SG4	No	865	2	11.5
22-Feb-11	61252	29056.5	SG1018	SG4	No	893.6	2.3	11.5
28-Jul-11	63024	26466.9	SG1018P	SG4	No	869.2	2.6	14.4
29-Jul-11	63030	25292.5	SG1018P	SG4	No	863.8	3.4	14.3
29-Jul-11	63032	26501.9	SG1018P	SG4	No	867.6	3.3	14.4
29-Jul-11	63036	28627.3	SG1018	SG4	No	860.8	3.4	14.4
29-Jul-11	63038	28526.5	SG1018	SG4	No	892.6	3.3	14.3
29-Jul-11	63041	25824.2	SG1018	SG4	No	861	2.5	14.4
13-Jan-12	64674	29472.7	SG1018	No	No	860	2.2	7.2
13-Jan-12	64676	29864.8	SG1018	No	No	858	2	7.5
13-Jan-12	64677	30049.4	SG1018	No	No	431	2	7.5
13-Jan-12	64678	30202.6	SG1018	No	No	414	2	7.5
13-Jan-12	64679	30218.3	SG1018	No	No	412	1.9	12.4
13-Jan-12	64680	29944.6	SG1018	No	No	409	1.9	12.5
13-Jan-12	64681	29720.9	SG1018	No	No	841	2.2	12.4
13-Jan-12	64682	29612	SG1018	No	No	865	2.3	12.9
13-Jan-12	64684	29954.8	SG1018	No	No	843	2	12.5

Table 9.4. Summary of all ^{3}He^{3}He experiments conducted

		Laser				Target		
Date	Shot	Energy (J)	Pulse	DPP	SSD	Dia (μm)	Wall (μm)	^{3}He (atm)
13-Jan-12	64685	30162	SG1018	No	No	405	2	12.5
13-Jan-12	64686	29840.8	SG1018	No	No	849	2.2	12.9
9-Aug-12	67085	29246.3	SG1018	SG4	No	945	2.6	20
9-Aug-12	67086	29505.9	SG1018	SG4	No	900	2.6	20
9-Aug-12	67087	29480.7	SG1018	SG4	No	997	2.7	20
9-Aug-12	67089	29053.9	SG1018	SG4	No	917	2.7	20
17-Jul-13	70411	16809.8	SG0604	SG4	No	958	2.13	22.449
17-Jul-13	70412	17080	SG0604	SG4	No	949	2.15	22.612

9.9 References

1. W. A. Fowler, "Experimental and theoretical nuclear astrophysics: the quest for the origin of the elements," Rev. Mod. Phys., **56**, 149–179 (1984).
2. E. G. Adelberger, S. M. Austin, J. N. Bahcall *et al.*, "Solar fusion cross sections," Rev. Mod. Phys., **70**, 1265–1291 (1998).
3. E. G. Adelberger, A. García, R. G. H. Robertson *et al.*, "Solar fusion cross sections. ii. the *pp* chain and cno cycles," Rev. Mod. Phys., **83**, 195–245 (2011).
4. M. R. Dwarakanath and H. Winkler, "^{3}He(^{3}He, $2p$)^{4}He Total Cross-Section Measurements Below the Coulomb Barrier," Phys. Rev. C, **4**, 1532–1540 (1971).
5. M. R. Dwarakanath, "^{3}He(^{3}He, $2p$)^{4}He and the termination of the proton-proton chain," Phys. Rev. C, **9**, 805–808 (1974).
6. A. Krauss, H. Becker, H. Trautvetter *et al.*, "Astrophysical S(E) factor of 3He(3He, 2p)4He at solar energies," Nuclear Physics A, **467**(2), 273 – 290 (1987).
7. M. Junker, A. D'Alessandro, S. Zavatarelli *et al.*, "Cross section of ^{3}He(^{3}He, $2p$)^{4}He measured at solar energies," Phys. Rev. C, **57**, 2700–2710 (1998).
8. N. Kudomi, M. Komori, K. Takahisa *et al.*, "Precise measurement of the cross section of ^{3}He(^{3}He, $2p$)^{4}He by using ^{3}He doubly charged beam," Phys. Rev. C, **69**, 015,802 (2004).
9. D. T. Casey, J. A. Frenje, M. Gatu Johnson *et al.*, "Measurements of the $\mathbf{T}(t, 2n)^4$He neutron spectrum at low reactant energies from inertial confinement implosions," Phys. Rev. Lett., **109**, 025,003 (2012).
10. D. B. Sayre, C. R. Brune, J. A. Caggiano *et al.*, "Measurement of the $t + t$ neutron spectrum using the national ignition facility," Phys. Rev. Lett., **111**, 052,501 (2013).
11. A. M. Lane and R. G. Thomas, "R-matrix theory of nuclear reactions," Rev. Mod. Phys., **30**, 257–353 (1958).
12. F. Barker, "Consistent description of unbound states observed in scattering and reactions," Australian Journal of Physics, **41**, 743–764 (1988).
13. T. Boehly, D. Brown, R. Craxton *et al.*, "Initial performance results of the OMEGA laser system," Optics Communications, **133**(1-6), 495–506 (1997).
14. F. H. Séguin, J. A. Frenje, C. K. Li *et al.*, "Spectrometry of charged particles from inertial-confinement-fusion plasmas," Rev. Sci. Instrum., **74**(2), 975–995 (2003).
15. F. H. Séguin, N. Sinenian, M. Rosenberg *et al.*, "Advances in compact proton spectrometers for inertial-confinement fusion and plasma nuclear science," Rev. Sci. Instrum., **83**(10), 10D908 (2012).
16. D. G. Hicks *et al.*, "Charged-particle acceleration and energy loss in laser-produced plasmas," Phys. Plasmas, **7**(12), 5106–5117 (2000).

17. N. Sinenian, M. J.-E. Manuel, J. A. Frenje *et al.*, "An empirical target discharging model relevant to hot-electron preheat in direct-drive implosions on OMEGA," Plasma Physics and Controlled Fusion, **55**(4), 045001 (2013).

18. N. Sinenian, M.-E. Manuel, A. Zylstra *et al.*, "Upgrade of the MIT Linear Electrostatic Ion Accelerator (LEIA) for nuclear diagnostics development for Omega, Z and the NIF," Rev. Sci. Instrum., **83**(4), 043502 (2012).

19. C. Wong, J. Anderson and J. McClure, "Neutron spectrum from the t+t reaction," Nuclear Physics, **71**, 106–112 (1965).

10

pD Experiments

10.1 Introduction

Deuterons and protons can fuse via the reaction

$$\mathrm{p} + \mathrm{D} \;\rightarrow\; {}^{3}\mathrm{He} + \gamma \quad (Q = 5.5 \text{ MeV}). \tag{10.1}$$

As the primary reaction for generation of ^{3}He in nucleosynthesis processes, this reaction is critically important for many astrophysical systems such as main-sequence stars, brown dwarfs, protostars, and the universe during the Big Bang.

In the stellar main sequence (see Section 7.2), hydrogen is burned to form helium. The first step is the weak reaction p(p,e$^+\nu$)d, which creates a deuteron. The reaction then proceeds via the d(p,γ)^{3}He reaction. Since the p+p fusion reaction is a weak process it is the rate-limiting step and thus sets the overall energy generation rate. The pD cross section (reaction rate) only affects the equilibrium concentration of deuterons within the star.

During the stellar formation process, a cloud of interstellar gas contracts gravitationally (the Kelvin-Helmholtz process) until the central temperature reaches the proton-proton ignition temperature ($\sim 10^7$ K). The contracting pre-stellar material is referred to as a 'proto-star'. Until the central temperature reaches $\sim 10^6$ K the gravitational contraction dominates. At that temperature, however, primordial deuterium in the proto-star can burn via this reaction, generating total energy comparable to the gravitational potential energy[1]. This halts the Kelvin-Helmholtz contraction until the primordial deuterium is exhausted, thus prolonging the overall lifespan of the protostar. The pD reaction rate at very low energy is thus critical for modeling protostellar evolution.

Similarly, in 'brown dwarf' stars, which are not massive enough to ignite hydrogen fusion ($\lesssim 0.07$ $M_\odot$) but larger than giant planets ($\gtrsim$ 0.01 $M_\odot$), deuterium burning can generate substantial amounts of thermonuclear energy[2–4]. The internal dynamics of these objects depends sensitively on the pD reactivity at low temperature.

The third relevance for astrophysics is Big-Bang Nucleosynthesis (BBN, see Section 7.1), in which the pD reaction generates ^{3}He needed for the reaction chain to proceed to heavier nuclei such as Li and Be[5,6].

This reaction has been studied at low energy in several accelerator (beam-target) experiments[7–9] and theoretical work[10–12]. The resulting data from these experiments must be corrected for bound-electron screening and thick-target effects, potentially introducing systematic uncertainties. Achieving low energies relevant for astrophysical nucleosynthesis is difficult as well, and may be improved upon using inertially-confined plasmas.

10.2 Experiment

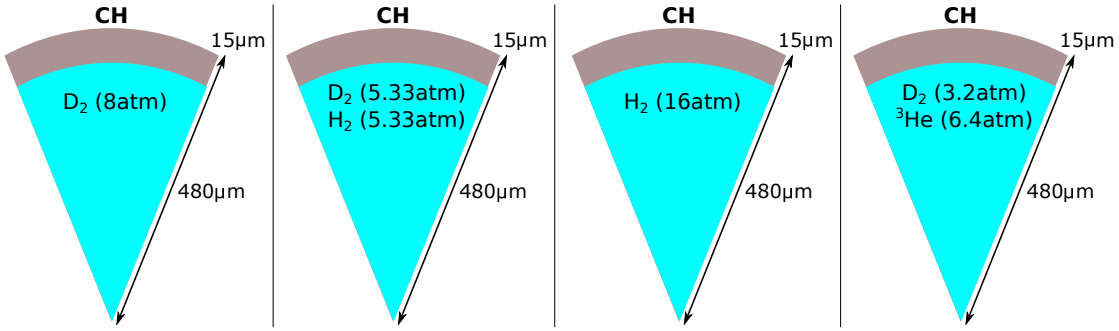

Figure 10.1. Targets used for the pD experiments.

For the first time, the pD reaction was studied using inertially-confined laboratory plasmas. Plastic (CH) shells filled with various fuel mixtures were imploded with the OMEGA laser[13]. The targets are shown in Fig. 10.1; the CH shells were nominally 15μm thick with an outer diameter of 860 μm and a 0.1μm Al overcoating. The shell was driven by the laser irradiation at 3ω (351nm) using SG4 DPP, DPR, and SSD smoothing. The pulse duration was 1ns and the total energy delivered was approximately 25kJ. Four different target fills were used, as shown in Fig. 10.1. The primary experiment, studying pD fusion, used an equimolar mix of D_2 and H_2 fill gas with 5.33atm of each. Background characterization shots were conducted with either pure D_2 or pure H_2 fills, using a mass-equivalent fill of 8atm of D_2 or 16atm of H_2 gas. While pure 'hydro-equivalence' is not possible between these gas mixes, keeping the mass density constant maintains similar hydrodynamics between the fills. Finally, a mass-equivalent equimolar mixture of D_2 and ^{3}He gas (3.2 and 6.4atm, respectively) was used as a calibration for the Cherenkov detector. Detailed setup parameters for each shot, including metrologized target information, are shown in Table 10.1. The H_2-filled shots were designed as a background test for the Cherenkov detector, since no fusion reactions should occur in these implosions. As expected, all nuclear diagnostics showed no evidence of nuclear reactions in the H_2 implosions. The primary GCD-3 setup parameters, the gas fill and type, are also shown in Table 10.1. The shots using C_2F_6 gas did not acquire good data, see Section 10.4.2 for more details.

10.3 DD and D^{3}He Nuclear Data

Nuclear diagnostics were used to measure the DD and D^{3}He fusion products to characterize these implosions. nTOF spectrometers[14] measured the DD neutron yield and burn-averaged ion temperature, and the NTD measured bang time[15]. On D^{3}He gas-filled implosions, compact Wedge Range Filters (WRFs)[16] were used to measure the D^{3}He yield.

The resulting DD nuclear data are shown in Fig. 10.2 for the D^{3}He, DD, and HD shots (color-coded). The DD yield was the highest on the pure D_2 filled implosions since the yield $\propto n_D^2$. We observe that the targets filled with a given type of fuel had a similar nuclear performance. All implosions had similar burn-averaged ion temperatures and bang times.

The target dimensions also affect the nuclear data. The series of implosions using thicker shells (74608−74613, see Table 10.1) have slightly lower yields and later bang times.

The DD nuclear data are compared to 1-D LILAC simulations[17] in Figure 10.3. Simulated

Table 10.1. Target and GCD-3 setup information for the pD experiments. The GCD-3 was filled with 400psi of gas for the data shots, and lower pressures for background tests.

	Target				**GCD-3**	
	Gas		Capsule		Gas	
Shot	Type	P (atm)	OD (μm)	Thick (μm)	Type	P (psi)
74285	D_2+^{3}He	9.5	866	14.7	CO_2	400
74286	D_2+^{3}He	9.6	874	14.7	CO_2	400
74287	D_2	8.0	867	14.7	CO_2	400
74288	D_2	8.0	876	14.6	CO_2	400
74289	H_2+D_2	10.6	868	14.7	CO_2	400
74290	H_2+D_2	10.7	872	14.8	CO_2	400
74292	H_2	15.9	872	14.8	CO_2	400
74293	H_2+D_2	9.9	871	14.7	CO_2	400
74294	H_2+D_2	10.3	873	14.5	CO_2	400
74295	H_2	15.6	875	14.5	CO_2	400
74296	D_2+^{3}He	9.6	865	14.7	CO_2	400
74297	D_2	8.0	868	14.7	-	0
74602	D_2+^{3}He	9.8	868	15.7	C_2F_6	400
74603	D_2+^{3}He	9.8	867	15.8	C_2F_6	400
74604	D_2	11.1	870	15.7	C_2F_6	400
74605	H_2	16.1	875	15.6	C_2F_6	400
74606	H_2+D_2	11.1	867	15.6	C_2F_6	400
74607	H_2+D_2	10.7	874	15.6	C_2F_6	400
74608	H_2+D_2	11.1	867	15.5	CO_2	400
74609	H_2+D_2	10.9	869	15.5	CO_2	400
74611	H_2+D_2	11.0	867	15.6	CO_2	400
74612	D2	8.1	870	15.8	CO_2	400
74613	D2	8.0	873	16.0	CO_2	400
74614	H_2+D_2	10.7	871	14.4	CO_2	100
74615	H_2+D_2	10.9	868	14.7	CO_2	100

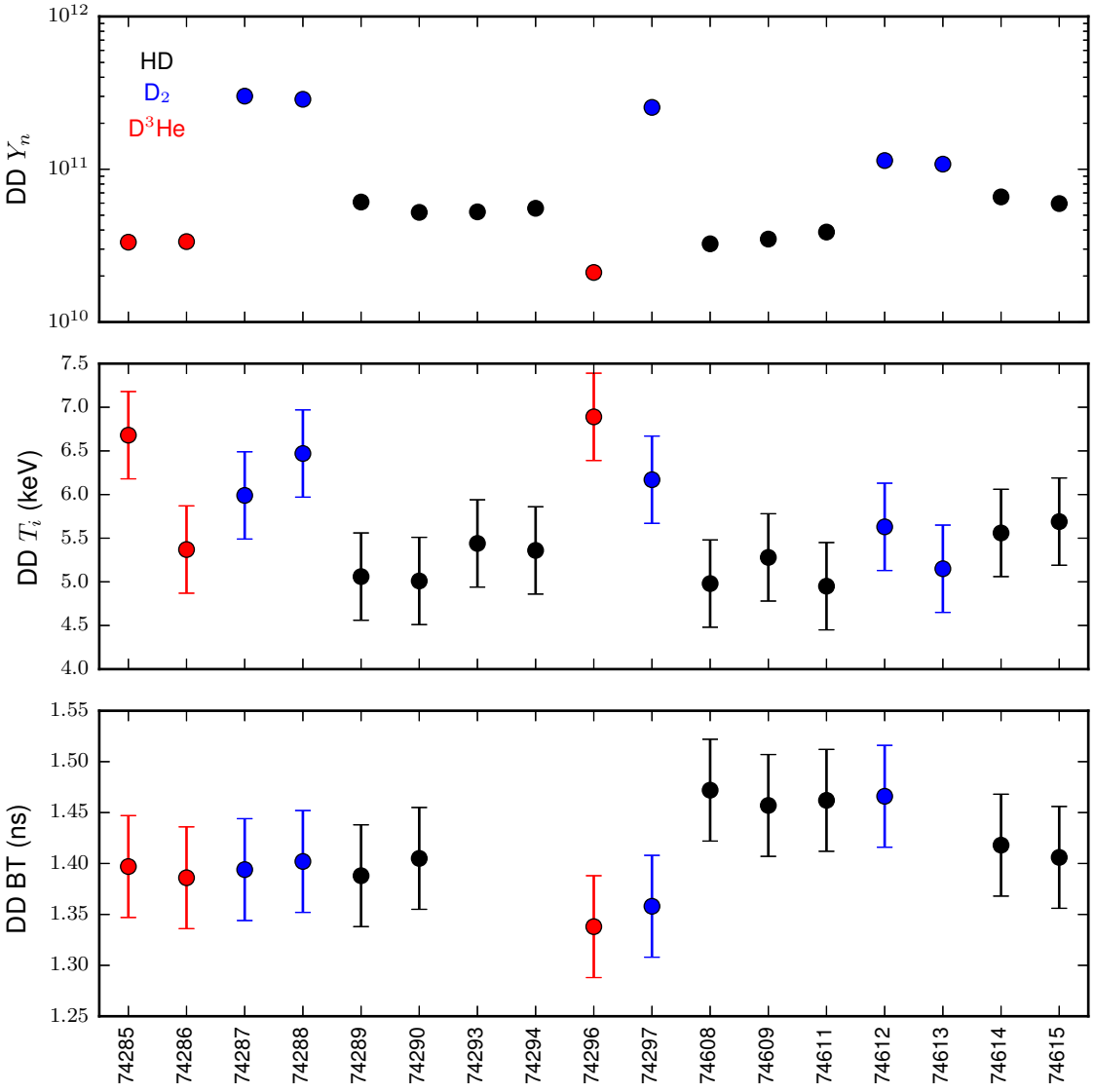

Figure 10.2. DD-n nuclear data: total yield (top), burn-averaged ion temperature (center, from Doppler width), and bang time (bottom). Marker colors correspond to shot type: HD (black), D_2 (blue), and D^3He (red).

yields are higher than experiment by a factor of $5-10\times$ (yield over clean (YOC) $\sim 0.1-0.2$) while the simulated ion temperatures are comparable to experiment.

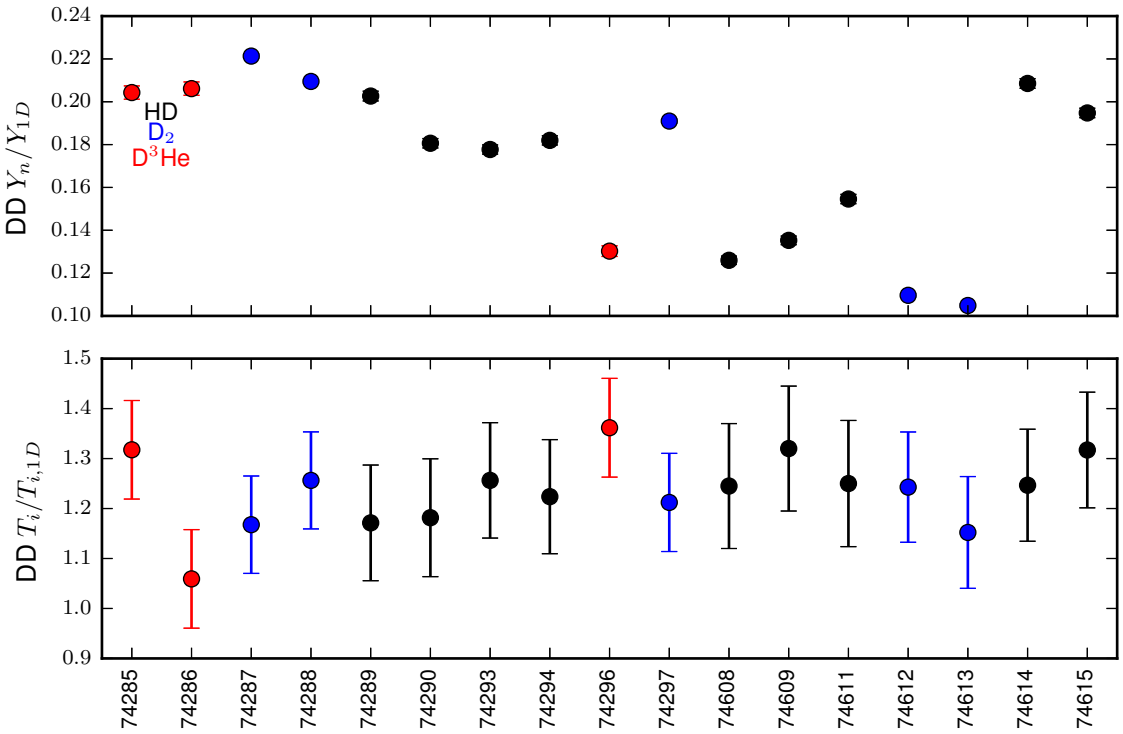

Figure 10.3. DD-n nuclear data (Fig. 10.2) compared to LILAC 1-D simulations: experimental yield over simulated yield (top), temperature over 1-D determined T_i (center), and bang time difference (bottom). Marker colors correspond to shot type: HD (black), D_2 (blue), and D^3He (red).

The D^3He nuclear yield is shown in Fig. 10.4 (left) and compared to simulation (right). Similar YOC is observed for the D^3He and DD reactions. The nuclear yield $\propto n^2\langle\sigma v\rangle$ where $\langle\sigma v\rangle$ is a strong function of T_i. Since the two reactions have similar yield, and the simulated burn-averaged ion temperature is close to experiment (Fig. 10.2), this suggests that the simulated burn volume is smaller in experiment than in simulation. This could occur due to a mix region developing around the fuel-shell interface during the deceleration phase.

The simulated performance is further explored by looking at the relative performance of the three fuel types. Fuel stratification or segregation, reported in several experiments[18–20], which may be due to diffusion processes[21,22] or ion thermal decoupling[23], can have an impact on the performance.

The YOC for a reaction (x) is defined relative to the 1-D simulation as $YOC_x \equiv Y_x/Y_{x,1D}$, where the uncertainty in YOC is driven by the uncertainty in the measurement ($\delta YOC_x = \delta Y_x/Y_{x,1D}$). The average YOC over a set of shots ($i = 1-N$) is then calculated from a weighted mean:

$$\overline{YOC_x} = \frac{\sum_i \left(YOC_{x,i}/\delta YOC_{x,i}^2\right)}{\sum_i \delta YOC_{x,i}^{-2}}. \tag{10.2}$$

Because of shot-to-shot scatter not accounted for in the simulation, the YOC data vary more than expected on the basis of the error bars ($\chi^2 \gg 1$). This 'over-dispersion' can be corrected for in the

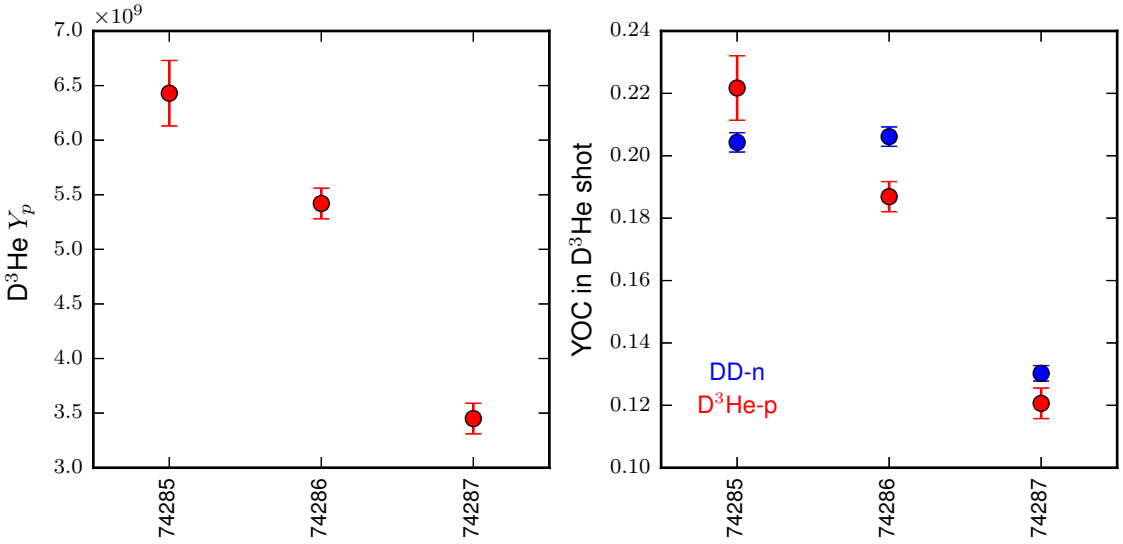

Figure 10.4. WRF measured D^3He-proton yields (left), and comparison to simulation (right) for both DD-n and D^3He-p yields in the D^3He gas-filled implosions.

uncertainty of the weighted mean by correcting for the fact that $\chi^2 \gg 1$ by:

$$\delta\overline{YOC_x} = \frac{1}{\sum_i \delta YOC_{x,i}^{-2}} \times \chi^2, \tag{10.3}$$

$$= \frac{1}{\sum_i \delta YOC_{x,i}^{-2}} \times \frac{1}{N-1} \sum_i \frac{(YOC_{x,i} - \overline{YOC_x})^2}{\delta YOC_{x,i}^2}. \tag{10.4}$$

The calculated average YOC values using this method are shown in Fig. 10.5 for two scenarios. First, the DD-n YOC was calculated for the three nuclear fuel types (D_2, D^3He, and HD), shown in the left of Fig. 10.5. In this case, no statistically-significant difference is observed between the fuel types. Secondly, both the DD-n and D^3He-p YOC were calculated in the D^3He gas-filled implosions, shown at right in Fig. 10.5. In this case, the two reactions occurring simultaneously in the same implosions show the same YOC. The combination of these two results show that negligible species separation or 'yield anomaly' effects are occurring in this type of implosion, which is an important observation for the S-factor analysis discussed in Section 10.5.

10.4 Cherenkov Data and Analysis

Cherenkov radiation is electromagnetic radiation emitted by a charged particle passing through a dielectric medium with a velocity higher than the medium's phase velocity of light (c/n where n is the index of refraction). Typically Cherenkov radiation is in a visible part of the spectrum, such as the blue light associated with water-moderated nuclear reactors. In ICF diagnostic techniques, energetic γ rays can be detected if they Compton scatter energetic electrons into a dielectric medium. The light production has a threshold depending on the γ-ray energy and dielectric medium. Typically for ICF diagnostics, a gas-filled chamber serves as the dielectric medium with a photomultiplier tube (PMT) to detect the Cherenkov light[24].

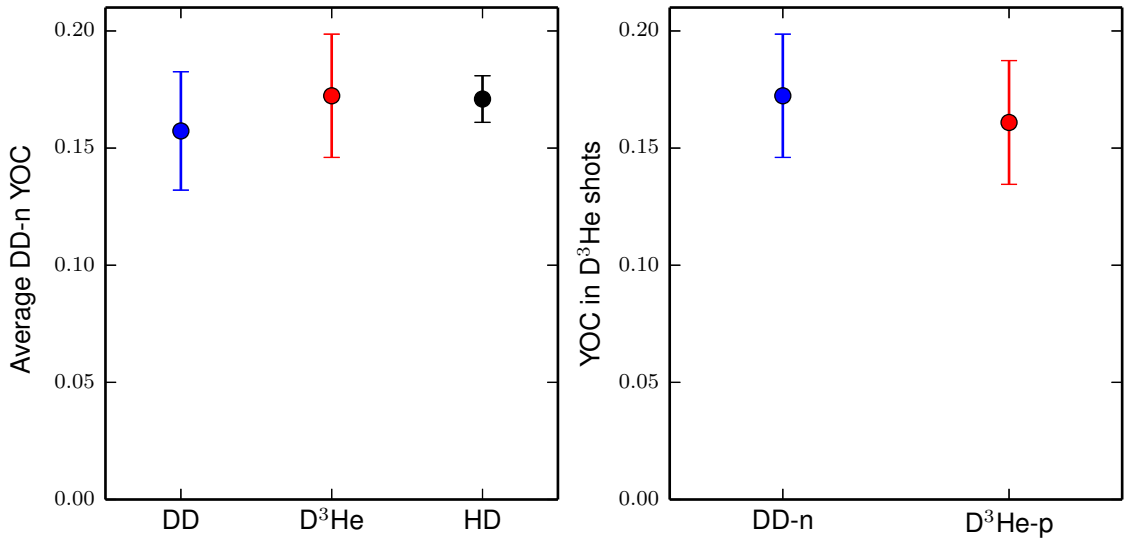

Figure 10.5. Left: average DD-n YOC for the three implosion types (D_2, D^3He, or HD fuel). Right: average DD-n and D^3He-p YOC in D^3He gas-filled implosions.

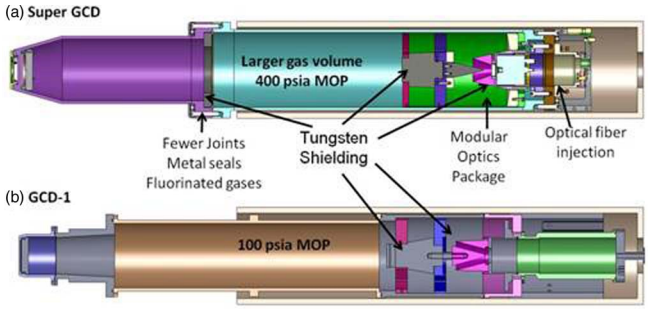

Figure 10.6. **(a)** 'Super' GCD (GCD-3) with larger gas volume at higher pressure, 400 psi Maximum Operating Pressure (MOP), and with improved optics package and shielding. **(b)** Previous design (GCD-1).

10.4.1 The GCD-3 Detector

Measuring the relatively low γ-ray energy from this reaction (5.5 MeV, Eq. 10.1) requires a gas with a high n for the Cherenkov detector, which typically requires high pressure and/or flourinated gases. Simultaneously, the relatively low cross section of the p+D reaction requires a large-solid-angle detector. This capability was implemented as the 'super' GCD (GCD-3)[25], shown schematically in Fig. 10.6. The key feature of the GCD-3 for this measurement is the low threshold. With 400psi of CO_2 fill, the γ detection threshold is $\sim$ 3 MeV, which can be reduced to $\sim$ 2 MeV with 400psi of C_2F_6 gas.

The response curves for the GCD-3 are shown in Fig. 10.7 with 100 or 400 psi of CO_2 or C_2F_6 gas, and are compared to the previous system (GCD-1 at 100psi of CO_2). When using 100 psi of CO_2 in either system, the 5.5 MeV γ ray from the p+D reaction cannot be measured. The new GCD-3 system is capable of detecting this γ ray with high sensitivity using a 400 psi fill of either gas.

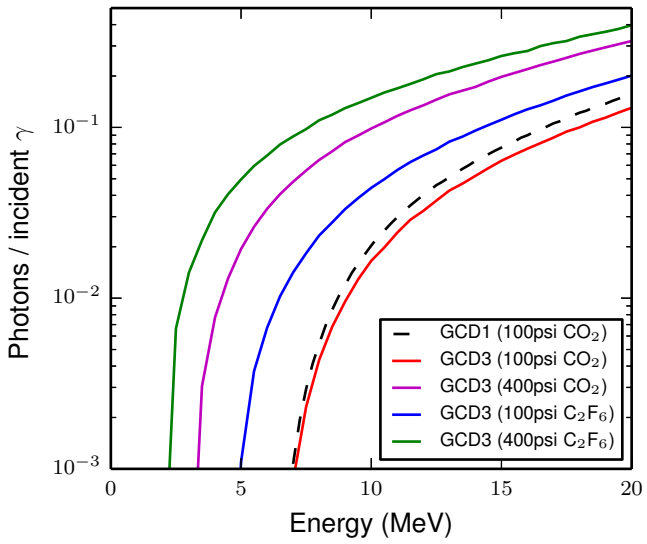

Figure 10.7. GCD-3 response curves with 100 or 400 psi of CO_2 or C_2F_6 gas, compared to the best performance of the previous GCD-1 system (100psi of CO_2, black dashed curve).

10.4.2 C_2F_6 Fluorescence

Several shots utilized C_2F_6 gas as the dielectric medium in the GCD-3 detector, since it was predicted to have a higher sensitivity to the γ rays (see Fig. 10.7). Unfortunately, the Cherenkov signals measured using C_2F_6 gas shows anomalously high and broad signals, several orders of magnitude more than fusion signal. An example of this is shown in Fig. 10.8 for three D^3He shots. When using CO_2 gas fill (shots 74285 and 74286) good Cherenkov signal is observed. On a similar shot (74603) using C_2F_6 gas, however, anomalous signal due to fluorescence is observed.

10.4.3 Signal analysis

The Cherenkov light production is detected with a PMT and recorded using a fast digital scope (SCD5000). The raw signals are analyzed using the following procedure. First, the SCD signal is corrected for electrical splits and attenuators used in the experiment to recover the signal level at the PMT output. Since peak nuclear production is defined as bang time, the scope trace is aligned in time such that the peak Cherenkov signal is at $t = 0$. The trace before and after the Cherenkov signal is used in a background subtraction. At this stage the raw data may be compared. The Cherenkov signals for several shot types are shown in Fig. 10.9.

The D^3He-γ data are used as a calibration (see Section 10.4.4). The H_2 null shot demonstrates that the signal observed is due to a nuclear process and not due to another process in the implosions (i.e. laser-plasma interactions generating hot electrons). Since the data are shown yield normalized, the DD curves represent the primary source of background in the pD measurement – due to the DD-γ (branching ratio $\sim 10^{-7}$) or (n, γ) reactions from the DD-n. The remaining signal in the pD implosions is attributed to the p+D γ ray (Eq. 10.1) at 5.5 MeV.

This can be verified with a threshold scan. By reducing the GCD-3 gas fill pressure from 400 to 100 psi, the γ-ray energy threshold increases to 6.3 MeV. This threshold scan is shown in Fig. 10.10. The data show that the Cherenkov signal disappears in the HD implosions as the threshold is increased. This demonstrates that the signal is due to a low-energy γ ray, i.e. the p+D fusion γ.

To calculate a total γ-ray yield, the PMT signal must be integrated to calculate the total signal.

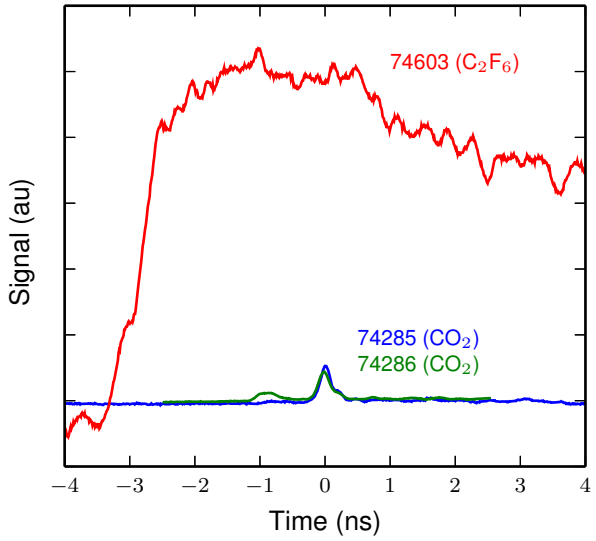

Figure 10.8. Cherenkov signal versus time for three D^3He gas-filled implosions, with $t = 0$ approximately at bang time. Shots 74285 and 74286 (blue and green curves) used CO_2 and show a clear Cherenkov signal from D^3He-γ. The shot using C_2F_6 fill (74603, red) shows an anomalous signal, both much higher in magnitude and wider than possible from fusion alone, but could be explained by fluorescence of the gas or a contaminant in the gas.

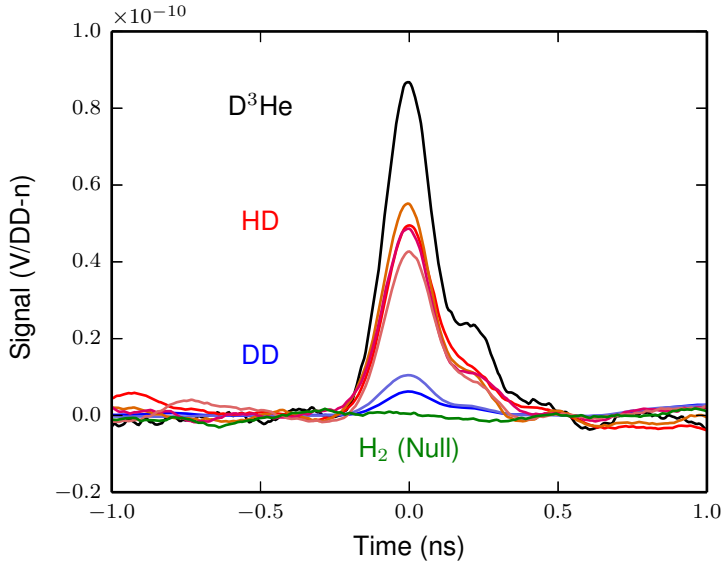

Figure 10.9. PMT signal (normalized to DD yield) for the three nuclear shot types: D^3He (black), four HD implosions (red), and two D_2 implosions (blue). The difference between the HD and DD traces is the signal due to the p+D fusion γ. A H_2-filled implosion (green curve) shows no Cherenkov signal.

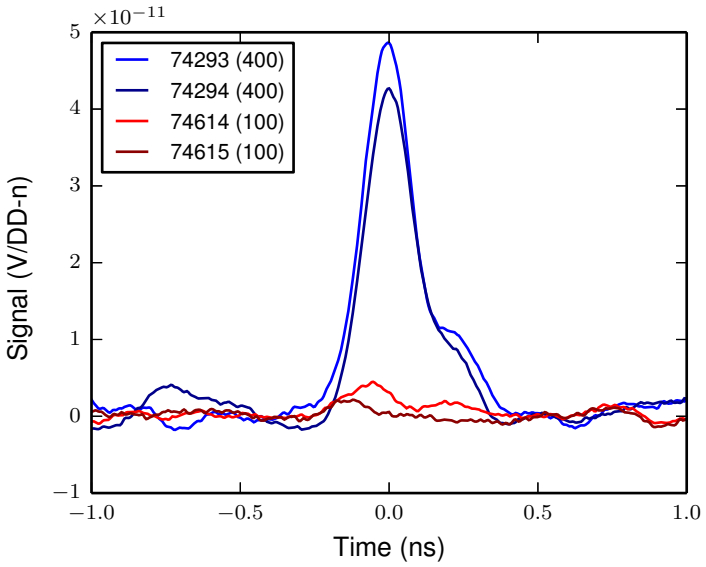

Figure 10.10. HD-filled implosions where the GCD-3 was filled with either 400psi (blue curves, $\sim$ 3 MeV threshold) or 100psi (red curves, $\sim$ 6.3 MeV threshold) of CO_2. The dramatic reduction in signal demonstrates that the signal observed at 400psi is due to a low-energy γ ray.

The raw data are fit with a double Gaussian curve in time, shown in Fig. 10.11 for shot 74290, a HD-filled implosion. A double Gaussian is used to account for the PMT ring, which creates the 'shoulder' on the falling edge of the main signal. The area under the double-Gaussian fit corresponds to the total signal in V×s, with an uncertainty associated with the best fit (from reduced-χ^2).

The γ-ray yield can be calculated for a given reaction x from the integrated signal ($V \times s$) using the detector equation

$$Y_x = \frac{V \times s}{\Omega \times R \times e \times \mathrm{QE} \times G} \times \frac{1}{C_x}, \tag{10.5}$$

where Ω is the detector solid angle, R is the scope input impedance (50 Ohm), e is the fundamental charge, QE is the PMT quantum efficiency, and G is the PMT gain. C_x is the effective GCD response for reaction x in photons collected per incident γ.

10.4.4 GCD-3 D^3He calibration

The GCD response function is calculated using GEANT4 Monte-Carlo simulations[26] and normalized using experimental calibration data[27]. This calibration factor accounts for systematic uncertainties in the instrument light collection, uncertainties in modeling the Cherenkov production, and accounts for uncertainties in the PMT response. This results in a multiplicative calibration factor (typically < 1 and dominated by the light production and transport). In this experiment, D^3He implosions were conducted as calibration shots using the same detector setup, with the calibration set using published data for the D^3He reaction branching ratio[28].

Three D^3He-filled implosions are used in this calibration. The raw data are shown in Fig. 10.12a. These data are analyzed using the procedure already described. A preliminary calibration factor* of 0.53 was used with the calculated instrument response to D^3He-γs to infer a D^3He γ-ray

*From a cross-calibration to the GCD-1 instrument using the DT-γ from separate DT-filled implosions a preliminary calibration factor of 0.53 was inferred. (H. Herrmann, private communication).

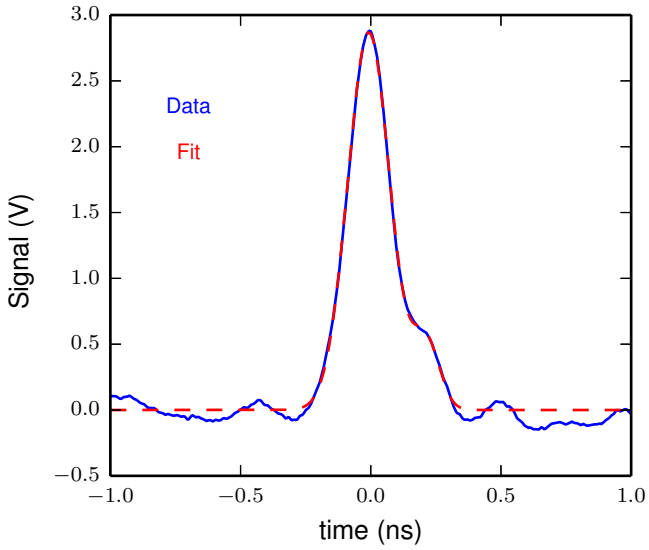

Figure 10.11. Double-Gaussian fit to the raw PMT signal for shot 74290 (HD). The shoulder on the late-time side of the main peak (at ~ 0.2ns) is a PMT ring.

yield. This yield can be compared to the expected γ yield using the known D^3He branching ratio[28] and measurements of the proton yield from WRF spectrometers[16,29]. This is shown in Fig. 10.12, where the data is used to refine the initial calibration estimate.

In this calibration, the sources of uncertainty include the integrated signal uncertainty and a statistical uncertainty from the number of productive Compton-scattered electrons in the system, which is the statistically-limiting step of the Cherenkov detector technique. The statistical uncertainty in the D^3He proton yield measurement is also included. When the integrated D^3He-γ signal is calculated the DD-induced background is subtracted, which introduces an additional uncertainty. The major systematic uncertainty is from the uncertainty in the D^3He branching ratio[28]. The calibration factor is calculated as a weighted mean of the three D^3He shots and found to be $0.50 \pm \pm 0.20$.

10.4.5 pD fusion yield

With this calibration factor, the pD fusion yield can be calculated. The primary source of background is from DD fusion reactions, which is characterized with the D_2-filled implosions. An average integrated signal per DD-n is calculated on the DD shots for the background subtraction. On each HD implosion, the measured DD-n yield is then used to subtract the background. The uncertainty in DD-n yield and the background signal per DD-n is included in the statistical uncertainty for the integrated signal on each HD implosion.

On each implosion the γ yield is then calculated using Eq. 10.5, the 5.5 MeV γ-ray response, and the calibration factor (Section 10.4.4). The statistical uncertainty in γ yield results from uncertainty in the integrated signal, DD background subtraction, Compton electron statistics, and the statistical uncertainty in the calibration. The systematic uncertainty results from the significant systematic uncertainty in the calibration.

A total of seven HD-fueled implosions have been diagnosed using GCD-3 with 400psi of CO_2 fill (see Table 10.1), which are shown in Fig. 10.13. The error bars shown are statistical only.

(a) Raw PMT signals for the D^3He shots

(b) Calibration for D^3He (blue) relative to initial estimate (black). Only statistical uncertainties shown.

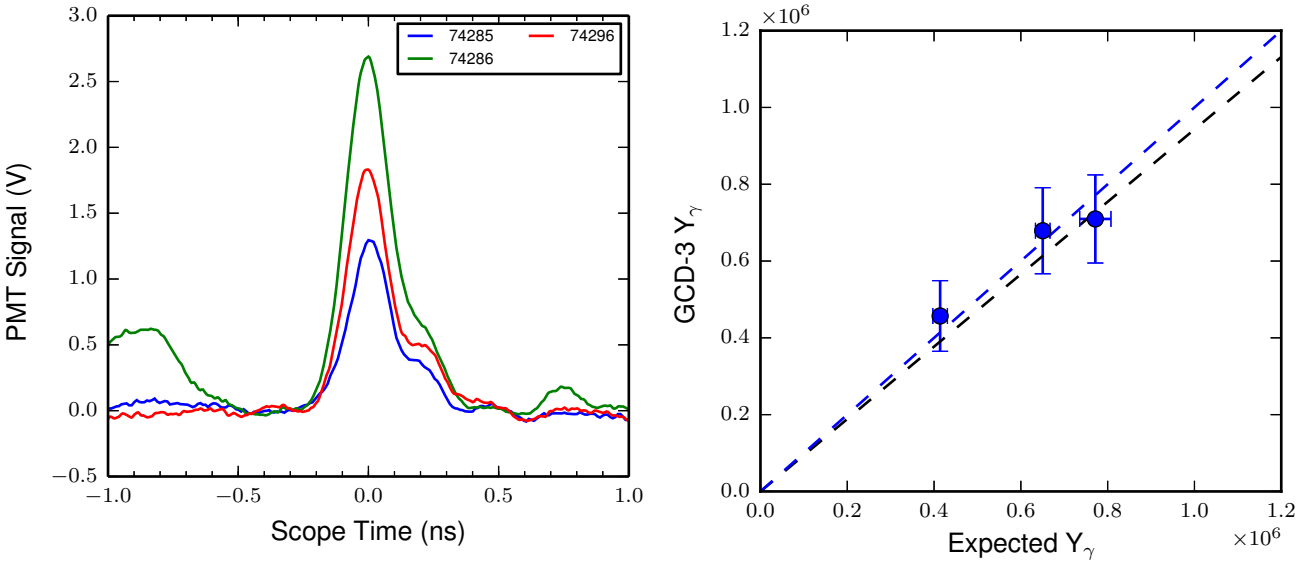

Figure 10.12. D^3He data used for calibration of the GCD-3 instrument.

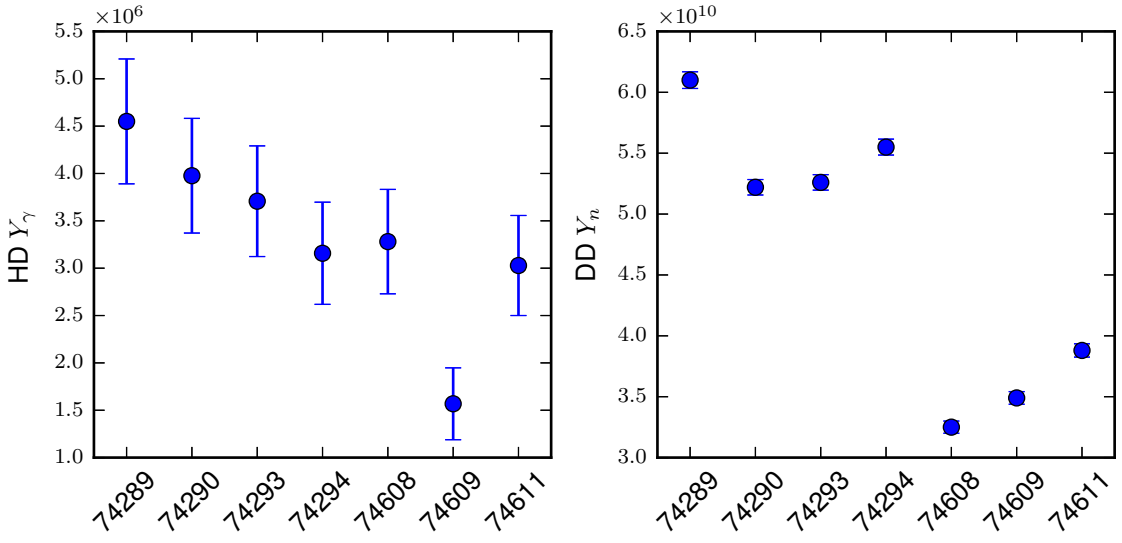

Figure 10.13. Left: calculated pD γ yield for seven data shots, showing statistical uncertainties only. Right: DD-n yield for the same shots.

10.5 S-factor analysis

The S-factor for the p+D reaction can be calculated from the pD-γ yield using the DD reaction as a reference. The yields for the two reactions are

$$Y_{pD} = \int d\vec{r}dt\ n_H n_D \langle\sigma v\rangle_{pD}, \tag{10.6}$$

$$Y_{DD} = \int d\vec{r}dt\ \frac{n_D^2}{2}\langle\sigma v\rangle_{DD}, \tag{10.7}$$

where n_H and n_D are the proton and deuteron number densities, respectively, and $\langle\sigma v\rangle$ is the fusion reactivity as a function of temperature; n and T_i are typically unknown functions of space and time. The ratio of the two yields is

$$\frac{Y_{pD}}{Y_{DD}} = 2\int d\vec{r}dt\ \frac{n_H}{n_D}\frac{\langle\sigma v\rangle_{pD}}{\langle\sigma v\rangle_{DD}}. \tag{10.8}$$

If there are no 'profile' or species-separation effects occuring in these implosions, as shown in Section 10.3, then the yield ratio is given by

$$\frac{Y_{pD}}{Y_{DD}} = 2\frac{n_H}{n_D}\frac{\langle\sigma v\rangle_{pD}}{\langle\sigma v\rangle_{DD}}. \tag{10.9}$$

where the reactivities are burn-averaged. This assumes that the density and temperature profiles for each reaction are the same, thus the burn duration and volume are also identical. Since these are both non-resonant reactions in this energy range, the reactivity can be written:

$$\langle\sigma v\rangle = \frac{8}{\pi\sqrt{3}}\frac{\hbar}{m_r Z_1 Z_2 e^2} S\xi^2 e^{-3\xi}, \tag{10.10}$$

which is Eq. 1.56 in Atzeni (Ref. 30), where Z_1 and Z_2 are the reactant charges, m_r is their reduced mass, S is the S-factor, and ξ is related to the Gamow energy (ϵ_G):

$$\xi = \left(\frac{\epsilon_G}{4k_B T}\right)^{1/3}, \tag{10.11}$$

$$= \left[\frac{(\pi\alpha Z_1 Z_2)^2 2m_r c^2}{4k_B T}\right]^{1/3}, \tag{10.12}$$

$$= 6.2696(Z_1 Z_2)^{2/3} A_r^{1/3} T^{-1/3}. \tag{10.13}$$

Using this formalism, the yield ratio can then be written as

$$\frac{Y_{pD}}{Y_{DD}} = 2\frac{n_H}{n_D}\frac{A_{pD}^{-1} S_{pD}\xi_{pD}^2 e^{-3\xi_{pD}}}{A_{DD}^{-1} S_{DD}\xi_{DD}^2 e^{-3\xi_{DD}}}, \tag{10.14}$$

which is inverted to give an expression for the pD S-factor:

$$S_{pD} = S_{DD} \times \frac{Y_{pD}}{Y_{DD}} \times \left[\frac{n_D}{2n_H}\frac{A_{pD}}{A_{DD}}\frac{\xi_{DD}^2 e^{-3\xi_{DD}}}{\xi_{pD}^2 e^{-3\xi_{pD}}}\right]. \tag{10.15}$$

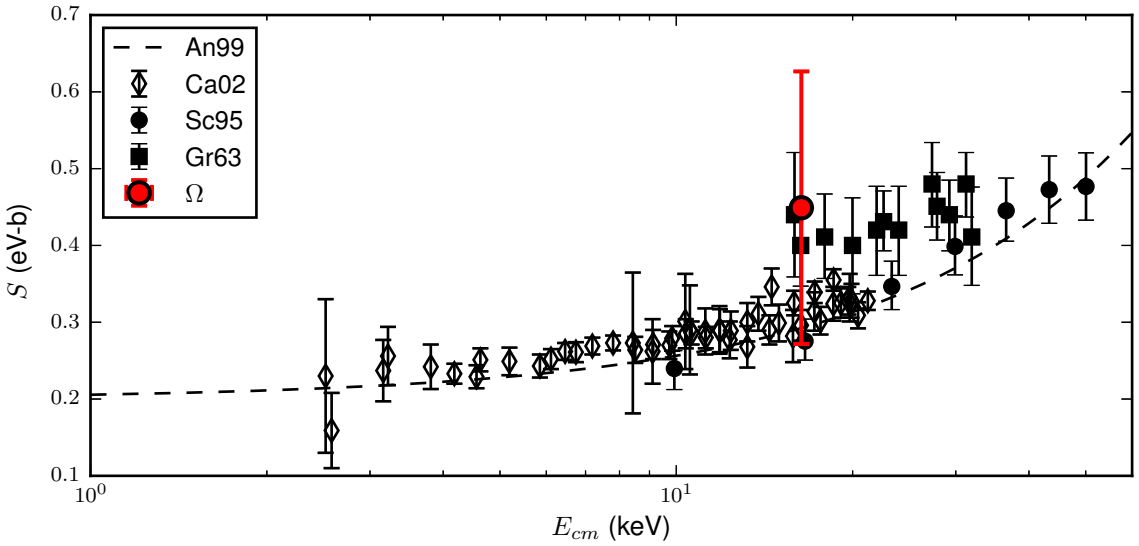

Figure 10.14. S-factors for this work (red point) and several accelerator experiments[7–9]. An adopted S-factor[31] is shown in the black dashed curve.

The DD S-factor is well known from accelerator experiments, the two yields are measured experimentally, and the factor in square brackets is calculated using the DD-n Doppler ion temperature, which is ~ 0.1 for $T_i \sim 5$ keV. The average center-of-mass energy (E_{cm}) for the reactions, the Gamow peak energy, is $\xi k_B T$ and thus is calculated for the DD and pD reactions separately, though using the same thermal temperature.

An S-factor is calculated for each of the seven shots, which are then used to calculate a weighted mean value:

$$S_{pD} = 0.45 \pm 0.03_{\text{stat}} \pm 0.17_{\text{sys}} \text{ eV-b}, \quad \text{at } E_{cm} = 16.3 \pm 0.4 \text{ keV}. \tag{10.16}$$

Within experimental uncertainty, agreement is found with the previous accelerator data and adopted $S(E)$ curve (see Fig. 10.14). The uncertainty is dominated by the systematic calibration uncertainty.

10.6 Conclusion

The p + D $\rightarrow^3$ He + γ (5.5 MeV) reaction is important for several astrophysical systems: energy generation in protostars and brown dwarfs via burning of the primordial D, and for ^{3}He production during BBN. The reaction has been studied at low (astrophysically-relevant) energies in several accelerator (beam-target) experiments[7–9] and theoretical work[10–12]. Experimentally, these accelerator experiments must correct for bound-electron screening and thick-target effects, potentially introducing systematic uncertainties.

In this work, inertially-confined plasmas were used to generate p+D reactions in a thermal plasma. The resulting γ rays were measured with a Cherenkov detector and used to determine an absolute value of the astrophysical S-factor. The result in this work agrees with accelerator data when considering the uncertainties, particularly the systematic due to the instrument calibration. This is the first direct comparison of accelerator- and plasma-measured fusion cross sections relevant to astrophysics.

10.7 References

1. S. W. Stahler, "Deuterium and the stellar birthline," The Astrophysical Journal, **332**, 804–825 (1988).
2. S. S. Kumar, "The Structure of Stars of Very Low Mass." The Astrophysical Journal, **137**, 1121 (1963).
3. C. Hayashi and T. Nakano, "Evolution of stars of small masses in the pre-main-sequence stages," Progress of Theoretical Physics, **30**(4), 460–474 (1963).
4. V. Joergens, *50 Years of Brown Dwarfs* (Springer, 2014).
5. C. Grupen, *Big Bang Nucleosynthesis* (Astroparticle Physics, Springer, 2005).
6. R. N. Boyd, C. R. Brune, G. M. Fuller *et al.*, "New nuclear physics for big bang nucleosynthesis," Phys. Rev. D, **82**, 105005 (2010).
7. G. Griffiths, M. Lal and C. Scarfe, "The reaction d (p, γ) he3 below 50 kev," Canadian Journal of Physics, **41**(5), 724–736 (1963).
8. G. Schmid, R. Chasteler, C. Laymon *et al.*, "Polarized proton capture by deuterium and the h 2 (p, γ) he 3 astrophysical s factor," Physical Review C, **52**(4), R1732 (1995).
9. C. Casella, H. Costantini, A. Lemut *et al.*, "First measurement of the d (p, γ) 3 he cross section down to the solar gamow peak," Nuclear Physics A, **706**(1), 203–216 (2002).
10. M. Viviani, R. Schiavilla and A. Kievsky, "Theoretical study of the radiative capture reactions $h^2(n,\gamma)^3h$ and $h^2(p,\gamma)^3he$ at low energies," Physical Review C, **54**(2), 534 (1996).
11. G. Schmid, M. Viviani, B. Rice *et al.*, "Effects of Non-nucleonic Degrees of Freedom in the D($\vec{p}$, γ)^{3}He and p($\vec{d}$,γ) ^{3}He Reactions," Physical review letters, **76**(17), 3088 (1996).
12. H. Sadeghi, H. Khalili and M. Godarzi, "Astrophysical s-factor of the d (p,?) 3he process by effective field theory," Chinese Physics C, **37**(4), 044,102 (2013).
13. T. Boehly, D. Brown, R. Craxton *et al.*, "Initial performance results of the OMEGA laser system," Optics Communications, **133**(1-6), 495–506 (1997).
14. V. Y. Glebov, D. D. Meyerhofer, T. C. Sangster *et al.*, "Development of nuclear diagnostics for the National Ignition Facility (invited)," Rev. Sci. Instrum., **77**(10), 10E715 (2006).
15. C. Stoeckl, V. Y. Glebov, S. Roberts *et al.*, "Ten-inch manipulator-based neutron temporal diagnostic for cryogenic experiments on omega," Review of scientific instruments, **74**(3), 1713–1716 (2003).
16. F. H. Séguin, J. A. Frenje, C. K. Li *et al.*, "Spectrometry of charged particles from inertial-confinement-fusion plasmas," Rev. Sci. Instrum., **74**(2), 975–995 (2003).
17. J. Delettrez, R. Epstein, M. Richardson *et al.*, "Effect of laser illumination nonuniformity on the analysis of time-resolved x-ray measurements in uv spherical transport experiments," Physical Review A, **36**(8), 3926 (1987).
18. J. R. Rygg, J. A. Frenje, C. K. Li *et al.*, "Tests of the hydrodynamic equivalence of direct-drive implosions with different d2 and he3 mixtures," Physics of Plasmas, **13**(5), 052702 (2006).
19. H. W. Herrmann, J. R. Langenbrunner, J. M. Mack *et al.*, "Anomalous yield reduction in direct-drive deuterium/tritium implosions due to h3e additiona)," Physics of Plasmas, **16**(5), 056312 (2009).
20. D. T. Casey, J. A. Frenje, M. Gatu Johnson *et al.*, "Evidence for stratification of deuterium-tritium fuel in inertial confinement fusion implosions," Phys. Rev. Lett., **108**, 075,002 (2012).
21. P. Amendt, O. L. Landen, H. F. Robey *et al.*, "Plasma barodiffusion in inertial-confinement-fusion implosions: Application to observed yield anomalies in thermonuclear fuel mixtures," Phys. Rev. Lett., **105**, 115,005 (2010).
22. G. Kagan and X.-Z. Tang, "Thermo-diffusion in inertially confined plasmas," Physics Letters A, **378**(21), 1531 – 1535 (2014).
23. H. G. Rinderknecht, J. Rosenberg, M. K. Li, C. *et al.*, "Ion thermal decoupling and species separation in shock-driven implosions," Phys. Rev. Lett., **114**, 025,001 (2015).
24. J. Mack, R. Berggren, S. Caldwell *et al.*, "Observation of high-energy deuterium-tritium fusion gamma rays using gas Cherenkov detectors," Nuclear Instruments and Methods in Physics Research Section A: Accelerators, Spectrometers, Detectors and Associated Equipment, **513**(3), 566 – 572 (2003).
25. H. W. Herrmann, Y. H. Kim, C. S. Young *et al.*, "Extended performance gas cherenkov detector for gamma-ray detection in high-energy density experimentsa)," Review of Scientific Instruments, **85**(11), 11E124 (2014).

26. M. S. Rubery, C. J. Horsfield, H. Herrmann *et al.*, "Monte carlo validation experiments for the gas cherenkov detectors at the national ignition facility and omega," Review of Scientific Instruments, **84**(7), 073504 (2013).

27. Y. Kim, J. Mack, H. Herrmann *et al.*, "D-T gamma-to-neutron branching ratio determined from inertial confinement fusion plasmas," Phys. Plasmas, **19**, 056313 (2012).

28. F. E. Cecil, D. M. Cole, R. Philbin *et al.*, "Reaction ^{2}H(^{3}he,γ)^{5}li at center-of-mass energies between 25 and 60 kev," Phys. Rev. C, **32**, 690–693 (1985).

29. F. H. Séguin, N. Sinenian, M. Rosenberg *et al.*, "Advances in compact proton spectrometers for inertial-confinement fusion and plasma nuclear science," Rev. Sci. Instrum., **83**(10), 10D908 (2012).

30. S. Atzeni and J. Meyer-Ter-Vehn, *The Physics of Inertial Fusion: Beam Plasma Interaction, Hydrodynamics, Hot Dense Matter*, International Series of Monographs on Physics (Oxford University Press, 2004).

31. C. Angulo, M. Arnould, M. Rayet *et al.*, "A compilation of charged-particle induced thermonuclear reaction rates," Nuclear Physics A, **656**(1), 3 – 183 (1999).

Part IV

Conclusion and Appendices

11

Conclusion

In this thesis, fusion product spectroscopy was used to study inertial fusion implosions, measure charged-particle stopping power in dense plasma, and study three fusion reactions relevant to stellar and Big-Bang nucleosynthesis. These experiments were conducted at OMEGA and the NIF.

In the first project, compact proton spectrometers were implemented on the NIF to measure D^3He fusion protons emitted from 'surrogate' implosions, where the cryogenic ice layer of ignition targets is replaced with an equivalent mass of ablator. These proton spectrometers may be fielded in up to eight locations, located near the north pole and equator. In the implosion, spherical convergence of the final merged shock produces a brief period of fusion burn known as the 'shock' burn. The shock burn is subsequently followed by the main 'compression' burn several hundred ps later. The downshift of the shock-produced D^3He protons is used to infer the areal density (ρR) and shell center-of-mass radius (R_{cm}) while the implosion is in flight, at a convergence ratio (CR) ~ 4. Additionally, the shock strength is inferred from the proton yield. In this work, the effects of several laser pulse design parameters on the shock dynamics have been studied. First, higher shock ρRs were observed for 'no-coast' implosions, where the laser drive is kept on for longer (i.e. until closer to the bang time). Higher ρR corresponds to a higher convergence (lower R_{cm}) at the shock-bang time. This data is combined with in-flight x-ray radiography to estimate the shock-bang time. The time difference between shock- and compression-bang time is found to decrease substantially for the no-coast implosions, in contradiction to hydrodynamic simulations. Physically, this corresponds to a shorter implosion deceleration phase, which could be caused in part by inaccurate modeling of the late-time drive pressure, more rapid deceleration of the compressed shell than expected, or significant mix in the no-coast implosions. Secondly, the shock strength inferred from the proton yield is found to depend strongly on the laser rise time from the foot of the pulse to peak power. A stronger shock is launched for a faster rise. This data is the only metric for shock heating of the gas at the center of the implosion, which is related to the initial adiabat of the material that will form the hot spot. In addition, with the multiple detector locations, at the pole and equator, low-mode asymmetries in the implosion were measured. At the shock-bang time ($CR \sim 4$), large ρR asymmetries were routinely observed and interpreted as P_2 shape perturbations with amplitudes $10 - 30\%$. When compared to compression-bang-time x-ray imaging, sensitive to the hot spot shape, positive correlation and comparable amplitudes between the two metrics were observed for two independent sets of data. The positive correlation means that the asymmetries do not change sign during deceleration, while the comparable amplitude suggests that these asymmetries do not grow during deceleration. This is in contradiction to several hydrodynamic growth models, both analytic and computational, which may be explained by the hot spot at compression not representing the asymmetry of the shell, or that significant residual kinetic energy may be present in these implosions that would not be accounted for in the growth models.

In a set of dedicated experiments on the OMEGA laser, the same type of WRF proton spectrometers were used to accurately measure charged-particle stopping power in dense plasma. D^{3}He protons were generated in a shock-driven 'exploding pusher' implosion to probe Be that was isochorically heated by x rays to WDM conditions, which were moderately-coupled $\left[(e^2/a)/(k_BT_e + E_F) \sim 0.3\right]$ and moderately-degenerate $[k_BT_e/E_F \sim 2]$. These are the first high-accuracy measurements of charged-particle energy loss through dense plasma; the data show an increased loss relative to cold matter, consistent with a reduced mean ionization potential. The data agree with stopping models based on an *ad-hoc* treatment of free and bound electrons, as well as the average-atom local-density approximation; this work is the first test of these theories in WDM plasma. Stopping-power experiments using petawatt lasers (OMEGA EP) have also been attempted, but several challenges in the production of appropriate subject plasmas and proton sources currently prevent accurate measurements.

Lastly, nuclear diagnostics have been used to study several reactions relevant to nuclear astrophysics. The ^{3}He+^{3}He reaction, the last step of the solar proton-proton I chain, was studied at OMEGA. Proton spectra from the reaction were measured at low reactant center-of-mass energy (E_{cm}). For the first time, this data is used to constrain phenomenological R-matrix nuclear models. Knowledge of the spectral shape is important for interpretation of accelerator data at even lower E_{cm}, which is used to determine the reaction rate inside stars. The T+^{3}He reaction was also studied in OMEGA implosions. The capture branch of this reaction can generate ^{6}Li and was hypothesized to potentially resolve anomalous ^{6}Li abundances via production during BBN. The OMEGA data was found to invalidate this hypothesis, as the cross section is too low for significant ^{6}Li production via this mechanism. The proton spectrum from T+^{3}He is also being used to constrain R-matrix theory. The third reaction studied was p+D, which is responsible for energy production in brown dwarfs and protostars. The γ ray was measured, and the inferred cross section agrees with previous accelerator data. This is the first direct comparison of plasma and accelerator data for an astrophysical reaction, and increases confidence in the reaction rate.

On the whole, this work contributes to the national quest for fusion ignition at NIF, our understanding of dense plasma physics, and the study of astrophysical nucleosynthesis. Future work is expected in all three areas. On the NIF, lower-convergence (higher-adiabat) experiments are being conducted to study the shock dynamics in a simpler implosion. Preliminary data are presented in Appendix J. By testing hydrodynamic models in these simpler implosions, further physics understanding may be obtained of the low-adiabat experiments in this work. On the stopping power, NIF experiments next year will extend this work into a strongly-coupled and degenerate plasma regime, to distinguish the bound-free and local-density approximation models. All of the astrophysical nuclear reactions in this work can be studied further. For the ^{3}He^{3}He reaction, new diagnostic capability could enable measurements of the low-energy part of the proton spectrum. The T^{3}He-γ data quality will be substantially improved by reducing the DT-γ background by using higher-purity fuel. Lastly, the pD reaction measurement can be improved by a better calibration of the Cherenkov detector, potentially enabling this technique to distinguish between discrepant low-energy accelerator experiments.

Appendices

Appendix A

Using high intensity laser-generated energetic protons to radiograph directly driven implosions

A.1 Introduction

A.1.1 Previous techniques

One successful technique for studies of ICF implosions has been radiography using either x-rays [1,2] or charged particles; the latter will be the focus of this Appendix. Within the past several years short-pulse-generated proton radiography has been demonstrated by Mackinnon et al. for 6 beam implosions on the Vulcan laser [3]. Backlighting full-energy OMEGA implosions, as demonstrated in this work, reveals filamentary EM field structures in the corona that were not observed by Mackinnon et al [3], but were observed by Rygg et al [4], who used a fusion-based charged-particle backlighter technique developed at OMEGA [5]. This method uses 3 and 15 MeV protons (from DD and D^3He fusion), produced in a 80-130ps burn with a typical source size of 40-50μm FWHM. This technique has been used to successfully study direct-drive implosions [6,4,7], indirect-drive implosions [8–10], and electromagnetic fields in HED plasmas [11–15].

A.1.2 Energetic proton production

It is well known that the interaction of a high-intensity laser with matter can create energetic electrons and ions [16,17]. Relevant to this work is the Target Normal Sheath Acceleration (TNSA) mechanism [18] at laser intensities on the order of 10^{19} W/cm^2. During the initial laser interaction with a solid target, electrons are accelerated to high energy, and propagate away from the target at nearly the speed of light, c. This sets up strong 'sheath' electric fields, which can accelerate ions to high energy. Hydrocarbon contaminants on the target are known to cause the production of protons with energies up to 60 MeV [19]. Ion acceleration mechanisms, including TNSA, have been extensively studied experimentally [20,18,21,22,19,23–37] and computationally [38–41]. Other proposed applications for this technique include compact medical and research accelerators [42], and proton fast ignition [43].

A.1.3 Challenges and benefits of TNSA backlighting

These TNSA-generated proton beams can be used as a backlighter for probing ICF and HED plasmas. This has been proposed and used in the literature [44–47], first demonstrated for 6 beam spherical implosions using Vulcan [3], and recently in experiments on OMEGA EP [48–50]. Backlighting

full-scale implosions at OMEGA or the NIF comes with a unique set of challenges and benefits for this technique. These challenges include designing the backlighter to ensure an adequate fluence and energy of backlighting protons. This requires compensating for several effects, such as x-ray crosstalk, return current, and preplasma from the implosion[51]. The beam divergence, magnification required, and desired radiography time window require experimental optimization.

The benefits of TNSA proton backlighting over previous proton backlighting, i.e. with fusion-generated protons, are better temporal resolution (∼10ps versus ∼100ps), better spatial resolution (∼10μm versus 40-50μm), and the ability to radiograph at several time steps during one implosion. Spatial and temporal resolution are quoted on the basis of previous TNSA proton production and radiography work in the literature[45,29,52]. Information on the spectral resolution is also available in works. The fusion backlighter offers better energy resolution and spatial uniformity than the TNSA backlighter, but which technique is optimal depends on the experiment. This work focuses on solutions to the unique challenges when using TNSA to backlight 60-beam OMEGA implosions, and presents the first radiographs of such implosions.

A.2 Experimental Overview

The OMEGA and OMEGA EP lasers (see Sections 1.3.2 and 1.3.3) are used for this experiment. All 60 OMEGA beams drove the subject spherical capsule implosion. A top-level schematic of the experiment is shown in Fig. A.1. The target was a 20-40μm thick CH shell of outer diameter 860μm filled with ^{4}He gas at 18atm. The OMEGA pulse shape was a 3.5ns 17kJ 'shock ignition' pulse[53] using smoothing by spectral dispersion[54] and SG4 phase plates[55], as the primary physics goal is to study the shock propagation in the imploded capsule[56]. The capsule drive pulse was started several ns before the backlighter was fired, as the most interesting physics occurs when the shock is launched, as well as near peak neutron production and stagnation. The backlighter foil used was 10μm thick Au. A 1ps 300J OMEGA EP short-pulse beam was used for TNSA backlighting, with a focal spot size ∼ 40μm in diameter for an intensity $\approx 2 \times 10^{19}$ W/cm^2.

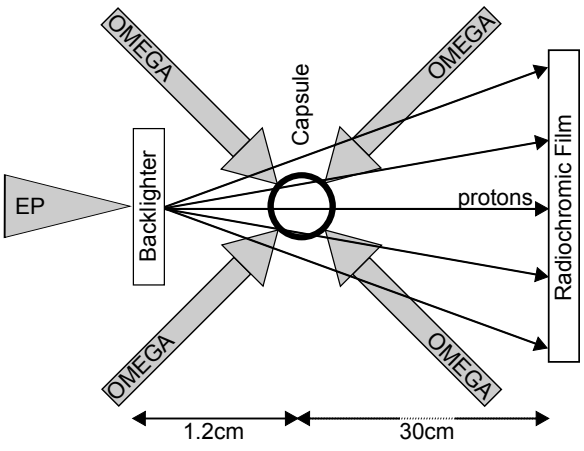

Figure A.1. Top-level schematic of the experiment. Sixty OMEGA beams drive a spherical implosion, which is backlit by the EP laser-generated protons and imaged on a radiochromic film detector.

A.3 Backlighter design

As listed in the introduction, there are three main mechanisms that could degrade the backlighter performance:

A.3.1 Preplasma

It is known that any prepulse before the proton-generating main laser pulse can create a 'preplasma' at the target that dramatically reduces the backlighter performance[23]. In this experiment, the subject capsule was imploded via sixty OMEGA beams via ablation pressure. The ablated mass was ejected outwards to large radii, forming a large coronal plasma around the implosion. Since the capsule drive started several ns before being radiographed, the coronal plasma can reach the backlighter. In a simple geometry, shown in Fig. A.2, the coronal plasma flows around the backlighter foil and can impede the short-pulse beam propagation to the foil surface. This has the same effect as preplasma: the conversion efficiency from laser energy to energetic protons is greatly reduced. Additionally, coronal plasma at the backlighter foil can short out the sheath field due to Debye screening; this will also reduce the conversion efficiency. The backlighter shielding must therefore be designed to impede the coronal plasma flow so that it does not interact with the foil.

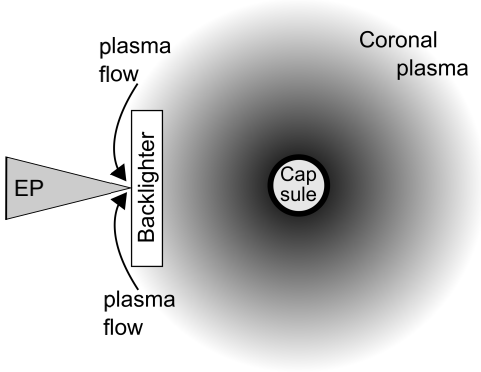

Figure A.2. A coronal plasma forms around an imploding capsule due to ablation blowoff from the OMEGA drive. The coronal plasma can flow around the backlighter foil to reach the region where the short pulse beam propagates. This impedes the short-pulse propagation to the focal point, leading to reduced proton maximum energy and yield.

A.3.2 X-ray crosstalk

X-ray imaging of capsule implosions shows that the capsule emits x-rays during the drive[57]. These x-rays are emitted isotropically, which means that some of the x rays are incident upon the backlighter foil. This is shown schematically in Fig. A.3. The x rays efficienctly heat the Au backlighter foil, which can create some preplasma on the back surface ∼ns before the short-pulse beam is incident on the foil. This would be a similar effect to a prepulse on the short-pulse beam, or interference by coronal plasma. To mitigate this effect the backlighter foil must be shielded from 'crosstalk' from the capsule.

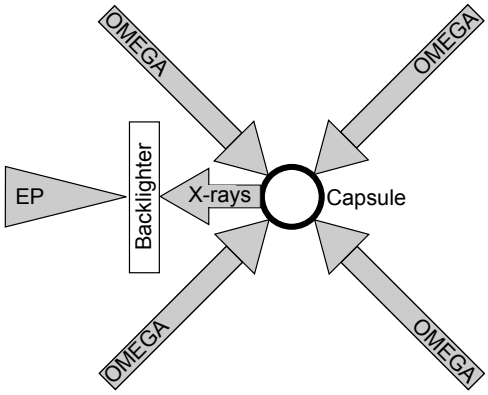

Figure A.3. 60 OMEGA beams driving a capsule implosion. X-rays from the capsule can preheat the backlighter foil, which reduces the backlighter performance.

A.3.3 Return current

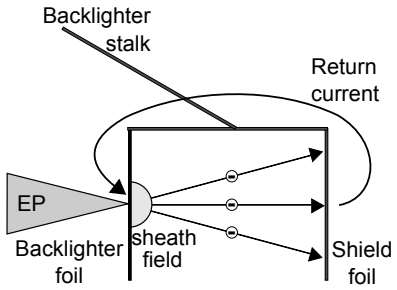

Figure A.4. If there is a pathway for fast electrons to form a return current to the backlighter foil within the backlighter pulse, then the sheath field can be neutralized. This reduces TNSA production. Return current can be mitigated by ensuring that the target scale lengths are large enough that the current cannot flow during the pulse duration.

In the TNSA mechanism fast electrons set up the strong electric sheath field, which accelerates the protons of interest for TNSA backlighting. If, for example, a shield foil is placed in front (toward the implosions) of the backlighter foil to shield from x-ray crosstalk (previous section), as shown in Fig. A.4, then there is a potential for the fast electrons to generate a return current loop back to the backlighter foil. This would neutralize the acceleration sheath field, and reduce the backlighter proton performance.

Therefore, the backlighter size must be greater than the scale length $\ell = c\tau$, where τ is the laser pulse length, and the electrons are ultra-relativistic ($v \approx c$). With a 1ps pulse $\ell \sim 0.3$mm, and at $\tau = 10$ps the scale length $\ell \sim 3$mm. Since typical backlighter sizes are of order mm, this is a design concern for 10ps pulses but not 1ps ones.

A.3.4 Resulting Design

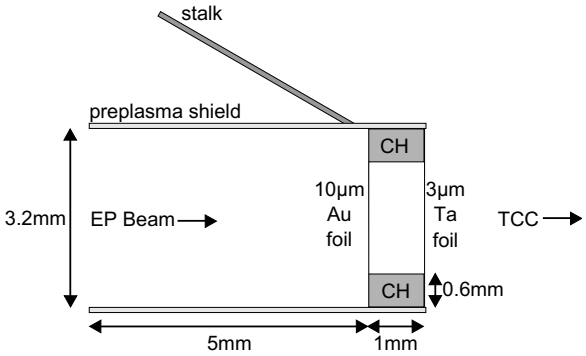

Figure A.5. A cross section of the backlighter design used in these experiments. Shown is a cross-section, where the design has cylindrical symmetry around the central axis (except for the target positioner stalk). The 10μm Au TNSA foil and 3μm Ta preplasma shield are mounted on a CH washer, which is inserted into a cylindrical preplasma shield.

A backlighter for TNSA radiography has been designed to mitigate these issues. A schematic is shown in Fig. A.5, and fabricated backlighters are shown in Fig. A.6.

The 10μm Au foil is the actual backlighter foil target. The foil is glued to a 1mm thick CH washer. On the other end of the washer, a 3μm Ta foil acts as a x-ray cross-talk shield. The washer is encased in a thin brass cylindrical shell that forms a shield to impede coronal plasma flow to the backlighter foil. As shown in Fig. A.5 the EP beam comes in from the left, and TCC is to the right. As a 1ps pulse is used in these experiments, there is no potential for return current issues due to the scale lengths of this backlighter design.

A.4 Experimental Optimization

The experimental configuration, i.e. separation between backlighter, subject, and imaging plane, must be adjusted to optimize the backlighter performance, magnification, and radiography timing.

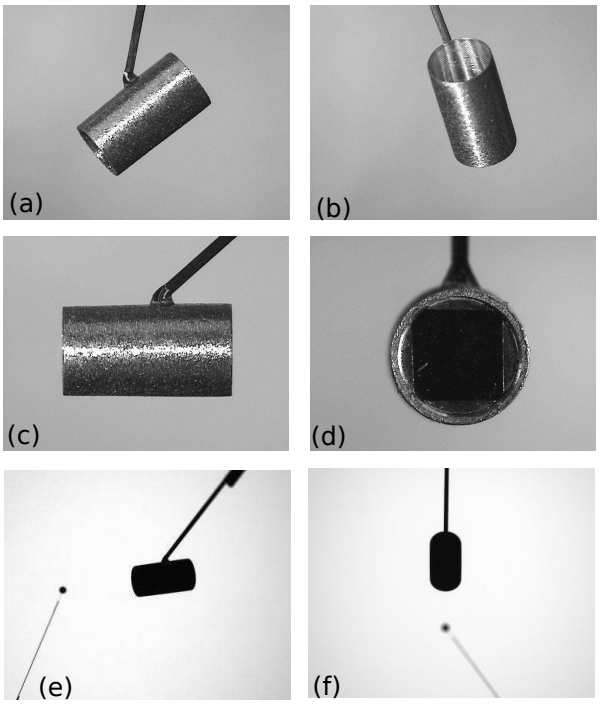

Figure A.6. Images of fielded backlighters. (a,b) two isometric views of a backlighter, (c) side-on view of backlighter, (d) view from TCC of backlighter, (e,f) shadowgraphs of pre-shot backlighter and capsule in OMEGA target chamber.

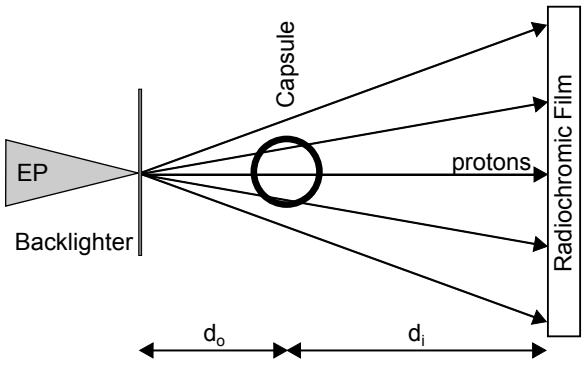

Figure A.7. Schematic of the experimental geometry. The radiography time-of-flight and magnification depend on the backlighter-object distance (d_o) and object-film distance (d_i). Optimized values, as used in these experiments, are $d_o = 1.2$cm and $d_i \sim 30$cm.

The backlighter-capsule distance d_o and the capsule-film distance d_i are shown in Fig. A.7.

The TNSA-generated proton beam has a cone-shaped emission, so for a given beam intensity a larger d_i results in less fluence on the detector. In joint radiography experiments we observed that the film pack performs well for $d_i \sim 30$cm.

The magnification is

$$M = \frac{d_i + d_o}{d_o} = 1 + \frac{d_i}{d_o}. \tag{A.1}$$

Since the interesting physics in a capsule implosions happens at small radii, ≤ 200 μm, the magnification must be at least 25 for detectable features. With $d_i \approx 30$ cm, this constrains $d_o \leq 1.25$ cm. Depending on the experimental goals a higher magnification may be desirable.

The radiography time-of-flight depends on the choice of d_o. Since the TNSA mechanism produces a falling exponential distribution with proton energy[19], low- (several MeV) and high- (several tens of MeV) energy protons can be used to backlight the implosion at differing times of flight[45,3]. All protons are born essentially simultaneously, within 1-10ps depending on the high-intensity laser pulse length, so protons with a certain energy backlight the implosion at a time

$$t = \tau + d_o/v_p, \tag{A.2}$$

where τ is the short-pulse laser delay, and $v_p = v_p(E)$ is the proton velocity. The time window radiographed in one shot is given by

$$\delta t = d_o \left(\frac{1}{v_{p,min}} - \frac{1}{v_{p,max}} \right) \tag{A.3}$$

where $v_{p,min}$ and $v_{p,max}$ are the minimum and maximum energies, respectively, for which usable radiographs can be obtained. Ideally this should ≥ 150ps to allow radiography of a large total time window of the implosion physics. This is easily achievable with the film pack design in this paper for $d_o = 1.2$cm, as will be shown in the next section.

A.5 Film pack design

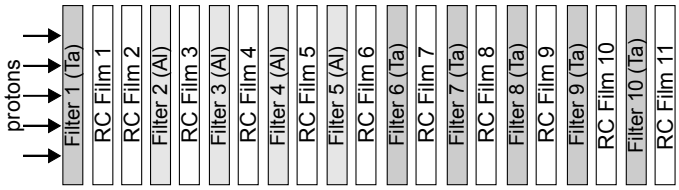

Figure A.8. Radiochromic (RC) film pack design for proton radiography. The pack consists of interleaved filters (Al or Ta) and films.

The film pack used in these experiments is shown in Fig. A.8. Protons from the backlighter are incident from the left. A series of Al or Ta filters and Gafchromic® HD-810 radiochromic films[58] are interleaved. The filter pack transverse size is 10cm × 10cm. Each filter is measured with a micrometer since the thickness tolerance is generally 10% (standard filter stock from Goodfellow®[59]). Each filter's material and measured thickness is listed in Table A.1.

With known filter thicknesses and composition information on the HD-810 film, the proton energy that each film is primarily sensitive to, ϵ, is calculated using SRIM[60] stopping-power tables.

Table A.1. Film pack filter materials and thicknesses

Filter	Material	Thickness (μm)
1	Ta	42
2	Al	29
3	Al	106
4	Al	205
5	Al	480
6	Ta	390
7	Ta	407
8	Ta	534
9	Ta	1027
10	Ta	1026

This is done by calculating the deposited energy for each incident proton energy for initial proton energies from 0 to 60 MeV. This is shown for RC film 5 in Fig. A.9.

ϵ is used to calculate a time-of-flight corresponding to each film, i.e. when that radiograph of the subject was taken. This information is given in Table A.2.

Table A.2. Film pack proton energy of maximum sensitivity (ϵ) for each film, and time-of-flight (TOF) to the subject implosion d_o/v_p for $d_o = 1.2$cm.

Film	ϵ (MeV)	TOF (ns)
1	3.8	0.64
2	5.2	0.54
3	6.6	0.48
4	8.6	0.42
5	11.2	0.37
6	15.3	0.32
7	22.8	0.26
8	29.4	0.23
9	36.8	0.21
10	48.4	0.18
11	58.4	0.17

In future experiments, the magnification will be increased by decreasing d_o. In this case it is useful to show how the sample timing changes with d_o. The TOF curves for a range of proton energies, with chosen films marked (corresponding to Table A.2, are shown in Fig. A.10 for $d_o = 0.6, 0.9, 1.2$ cm.

Another film pack consideration is the film sensitivity to higher-energy protons, shown in Fig. A.9. The peak sensitivity (Fig. A.9) is narrow due to the Bragg peak, but the integrated tail as shown for a single film sensitivity is significant. The TNSA proton mechanism produces a falling

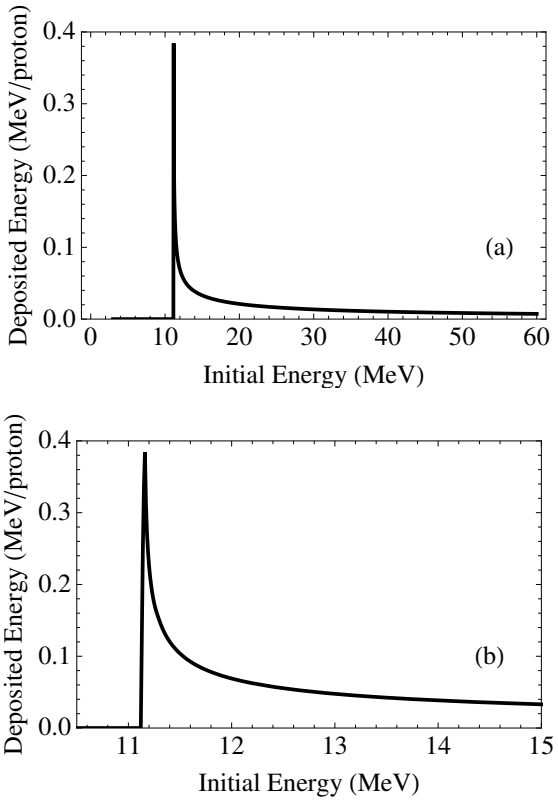

Figure A.9. (a) Deposited energy (sensitivity) versus proton energy for film 5, chosen as an example of typical behavior. (b) Zoomed in view of the peak structure.

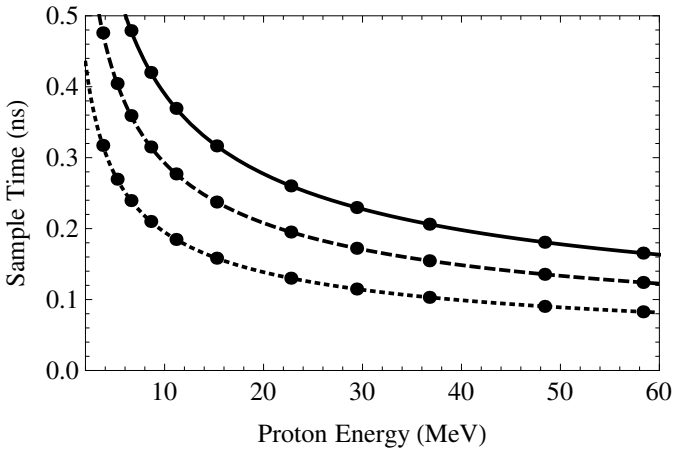

Figure A.10. Time-of-flight curves for d_o = 0.6cm (dotted line), = 0.9cm (dashed line), and = 1.2cm (solid line). The points mark specific films in this design (see Table A.2).

exponential energy distribution that suppresses detection of the high-energy tail. The approximate distribution is folded with the sensitivities calculated for each film, as shown in Fig. A.11 and A.12. In future shots, the last 2-3 films will be replaced by higher sensitivity Gafchromic® MD-V2-55 films.

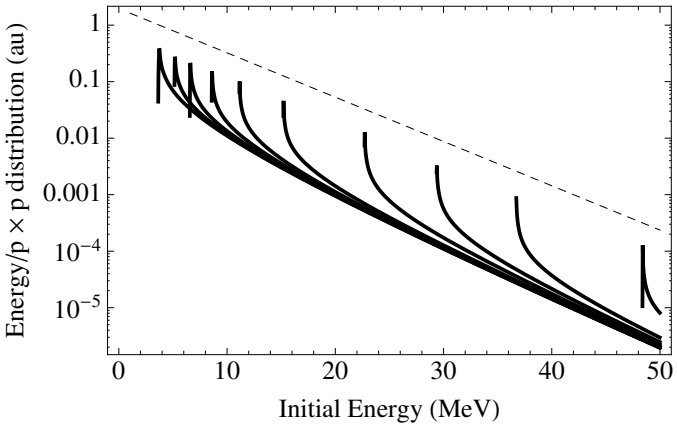

Figure A.11. Energy deposited per proton, folded with an assumed exponential proton distribution and plotted versus initial energy. Ten of eleven films are shown, from film 1 to 10 from left to right (Film 11 is off scale to the right). The dashed line represents the assumed exponential normalized source distribution[19].

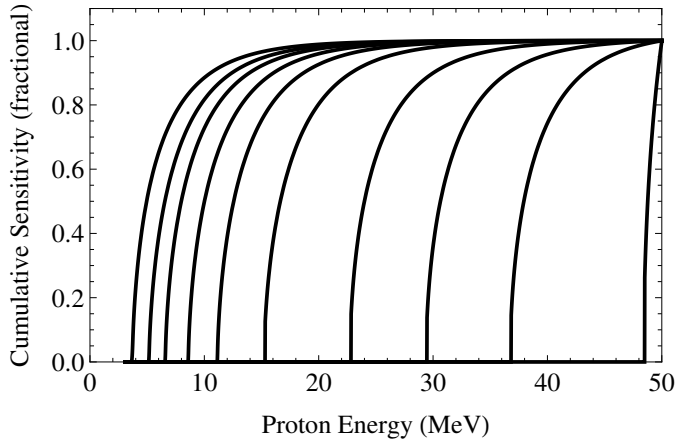

Figure A.12. Cumulative energy deposited for protons with energy $\leq E$ vs E (i.e. integration of Fig. A.11. Each film is normalized to the total energy deposited. Ten of eleven films are shown, from film 1 to 10 from left to right (Film 11 is off scale to the right).

In future experiments, the proton spectrum can be measured by taking a backlighter-only shot. With a microdensitometer or optical microscope to measure the film optical density and known film response, the exact proton fluence can be calculated using this sensitivity method[61].

A.6 Results

Using the techniques outlined in this Appendix, a series of radiographs were taken of the filamentary electromagnetic field structure around an imploded capsule. Four sequential films are shown in Fig. A.13. This data was taken with the film pack configured as discussed in Section A.5. A 17kJ shock ignition pulse (FIS3601P)[53] drove the capsule using all 60 OMEGA beams, and a 300J 1ps EP pulse generated the backlighting protons, using the backlighter design in Section A.3. For this shot $d_o = 1.2$cm and d_i=30cm, so the magnification was 26 and the RC film field of view was 3.8mm at the target plane. Timing of the short-pulse beam relative to the implosion drive, and subsequent proton sampling times, is shown in Fig. A.13e.

The filamentary structures that dominate the radiographs in Fig. A.13 are the result of proton deflections resulting from the Lorentz force. Large self-generated fields have been previously

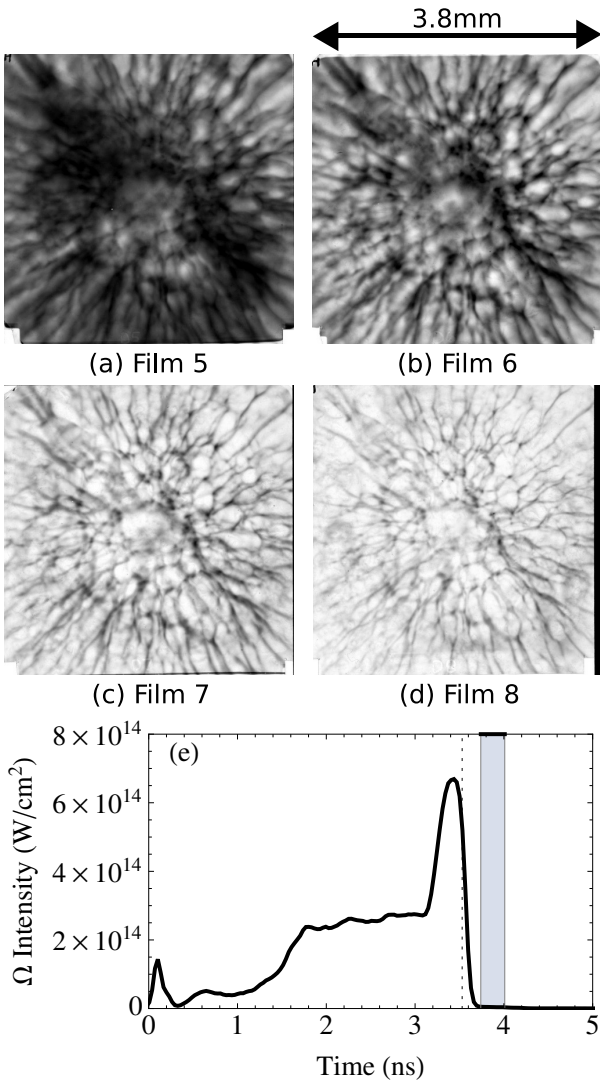

Figure A.13. (a-d) A series of radiographs of the filametary field structure around an imploded capsule (OMEGA shot 61250). For film energies and timing, see Table A.2. (e) Timing for OMEGA shot 61250, corresponding to radiographs presented in (a-d). The black curve represents the average OMEGA implosion drive intensity (pulse shape FIS3601P). The vertical dashed line shows when the EP short pulse beam was fired. The gray box represents the sample times for Films 3 through 9, which recorded useful data on this implosion (see also Table A.2).

observed in the coronae of directly-driven ICF implosions, and the physics of these fields has been studied by Séguin et al[62]. Previous TNSA-backlit implosions[3] did not show such filamentary structures, but other experiments have[4]. This was due to much lower laser intensity on the implosion target in these previous TNSA experiments, and demonstrates the importance of this backlighting capability for full-energy implosions. These filamentary structures are not seen in indirect-drive implosions[9]. Additionally, the protons are sensitive to the line integrated areal density between the backlighter and film through the charged-particle stopping power

$$\Delta E = \int \frac{dE}{d\rho R} \mathrm{d}\rho \mathrm{R}, \tag{A.4}$$

which will be used in future experiments.

A.7 Diagnosing failed radiography

If a radiography shot fails it is important to troubleshoot the failure with the smallest number of additional shots and least amount of time, given the experimental constraints at facilities like OMEGA and OMEGA EP. On a typical joint shot day, a PI can expect 6 ± 1 radiography shots. Two common failure modes were observed backlighting implosions: preplasma, and excessive beam divergence.

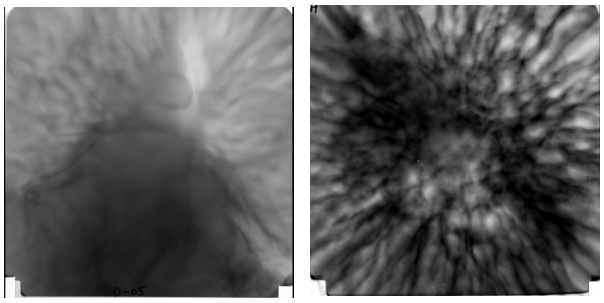

(a) Film 5, Shot 59141 (b) Film 5, Shot 61250

Figure A.14. Comparison of 60-beam OMEGA radiographs using backlighters without (left) and with (right) a preplasma shield, as discussed in Section A.3. The implosion is at the center of each image; (a) is dominated by large-scale diffuse structure when the coronal plasma interacts with the backlighter foil, and (b) is dominated by a radiograph of filamentary field structures around the implosion when the coronal plasma is shielded.

The preplasma issue, as discussed in Section A.3.1 and Fig. A.2, can seriously degrade the backlighter performance. When the coronal plasma interferes with the EP beam propagation, the proton beam emission is more diffuse, and the highest energy proton produced is low (10-20 MeV instead of ~ 50). Diffuse large-scale structures have been observed in this case, as shown in Fig. A.14. The left image of Fig. A.14 shows a radiograph where the backlighter did not have a preplasma shield, and the right image had a shield as discussed in Section A.3. On the left some filamentary structure is observed in the top left and top right, but most of the image is dominated by a large diffuse structure resulting from the coronal plasma interaction with the backlighter. On the right, with a shield, a radiograph of the entire implosion is obtained, demonstrating the backlighter performance improved with the shield.

If the film pack is too far away (d_i is too large) then the divergence of the TNSA proton beam causes the fluence on the detector to be too low. If this is the case, then it affects the high-energy

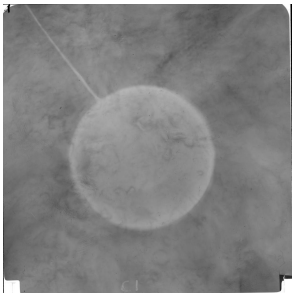

Figure A.15. Film 1, $d_i = 69$cm, OMEGA shot 61247. The image is of an undriven implosion. In this case, d_i is too large so only the lowest-proton-energy film recorded useful data because of the beam divergence. On a nominal performance backlighter shot, with d_i optimized, Film 1 saturates.

films first due to the exponential distribution. Thus a low proton energy cutoff ($10-20$ MeV instead of ~ 50) but sharp radiographs at low energy results from d_i being too large. This is shown in Fig. A.15, a radiograph of an unimploded capsule with the lowest energy film at $d_i = 69$ cm. The higher energy films did not have visible radiographs. With an optimal distance of 30 cm, the higher fluence saturates the lowest energy film but at higher energies excellent radiographs are obtained (shown in Fig. A.13).

A.8 Backlighter Uniformity

Recent data taken demonstrates the general uniformity of the TNSA backlighter. This data is shown in Fig. A.16. The image is from a 40J 1ps short-pulse shot onto a normal backlighter target, but without an implosion target in place. The primary purpose of the shot was facility timing. We can see low-amplitude large-scale spatial variations of the order of the image size, but no higher-order source nonuniformities that could be confused with physics effects seen in the implosion (Fig. A.13).

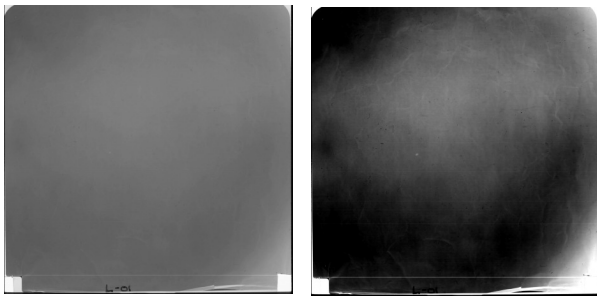

Figure A.16. Film 1, OMEGA Shot 63031. (a) normal film scan, (b) enhanced contrast image. The EP backlighter was fired at reduced energy (40J) for timing purposes without an implosion target in place. This experiment gave a measurement of the backlighter uniformity. Here we can see some low-amplitude large-scale spatial non-uniformities, but clearly distinct from implosion effects in Fig. A.13.

In future experiments this could be investigated for a full-energy backlighter drive, which was not done in present experiments due to a limited number of shots. Additionally, in experiments where precise spectral information is required, a source proton spectrum could be measured on a

similar full-energy null shot. This would be particularly important for measuring areal densities of imploded shells with proton backlighters.

A.9 Conclusions and Future Work

Petawatt-class lasers with kilojoule-picosecond pulses offer new opportunities for ICF and HEDP radiography, using the TNSA mechanism for proton backlighting. This technique offers better spatial and temporal resolution but poorer spatial uniformity and energy resolution than previous fusion-based proton backlighters. It also offers a wide range of proton energies, which is beneficial for mapping out field structures in ICF and HEDP plasmas. We present the first results of using TNSA proton backlighting to image 60-beam OMEGA implosions. In such experiments there are several challenges to using the TNSA mechanism to generate backlighting protons, such as avoiding preplasma, crosstalk, return current, and optimizing the experimental configuration to achieve the desired magnification, timing, and fluence at the radiochromic film detector. This work presents solutions to these issues that will allow future joint OMEGA and OMEGA EP experiments to use TNSA backlighting to study ICF and HEDP physics. In contrast to previous TNSA implosion radiography[3], we observe strong filamentary EM field structures[62] around the implosion that result from higher implosion drive intensity and illustrate the need for the capability to backlight full-energy implosions.

This technique will be applied to study shock propagation in shock ignition implosions at OMEGA, in particular using high-energy protons to probe the electromagnetic field structure at the shock front. The improved spatial and temporal resolution will be used to study electromagnetic fields in hohlraums around the laser entrance hole (LEH) and at plasma bubbles formed at the wall, expanding on previous efforts[8–10].

The future NIF Advanced Radiographic Capability (ARC)[63] will allow the study of full-scale NIF experiments using a petawatt-class laser. Radiography using NIF ARC will be at similar backlighter drive conditions to OMEGA EP (kilojoule-picosecond pulses), and with additional but similar challenges to those discussed in this work due to 60 times more subject drive energy at NIF. NIF ARC proton radiography will provide an important tool for studies of electromagnetic field structures in megajoule indirect- and direct- drive implosions. It will be important to transfer experience with TNSA backlighting from full-scale joint OMEGA experiments, as discussed in this work, to future radiography experiments using ARC on the NIF.

A.10 References

1. R. Tommasini, A. MacPhee, D. Hey *et al.*, "Development of backlighting sources for a Compton radiography diagnostic of inertial confinement fusion targets (invited)," Rev. Sci. Instrum., **79**, 10E901 (2008).
2. F. Marshall, P. McKenty, J. Delettrez *et al.*, "Plasma-Density Determination from X-Ray Radiography of Laser-Driven Spherical Implosions," Physical review letters, **102**(18), 185004 (2009).
3. A. J. Mackinnon, P. K. Patel, M. Borghesi *et al.*, "Proton Radiography of a Laser-Driven Implosion," Phys. Rev. Lett., **97**(4), 045001 (2006).
4. J. Rygg, F. Séguin, C. Li *et al.*, "Proton radiography of inertial fusion implosions," Science, **319**(5867), 1223 (2008).
5. C. Li, F. Seguin, J. Frenje *et al.*, "Monoenergetic proton backlighter for measuring E and B fields and for radiographing implosions and high-energy density plasmas (invited)," Rev. Sci. Instrum., **77** (2006).
6. C. Li, F. Séguin, J. Rygg *et al.*, "Monoenergetic-proton-radiography measurements of implosion dynamics in direct-drive inertial-confinement fusion," Physical review letters, **100**(22), 225001 (2008).

7. C. Li, F. Séguin, J. Frenje *et al.*, "Study of direct-drive capsule implosions in inertial confinement fusion with proton radiography," Plasma Physics and Controlled Fusion, **51**, 014003 (2009).
8. C. Li, F. Séguin, J. Frenje *et al.*, "Observations of electromagnetic fields and plasma flow in hohlraums with proton radiography," Physical review letters, **102**(20), 205001 (2009).
9. C. Li, F. Séguin, J. Frenje *et al.*, "Charged-Particle Probing of X-ray–Driven Inertial-Fusion Implosions," Science, **327**(5970), 1231 (2010).
10. C. Li, F. Séguin, J. Frenje *et al.*, "Diagnosing indirect-drive inertial-confinement-fusion implosions with charged particles," Plasma Physics and Controlled Fusion, **52**, 124027 (2010).
11. C. Li, F. Séguin, J. Frenje *et al.*, "Measuring E and B fields in laser-produced plasmas with monoenergetic proton radiography," Physical review letters, **97**(13), 135003 (2006).
12. C. Li, F. Séguin, J. Frenje *et al.*, "Observation of the decay dynamics and instabilities of megagauss field structures in laser-produced plasmas," Physical review letters, **99**(1), 15001 (2007).
13. C. Li, F. Séguin, J. Frenje *et al.*, "Observation of megagauss-field topology changes due to magnetic reconnection in laser-produced plasmas," Physical review letters, **99**(5), 55001 (2007).
14. R. Petrasso, C. Li, F. Seguin *et al.*, "Lorentz Mapping of Magnetic Fields in Hot Dense Plasmas," Physical review letters, **103**(8), 85001 (2009).
15. C. Li, F. Séguin, J. Frenje *et al.*, "Proton radiography of dynamic electric and magnetic fields in laser-produced high-energy-density plasmas," Physics of Plasmas, **16**, 056304 (2009).
16. J. Badziak, "Laser-driven generation of fast particles," Opto-Electronics Review, **15**(1), 1–12 (2007).
17. P. Norreys, "Laser-driven particle acceleration," Nature Photonics, **3**(8), 423–425 (2009).
18. S. Hatchett, C. Brown, T. Cowan *et al.*, "Electron, photon, and ion beams from the relativistic interaction of Petawatt laser pulses with solid targets," Physics of Plasmas, **7**, 2076 (2000).
19. R. Snavely, M. Key, S. Hatchett *et al.*, "Intense high-energy proton beams from petawatt-laser irradiation of solids," Physical Review Letters, **85**(14), 2945–2948 (2000).
20. A. Fews, P. Norreys, F. Beg *et al.*, "Plasma ion emission from high intensity picosecond laser pulse interactions with solid targets," Physical review letters, **73**(13), 1801–1804 (1994).
21. K. Krushelnick, E. Clark, M. Zepf *et al.*, "Energetic proton production from relativistic laser interaction with high density plasmas," Physics of Plasmas, **7**, 2055 (2000).
22. A. Maksimchuk, S. Gu, K. Flippo *et al.*, "Forward ion acceleration in thin films driven by a high-intensity laser," Physical Review Letters, **84**(18), 4108–4111 (2000).
23. A. Mackinnon, M. Borghesi, S. Hatchett *et al.*, "Effect of plasma scale length on multi-MeV proton production by intense laser pulses," Physical Review Letters, **86**(9), 1769–1772 (2001).
24. A. Mackinnon, Y. Sentoku, P. Patel *et al.*, "Enhancement of proton acceleration by hot-electron recirculation in thin foils irradiated by ultraintense laser pulses," Physical review letters, **88**(21), 215006 (2002).
25. M. Roth, A. Blazevic, M. Geissel *et al.*, "Energetic ions generated by laser pulses: A detailed study on target properties," Physical Review Special Topics-Accelerators and Beams, **5**(6), 61301 (2002).
26. M. Roth, M. Allen, P. Audebert *et al.*, "The generation of high-quality, intense ion beams by ultra-intense lasers," Plasma physics and controlled fusion, **44**, B99 (2002).
27. M. Zepf, E. Clark, F. Beg *et al.*, "Proton acceleration from high-intensity laser interactions with thin foil targets," Physical review letters, **90**(6), 64801 (2003).
28. M. Allen, P. Patel, A. Mackinnon *et al.*, "Direct experimental evidence of back-surface ion acceleration from laser-irradiated gold foils," Physical review letters, **93**(26), 265004 (2004).
29. M. Borghesi, A. J. Mackinnon, D. H. Campbell *et al.*, "Multi-MeV Proton Source Investigations in Ultraintense Laser-Foil Interactions," Phys. Rev. Lett., **92**(5), 055003 (2004).
30. J. Fuchs, P. Antici, E. D'Humieres *et al.*, "Laser-driven proton scaling laws and new paths towards energy increase," Nature Physics, **2**(1), 48–54 (2005).
31. J. Fuchs, Y. Sentoku, S. Karsch *et al.*, "Comparison of laser ion acceleration from the front and rear surfaces of thin foils," Physical Review Letters, **94**(4), 45004 (2005).
32. L. Romagnani, J. Fuchs, M. Borghesi *et al.*, "Dynamics of electric fields driving the laser acceleration of multi-MeV protons," Physical review letters, **95**(19), 195001 (2005).

33. M. Borghesi, J. Fuchs, S. Bulanov *et al.*, "Fast ion generation by high-intensity laser irradiation of solid targets and applications," Fusion science and technology, **49**(3), 412–439 (2006).
34. D. Neely, P. Foster, A. Robinson *et al.*, "Enhanced proton beams from ultrathin targets driven by high contrast laser pulses," Applied physics letters, **89**, 021502 (2006).
35. S. Kar, K. Markey, P. T. Simpson *et al.*, "Dynamic Control of Laser-Produced Proton Beams," Phys. Rev. Lett., **100**(10), 105004 (2008).
36. K. Flippo, T. Bartal, F. Beg *et al.*, "Omega EP, laser scalings and the 60 MeV barrier: First observations of ion acceleration performance in the 10 picosecond kilojoule short-pulse regime," in "Journal of Physics: Conference Series," volume 244 (2010).
37. L. Willingale, G. M. Petrov, A. Maksimchuk *et al.*, "Front versus rear side light-ion acceleration from high-intensity lasersolid interactions," Plasma Physics and Controlled Fusion, **53**(1), 014011 (2011).
38. A. Pukhov, "Three-dimensional simulations of ion acceleration from a foil irradiated by a short-pulse laser," Physical Review Letters, **86**(16), 3562–3565 (2001).
39. S. Wilks, A. Langdon, T. Cowan *et al.*, "Energetic proton generation in ultra-intense laser–solid interactions," Physics of Plasmas, **8**, 542 (2001).
40. Y. Sentoku, T. Cowan, A. Kemp *et al.*, "High energy proton acceleration in interaction of short laser pulse with dense plasma target," Physics of Plasmas, **10**, 2009 (2003).
41. G. M. Petrov, L. Willingale, J. Davis *et al.*, "The impact of contaminants on laser-driven light ion acceleration," Physics of Plasmas, **17**(10), 103111 (2010).
42. K. FLIPPO, B. HEGELICH, B. ALBRIGHT *et al.*, "Laser-driven ion accelerators: Spectral control, monoenergetic ions and new acceleration mechanisms," Laser and Particle Beams, **25**, 3–8 (2007).
43. M. Roth, T. Cowan, M. Key *et al.*, "Fast ignition by intense laser-accelerated proton beams," Physical Review Letters, **86**(3), 436–439 (2001).
44. E. Clark, K. Krushelnick, J. Davies *et al.*, "Measurements of energetic proton transport through magnetized plasma from intense laser interactions with solids," Physical Review Letters, **84**(4), 670–673 (2000).
45. M. Borghesi, A. Schiavi, D. Campbell *et al.*, "Proton imaging: a diagnostic for inertial confinement fusion/fast ignitor studies," Plasma physics and controlled fusion, **43**, A267 (2001).
46. M. Borghesi, D. Campbell, A. Schiavi *et al.*, "Electric field detection in laser-plasma interaction experiments via the proton imaging technique," Physics of Plasmas, **9**, 2214 (2002).
47. J. Cobble, R. Johnson, T. Cowan *et al.*, "High resolution laser-driven proton radiography," Journal of applied physics, **92**, 1775 (2002).
48. L. Willingale, A. Thomas, P. Nilson *et al.*, "Fast advection of magnetic fields by hot electrons," Physical Review Letters, **105**(9), 95001 (2010).
49. L. Willingale, P. Nilson, M. Kaluza *et al.*, "Proton deflectometry of a magnetic reconnection geometry," Physics of Plasmas, **17**, 043104 (2010).
50. L. Willingale, P. Nilson, A. Thomas *et al.*, "High-Power, Kilojoule Class Laser Channeling in Millimeter-Scale Underdense Plasma," Physical Review Letters, **106**(10), 105002 (2011).
51. M. Kaluza, J. Schreiber, M. Santala *et al.*, "Influence of the laser prepulse on proton acceleration in thin-foil experiments," Physical Review Letters, **93**(4), 45003 (2004).
52. A. J. Mackinnon, P. K. Patel, R. P. Town *et al.*, "Proton radiography as an electromagnetic field and density perturbation diagnostic (invited)," Rev. Sci. Instrum., **75**(10), 3531–3536 (2004).
53. R. Betti, C. D. Zhou, K. S. Anderson *et al.*, "Shock Ignition of Thermonuclear Fuel with High Areal Density," Phys. Rev. Lett., **98**, 155001 (2007).
54. S. Skupsky, R. W. Short, T. Kessler *et al.*, "Improved laser-beam uniformity using the angular dispersion of frequency-modulated light," Journal of Applied Physics, **66**(8), 3456–3462 (1989).
55. Y. Lin, G. N. Lawrence and T. J. Kessler, "Distributed phase plates for super-Gaussian focal-plane irradiance profiles," Opt. Lett., **20**(7), 764–766 (1995).
56. D. Meyerhofer, R. McCrory, R. Betti *et al.*, "High-performance inertial confinement fusion target implosions on OMEGA," Nuclear Fusion, **51**(5), 053010 (2011).
57. D. K. Bradley, P. M. Bell, J. D. Kilkenny *et al.*, "High-speed gated x-ray imaging for ICF target experiments (invited)," Rev. Sci. Instrum., **63**(10), 4813–4817 (1992).

58. "Ashland corp." http://www.gafchromic.com/ (2012).

59. "Goodfellow corp." http://www.goodfellow.com/ (2012).

60. J. Ziegler, J. Biersack and U. Littmark, *The stopping and range of ions in matter* (Pergamon, New York, 1985).

61. D. Hey, M. Key, A. Mackinnon *et al.*, "Use of GafChromic film to diagnose laser generated proton beams," Rev. Sci. Instrum., **79**, 053501 (2008).

62. F. H. Séguin, C. K. Li, M. J.-E. Manuel *et al.*, "Time evolution of filamentation and self-generated fields in the coronae of directly driven inertial-confinement fusion capsules," Physics of Plasmas, **19**(1), 012701 (2012).

63. C. Barty, M. Key, J. Britten *et al.*, "An overview of LLNL high-energy short-pulse technology for advanced radiography of laser fusion experiments," Nuclear Fusion, **44**(12), S266 (2004).

Appendix B

A compact neutron spectrometer for characterizing inertial confinement fusion implosions at OMEGA and the NIF

B.1 Introduction

In ICF implosions at OMEGA[1] and the National Ignition Facility (NIF)[2] (see Chapter 1), the spherical shell of fuel is ablatively driven inwards at implosion velocities of $\sim$ 370 km/s. This imploding shell is decelerated by the hot spot, which reaches pressures of $\sim$ 300 GBar in ideal fusion target designs[3–5]. Efficient conversion of this implosion kinetic energy into hot spot thermal energy is essential for achieving ignition. Any residual fuel kinetic energy at peak compression represents a deficit in thermal energy, which will significantly reduce the fusion burn rate in the hot spot and can cause the implosion to fail to ignite.

Neutron spectroscopy has been identified as a promising technique for diagnosing residual kinetic energy in the fuel[6,7], in addition to well-established measurements of areal density, total yield, and ion temperature[8]. Neutron spectroscopy techniques in-use at the OMEGA and NIF facilities include neutron time-of-flight (nTOF)[9,10], nuclear activation[11,12], and recoil spectroscopy[13–18].

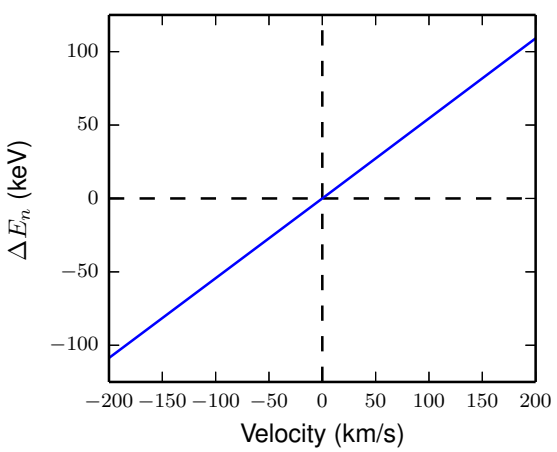

Figure B.1. Neutron Doppler shift (ΔE_n) versus fuel bulk velocity in the direction of the spectrometer.

The primary signature of residual kinetic energy would be a Doppler shift of the neutron spectrum; for relevant conditions the Doppler shift is approximately linear through relativistic kinematics (see Appendix B.2). This is shown in Fig. B.1 for neutrons produced via the deuterium-tritium

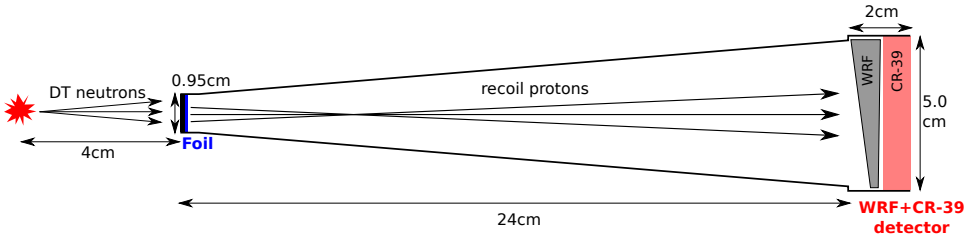

Figure B.2. Conceptual spectrometer design. A small fraction of the DT neutrons generated in the implosion (at left) hit a CH_2 foil, and elastically scatter protons. Forward-scattered protons are detected by a wedge-range-filter (WRF) and CR-39 package (far right). From the measured recoil-proton spectrum, the spectrum of the emitted neutrons can be inferred. The dimensions shown are for an optimal design at OMEGA-relevant conditions.

(DT) fusion reaction, expressed as

$$\mathrm{D} + \mathrm{T} \;\rightarrow\; \alpha + \mathrm{n}\ (14.03\ \mathrm{MeV}), \tag{B.1}$$

where the neutron birth energy is 14.03 MeV at zero temperature and is upshifted for finite temperatures[19]. The spectral Doppler shifts will be of order a few tens of keV for DT neutrons if the residual velocity is a significant fraction of the 370 km/s implosion velocity at NIF.The magnitude of observed energy shift depends on the direction of bulk flow velocity ($\vec{v_b}$) relative to the detector ($\hat{r}$):

$$v = \vec{v_b} \cdot \hat{r} = v_b \cos\theta, \tag{B.2}$$

which necessitates that spectrometers be placed in at least three quasi-orthogonal lines of sight to fully diagnose residual kinetic energy through Doppler shifts of the mean neutron energy. As shown by Eq. B.2, a single detector is only sensitive to the velocity collinear with the line of sight. In recent experiments at the NIF velocities (Doppler shifts) up to $\sim$ 200 km/s (100 keV) have been observed[6]. The ignition point design[4] accelerates $\sim$ 0.17 mg of DT fuel to an implosion velocity $\sim$ 370 km/s corresponding to 11kJ of kinetic energy. Diagnosing residual kinetic energy of 250(1000)J, representing approximately 2.5(10)% of the total kinetic energy, would correspond to bulk velocities of $\sim$ 50(100) km/s or neutron Doppler shifts of $\sim$ 25(50) keV. For NIF, this suggests a desired measurement accuracy of $\pm$50 keV or more ideally $\pm$20 keV.

This paper describes a new uniquely-compact neutron spectrometer based on the recoil technique for diagnosing ICF implosions. A CH foil is used to generate recoil protons, which are detected with a Wedge Range Filter proton spectrometer[20,21]. This design is advantageous for measurements of the residual kinetic energy, since many spectrometers could easily be fielded around the implosion. The proton spectrometer is unshielded (exposed directly to the primary neutron flux), allowing S/B of order 1 for the primary neutron peak[13]. This is in contrast to the 'magnetic recoil spectrometer' (MRS) system using dipole magnetic dispersion[13–15], which improves the S/B significantly since the charged particles can be bent around shielding to reduce background[15,22]. However, the MRS is a large investment, and only one has been built on each facility (OMEGA and the NIF). Recoil spectrometers have also been developed at other facilities using telescope systems[23–26]. We note that we have also developed a related concept[27] for a compact spectrometer designed for lower-energy neutrons($\sim 1-5$ MeV).

This paper is organized as follows: Section B.3 describes the concept and design of the instrument, Section B.4 presents response calculations for data analysis, Section B.5 reports data from the first use of this system on OMEGA, applications of this diagnostic to ICF physics are discussed

in Section B.9, and the paper is concluded in Section B.10.

B.2 Neutron Kinematics

The fusion kinematics used in this work follow the relativistic calculations of Ballabio (Ref. [28]), which provide small corrections to the standard classical kinematics [19]. In particular, for the mean neutron birth energy E_n and width σ_n we use Eqs. 10 and 17 respectively of Ref. [28].

The mean neutron birth energy $E_n(T_i)$ is used to calculate the initial velocity: $\gamma_0 = 1 + E_n/(m_n c^2)$ and $v_0 = c\sqrt{1-\gamma_0^{-2}}$. For a given bulk velocity v_b in the detector direction the velocities add relativistically:

$$v' = \frac{v_0 + v_b}{1 + v_0 v_b/c^2},\ \gamma' = 1/\sqrt{1-(v'/c)^2}, \tag{B.3}$$

with Doppler shifted energy given by

$$E_n' = (\gamma' - 1)m_n c^2,\ \Delta E_n = E_n' - E_n, \tag{B.4}$$

where ΔE_n is the energy shift as plotted in Fig. B.1.

For the effect of symmetric radial fuel velocity $\vec{v} = v_r \hat{r}$ with v_r constant, the center of mass of the implosion is not moving but the width of the neutron spectrum will be broadened by the radial velocity. With the detector at $\theta = \phi = 0$ in spherical coordinates, the broadened spectrum is given by:

$$Y_n'(E) = \int_0^{\pi} d\theta \sin\theta \int_0^{2\pi} d\phi \frac{1}{\sqrt{2\pi}\sigma_n} e^{-[E - E_n'(v_r \cos\theta)]^2/2\sigma_n^2}, \tag{B.5}$$

where for a given location θ, ϕ the neutron spectrum is taken as Gaussian in shape with intrinsic thermal birth width σ_n and shifted energy E_n' using $v_b = v_r \cos\theta$ in the analysis of Eqs. B.3 and B.4. The resulting spectrum $Y_n'(E)$ is evaluated numerically. Example calculations with v_r =0, 100, and 200 km/s are shown in Fig. B.3.

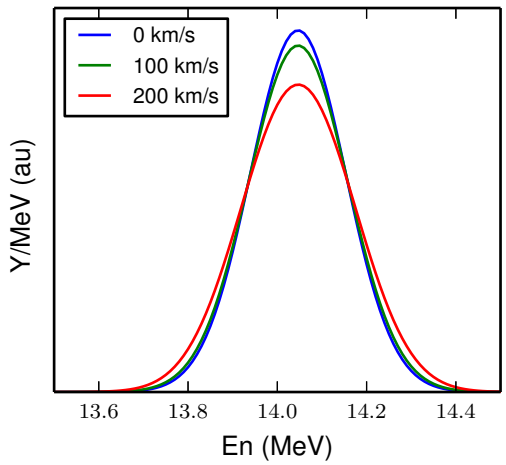

Figure B.3. Neutron spectra for symmetric radial flow velocities of 0, 100, and 200 km/s with T_i = 5 keV. Spectra are area normalized.

From the calculated spectrum with radial flow, a Gaussian width σ_n' is calculated, and the extra width due to the radial flow σ_r is obtained from:

$$\sigma_r = \sqrt{\sigma_n'^2 - \sigma_n^2}. \tag{B.6}$$

The additional broadening due to radial flow is plotted in Fig. B.4

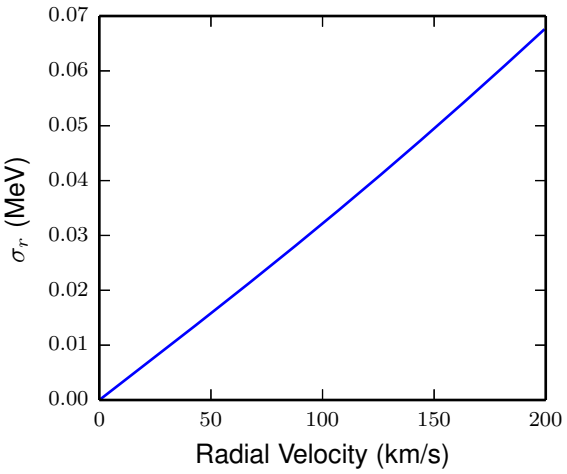

Figure B.4. Extra broadening in the observed neutron spectrum caused by symmetric radial flow.

B.3 Spectrometer Design

The conceptual design of the instrument is shown in Fig. B.2. A small fraction of the neutrons emitted from the implosion hit a foil, in this case CH_2, and elastically scatter protons, some of which are detected by a proton spectrometer (WRF+CR-39).

The energy of a recoil proton is directly related to the incident neutron energy through the scattering angle, as described by

$$E_r = E_n \cos^2 \theta, \tag{B.7}$$

where E_r and E_n are the recoil and neutron energies, respectively, and θ is the scattering angle. Given the geometry, the detector efficiency can be written semi-analytically[15], but the characterization of the energy response will depend on numerical modeling of the charged-particle stopping powers in the foil[29] and also on the WRF response itself. Monte Carlo simulations are therefore used to model the instrument response function (IRF).

In this work, two types of proton spectrometers are used: an aluminum or 'Al' wedge which varies in thickness from $\sim$ 140 to 2000μm and is approximately 2 cm square in lateral dimensions, and a ceramic (alumina) narrow-band 'NB' wedge which varies in thickness from $\sim$ 100 to 800μm with lateral dimensions of $\sim 1 \times 4$ cm. For the NB wedges, the dispersion direction is the longer axis, and two wedges can be run simultaneously and adjacently within a single package. Both designs were tested; the NB WRFs have a higher efficiency at the cost of less energy resolution. Positioned behind the wedge material is a piece of CR-39 solid-state nuclear track detector[30–32], which records the location and energy of the protons that have penetrated the wedge. From the CR-39 track distribution, a proton energy spectrum is inferred[20,21]. Each wedge is individually calibrated on an electrostatic accelerator fusion product source[33].

The key parameters for the instrument are the foil dimensions (diameter and thickness), foil distance from the implosion, detector lateral dimensions, and foil-to-detector distance. It is important to note that there is a direct tradeoff between energy resolution and detection efficiency[34]. To find the optimal design for the instrument, series of simulations were conducted in which the key parameters were varied until maximum efficiency for a specified energy resolution was found. This modeling was also constrained by the geometric limits of TIM diagnostics on the OMEGA facility,

and with the requirement that S/B must be $\gtrsim 0.5$ for OMEGA experiments with $Y_n = 10^{12} - 10^{13}$. For these conditions, the optimal design is a foil radius of $\sim$ 1cm, with the foil positioned $\sim$ 4cm from the implosion, and a foil-detector distance of $\sim$ 25cm. Additionally, the existing WRF designs[20,21] were found to perform adequately, and are thus used in this design.

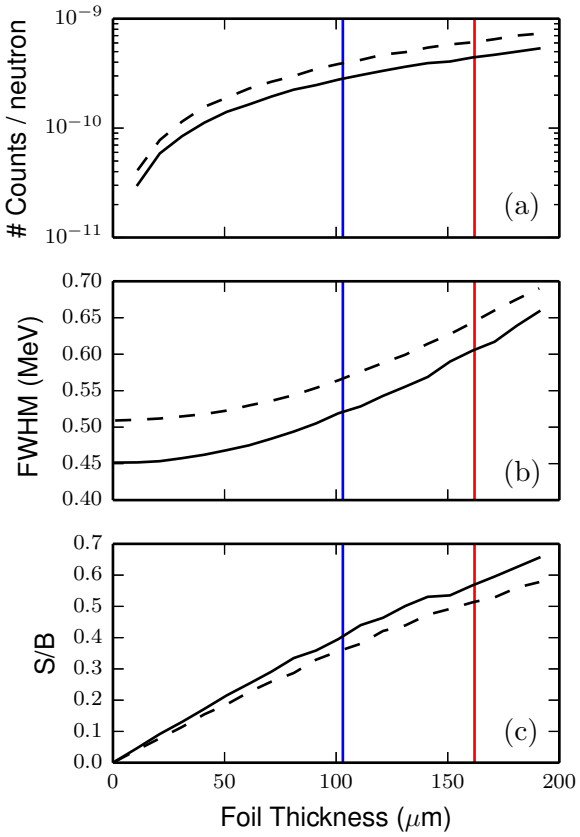

Figure B.5. Performance of the optimal nWRF design as a function of foil thickness. **(a)** Number of counts recorded per neutron generated (efficiency). **(b)** Resolution, shown as FWHM. For thin foils, the resolution is dominated by geometric broadening and the WRF response. **(c)** Signal to background (S/B). In all plots, solid curves correspond to Al WRFs and dashed curves correspond to NarrowBand (NB) WRFs. Foils used in the experiments (Sec. B.5) are shown by blue (103μm) and red (162μm) vertical lines.

Depending on application and experimental goals, the foil thickness can be changed easily , affecting the number of counts recorded, S/B, and resolution. This is shown in Fig. B.5 for both types of WRF (Al and NB), where these three quantities are plotted for foil thicknesses up to 200μm. For very thin foils, the instrument resolution (FWHM) is dominated by 'geometrical broadening', where the proton spectrometer sees a range of recoil angles due to the lateral spatial extent of the foil (see Fig. B.2 and Eq. B.7). Since the signal and primary source of background (direct neutron interaction, see Appendix B.7) scale linearly with primary yield, S/B depends only on the instrument configuration.

The final dimensions are shown in Fig. B.2. The engineering design is based on a x-ray camera already in use on the OMEGA facility. A CAD drawing of the instrument is shown in Fig. B.6. The WRF proton spectrometer is held in a detector pack, while the foil is assembled as a 'nose cone' at the front of the instrument. A 1mm thick Ta blast filter is placed between TCC and the foil. Images of the foil assembly and detector pack are shown in Fig B.6b-d. The foil and detector can be changed between shots. For different experimental conditions (for example, either lower or higher yields) different optimal designs can be used.

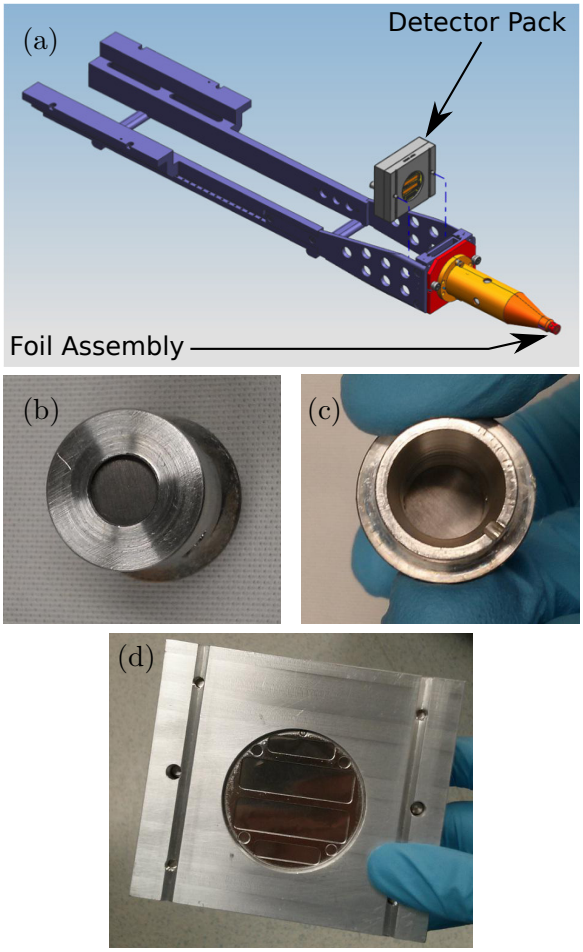

Figure B.6. **(a)** 3-D CAD model of the instrument. The proton spectrometer is housed in the gray box, which is attached at the rear of a conical nose assembly. The foil assembly is at the tip in the lower right. The rail structures in the upper left interface with the facility instrument manipulator. **(b-c)** Photos of a sample foil assembly, viewed from and towards TCC respectively. **(d)** Detector pack. A NB WRF proton spectrometer is held at the center.

B.4 Instrument Response Function (IRF) modeling

A Monte Carlo code is used to simulate the n-p scattering in the foil, ranging of the recoil protons in the foil, transport of the recoil protons through the diagnostic geometry to the WRF detector, and the response of the WRF detector to protons. For a given neutron energy, recoil protons are tracked and the proton spectrometer response is simulated, such that an apparent proton spectrum on the detector is calculated for a given neutron energy. This is shown in Fig. B.7 for 14.05 MeV neutrons incident on two foils (103 and 162 μm thick) and for both types of WRF used (Al and NB).

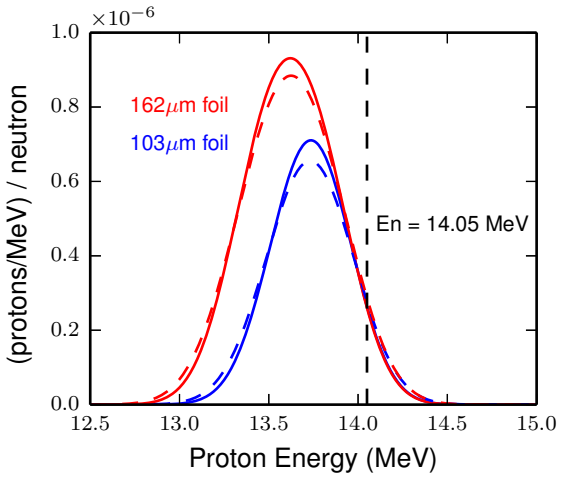

Figure B.7. Proton spectrum for 14.05 MeV monoenergetic neutrons. Shown are calculations for 103μm (blue) and 162μm (red) thick foils. Solid spectra are for Al WRFs, and dashed spectra are for NB WRFs.

The curves in Fig. B.7 are normalized per neutron produced, and the apparent proton yield is calculated as a 4π equivalent yield*. Using the 162μm foil results in more proton signal due to the higher areal number density of the thicker foil. Similarly, the thicker foil generates a lower average proton energy, since the emerging protons are on average downshifted more in the thicker foil. The slight differences between WRF types arise from subtle differences in the WRF geometry, which affects the scattering angles for protons used in the analysis.

To calculate an IRF, a series of calculations are performed for the neutron energy range of interest, with a proton spectrum calculated for each neutron energy, thus generating a response matrix. In the data analysis, we convolve a trial Gaussian neutron spectrum with the IRF matrix to calculate a modeled proton spectrum. Thus, we can forward fit the data using the IRF.

B.5 OMEGA Results

A series of eight implosions were conducted on the OMEGA laser to test this new spectrometer. The targets used were 15μm thick CH shells with a diameter of 865μm, filled with 15atm of approximately equimolar DT gas. The targets were driven using 60 laser beams at 351nm wavelength, with a 1ns square laser pulse, 25.4 kJ average energy, and SSD[35], DPR[36], and SG4 DPP[37] smoothing techniques. These targets are commonly used for diagnostic development, and typically produce $(2-3)\times10^{13}$ DT-n and ion temperatures ~ 6 keV. Both types of WRF (Al and NB) and the two foil thicknesses (103 and 162 μm) were used in these first tests. Sample data for shot 70740 using a

*A 4π equivalent yield being the local value of fluence / steradian multiplied by 4π. This is convenient for forward-fitting the WRF analysis, which implicitly assumes isotropic emission.

Al WRF and a 103μm foil are shown in Fig. B.8. The data are shown with error bars. The modeled neutron spectrum (red, Gaussian in shape) is convolved with the IRF to produce a modeled proton spectrum (blue). The inferred neutron yield is $Y_n = (3.4 \pm 0.4) \times 10^{13}$, the neutron energy is $E_n = 14.05 \pm 0.06_{ran} \pm 0.05_{sys}$ MeV, and the width of the neutron spectrum is $\sigma_n = 0.19 \pm 0.06$ MeV.

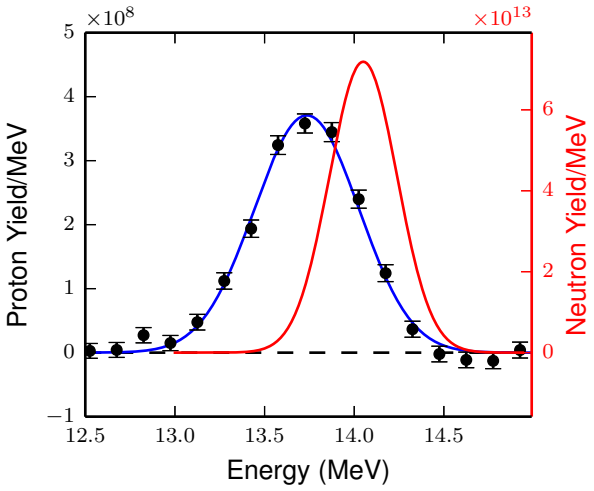

Figure B.8. Forward fit analysis of shot 70740, using a Al WRF and 103μm foil. The modeled neutron spectrum (red) is convolved with the IRF and adjusted to generate the best fit modeled proton spectrum (blue). The reduced χ^2 for the fit is 0.98.

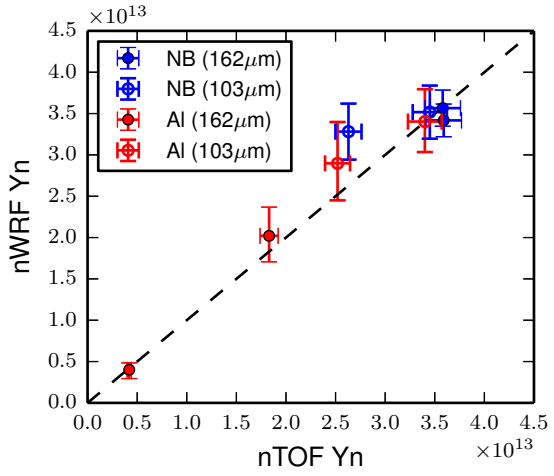

Figure B.9. Neutron yields measured by the nWRF versus standard nTOF neutron yield, for both Al and NB wedges used with either a 103μm or 162μm foil.

As a first fidelity test, this data was compared to the yield measured by the standard suite of nTOF detectors on OMEGA. This comparison, which is shown in Fig. B.9 for all eight shots, indicate an excellent agreement between the two measurements. On one shot (70736) the yield was low compared to the typical $(2-3) \times 10^{13}$. The good agreement with the nTOF system demonstrates that the first-principles IRF calculations described in the previous section accurately capture the scattering dynamics well in the foil and recoil proton response.

For the neutron energy, there is no other diagnostic to readily compare to. The measured energies are shown relative to the mean for each WRF spectrometer in Fig B.10 for the Al (red) and NB (blue) WRFs, and for each foil thickness: 162μm at left, and 103μm at right. The error bars shown are random only. The systematic uncertainties primarily due to the WRF calibration using the accelerator technique[33] are too large for the applications of this diagnostic, and we therefore

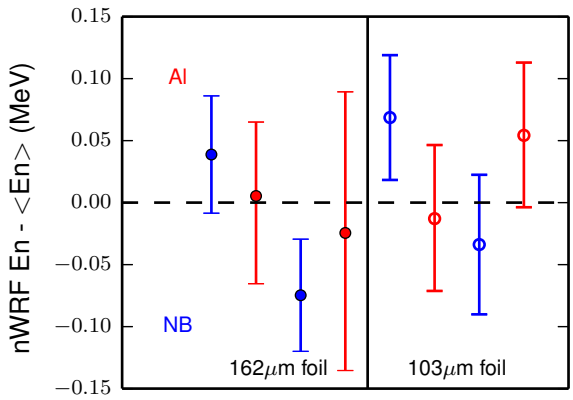

Figure B.10. Mean neutron energies measured with the nWRF spectrometer for all eight shots, relative to the mean for each WRF spectrometer measurement. Shots using the 162μm foil are shown to the left, and shots with the 103μm foil are shown to the right. The Al WRF data is shown in red, and the NB data in blue.

calibrate the system *in-situ* using symmetrically-driven low-convergence implosions.

B.6 Error Analysis

The measurement uncertainties are mainly due to uncertainties in the proton-spectrometer analysis and uncertainties in the forward fit to the proton spectrum. For shot 70740 (see Fig. B.8), the uncertainties in mean proton energy E_p, proton spectral width σ_p and proton yield Y_p are given in Table B.1, broken up into random, statistical, and systematic. The random uncertainties are normally distributed shot-to-shot errors, largely resulting from CR-39 response variation, which are separated from the purely statistical (i.e. counting) uncertainties.

Table B.1. Proton spectrometer uncertainties for shot 70740

Quantity	Random Uncertainty	Statistical Uncertainty	Systematic Uncertainty
E_p (MeV)	±0.050	±0.030	±0.050
σ_p (MeV)	±0.026	±0.030	-
Y_p	±6.6%	±10.3%	-

The statistical errors are retained as the error bars on the data points in the spectra (i.e. Fig. B.8), and thus propagate to an error in the forward fit, which is calculated through a χ^2 analysis of the best fit and thus also include additional uncertainty from the fit itself. The non-statistical random and systematic errors are separately propagated to the total uncertainties in derived neutron quantities. The neutron uncertainties are summarized in Table B.2.

B.7 Direct Neutron Background

The primary source of background in this measurement is direct neutron interaction with the WRF or the CR-39 detector; in either case neutrons can undergo (n,p) scattering or other reactions that generate particle tracks in the CR-39 detector, and which must be excluded in the analysis via

Table B.2. Neutron uncertainties for shot 70740

Quantity	Forward Fit† Uncertainty	Random‡ Uncertainty	Systematic Uncertainty
E_n (MeV)	$^{+0.032}_{-0.030}$	$^{+0.059}_{-0.058}$	± 0.053
σ_n (MeV)	$^{+0.044}_{-0.048}$	$^{+0.053}_{-0.056}$	-
Y_n	$^{+9.4}_{-9.1}\%$	$^{+11.5}_{-10.9}\%$	-

background subtraction. The S/B is a crucial metric for these sorts of systems, and understanding the background is essential.

Previous work[38] studied the fluence of direct neutron tracks in CR-39 detectors with aluminum filters in front of the CR-39, and the results from that study are directly applicable to the Al WRF data in this work. The background level is shown in Fig. B.11 as the fluence of background tracks on the CR-39 versus neutron yield.

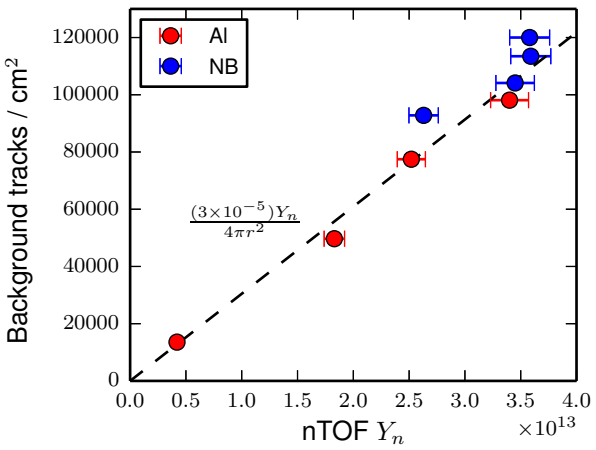

Figure B.11. Measured neutron background versus neutron yield, for the data in this work versus the expected scaling from Ref.[38] (dashed line).

As expected there is a clear linear relationship between the neutron yield and background level. Additionally, we show the background level that would be expected from the 'frontside' data of Ref.[38], for the 2h CR-39 etch time used in this work, that is $(3 \times 10^{-5})Y_n/(4\pi r^2)$ where $r = 28$cm is the distance from the implosion to the CR-39 detector. We see excellent agreement between the calibration of Ref.[38] and the observed background levels in this work. We note that the NB WRFs (which are made of alumina) could have a slightly different scaling relation between neutron yield and background level due to different neutron scattering cross-sections, which may be observed in Fig. B.11. This demonstrates that the background levels are well understood in this type of data.

At high neutron yields, signal and background track densities are high, necessitating short etch times to avoid track overlap.[39]

B.8 Ion Temperature and Radial Velocity

In the previous section we saw that the width of the neutron spectrum is related to both the ion temperature and any symmetric radial motion of the implosion. The forward-fit analysis (see Sec. B.5) calculates the Gaussian width σ with associated error bars. If that value is taken directly and used to infer the temperature we obtain the data shown in Fig. B.12, which is compared to the nTOF-measured Ti.

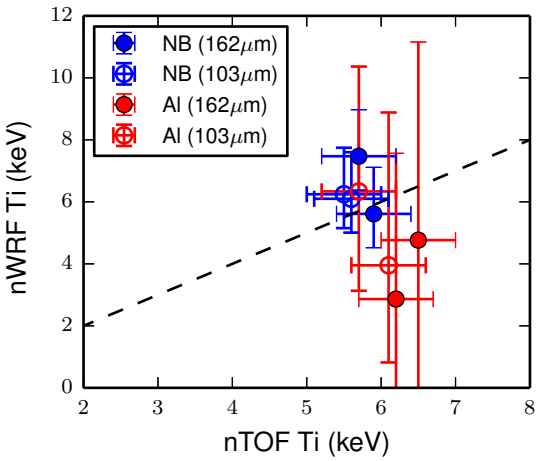

Figure B.12. Ion temperature determined from the nWRF data versus the standard nTOF measurement of T_i.

The large error bars associated with the nWRF T_i measurements result from the fact that the instrumental response width is larger than the thermal width for these conditions, and uncertainties in the width from the proton spectroscopy and forward fit are amplified since $T_i \propto \sigma^2$. The former is illustrated by Fig. B.13, which shows the 1σ widths for the instrument response (~ 250 keV), the thermal width (in red), and the total width (in blue). The curves are calculated for the 103μm foil. In this case, the thermal width dominates the instrumental only for $T_i \gtrsim 10$ keV. The NB WRFs perform better than the Al for the temperature determination (demonstrated by smaller error bars in Fig. B.12) due to smaller uncertainties in the proton spectroscopy for that design.[20,21]

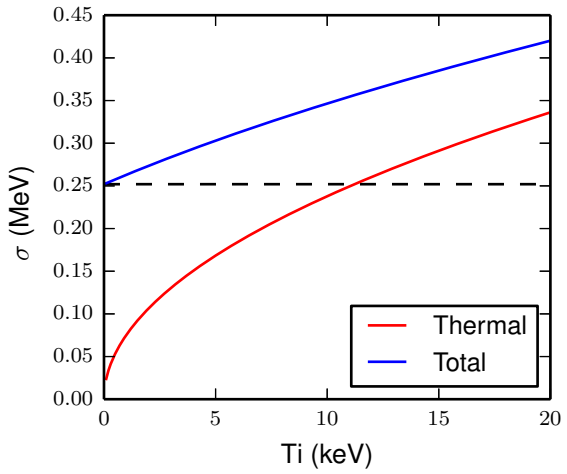

Figure B.13. Broadening (σ) from the instrumental response (dashed line), the thermal width (red), and the total resulting width (blue).

For thin-glass 'exploding pusher' targets on OMEGA, temperatures of $10 - 20$ keV can be achieved, and in this regime the current nWRF configuration would obtain a precise measurement

of T_i. Alternatively, thinner foil configurations could be explored to reduce the instrumental width, but at the cost of reduced S/B.

Using the width, symmetric radial flows could similarly be investigated, or differences in ion temperature at various lines of sight around the implosion could be investigated. This would also be a signature of residual kinetic energy. However, we can see in Fig. B.4 that the broadening from radial flow is small compared to both the instrumental width and thermal width for these experiments (see Fig. B.13). This implies that a measurement of symmetric radial flow velocities would require a significantly reduced instrumental width and implosions with much lower thermal widths, i.e. with $T_i \sim 1-2$ keV.

B.9 Applications

The primary application for this diagnostic is to measure the mean neutron energy precisely in several directions to infer the bulk velocity of the DT fuel. For this measurement, the uncertainties in mean energy must be reduced. For example, a velocity measurement to a precision of ± 50 km/s would require an uncertainty in neutron energy of about ± 30 keV (see Fig. B.1).

As mentioned in the previous section, systematic calibration uncertainties will be eliminated by shooting symmetric low-velocity implosions as a reference, and then shoot implosions of interest or implosions with seeded asymmetries and measure their relative velocity. This would eliminate systematic uncertainties. Another option being pursued is using a DT-n source[40] to calibrate the entire system to a much better precision than can be done currently.

The overall random error bars are $\sim \pm 50$ keV for this dataset, which is a result of a combination of fitting uncertainties and uncertainties in the WRF analysis (see Appendix B.6). With improved WRF detectors we expect to reduce this uncertainty to $\pm 30-40$ keV on a per-shot basis. This still corresponds to a fairly large velocity of $\pm 50-75$ km/s. Since these uncertainties are normally distributed, a series of several shots could be conducted at identical conditions to reduce the energy (velocity) uncertainty to approximately $15-20$ keV ($25-38$ km/s).

Since the implosion residual velocity vector is generally 3-D, at least 3 orthogonal lines of sight are required to determine the residual kinetic energy. On the OMEGA laser facility, this diagnostic is fielded in a TIM, and thus up to six could be fielded around an implosion with good 4π coverage to measure the velocity vector in 3-D. On the NIF, the x-ray imaging diagnostics fielded in the diagnostic manipulators (DIMs) could be modified to create a nWRF by replacing the pinhole assembly with a scattering foil, and the kinematic base filter pack with a WRF detector, forming a system with comparable dimensions to the system used on OMEGA in this work. The DIMs are located at target chamber coordinates (polar angle θ, azimuthal angle ϕ) of (0,0), (90,78), and (90,315). Fielded simultaneously in all three DIMs, this system could measure the 3-D velocity vector in NIF implosions.

The current nWRF design can operate between $10^{12}-10^{14}$ DT neutron yield on OMEGA, though the data presented in this work span $4\times10^{12}-4\times10^{13}$ (see Fig. B.9). At higher yields, CR-39 track saturation[39] is an issue, which can be mitigated by the use of thinner and/or smaller foils at the cost of the signal to background ratio. At lower yields, signal statistics can become poor, necessitating the use of thicker foils at the cost of poorer energy resolution. On the OMEGA facility, no current measurement of bulk velocity exists, so the implementation of this new diagnostic enables physics studies of residual kinetic energy. However, the instrument is incompatible with the stand-off requirements for cryogenic targets on OMEGA. The primary application on OMEGA is to use this instrument to benchmark implosion physics models by imposing known flux asymmetries on warm targets and accurately measuring the resulting residual kinetic energy.

On the NIF, both the MRS and nTOF neutron spectrometers are currently used to measure DT-n Doppler shifts and infer bulk velocity. The MRS measures bulk velocities to ±30 km/s,[6] and the nTOF detectors measure velocity to ±20 km/s.[41] Therefore on the NIF this technique would not represent an improvement in precision over current techniques, but it would enable verification of existing measurements and a relatively inexpensive expansion of the measurement to new locations: for example, at the north pole where there is no current velocity measurement.

B.10 Conclusions

A compact neutron spectrometer has been developed and implemented on the OMEGA laser facility for measurements of the DT neutron spectrum. A proton spectrometer is used to detect recoil protons from elastic neutron scattering in a CH_2 foil. Monte Carlo simulations are used to characterize the instrument response, which is used in a forward-fitting process of the proton data to infer the incident neutron spectrum. The neutron mean energy is determined to ±50 keV precision, and the neutron yield is determined to ±10%. By placing several recoil spectrometers around an implosion, the mean energy of neutrons emitted in the different directions can be determined and used to study the residual implosion kinetic energy at peak compression in implosions at the OMEGA facility. We also discuss improvements to the system to reduce the uncertainty in mean energy in a single direction to $\pm 15 - 20$ keV.

B.11 References

1. T. Boehly, D. Brown, R. Craxton *et al.*, "Initial performance results of the OMEGA laser system," Optics Communications, **133**(1-6), 495–506 (1997).
2. G. Miller, E. Moses and C. Wuest, "The National Ignition Facility: enabling fusion ignition for the 21st century," Nuclear Fusion, **44**, S228 (2004).
3. J. Nuckolls, L. Wood, A. Thiessen *et al.*, "Laser Compression of Matter to Super-High Densities: Thermonuclear (CTR) Applications," Nature, **239**, 139–142 (1972).
4. J. Lindl, "Development of the indirect-drive approach to inertial confinement fusion and the target physics basis for ignition and gain," Phys. Plasmas, **2**, 3933–4024 (1995).
5. S. W. Haan *et al.*, "Design and modeling of ignition targets for the National Ignition Facility," Phys. Plasmas, **2**, 2480 (1995).
6. M. Gatu Johnson, D. T. Casey, J. A. Frenje *et al.*, "Measurements of collective fuel velocities in deuterium-tritium exploding pusher and cryogenically layered deuterium-tritium implosions on the NIF," Physics of Plasmas, **20**(4), 042707 (2013).
7. J. Kilkenny *et al.*, submitted to EPJ Web of Conferences (2013).
8. M. Gatu Johnson, J. A. Frenje, D. T. Casey *et al.*, "Neutron spectrometryAn essential tool for diagnosing implosions at the National Ignition Facility (invited)a)," Rev. Sci. Instrum., **83**(10), 10D308 (2012).
9. V. Y. Glebov, D. D. Meyerhofer, T. C. Sangster *et al.*, "Development of nuclear diagnostics for the National Ignition Facility (invited)," Rev. Sci. Instrum., **77**(10), 10E715 (2006).
10. C. J. Forrest, P. B. Radha, V. Y. Glebov *et al.*, "High-resolution spectroscopy used to measure inertial confinement fusion neutron spectra on Omega (invited)," Rev. Sci. Instrum., **83**(10), 10D919 (2012).
11. D. L. Bleuel, C. B. Yeamans, L. A. Bernstein *et al.*, "Neutron activation diagnostics at the National Ignition Facility (invited)," Rev. of Sci. Instrum., **83**(10), 10D313 (2012).
12. C. B. Yeamans, D. L. Bleuel and L. A. Bernstein, "Enhanced NIF neutron activation diagnosticsa)," Rev. of Sci. Instrum., **83**(10), 10D315 (2012).
13. J. A. Frenje, D. T. Casey, C. K. Li *et al.*, "First measurements of the absolute neutron spectrum using the magnetic recoil spectrometer at OMEGA (invited)," Rev. Sci. Instrum., **79**(10), 10E502 (2008).

14. J. A. Frenje, D. T. Casey, C. K. Li *et al.*, "Probing high areal-density cryogenic deuterium-tritium implosions using downscattered neutron spectra measured by the magnetic recoil spectrometer," Physics of Plasmas, **17**(5), 056311 (2010).
15. D. Casey, *Diagnosing Inertial Confinement Fusion Implosions at OMEGA and the NIF Using Novel Neutron Spectrometry*, Ph.D. thesis, Massachusetts Institute of Technology (2012).
16. D. T. Casey, J. A. Frenje, M. Gatu Johnson *et al.*, "Measuring the absolute deuteriumtritium neutron yield using the magnetic recoil spectrometer at OMEGA and the NIF," Rev. Sci. Instrum., **83**(10), 10D912 (2012).
17. D. T. Casey, J. A. Frenje, M. Gatu Johnson *et al.*, "The magnetic recoil spectrometer for measurements of the absolute neutron spectrum at OMEGA and the NIF," Rev. Sci. Instrum., **84**(4), 043506 (2013).
18. J. Frenje, R. Bionta, E. Bond *et al.*, "Diagnosing implosion performance at the National Ignition Facility (NIF) by means of neutron spectrometry," Nuclear Fusion, **53**(4), 043014 (2013).
19. H. Brysk, "Fusion Neutron Energies and Spectra," Plasma Physics, **15**, 611–617 (1973).
20. F. H. Séguin, J. A. Frenje, C. K. Li *et al.*, "Spectrometry of charged particles from inertial-confinement-fusion plasmas," Rev. Sci. Instrum., **74**(2), 975–995 (2003).
21. F. H. Séguin, N. Sinenian, M. Rosenberg *et al.*, "Advances in compact proton spectrometers for inertial-confinement fusion and plasma nuclear science," Rev. Sci. Instrum., **83**(10), 10D908 (2012).
22. D. T. Casey, J. A. Frenje, F. H. Séguin *et al.*, "The coincidence counting technique for orders of magnitude background reduction in data obtained with the magnetic recoil spectrometer at OMEGA and the NIF," Rev. Sci. Instrum., **82**(7), 073502 (2011).
23. G. Morgan, D. Olsen and J. McConnell, "A proton-recoil telescope for in-line absolute neutron fluence measurements," Nuclear Instruments and Methods, **157**(3), 525 – 535 (1978).
24. N. P. Hawkes, P. van Belle, D. S. Bond *et al.*, "A 14 MeV neutron spectrometer for the Joint European Torus deuterium-tritium experiments," Rev. Sci. Instrum., **70**(1), 1134–1136 (1999).
25. M. J. Moran, V. Y. Glebov, C. Stoeckl *et al.*, "PROTEX: A proton-recoil detector for inertial confinement fusion neutrons," Rev. Sci. Instrum., **76**(2), 023506 (2005).
26. S. W. Conroy, M. Weiszflog, E. Andersson-Sunden *et al.*, "Neutron spectrometer for ITER using silicon detectors," Rev. Sci. Instrum., **79**(10), 10E508 (2008).
27. F. H. Séguin, M. G. Johnson, N. Sinenian *et al.*, Bull. Am. Phys. Soc., **57**(12), 345 (2012).
28. L. Ballabio, J. Källne and G. Gorini, "Relativistic calculation of fusion product spectra for thermonuclear plasmas," Nuclear Fusion, **38**(11), 1723 (1998).
29. J. Ziegler, J. Biersack and U. Littmark, *The stopping and range of ions in matter* (Pergamon, New York, 1985).
30. A. Fews and D. L. Henshaw, "High resolution alpha particle spectroscopy using CR-39 plastic track detector," Nuclear Instruments and Methods in Physics Research, **197**(23), 517 – 529 (1982).
31. A. P. Fews and D. L. Henshaw, "High resolution alpha-particle spectroscopy using CR-39 plastic track detector," Nuclear Instruments and Methods in Physics Research, **223**(23), 609 – 616 (1984).
32. N. Sinenian, M. Rosenberg, M. Manuel *et al.*, "The response of CR-39 nuclear track detector to 19 MeV protons," Rev. Sci. Instrum., **82**, 103303 (2011).
33. N. Sinenian, M.-E. Manuel, A. Zylstra *et al.*, "Upgrade of the MIT Linear Electrostatic Ion Accelerator (LEIA) for nuclear diagnostics development for Omega, Z and the NIF," Rev. Sci. Instrum., **83**(4), 043502 (2012).
34. J. A. Frenje, K. M. Green, D. G. Hicks *et al.*, "A neutron spectrometer for precise measurements of DT neutrons from 10 to 18 MeV at OMEGA and the National Ignition Facility," Rev. Sci. Instrum., **72**(1), 854–858 (2001).
35. S. Skupsky, R. W. Short, T. Kessler *et al.*, "Improved laser-beam uniformity using the angular dispersion of frequency-modulated light," Journal of Applied Physics, **66**(8), 3456–3462 (1989).
36. D. D. Meyerhofer, J. A. Delettrez, R. Epstein *et al.*, "Core performance and mix in direct-drive spherical implosions with high uniformity," Physics of Plasmas, **8**(5), 2251–2256 (2001).
37. Y. Lin, G. N. Lawrence and T. J. Kessler, "Distributed phase plates for super-Gaussian focal-plane irradiance profiles," Opt. Lett., **20**(7), 764–766 (1995).
38. J. A. Frenje, C. K. Li, F. H. Sguin *et al.*, "Absolute measurements of neutron yields from DD and DT implosions at the OMEGA laser facility using CR-39 track detectors," Rev. Sci. Instrum., **73**(7), 2597–2605 (2002).

39. A. Zylstra, J. Frenje, F. Séguin *et al.*, "A new model to account for track overlap in cr-39 data," Nuclear Instruments and Methods in Physics Research Section A: Accelerators, Spectrometers, Detectors and Associated Equipment, **681**(0), 84 – 90 (2012).

40. C. L. Ruiz, G. A. Chandler, G. W. Cooper *et al.*, "Progress in obtaining an absolute calibration of a total deuteriumtritium neutron yield diagnostic based on copper activationa)," Rev. Sci. Instrum., **83**(10), 10D913 (2012).

41. R. Hatarik *et al.*, to be submitted to Phys. Rev. Lett. (2015).

Appendix C

Increasing the energy dynamic range of solid-state nuclear track detectors using multiple surfaces

C.1 Introduction

Solid-State Nuclear Track Detectors (SSNTDs) were developed in the beginning of the 1950s with LiF[1] and mica[2]. When a high energy charged particle is incident upon the solid dielectric detector it ionizes the matter along its path. The damaged region corresponding to the particle trajectory is chemically altered due to the ionization. If the detector is then exposed to a chemical etchant such that the etch rate for the damaged material is greater than for the undamaged material a physical 'pit' or 'track' is created. These tracks can then be observed with an optical microscope. SSNTDs are in widespread use today.

In Inertial Confinement Fusion (ICF) experiments, CR-39 was used in the first direct measurement of fuel ρR[3]. More recently, diagnostics based on SSNTDs, such as CR-39, have been used to measure absolute spectra of various fusion products (see Chapter 2 and Refs. 4–6).

Recent techniques in imaging ICF implosions using proton backlighter radiography[7] in fast-ignition relevant[8] and indirect-drive[9] configurations have led to important physics results. Proposed future experiments include direct-drive radiography and warm/hot matter stopping power experiments. In these studies of electromagnetic fields in ICF implosions it is necessary to spatially resolve the imaging particle energies across the detector. For this the detector response as a function of energy must be characterized. This has been carefully studied for a particle incident on the front surface of a CR-39 SSNTD[4,10].

In the proton radiography experiments a detector pack consisting of two pieces of CR-39 is assembled as shown in Fig. C.1. A thin Ta filter (generally $\geq 5\mu$m) is placed in front to range out fast ablator ions produced in laser-plasma interactions[11]. The Al filter between the two CR-39 detectors is usually chosen to optimize the high-energy proton (from D+^{3}He) detection on the second piece of CR-39. This allows simultaneous imaging of both high and low energy particles from the fusion reactions

$$\mathrm{D} + {}^3\mathrm{He} \rightarrow {}^4\mathrm{He}(3.6\ \mathrm{MeV}) + \mathrm{p}(14.7\ \mathrm{MeV}), \tag{C.1}$$

$$\mathrm{D} + \mathrm{D} \rightarrow \mathrm{T}(1.01\ \mathrm{MeV}) + \mathrm{p}(3.02\ \mathrm{MeV}). \tag{C.2}$$

Additional reactions generally relevant to ICF are the second branch DD reaction (D + D $\rightarrow$ n +^{3} He) and the DT reaction (D + T $\rightarrow$ n +^{4} He) but none of these products has been used in

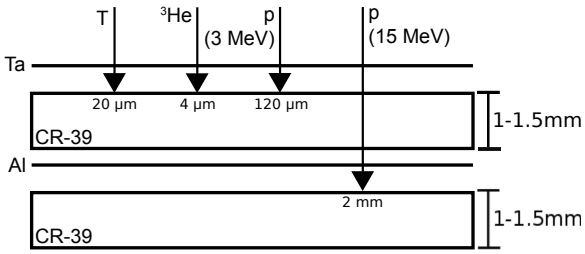

Figure C.1. SSNTD configuration for proton radiography using fusion products (Eqs C.1 and C.2). The maximum range (i.e. with 0μm of Ta filtering in front) of each particle in CR-39 is shown. The low energy particles (T, ^{4}He, and 3 MeV p) are recorded on the first CR-39 detector. The 14.7 MeV p are too energetic to be seen on the front of the first detector since the track size $\sim dE/dx$. However, they are recorded both on the back surface of the first detector and the front surface of the second detector.

the radiography experiments so far. These backlighting particles are generated in a thin-glass shell (low ρR) implosion in a short ($\sim$ 80ps duration) shock coalescence burn[7]. In principle all four fusion products from Eqs C.1 and C.2 can be used for radiography; in practice the 3 and 14.7 MeV protons are the most useful[7,9,12]. Proof-of-principle simultaneous detection of p, T, ^{3}He, and ^{4}He, from DD and D^{3}He fusion on an accelerator fusion product source, is shown in Fig. C.2.

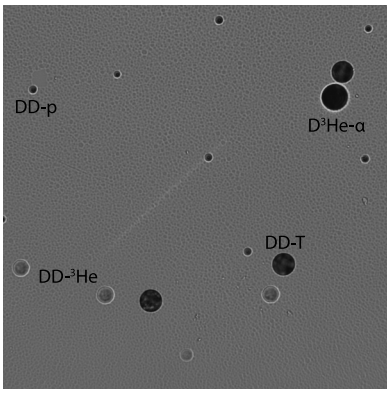

Figure C.2. Four types of particle track in CR-39 after a 3 hour etch. Shown are DD-p (D$\approx$ 4μm), DD-^{3}He (D$\approx$ 9μm), DD-T (D$\approx$ 13μm), and D^{3}He-^{4}He (D$\approx$ 14μm). For DD-p, DD-T, and D^{3}He-^{4}He the track contrast is $\geq$ 90% as defined in this work; the DD-^{3}He have contrast $60-70\%$ (see Appendix C.9). The 14.7 MeV D^{3}He protons are undetectable in this scheme, since they are not ranged down into the detectable energy range. The CR-39 was filtered with only 1μm of alumized mylar to allow detection of the ^{3}He ions. The image size is 208μm square.

The response of CR39 to energetic charged particles has been extensively studied experimentally[13,4,10,14–23] and theoretically[24] for particles incident on the front surface of the detector. In this work, as well as several of the cited works, TasTrak® CR-39 was used. Since the highest energy protons traverse the entire first detector an image will also be generated on the back surface of the first detector, if the energy loss is enough that the proton energy at the back surface is in the detectable range (0-8 MeV). These protons generally lose 8-11 MeV through the first CR-39 detector in the proton radiography experiments. The energy characteristics of the detector response on the back surface are found to be significantly different from the previously-measured front surface. To accurately infer an energy of the incident particles from this data, the detector energy response must be characterized for charged particles traversing the entire SSNTD, which is the focus of this work.

The paper is structured as follows. Section C.2 gives a simple model for track formation in SSNTDs. Section C.3 describes the experimental setup used to characterize the detector energy response. Section C.4 shows and discusses the experimental results. Section C.5 presents a simple Monte Carlo simulation of the track formation process, which is interpreted in Section C.6. Finally, the paper is concluded in Section C.7.

C.2 Track formation

The theory of track formation in SSNTDs is well-developed[25,26]. In the idealized case the particle's energy deposition in the bulk material creates a region in which the chemical composition of the material is altered. This results in different chemical etch rates of the undamaged and damaged material: the bulk (v_b) and track (v_t) etch rates.

A detector schematic before and after the etch process is shown in Fig. C.3(a) and C.3(b), respectively. In typical SSNTDs $v_t > v_b$ which results in a conical track defined by the track depth h and angle θ. In particular, we can write that

$$\sin\theta = \frac{v_b}{v_t}. \tag{C.3}$$

In the case of normal particle incidence and constant track etch rate, the track depth is

$$h = (v_t - v_b)\tau \tag{C.4}$$

for some etch duration τ. Then we can write that the track diameter is

$$D = 2h\tan\theta = 2h\sqrt{\frac{v_b^2}{v_t^2 - v_b^2}}. \tag{C.5}$$

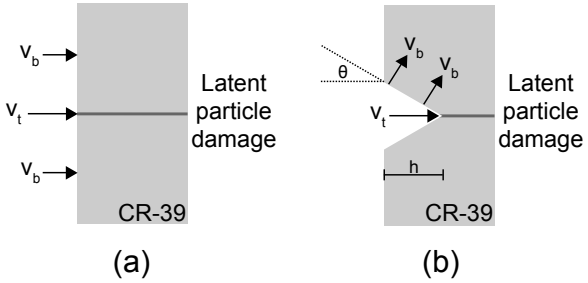

Figure C.3. An overview of the track etching process in SSNTDs. Fig. (a) shows the SSNTD at the start of the etch process. The latent particle damage is unobservable with conventional techniques ($\sim$ 5 nm in size). Fig. (b) shows that after some etch time a track is developed. Typical track diameters are $2 - 30\mu$m depending on particle species, energy, and etch time.

The track etch rate v_t is a monotonically increasing function of the energy lost to low-energy electrons, which create the latent damage in the material. Higher-energy electrons do not locally deposit their energy and thus do not contribute to track formation. In the literature the energy loss rate to low-energy electrons (below some critical recoil energy) is referred to as the restricted energy loss rate, which then depends on dE/dx for the incident particle. We can thus see how the diameter of a track will corresponds to its energy, based on Eq. C.5.

Typically the bulk etch rate is $2 - 3$ μm/hr, the track etch rate is $4 - 6$ μm/hr, giving a typical

ratio in Eq. C.3 as 1/2 and a typical track depth of $2-3$ μm/hr by Eq. C.4. The range of detectable track diameters is typically $2-30$ μm depending on particle type and energy. These typical numbers can vary between CR-39 manufacturing batches.

C.3 Experimental Overview

Experimental studies of the properties of CR-39 SSNTDs have been conducted using an accelerator-based fusion products source[27]. In these experiments, we use a 140 kV linear electrostatic accelerator. Either D or ^{3}He beams were incident on a ErD_2 target. These targets were additionally doped with ^{3}He. Therefore we were able to produce the fusion products in Eqs C.1 and C.2 with typical reaction rates of order 10^6 and 10^5 s^{-1} for DD and D^{3}He respectively using a D beam.

In these experiments, CR-39 detectors were exposed to D^{3}He protons with different energies, depending on the filtering in front of the CR-39 (see Fig. C.4). These proton spectra were measured with a silicon surface barrier detector, which had been calibrated with a ^{226}Ra alpha source to an accuracy of ± 75 keV.

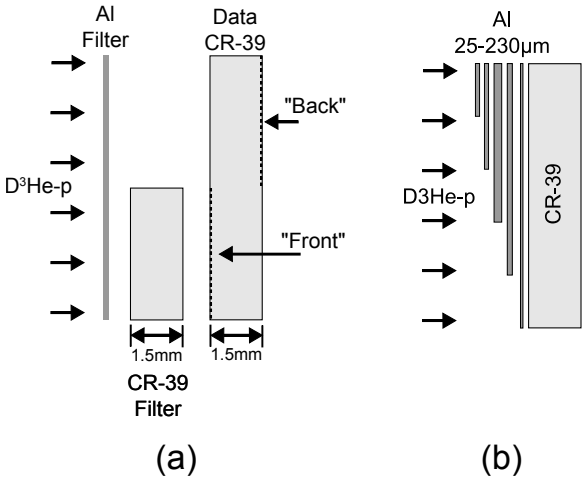

Figure C.4. Filtering configuration for the accelerator fusion product source experiments. Fig. (a) shows that filters for equivalent known energy distributions at the front and back surface of a single detector using both Al and a CR-39 filter. Fig. (b) shows that several energy windows are created through different Al thicknesses. Figs (a) and (b) are orthogonal depictions of the filter pack. For a given Al thickness, a CR-39 filter is used to create identical energy distributions at the front and back surface of the data CR-39 (a). In an orthogonal direction, multiple Al thicknesses are used to vary the energy distribution over five windows (b).

The filter configuration shown schematically in Fig. C.4 is used to range D^{3}He protons to $2.5-6.5$ MeV. Images of the filter pack are shown in Fig. C.5. Equivalent energy distributions are created on the front and back surfaces of the CR-39 through the use of a CR-39 filter*, as shown in Figure C.4(a). This allows investigation of fundamental differences in the detector behavior for protons at the front and back surface. Several discrete energy windows are created by varying the aluminum filter in front of the detector (Figure C.4(b)). Thus a single piece of CR-39 is exposed to five distinct proton energy distributions on both the front and back surfaces.

After exposure, the CR-39 SSNTDs were etched in a 6 molar NaOH solution for $2-6$ hours.

*As the thickness of CR-39 stock can change, the CR-39 filter thickness was verified to be within $\pm$ 20μm of the data CR-39 thickness

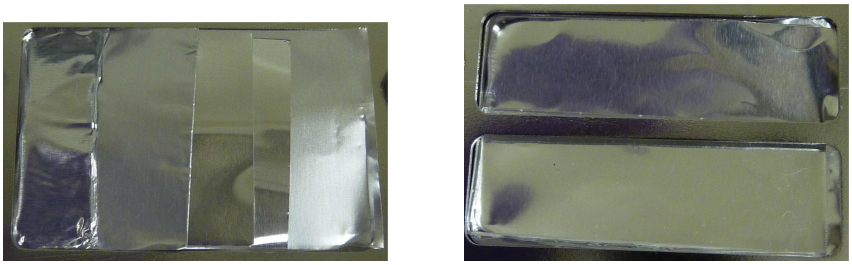

(a) **(b)**

Figure C.5. Images of the filter pack used in this experiment. (a) Front view (looking along proton trajectory) of filter pack. Five energy windows are created via varying the aluminum thickness, which increases from right to left. (b) Back view (looking towards proton source) of filter pack. The CR-39 filter is visible in the bottom half.

Digital microscope systems with automatic track image recognition algorithms are used to identify the diameter, eccentricity, and contrast of each track on the detector.

C.4 Results

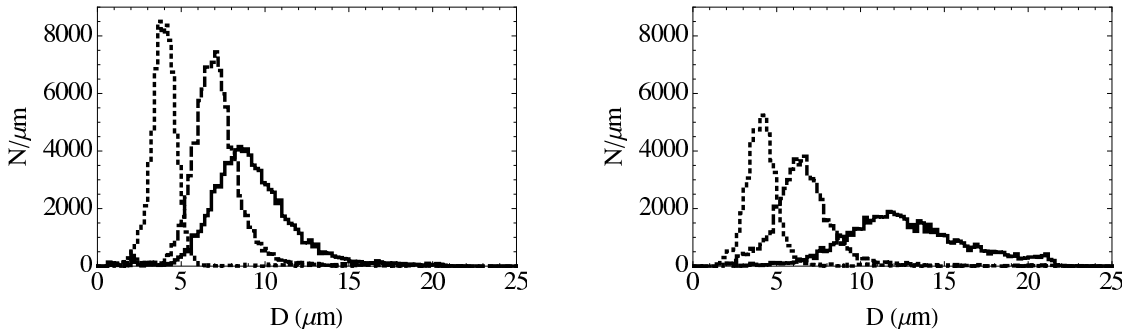

(a) Front **(b)** Back

Figure C.6. Sample track diameter spectra on a single CR-39 detector for the front (a) and back (b) sides of the CR-39 SSNTD after 6 hours etching time. The incident energy distributions observed are identical in each case (see Fig. C.4) with mean energies of 2.55 MeV (solid line), 4.14 MeV (dashed line), and 5.68 MeV (dotted line). Contrast plots for the 2.55 MeV data are shown in Fig. C.8.

Sample diameter distributions are plotted for several energies in Fig C.6. Figure C.6(a) shows the resulting track diameter distributions detected on the front surface of the CR-39 while Figure C.6(b) shows the diameter distributions for the back surface. In the lowest energy window we can clearly see that the back surface diameter distributions have larger means and standard deviations than on the front. Additionally, the lowest energy spectrum on the back surface displays a sharp cutoff at $D \approx 22\mu$m.

In Figure C.7 the mean diameter versus proton energy is illustrated for 2, 4, and 6 hour etch times for the front (solid line) and back (dashed line) surfaces. The back surface systematically shows larger diameters for all etch times at low energies. The front vs back surface discrepancy is larger for lower energies and the two D vs E trends converge at high energies (≈ 6 MeV). The highest energy window (~ 6.5 MeV) was not detectable at the 2 hour etch time.

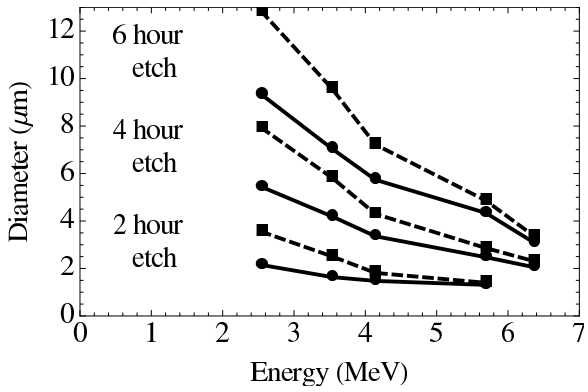

Figure C.7. Diameter of tracks observed versus energy for 2, 4, and 6 hours etch time. Solid lines represent the front CR-39 surface, dashed lines represent the back surface. Example distributions are shown in Fig. C.6

Contour plots of the number of tracks observed versus diameter and contrast, which is defined as the minimum light transmission through the track normalized to the background level during the optical scan, are plotted in Figure C.8 for the front surface (a) and back surface (b). A perfectly dark track corresponds to 100% contrast and a very faint track would have low contrast. For an example of how this contrast definition compares to microscope images see Fig. C.2, which shows both high- and low- contrast particle tracks, and Appendix C.9 which shows the resulting contrast contour plot. At small diameters and low contrast intrinsic noise (defects in the CR-39) is observed. This intrinsic noise is eliminated in a normal analysis through contrast and diameter limits. The contrast contour plots show a clear qualitative difference in behavior between the data on the front and back surfaces. On the front surface we see the data region curves to lower contrast (as defined) for the extreme diameters. On the back surface contrast plot we observe that the data contrast is independent of track diameter.

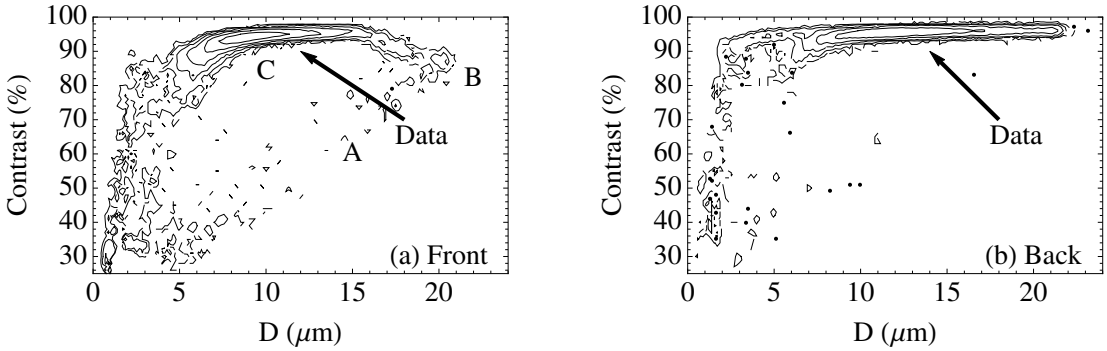

Figure C.8. Contour plots of the number of tracks versus track contrast and diameter for the same piece of CR-39 in Fig. C.6. Data for 2.55 MeV protons is shown for the front side (top, with regions of data identified with stopping power regimes) and the back side (bottom). Intrinsic CR-39 noise appears in the low-contrast low-diameter regime. Contours represent a constant number of tracks per unit contrast and diameter; the values of this quantity corresponding to plotted contours form a geometric series with a ratio of 3. As defined in this work a high contrast number is a dark track, while a low contrast number is a light track (see Fig. C.2).

The stopping power for a proton in the detector is calculated with SRIM software[28] and plotted in Figure C.9. The proton Bragg peak in the CR-39 is observed at around 100keV. For most of the detected protons, since the distribution mean is of order MeV, we are dealing exclusively with average ion energies higher than the Bragg peak. Therefore, as a proton traverses the detector, its energy decreases and dE/dx increases for the front surface(see Fig. C.9). Since the amount

of damage done to the CR-39 increases monotonically with the increasing stopping power we can say that the size of the latent damage track created by the particle will be increasing along the direction of the particle trajectory. This is annotated in Figs. C.9 and C.8(a) by the label **C**.

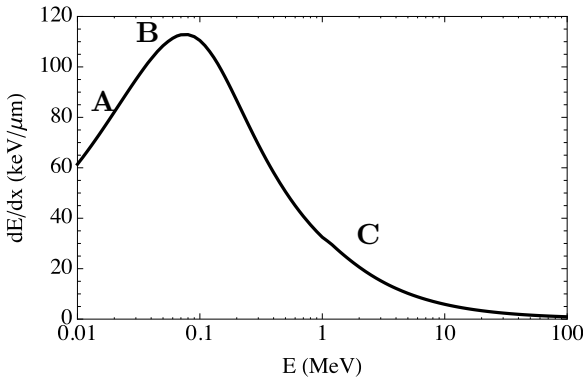

Figure C.9. Stopping power for protons in CR-39, given as change in energy per unit length. Protons of order MeV (**C**) create small dark tracks. Around the Bragg peak (**B**) protons create large tracks due to the large dE/dx. For protons that stop in the etched plastic (**A**) the track etches away and becomes light and hard to detect. These features are labeled in Fig. C.8(a)

Since the distribution functions in this experiment are so broad (see Fig. C.6 and Appendix C.8) there is a low-energy tail which also samples energies near the Bragg peak. Protons near the Bragg peak create very large tracks due to the high stopping power (annotated in Figs. C.9 and C.8(a) by the label **B**). But if the proton stops within the CR-39 material removed during the etch (bulk material removed is $\sim 2\mu$m/hr) then the track shape deviates significantly from conical once the etch proceeds past the end of the latent track. In this case the measured track contrast decreases (lighter tracks) and the diameter decreases, as annotated in Figs. C.9 and C.8(a) by the label **A**.

C.5 Simulated response

To explore the CR-39 response to protons of various energies, a simple Monte Carlo track formation code was developed and used. Incident particles sampled from an arbitrary energy distribution are ranged in the detector material using SRIM-calculated stopping powers[28]. This defines the formation of the latent track. The etching process is then simulated for a given etch time using a model previously developed with nominal parameters for CR-39[29]. Transmission of a uniform backlight through the track using Fresnel's equations then simulates the automated microscope-based scanning process. Refraction in the conical track defines the observed diameter and contrast of a track.

The simulated results are shown in Fig. C.10 for a uniform energy distribution from 0.1-10.0 MeV to sample the full range of track behavior. Many of the interesting features in the contrast-diameter space (such as labels **A** and **B** in Fig. C.8(a)) come from the low-energy tail of the distribution, which is created by straggling and blooming effects in the filter. This is more difficult to model, so the uniform energy distribution is used to map out the trajectory of tracks as the energy is changed in the contrast-diameter space.

The simulated data on the detector front surface is shown in Fig. C.10(a), and the simulated back surface data shown in Fig. C.10(b). From these distributions, we can clearly see that the simulation qualitatively matches features of the data as shown in Fig. C.8. The front surface data

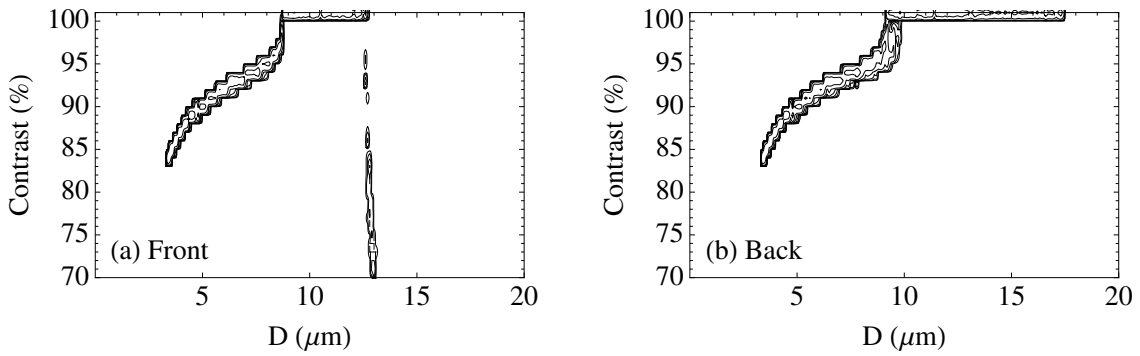

Figure C.10. Simulated contour plots of the number of tracks observed (arbitrary) versus track contrast and diameter. Plots are shown for the front (a) and back (b) surfaces. Contours represent a constant number of tracks per unit contrast and diameter; the values of this quantity corresponding to plotted contours form a geometric series with a ratio of 3.

shows a low-contrast tail at the maximum observed diameter which is not observed on the back surface. Additionally, the maximum diameter observed is larger on the back surface. Both of these effects are observed in the data.

Additionally, the simulation reproduces the effect that the back surface diameters are larger than the front, although the simulated effect is much smaller than the data indicates. Differences between the simulation and data are likely explained by the choice of the two free parameters in the track formation model[29].

C.6 Interpretation

The only difference between the front and back surface simulation is the sign of $d/d\chi(dE/dx)$ where χ is the distance of the etch into the bulk detector material: dE/dx increases along the etch direction for data on the front surface whereas it decreases along the etch direction on the back surface. This indicates that the observed differences in the data for the front and back surfaces is due to energy deposition effects in the SSNTD, which is known to affect the resulting track shape[25]. The ratio of track to bulk etch rate, as discussed in Sec. C.2, defines the track cone angle. If the stopping power along the track length is constant then the cone angle is constant and the overall track shape is perfectly conical. However, when the stopping power (and thus track etch rate) changes as a function of distance along the track then the cone angle changes over the track. This causes curvature of the track surface, as discussed in detail by Henke and Benton[25]. We therefore interpret the difference in front vs back diameter versus particle energy (Fig. C.7) as a result of the track formation process with $d/d\chi(dE/dx)$ positive (front) versus negative (back).

The other major feature is the different behavior at large diameters between the front and back (Fig. C.8). In the front side data around the maximum proton diameter the contrast of data tracks (as defined) tends to decrease. This is a common feature of CR-39 data. The maximum proton diameter occurs for proton energies near the Bragg peak since the track size $\sim dE/dx$. However, the range of protons near the Bragg peak in CR-39 is about the same as the bulk material removed during the etching process (~ 2 μm/hr). Therefore these large-diameter proton tracks are etched beyond the end of the track, which increases the light transmission (leading to lower contrast or lighter tracks in Fig. C.8) and decreases the observed diameter. The back side data also has the maximum proton diameter observed for tracks where the proton energy was near the Bragg

peak, but in this case as the bulk material is etched away tracks do not disappear since the etch direction is opposite to the particle velocity. This causes the characteristic flat contrast shape at large diameters as observed in the data. In this case, the maximum proton diameter is also closer to the theoretical maximum ($2v_b \times \tau$) since tracks do not disappear or 'etch away' during the etch process.

C.7 Conclusions

Distinct energy calibrations have been measured on an accelerator-based fusion products source for both the front and back surfaces of CR-39, a solid-state nuclear track detector. We observe significant differences in track formation for identical energy distributions between the two surfaces, which result from a dependence of the final track shape on whether dE/dx increases or decreases along the track etch direction. This is verified by simulated data using a Monte Carlo track formation code. The observed effects illustrate that equivalent distributions create larger track diameters on the back, and that the back side tracks have consistent contrast while on the front side low energy proton tracks are etched away. This demonstrates the importance of separate front and back surface energy calibrations for CR-39 based proton diagnostics in ICF experiments, such as in proton radiography. Characterizing both detector surfaces thus extends, in a practical fashion, the range of detectable energies on a single piece of CR-39 by up to 7-8 MeV.

C.8 Distribution Width

In this experiment many important effects are observed for protons near the Bragg peak (see Figs. C.9, C.8, and C.10). It is important to note that these observations are possible even though the mean energies of each proton distribution are all over order several MeV. This is because the diameter distributions, as shown in Fig. C.6 have standard deviations up to $\sim 3\mu$m resulting from ranging down the protons from 14.7 MeV. In this experiment each energy window has approximately 2×10^4 particles, so with a sufficiently broad distribution we can sample a wide range of track behavior. Thus the low-energy tail of the energy distribution allows us to probe behavior close to the Bragg peak for proton distributions of order MeV.

C.9 Track constrast

The contrast contour plot for the 4 particle data in Fig. C.2 is shown in Fig. C.12. The fusion product energies are given in Eqs. C.1 and C.2. The protons, tritons, and alphas have ranges greater than the etch distance and thus have fully-formed high-contrast (dark) tracks. When the cone angle is above a critical value then all light is reflected out, and in theory the track contrast is 100%. This is true for the protons, tritons, and alphas. The diameter of each species track is related to the stopping power as discussed in Sec. C.2. The DD-^{3}He particles have a shorter range than the bulk amount of material removed during the etch and thus the tracks are being 'etched out', resulting in the significantly lower contrast.

C.10 Shot Numbers

For reference purposes, facility shot numbers for all data given in this paper are tabulated in Table C.1.

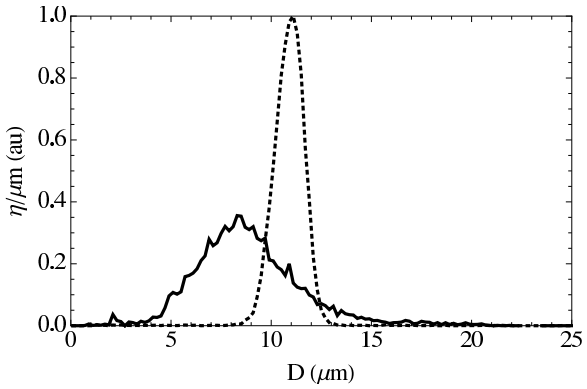

Figure C.11. Sample track diameter spectra on CR-39 detector for D^3He-p ranged down to 2.55 MeV (solid line) versus DD-p (see C.2) ranged down to 2.4 MeV (dotted line). The two distributions are area normalized and plotted in arbitrary units per μm. The observed distribution widths are $\sigma = 0.72\mu$m for the DD-p versus $\sigma = 2.69\mu$m for the D^3He-p. This is due to broadening of the initial spectrum due to dispersion, straggling, and blooming in the filtering for D^3He as the energy loss is approximately 12 MeV. Some of the discrepancy in the mean is due to piece-to-piece CR39 variation.

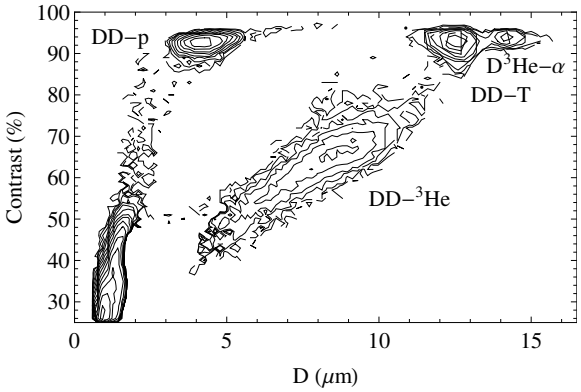

Figure C.12. Contour plots of the number of tracks versus track contrast and diameter for the same piece of CR-39 in Fig. C.2. The four particle species visible are labeled on the plot, compare to the microscope image in Fig. C.2. Intrinsic CR-39 noise appears in the low-contrast low-diameter regime. Contours represent a constant number of tracks per unit contrast and diameter; the values of this quantity corresponding to plotted contours form a geometric series with a ratio of 2. As defined in this work a high contrast number is a dark track, while a low contrast number is a light track.

Figure	Shot Number
2	A2010083101
6	A2010021204
7	A2010021203-5
8	A2010021204
11	A2010021204 A2010020101
12	A2010083101

Table C.1. Shot numbers for data shown in each figure.

C.11 References

1. D. Young, "Etching of radiation damage in lithium fluoride," Nature, **182** (1958).
2. E. Silk and R. Barnes, "Examination of fission fragment tracks with an electron microscope," Philosophical Magazine, **4**(44), 970–972 (1959).
3. S. Kacenjar, S. Skupsky, A. Entenberg *et al.*, "Direct Measurement of the Fuel Density-Radius Product in Laser-Fusion Experiments," Phys. Rev. Lett., **49**(7), 463–467 (1982).
4. F. H. Séguin, J. A. Frenje, C. K. Li *et al.*, "Spectrometry of charged particles from inertial-confinement-fusion plasmas," Rev. Sci. Instrum., **74**(2), 975–995 (2003).
5. J. A. Frenje, K. M. Green, D. G. Hicks *et al.*, "A neutron spectrometer for precise measurements of DT neutrons from 10 to 18 MeV at OMEGA and the National Ignition Facility," Rev. Sci. Instrum., **72**(1), 854–858 (2001).
6. J. A. Frenje, C. K. Li, F. H. Sguin *et al.*, "Absolute measurements of neutron yields from DD and DT implosions at the OMEGA laser facility using CR-39 track detectors," Rev. Sci. Instrum., **73**(7), 2597–2605 (2002).
7. C. K. Li, F. H. Séguin, J. A. Frenje *et al.*, "Monoenergetic proton backlighter for measuring E and B fields and for radiographing implosions and high-energy density plasmas (invited)," Rev. Sci. Instrum., **77**(10), 10E725 (2006).
8. J. Rygg, F. Seguin, C. Li *et al.*, "Proton radiography of inertial fusion implosions," Science, **319**(5867), 1223 (2008).
9. C. Li, F. Seguin, J. Frenje *et al.*, "Charged-Particle Probing of X-ray-Driven Inertial-Fusion Implosions," Science, **327**(5970), 1231 (2010).
10. N. Sinenian, M. Rosenberg, M. Manuel *et al.*, "The response of CR-39 nuclear track detector to 19 MeV protons," Rev. Sci. Instrum., **82**, 103303 (2011).
11. D. Hicks, C. Li, F. Séguin *et al.*, "Observations of fast protons above 1 MeV produced in direct-drive laser-fusion experiments," Physics of Plasmas, **8**, 606 (2001).
12. C. Li, F. Séguin, J. Frenje *et al.*, "Diagnosing indirect-drive inertial-confinement-fusion implosions with charged particles," Plasma Physics and Controlled Fusion, **52**, 124027 (2010).
13. A. Fews and D. L. Henshaw, "High resolution alpha particle spectroscopy using CR-39 plastic track detector," Nuclear Instruments and Methods in Physics Research, **197**(23), 517 – 529 (1982).
14. R. Fleischer, P. Price and R. Walker, *Nuclear tracks in solids: principles and applications* (University of California Press, 1975).
15. B. Cartwright, E. Shirk and P. Price, "A nuclear-track-recording polymer of unique sensitivity and resolution," Nuclear Instruments and Methods, **153**(2-3), 457–460 (1978).
16. E. da Fonseca, T. Knöfel and O. Tavares, "Bulk Etching Characteristics of CR-39 Track Detectors in Hydroxide Solutions," Centro Basileiro de Pesquisas Fisicas, **13** (1983).
17. H. Khan, A. Brandt Naeem *et al.*, "Track-registration-and-development characteristics of CR-39 plastic track detector," Nuclear Tracks and Radiation Measurements (1982), **7**(3), 129–139 (1983).
18. J. Charvát and F. Spurnı, "Optimization of etching characteristics for cellulose nitrate and CR-39 track detectors," International Journal of Radiation Applications and Instrumentation. Part D. Nuclear Tracks and Radiation Measurements, **14**(4), 447–449 (1988).
19. P. Stafford, J. Horton, K. Hogstrom *et al.*, "The critical angle dependence of CR-39 nuclear track detectors for 3-10 MeV protons and 7-15 MeV alpha particles," International Journal of Radiation Applications and Instrumentation. Part D. Nuclear Tracks and Radiation Measurements, **14**(3), 373–378 (1988).
20. R. Mishra, C. Orlando, L. Tommasino *et al.*, "A better understanding of the background of CR-39 detectors," Radiation Measurements, **40**(2-6), 325–328 (2005).
21. Matiullah, S. Rehman, S. Rehman *et al.*, "Discovery of new etchants for CR-39 detector," Radiation Measurements, **39**(3), 337 – 343 (2005).
22. K. Chan, B. Lau, D. Nikezic *et al.*, "Simple preparation of thin CR-39 detectors for alpha-particle radiobiological experiments," Nuclear Instruments and Methods in Physics Research Section B: Beam Interactions with Materials and Atoms, **263**(1), 290–293 (2007).
23. K. Chan, F. Ng, D. Nikezic *et al.*, "Bulk and track etch properties of CR-39 SSNTD etched in NaOH/ethanol," Nuclear Instruments and Methods in Physics Research Section B: Beam Interactions with Materials and Atoms, **263**(1), 284–289 (2007).

24. S. Durrani and R. Bull, *Solid state nuclear track detection* (Pergamon Books Inc., Elmsford, NY, 1987).

25. R. Henke and E. Benton, "On geometry of tracks in dielectric nuclear track detectors," Nuclear Instruments and Methods, **97**(3), 483–489 (1971).

26. D. Nikezic and K. Yu, "Formation and growth of tracks in nuclear track materials," Materials Science and Engineering: R: Reports, **46**(3-5), 51–123 (2004).

27. S. McDuffee, J. Frenje, F. Séguin *et al.*, "An accelerator based fusion-product source for development of inertial confinement fusion nuclear diagnostics," Rev. Sci. Instrum., **79**, 043302 (2008).

28. J. Ziegler, J. Biersack and U. Littmark, *The stopping and range of ions in matter* (Pergamon, New York, 1985).

29. D. Hicks, *Charged-particle spectroscopy: a new window on inertial confinement fusion*, Ph.D. thesis, Massachusetts Institute of Technology (1999).

Appendix D

A new model to account for track overlap in CR-39 data

D.1 Introduction

Solid-state nuclear track detectors have been developed for several decades[1–4]. CR-39 itself was developed as a nuclear track detector starting in the 1980s[5]. Significant work characterizing the response of CR-39 has been published in the last three decades; a recent comprehensive paper on the response of CR-39 to protons has been published by Sinenian et al. along with a comprehensive bibliography of studies on CR-39[6]. In many applications at modern ICF facilities such as OMEGA and the NIF, charged-particle fluxes of $10^5 - 10^7$ cm^{-2} are possible or expected. As typically a few percent of particle tracks are observed to overlap at track densities of order 10^4 cm^{-2}, these are well into the current saturation regime. For example, an image of CR-39 exposed to 1.8×10^5 protons/cm^2 is shown in Fig. D.1, which clearly shows significant track overlap. Recent work has been published on CR-39 data in extremely high fluence environments, such as short-pulse laser ion acceleration[7,8].

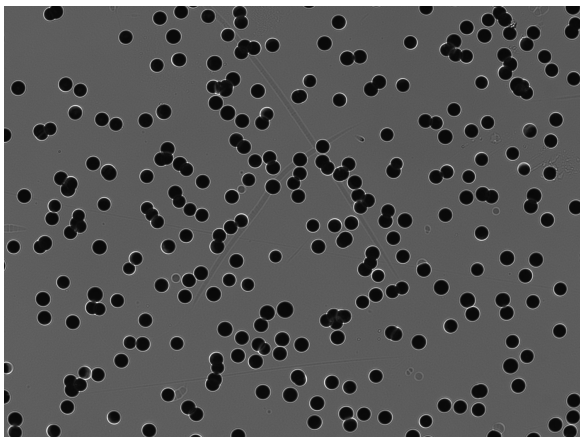

Figure D.1. High-fluence, 1.8×10^5 tracks/cm^2 of 3 MeV DD-p, CR-39 with significant overlap observable after being etched for 6 hours. The average track diameter is 10.63μm with a standard deviation of 0.54μm. The image was taken with an optical microscope system with a frame area of 1.36×10^{-3} cm^2 (431μm $\times$ 315.5μm).

Extending the upper fluence limit of CR-39 would allow: high-contrast charged-particle spectroscopy (e.g. simultaneous measurements of fusion products with reactivities differing by orders of magnitude), higher signal-to-background neutron spectroscopy of ignited implosions through increased allowable instrument efficiency, higher-contrast proton radiography of mass and EM field distributions, and simple extensions of various existing CR-39 based diagnostics to higher yields. These potential applications clearly motivate development of methods to operate CR-39 detectors into track-overlap saturation regimes, which is quantitatively addressed in this Appendix.

In addition to the modeling work, experimental data is presented in this Appendix from CR-39 diagnostics used on implosions at the OMEGA laser facility[9] and from the MIT Linear Electrostatic Ion Accelerator (LEIA)[10,11].

D.2 Analytic model of track overlap

A complete recurrence-relation model of mono-energetic tracks has been derived[12]. For our purposes it is sufficient to present an integral equation model for single and double tracks at low densities, which illustrates important scalings. This model can be derived by first defining probabilities for a new track being single, double, etc. Let η be the total density of tracks. Then,

$$P_1(\eta) = 1 - \sum_{i=1}^{\infty} \bar{A}_i N_i \tag{D.1}$$

$$P_n(\eta) = \bar{A}_{n-1} N_{n-1}, \quad n > 1 \tag{D.2}$$

where P_i is the probability that a new particle track on the detector will have an 'overlap fraction' i(where $i = 1$ is a single track, $i = 2$ is two tracks overlapping each other, $i = 3$ is a cluster of three mutually overlapping tracks, etc).$\bar{A}_i$ is the cross-section of a track, i.e. the area in which a new particle track will overlap with it (see Fig. D.2), with overlap fraction i and N_i is the density of tracks with overlap fraction i.

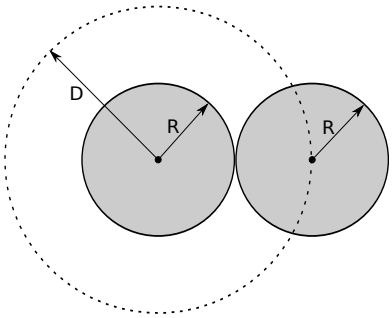

Figure D.2. Of relevance for track overlap calculations is the effective cross-section of a track for another track to overlap with it. As illustrated in the figure, for tracks of radius R any track lying within a one diameter separation overlaps, thus $\bar{A}_1 = \pi \bar{D}^2$.

Now assume that $N_i = 0 \ \ \forall \ \ i > 2$. We can write the two probabilities as

$$P_1(\eta) = 1 - \bar{A}_1 N_1 - \bar{A}_2 N_2, \tag{D.3}$$

$$P_2(\eta) = \bar{A}_1 N_1. \tag{D.4}$$

Therefore using Eqs D.1 and D.2 with D.3 and D.4,

$$N_1(\eta) = \int_0^{\eta} (P_1(\eta') - P_2(\eta')) d\eta' = \eta(1 - \bar{A}_1 \eta), \tag{D.5}$$

$$N_2(\eta) = \int_0^{\eta} 2P_2(\eta') d\eta' = \bar{A}_1 \eta^2 (1 - \frac{2}{3} \bar{A}_1 \eta), \tag{D.6}$$

where in Eq. D.5 we have approximated $2\bar{A}_1 N_1 + \bar{A}_2 N_2 \approx 2\bar{A}_1 \eta$, neglecting second-order geometric effects of double tracks, to simplify integration for N_1. The factor of 2 in the latter equation results from the fact that a newly-placed track which hits an existing track results in two

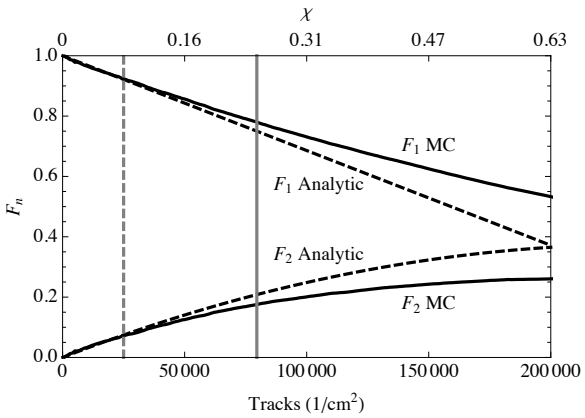

Figure D.3. Comparison of Monte Carlo F_1 and F_2 (solid lines) to the analytic model for F_1 and F_2 (dashed lines). The track diameter is 10 μm, the models are plotted versus track fluence and χ. The analytic model begins to fail for $\chi \sim 0.25$, indicated by the solid vertical gray line. Typical track fluences are ≤ 25000, indicated by the dashed vertical gray line. The Monte Carlo statistics are good enough that scatter is not visible on this scale.

tracks with overlap fraction 2. The overlap fraction F is defined as

$$F_i(\eta) = N_i(\eta)/\eta. \tag{D.7}$$

So for an average* track diameter $\bar{D}$, we have $\bar{A}_1 = \pi\bar{D}^2$ and if we define the dimensionless parameter $\chi \equiv \eta \times (\pi\bar{D}^2)$,

$$F_1(\chi) = 1 - \chi \tag{D.8}$$
$$F_2(\chi) = \chi\,(1 - 2\chi/3) \tag{D.9}$$

This model is plotted as a function of χ versus a full Monte Carlo simulation in Fig. D.3, which shows that the analytic model is accurate for overlap fractions up to $\sim 25\%$ (here, track densities up to $\sim 8 \times 10^4/\text{cm}^2$).

The analytic model can be used to estimate amounts of overlap in various diagnostic scenarios. In particular, we consider here the NIF Magnetic Recoil Spectrometer (MRS)[13], which must diagnose a range of implosions from dud THD tuning-campaign implosions ($\text{Y}_\text{n} \sim 10^{14}$) to ignited, burning plasmas ($\text{Y}_\text{n} \sim 10^{19}$). For example, a break-even NIF implosion has $Y_n \sim 10^{18}$. Since the amount of overlap strongly depends on the average track diameter (Eqs D.5 and D.6) we vary the track diameter and plot the counting error due to overlap versus the primary neutron yield in Fig. D.4. At diameters $1 - 2\mu$m the data would be indistinguishable from intrinsic noise in the CR-39, placing a lower limit on the fluence dynamic range gain achievable with short etch times.

This information can also be plotted as the maximum allowable yield versus track diameter, Fig. D.5. This is calculated for six MRS configurations; in high-yield implosions the efficiency can be reduced to avoid track overlap via thinner foils and smaller apertures, but this has the undesirable effect of simultaneously lowering the signal-to-background ratio.

*Since the track area $\propto D^2$ this is only valid in the limit where the distribution width σ obeys $\sigma/D \ll 1$. For wide distributions the overlap is more heavily weighted towards the higher diameter part of the distribution. In Fig. D.8, we see that $\sigma/D \leq 0.3$ has no effect on overlap calculations.

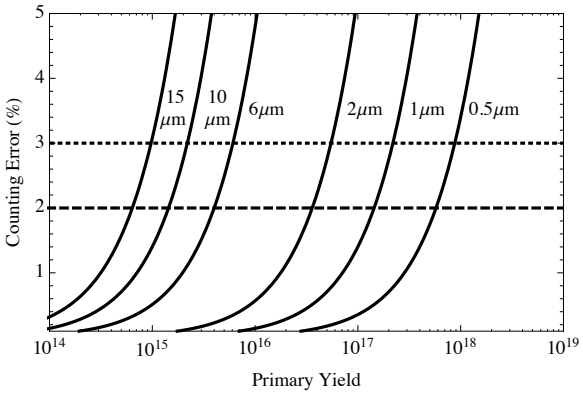

Figure D.4. Counting error due to track overlap versus primary neutron yield for a variety of track diameters ($0.5-15\mu$m). This is calculated for the NIF Magnetic Recoil Spectrometer (MRS) efficiency using a 20 cm^2 aperture and 138.2μm CD foil. The dashed and dotted lines represent $2-3\%$ counting error, the maximum allowable error for this application.

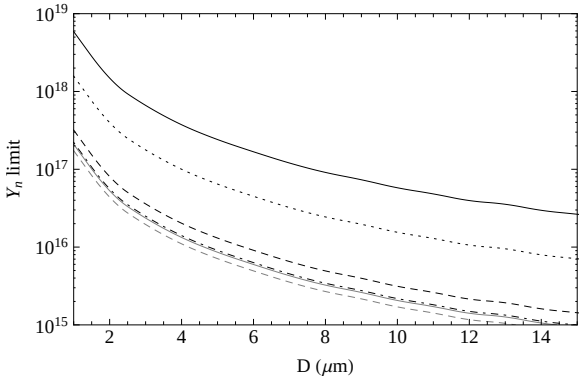

Figure D.5. Using the results of Fig. D.4, the allowable Y_n for a 3% counting error is plotted versus track diameter for the NIF MRS efficiency using a the configurations in Table D.1, from top to bottom: solid (#1), dotted (#2), dashed (#3), dot-dashed (#4), solid gray (#5), and dashed gray (#6).

Number	Foil (μm)	Aperture (cm^2)	Efficiency [Tracks/(DT-n cm^2)]
1	25	1	3.24×10^{-13}
2	25	6	1.21×10^{-12}
3	47.4	20	5.98×10^{-12}
4	100.4	20	8.61×10^{-12}
5	138.2	20	9.1×10^{-12}
6	259.2	20	1.1×10^{-11}

Table D.1. MRS Configurations, with calculated efficiency (signal + background). Configurations 3-6 are currently in use at the NIF.

D.3 Simulation code

A Monte Carlo track overlap code has been developed for computational studies of this problem. The code randomly places tracks using a uniform spatial distribution in the simulation plane. Track diameters are chosen from Gaussian or arbitrary distributions. The code incrementally adds a number of tracks dN and computes the overlap fractions at each step. A buffer region outside of the proper simulation area ensures accurate counting without edge effects (see Fig. D.6).

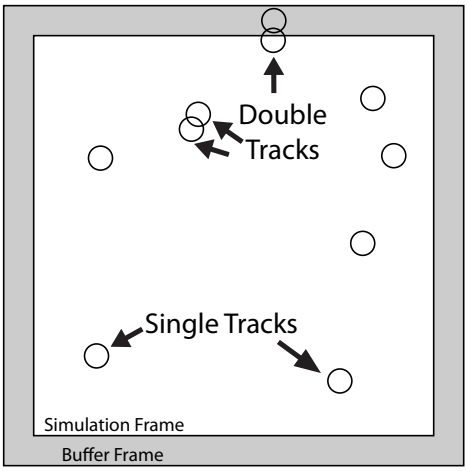

Figure D.6. An example simulation frame with six single tracks and three double tracks.

The problem is polynomial run time in the total number of tracks, increment dN, and the total fraction of tracks overlapping. While polynomial algorithms are in general computationally easy, the large Ns required can cause long run times. For that reason the simulation plane is split into multiple areas for parallel processing.

D.4 Simulation results

In this section, we present simulation results under various conditions to both illustrate the versatility of the code as well as examine properties of track overlap in CR-39 and other similar detectors. For the former, we first show the fractions F_n for $n = 1, 2, 3$ and $n \geq 4$ versus track density χ in Fig. D.7. We can see that the track overlap becomes significant when χ is a few tenths. The parameter χ is 'universal' for any diameter and fluence combination through $\chi \equiv \eta \times (\pi \bar{D}^2)$, so the curves in Fig. D.7 vs χ apply to any narrow distribution.

In this problem a 'narrow' distribution refers to the case when σ/D is small compared to 1, as in Section D.2. Since the Monte Carlo code can sample arbitrary distributions we can explore this regime with Gaussian distributions. For example, for $D = 6$ μm we take $\sigma = 0, 0.5, 1.0, 2.0$ μm and plot F_1 and F_2 versus χ, Fig. D.8, we can clearly see that there is no effect on $F_1(\chi)$ for Gaussian distributions up to $\sigma/D \sim 1/3$. However, if we instead plot $F_2(\chi)$ we can see deviations for χ of order unity between the various distributions. We therefore conclude that the distribution width is a second-order effect in that it does not change the fraction of tracks that are non-overlapping for reasonable χ. For higher n there is an effect for $\sigma/D \gtrsim 0.1$

Similar effects can result from non-Gaussian diameter distributions, which occur in real data. Fig. D.9 shows a track diameter distribution from ~ 3 MeV protons incident on a CR-39 detector. There are small components in the distribution at much larger track diameters than the mean, at $D \sim 18$ and 27 μm.

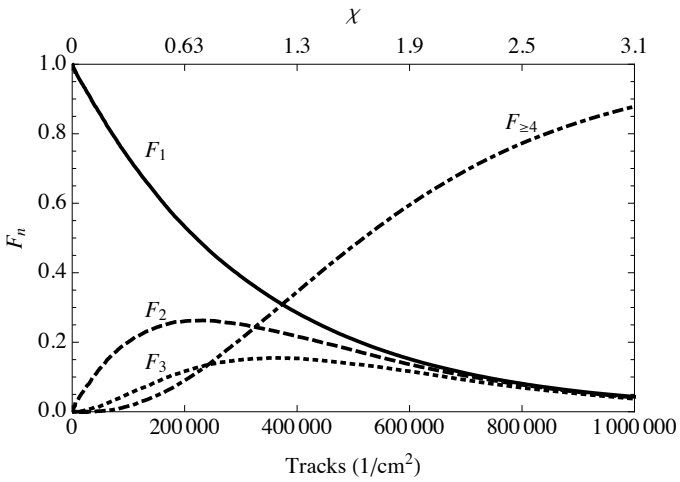

Figure D.7. F_n versus track density for 10 μm tracks and $n = 1$ (solid line), $n = 2$ (dashed line), $n = 3$ (dotted line), and a sum of all $n \geq 4$ (dot-dashed line). When plotted versus *chi* the shape of the curve is 'universal' for any diameter through the relation $\chi \equiv \eta \times (\pi \bar{D}^2)$. In Fig. D.3, we can see that the analytic model is only valid until $\chi \sim 0.25$, compared to the Monte Carlo code which can be run to high χ.

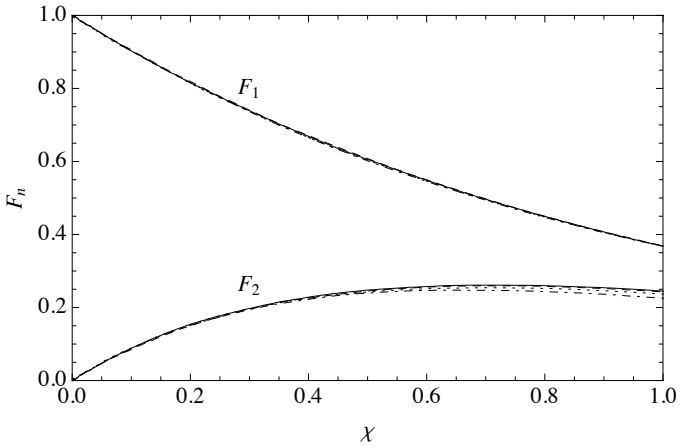

Figure D.8. F_1 and F_2 vs χ for track $D = 6$ μm and $\sigma = 0$ (solid line), 0.5 (dashed line), 1.0 (dotted line), and 2.0 (dot-dashed line) μm. The curves overlap significantly for F_1, and show small deviation with σ at $\chi \sim 1$.

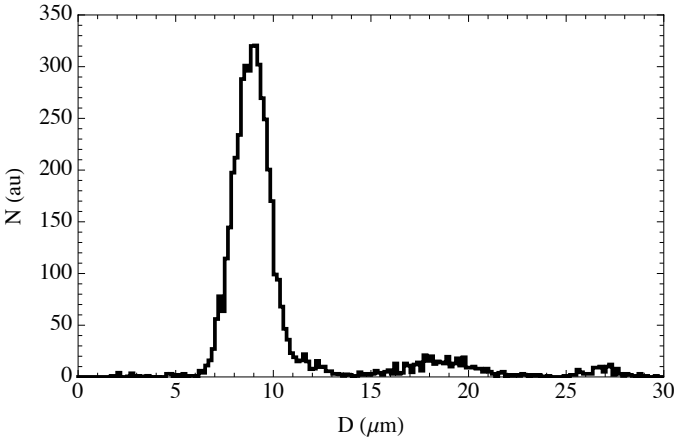

Figure D.9. A diameter distribution from real CR-39 data with a primary proton signal at $D \sim 9$ μm and weaker non-Gaussian components at larger diameters ($D \sim 18$ and 27 μm).

The track overlap for the distribution in Fig. D.9 was simulated when considering the whole distribution and a Gaussian fit to the prominent peak at $D \sim 9$ μm. The results are shown in Fig. D.10. Similarly to the effect of the distribution standard deviation we see no difference in the fraction of single tracks for the raw distribution compared to the Gaussian distribution. However, the double track fraction F_2 shows a deviation indicating that non-Gaussian distributions are also a second-order effect changing overlap fractions F_n for $n \geq 2$.

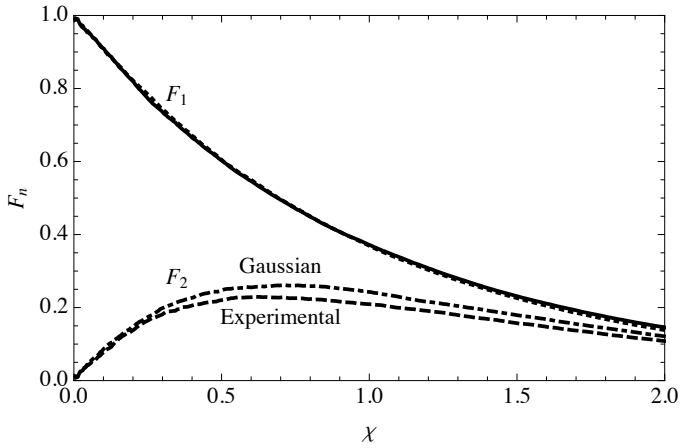

Figure D.10. Simulations of F_1 and F_2 for the experimental diameter distribution (solid and dashed lines, respectively) and a Gaussian fit to the primary component at $D \sim 9$ μm (dotted and dot-dashed, respectively).

D.5 Post-hoc overlap correction algorithm

The Monte Carlo simulation is also used for a post-hoc correction of track overlap in data. In experimental data it is difficult to analyze an overlapping track structure due to complicated geometry and the stochastic track placement (e.g. see Fig. D.1). If the number of non-overlapping tracks is known, on the other hand, it can be related via theory or simulation to the total number of tracks (see Sec. D.2 or D.4).

To discriminate against overlapping tracks, which are still detected by the automated optical microscope system used to process CR-39[14], it is necessary to discriminate between single and overlapping tracks in this method. In principle this can be done by using the track eccentricity information; e.g. two overlapping non-concentric tracks will form a quasi-elliptical shape with non-zero eccentricity and larger diameter than a single track. As a demonstration, Fig. D.11 shows a contour plot of CR-39 data with overlap. The single tracks are clustered at $D \sim 11$ μm and eccentricity of about a few percent. The overlapping tracks appear at larger diameter and eccentricities of several tens of percent. Additionally, we note that inferred diameter is proportional to eccentricity as expected from geometry. In this case, the data could be limited to eccentricities below $8 - 10\%$ to reject overlapping tracks while retaining single tracks.

Once the data is discriminated to single tracks only, the measured track distribution is used as a source function in the Monte Carlo simulation. The code then incrementally increases the track fluence until it matches the observed fluence of single tracks, at which point the code reports the total fluence necessary to match the data.

Experimental tests of this method have been performed using a linear electrostatic ion accelerator (LEIA) fusion products source at MIT[10,11], and with capsule implosions at the OMEGA laser[9]. In the accelerator experiment we used energetic protons from the reaction

$$\mathrm{D} + \mathrm{D} \rightarrow \mathrm{T}(1.01\ \mathrm{MeV}) + \mathrm{p}(3.02\ \mathrm{MeV}), \tag{D.10}$$

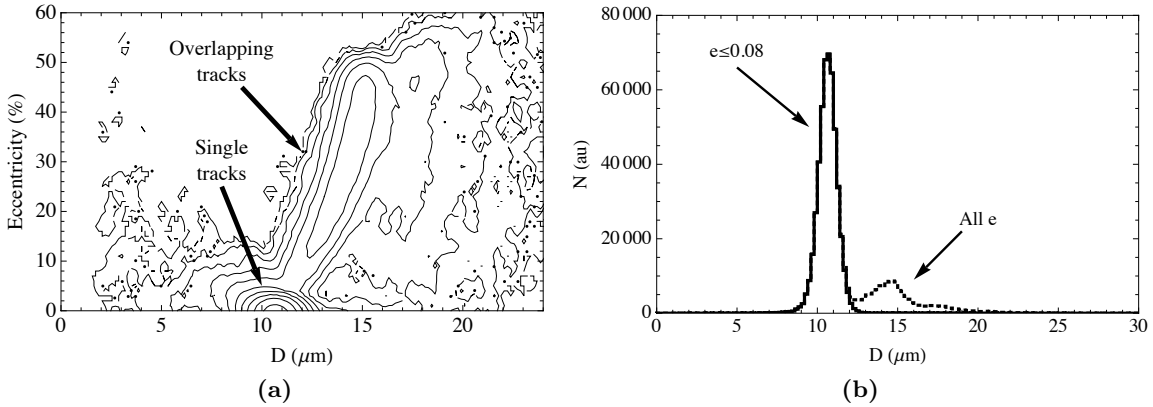

Figure D.11. (a) Contour plot of number of tracks versus track eccentricity and diameter, for overlapping data etched to 6 hours. The diameter is defined as $D = 2\sqrt{A/\pi}$ where A is the total measured track area. Single tracks are visible near zero eccentricity (perfectly round) and $D \sim 11$ μm while overlapping tracks have more eccentricity and larger diameters. The ratio of adjacent contours is 2. (b) Diameter histogram for the same data, with an eccentricity limit of 8% (solid) and without limit (dotted). The eccentricity is defined as for a geometric ellipse; $e \leq 0.08$ means that tracks are only accepted if they are between perfectly circular ($e = 0$) and 8% out of round ($e = 0.08$).

Figure D.12. Experimental test of the algorithm performance. Data points are plotted as inferred counting error vs overlap fraction. Two datasets are shown: accelerator DD-p (circles) and OMEGA D^3He-p (open squares). A naïve counting scheme, without overlapped tracks counted, would lie on the 45° line (dashed).

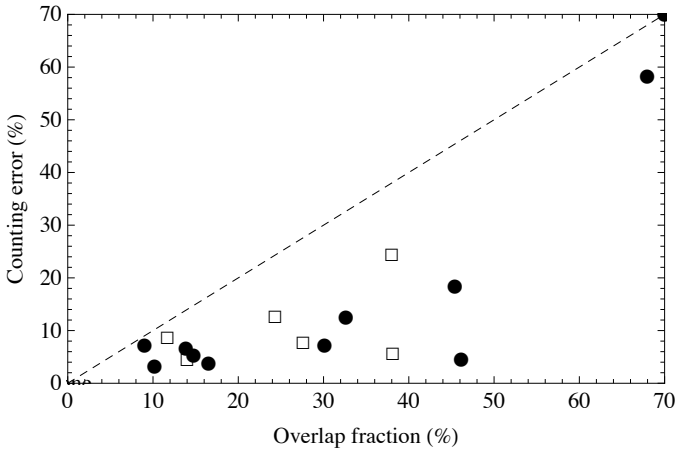

and in the OMEGA experiments from the reaction

$$\mathrm{D} + {}^{3}\mathrm{He} \rightarrow {}^{4}\mathrm{He}(3.6\ \mathrm{MeV}) + \mathrm{p}(14.7\ \mathrm{MeV}), \tag{D.11}$$

to expose CR-39 samples to various proton fluences. The CR-39 was etched for a short enough period of time that there was minimal overlap and the fluence recorded. We then etched the CR-39 further until significant overlap occured, and rescanned the same area again. This allows an accurate determination of the counting precision with induced track overlap.

The results of this experiment are shown in Fig. D.12, plotted as the measured counting error in the overlapping data versus the fraction of tracks overlapping. In the naïve case, with all overlapping tracks thrown away and no correction, the trend would be a 45° line (dashed line). For relatively low amounts of overlap $10-20\%$, the algorithm has a counting error $< 10\%$. For higher overlap fractions $\sim 30-45\%$ the counting error increases to $\sim 10-20\%$. Finally, at very high overlap fractions (70%) the algorithm breaks down and the counting error becomes very large.

The algorithmic accuracy is primarily limited by the single vs overlapping track discrimination (via eccentricity cuts in the CR-39 analysis), as well as statistics in determining fluence and diameter distributions in both the data and calculation. For these reasons the current results are a limitation of the method.

By comparison to Fig. D.7, where the overlap fractions are plotted versus fluence, we can see that in applications were $\sim 10\%$ counting accuracy is acceptable this technique can extend the upper fluence limit of CR-39 by about a factor of $3-4$.

D.6 Conclusions

The solid-state nuclear track detector CR-39 is used in various diagnostics at laser ICF facilities, where high track fluences are easily achievable. Previous counting techniques were limited to regimes in which the physical overlap of particle tracks was small, which defined the upper limit of dynamic range for many of these diagnostics. In the low-overlap regime the overlapping fraction of tracks scales as $\chi \equiv \eta \times (\pi \bar{D}^2)$ where η is the density of tracks and $\bar{D}$ is the average track diameter, derived in a simple theory. A Monte Carlo simulation code has been developed to study the effects of track overlap in these detectors under various scenarios. Illustrative examples of simulation results are presented. We report on a post-hoc overlap correction algorithm, which uses Monte Carlo simulations to correct for overlap in CR-39 data based on matching simulated single track results to the data. In applications where counting accuracy $\sim 10\%$ is acceptable, this technique can extend the upper fluence limit by a factor of $3-4$x. Future work will focus on the development of a new algorithm to recognize overlapping tracks based on shape during the optical microscope scan, which will allow for diameter measurements and more accurate counting in high-fluence scenarios.

For applications such as high-precision counting (to a few percent for MRS data) or diameter identification of overlapping tracks for complicated distributions (i.e. Wedge Range Filter[14] data) another technique is required. The future work of this project includes the development of an algorithm to recognize overlapping tracks during the optical microscope scan by the track shape. Benchmarking this algorithm will then allow its application to diagnostics at laser fusion facilities. We will also study the response of CR-39 track detectors at short etch times ($1-2$ hours, versus typical 6) to characterize the minimum etch time necessary to distinguish data from noise; this short-etch technique will also be useful for extending the upper fluence range of these detectors.

Table D.2. Shot numbers for experimental data shown in each figure.

Figure	Shot Number
1	A2010020104
9	A2009102201
11	A2010020104
12	A2010020101-4 A2010021701-3 Ω62407-8
A.13	Ω62407
A.14	Ω62407
B.15	A2010020102-4

D.7 Diameter distribution evolution

As an example, we provide contour plot of number of tracks versus track eccentricity and diameter as well as diameter histograms for a dataset with overlap induced via progressive etches. Filters are used to reduce the proton energy from 14.7 MeV (undetectable with CR-39) to ~ 4 MeV, which is in the detectable regime. All CR-39 used in this study was etched with a 6 molar NaOH solution at 80° C.

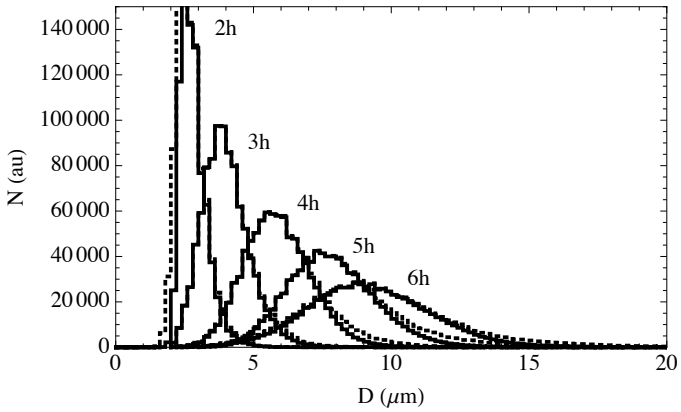

Figure D.13. Diameter distributions for D^3He-p data etched to 2-6h. Solid traces are for eccentricities less than 15%, while dotted curves are summed over all eccentricities. The data presented in this plot is the same as in Fig. D.14.

D.8 Fluence Examples

For reference, we present example microscope images for various fluences of DD-p on CR-39 in Fig. D.15.

D.9 Shot Numbers

Facility shot numbers (A denotes MIT linear electrostatic ion accelerator, Ω denotes the OMEGA laser facility) for all data given in this paper are tabulated in Table D.2.

D.10 References

1. D. Young, "Etching of radiation damage in lithium fluoride," Nature, **182** (1958).

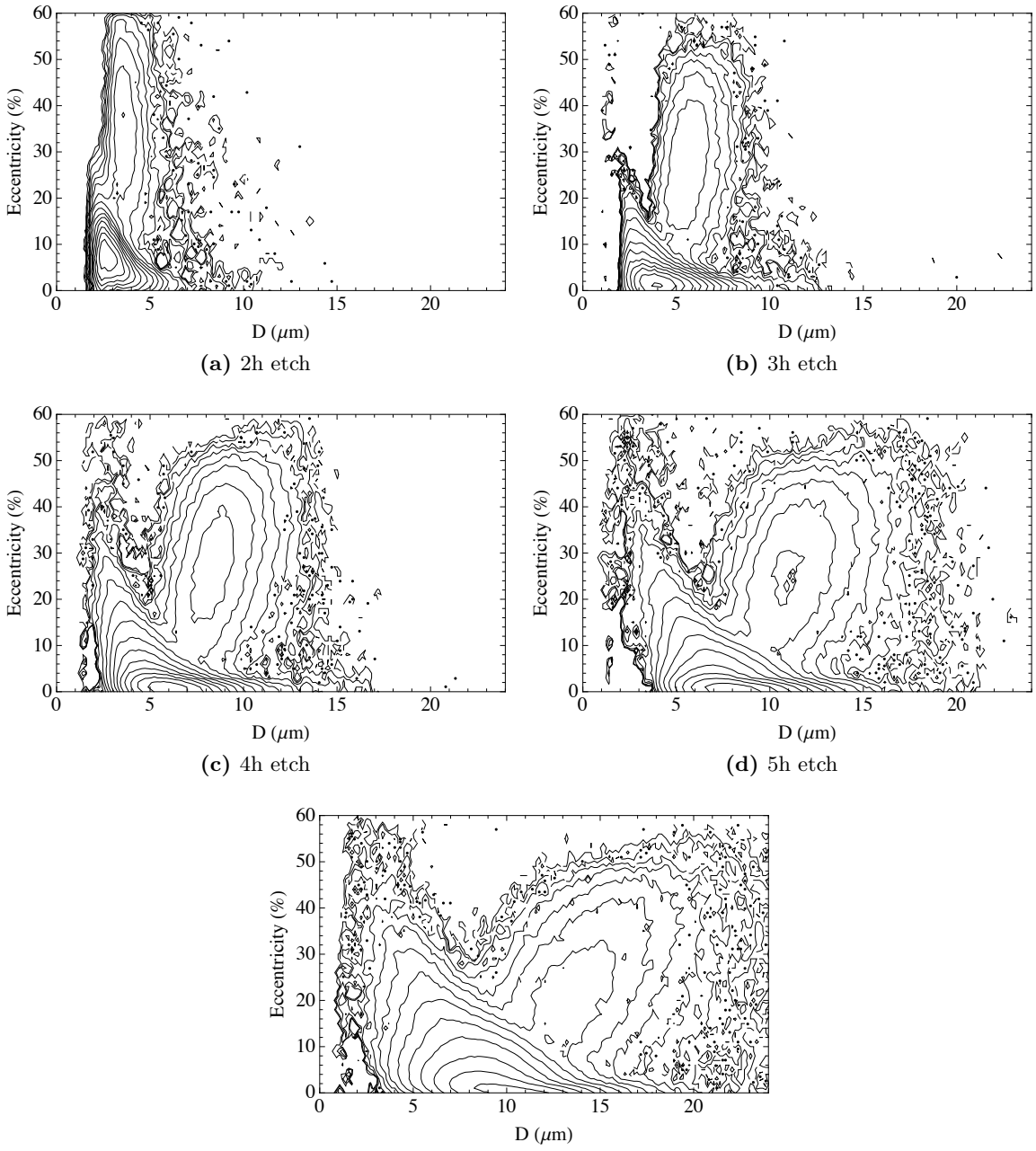

(a) 2h etch

(b) 3h etch

(c) 4h etch

(d) 5h etch

(e) 6h etch

Figure D.14. Contour plots of number of tracks versus track eccentricity and diameter, for overlapping D^3He-p data etched to 2-6 hours. Single tracks are visible near zero eccentricity (perfectly round) while overlapping tracks have more eccentricity and larger diameters. The ratio of adjacent contours is 2. The data presented in this plot is the same as in Fig. D.13.

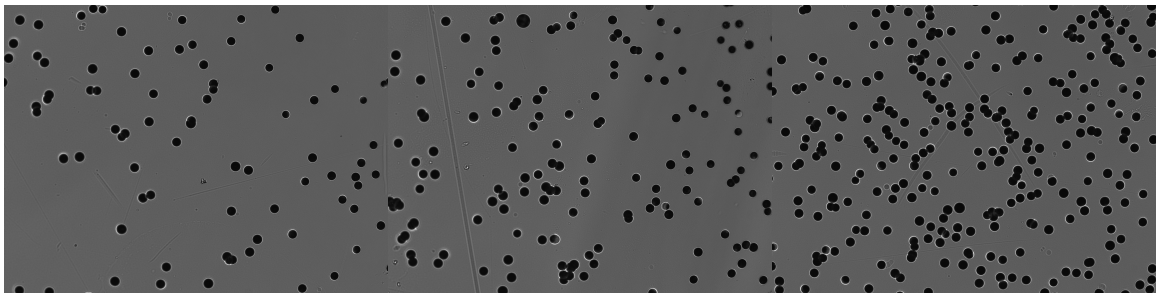

(a) $\eta = 4.4\times10^4$ p/cm^2, or $\chi = 0.16$**(b)** $\eta = 8.9\times10^4$ p/cm^2, or $\chi = 0.33$**(c)** $\eta = 1.8\times10^5$ p/cm^2, or $\chi = 0.63$

Figure D.15. Varying fluences of 3 MeV DD-p, CR-39 with overlap observable after being etched for 6 hours. The image was taken with an optical microscope system with a frame area of 1.36×10^{-3} cm^2 (431μm $\times$ 315.5μm). 25μm Aluminum filtering was used to remove couplementary particles (T, ^{3}He, ^{4}He) from DD and D^{3}He fusion. Neutrons from DD fusion are also incident on the CR-39, but the detection efficiency for neutrons (due to scattered protons in the CR-39) is 10^{-4} below the proton detection efficiency and the neutrons are therefore negligible in this work.

2. E. Silk and R. Barnes, "Examination of fission fragment tracks with an electron microscope," Philosophical Magazine, **4**(44), 970–972 (1959).
3. R. Fleischer, P. Price and R. Walker, *Nuclear tracks in solids: principles and applications* (University of California Press, 1975).
4. S. Durrani and R. Bull, *Solid state nuclear track detection* (Pergamon Books Inc., Elmsford, NY, 1987).
5. A. Fews and D. L. Henshaw, "High resolution alpha particle spectroscopy using CR-39 plastic track detector," Nuclear Instruments and Methods in Physics Research, **197**(23), 517 – 529 (1982).
6. N. Sinenian, M. Rosenberg, M. Manuel *et al.*, "The response of CR-39 nuclear track detector to 19 MeV protons," Rev. Sci. Instrum., **82**, 103303 (2011).
7. S. Gaillard, J. Fuchs, N. Renard-Le Galloudec *et al.*, "Study of saturation of CR39 nuclear track detectors at high ion fluence and of associated artifact patterns," Rev. Sci. Instrum., **78**, 013304 (2007).
8. D. Gautier, J. Kline, K. Flippo *et al.*, "A simple apparatus for quick qualitative analysis of CR39 nuclear track detectors," Rev. Sci. Instrum., **79**, 10E536 (2008).
9. T. Boehly, D. Brown, R. Craxton *et al.*, "Initial performance results of the OMEGA laser system," Optics Communications, **133**(1-6), 495–506 (1997).
10. S. McDuffee, J. Frenje, F. Séguin *et al.*, "An accelerator based fusion-product source for development of inertial confinement fusion nuclear diagnostics," Rev. Sci. Instrum., **79**, 043302 (2008).
11. N. Sinenian, M.-E. Manuel, A. Zylstra *et al.*, "Upgrade of the MIT Linear Electrostatic Ion Accelerator (LEIA) for nuclear diagnostics development for Omega, Z and the NIF," Rev. Sci. Instrum., **83**(4), 043502 (2012).
12. T. Yamauchi, "Studies on the nuclear tracks in CR-39 plastics," Radiation Measurements, **36**(1-6), 73–81 (2003).
13. J. A. Frenje, D. T. Casey, C. K. Li *et al.*, "Probing high areal-density cryogenic deuterium-tritium implosions using downscattered neutron spectra measured by the magnetic recoil spectrometer," Physics of Plasmas, **17**(5), 056311 (2010).
14. F. H. Séguin, J. A. Frenje, C. K. Li *et al.*, "Spectrometry of charged particles from inertial-confinement-fusion plasmas," Rev. Sci. Instrum., **74**(2), 975–995 (2003).

Appendix E

Measurements of hohlraum-produced fast ions

E.1 Introduction

Understanding hohlraum physics is crucial to achieving ignition at the NIF using the indirect-drive scheme (see Chapter 1); many fundamental hohlraum-physics problems can be more easily studied at smaller-scale facilities such as OMEGA at the University of Rochester[1]. Fast ions and hot electrons produced in laser-plasma interactions (LPI) are known effects, and studied theoretically[2–5] and experimentally[6,7]. In ICF ignition experiments, hot electrons produced by LPI are energetic enough to penetrate the ablator material and deposit energy in the cryogenic fuel, which increases the fuel adiabat and thus reduces the fuel compressibility. Therefore, understanding hot electron production and preheat is critical for achieving ignition[8].

Additionally, strong electrostatic fields around direct-drive implosions were discovered[9] and studied[10] three decades ago. More recent experiments extensively studied these electric fields[11] and related production of fast ions[12] in direct-drive implosions.

Fast ion production has not been studied in hohlraum experiments, as relevant to the NIC. The NIC design uses gas-filled hohlraums to impede plasma flow at the hohlraum wall[13–15]. This requires a thin window at the laser entrance hole (LEH) to contain the initial gas fill. Since the laser beams overlap at the LEH, this can create complex LPI. Recent experiments measured hot electron production due to LPI at the LEH[16], and attributed the hot electron production to the two-plasmon decay (TPD) instability[17,18].

In this Appendix, the first measurements of fast ions produced in both vacuum and gas-filled hohlraum experiments are presented. Fast ion measurements were conducted with the OMEGA Charged-Particle Spectrometer (CPS) 2, or flat-filtered CR-39. Using three geometries: 2.4mm diameter (scale 1.5) half hohlraums and hohlraums, and 1.2mm diameter (scale 0.75) hohlraums. Experimental configurations were designed and analyzed using VISRAD software[19].

E.2 Charged-Particle Spectrometer Results

E.2.1 Experimental Design

E.2.1.1 Scale 1.5 Halfraums

Fig. E.1 shows the OMEGA scale 1.5 hohlraum used in these experiments. These hohlraums had a 100% LEH composed of 0.6μm polyimide window. The gas fill was $0.04 - 0.1$ n_c neopentane. The hohlraums are driven from one side only, with 15 beams in 2 cones (Cone 2 at 42° and Cone 3 at 59°), with beams pointed at the LEH center, at a maximum total drive energy of 5.8kJ. The

laser drive was a 1ns square pulse (SG1018) using SG4 phase plates and SSD. The hohlraum axis is aligned along the P6-P7 axis in the OMEGA target chamber.

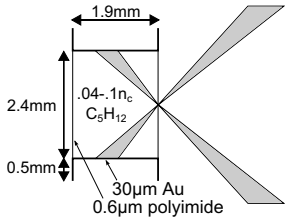

Figure E.1. Cartoon of an OMEGA scale 1.5 halfraum with 100% LEH and gas fill, driven from one side.

The halfraums can be driven from either side. This is shown in Fig. E.2. The drive side is hereafter referred to as either P6 or P7, as shown in Fig. E.2. The line of sight for CPS 2, which was used for the fast-ion measurement, is also illustrated in the figure.

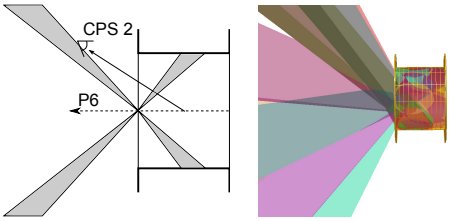

(a) P6 Drive Cartoon

(b) P6 Drive Visrad

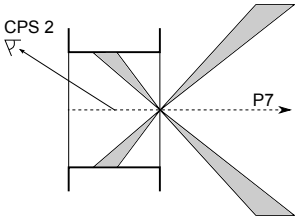

(c) P7 Drive Cartoon

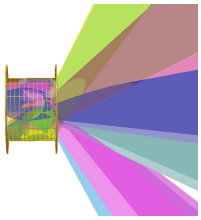

(d) P7 Drive Visrad

Figure E.2. The halfraums can be driven from either side. (a,c) Cartoons of halfraum geometry with P6 or P7 drive, respectively. The CPS 2 line of sight is also shown in these figures. (b,d) Visrad CAD models of halfraum geometry with P6 or P7 drive, respectively.

Drive intensities are calculated for both P6 and P7 drives at the halfraum wall as well as the LEH window, shown in Figs. E.3 and E.4, shown as viewed from the CPS 2 line of sight. Shown is a full energy halfraum drive, 5.8kJ. Shots were also taken at 1/5 drive energy, in which the calculated intensities should be divided by five. We observe from Figs. E.3 and E.4 that the peak intensity is $\approx 10^{14}$ W/cm^2 at the halfraum wall, and $\approx 10^{15}$ W/cm^2 at the LEH. In the case where the halfraum is driven from P7 then CPS 2 does not have a clear view of the center of the LEH window.

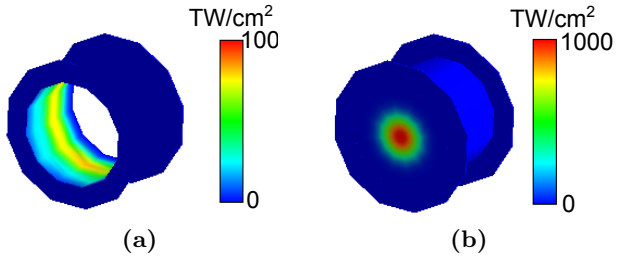

Figure E.3. P6 drive intensities at the hohlraum wall (a) and at the LEH (b), as viewed from CPS 2.

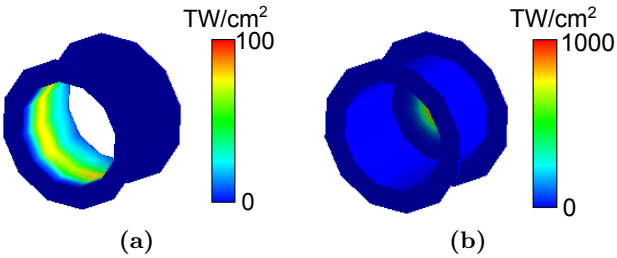

Figure E.4. P7 drive intensities at the hohlraum wall (a) and at the LEH (b), as viewed from CPS 2.

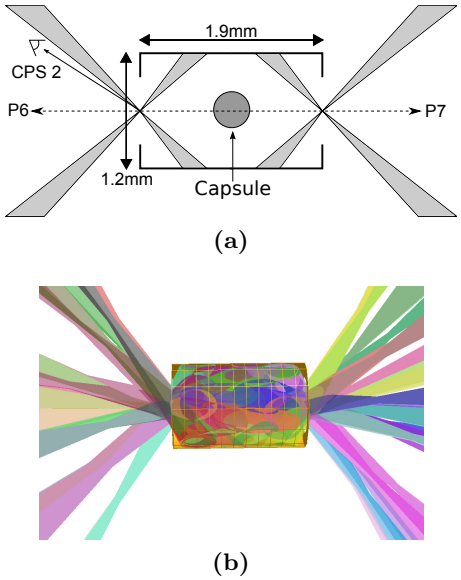

Figure E.5. (a) Cartoon of an OMEGA scale 0.75 hohlraum with 66% LEH. (b) VISRAD CAD model.

E.2.1.2 Scale 0.75 Hohlraums

Data was also taken on scale-0.75 hohlraums with a 66% LEH and no gas fill, as shown schematically in Fig. E.5. The hohlraums contained a gas-filled capsule. The hohlraum was oriented along the P6-P7 axis as in the other experiments. The hohlraum was driven by 40 beams in cones 1 (21.4°), 2 (42°), and 3 (59°) with a total energy of 20kJ using the main driver without phase plates. The resulting intensity map on the hohlraum wall is shown in Fig. E.6, as viewed from the CPS 2 line of sight.

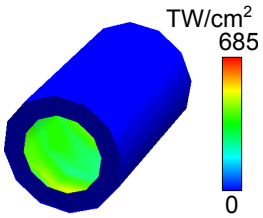

Figure E.6. Drive intensity at the hohlraum wall for the scale 0.75 hohlraum, as viewed from the CPS 2 line of sight.

E.2.2 Results

E.2.2.1 Scale 1.5 Halfraums

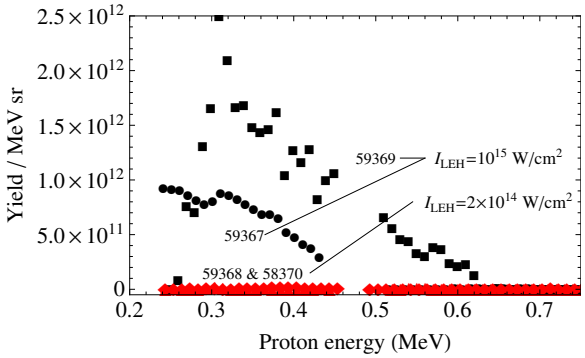

Figure E.7. Charged particle spectra from four OMEGA scale 1.5 gas-filled halfraum shots: 58367 (P7 drive, black circles), 58369 (P6 drive, black squares), 58368 (P7 drive, red triangles), and 58370 (P6 drive, red diamonds). See Table E.1 for experimental configurations.

The CPS-measured charged particle spectra for halfraum shots (as described in Sec. E.2.1.1) are shown in Fig. E.7. Data from four OMEGA shots are overplotted. The experimental configuration is summarized in Table E.1. We can see significant charged-particle production (of order 10^{12} fast protons per MeV per steradian) in two spectra of Fig. E.7. These are the higher drive energy (5.8kJ) and thus higher intensity at the hohlraum wall (10^{14} W/cm^2) shots, with the halfraum driven from P7 (Shot 58367) and P6 (Shot 58369). We observe a higher flux of protons and a higher maximum energy for the halfraum driven from P6. This could be because of a preferential acceleration direction due to the plasma waves propagating along the density gradient in the resonance absorption mechanism: In the P6 drive case the diagnostic line of sight is close to the laser propagation angle (Fig. E.3), but this is not the case for the P7 drive (Fig. E.4).

Table E.1. Experimental configuration for halfraum shots.

Shot	Drive	Energy (kJ)	I_{LEH} (W/cm^2)	I_{Wall} (W/cm^2)
58367	P7	5.8	10^{15}	10^{14}
58368	P7	1.2	2×10^{14}	2×10^{13}
58369	P6	5.8	10^{15}	10^{14}
58370	P6	1.2	2×10^{14}	2×10^{13}

E.2.2.2 Scale 0.75 Hohlraums

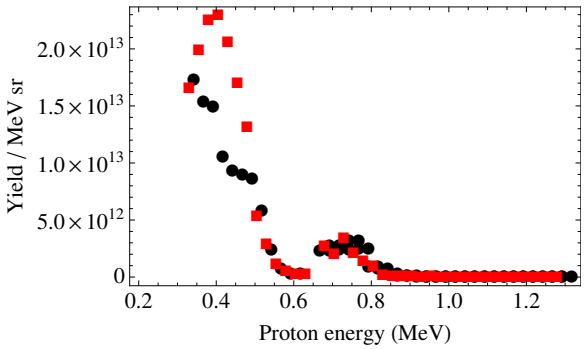

Figure E.8. Charged particle spectra from two OMEGA scale 0.75 vacuum hohlraum shots: 35769 (black circles) and 35770 (red squares). See Section E.2.1.2 for experimental configuration. The laser intensity at the hohlraum wall was 3.5×10^{14}.

The fast ion spectra for two scale 0.75 hohlraum shots, as measured by CPS 2, is shown in Fig. E.8. Significant fast ions are observed, at higher fluence per solid angle than the halfraum case in Sec. E.2.2.1 by about an order of magnitude, which is discussed in the following section. Shot 35770 had about 700J more laser energy due to shot-to-shot variations, which explains the higher proton fluence observed.

Fig. E.8 also shows a repeatable peak feature at 700-800 keV. In direct-drive implosions, structure in fast ion spectra has been observed[12]. Recent radiography results show charge shells, which are hypothesized as ion acoustic perturbations in the coronal plasma associated with the charged-particle spectral shape[20]. A similar mechanism might be occurring in these hohlraums, which could be investigated with high-resolution charged-particle radiography.

E.3 Flat-filtered CR-39 Results

E.3.1 Scale 1.5 Hohlraum Design

The 1.5-scale hohlraum is essentially two 1.5-scale halfraums combined, as shown in Fig. E.9. The hohlraum is driven from both sides. In this experiment, the full hohlraums had a solid CH capsule in the center, and either a $0.1n_c$ neopentane gas fill or vacuum. The vacuum hohlraums were shot with or without a CH liner on the inner wall. The drive was the same for each side as the equivalent

halfraum case, Figs. E.3 and E.4, to generate the same peak intensities at the wall and LEH. The total drive energy is 11.6kJ.

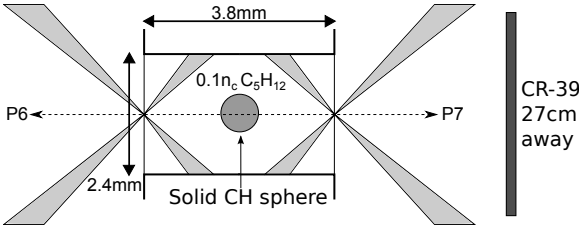

(a)

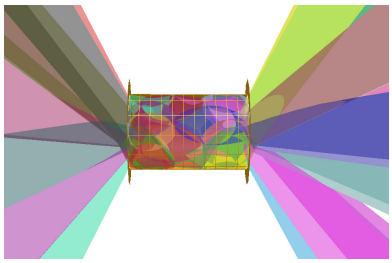

(b)

Figure E.9. (a) Cartoon of an OMEGA scale 1.5 hohlraum with 100% LEH and gas fill. (b) VISRAD CAD model of hohlraum geometry with beams.

E.3.2 Results

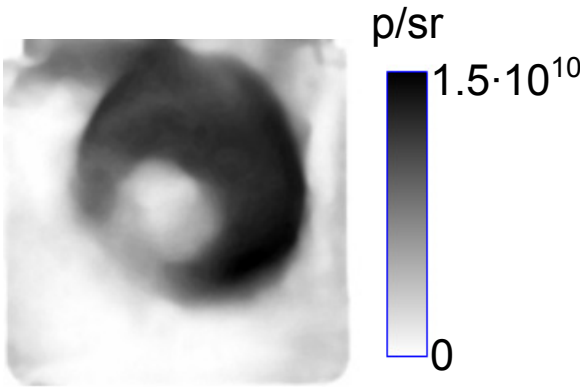

Figure E.10. Flat-filtered CR-39 'radiograph' of a 11.6kJ gas-filled hohlraum implosion with no proton backlighter, plotted as a proton fluence image. The minimum proton energy observable is 1.2 MeV. The CR-39 was placed at 27cm towards P7 (see Fig. E.9).

Flat-filtered CR-39 was fielded 27cm away from the target for full gas-filled hohlraum shots, as described in Sec. E.3.1 and shown in Fig. E.9. The result from this measurement is shown in Fig. E.10. The CR-39 is filtered with $\sim 7.5\mu$m of Ta, which gives a minimum detected proton energy of 1.2 MeV. This is at a higher energy than measured in Fig. E.7, and the proton fluence for all $E_p > 1.2$MeV is of order 10^{10} protons per steradian. In the center of Fig. E.10 we can see a shadow

of the capsule in the hohlraum, since it ranges out any protons incident upon it. Protons from the P6-side of the hohlraum (left side of Fig. E.9) can be stopped by the capsule since the detector is placed towards P7 (also shown in Fig. E.9). The shadow effect shows proton emission towards TCC. Combined with the halfraum data shown in Fig. E.7, this further demonstrates that the fast ion emission is in both directions along the hohlraum axis.

In identical radiography experiments using lined and unlined vacuum hohlraums, as recently published[14], the proton fluence on the front piece of flat-filtered CR-39 is of order 10^8 p/sr, which is two orders of magnitude below the fluence observed in Fig. E.10. In those previous experiments a fusion proton backlighter was used with $Y \approx 10^9$, which accounts for the proton fluence observed[14]. In these experiments, with identical drive, the two order of magnitude increase in proton fluence on the detector can only be explained by fast protons produced in the hohlraum LEH or gas fill.

E.4 Interpretation

First, we consider the charged particle spectra presented in Sec. E.2.2.2. Since fast protons are observed in the vacuum scale 0.75 hohlraums (Fig. E.8) we conclude that these fast protons cannot be produced by any LPI mechanism at the LEH window. This production mechanism is therefore associated with the general hohlraum charging, as discovered using charged-particle radiography[13], which creates $\vec{E}$ fields of order 10^9 V/m. Such strong fields can create runaway ions. The higher yield of fast ions below 1 MeV in the scale 0.75 experiments compared to the scale 1.5 halfraums (Fig. E.8 vs E.7) is likely due to a $\sim 4\times$ higher total laser energy and intensity at the hohlraum wall in the scale 0.75 experiments (compare Fig. E.6 to Figs. E.3 and E.4).

Since energetic (≥ 1.2 MeV) fast protons are only observed in gas-filled hohlraums we associate this production mechanism with thin plastic LEH window or gas fill.

To explain these observations, we must consider the fundamental LPI instabilities. In general, potentially applicable and well-known LPI mechanisms are: Resonance Absorption (RA), Parametric Decay Instability (PDI), Two-Plasmon Decay (TPD), Stimulated Brillouin Scattering (SBS), and Stimulated Raman Scattering (SRS). For more detail on laser-plasma interaction physics, see Kruer[18].

In general, it is known that fast ion production in laser plasmas is associated with prior hot electron generation, as the runaway hot electrons set up strong $\vec{E}$ fields that accelerate the ions. We therefore focus on mechanisms which can generate hot electrons in this indirect-drive implosion geometry: RA, PDI, TPD, and SRS.

E.4.1 Hohlraum mechanisms

An important recent and related result from Li et al.[13] is that large hohlraum fields were observed at the beginning of the laser drive, reaching a strength $|\vec{E}| = 2$ GV/m within the first few hundred ps and monotonically decaying afterwards (see their Fig. 4). Therefore, the hohlraum charging mechanism must generate hot electrons early in time. Since SRS and TPD only occur in underdense plasmas, $\leq n_c/4$ and $n_c/4$, respectively, where n_c is the critical density, these mechanisms would require a large-volume ablated low-density gold plasma. Since previous proton radiography experiments showed that the timescale for hohlraum wall motion[14] is longer than the $\vec{E}$ field generation time[13], SRS and TPD in the ablated wall plasma cannot explain the data.

RA and PDI, which occur at the critical density, are more applicable to the laser-hohlraum wall interaction. RA requires a density gradient from the turning point to the critical density, with a scale length $L = k^{-1}(2\sin^2\alpha)^{-3/2}$, where α is the angle of incidence and k is the wavenumber of a laser photon. Since α is tens of degrees, the term in parentheses is of order unity, and L is of

order $1/k$ which is small. Therefore RA will occur early in time when the wall plasma has small gradient lengths. Alternatively, PDI requires a volume of plasma near n_c, which means that it will be more efficient later in time when the gold plasma gradient scales are longer. Since the previously published data[13,14] demonstrate that the hohlraum potential is built up early in time, we associate the hohlraum-charging fast ions with RA.

E.4.2 LEH or gas mechanisms

The TPD instability threshold of $(3-5)\times 10^{14}$ observed by Regan et al[16] is surpassed at the LEH for full-energy shots, and the entire gas fill is at $n < n_c/4$ so SRS can occur throughout the hohlraum volume for gas-filled experiments. TPD only happens around $n_c/4$. This is applicable to the exploding window plasma where a large amount of material is at (or close to) this density as the window rarefies into vacuum on one side and low-density gas on the other. SRS is applicable to the gas fill, which has the longest scale length of low-density plasma, or the exploded window plasma late in time. While these experiments clearly demonstrate fast proton production at $E_p \geq 1.2$ MeV (Sec. E.3.2 and Fig. E.10), it is not possible to distinguish between the two potential mechanisms.

E.5 Estimates of conversion efficiency to protons

E.5.1 Hohlraum Resonance Absorption

We can make simple estimates of the conversion efficiency for the 'hohlraum charging' production mechanism due to RA from the spectra shown in Figs. E.7 and E.8. The total energy in the fast ion population is

$$E = \iint d\Omega dE \, \frac{dY(E,\Omega)}{dE d\Omega} \times E. \tag{E.1}$$

If we assume that the emission is approximately isotropic far from the target, then

$$E_{\mathrm{hc}} = 4\times 10^6 \pi e \int_0^\infty \frac{dY(E)}{dE d\Omega} dE \tag{E.2}$$

where E_{hc} is in J, e is the fundamental charge, and Y is expressed in number per MeV·sr as in Figs. E.7 and E.8. Here E_{hc} specifically denotes the energy in fast protons due to the hohlraum charging.

Integrating the spectra for the shots shown in Figs. E.7 and E.8 we calculate the total energy in fast ions and conversion efficiencies ϵ shown in Table E.2.

Table E.2. Determined conversion efficiencies and total energy carried by fast protons due to the 'hohlraum charging' mechanism.

Shot	Drive (kJ)	E_{hc} (J)	ϵ_{hc}
58367	5.8	0.3	6×10^{-5}
58369	5.8	0.7	1×10^{-4}
35769	20	5.5	3×10^{-4}
35770	20	7.9	4×10^{-4}

E.5.2 LEH window TPD or gas-fill SRS

From the data presented in Sec. E.3 we can make order of magnitude estimates of the conversion efficiency for fast ion production due to TPD or SRS when the LEH intensity is about 10^{15} W/cm^2. We assume that the fast ion emission is symmetric around the hohlraum axis and Gaussian with scale θ_0 in the angle from the hohlraum axis. That is, with $\theta = 0$ along the hohlraum axis, the fluence emitted per steradian is

$$F(\theta, \phi) = \frac{Y_p}{4\pi} \frac{\alpha(\theta_0)}{\sqrt{2\pi}\theta_0} e^{-\theta^2/2\theta_0^2}, \tag{E.3}$$

where Y_p is the total yield of produced protons and α is a function of θ_0 involving the error function. $\alpha(\theta_0)$ is of order unity.

The simplest case is the hohlraum experiment (Sec. E.3.2), in which case we know F at $\theta \sim 0$ for protons with energies above 1.2 MeV. Setting $F = 1.5 \times 10^{10}$ protons per steradian and assuming $\theta_0 = 20$ degrees with symmetric emission forwards and backwards from both hohlraum ends we get $Y_p \sim 3 \times 10^{11}$. As these protons must all be at least 1.2 MeV, the total energy in fast protons with $E_p \geq 1.2$ MeV is $E_{\mathrm{TPD/SRS}} \gtrsim 60$mJ. As a fraction of the incident laser energy, the conversion efficiency for this population is $\epsilon_{\mathrm{TPD/SRS}} \gtrsim 5 \times 10^{-6}$. For the short etch times used, an upper bound on proton energies observed is $\sim 3 - 4$ MeV, implying that $\epsilon_{\mathrm{TPD/SRS}} \lesssim 2 \times 10^{-5}$

We note that from Eq. E.3 that for a given fluence at $\theta = 0$ the inferred proton yield scales with $\theta_0/\alpha(\theta_0)$. For $10 \leq \theta_0 \leq 40$, the inferred yield and conversion efficiency will scale by a factor of 4 from the assumption $\theta_0 = 20$ degrees.

E.6 Conclusions

Measurements taken of proton fluence and spectra from OMEGA hohlraum and halfram experiments demonstrate that fast ions are produced in indirect-drive implosions. The data consist of proton spectra from $300 - 800$ keV, as well as fluence measurements of protons with energy greater than 1.2 MeV.

Observations of fast protons with energies from 300 to 800 keV are observed in both vacuum and gas-filled hohlraums. These protons are associated with the general hohlraum charging seen in charged-particle radiography. We argue that this mechanism is RA, and estimate a conversion efficiency of $\sim (1 - 4) \times 10^{-4}$, depending on the hohlraum and drive. In the flat-filtered CR-39 data significant high-energy (≥ 1.2 MeV) fast protons are observed only for gas-filled hohlraums; we associate this production mechanism with the TPD instability at the exploding window plasma, which is in agreement with observations by Regan et al., or with SRS throughout the underdense gas fill. This mechanism has an estimated conversion efficiency from the main drive of $(0.5 - 2) \times 10^{-5}$ depending on assumptions made.

Future experiments could use several flat-filtered CR-39 detectors to angularly resolve the fast ion emission. The experiment could also be conducted in a geometry that would allow measurements with both magnetic charged particle spectrometers on OMEGA, which could allow a calculation of the emission angle θ_0.

We will also explore advanced radiography measurements of hohlraums using EP-generated protons. This will have the advantage of better spatial and temporal resolution over previous techniques, and could be used to study field structures and mass distributions in the exploding window plasma and plasma bubbles formed on the hohlraum wall. Such measurements would shed light on the fundamental plasma physics behind these observed phenomena.

Previous direct-drive experiments with Au spheres have shown discrepancies in fast proton production[7,12], which could be due to inconsistent hydrogen contaminant levels on the surface, or different plasma scale lengths relative to lower-Z ablators. This could be further investigated on OMEGA.

In addition to fast proton studies, a significant amount of energy can be carried away by heavier ions in direct-drive experiments. The proton measurements imply general ion acceleration, but measuring heavy fast ions produced in indirect-drive experiments would be an important extension of these results.

Simplified experiments to individually measure fast ion production due to indirect-drive relevant mechanisms are motivated by these observations, in particular to determine if SRS in gas filled hohlraums creates an appreciable population of fast ions compared to TPD at the LEH window. Furthermore, this experimental work motivates theoretical and computational study of fast ion production in indirect-drive laser fusion experiments.

E.7 References

1. T. Boehly, D. Brown, R. Craxton *et al.*, "Initial performance results of the OMEGA laser system," Optics Communications, **133**(1-6), 495–506 (1997).
2. J. Crow, P. Auer and J. Allen, "The expansion of a plasma into a vacuum," Journal of Plasma Physics, **14**(01), 65–76 (1975).
3. R. Craxton and M. Haines, "J× B acceleration of fast ions in laser-target interactions," Plasma Physics, **20**, 487 (1978).
4. Y. Kishimoto, K. Mima, T. Watanabe *et al.*, "Analysis of fast-ion velocity distributions in laser plasmas with a truncated Maxwellian velocity distribution of hot electrons," Physics of Fluids, **26**, 2308 (1983).
5. M. Haines, "Saturation mechanisms for the generated magnetic field in nonuniform laser-matter irradiation," Physical review letters, **78**(2), 254–257 (1997).
6. T. Tan, G. McCall and A. Williams, "Determination of laser intensity and hot-electron temperature from fastest ion velocity measurement on laser-produced plasma," Physics of Fluids, **27**, 296 (1984).
7. S. Gitomer, R. Jones, F. Begay *et al.*, "Fast ions and hot electrons in the laser–plasma interaction," Physics of Fluids, **29**, 2679 (1986).
8. J. Lindl, "Development of the indirect-drive approach to inertial confinement fusion and the target physics basis for ignition and gain," Phys. Plasmas, **2**, 3933–4024 (1995).
9. Y. Gazit, J. Delettrez, T. Bristow *et al.*, "Effect of electrostatic fields on charged reaction products in six-beam symmetrical implosion experiments," Physical Review Letters, **43**(26), 1943–1947 (1979).
10. J. Delettrez, A. Entenberg, Y. Gazit *et al.*, "Time decay of electric fields probed by charged reaction products in six-beam symmetrical implosion experiments," Nuclear fusion, **23**, 1135 (1983).
11. D. Hicks, C. Li, F. Séguin *et al.*, "Charged-particle acceleration and energy loss in laser-produced plasmas," Physics of Plasmas, **7**, 5106 (2000).
12. D. Hicks, C. Li, F. Séguin *et al.*, "Observations of fast protons above 1 MeV produced in direct-drive laser-fusion experiments," Physics of Plasmas, **8**, 606 (2001).
13. C. Li, F. Séguin, J. Frenje *et al.*, "Observations of electromagnetic fields and plasma flow in hohlraums with proton radiography," Physical review letters, **102**(20), 205001 (2009).
14. C. Li, F. Séguin, J. Frenje *et al.*, "Charged-Particle Probing of X-ray–Driven Inertial-Fusion Implosions," Science, **327**(5970), 1231 (2010).
15. C. Li, F. Séguin, J. Frenje *et al.*, "Diagnosing indirect-drive inertial-confinement-fusion implosions with charged particles," Plasma Physics and Controlled Fusion, **52**, 124027 (2010).
16. S. Regan, N. Meezan, L. Suter *et al.*, "Suprathermal electrons generated by the two-plasmon-decay instability in gas-filled Hohlraums," Physics of Plasmas, **17**, 020703 (2010).
17. A. Simon, R. Short, E. Williams *et al.*, "On the inhomogeneous two-plasmon instability," Physics of Fluids, **26**, 3107 (1983).

18. W. Kruer, *The physics of laser plasma interactions* (Reading, MA (US); Addison-Wesley Publishing Co., 1988).
19. J. MacFarlane, "VISRAD–A 3-D view factor code and design tool for high-energy density physics experiments," Journal of Quantitative Spectroscopy and Radiative Transfer, **81**(1-4), 287–300 (2003).
20. F. H. Séguin, C. K. Li, M. J.-E. Manuel *et al.*, "Time evolution of filamentation and self-generated fields in the coronae of directly driven inertial-confinement fusion capsules," Physics of Plasmas, **19**(1), 012701 (2012).

Appendix F

HYADES simulations of ICF experiments

The HYADES code[1] is a 1-D radiation-hydrodynamics simulation tool, which uses Lagrangian hydrodynamics, with problems specified in planar, cylindrical, or spherical geometry. It is a three-temperature code where electrons, ions, and the radiation field have independent temperatures. In mixtures with multiple ion species, they are treated as a single ion fluid. Radiative energy transport can be treated with either a single- or multi-group diffusion model. All energy transport is modeled using the diffusion approximation.

Material equation of state is specified by a tabular library (LANL Sesame), an ideal-gas, or a quotidian equation of state (QEOS). Ionization may be treated with several models: Saha, Thomas-Fermi, and LTE or non-LTE average atom. Energy sources may be added to drive the system including laser sources, radiation flux sources, pressure and temperature sources, or direct energy deposition.

HYADES is deck-based, where the user specifies the problem in a text input file, which is input to the HYADES executable. A sample deck is shown below for a post-shot simulation of OMEGA shot 69055, shot on March 14$^{\text{th}}$, 2013. The capsule is 2.2μm SiO_2 with an outer diameter of 854μm. It was driven by a 600ps square pulse, with 14.6kJ of total energy. The measured absorption fraction is 59%.

```
 D2(8.37)3He(14.13) SiO2(2.2) 854um OD
c
c Author: A Zylstra
c Date: 3/13/2013
c
c ------- Define some parameters ------

c Inner radius of the capsule
 define r1 4.302e-2
c third through shell
 define r2 4.3135e-2
c outer radius
 define r3 4.325e-2
c Gas fill info
 define den 3.0916e-3
c
c ------ ACTUAL DECK ------
c
```

```
19 c Spherical geometry
20 geometry 3
21 c
22 c  gas zones of gas divided into two regions
23 c
24 mesh 1 101 0. r1 0.99
25 region 1 100 1 den
26 material 1 1. 2. 0.542
27 material 1 2. 3. 0.458
28 c ideal gas eos
29 eos 999 1
30 c shell zones of SiO2 feathered inward and outward
31 c
32 mesh 101 131 r1 r2 1.1
33 mesh 131 201 r2 r3 0.9
34 region 101 200 2 2.15
35 material 2 8. 16. 2.
36 material 2 14. 28. 1.
37 eos /Applications/hyades/EOS-Opacity/EOS/eos_21.dat 2
38 eosxtrp 2 1 2 1 2
39 c
40 c 0.351 um laser source incident on outer surface
41 c Laser info
42 source laser .351 -201
43 sourcem 0.59
44 tv 0. 0.
45 tv 0.1e-9 2.43e+20
46 tv 0.6e-9 2.43e+20
47 tv 0.7e-9 0.
48 c
49 c Set some physics parameters
50 c
51 parm flxlem .07
52 c timing
53 parm editdt 1.e-11
54 parm tstop 1.2e-9
55 parm nstop 1.e+6
56 parm itmcyc 10
57 c
58 pparray r rcm dene deni rho rhodr te ti tauei ucm xmass vol
59 parm postdt 10.e-12
60
```

The first line is a problem description. Any line beginning with c is a comment. Lines 8 through 15 define several variables: the capsule dimensions and gas fill density. The deck is written this way to make variation of these parameters easier and more transparent. The spherical geometry is defined on line 20. The Lagrangian mesh for the gas material is defined on lines 24-27, and an ideal-gas equation of state is used for the gas material (line 29). The Lagrangian zones for the shell

material are defined on lines 32-36, with a tabular equation-of-state used (lines 37-38). The energy is deposited as a laser source, defined on lines 42-47: the laser intensity starts at 0, increases over 100ps to a peak power of 2.43×10^{20} erg/s (24.3 TW), remains at the peak power level for 500ps, and decreases to 0 over a 100ps ramp. An electron flux limiter of 0.07 is used (line 51). Finally, the timing control (lines 53-56) and post-processor output (lines 58-59) are defined at the end of the file.

The simulation is run from the command line as follows:

```
hyades -c D3He
ppf2ncdf D3He D3He
mv D3He.cdf D3He.nc
```

The first command runs the simulation. The second two commands convert the HYADES output into a netCDF file, which is significantly easier to use in post-processing codes due to a modular storage scheme (similar to HDF).

HYADES itself generates plasma conditions (density, temperature, etc) as a function of time and space. Observables are calculated with a 'post-processor' code. The nuclear results of this simulation are shown in Table F.1, and several summary plots are shown in Fig. F.1. The nuclear results are calculating using parameterized cross sections[2].

Table F.1. Simulated nuclear results for shot 69055

Reaction	Yield	T_i (keV)	BT (ns)
D^3He	9.96×10^{10}	25.2	0.61
DD-p	6.51×10^{10}	14.2	0.64
DD-n	6.88×10^{10}	14.5	0.64

Shot 69055 is clearly a shock-driven ('exploding pusher') case, with low convergence. HYADES may also be used to simulate higher-convergence implosions. An example of this is a 15μm CH shell, similar D^3He gas fill, and a 1ns square pulse drive. The nuclear results are summarized in Table F.2 and several summary plots are shown in Fig. F.2.

Table F.2. Nuclear results for simulation of a hypothetical 15μm CH shell

Reaction	Yield	T_i (keV)	BT (ns)
D^3He	2.30×10^{10}	4.86	1.54
DD-p	2.00×10^{11}	4.54	1.54
DD-n	2.02×10^{11}	4.54	1.54

F.1 References

1. J. T. Larsen and S. M. Lane, "HYADES-A plasma hydrodynamics code for dense plasma studies," Journal of Quantitative Spectroscopy and Radiative Transfer, **51**(1-2), 179 – 186 (1994), special Issue Radiative Properties of Hot Dense Matter.

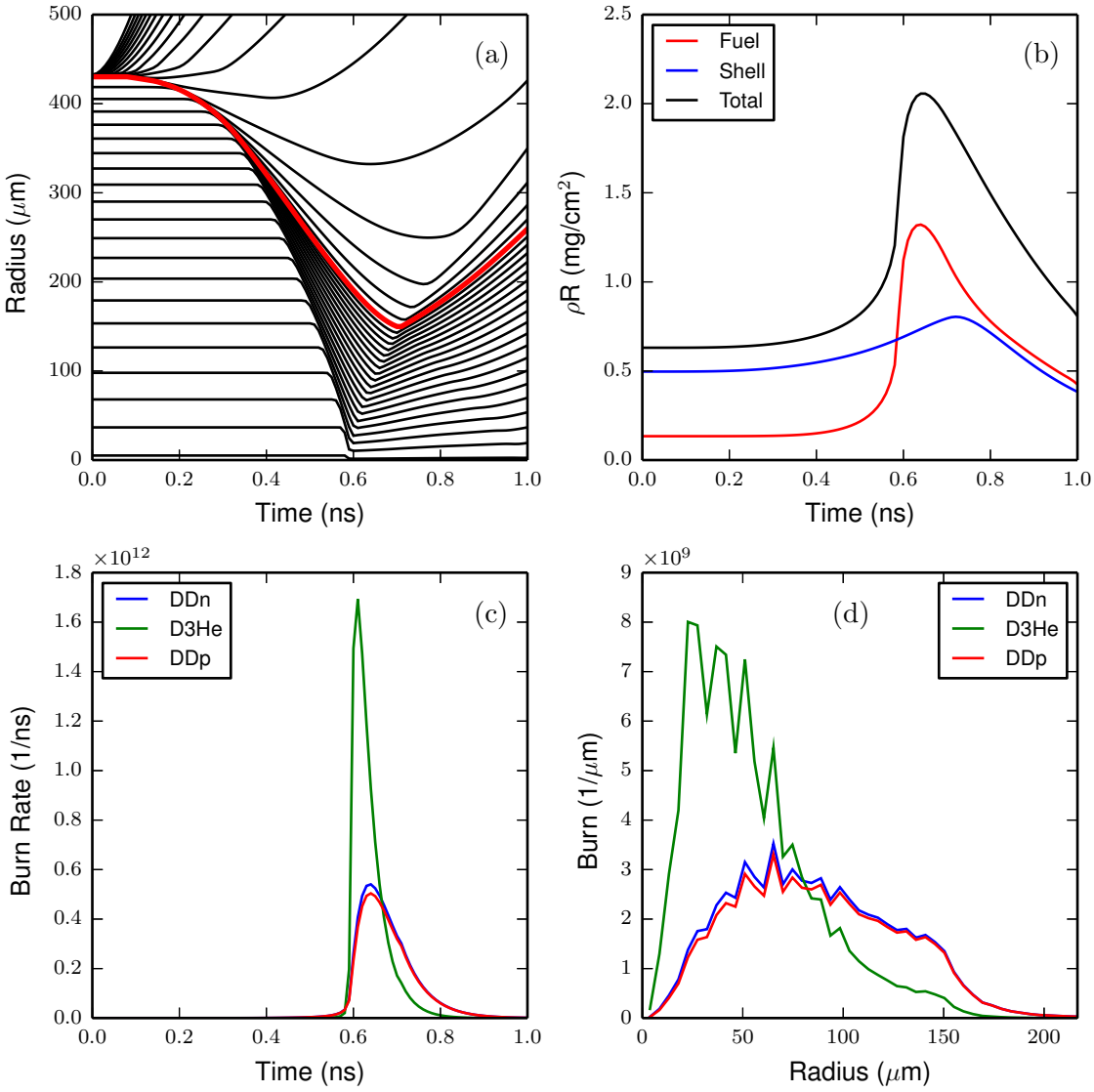

Figure F.1. Post-processed results for the simulation of OMEGA shot 69055. **(a)** Lagrangian mass-element trajectories for every fifth zone. The red curve is the fuel-shell interface. **(b)** ρR evolution for the fuel, shell (ablated and remaining), and total (sum of the two) during the implosion. **(c)** Burn rate for the DD and D^{3}He reactions. **(d)** Spatial burn profile for DD and D^{3}He reactions.

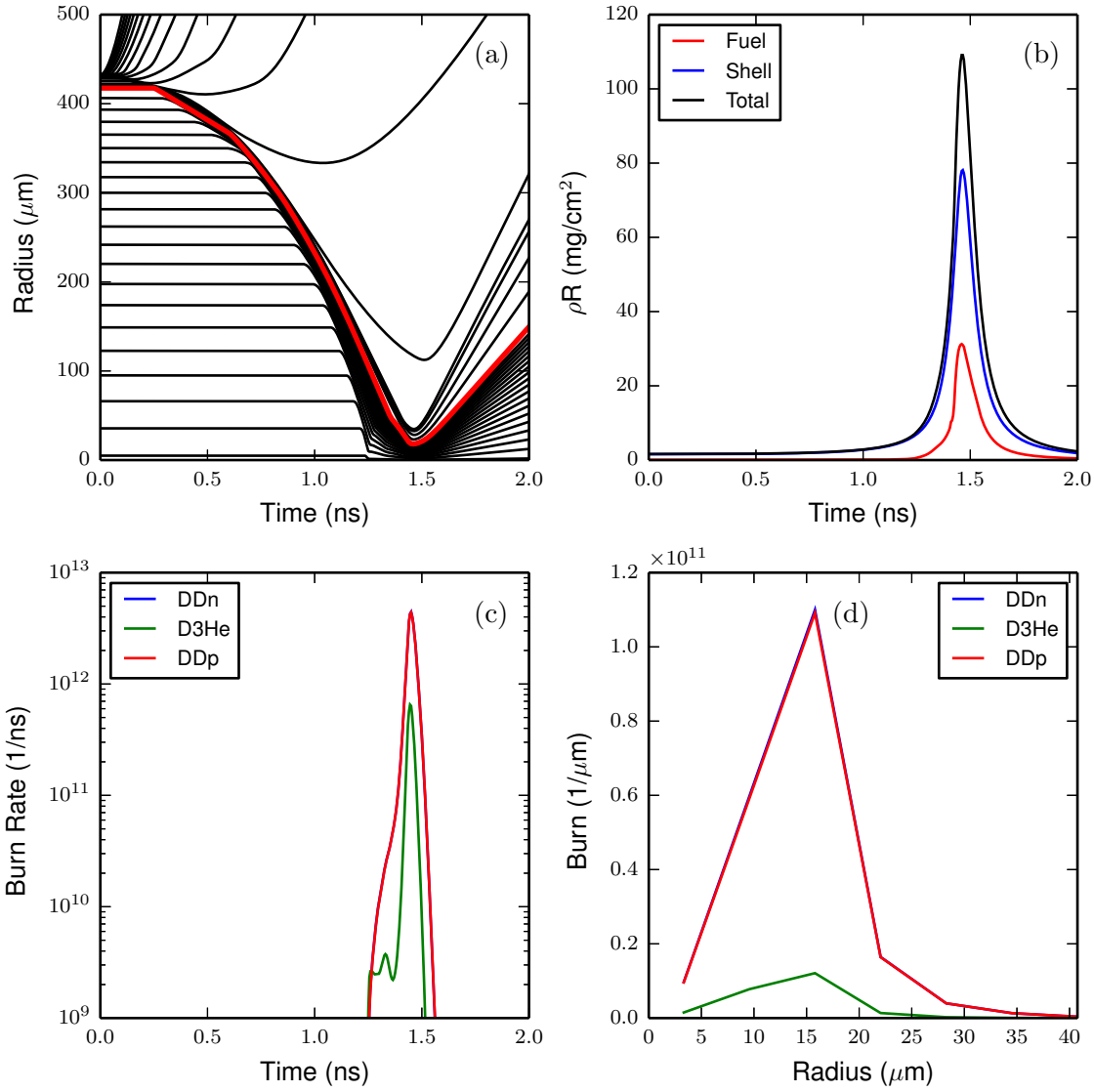

Figure F.2. Post-processed results for the simulation of a hypothetical OMEGA shot with a 15μm CH shell. **(a)** Lagrangian mass-element trajectories for every fifth zone. The red curve is the fuel-shell interface. **(b)** ρR evolution for the fuel, shell (ablated and remaining), and total (sum of the two) during the implosion. **(c)** Burn rate for the DD and D^{3}He reactions. **(d)** Spatial burn profile for DD and D^{3}He reactions.

2. H.-S. Bosch and G. Hale, "Improved Formulas for Fusion Cross-Sections and Thermal Reactivities," Nuclear Fusion, **32**, 611–631 (1992).

Appendix G

Evaluation of dE/dx models and scattering

G.1 Brown-Preston-Singleton (BPS) model

The BPS stopping power model[1] treats ion slowing in plasmas due to short-range Coulomb collisions and long-range dielectric effects; it also considers a quantum correction to the previous two. These terms form the stopping of charged particles in plasmas:

$$\frac{dE}{dx} = \frac{dE^{CS}}{dx} + \frac{dE^{CR}}{dx} + \frac{dE^{Q}}{dx}. \tag{G.1}$$

Each term is evaluated for a single plasma species (denoted with subscript f), and the total stopping is a sum over all plasma species.

G.1.1 Short-range Coulomb collisions

The short-range classical stopping term is given by Eq. 3.3 of Ref. 1:

$$\begin{aligned}\frac{dE^{CS}}{dx} &= \frac{e_t^2}{4\pi}\frac{\kappa_f^2}{m_t v_t}\sqrt{\frac{m_f}{2\pi\beta_f}} \times \\ &\int_0^1 du\sqrt{u}\exp(-\beta_f m_f v_t^2 u/2) \times \\ &\left\{\left[-\ln\left(\beta_f\frac{e_t e_f K}{4\pi}\frac{m_f}{m_{tf}}\frac{u}{1-u}\right)+2-2\gamma\right]\left[\beta_f M_{tf} v_t^2 - \frac{1}{u}\right]+\frac{2}{u}\right\}.\end{aligned} \tag{G.2}$$

In this expression, f denotes field particle and t denotes test particle. u is a variable of integration. The parameters are:

- e_t and e_f are the particle charges in Lorentz-Heaviside units (conversion from electrostatic units (ESU) is given by: $e_{LH} = e_{ESU}\sqrt{4\pi}$).
- m_t and m_f are the particle masses.
- v_t is the test particle velocity.
- β_f is the normalized field species temperature $\beta_f \equiv 1/k_B T_f$ (where k_B is Boltzmann's constant).
- $\kappa_f = \beta_f e_f^2 n_f$ is the Debye wavenumber for field species f (n_f is the particle number density).

- K is an arbitrary wavenumber, taken as $K = \kappa_e$. The effect of K on the short- and long-range classical stopping cancel in the final summed dE/dx.
- γ is the Euler-Mascheroni constant ($\gamma = 0.5772...$).

These parameters may be directly evaluated when the test and field particle conditions are specified. The integral in Eq. G.2 can thus be solved numerically. Care must be taken since the integral is singular at $u = 0, 1$. The numerical integration can either be done over the range $0 \to 1$ using a technique that is robust to singularities, or the integration limits can be changed to $\delta \to (1 - \delta)$ without loss of precision where $\delta \ll 1$.

G.1.2 Long-range dielectric response

The long-range dielectric response term is given by:

$$\begin{aligned}\frac{dE^{CR}}{dx} &= \frac{e_t^2}{4\pi}\frac{i}{2\pi}\int_{-1}^{1} du\; u\frac{\rho_f(uv_t)}{\rho_{tot}(uv_t)}F(uv_t)\ln\left(\frac{F(uv_t)}{K^2}\right) \\ &\quad -\frac{e_t^2}{4\pi}\frac{i}{2\pi}\frac{1}{\beta_f m_t v_t^2}\left[F(v_t)\ln\left(\frac{F(v_t)}{K^2}\right) - F^*(v_t)\ln\left(\frac{F^*(v_t)}{K^2}\right)\right]. \end{aligned} \tag{G.3}$$

Relative to the expression given in Ref 1, the variable of integration has been changed by substitution $\cos\theta \to u$, and otherwise the expression is unchanged. The 'spectral weights' are given by

$$\rho_f(v) = \kappa_f^2 v\sqrt{\frac{\beta_f m_f}{2\pi}}\exp\left(-\frac{1}{2}\beta_f m_f v^2\right), \tag{G.4}$$

$$\rho_{tot}(v) = \sum_i \rho_i(v). \tag{G.5}$$

The function F is derived from the leading-order plasma dielectric susceptibility. Brown-Preston-Singleton define it as

$$F(u) = -\int_{-\infty}^{\infty} dv \frac{\rho_{tot}(v)}{u - v + i\eta}, \tag{G.6}$$

in the limit $\eta \to 0^+$. The integrand is clearly singular at $v = u + i\eta$, but can be reformulated using complex analysis. First, it is convenient to consider only a single plasma species at a time so that $\rho_{tot} \to \rho_f$, which we write in the form

$$\rho_f(v) = \rho v \exp(-av^2), \tag{G.7}$$

where $\rho = \kappa_f^2\sqrt{\beta_f m_f/2\pi}$ and $a = \beta_f m_f/2$ are constants. Then, the integral for F may be rewritten in the form

$$F_f = \rho\int_{-\infty}^{\infty} dv \frac{v\exp(-av^2)}{u - v + i\eta}. \tag{G.8}$$

This integral can be evaluated using Cauchy's integral theorem[2], which gives the result:

$$\begin{aligned} F_f &= \rho\Bigg\{-\sqrt{\frac{\pi}{a}} + \exp\left[-a(u+i\eta)^2\right](u+i\eta) \\ &\quad \times\left[\pi\mathrm{erfi}\left(\sqrt{a}(u+i\eta)\right) + \ln(-u-i\eta) - \ln(u+i\eta)\right]\Bigg\}. \end{aligned} \tag{G.9}$$

Here erfi is the imaginary error function:

$$\mathrm{erfi}(z) \equiv -i\mathrm{erf}(iz), \tag{G.10}$$

which may also be written in terms of Dawson's integral F_D:

$$\mathrm{erfi}(z) = \frac{2}{\sqrt{\pi}} e^{z^2} F_D(z), \tag{G.11}$$

which is a convenient form for evaluation, since Dawson's integral is often implemented in scientific numerical libraries (e.g. the GNU Scientific Library for C++). In the evaluation of F_f, a small but non-zero value of η may be arbitrarily chosen, for example $\eta = 10^{-6}$. The value of η chosen has no effect on the calculated stopping power.

In this form, $F(u)$ is evaluated by summing over all plasma species. F must also be evaluated in the complex plane, but the final result from this evaluation is real due to the pre-factor of i in Eq. G.3. In the evaluation of Eq. G.3, F^* is obtained by the reflection property $F^*(u) = F(-u)$ (see Eq. 3.13 in Ref. 1).

G.1.3 Quantum correction

The quantum correction to the classical stopping power (the sum of Eqs G.2 and G.3) is given by

$$\begin{aligned}\frac{dE^Q}{dx} &= \frac{e_t^2}{4\pi}\frac{\kappa_f^2}{2\beta_f m_t v_t^2}\sqrt{\frac{\beta_f m_f}{2\pi}}\int_0^\infty dv_{tf}\left\{2\mathrm{Re}\psi(1+i\eta_{tf}) - \ln\eta_{tf}^2\right\} \\ &\times\left\{\left[1+\frac{M_{tf}}{m_f}\frac{v_t}{v_{tf}}\left(\frac{1}{\beta_f m_f v_t v_{tf}}-1\right)\right]\exp\left[-\frac{1}{2}\beta_f m_f (v_t - v_{tf})^2\right]\right. \\ &\left.-\left[1+\frac{M_{tf}}{m_f}\frac{v_t}{v_{tf}}\left(\frac{1}{\beta_f m_f v_t v_{tf}}+1\right)\right]\exp\left[-\frac{1}{2}\beta_f m_f (v_t + v_{tf})^2\right]\right\}.\end{aligned} \tag{G.12}$$

In this equation, we have:

$$v_{tf} \equiv |\vec{v_t} - \vec{v_f}|, \tag{G.13}$$

$$\eta_{tf} \equiv \frac{e_t e_f}{4\pi\hbar v_{tf}}. \tag{G.14}$$

The function ψ is the logarithmic derivative of the gamma function:

$$\psi(z) \equiv \frac{d}{dz}\ln\Gamma(z). \tag{G.15}$$

This function is also typically present in commonly used numerical libraries.

The integration in Eq. G.12 must also be performed numerically. The limits $0 \to \infty$ are unnecessary, since the integrand is primarily significant in the region $v_t \sim v_f$. Without loss of precision, the integration limits may be changed to $v_{min} \to v_{max}$ where

$$v_{min} = \min(v_f, v_t) \;/\; 5, \tag{G.16}$$

$$v_{max} = \max(v_f, v_t) \times 5. \tag{G.17}$$

The factor of 5 is arbitrary, but numerical convergence can be easily verified. For typical stopping calculations, increasing the integration limits has negligible effect on the calculated quantum

correction term.

G.2 Modified Li-Petrasso formalism

The published Li-Petrasso[3,4] stopping power is expressed as

$$\frac{dE}{dx} = -\left(\frac{Z_t e}{v_t}\right)^2 \omega_{pf}^2 \left\{ G(x^{t/f}) \ln \Lambda_b + \Theta(x^{t/f}) \ln\left(1.123\sqrt{x^{t/f}}\right)\right\}, \tag{G.18}$$

see Eq. 3 of 3. Here, Z_t is the test particle charge in atomic units, e is the fundamental charge, v_t is the velocity, and ω_{pf} is the plasma frequency for field particle species f (defined $\omega_{pf} = \sqrt{4\pi n_f e_f^2/m_f}$ where e_f is the field particle charge, m_f is the mass, and n_f is the particle number density. The parameter $x^{t/f}$ is a dimensionless ratio of test to field particle velocity, which will be discussed later. In plasmas with multiple species (e.g. electrons and ions), the total stopping power should be written as

$$\frac{dE}{dx} = \sum_f \frac{dE}{dx}_f. \tag{G.19}$$

The pre-factor in Eq. G.18 gives the overall normalization. Inside the brackets, the term $G(x^{t/f}) \ln \Lambda_b$ represents the stopping power from binary Coulomb collisions, and the term $\Theta(x^{t/f}) \ln\left(1.123\sqrt{x^{t/f}}\right)$ represents slowing due to collective plasma effects (i.e. dielectric response).

The value of x in this term is different than x in the binary stopping term; in the dielectric term the parameter $\sqrt{x}$ should be replaced by $v_t/\omega_{pf}\lambda_D$ where λ_D is the Debye length $\left(=\sqrt{k_B T_f/4\pi n_f e_f^2}\right)$, as noted in Ref. 4. Also, as the form of the collective effects term published in Ref. 3 was derived under the assumption that $x^{t/f} \gg 1$[5], we generalize Eq. G.18 by writing

$$\frac{dE}{dx} = -\left(\frac{Z_t e}{v_t}\right)^2 \omega_{pf}^2 \left\{ G(x^{t/f}) \ln \Lambda_b + \left(\frac{\omega_{pf}\lambda_D}{v_t}\right) K_0\left(\frac{\omega_{pf}\lambda_D}{v_t}\right) K_1\left(\frac{\omega_{pf}\lambda_D}{v_t}\right)\right\}, \tag{G.20}$$

where K_0 and K_1 are the irregular modified cylindrical Bessel function of zeroth and first order, respectively. This expression should be accurate for all values of $x^{t/f}$.

The binary collision term's factor of G is sometimes referred to as the Chandrasekhar function,

$$G\left(x^{t/f}\right) = \mu\left(x^{t/f}\right) - \frac{m_f}{m_t}\left\{\frac{d\mu\left(x^{t/f}\right)}{dx^{t/f}} - \frac{1}{\ln\Lambda_b}\left[\mu\left(x^{t/f}\right) + \frac{d\mu\left(x^{t/f}\right)}{dx^{t/f}},\right]\right\} \tag{G.21}$$

where

$$\mu\left(x^{t/f}\right) = \frac{2}{\sqrt{\pi}}\int_0^{x^{t/f}} e^{-\xi}\sqrt{\xi}d\xi, \tag{G.22}$$

$$= \frac{\sqrt{\pi}}{2}\mathrm{erf}\left(\sqrt{x^{t/f}}\right) - \sqrt{x^{t/f}}e^{-x^{t/f}}, \tag{G.23}$$

$$\frac{d\mu\left(x^{t/f}\right)}{dx^{t/f}} = \sqrt{x^{t/f}}e^{-x^{t/f}}. \tag{G.24}$$

G is evaluated where $x^{t/f} = v_t^2/v_f^2$ and $v_f^2 = 2k_B T_f/m_f$. In these equations, erf is the error function,

which is commonly available in numerical libraries for quick evaluation.

The last part of the stopping equation is the Coulomb logarithm, $\ln \Lambda_b$, in the Li-Petrasso paper given by

$$\ln \Lambda_b = \ln \left(\frac{\lambda_D}{p_{min}} \right), \tag{G.25}$$

which is an approximation by Trubnikov[6] in the limit $\lambda_D \gg p_{min}$. A more general form is given by

$$\ln \Lambda_b = \frac{1}{2} \ln \left[1 + \left(\frac{\lambda_D}{p_{min}} \right)^2 \right]. \tag{G.26}$$

For the Coulomb logarithm, Li and Petrasso use the electron Debye length. Here, the Debye length is taken as a total Debye length for all species in the plasma, as it represents the absolute screening length:

$$\lambda_D = \frac{1}{\sqrt{\sum_f 4\pi n_f e_f^2 / k_B T_f}}. \tag{G.27}$$

The term p_{min} corresponds to a minimum impact parameter (maximum momentum transfer) collision, and is given by Li-Petrasso as

$$p_{min} = \sqrt{p_\perp^2 + \left(\frac{\hbar}{2 m_r u} \right)^2}, \tag{G.28}$$

where $p_\perp = e_t e_f / m_r u^2$ is the classical impact parameter, and the second term represents maximum momentum transfer in the regime where the quantum de Broglie wavelength may be greater than the classical minimum impact parameter. In this equation, m_r is the reduced mass of test and field particles, and u is a relative velocity between test and field particles which is not given explicitly in the Li-Petrasso work. u is defined here by integrating the complete Maxwellian field particle distribution in three dimensions:

$$u \equiv \int_{-\infty}^{\infty} \int_{-\infty}^{\infty} \int_{-\infty}^{\infty} \sqrt{(v_t - v_x)^2 + v_y^2 + v_z^2}\; A e^{-m_f v^2 / 2 k_B T_f} dv_x dv_y dv_z, \tag{G.29}$$

where A is the normalization of the distribution function and v_t is the test particle velocity, which is taken as $\vec{v_t} \parallel \hat{x}$ without loss of generality. In the exponent, $v = \sqrt{v_x^2 + v_y^2 + v_z^2}$. When the test particle is slow ($v_t \ll v_{th}$),

$$\sqrt{(v_t - v_x)^2 + v_y^2 + v_z^2} \to \sqrt{v_x^2 + v_y^2 + v_z^2} = v, \tag{G.30}$$

which means that the relative velocity reduces to

$$u = \int_0^{\infty} v A e^{-m v^2 / 2 k_B T_f} dv = \sqrt{\frac{8 k_B T_f}{\pi m_f}}. \tag{G.31}$$

In the high-velocity limit ($v_t \gg v_{th}$),

$$\sqrt{(v_t - v_x)^2 + v_y^2 + v_z^2} \to v_t, \tag{G.32}$$

and the relative velocity reduces to

$$u = v_t. \tag{G.33}$$

For intermediate values one can construct a 'simple relative velocity' from these two results, rather than evaluating the integral over the distribution function. This velocity is given by:

$$u_s = \sqrt{v_t^2 + \left(\frac{8k_B T_f}{\pi m_f}\right)^2}. \tag{G.34}$$

When $v_t \sim v_{th}$, this expression has an error of about 2.5%. Generally, this is acceptable since u only appears in the Coulomb logarithm. However, it is also straightforward to directly evaluate the integral of the distribution function, which results in the expression

$$u = \sqrt{\frac{2k_B T_f}{\pi m_f}} \exp\left[-\frac{m_f v_t^2}{2k_B T_f}\right] + v_t \left(1 + \frac{k_B T_f}{m_f v_t^2}\right) \operatorname{erf}\left[\sqrt{\frac{m_f v_t^2}{2k_B T_f}}\right]. \tag{G.35}$$

Li and Petrasso also note that "in the low-temperature, high-density regime, electron (not ion) quantum degeneracy effects must be considered in calculating λ_D and p_{min}", as prescribed in their 1995 Phys. Plasmas paper[7]. Here, an effective field particle temperature correction is used following Drake[8]. The total pressure (p_e) of quasi-degenerate electron fluid may be written as (Drake Eq. 3.22)

$$\frac{3}{2} p_e = n_e k_B T_e \frac{F_{3/2}\left(\frac{\mu_e}{k_B T_e}\right)}{F_{1/2}\left(\frac{\mu_e}{k_B T_e}\right)}, \tag{G.36}$$

which leads to an 'effective temperature' (T_{eff})

$$T_{eff} = T_e \frac{F_{3/2}\left(\frac{\mu_e}{k_B T_e}\right)}{F_{1/2}\left(\frac{\mu_e}{k_B T_e}\right)}. \tag{G.37}$$

In this expression, $F_{1/2}$ and $F_{3/2}$ are the Fermi integrals

$$F_j(x) = \frac{1}{\Gamma(j+1)} \int_0^\infty dt \frac{t^j}{\exp(t-x)+1}, \tag{G.38}$$

and μ_e is the chemical potential, which can be obtained from the fit by Drake Eq. 3.20[8]

$$\frac{\mu_e}{k_B T_e} = -\frac{3}{2} \ln \Theta + \ln\left(\frac{4}{3\sqrt{\pi}}\right) + \frac{0.25054\Theta^{-1.858} + 0.072\Theta^{-1.858/2}}{1 + 0.25054\Theta^{-0.868}}, \tag{G.39}$$

where Θ is the ratio of temperature to Fermi temperature, given by:

$$\Theta = \frac{T_e}{T_F} = T_e \left[\left(\frac{8\pi}{3n_e}\right)^{2/3} \frac{2m_e k_B}{h^2}\right]. \tag{G.40}$$

To express the modified Li-Petrasso formalism, we use Eq. G.20 with the Chandrasekhar function defined by Eq. G.21, and the Coulomb logarithm calculated from Eqs. G.26, G.27, G.28, and G.35 with a quantum correction given by Eqs. G.36 to G.40. The results of these changes are significant in the small $\log \Lambda$ regime, i.e. at high density. A comparison to the published version of

the theory is shown in Fig. G.1

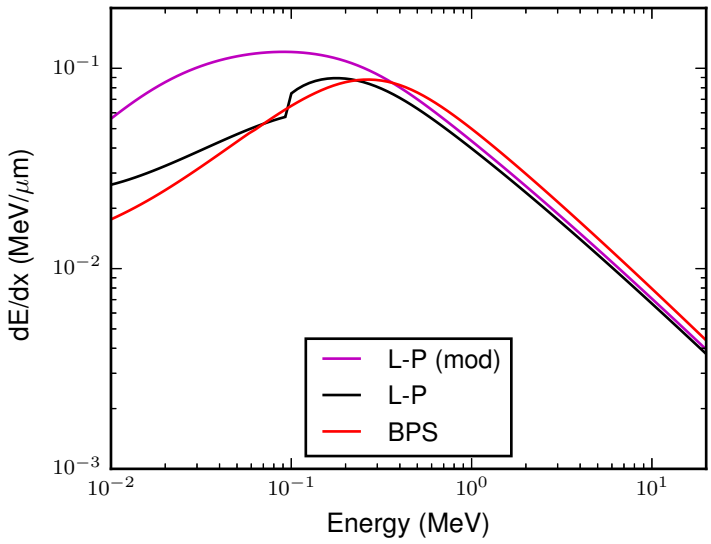

Figure G.1. Comparison of the published Li-Petrasso stopping theory (black) to the modified theory presented in this work (magenta) and the BPS theory (red). The projectile is a proton traversing a fully-ionized solid-density Be plasma at $T_e = T_i = 50\text{eV}$.

G.3 Results

In addition to the BPS and Li-Petrasso theories, Zimmerman's parameterization[9] of the Maynard-Deutsch theory[10,11], Grabowski's classical molecular dynamics results[12], and cold-matter tabular stopping power from the SRIM code[13] are used in this work. A comparison of these models is shown in Fig. G.2 for a variety of ICF-relevant plasmas.

In addition, we directly compare the Zimmerman parameterization of the Maynard-Deutsch theory and Li-Petrasso theory over a wide range of parameters in Fig. G.3. The theories disagree around the Bragg peak, with the Li-Petrasso theory giving a higher stopping power. This causes the vertical bands of red at $20 - 30$ keV for D^3He protons, and around $1 - 2$ keV for the DT-αs. At high densities, the theories begin to break down leading to large disagreements.

The Zimmerman stopping power is similarly compared to the BPS theory in Fig. G.4. At high densities (in the strongly-coupled regime) the theories again encounter difficulties. In this case of BPS , this is in part due to the fact that it does not treat degeneracy of the field particles, which is very important at the high end of the densities plotted. However, in comparison to Fig. G.3, it is apparent that the Zimmerman and BPS theories are in good agreement with each other over a wide range of conditions.

G.4 Large-angle Coulomb scattering

As an energetic charged particle slows in a plasma, rare large-angle ion-ion scattering events can potentially create a substantial difference between the path and linear stopping powers. This is illustrated by Fig. G.5.

If scattering causes deflections of the ion, then the path (s) is longer than the linear distance (x). When calculating the stopping power, the linear-distance dE/dx must be greater than or

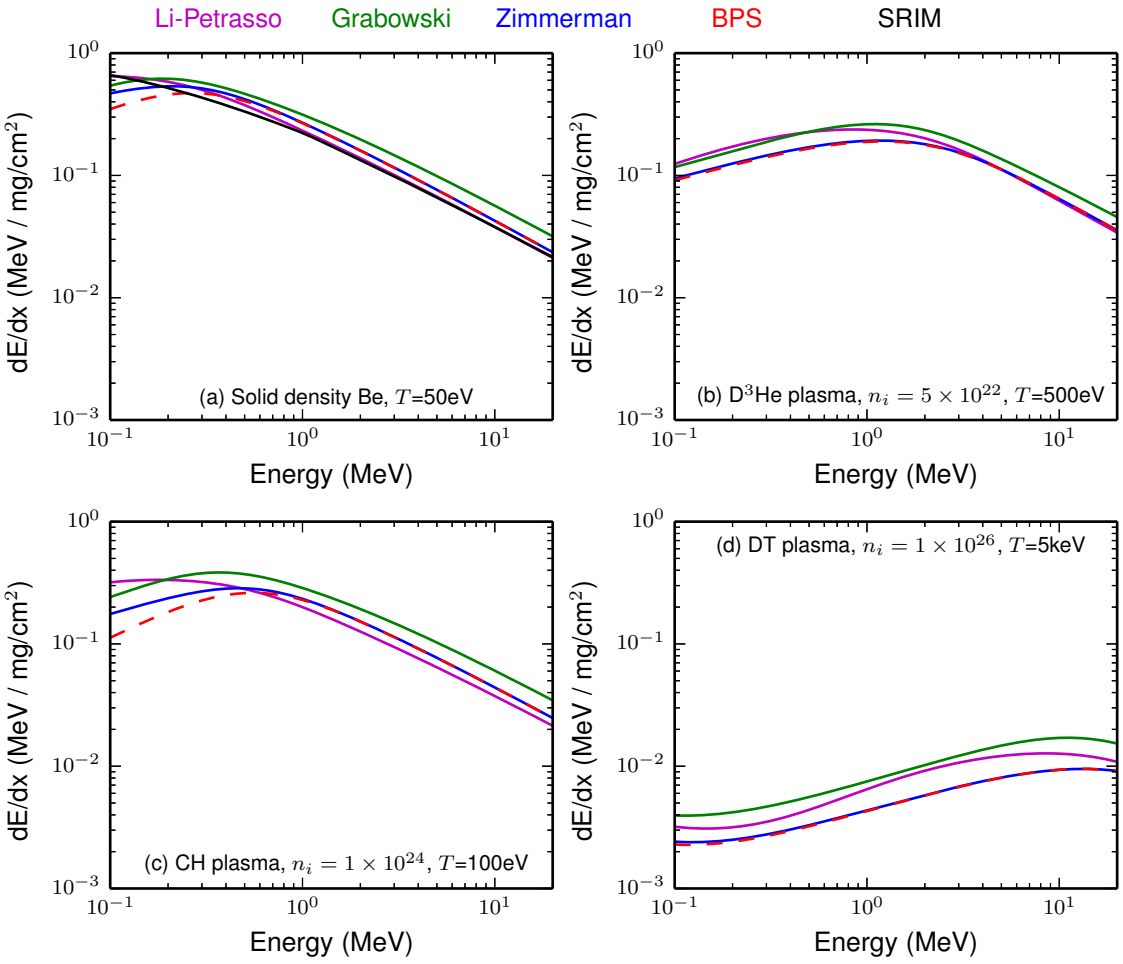

Figure G.2. Comparison of several stopping theories for protons slowing in various ICF-relevant plasmas. **(a)** Fully-ionized solid-density Be at 50eV (WDM regime), **(b)** in a D^3He plasma at 500 eV, **(c)** in a CH plasma at 10^{24}/cc and 100eV, relevant to dense shells, and (d) in a high-density and hot DT plasma, relevant to ignition targets.

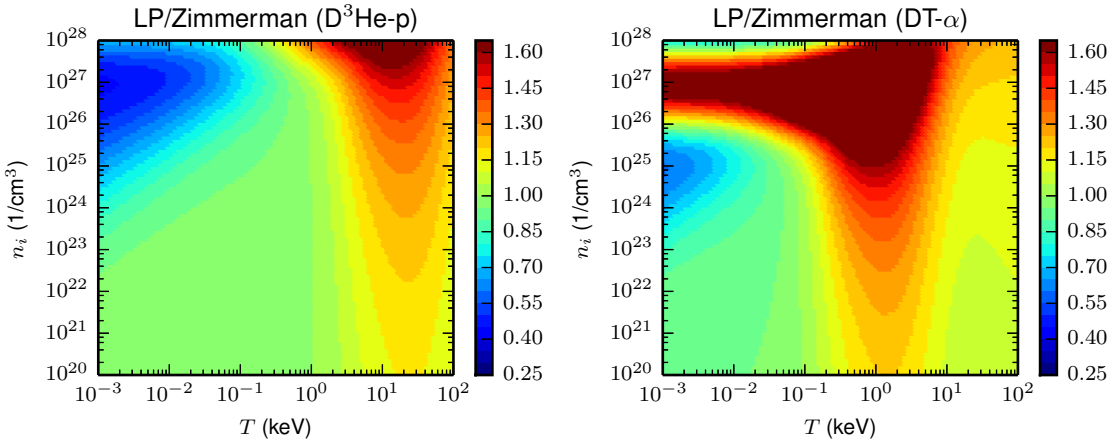

Figure G.3. Ratio of Li-Petrasso and Zimmerman stopping powers for D^3He-p (14.7 MeV) and DT-α (3.5 MeV) slowing in a DT plasma at various densities and temperatures ($T = T_e = T_i$). Large disagreement around $T = 20$keV for the D^3He-p, and $1 - 2$ keV for the DT-α, corresponds to the Bragg peak.

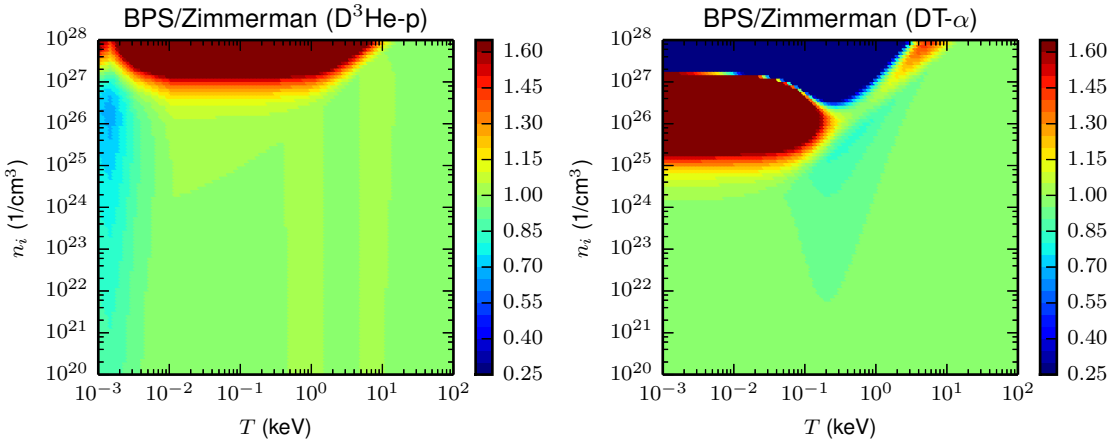

Figure G.4. Ratio of Zimmerman and BPS stopping powers for D^3He-p (14.7 MeV) and DT-α (3.5 MeV) slowing in a DT plasma at various densities and temperatures ($T = T_e = T_i$).

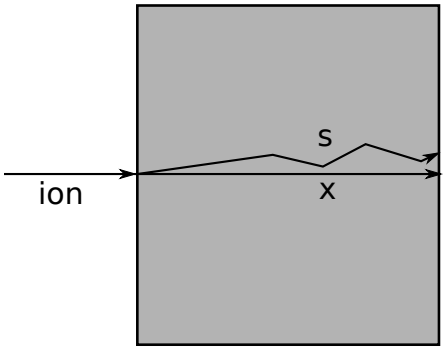

Figure G.5. When slowing in material, an ion's path (s) is longer than the linear distance (x) due to scattering.

approximately the path-integrated stopping power dE/ds. These are related by[14]

$$\frac{dE}{dx} = \langle \cos\theta \rangle^{-1} \frac{dE}{ds}, \tag{G.41}$$

where $\langle \cos\theta \rangle$ is a measure of the mean deflection angle. Li et al. derive multiple scattering deflection from a diffusion equation, which results in

$$\langle \cos\theta \rangle = \exp\left[-\int_{E_0}^{E_1} \kappa_1(E) \left(\frac{dE}{ds} \right)^{-1} dE \right], \tag{G.42}$$

where the integration is from the particle's initial (E_0) to final (E_1) energies. κ_1 is related to the diffusion cross section:

$$\kappa_1(E) = 2\pi n_i \int_0^{\pi} \left(\frac{d\sigma}{d\Omega} \right) (1 - \cos\theta) \sin\theta d\theta, \tag{G.43}$$

which depends on the differential cross section for Coulomb collisions,

$$\frac{d\sigma}{d\Omega} = \frac{b_{90}^2}{4} \frac{1}{\sin^4(\theta/2)}. \tag{G.44}$$

The so-called '90° impact parameter' (b_{90}) depends on the properties of the two scattering particles,

$$b_{90} \equiv \frac{Z_t Z_i e_0^2}{4\pi\epsilon_0} \frac{1}{m_\mu v_{rel}^2}, \tag{G.45}$$

where Z_t and Z_i are the ion charges, e_0 is the fundamental charge, and m_μ is the reduced mass. Generally a subscript t denotes 'test' particle or projectile quantities, and a subscript i denotes field ion quantities. v_{rel} is the relative velocity between the two particles, for thermal field particles (Eq. G.34),

$$v_{rel} = \sqrt{v_t^2 + \frac{8k_B T_i}{\pi m_i}}. \tag{G.46}$$

b_{90} depends strongly on the relative velocity ($\propto v_{rel}^{-2}$), and thus the differential cross section $d\sigma/d\Omega \propto v_{rel}^{-4}$. With these specified, the deflection $\langle \cos\theta \rangle$ can be calculated. The effect of scattering on proton slowing depends on the conditions. For example, for a 15 MeV proton slowing in WDM Be, the

quantity $\langle\cos\theta\rangle$ is plotted versus final proton energy in Fig. G.6. To further demonstrate this effect, three scenarios for particle scattering are shown in Table G.1.

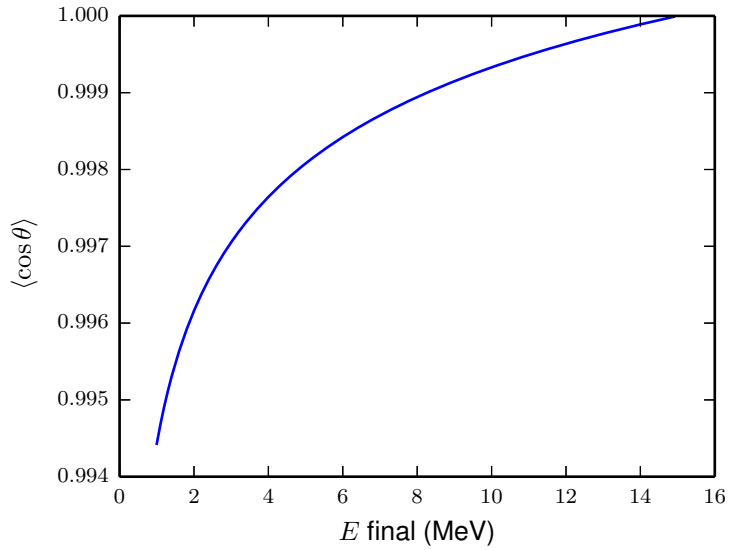

Figure G.6. Difference between path length and linear distance (expressed as $\langle\cos\theta\rangle$) as a 15 MeV proton slows down in WDM Be.

Table G.1. Calculated scattering effects (as $\langle\cos\theta\rangle$) for a variety of charged-particle stopping scenarios: a WDM Be stopping-power experiment, for D^3He protons ranging in the shell of an implosion, and for DT-αs stopping in an ignition implosion hot spot. Z_t and A_t are the test particle charge and mass; Z_i, A_i, n_i, and $T = T_e = T_i$ define the plasma conditions. The initial (E_0) and final (E_1) particle energies result in a given $\langle\cos\theta\rangle$.

	Z_t	A_t	Z_i	A_i	n_i (1/cm^3)	T (eV)	E_0 (MeV)	E_1 (MeV)	$\langle\cos\theta\rangle$
WDM Be	1	1	4	9	1.2×10^{23}	35	15	12	0.9996
CH shell	1	1	6	12	1×10^{24}	500	15	12	0.9994
DT hot spot	2	4	1	2.5	2.5×10^{25}	5000	3.5	0.1	0.8666

These results can also be compared to a TRIM[13] simulation, which is a Monte Carlo calculation of charged-particle transport through cold material. The D^3He protons traversing a Be target, as in the WDM stopping-power experiment, was simulated with TRIM and the results are shown in Fig. G.7. In the TRIM simulation the protons travel through a $L = 532.1$ μm thick region of Be along the z axis; the transverse displacement at the exit plane $r = \sqrt{x^2 + y^2}$ is shown in Fig. G.7a. The corresponding average angular displacement as the protons traverse the sample, $\langle\theta\rangle = \arctan(r/L)$, is shown as the second abscissa. TRIM also calculates the particle's trajectory as it exists the Be sample, the final angle relative to the initial trajectory is shown as the exit angle θ in Fig. G.7b.

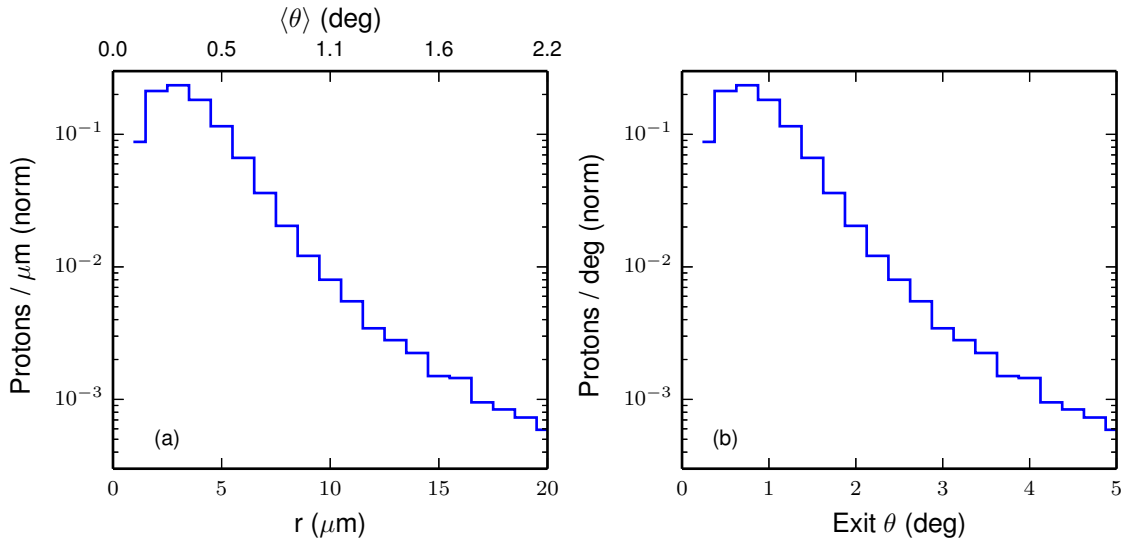

Figure G.7. TRIM calculation of proton scattering in cold solid Be. **(a)**: The displacement perpendicular to the original trajectory and corresponding average angular displacement ($\langle\theta\rangle$). **(b)**: The proton's exit angle distribution after transiting the Be.

G.5 Dielectric Response (non-degenerate vs degenerate)

The dielectric response in stopping-power theories is typically written as

$$\frac{dE}{dx} = \frac{4\pi n_f Z_t^2 e^4}{m_e v_t^2} L = \left(\frac{Z_t e \omega_{pf}}{v_t}\right)^2 L, \tag{G.47}$$

where Z_t and v_t are the test-particle charge and velocity, e is the fundamental charge, and ω_{pf} is the field-particle plasma frequency. L is the 'stopping number', also referred to sometimes as the Coulomb logarithm. In the dielectric formalism it is written

$$L = \frac{i}{\pi \omega_{pf}^2} \int_0^\infty \frac{dk}{k} \int_{-kv}^{kv} \omega d\omega \left[\epsilon^{-1}(k,\omega) - 1\right], \tag{G.48}$$

where ϵ is the wave-number and frequency dependent dielectric constant. The dielectric constant is easiest to evaluate when a simplifying assumption can be made about the field particle distribution function.

G.5.1 Fully-degenerate electron gas

Lindhard first treated this problem using a fully-degenerate simplification[15–17], i.e. that the electrons obey a Fermi-Dirac distribution. In this case, the stopping number can be shown to reduce to[16]

$$L = \frac{6}{\pi} \int_0^{v_t/v_F} u du \int_0^\infty dz \frac{z^3 f_2(u,z)}{\left[z^2 \chi^2 f_1(u,z)\right]^2 + \left[\chi^2 f_2(u,z)\right]^2}, \tag{G.49}$$

where a change of variables was made to $z = k/2k_F$ and $u = \omega/kv_F$ in terms of the Fermi wavenumber and velocity. $\chi^2 = e^2/\pi\hbar v_F$ is a parameter, and the two functions are given by

$$f_1(u,z) = \frac{1}{2}\frac{1}{8z}\left[1-(z-u)^2\right]\left|\ln\left(\frac{z-u+1}{z-u-1}\right)\right| + \frac{1}{8z}\left[1-(z+u)^2\right]\left|\ln\left(\frac{z+u+1}{z+u-1}\right)\right| \tag{G.50}$$

and

$$f_2(u,z) = \begin{cases} \frac{\pi u}{2} & z+u \le 1 \\ \frac{\pi}{8z}\left[1-(z-u)^2\right] & |z-u| < 1 < z+u \\ 0 & |z-u| \ge 1 \end{cases} \tag{G.51}$$

G.5.2 Maxwellian electron gas

Another simplification is to take the field electrons as a Maxwellian gas, in which case Jackson[18] shows that the dielectric response (pg. 451, Eq. 13.86)

$$\epsilon(\omega) = 1 - \frac{\omega_{pf}^2}{\omega^2 + i\omega\Gamma}, \tag{G.52}$$

where Γ is a small damping constant ($\Gamma \ll \omega_{pf}$), so that the stopping number simplifies to (Eq. 13.88)

$$L = \ln\left(\frac{1.123 k_D v_t}{\omega_{pf}}\right), \tag{G.53}$$

where k_D is the Debye wave number.

G.5.3 Comparison

A comparison of the stopping power resulting from these two limits of the dielectric function is shown in Fig. G.8.

G.6 References

1. L. S. Brown, D. L. Preston, and R. L. Singleton Jr., "Charged particle motion in a highly ionized plasma," Physics Reports, **410**(4), 237 – 333 (2005).
2. H. Arfken and G. Weber, *Mathematical Methods for Physicists* (Elsevier Press, 2006).
3. C. Li and R. Petrasso, "Charged-particle stopping powers in Inertial Confinement Fusion Plasmas," Phys. Rev. Lett., **70**(20), 3059 (1993).
4. C. Li and R. Petrasso, "Erratum: Charged-particle stopping powers in Inertial Confinement Fusion Plasmas," Phys. Rev. Lett. (2015).
5. C. Li, *Conceptual study of moderately-coupled plasmas and experimental comparison of laboratory x-ray sources* (MIT, 1993).
6. B. Trubnikov, *Particle Interactions in a Fully Ionized Plasma* (Consultant's Bureau, 1965).
7. C. Li and R. D. Petrasso, "Effects of scattering upon energetic ion energy loss in plasmas," Physics of Plasmas, **2**(6), 2460–2464 (1995).
8. R. Drake, *High-Energy-Density Physics* (Springer, 2006).
9. G. Zimmerman, "Recent Developments in Monte Carlo Techniques," LLNL report, UCRL-JC-105616 (1990).
10. G. Maynard and C. Deutsch, "Energy loss and straggling of ions with any velocity in dense plasmas at any temperature," Phys. Rev. A, **26**, 665 (1982).

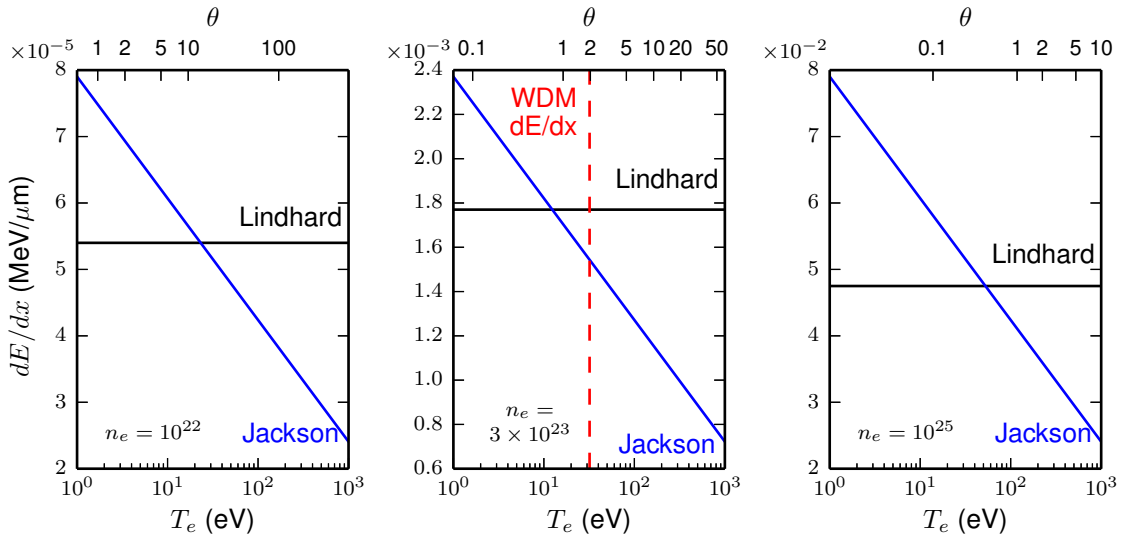

Figure G.8. Comparison of Lindhard (fully degenerate) and Jackson (non-degenerate) dielectric response stopping power for 15 MeV protons in plasmas of varying density: $n_e = 10^{22}$ 1/cm^3 (left), 3×10^{23} (center), and 10^{25} (right). The temperature is changed so that the plasma varies from degenerate to non-degenerate conditions, indicated by values of $\theta = k_B T_e / E_F$.

11. G. Maynard and C. Deutsch, "Born random phase approximation for ion stopping in an arbitrary degenerate electron fluid," J. Physique, **46**, 1113–1122 (1985).
12. P. E. Grabowski, M. P. Surh, D. F. Richards *et al.*, "Molecular Dynamics Simulations of Classical Stopping Power," Phys. Rev. Lett., **111**, 215002 (2013).
13. J. Ziegler, J. Biersack and U. Littmark, *The stopping and range of ions in matter* (Pergamon, New York, 1985).
14. C. K. Li and R. D. Petrasso, "Stopping of directed energetic electrons in high-temperature hydrogenic plasmas," Phys. Rev. E, **70**, 067,401 (2004).
15. J. Lindhard, "On the Properties of a Gas of Charged Particles," Mat. Fys. Medd. Dan. vid. Selsk., **27** (1954).
16. G. J. Iafrate and J. F. Ziegler, "Numerical evaluation of lindhards theory of stopping power for a charged particle in a freeelectron gas," Journal of Applied Physics, **50**(9), 5579–5581 (1979).
17. G. J. Iafrate, J. F. Ziegler and M. J. Nass, "Application of lindhards dielectric theory to the stopping of ions in solids," Journal of Applied Physics, **51**(2), 984–987 (1980).
18. J. Jackson, *Classical Electrodynamics* (Wiley, New York, 1975).

Appendix H

NIF summary tables

Table H.1. Summary of NIF shots

		Laser							DD-n	
Shot	Type	Energy (MJ)	Power (TW)	Absorption (%)	Rise Time (ns)	T_r (eV)	Coast Time (ns)	X-ray BT (ns)	Y_n ($\times 10^{11}$)	T_i (keV)
N101004-002-999	Symcap	1.00	289	84.9 ± 2.5	2	279 ± 4			3.3 ± 0.3	2.7 ± 0.1
N101019-003-999	CSymcap	1.02	295	85.5 ± 2.2	2	276 ± 4			1.9 ± 0.1	2.5 ± 0.1
N101022-001-999	CSymcap	1.01	292	86.1 ± 1.8	2	282 ± 4			2.4 ± 0.1	2.6 ± 0.1
N101027-001-999	Symcap	1.03	286	87.3 ± 2.4	2	284 ± 4			3.7 ± 0.2	2.8 ± 0.1
N101102-002-999	Symcap	1.22	395	87.5 ± 2.3	2	295 ± 4			7.9 ± 0.6	3.5 ± 0.3
N101111-001-999	CSymcap	1.16	371	88.6 ± 1.7	2	290 ± 4			3.2 ± 0.3	2.6 ± 0.1
N101211-002-999	Symcap	1.02	292	89.5 ± 2.1	2	282 ± 4			4.7 ± 0.3	2.9 ± 0.1
N101218-002-999	ConvAbl	1.00	281	90.4 ± 2.3	2	275 ± 4			1.0 ± 0.2	2.4 ± 0.2
N101220-001-999	ConvAbl	1.10	308	89.5 ± 1.9	2	280 ± 4			4.1 ± 0.3	2.7 ± 0.2
N110113-003-999	Symcap	1.06	307	86.0 ± 2.6	2	282 ± 4			4.0 ± 0.2	2.7 ± 0.2
N110204-001-999	ConvAbl	1.30	385	86.6 ± 2.1	1	293 ± 5			4.2 ± 0.2	3.0 ± 0.1
N110208-001-999	Symcap	1.30	377	85.0 ± 2.5	1	299 ± 4			7.5 ± 0.3	3.2 ± 0.1
N110211-001-999	Symcap	1.23	370	85.4 ± 2.5	1	298 ± 4			5.4 ± 0.2	3.1 ± 0.2
N110214-001-999	Symcap	1.28	392	83.7 ± 2.8	1	308 ± 4			6.2 ± 0.3	3.1 ± 0.2
N110527-001-999	Symcap	1.31	430	87.1 ± 2.3	2	300 ± 4	2.0 ± 0.1	22.52 ± 0.04	2.5 ± 0.4	3.2 ± 0.2
N110612-003-999	Symcap	1.33	395	82.9 ± 2.7	2	301 ± 4	1.6 ± 0.1	21.23 ± 0.10	6.5 ± 0.3	2.9 ± 0.1
N110625-001-999	ConvAbl	1.33	410	82.5 ± 2.9	2	301 ± 4	2.1 ± 0.0	22.39 ± 0.04	2.2 ± 0.1	2.3 ± 0.1
N110627-001-999	ConvAbl	1.33	414	83.0 ± 3.1	2	300 ± 4	2.1 ± 0.1	22.42 ± 0.05	7.2 ± 0.4	2.9 ± 0.1
N110630-001-999	ConvAbl	1.42	414	81.7 ± 2.9	2	305 ± 4	1.9 ± 0.0	22.41 ± 0.04	3.9 ± 0.2	2.5 ± 0.1
N110728-001-999	Symcap	1.39	444	82.9 ± 2.7	2	297 ± 4	1.9 ± 0.1	22.52 ± 0.04	4.2 ± 0.4	2.5 ± 0.2
N110731-002-999	Symcap	1.36	439	81.4 ± 2.9	2	292 ± 4	1.9 ± 0.1	22.45 ± 0.04	3.5 ± 0.4	2.5 ± 0.2
N110807-002-999	Symcap	1.35	436	83.7 ± 3.0	2	293 ± 4	1.9 ± 0.1	22.43 ± 0.04	3.0 ± 0.4	2.5 ± 0.2
N110821-002-999	Symcap	1.38	436	85.9 ± 2.9	2	298 ± 4	1.9 ± 0.1	22.46 ± 0.04	7.1 ± 0.3	3.1 ± 0.2
N110919-001-999	Symcap	1.37	436	83.8 ± 2.7	2	301 ± 4	1.8 ± 0.1	22.40 ± 0.04	3.5 ± 0.4	2.7 ± 0.2
N111007-002-999	ConvAblW	1.29	418	83.8 ± 3.1	2	289 ± 4	2.5 ± 0.0	22.46 ± 0.04	2.9 ± 0.1	2.4 ± 0.1
N111009-001-999	ConvAbl	1.52	403	83.3 ± 2.6	2	300 ± 4	1.7 ± 0.0	22.42 ± 0.04	7.4 ± 0.3	2.9 ± 0.1
N111011-004-999	ConvAbl	1.27	404	85.7 ± 3.2	2	292 ± 4	2.5 ± 0.0	22.55 ± 0.04	4.7 ± 0.2	2.5 ± 0.1
N111013-001-999	Symcap	1.24	436	84.0 ± 2.6	2	284 ± 4	2.5 ± 0.1	22.54 ± 0.04	3.0 ± 0.2	2.4 ± 0.2
N111014-001-999	Symcap	1.26	436	84.4 ± 2.6	2	289 ± 4	2.4 ± 0.1	22.46 ± 0.04	4.0 ± 0.3	2.5 ± 0.2
N111016-002-999	Symcap	1.24	440	81.5 ± 3.7	2	288 ± 4	2.5 ± 0.1	22.52 ± 0.04	4.1 ± 0.3	2.4 ± 0.2
N111018-001-999	Symcap	1.23	437	83.8 ± 2.8	2	291 ± 4	2.3 ± 0.1	22.30 ± 0.04	6.3 ± 0.3	2.8 ± 0.1

Table H.1. Summary of NIF shots

		Laser							DD-n	
Shot	Type	Energy (MJ)	Power (TW)	Absorption (%)	Rise Time (ns)	T_r (eV)	Coast Time (ns)	X-ray BT (ns)	Y_n ($\times 10^{11}$)	T_i (keV)
N111019-002-999	Symcap	1.24	438	83.6 ± 2.8	2	280 ± 4	2.6 ± 0.1	22.58 ± 0.04	3.0 ± 0.2	2.3 ± 0.2
N111022-002-999	Symcap	1.24	439	84.5 ± 2.5	2	288 ± 4	2.4 ± 0.1	22.44 ± 0.04	3.3 ± 0.2	2.5 ± 0.2
N111106-002-999	Symcap	1.27	439	83.2 ± 2.8	2	288	2.5 ± 0.1	22.69 ± 0.04	2.7 ± 0.2	2.1 ± 0.1
N111109-002-999	Symcap	1.26	430	86.2 ± 3.4	2	291 ± 4	2.4 ± 0.1	22.63 ± 0.04	3.1 ± 0.2	2.3 ± 0.2
N111115-002-999	Symcap	1.24	430	80.3 ± 2.8	2	291 ± 4	2.4 ± 0.1	22.53 ± 0.04	2.9 ± 0.2	2.2 ± 0.2
N111117-002-999	Symcap	1.25	436	83.7 ± 2.7	2	291 ± 4	2.5 ± 0.1	22.69 ± 0.04	2.7 ± 0.2	2.2 ± 0.2
N111119-002-999	ConvAblW	1.17	405	84.5 ± 2.6	2	286 ± 4	2.5 ± 0.0	22.51 ± 0.04	2.1 ± 0.2	2.1 ± 0.1
N111120-002-999	Symcap	1.50	446	84.1 ± 2.8	2	301 ± 4	1.7 ± 0.1	22.37 ± 0.04	5.0 ± 0.3	2.8 ± 0.1
N111218-001-999	ConvAblW	1.20	407	82.4 ± 3.0	2	294 ± 4	2.6 ± 0.1	22.51 ± 0.10	7.2 ± 0.4	2.2 ± 0.1
N111219-001-999	ConvAblW	1.41	417	84.6 ± 2.6	2	294 ± 4	1.9 ± 0.1	22.38 ± 0.10	4.4 ± 0.3	2.4 ± 0.1
N111220-001-999	ConvAblW	1.42	421	82.7 ± 2.8	3	295 ± 4	1.8 ± 0.1	22.47 ± 0.10	2.7 ± 0.2	2.4 ± 0.1
N111220-002-999	ConvAblW	1.41	421	83.7 ± 2.7	1	296 ± 4	2.0 ± 0.1	22.21 ± 0.10	3.8 ± 0.3	2.5 ± 0.1
N111221-001-999	Symcap	1.44	405	85.9 ± 2.4	1	304 ± 4	1.8 ± 0.0	22.01 ± 0.10	7.4 ± 0.4	3.0 ± 0.1
N120119-006-999	ConvAblW	1.40	419	83.9 ± 2.8	3	295 ± 4	1.9 ± 0.1	22.86 ± 0.05	3.2 ± 0.2	2.4 ± 0.2
N120306-003-999	ConvAbl	1.53	332	83.8 ± 2.9	3	306 ± 4	1.0 ± 0.1	23.00 ± 0.05	5.1 ± 0.2	2.5 ± 0.2
N120324-002-999	ConvAbl	1.52	327	83.5 ± 2.5	3		0.9 ± 0.1	22.91 ± 0.05	5.0 ± 0.3	2.4 ± 0.1
N120408-001-999	ConvAbl	1.52	333	81.3 ± 3.0	3	313 ± 4	0.9 ± 0.1	22.91 ± 0.05	2.7 ± 0.1	2.3 ± 0.1
N120409-001-999	ConvAbl	1.65	383	85.7 ± 2.2	2		1.0 ± 0.1	22.71 ± 0.05	3.1 ± 0.3	2.6 ± 0.1
N120418-001-999	ConvAbl	1.70	384	82.0 ± 2.7	3		1.1 ± 0.1	23.93 ± 0.05	5.9 ± 0.3	2.6 ± 0.1
N120421-006-999	ConvAbl	1.63	360	85.1 ± 2.7	3	313 ± 4	1.0 ± 0.1	22.59 ± 0.06	0.9 ± 0.1	1.5 ± 0.1
N120629-002-999	ConvAblW	1.34	328	84.2 ± 2.2	3	303 ± 4	1.6 ± 0.1	22.91 ± 0.06	2.7 ± 0.2	2.3 ± 0.1
N120703-001-999	Symcap	1.89	424	88.2 ± 1.8	3	321 ± 4	0.9 ± 0.1	24.30 ± 0.06	4.5 ± 0.3	2.4 ± 0.1
N120705-002-999	Symcap	1.85	523	83.8 ± 1.7	2	330 ± 4	1.3 ± 0.1	23.80 ± 0.06	5.9 ± 0.3	3.4 ± 0.2
N120709-003-999	ConvAblW	1.57	352	84.7 ± 2.6	3	309 ± 4	1.1 ± 0.1	23.05 ± 0.06	2.2 ± 0.2	2.1 ± 0.2
N120726-003-999	Symcap	1.37	412	83.7 ± 2.2	2	296 ± 4	2.3 ± 0.1	24.30 ± 0.06	3.1 ± 0.1	2.2 ± 0.1
N120729-002-999	Symcap	1.47	435	85.6 ± 2.0	2	307 ± 5	1.9 ± 0.1	22.52 ± 0.06	3.5 ± 0.3	2.5 ± 0.2
N120814-002-999	ConvAbl	1.73	380	87.8 ± 1.7	3	317 ± 5	1.0 ± 0.1	24.41 ± 0.06	4.6 ± 0.3	2.7 ± 0.2
N120906-001-999	Symcap	1.45	434	84.1 ± 2.1	2	299 ± 4	1.9 ± 0.1	22.55 ± 0.05	6.4 ± 0.2	2.9 ± 0.1
N120909-001-999	Symcap	1.43	428	86.5 ± 2.1	2	297 ± 4	2.0 ± 0.1	22.62 ± 0.05	5.9 ± 0.5	2.5 ± 0.1
N120910-001-999	Symcap	1.46	437	86.0 ± 1.9	2	298 ± 4	2.1 ± 0.1	22.69 ± 0.05	6.2 ± 0.5	2.6 ± 0.1
N121003-001-999	Symcap	1.37	391	83.6 ± 2.2	2	297 ± 4	2.5 ± 0.1	24.47 ± 0.06	2.2 ± 0.1	2.2 ± 0.2

Table H.1. Summary of NIF shots

		Laser							DD-n	
Shot	Type	Energy (MJ)	Power (TW)	Absorption (%)	Rise Time (ns)	T_r (eV)	Coast Time (ns)	X-ray BT (ns)	Y_n ($\times 10^{11}$)	T_i (keV)
N121004-005-999	ConvAbl2D	1.42	422	86.5 ± 2.2	2	316 ± 5	2.1 ± 0.1	24.27 ± 0.06	1.9 ± 0.1	2.2 ± 0.2
N121007-001-999	ConvAbl	1.68	470	85.5 ± 2.2	2	323 ± 5	1.7 ± 0.1	24.16 ± 0.06	40.0 ± 2.0	2.4 ± 0.1
N121008-002-999	ConvAblW	1.28	313	85.7 ± 2.4	3	299 ± 4	1.7 ± 0.1	23.08 ± 0.09	1.3 ± 0.1	2.2 ± 0.2
N121130-001-999	SymcapHF	1.27	350	83.8 ± 2.5	2		2.2 ± 0.1	16.66 ± 0.05	4.3 ± 0.3	2.2 ± 0.1
N121202-001-999	ConvAbl2D	1.28	365	86.4 ± 2.3	2	318 ± 5	2.0 ± 0.1	22.57 ± 0.09	1.7 ± 0.1	2.0 ± 0.1
N121210-001-999	ConvAbl2D	1.28	365	86.4 ± 2.2	2	318 ± 5	2.0 ± 0.1	22.89 ± 0.09	1.2 ± 0.1	1.9 ± 0.2
N121218-004-999	ConvAbl2D	1.29	363	87.5 ± 2.2	2	318 ± 5	2.0 ± 0.1	22.92 ± 0.09	2.3 ± 0.1	2.2 ± 0.2
N121219-001-999	ConvAbl2D	1.29	345	87.5 ± 2.2	2	317 ± 5	2.0 ± 0.1	22.91 ± 0.09	2.1 ± 0.1	2.2 ± 0.2
N130108-001-999	SymcapHF	1.27	350	88.0 ± 2.5	2	311 ± 5	2.1 ± 0.1	16.63 ± 0.05	2.4 ± 0.1	2.2 ± 0.1
N130211-003-999	ConvAbl2D	1.28	358	90.8 ± 3.0	2		2.0 ± 0.1	22.88 ± 0.09	2.2 ± 0.2	2.3 ± 0.5
N130212-001-999	ConvAbl2D	1.27	358	89.8 ± 3.0	2		2.2 ± 0.1	23.03 ± 0.09	2.4 ± 0.1	2.4 ± 0.2
N130213-002-999	ConvAbl2D	0.96	243	91.2 ± 3.0	2		2.7 ± 0.1	23.56 ± 0.09	0.6 ± 0.0	2.0 ± 0.2
N130226-002-999	ConvAbl2D	1.28	358	90.3 ± 3.0	2		1.9 ± 0.1	22.80 ± 0.09	3.5 ± 0.2	1.8 ± 0.1
N130227-002-999	ConvAbl2D	1.28	361	89.3 ± 3.0	2		2.1 ± 0.1	22.92 ± 0.09	3.4 ± 0.2	1.8 ± 0.1
N130303-001-999	ConvAbl2DHF	1.26	328	90.6 ± 3.0	2		2.2 ± 0.1	16.76 ± 0.05	2.7 ± 0.1	2.2 ± 0.1
N130313-003-999	ConvAbl2D	1.28	362	87.7 ± 3.0	2		2.0 ± 0.1	22.87 ± 0.06	2.1 ± 0.1	2.2 ± 0.1
N130314-003-999	ConvAbl2D	1.28	358	89.9 ± 3.0	2		2.1 ± 0.1	23.44 ± 0.06	1.9 ± 0.1	2.0 ± 0.2
N130411-002-999	ConvAbl2D	1.27	355	87.3 ± 3.0	2		2.1 ± 0.1	23.02 ± 0.06	1.6 ± 0.1	1.8 ± 0.1
N130425-003-999	Symcap	1.31	363	90.9 ± 2.1	2		2.0 ± 0.1	23.33 ± 0.05	2.8 ± 0.1	2.2 ± 0.2
N130502-002-999	SymcapRugby	1.29	379	93.0 ± 0.4	2		2.2 ± 0.1	22.21 ± 0.06	1.8 ± 0.1	2.1 ± 0.2
N130508-002-999	ConvAbl2DHF	1.28	354	85.4 ± 2.5	2		2.5 ± 0.1	17.07 ± 0.05	1.5 ± 0.1	2.0 ± 0.2
N130520-002-999	ConvAbl2D	1.48	367		3		1.4 ± 0.0	22.79 ± 0.06	1.2 ± 0.1	1.9 ± 0.3
N130630-002-999	ConvAbl2D	1.31	367		2		2.1 ± 0.1	23.42 ± 0.06	2.6 ± 0.1	2.2 ± 0.1
N130711-002-999	ConvAbl2DP	1.29	360		2		2.0 ± 0.1	23.41 ± 0.06	2.3 ± 0.2	2.7 ± 0.4
N130811-001-999	ConvAbl2DHDC	1.26	349	86.4 ± 2.4	2		3.2 ± 0.1	13.46 ± 0.06	0.8 ± 0.1	1.5 ± 0.2
N131118-003-999	ConvAbl2DHF									
N140601-001-999	ConvAblHF									

Table H.2. NIF shot target parameters

	Hohlraum					Capsule					
			Fill	Length	Diameter		Thickness	Radius	Fill		
Shot	Material	Gas	(mg/cc)	(mm)	(mm)	Material	(μm)	(μm)	P (atm)	f_D	f_{3He}
N101004-002-999	Au	He	0.96	10.01	5.44	CH	200.5	1111	50	0.3	0.7
N101019-003-999	Au	He	0.96	10.01	5.44	CH	192.8	1118	50	0.3	0.7
N101022-001-999	Au	He	0.96	10.01	5.44	CH	188.3	1113	50	0.3	0.7
N101027-001-999	Au	He	0.96	10.01	5.44	CH	199.8	1118	50	0.3	0.7
N101102-002-999	Au	He	0.96	10.01	5.44	CH	201.2	1114	50	0.3	0.7
N101111-001-999	Au	He	0.96	10.01	5.44	CH	202.9	1135	50	0.3	0.7
N101211-002-999	Au	He	0.96	10.01	5.44	CH	204.1	1132	50	0.3	0.7
N101218-002-999	Au	He	0.96	10.01	5.44	CH	201.3	1128	50	0.3	0.7
N101220-001-999	Au	He	0.96	10.01	5.44	CH	200.7	1124	50	0.3	0.7
N110113-003-999	Au	He	0.96	10.01	5.44	CH	199.8	1118	50	0.3	0.7
N110204-001-999	Au	He	0.96	10.01	5.44	CH	203.0	1119	50	0.3	0.7
N110208-001-999	Au	He	0.96	10.01	5.44	CH	199.8	1118	50	0.3	0.7
N110211-001-999	Au	He	0.96	10.01	5.44	CH	199.8	1118	50	0.3	0.7
N110214-001-999	Au	He	0.96	10.01	5.44	CH	199.8	1118	50	0.3	0.7
N110527-001-999	Au	He	0.96	10.01	5.44	CH	206.0	1124	50	0.3	0.7
N110612-003-999	Au	He	0.96	10.01	5.44	CH	199.8	1118	50	0.3	0.7
N110625-001-999	Au	He	0.96	10.01	5.44	CH	203.4	1113	50	0.3	0.7
N110627-001-999	Au	He	0.96	10.01	5.44	CH	209.8	1144	50	0.3	0.7
N110630-001-999	Au	He	0.96	10.01	5.44	CH	209.2	1140	50	0.3	0.7
N110728-001-999	Au	He	0.96	9.43	5.75	CH	205.0	1133	50	0.3	0.7
N110731-002-999	Au	He	0.96	9.43	5.75	CH	201.0	1129	50	0.3	0.7
N110807-002-999	Au	He	0.96	9.43	5.75	CH	200.0	1117	50	0.3	0.7
N110821-002-999	Au	He	0.96	9.43	5.75	CH	207.1	1139	50	0.3	0.7
N110919-001-999	U	He	0.96	10.01	5.44	CH	206.0	1124	50	0.3	0.7
N111007-002-999	Au	He	0.96	9.43	5.75	CH	205.5	1131	50	0.3	0.7
N111009-001-999	Au	He	0.96	9.43	5.75	CH	206.4	1136	50	0.3	0.7
N111011-004-999	Au	He	0.96	9.43	5.75	CH	206.3	1138	50	0.3	0.7
N111013-001-999	Au	He	0.96	9.43	5.75	CH	207.6	1134	50	0.3	0.7
N111014-001-999	Au	He	0.96	9.43	5.75	CH	209.7	1139	50	0.3	0.7
N111016-002-999	Au	He	0.96	9.43	5.75	CH	210.2	1143	50	0.3	0.7

Table H.2. NIF shot target parameters

	Hohlraum					Capsule					
			Fill	Length	Diameter		Thickness	Radius	Fill		
Shot	Material	Gas	(mg/cc)	(mm)	(mm)	Material	(μm)	(μm)	P (atm)	f_D	f_{3He}
N111018-001-999	U	He	0.96	9.43	5.75	CH	209.4	1144	50	0.3	0.7
N111019-002-999	Au	He	0.96	9.32	5.75	CH	208.8	1148	50	0.3	0.7
N111022-002-999	Au	He	0.96	9.32	5.75	CH	208.1	1140	50	0.3	0.7
N111106-002-999	Au	He	0.96	9.32	5.75	CH	208.7	1146	50	0.3	0.7
N111109-002-999	Au	He	0.96	9.32	5.75	CH	207.8	1134	50	0.3	0.7
N111115-002-999	Au	He	0.96	9.43	5.75	CH	200.0	1116	50	0.3	0.7
N111117-002-999	Au	He	0.96	9.32	5.75	CH	206.7	1134	50	0.3	0.7
N111119-002-999	Au	He	0.96	9.43	5.75	CH	205.7	1130	50	0.3	0.7
N111120-002-999	Au	He	0.96	9.32	5.75	CH	207.3	1136	50	0.3	0.7
N111218-001-999	Au	He	0.96	9.32	5.75	CH	206.3	1131	50	0.5	0.5
N111219-001-999	Au	He	0.96	9.32	5.75	CH	209.3	1144	50	0.3	0.7
N111220-001-999	Au	He	0.96	9.32	5.75	CH	208.4	1135	50	0.3	0.7
N111220-002-999	Au	He	0.96	9.32	5.75	CH	206.6	1133	50	0.3	0.7
N111221-001-999	U	He	0.96	9.43	5.75	CH	208.6	1147	50	0.3	0.7
N120119-006-999	Au	He	0.96	9.32	5.75	CH	208.5	1137	50	0.3	0.7
N120306-003-999	U	He	0.96	9.43	5.75	CH	208.2	1139	50	0.3	0.7
N120324-002-999	U	He	0.96	9.43	5.75	CH	208.7	1142	50	0.3	0.7
N120408-001-999	U	He	0.96	9.43	5.75	CH	206.8	1144	50	0.3	0.7
N120409-001-999	U	He	0.96	9.43	5.75	CH	207.2	1146	50	0.3	0.7
N120418-001-999	U	He	0.96	9.43	5.75	CH	231.3	1169	50	0.3	0.7
N120421-006-999	Au	He	0.96	9.43	5.75	CH	202.7	1128	50	0.3	0.7
N120629-002-999	U	He	0.96	9.43	5.75	CH	207.4	1139	50	0.3	0.7
N120703-001-999	Au	He	0.96	9.43	5.75	CH	228.2	1163	50	0.3	0.7
N120705-002-999	U	He	0.96	9.43	5.75	CH	229.0	1157	50	0.3	0.7
N120709-003-999	Au	He	0.96	9.43	5.75	CH	203.2	1128	50	0.3	0.7
N120726-003-999	Au	He	0.96	9.43	5.75	CH	224.4	1148	50	0.3	0.7
N120729-002-999	Au	He	0.96	9.32	5.75	CH	208.3	1136	50	0.3	0.7
N120814-002-999	U	He	0.96	9.43	5.75	CH	228.6	1166	50	0.3	0.7
N120906-001-999	Au	He	0.96	9.32	5.75	CH	208.5	1135	50	0.3	0.7
N120909-001-999	Au	He	0.96	9.32	5.75	CH	209.2	1141	50	0.3	0.7

Table H.2. NIF shot target parameters

	Hohlraum					Capsule					
			Fill	Length	Diameter		Thickness	Radius	Fill		
Shot	Material	Gas	(mg/cc)	(mm)	(mm)	Material	(μm)	(μm)	P (atm)	f_D	f_{3He}
N120910-001-999	Au	He	0.96	9.32	5.75	CH	209.8	1143	50	0.3	0.7
N121003-001-999	Au	He	0.96	9.43	5.75	CH	228.5	1151	50	0.3	0.7
N121004-005-999	Au	He	0.96	9.43	5.75	CH	227.3	1157	50	0.3	0.7
N121007-001-999	U	He	0.96	9.43	5.75	CH	229.2	1169	50	1.0	0.0
N121008-002-999	U	He	0.96	9.43	5.75	CH	208.7	1136	50	0.3	0.7
N121130-001-999	Au	He	1.45	9.43	5.75	CH	211.0	1130	50	0.3	0.7
N121202-001-999	Au	He	0.96	9.43	5.75	CH	207.8	1111	50	0.3	0.7
N121210-001-999	Au	He	0.96	9.43	5.75	CH	209.8	1120	50	0.3	0.7
N121218-004-999	Au	He	0.96	9.72	5.75	CH	209.3	1132	50	0.3	0.7
N121219-001-999	Au	He	0.96	9.12	5.75	CH	209.4	1129	50	0.3	0.7
N130108-001-999	Au	He	1.60	9.43	5.75	CH	209.9	1120	50	0.3	0.7
N130211-003-999	Au	He	0.96	10.13	5.75	CH	207.4	1131	50	0.3	0.7
N130212-001-999	Au	He	0.96	10.43	5.75	CH	210.2	1139	50	0.3	0.7
N130213-002-999	Au	He	0.96	10.13	5.75	CH	208.5	1132	50	0.3	0.7
N130226-002-999	Au	He	0.96	10.13	5.75	CH	208.7	1125	50	0.3	0.7
N130227-002-999	Au	He	0.96	10.13	5.75	CH	209.2	1128	50	0.3	0.7
N130303-001-999	Au	He	1.60	9.43	5.75	CH	207.3	1107	50	0.3	0.7
N130313-003-999	Au	He	0.96	9.43	5.75	CH	206.5	1128	50	0.3	0.7
N130314-003-999	Au	He	0.96	10.13	5.75	CH	210.3	1139	50	0.3	0.7
N130411-002-999	Au	He	0.96	9.43	5.75	CH	210.7	1143	50	0.3	0.7
N130425-003-999	Au	He	0.96	10.13	5.75	CH	209.0	1141	50	0.3	0.7
N130502-002-999	Au	He	1.20	10.52	7.00	CH	210.3	1139	50	0.3	0.7
N130508-002-999	Au	He	1.60	10.13	5.75	CH	207.4	1141	50	0.3	0.7
N130520-002-999	Au	He	0.96	9.43	5.75	CH	207.1	1115	50	0.3	0.7
N130630-002-999	Au	He	0.96	10.13	5.75	CH	207.8	1138	50	0.3	0.7
N130711-002-999	Au	He	0.86	10.13	5.75	CH	207.1	1139	50	0.3	0.7
N130811-001-999	Au	He	1.60	10.13	5.75	HDC	86.2	1087	50	0.3	0.7
N131118-003-999	Au	He			5.75	CH	189.0	1121	50	0.3	0.7
N140601-001-999	Au	He				CH	206.9	1135	50	0.3	0.7

Table H.5. Summary of NIF WRF data

	DIM (0,0)		DIM (90,78)		
Shot	ρR (mg/cm^2)	R_{cm} (μm)	ρR (mg/cm^2)	R_{cm} (μm)	Y_p
N101004-002-999	73.3 ± 10.3	289 ± 50	97.9 ± 6.5	239 ± 34	$(8.4 \pm 0.6) \times 10^7$
N101019-003-999	68.6 ± 5.2	301 ± 46	82.0 ± 6.3	266 ± 39	$(4.5 \pm 0.3) \times 10^7$
N101022-001-999	87.8 ± 5.8	252 ± 36	94.2 ± 6.5	240 ± 34	$(1.9 \pm 0.2) \times 10^8$
N101027-001-999	80.6 ± 5.4	273 ± 40	92.5 ± 6.2	249 ± 36	$(1.4 \pm 0.1) \times 10^8$
N101102-002-999	74.2 ± 5.5	288 ± 43			$(1.0 \pm 0.0) \times 10^0$
N101111-001-999			84.7 ± 5.8	271 ± 39	$(2.1 \pm 0.6) \times 10^8$
N101211-002-999	80.3 ± 5.0	280 ± 41	91.6 ± 6.1	257 ± 37	$(1.9 \pm 0.1) \times 10^8$
N101218-002-999	109.6 ± 7.0	227 ± 32	82.1 ± 5.5	273 ± 40	$(6.2 \pm 0.6) \times 10^7$
N101220-001-999	87.8 ± 5.6	260 ± 37	91.5 ± 6.0	253 ± 36	$(1.7 \pm 0.1) \times 10^8$
N110113-003-999			99.4 ± 6.6	238 ± 34	$(1.1 \pm 0.1) \times 10^8$
N110204-001-999	101.8 ± 6.5	236 ± 33	90.6 ± 6.1	254 ± 37	$(2.3 \pm 0.1) \times 10^8$
N110208-001-999	80.3 ± 6.4	274 ± 41	89.0 ± 6.1	256 ± 37	$(2.4 \pm 0.1) \times 10^8$
N110211-001-999	93.2 ± 6.0	248 ± 35	85.9 ± 5.9	262 ± 38	$(1.6 \pm 0.1) \times 10^8$
N110214-001-999			91.1 ± 6.2	252 ± 36	$(2.5 \pm 0.2) \times 10^8$
N110527-001-999			105.3 ± 7.3	234 ± 33	$(1.1 \pm 0.2) \times 10^8$
N110612-003-999	78.6 ± 8.0	278 ± 43	92.1 ± 6.4	250 ± 36	$(2.4 \pm 0.4) \times 10^8$
N110625-001-999			110.4 ± 7.5	223 ± 31	$(1.2 \pm 0.2) \times 10^8$
N110627-001-999	94.1 ± 8.9	258 ± 39	106.8 ± 7.3	238 ± 34	$(3.6 \pm 0.6) \times 10^8$
N110630-001-999	97.7 ± 7.3	250 ± 36	108.1 ± 7.3	235 ± 33	$(2.3 \pm 0.3) \times 10^8$
N110728-001-999	108.4 ± 7.1	231 ± 33	85.0 ± 6.9	270 ± 40	$(3.8 \pm 1.3) \times 10^7$
N110731-002-999			81.5 ± 8.5	275 ± 43	$(2.3 \pm 0.7) \times 10^7$
N110807-002-999			91.0 ± 6.9	252 ± 37	$(4.3 \pm 0.6) \times 10^7$
N110821-002-999			92.3 ± 6.6	259 ± 37	$(9.9 \pm 1.8) \times 10^7$
N110919-001-999	110.5 ± 14.4	227 ± 36	108.9 ± 7.7	229 ± 32	$(9.8 \pm 0.8) \times 10^7$
N111007-002-999	89.0 ± 5.6	262 ± 37	76.6 ± 5.9	290 ± 43	$(7.1 \pm 1.1) \times 10^7$
N111009-001-999			85.4 ± 7.1	271 ± 40	$(4.6 \pm 1.3) \times 10^7$
N111011-004-999	87.6 ± 5.7	267 ± 39	79.5 ± 5.7	285 ± 42	$(1.1 \pm 0.1) \times 10^8$
N111013-001-999	91.5 ± 5.8	259 ± 37	86.9 ± 6.3	268 ± 39	$(6.3 \pm 1.4) \times 10^7$
N111014-001-999	87.7 ± 5.6	265 ± 40	86.0 ± 6.1	272 ± 40	$(1.4 \pm 0.1) \times 10^8$
N111016-002-999			86.4 ± 6.2	273 ± 40	$(1.5 \pm 0.1) \times 10^8$
N111018-001-999			103.2 ± 7.2	243 ± 35	$(2.5 \pm 0.2) \times 10^8$
N111019-001-999	89.0 ± 6.1	251 ± 36	83.8 ± 6.1	261 ± 38	$(1.2 \pm 0.1) \times 10^8$
N111022-002-999			83.6 ± 6.1	277 ± 41	$(1.5 \pm 0.3) \times 10^8$
N111106-002-999	96.5 ± 6.8	254 ± 36	79.6 ± 6.5	288 ± 43	$(9.2 \pm 2.6) \times 10^7$
N111109-002-999	94.5 ± 6.3	254 ± 36	82.7 ± 6.3	277 ± 41	$(8.1 \pm 2.1) \times 10^7$
N111115-002-999			84.2 ± 6.6	265 ± 39	$(6.5 \pm 0.9) \times 10^7$
N111117-002-999			78.4 ± 5.8	287 ± 43	$(7.4 \pm 0.7) \times 10^7$
N111119-002-999	77.0 ± 5.2	288 ± 43	76.4 ± 5.5	290 ± 43	$(5.5 \pm 0.9) \times 10^7$
N111120-002-999	102.6 ± 7.5	241 ± 35	90.2 ± 6.5	262 ± 38	$(1.6 \pm 0.2) \times 10^8$
N111218-001-999			82.8 ± 8.3	274 ± 43	$(3.0 \pm 1.2) \times 10^7$
N111219-001-999	93.2 ± 7.3	259 ± 38	92.1 ± 6.8	261 ± 38	$(1.1 \pm 0.2) \times 10^8$
N111220-001-999			86.3 ± 6.4	270 ± 40	$(7.2 \pm 1.5) \times 10^7$
N111220-002-999	93.4 ± 7.6	255 ± 37	87.0 ± 6.4	267 ± 39	$(1.6 \pm 0.3) \times 10^8$
N111221-001-999			106.7 ± 7.5	239 ± 34	$(3.5 \pm 0.3) \times 10^8$

Table H.5. Summary of NIF WRF data

	DIM (0,0)		DIM (90,78)		
Shot	ρR (mg/cm^2)	R_{cm} (μm)	ρR (mg/cm^2)	R_{cm} (μm)	Y_p
N120119-006-999	99.1 ± 9.4	247 ± 37			$(1.0 \pm 0.0) \times 10^0$
N120324-002-999			163.4 ± 11.4	183 ± 25	$(1.7 \pm 0.2) \times 10^7$
N120408-001-999	107.3 ± 8.1	236 ± 34	159.9 ± 11.0	186 ± 26	$(3.0 \pm 0.4) \times 10^7$
N120409-001-999	99.6 ± 6.4	248 ± 35	162.6 ± 10.8	185 ± 25	$(1.0 \pm 0.1) \times 10^8$
N120418-001-999	126.7 ± 9.3	227 ± 33	166.7 ± 12.0	193 ± 27	$(2.1 \pm 0.4) \times 10^7$
N120421-006-999	112.8 ± 8.7	224 ± 32	144.1 ± 9.7	193 ± 27	$(3.4 \pm 0.1) \times 10^7$
N120629-002-999	101.2 ± 6.8	244 ± 35	164.7 ± 11.2	182 ± 25	$(2.5 \pm 0.2) \times 10^7$
N120703-001-999			99.4 ± 6.7	261 ± 38	$(3.3 \pm 0.2) \times 10^7$
N120705-002-999	111.0 ± 7.5	243 ± 35	131.8 ± 8.3	219 ± 31	$(1.7 \pm 0.2) \times 10^8$
N120709-003-999	116.4 ± 7.7	220 ± 31	149.1 ± 10.4	189 ± 26	$(1.8 \pm 0.2) \times 10^7$
N120726-003-999	109.4 ± 8.0	241 ± 35	103.4 ± 6.7	249 ± 36	$(4.3 \pm 0.3) \times 10^7$
N120729-002-999			88.1 ± 5.5	266 ± 38	$(6.7 \pm 0.6) \times 10^7$
N120814-002-999			177.2 ± 12.2	185 ± 26	$(1.4 \pm 0.3) \times 10^7$
N120906-001-999			87.9 ± 6.0	266 ± 39	$(8.9 \pm 0.8) \times 10^7$
N120909-001-999	99.7 ± 6.3	248 ± 35	74.8 ± 9.9	300 ± 51	$(1.4 \pm 0.6) \times 10^7$
N120910-001-999	102.7 ± 7.1	244 ± 35	88.2 ± 5.9	269 ± 39	$(5.1 \pm 0.7) \times 10^7$
N121003-001-999	125.8 ± 7.6	223 ± 32			$(1.0 \pm 0.0) \times 10^0$
N121004-005-999	122.8 ± 11.0	228 ± 33	127.1 ± 8.3	223 ± 31	$(3.0 \pm 0.3) \times 10^7$
N121008-002-999	116.1 ± 7.6	224 ± 31	170.8 ± 11.7	178 ± 24	$(2.0 \pm 0.2) \times 10^7$
N121130-001-999	104.5 ± 6.7	238 ± 34	94.4 ± 6.0	254 ± 37	$(5.1 \pm 0.3) \times 10^7$
N121202-001-999	108.4 ± 8.4	227 ± 33	116.4 ± 7.5	217 ± 31	$(2.4 \pm 0.2) \times 10^7$
N121210-001-999	109.0 ± 7.3	229 ± 32	117.3 ± 7.5	218 ± 31	$(2.4 \pm 0.2) \times 10^7$
N121218-004-999	105.9 ± 6.8	236 ± 33	114.6 ± 7.3	224 ± 32	$(2.2 \pm 0.2) \times 10^7$
N121219-001-999	118.9 ± 7.8	219 ± 31	120.0 ± 8.0	216 ± 30	$(3.5 \pm 0.3) \times 10^7$
N130108-001-999	100.2 ± 6.3	241 ± 34	92.6 ± 5.9	253 ± 36	$(4.7 \pm 0.4) \times 10^7$
N130211-003-999	102.6 ± 8.4	240 ± 35	117.1 ± 7.4	221 ± 31	$(5.5 \pm 0.3) \times 10^7$
N130212-001-999	97.3 ± 6.0	251 ± 36	113.9 ± 7.5	227 ± 32	$(6.2 \pm 0.5) \times 10^7$
N130213-002-999	102.8 ± 7.0	240 ± 34	116.2 ± 7.8	221 ± 31	$(8.7 \pm 0.8) \times 10^6$
N130226-002-999	97.1 ± 7.2	247 ± 36	111.5 ± 7.1	227 ± 32	$(5.0 \pm 0.5) \times 10^7$
N130227-002-999	96.4 ± 5.9	249 ± 36	113.3 ± 7.3	225 ± 32	$(6.4 \pm 0.6) \times 10^7$
N130303-001-999	81.7 ± 6.7	271 ± 41	98.0 ± 6.6	239 ± 35	$(2.3 \pm 0.4) \times 10^7$
N130313-003-999	105.2 ± 7.1	235 ± 33	110.1 ± 6.8	228 ± 32	$(2.3 \pm 0.2) \times 10^7$
N130314-003-999	99.0 ± 6.5	249 ± 35	108.2 ± 6.9	233 ± 33	$(3.6 \pm 0.3) \times 10^7$
N130411-002-999	113.5 ± 7.2	229 ± 32	114.1 ± 7.6	227 ± 32	$(4.6 \pm 0.6) \times 10^7$
N130425-003-999	102.4 ± 6.4	243 ± 34			$(1.0 \pm 0.0) \times 10^0$
N130502-002-999	95.4 ± 6.2	255 ± 36	97.3 ± 6.2	251 ± 36	$(4.8 \pm 0.3) \times 10^7$
N130508-002-999	84.2 ± 5.8	275 ± 40	100.1 ± 6.2	246 ± 35	$(4.7 \pm 0.3) \times 10^7$
N130520-002-999			117.0 ± 7.5	217 ± 30	$(3.3 \pm 0.4) \times 10^7$
N130630-002-999			110.8 ± 7.5	229 ± 33	$(3.8 \pm 0.5) \times 10^7$
N130711-002-999			80.4 ± 5.2	282 ± 41	$(4.0 \pm 0.5) \times 10^7$
N130811-001-999			111.1 ± 7.8	268 ± 39	$(2.0 \pm 0.3) \times 10^7$
N131118-003-999	69.7 ± 4.8	282 ± 32	84.8 ± 5.8	246 ± 25	$(2.4 \pm 0.1) \times 10^8$
N140601-001-999	92.4 ± 6.8	257 ± 37	123.1 ± 8.3	215 ± 30	$(3.7 \pm 0.6) \times 10^7$

Table H.3. Calculated hohlraum thicknesses

Name	Drawing	Au (μm)	DU (μm)	Al (μm)	Bump Δx (μm)
ConA544AuCH5ST315ST	AAA09-119689_AD	32.5	0.0	74.1	−8.3
SymT544CH5P203Au18457D78S1,SYMCAP	AAA10-105540_AB	32.5	0.0	74.1	−8.3
Sym_544_U_CH5SP_T78_ST	AAA10-108628_AD	24.9	7.6	74.1	−8.3
Sym_544.921_Au_CH5SP_T78_ST	AAA10-117682_AA	32.6	0.0	74.1	−8.3
Sym_575.943_Au_CH5SP_T78_ST	AAA11-104824_AA	61.4	0.0	74.1	−9.5
ConA_544_Au_CH5S.12S_T315_ST	AAA11-107562_AA	32.5	0.0	74.1	−8.3
Sym_575.943_U_CH5.12SP_T78_ST	AAA11-109089_AA	23.7	7.3	74.1	−8.3
ConA_575_Au_CH5.12SP_T315_ST	AAA11-109146_AA	61.4	0.0	74.1	−9.5
ConAw_575.943_Au_CH5.12S_T315_ST	AAA11-112570_AA	61.4	0.0	74.1	−9.5
Sym_575.933_Au_CH5.12SP_T78_L337	AAA11-112577_AA	61.4	0.0	74.1	−9.5
ConAw_575.933_Au_CH5.12SP_T315_L337	AAA11-112582_AA	61.4	0.0	74.1	−9.5
SYM_575.933_AU_CH5.12SP_T78-89_L337	AAA11-118305_AA	61.4	0.0	74.1	−9.5
SYM_575.933_AU_CH5.21SP_T78-89_L337	AAA11-118317_AA	61.4	0.0	74.1	−9.5
CONAW_575.943_U_CH5.12SP_T78_L310	AAA11-118327_AA	23.7	7.3	74.1	−8.3
CONAW_575.943_U_CH5.26SP_T78_L310	AAA12-100808_AA	23.7	7.3	74.1	−8.3
CONAW_575.943_U_CH5.29SP_T78_L310	AAA12-100809_AA	23.7	7.3	74.1	−8.3
CONAW_575.943_AU_CH5.36P_T78_L310	AAA12-100847_AA	61.4	0.0	74.1	−9.5
CONA2D_575.1013_AU_CH5.12S_T78_L337	AAA12-102853_AA	33.3	0.0	72.9	0.0
CONAW_575.943_AU_CH5.39P_T78	AAA12-106036_AA	61.4	0.0	74.1	−9.5
SYM_575.943_U_CH5.29SP_T78-89_L310	AAA12-109405_AA	23.7	7.3	74.1	−8.3
CONA2D_575.943_AU_CH5.12S_T78_GE12	AAA12-110625_AA	33.3	0.0	72.9	0.0
SYMRC_575.943_AU_CH5.12S_T78-89_L310	AAA12-110631_AA	61.4	0.0	74.1	−9.5
CONA2D_575.943_AU_CH5.21S_T78_GE12	AAA12-112494_AA	33.3	0.0	72.9	0.0
CONA2D_575.973_AU_CH5.12S_T78_GE12	AAA12-117671_AA	33.3	0.0	72.9	0.0
CONA2D_575.913_AU_CH5.12S_T78_GE12	AAA12-117681_AA	33.3	0.0	72.9	0.0
CONA2D_575.1043_AU_CH5.12S_T78_L337	AAA12-118612_AA	33.3	0.0	72.9	0.0
CONA2D_575.1013_AU_CH5.47S_T78_L337	AAA12-119365_AA	33.3	0.0	72.9	0.0
ConA2D_Au_575.1013_337_HDC5.3_T_13-100813 - Rev AA	AAA13-100813_AA	32.4	0.0	72.9	0.0
SYM_575.1013_Au-HC_CH5.12S_T78-89_L337	AAA13-100793_AA	61.4	0.0	74.1	−9.5
ConA2D_Au_575.943_310_CH5.17SP_T_13-107795	AAA13-107795_AA	32.4	0.0	72.9	0.0
Sym_575.943_Au_CH5.12SP_T78_ST	AAA11-107650_AA	61.4	0.0	74.1	−9.5
CONAW_575.943_AU_CH5.12S_T78_ZN15-F100	AAA12-106656_AA	61.4	0.0	74.1	−9.5

Table H.4. Data summary of shots used in the shock dynamics analysis

Shot	Average ρR (mg/cm^2)	Equatorial Shock Yield	R_{cm} (μm)	Δ_{BT} (ns)
N110728-001-999	91±13	$(3.8 \pm 1.3) \times 10^7$	247±36	
N111007-002-999	80±6	$(7.1 \pm 1.1) \times 10^7$	269±40	
N111011-004-999	82±11	$(1.1 \pm 0.1) \times 10^8$	265±40	-0.75 ± 0.16
N111013-001-999	88±11	$(6.3 \pm 1.4) \times 10^7$	252±38	
N111014-001-999	87±6	$(1.4 \pm 0.1) \times 10^8$	255±40	
N111106-002-999	84±12	$(9.2 \pm 2.6) \times 10^7$	260±40	
N111109-002-999	86±12	$(8.1 \pm 2.1) \times 10^7$	256±39	
N111119-002-999	77±10	$(5.5 \pm 0.9) \times 10^7$	277±43	
N111120-002-999	94±12	$(1.6 \pm 0.2) \times 10^8$	242±36	
N111219-001-999	92±12	$(1.1 \pm 0.2) \times 10^8$	245±38	
N111220-002-999	89±12	$(1.6 \pm 0.3) \times 10^8$	251±38	
N120408-001-999	139±10	$(3.0 \pm 0.4) \times 10^7$	191±28	-0.34 ± 0.12
N120409-001-999	137±9	$(1.0 \pm 0.1) \times 10^8$	193±29	-0.38 ± 0.13
N120418-001-999	152±10	$(2.1 \pm 0.4) \times 10^7$	181±29	-0.31 ± 0.13
N120421-006-999	133±9	$(3.4 \pm 0.1) \times 10^7$	196±28	-0.46 ± 0.13
N120629-002-999	138±10	$(2.5 \pm 0.2) \times 10^7$	191±27	
N120709-003-999	137±9	$(1.8 \pm 0.2) \times 10^7$	192±28	
N120726-003-999	105±7	$(4.3 \pm 0.3) \times 10^7$	226±36	
N120909-001-999	81±13	$(1.4 \pm 0.6) \times 10^7$	266±42	
N120910-001-999	92±6	$(5.1 \pm 0.7) \times 10^7$	245±38	
N121008-002-999	149±11	$(2.0 \pm 0.2) \times 10^7$	183±26	
N121202-001-999	110±8	$(2.4 \pm 0.2) \times 10^7$	219±31	-0.60 ± 0.13
N121210-001-999	110±7	$(2.4 \pm 0.2) \times 10^7$	219±31	-0.60 ± 0.13
N121218-004-999	107±7	$(2.2 \pm 0.2) \times 10^7$	223±32	-0.60 ± 0.13
N121219-001-999	119±8	$(3.5 \pm 0.3) \times 10^7$	209±31	-0.57 ± 0.13
N130211-003-999	110±8	$(5.5 \pm 0.3) \times 10^7$	220±32	-0.58 ± 0.13
N130212-001-999	100±7	$(6.2 \pm 0.5) \times 10^7$	233±33	-0.61 ± 0.13
N130213-002-999	105±8	$(8.7 \pm 0.8) \times 10^6$	226±32	-0.79 ± 0.19
N130226-002-999	100±7	$(5.0 \pm 0.5) \times 10^7$	233±34	-0.71 ± 0.13
N130227-002-999	98±7	$(6.4 \pm 0.6) \times 10^7$	236±33	-0.71 ± 0.12

Table H.6. Summary of NIF asymmetry analysis

Shot	WRF $\Delta_{\ell=2}$	X-ray P2/P0	WRF M2/M0	X-ray M2/M0
N101004-002-999	0.23 ± 0.11	0.20 ± 0.06		
N101019-003-999	0.15 ± 0.05	0.41 ± 0.09		
N101022-001-999	0.05 ± 0.02			
N101027-001-999	0.11 ± 0.03			
N101211-002-999	0.11 ± 0.02			
N101218-002-999	-0.21 ± 0.02			
N101220-001-999	0.03 ± 0.02			
N110204-001-999	-0.09 ± 0.02			
N110208-001-999	0.08 ± 0.04			
N110211-001-999	-0.06 ± 0.02	0.05 ± 0.11		
N110612-003-999	0.13 ± 0.07			
N110627-001-999	0.10 ± 0.06			
N110630-001-999	0.08 ± 0.03			
N110728-001-999	-0.18 ± 0.04			
N110919-001-999	-0.01 ± 0.08			
N111007-002-999	-0.12 ± 0.03	0.24 ± 0.06		
N111011-004-999	-0.08 ± 0.03			
N111013-001-999	-0.04 ± 0.02	0.30 ± 0.04		
N111014-001-999	-0.01 ± 0.03	0.31 ± 0.04		
N111019-001-999	-0.05 ± 0.03			
N111106-002-999	-0.15 ± 0.04			
N111109-002-999	-0.10 ± 0.03			
N111119-002-999	-0.01 ± 0.03			
N111120-002-999	-0.10 ± 0.03	-0.09 ± -0.09		
N111219-001-999	-0.01 ± 0.04			
N111220-002-999	-0.05 ± 0.04			
N120408-001-999	0.29 ± 0.04			
N120409-001-999	0.36 ± 0.02			
N120418-001-999	0.19 ± 0.04			
N120421-006-999	0.18 ± 0.04			
N120629-002-999	0.36 ± 0.02			
N120705-002-999	0.12 ± 0.02			
N120709-003-999	0.18 ± 0.02			
N120726-003-999	-0.04 ± 0.03	-0.16 ± -0.01		
N120909-001-999	-0.22 ± 0.09			
N120910-001-999	-0.11 ± 0.03	-0.09 ± -0.06		
N121004-005-999	0.02 ± 0.05			
N121008-002-999	0.28 ± 0.02			
N121130-001-999	-0.08 ± 0.02			
N121202-001-999	0.05 ± 0.04		0.05 ± 0.05	0.07 ± 0.01
N121210-001-999	0.05 ± 0.02		0.06 ± 0.06	0.14 ± 0.03
N121218-004-999	0.06 ± 0.02		0.06 ± 0.06	0.10 ± 0.00
N121219-001-999	0.01 ± 0.02		0.01 ± 0.01	0.09 ± 0.01

Table H.6. Summary of NIF asymmetry analysis

Shot	WRF $\Delta_{\ell=2}$	X-ray P2/P0	WRF M2/M0	X-ray M2/M0
N130108-001-999	-0.06 ± 0.03			
N130211-003-999	0.10 ± 0.04		0.06 ± 0.06	0.06 ± 0.01
N130212-001-999	0.12 ± 0.02		0.11 ± 0.11	0.13 ± 0.01
N130213-002-999	0.09 ± 0.03		0.08 ± 0.08	0.12 ± 0.02
N130226-002-999	0.10 ± 0.04		0.10 ± 0.10	0.17 ± 0.01
N130227-002-999	0.12 ± 0.02		0.13 ± 0.13	0.20 ± 0.01
N130303-001-999	0.14 ± 0.06			
N130313-003-999	0.03 ± 0.03			
N130314-003-999	0.07 ± 0.03			
N130411-002-999	0.00 ± 0.02			
N130502-002-999	0.01 ± 0.03			
N130508-002-999	0.13 ± 0.03			
N131118-003-999	0.16 ± 0.03			

Appendix I

Additional T^3He experimental details

I.1 CPS 2 and MRS proton IRFs

The primary factor for determining the CPS 2 resolution is the slit used[1]. The finite slit width in the energy dispersion direction results in a distribution of inferred energies for a mono-energetic input. The resolution of the CPS 2 system is calculated via ray-tracing of particles incident upon the full extent of the slit. For any given detector location, this gives a minimum, maximum, and mean particle energy detected. The full width of energies detected (i.e., the resolution) is plotted vs mean energy in Fig. I.1. Three detector windows were used to cover a wide range of proton energies. At low energy, the dipole magnet has focusing characteristics, resulting in good resolution. At higher energies, the resolution is poor due to the use of a large slit (3mm), which was necessary to achieve decent statistics in the measured spectrum.

The MRS system is similar, with a dipole providing magnetic dispersion of different particle energies[2]. The IRF for several proton energies is shown in Fig. I.2. At energies where the signal splits between adjacent windows, the IRF is significantly broader. A simple FWHM can be calculated from a Gaussian fit to the IRF at various proton energies over the range of interest, which is shown in Fig. I.3. The peaks (high FWHM) correspond to signal splitting between windows. In any fitting to the measured proton spectrum, this must be accounted for.

I.2 Shot Summary Tables

Several summary tables for the T^3He experiments are included in this section: the laser and target conditions on each shot (Table I.1), and the basic nuclear observables for each shot (Table I.2).

I.3 Simulations

I.3.1 ARES

Simulations of these experiments were conducted with the ARES radiation-hydrodynamics code[3,4]. Simulation results for nuclear yields are summarized in Table I.3. The yield-over-clean results are shown in Fig. I.4.

I.3.2 HYADES

Similarly, nuclear observables were calculated using the radiation-hydrodynamics code HYADES[5] (see Appendix F). The calculations are summarized in Table I.4. The yield-over-clean is shown in

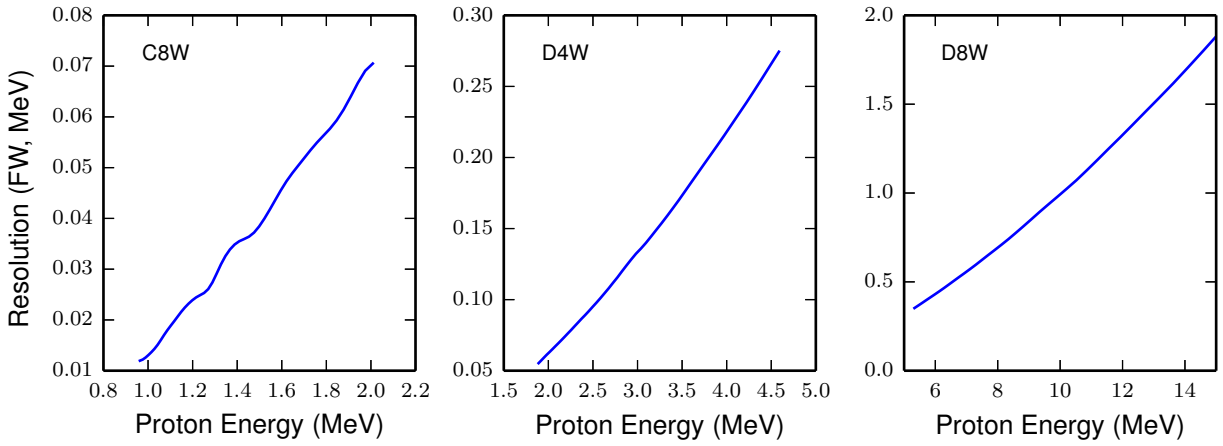

Figure I.1. Resolution (full width) of the CPS 2 proton measurement over three detector windows used (C8W, D4W, D8W) with a 3mm slit width.

Table I.1. Target and laser conditions for the T^3He experiments, plus nuclear bang time measured by NTD.

		Gas (atm)		Shell (μm)		Laser		
Shot	**Type**	**^{3}He**	**T_2**	**OD**	**Thick.**	**E (kJ)**	**Abs. (%)**	**BT (ps)**
70401	T_2	0	3.2	953	2.30	17.3	55 ± 6	680 ± 50
70402	T_2	0	3.2	953	2.27	17.8	62 ± 5	706 ± 50
70403	T_2	0	3.2	951	2.78	17.0	60 ± 4	870 ± 50
70404	T_2+^{3}He	15.7	3.2	1009	2.86	16.8	64 ± 4	904 ± 50
70405	T_2+^{3}He	16.1	3.2	967	2.53	16.9	69 ± 3	845 ± 50
70407	T_2+^{3}He	17.3	3.2	937	2.33	17.0	67 ± 5	803 ± 50
70408	T_2+^{3}He	17.7	3.2	1030	2.33	16.9	62 ± 6	822 ± 50
70409	T_2+^{3}He	17.1	3.2	899	2.29	16.9	70 ± 1	755 ± 50
70410	T_2+^{3}He	16.7	3.2	915	2.93	16.9	57 ± 5	881 ± 50
70411	^{3}He	22.4	0	958	2.23	16.8	66 ± 3	
70412	^{3}He	22.6	0	949	2.15	17.1	61 ± 2	

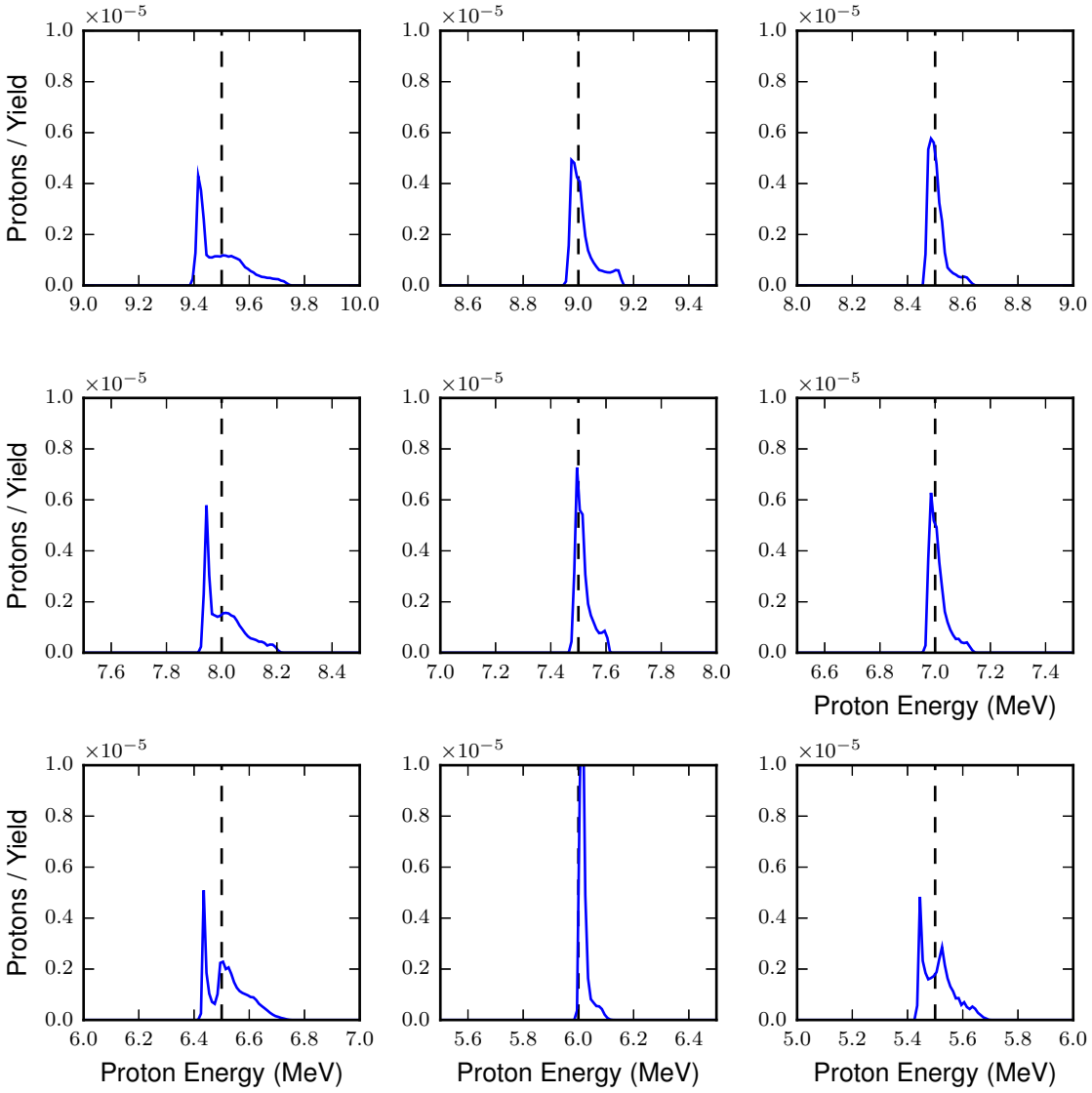

Figure I.2. MRS IRF for mono energetic protons from 5.5 to 9.5 MeV (dashed lines). The IRF is significantly broader where signal splits between multiple pieces of CR-39 in the MRS.

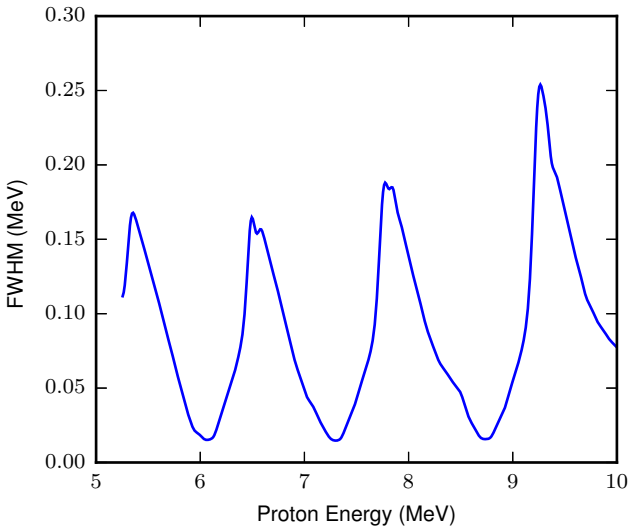

Figure I.3. MRS resolution (FWHM, MeV) versus mean proton energy for the range relevant to T^3He-p measurements.

Table I.2. Nuclear observables.

Shot	T_i (keV)		Yield			
	DT	**D^3He**	**DT** ($\times 10^{10}$)	**D^3He** ($\times 10^{8}$)	**TT-n** ($\times 10^{10}$)	**T^3He-D** ($\times 10^{9}$)
70401	21.5 ± 0.5		43.0 ± 2.6		16.8	
70402	20.9 ± 0.5		46.6 ± 2.8		18.3	
70403	20.9 ± 0.5		104 ± 6		37.1	
70404	12.6 ± 0.5	19.1 ± 1.1	11.8 ± 0.8	10.6 ± 0.1	3.4	1.75 ± 0.02
70405	13.3 ± 0.5	20.1 ± 0.5	8.7 ± 0.6	9.9 ± 0.1	2.4	1.45 ± 0.01
70407	12.2 ± 0.5	18.4 ± 0.7	6.1 ± 0.4	6.9 ± 0.1		1.06 ± 0.01
70408	12.9 ± 0.5	19.1 ± 0.6	7.7 ± 0.5	8.6 ± 0.1		1.23 ± 0.01
70409	11.1 ± 0.5	19.5 ± 0.6	5.0 ± 0.4	5.4 ± 0.1		0.96 ± 0.01
70410	13.1 ± 0.5	17.9 ± 0.5	9.6 ± 0.6	8.4 ± 0.1		1.22 ± 0.01

Table I.3. Simulated yields from ARES

Shot	**DT** ($\times 10^{11}$)	**TT-n** ($\times 10^{10}$)	**D^{3}He** ($\times 10^{8}$)	**T^{3}He-D** ($\times 10^{9}$)
70401	7.8	23.8		
70402	7.6	23.1		
70403	19.0	57.4		
70404	1.7	4.2	12.6	2.0
70405	1.4	3.5	11.7	2.0
70407	1.0	2.5	8.6	1.5
70408	1.2	2.8	10.1	1.7
70409	0.9	2.1	7.3	1.2
70410	1.3	3.1	9.2	1.4

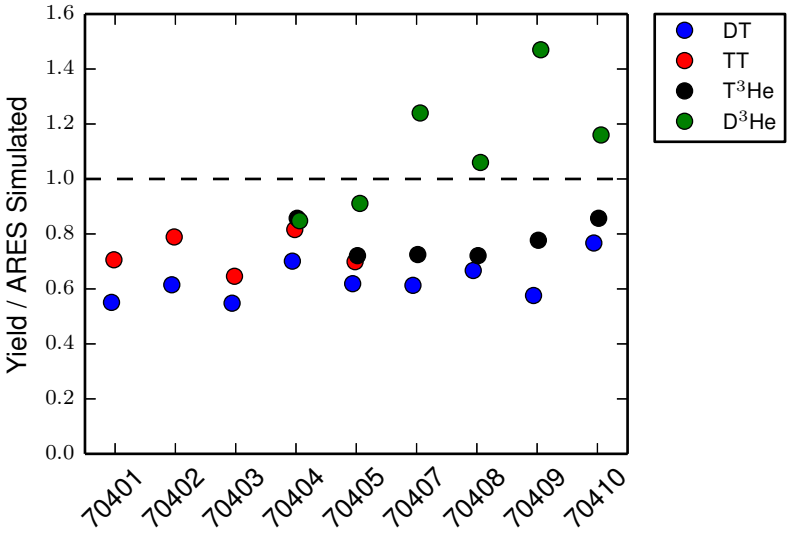

Figure I.4. Yield over clean for the T^{3}He experiments. Four nuclear yields (DT, TT, D^{3}He, T^{3}He) are shown. The ARES radiation-hydrodynamics code was used for the simulations.

Fig. I.5.

Table I.4. HYADES-simulated nuclear yields and burn-weighted ion temperatures for the T^3He experiments.

	T_i (keV)				Yield			
Shot	**DT**	**TT**	**D^3He**	**T^3He**	**DT** ($\times 10^{11}$)	**TT-n** ($\times 10^{10}$)	**D^3He** ($\times 10^9$)	**T^3He-D** ($\times 10^9$)
70401	29.7	31.6			15.4	59.3		
70402	29.9	31.8			15.7	60.5		
70403	30.4	32.3			20.4	80.1		
70404	15.4	17.4	26.5	25.3	2.0	5.4	3.3	4.2
70405	15.8	17.9	26.7	25.6	1.6	4.3	2.8	3.6
70407	15.5	17.6	26.7	25.5	1.2	3.1	2.1	2.7
70408	15.2	17.3	26.7	25.5	1.3	3.6	2.4	3.1
70409	15.4	17.5	26.4	25.3	1.0	2.7	1.8	2.2
70410	15.5	17.6	26.5	25.3	1.6	4.2	2.7	3.5

I.4 References

1. D. Hicks, *Charged-particle spectroscopy: a new window on inertial confinement fusion*, Ph.D. thesis, Massachusetts Institute of Technology (1999).
2. D. Casey, *Diagnosing Inertial Confinement Fusion Implosions at OMEGA and the NIF Using Novel Neutron Spectrometry*, Ph.D. thesis, Massachusetts Institute of Technology (2012).
3. R. M. Darlington, T. L. McAbee and G. Rodrigue, "A study of ALE simulations of Rayleigh-Taylor instability," Computer Physics Communications, **135**(1), 58 – 73 (2001).
4. J. Pino, private communication (2014).
5. J. T. Larsen and S. M. Lane, "HYADES-A plasma hydrodynamics code for dense plasma studies," Journal of Quantitative Spectroscopy and Radiative Transfer, **51**(1-2), 179 – 186 (1994), special Issue Radiative Properties of Hot Dense Matter.

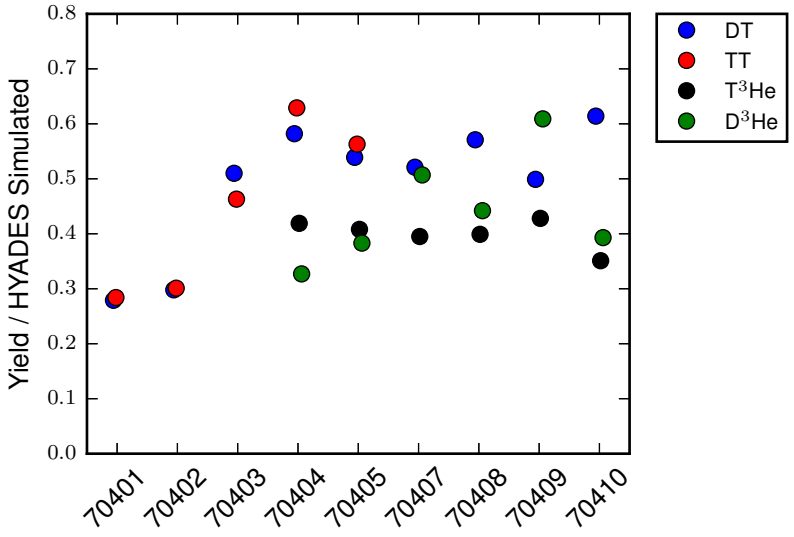

Figure I.5. Yield over clean for the T^3He experiments. Four nuclear yields (DT, TT, D^3He, T^3He) are shown. The HYADES radiation-hydrodynamics code was used for the simulations.

Appendix J

High-adiabat experiments at NIF

In the main body of this work, 'low-adiabat' surrogate shots were studied at NIF (Chapters 2, 3, and 4). Adiabat refers to the pressure of the dense fuel relative to the Fermi pressure ($\alpha \equiv P/P_F$), so lower adiabat shots can have higher convergence ratios, up to the $CR \sim 34$ designs considered during the National Ignition Campaign[1]. Those low-adiabat shots are poorly understood, whereas more recent high-adiabat layered implosions (the 'high-foot' campaign)[2] or indirect-drive exploding pushers[3] are much better modeled by hydrodynamic simulations.

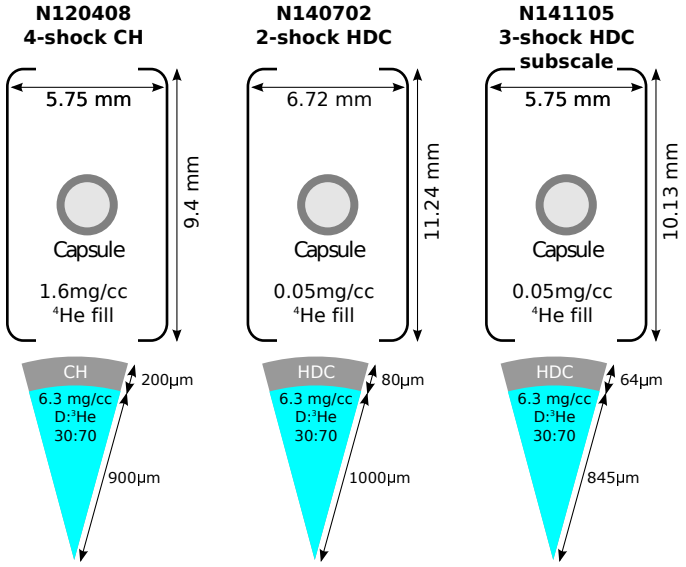

Figure J.1. Shot types. Left: A standard low-adiabat NIC-type shot using a gas-filled hohlraum and CH capsule. Center: the design for a near-vacuum hohlraum and HDC capsule. Right: the target design for a sub-scale NVH shot using a HDC capsule.

Higher-adiabat implosion designs are currently being studied with proton and shock diagnostics to determine if the anomalies observed in this thesis (Chapters 3, and 4) are present, or if simulations predict the experimental behavior. This Appendix presents the current status of that work. A summary of the shot types used is shown in Fig. J.1. At left is a standard low-adiabat 'NIC-type' shot, N120408, which used a 4-shock pulse in a gas-filled 5.75mm hohlraum to drive a CH target. The first new type of shot considered is a 2-shock pulse shape using a large (6.72mm diameter) near-vacuum hohlraum (NVH) to drive a high-density carbon (HDC, i.e. diamond) capsule, which was done in shot N140702. Alternatively, 'sub-scale' experiments are conducted using a 5.75mm diameter NVH to drive a smaller HDC capsule, as in shot N141105.

These shots are driven using different pulse shapes, predominantly distinguished by the number of shocks launched into the shell. The pulse shapes for the three shots are shown in Fig. J.2. The 2- and 3-shock designs are much shorter overall pulses due to the stronger initial shock(s), which allows use of the near-vacuum hohlraums since the wall motion is not as problematic for shorter laser pulses.

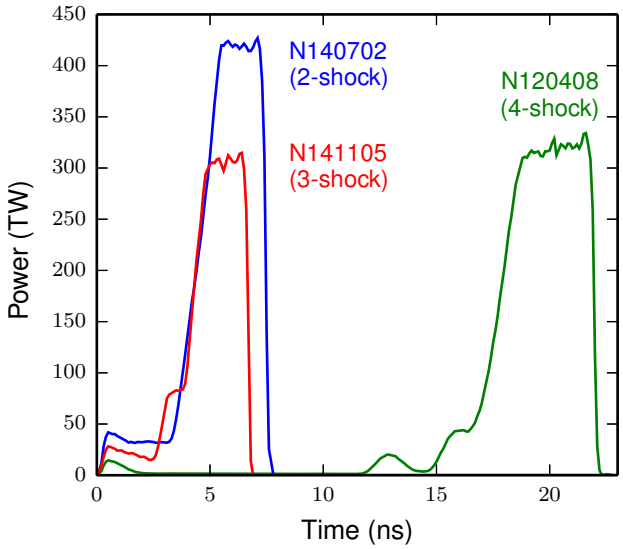

Figure J.2. Pulse shapes for the three shots: N120408 (4-shock), N140702 (2-shock) and N141105 (sub-scale 3-shock).

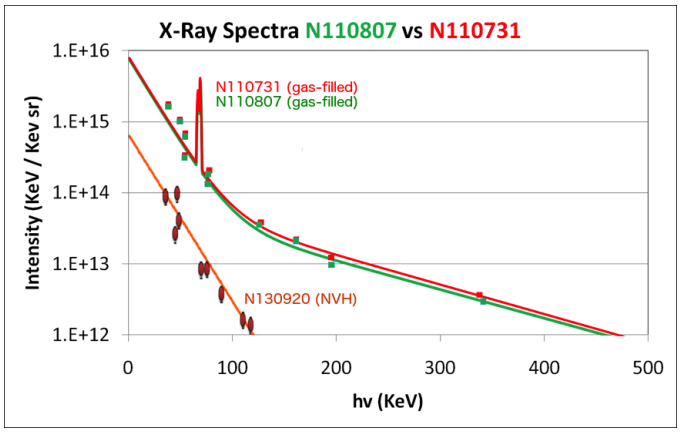

Figure J.3. Comparison of FFLEX-measured hard x-ray spectra for two gas-filled hohlraums (N110731 and N110807) to a NVH shot (N130920).

The lower-convergence NVH hohlraum shots have two important diagnostic advantages. First, the NVH have significantly-reduced hard x-ray background; with the lower background, the existing pTOF instrument[4] can measure the shock-produced D^3He-p for a direct measurement of the shock-bang time[5]. The hard x-ray spectrum, measured by FFLEX, is shown in Fig. J.3. Secondly, with the lower convergence the compression ρR is reduced to ~ 250 mg/cm^2, at which point the WRFs can measure the compression-produced D^3He protons. The data for one shot (N141105 are shown in Fig. J.4: the polar WRF spectra (a), equatorial WRF spectra (b), and the pTOF trace (c).

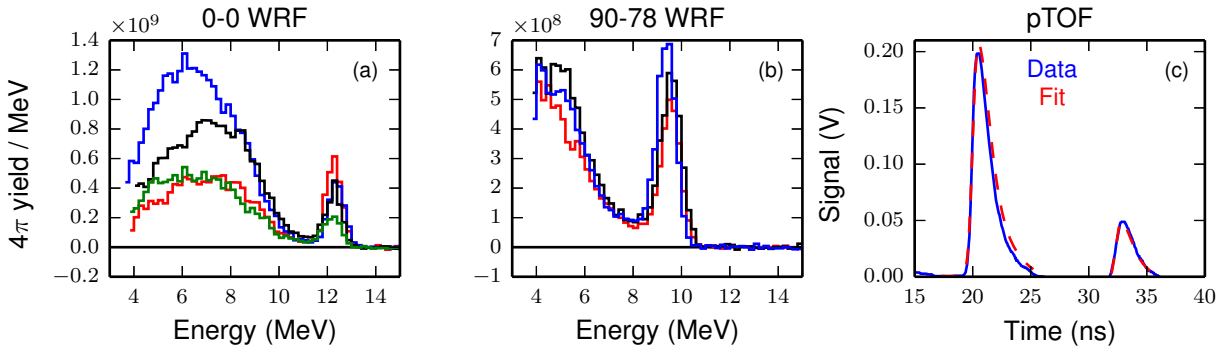

Figure J.4. Data for shot N141105. **(a)** Polar WRF spectra, showing shock-produced protons ($\sim$ 12 MeV) and compression protons ($\sim$ 6 MeV). **(b)** Equatorial WRF spectra (after the hohlraum wall), where the shock-produced protons are downshifted to $\sim$ 9 MeV and only the shoulder of the compression protons is visible. **(c)** pTOF data (blue) with forward fit (red) for the shock-produced D^3He-p ($\sim$ 20ns) and compression DD-n ($\sim$ 33 ns).

The WRF data are analyzed for the ρR at both shock and compression bang times. The data are fit with a double-Gaussian curve, shown for the #4 polar WRF on shot N141105 in Fig. J.5. The mean energies in each peak are used to infer the shock and compression ρR using the 1-D implosion model discussed in Chapter 2. In this case, the shock ρR is $79.6 \pm 4.2_{\text{ran}} \pm 11.0_{\text{sys}}$ and the compression ρR is $262.9 \pm 17.8_{\text{ran}} \pm 38.2_{\text{sys}}$. The shock and compression proton yields are also calculated from the fits.

Seven shots have been conducted in this experimental campaign to date. The experiments are summarized in Table J.1, with the WRF and pTOF data summarized in Table J.2. For the WRF data, the reported values are a weighted mean of the spectrometers within a single DIM (pole or equator), which reduces the random uncertainties. The data are also shown in Fig. J.6.

Table J.1. Shot parameters for the high-adiabat campaign.

				Laser		Coast
Shot	# Shocks	Scale	Ablator	Energy (MJ)	Power (TW)	time (ns)
N140702	2	672	HDC	1.37	420	2.19 ± 0.06
N140913	3	575	HDC	0.88	300	1.40 ± 0.05
N141105	3	575	HDC	0.88	300	1.21 ± 0.05
N141124	3	575	HDC	0.93	200	0.52 ± 0.02
N150107	3	575	HDC	0.89	300	1.33 ± 0.05
N150126	3	575	HDC	0.86	300	1.20 ± 0.05
N150128	3	620	HDC	1.44	400	1.37 ± 0.05

One primary goal of this campaign is to benchmark radiation-hydrodynamics simulations. Preliminary comparisons of some experimental data are shown in Fig. J.7, comparing the differential bang time, and Fig. J.8, which directly compares simulated and measured proton spectra.

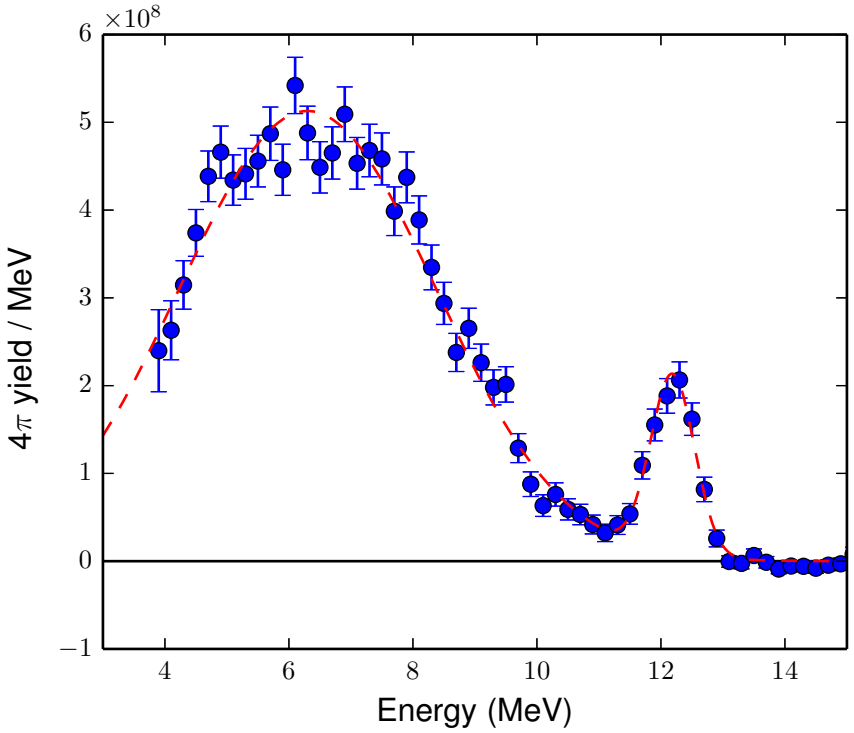

Figure J.5. Double-Gaussian fit (red) to the data (blue) for the #4 polar WRF on shot N141105.

Table J.2. WRF and pTOF data for the high-adiabat campaign.

	Pole		Equator	
Shot	Shock ρR (mg/cm^2)	Compression ρR (mg/cm^2)	Shock ρR (mg/cm^2)	pTOF ΔBT (ns)
N140702	$87.6 \pm 3.2_{\text{ran}} \pm 12.0_{\text{sys}}$	$279 \pm 13_{\text{ran}} \pm 40_{\text{sys}}$	$94.0 \pm 2.9_{\text{ran}} \pm 12.7_{\text{sys}}$	0.90 ± 0.10
N140913	$74.2 \pm 2.1_{\text{ran}} \pm 10.2_{\text{sys}}$	$253 \pm 8_{\text{ran}} \pm 37_{\text{sys}}$		0.63 ± 0.10
N141105	$76.2 \pm 2.0_{\text{ran}} \pm 10.5_{\text{sys}}$	$254 \pm 9_{\text{ran}} \pm 37_{\text{sys}}$	$76.2 \pm 2.4_{\text{ran}} \pm 10.6_{\text{sys}}$	0.55 ± 0.09
N141124	$83.6 \pm 2.7_{\text{ran}} \pm 11.3_{\text{sys}}$	$262 \pm 10_{\text{ran}} \pm 39_{\text{sys}}$	$78.9 \pm 2.9_{\text{ran}} \pm 10.8_{\text{sys}}$	0.67 ± 0.11
N150107	$73.0 \pm 3.0_{\text{ran}} \pm 10.0_{\text{sys}}$	$223 \pm 8_{\text{ran}} \pm 32_{\text{sys}}$	$74.4 \pm 3.0_{\text{ran}} \pm 10.1_{\text{sys}}$	0.50 ± 0.10
N150126	$76.8 \pm 2.4_{\text{ran}} \pm 10.3_{\text{sys}}$	$265 \pm 10_{\text{ran}} \pm 41_{\text{sys}}$	$74.8 \pm 2.5_{\text{ran}} \pm 10.2_{\text{sys}}$	0.55 ± 0.09
N150128	$108.7 \pm 2.9_{\text{ran}} \pm 14.7_{\text{sys}}$	$284 \pm 9_{\text{ran}} \pm 42_{\text{sys}}$	$102.7 \pm 3.0_{\text{ran}} \pm 14.0_{\text{sys}}$	0.67 ± 0.09

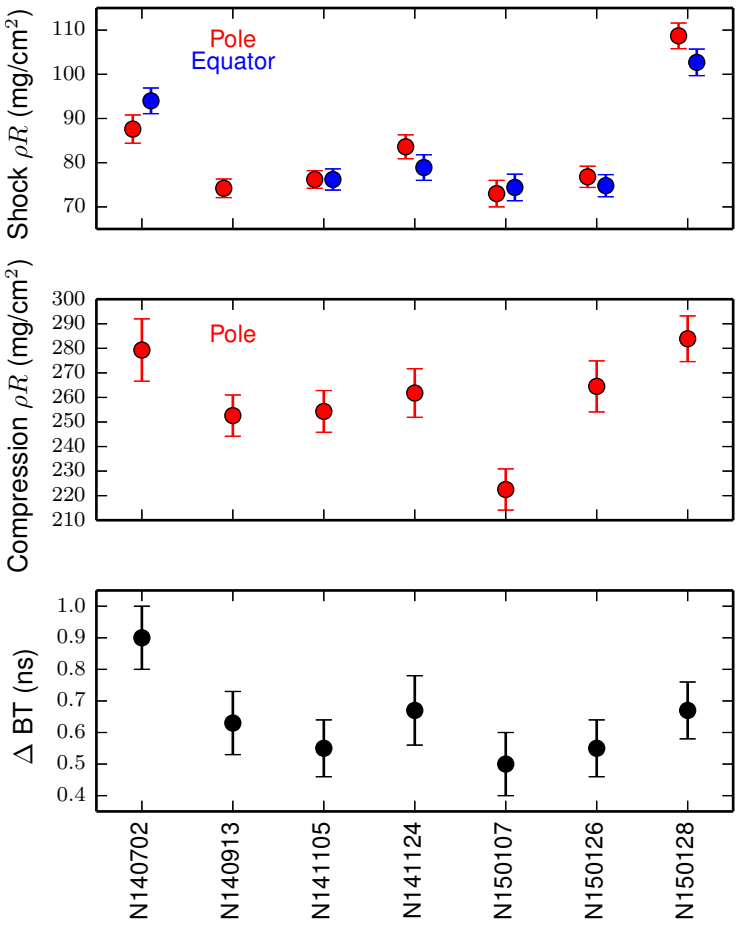

Figure J.6. Data for the high-adiabat campaign. Top: shock ρR on the pole (red) and equator (blue). Middle: polar compression ρR. Bottom: differential bang time measurement from pTOF.

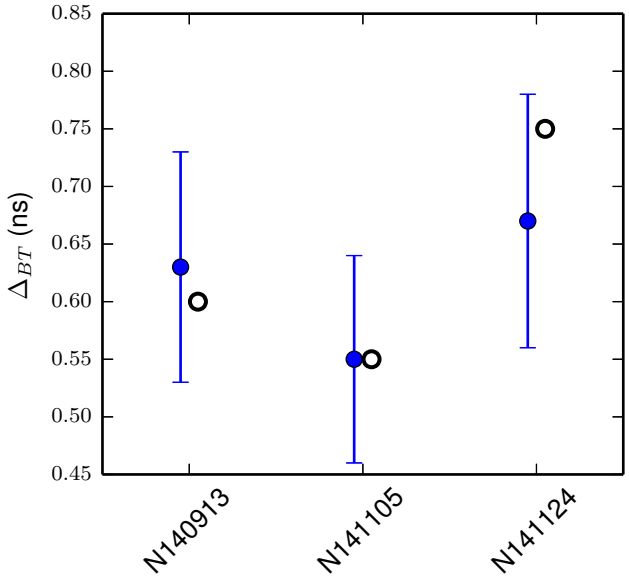

Figure J.7. Good agreement is observed in the shock-compression differential bang time (Δ_{BT}) between data (blue) and simulation (black) for three shots.

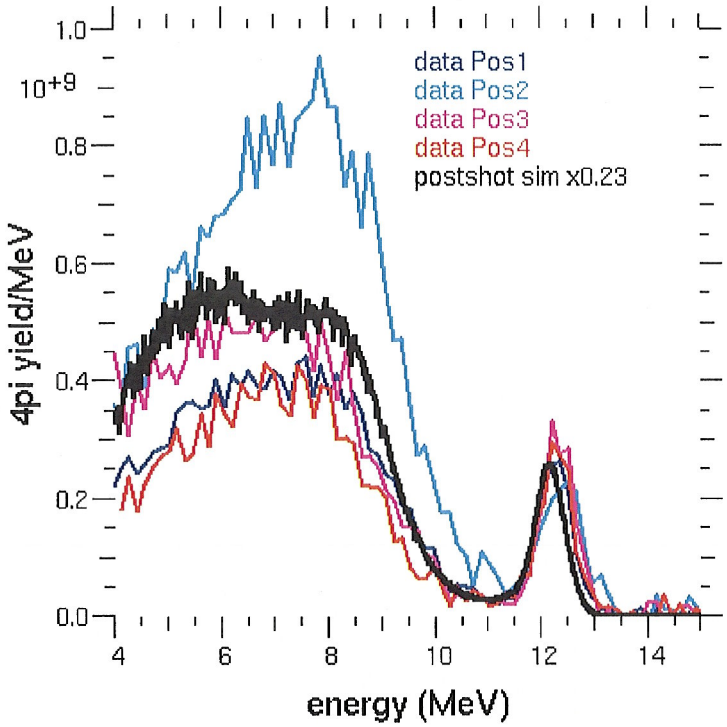

Figure J.8. Good agreement in the complete shape of the proton spectrum is observed for the polar direction on shot N140913. The simulated spectrum from a proton Monte Carlo package in HYDRA is shown in black, while the four polar WRF are in the colored curves.

For completeness, the raw data for the remaining shots are shown in Figs. J.9 (N140702), J.10 (N140913), J.11 (N141124), J.12 (N150107), J.13 (N150126), and J.14 (N150128).

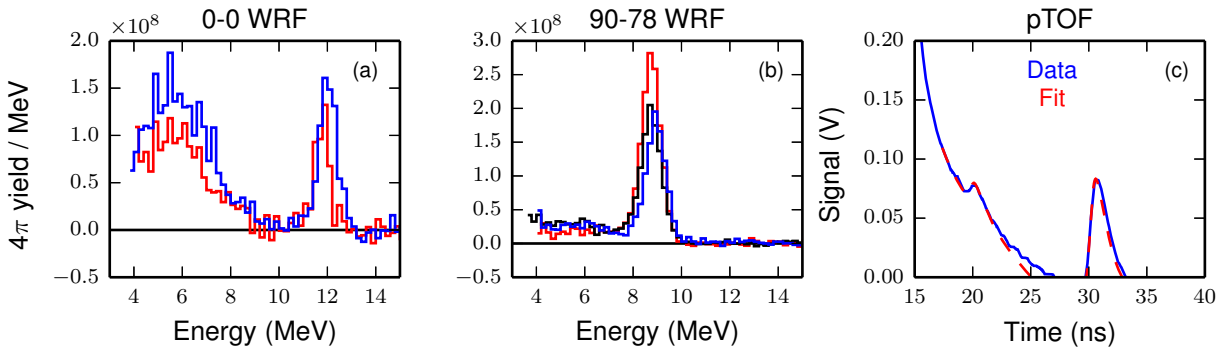

Figure J.9. Data for shot N140702: (a) polar WRF spectra, (b) equatorial WRF spectra, and (c) pTOF signal.

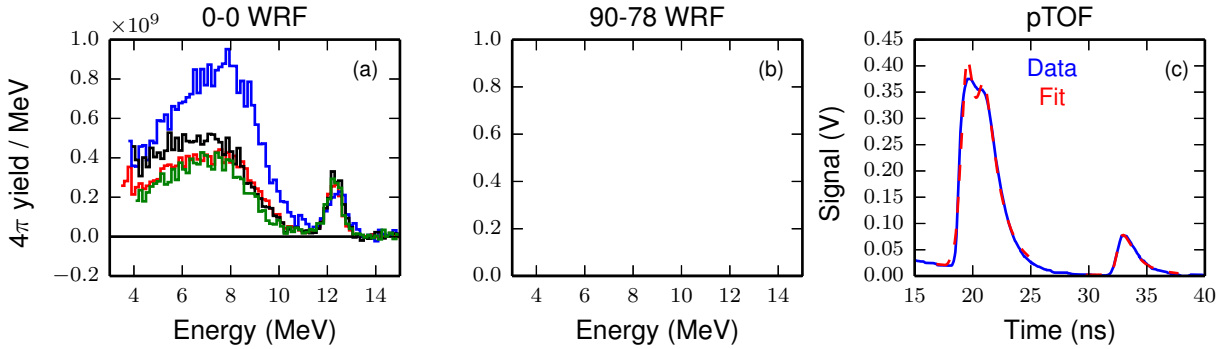

Figure J.10. Data for shot N140913: (a) polar WRF spectra, (b) equatorial WRF spectra (compromised by equatorial hohlraum thickness variation), and (c) pTOF signal.

J.1 References

1. J. Lindl, O. Landen, J. Edwards *et al.*, "Review of the National Ignition Campaign 2009-2012," Phys. Plasmas, **21**, 020501 (2014).
2. O. Hurricane, D. Callahan, D. Casey *et al.*, "Fuel gain exceeding unity in an inertially confined fusion implosion," Nature, **506**, 343 (2014).
3. S. Le Pape, L. Divol, L. Berzak Hopkins *et al.*, "Observation of a reflected shock in an indirectly driven spherical implosion at the national ignition facility," Phys. Rev. Lett., **112**, 225,002 (2014).
4. H. G. Rinderknecht, M. G. Johnson, A. B. Zylstra *et al.*, "A novel particle time of flight diagnostic for measurements of shock- and compression-bang times in d3he and dt implosions at the nifa)," Review of Scientific Instruments, **83**(10), 10D902 (2012).
5. H. Rinderknecht, *Studies of non-hydrodynamic processes in ICF implosions on OMEGA and the National Ignition Facility*, Ph.D. thesis, Massachusetts Institute of Technology (2015).

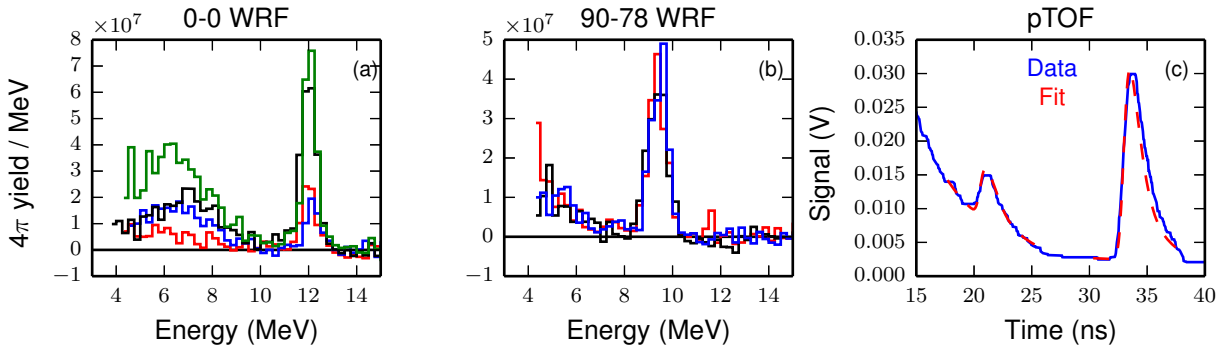

Figure J.11. Data for shot N141124: (a) polar WRF spectra, (b) equatorial WRF spectra, and (c) pTOF signal.

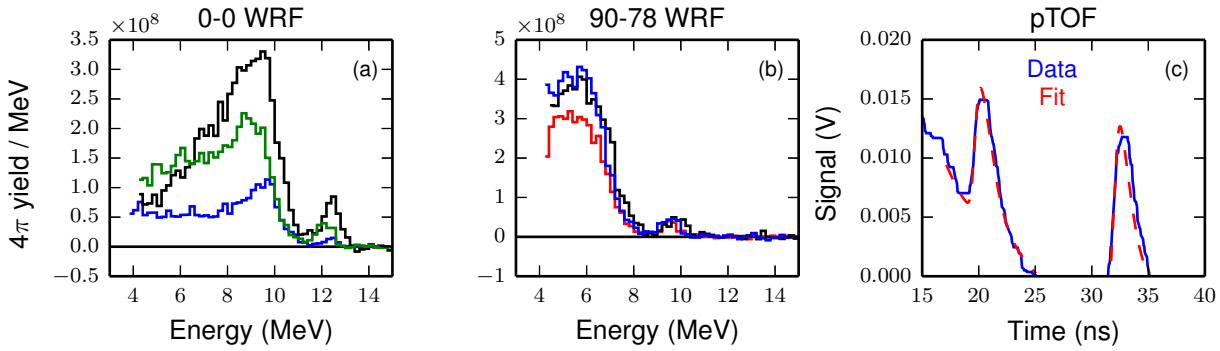

Figure J.12. Data for shot N150107: (a) polar WRF spectra, (b) equatorial WRF spectra, and (c) pTOF signal.

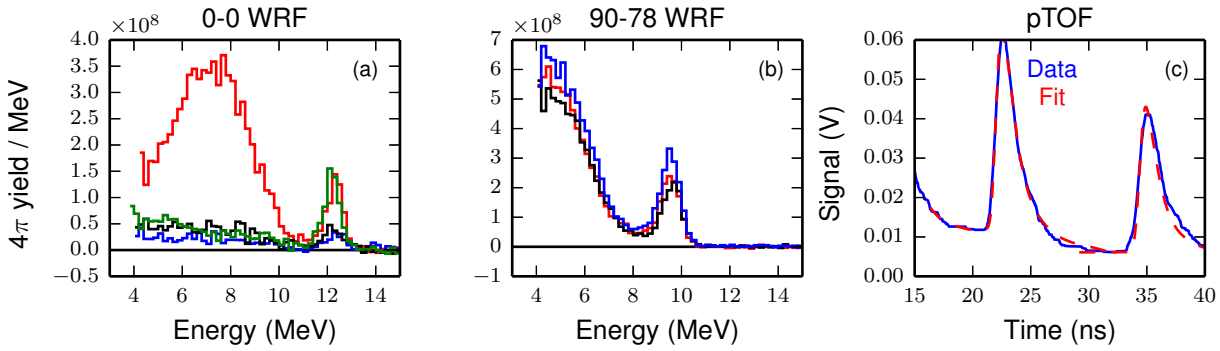

Figure J.13. Data for shot N150126: (a) polar WRF spectra, (b) equatorial WRF spectra, and (c) pTOF signal.

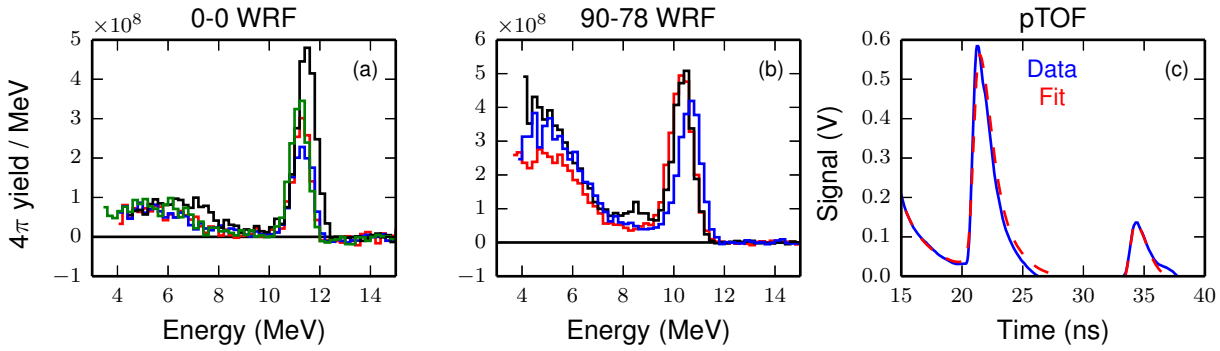

Figure J.14. Data for shot N150128: (a) polar WRF spectra, (b) equatorial WRF spectra, and (c) pTOF signal.

Appendix K

Detailed fusion-product kinematics

The fusion-product distribution moments (i.e. mean, width, ...) are critical quantities for interpreting data. The fusion kinematics used in this work follow the relativistic calculations of Ballabio (Ref.[1]), which provide small corrections to the standard classical kinematics[2].

For a generic two-body fusion reaction

$$X_1 + X_2 \rightarrow X_3 + X_4, \tag{K.1}$$

Ballabio gives the first spectral moment (mean energy) of product X_3 using relativistic kinematics as

$$\begin{aligned}\langle E_3 \rangle &= \left(\frac{(m_1+m_2)^2 + m_3^2 - m_4^2}{2(m_1+m_2)} - m_3 \right) \\ &+ \left(\frac{(m_1+m_2)^2 - m_3^2 + m_4^2}{2(m_1+m_2)^2} \langle K \rangle + \frac{(m_1+m_2)^2 + m_3^2 - m_4^2}{4(m_1+m_2)} \langle V^2 \rangle \right) + ...\end{aligned} \tag{K.2}$$

Eq. 10 in Ref. 1, where m represents the masses of the particles. K is the center-of-mass energy and V is the velocity of the center-of-mass frame, which are averaged over the reactions. The second moment (i.e. thermal width) of the product spectrum is given by

$$\begin{aligned}\sigma_{th}^2 &= \frac{1}{3} \left(\frac{(m_1+m_2)^2 + m_3^2 - m_4^2}{2(m_1+m_2)} - m_3 \right) \times \left(\frac{(m_1+m_2)^2 + m_3^2 - m_4^2}{2(m_1+m_2)} + m_3 \right) \langle V^2 \rangle \\ &+ \left[\frac{1}{4} m_3^2 \left(\langle V^4 \rangle - \langle V^2 \rangle^2 \right) + \left(\frac{m_4}{m_3+m_4} \right)^2 \left(\langle K^2 \rangle - \langle K \rangle^2 \right) \right. \\ &\left. + \frac{2 m_3 m_4}{3(m_3+m_4)} \langle V^2 \rangle \langle K \rangle \right],\end{aligned} \tag{K.3}$$

Eq. 17 in Ref. 1. The moments of V:

$$\langle V^2 \rangle = 3 \left(\frac{T_i}{m_1+m_2} \right), \tag{K.4}$$

$$\langle V^4 \rangle = 15 \left(\frac{T_i}{m_1+m_2} \right)^2, \tag{K.5}$$

are given by Eqs 34a-b in Ref. 1, where T_i is the (Maxwellian) reactant temperature. The moments of K depend on the specific reactivity, which is used in the parametrized form of Bosch and Hale

(Ref. 3) so that

$$\langle K \rangle = \frac{T_i}{\theta}\left(\frac{5}{6}+\xi\right)\frac{d\theta}{dT_i}, \tag{K.6}$$

$$\langle K^2 \rangle = \frac{T_i^4}{\theta^2}\left(\xi^2+\frac{1}{3}\xi-\frac{5}{36}\right)\left(\frac{d\theta}{dT_i}\right)^2+\frac{T_i^3}{\theta}\left(\frac{5}{6}+\xi\right)\left(\frac{d\theta}{dT_i}+T_i\frac{d^2\theta}{dT_i^2}\right), \tag{K.7}$$

from Eqs. 39 and 42 of Ref. 1. The reactivities are parameterized:

$$\xi = \left(\frac{B_G^2}{4\theta}\right)^{1/3}, \tag{K.8}$$

$$\theta = T_i\left[1-\frac{T_i(C_2+T_i(C_4+T_iC_6))}{1+T_i(C_3+T_i(C_5+T_iC_7))}\right]^{-1}, \tag{K.9}$$

$$\langle \sigma v \rangle = C_1\theta\sqrt{\frac{\xi}{m_r c^2 T_i^3}}e^{-3\xi}. \tag{K.10}$$

These are given in Bosch and Hale as Eqs 12-14. B_G is the Gamow energy, m_r is the reactant reduced mass, and the constants C are from a fit and are tabulated in Ref. 3 for the D+T, D+^{3}He, and D+D reactions.

While Eq. K.2 gives the product birth energy, in inertial fusion plasmas significant fuel motion (residual kinetic energy) may Doppler shift the observed particles. The mean birth energy $E_3(T_i)$ is used to calculate the initial velocity: $\gamma_0 = 1 + E_3/(m_3c^2)$ and $v_0 = c\sqrt{1-\gamma_0^{-2}}$. For a given bulk velocity v in the detector direction the velocities add relativistically:

$$v' = \frac{v_0+v_b}{1+v_0v_b/c^2},\ \gamma' = 1/\sqrt{1-(v'/c)^2}, \tag{K.11}$$

with Doppler shifted energy given by

$$E_3' = (\gamma'-1)m_3c^2,\ \delta E_3 = E_3' - E_3, \tag{K.12}$$

where δE_3 is the change in energy due to the bulk fuel velocity. There may also be some residual radial motion, which will broaden the spectrum. The Doppler-broadened spectrum is given by

$$Y_3'(E) = \int_0^{\pi} d\theta \sin\theta \int_0^{2\pi} d\phi \frac{1}{\sqrt{2\pi}\sigma_n} e^{-[E-E_3'(v_r\cos\theta)]^2/2\sigma_{th}^2}, \tag{K.13}$$

where θ and ϕ are spherical coordinates, E_3' is given by Eq. K.12, and σ_{th} is the birth thermal width given by Eq. K.3. The Doppler-broadened spectrum can be computed numerically and fit with a Gaussian to extract the extra broadening due to the radial motion (v_r).

The four quantities of most interest for fusion-product spectroscopy are the initial birth energy (E) and thermal width (σ_{th}), the Doppler shift due to unidirectional motion towards or away from the detector (δE), and the amount of additional broadening due to the radial motion (σ_r). These are plotted below for several reaction products: Figs K.1 (DT-n), K.2 (DT-α), K.3 (D^{3}He-p), K.4 (D^{3}He-α), K.5 (DD-n), K.6 (DD-p), K.7 (DD-T), and K.8 (DD-^{3}He).

For the Doppler shifts a temperature of 10 keV has been used in the calculations, though the final result is very insensitive to T_i. All calculations use the AME2003 atomic mass evaluations[4].

For convenient numerical evaluation, the four quantities are parameterized:

$$E = a_1 T_i^2 + a_2 T_i + a_3, \quad \text{(K.14)}$$

$$\sigma_{th} = \sqrt{b T_i}, \quad \text{(K.15)}$$

$$\delta E = c_1 v^2 + c_2 v, \quad \text{(K.16)}$$

$$\sigma_r = d_1 v_r^2 + d_2 v_r. \quad \text{(K.17)}$$

E is the particle energy in MeV, T_i is the temperature in energy units (keV), σ_{th} is the Gaussian width in keV, δE is the Doppler shift in keV for net velocity v (km/s) towards the detector, and σ_v is the additional Gaussian width in keV for a uniform radial velocity v_r (km/s). The coefficients (a, b, c, d) are tabulated for the reactions of interest in Tables K.1 (E), K.2 (σ_{th}), K.3 (δE), and K.4 (σ_v). In the tabulations the residual is calculated as the standard deviation between the parameterization and the actual kinematic calculation.

Table K.1. Parameterization coefficients for the mean birth energy (E)

	a_1	a_2	a_3	Residual
DT-n	-7.7166×10^{-5}	5.0979×10^{-3}	14.037	1.671×10^{-3}
DT-α	-1.9718×10^{-5}	2.4193×10^{-3}	3.5621	4.269×10^{-4}
D^{3}He-p	-5.2553×10^{-5}	7.2533×10^{-3}	14.650	1.151×10^{-3}
D^{3}He-α	-1.3426×10^{-5}	2.9698×10^{-3}	3.7156	2.940×10^{-4}
DD-n	-1.6029×10^{-5}	3.0531×10^{-3}	2.4526	4.737×10^{-4}
DD-p	-1.6330×10^{-5}	3.0074×10^{-3}	3.0253	4.959×10^{-4}
DD-T	-5.4723×10^{-6}	2.0051×10^{-3}	1.0124	1.662×10^{-4}
DD-^{3}He	-5.3729×10^{-6}	2.0206×10^{-3}	0.82118	1.588×10^{-4}

Table K.2. Parameterization coefficients for the thermal width (σ_{th})

	b	Residual
DT-n	5.6512×10^3	1.219×10^{-1}
DT-α	5.6862×10^3	1.581×10^{-1}
D^{3}He-p	5.8977×10^3	1.114×10^{-1}
D^{3}He-α	5.9302×10^3	1.552×10^{-1}
DD-n	1.2229×10^3	4.882×10^{-2}
DD-p	1.5091×10^3	4.262×10^{-2}
DD-T	1.5304×10^3	2.758×10^{-1}
DD-^{3}He	1.2440×10^3	3.056×10^{-1}

Table K.3. Parameterization coefficients for the net Doppler shift (δE)

	c_1	c_2	Residual
DT-n	5.3060×10^{-6}	5.4468×10^{-1}	3.667×10^{-6}
DT-α	5.2476×10^{-6}	2.7405×10^{-1}	1.845×10^{-6}
D^3He-p	5.3095×10^{-6}	5.5692×10^{-1}	3.749×10^{-6}
D^3He-α	5.2485×10^{-6}	2.8008×10^{-1}	1.886×10^{-6}
DD-n	5.2414×10^{-6}	2.2796×10^{-1}	1.535×10^{-6}
DD-p	5.2446×10^{-6}	2.5291×10^{-1}	1.703×10^{-6}
DD-T	5.2334×10^{-6}	1.4694×10^{-1}	9.892×10^{-7}
DD-^{3}He	5.2323×10^{-6}	1.3264×10^{-1}	8.929×10^{-7}

Table K.4. Parameterization coefficients for the Doppler velocity broadening (σ_v)

	d_1	d_2	Residual
DT-n	2.1142×10^{-5}	3.1323×10^{-1}	1.453×10^{-2}
DT-α	2.7536×10^{-6}	1.5806×10^{-1}	1.960×10^{-3}
D^3He-p	2.1661×10^{-5}	3.2027×10^{-1}	1.488×10^{-2}
D^3He-α	2.8180×10^{-6}	1.6154×10^{-1}	1.983×10^{-3}
DD-n	7.2490×10^{-6}	1.3118×10^{-1}	5.072×10^{-3}
DD-p	7.9835×10^{-6}	1.4555×10^{-1}	5.521×10^{-3}
DD-T	1.5914×10^{-6}	8.4740×10^{-2}	1.114×10^{-3}
DD-^{3}He	1.4437×10^{-6}	7.6492×10^{-2}	1.010×10^{-3}

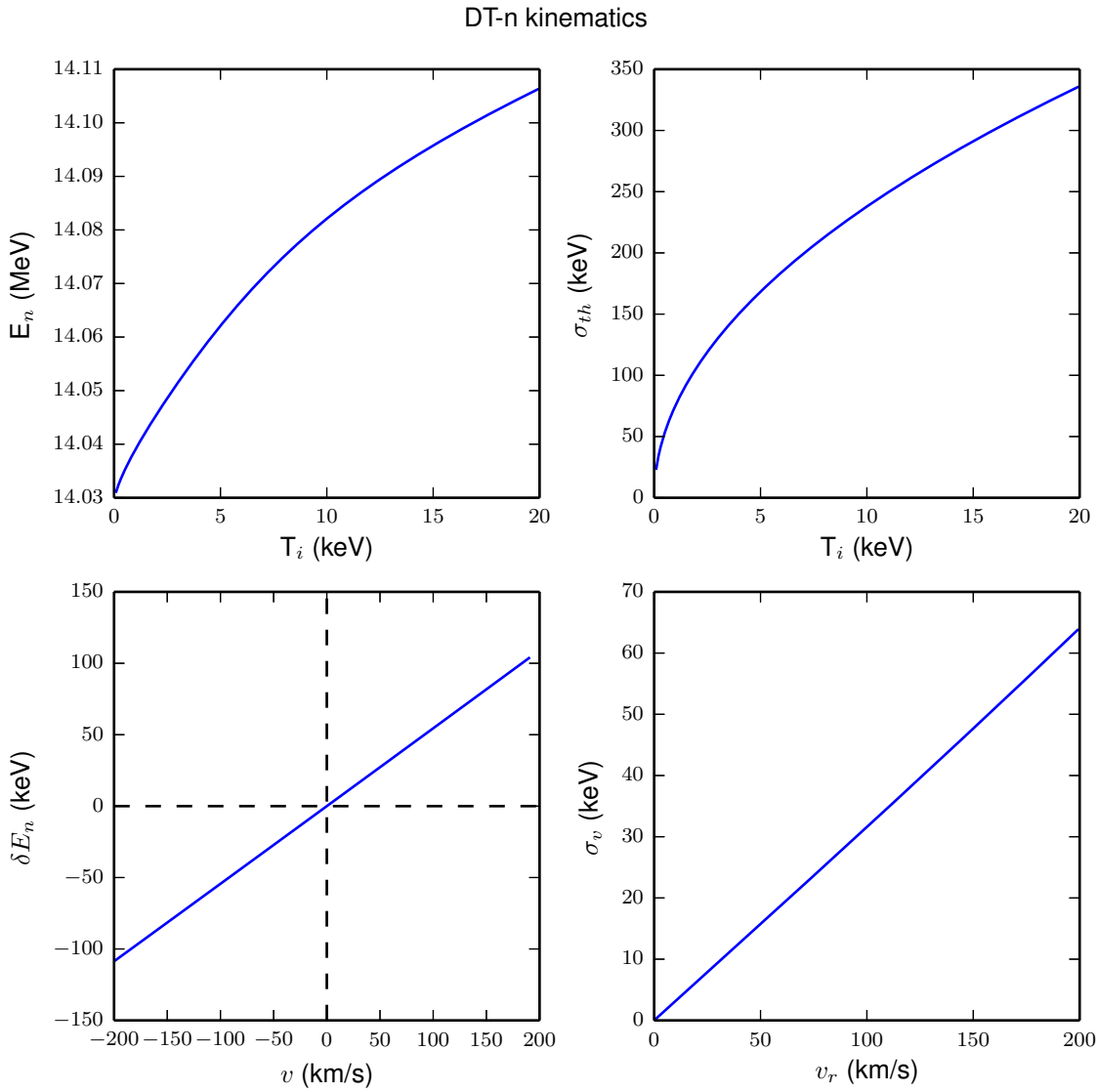

Figure K.1. DT-n kinematics: birth energy, thermal width, Doppler shift, and velocity Doppler broadening.

K.1 References

1. L. Ballabio, J. Källne and G. Gorini, "Relativistic calculation of fusion product spectra for thermonuclear plasmas," Nuclear Fusion, **38**(11), 1723 (1998).
2. H. Brysk, "Fusion Neutron Energies and Spectra," Plasma Physics, **15**, 611–617 (1973).
3. H.-S. Bosch and G. Hale, "Improved Formulas for Fusion Cross-Sections and Thermal Reactivities," Nuclear Fusion, **32**, 611–631 (1992).
4. G. Audi, A. Wapstra and C. Thibault, "The ame2003 atomic mass evaluation: (ii). tables, graphs and references," Nuclear Physics A, **729**(1), 337 – 676 (2003), the 2003 {NUBASE} and Atomic Mass Evaluations.

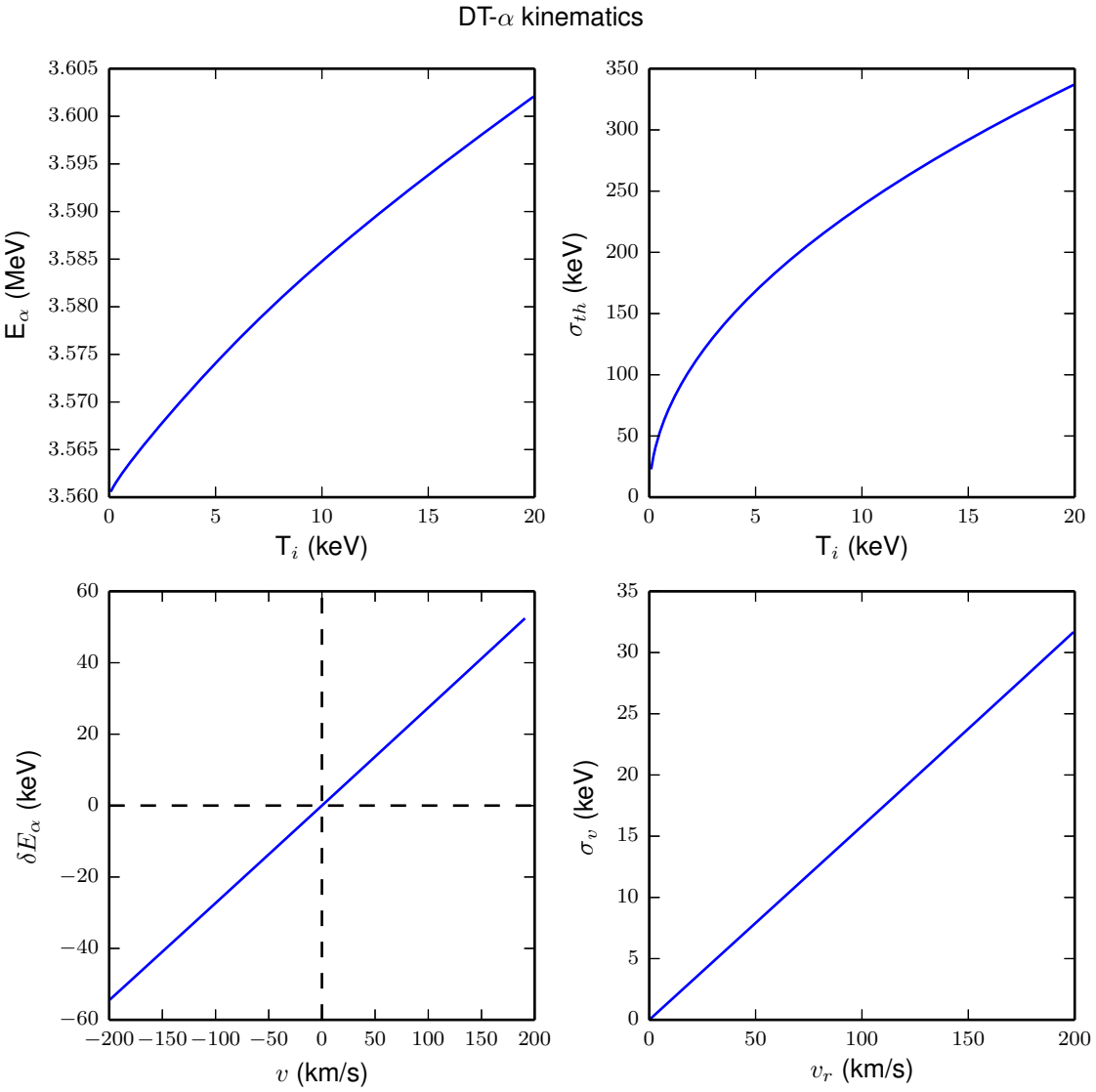

Figure K.2. DT-α kinematics: birth energy, thermal width, Doppler shift, and velocity Doppler broadening.

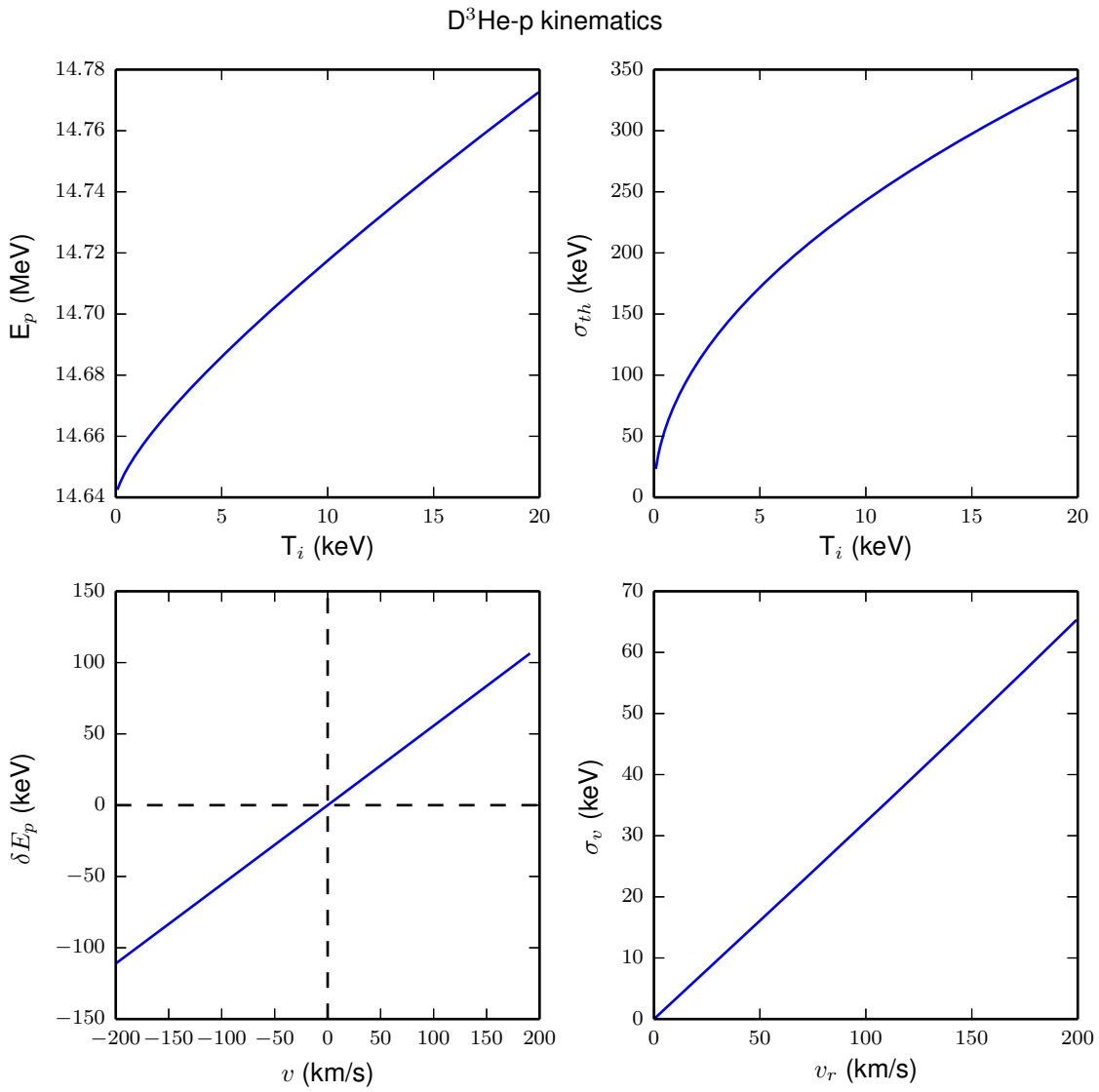

Figure K.3. D^{3}He-p kinematics: birth energy, thermal width, Doppler shift, and velocity Doppler broadening.

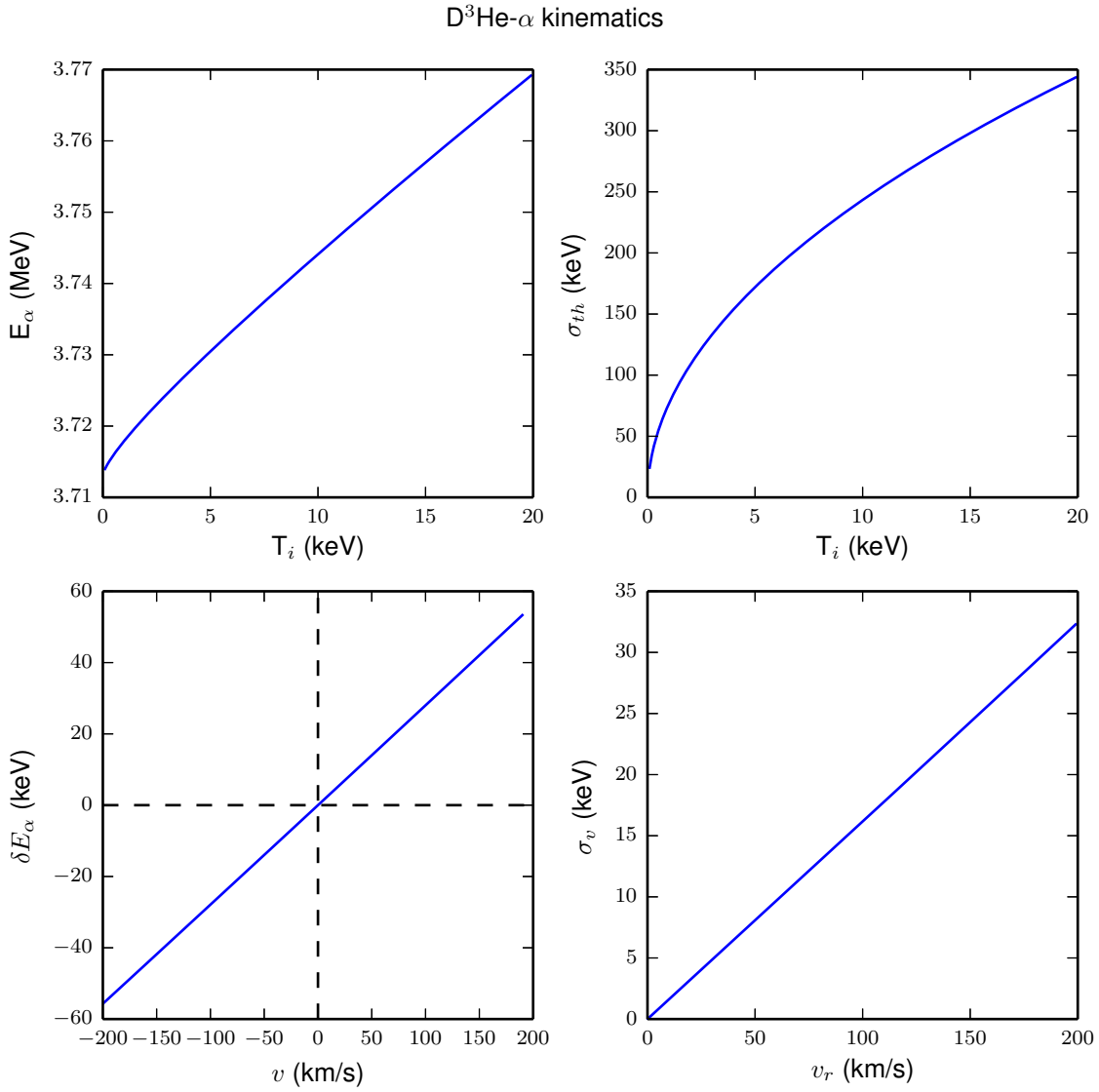

Figure K.4. D^{3}He-α kinematics: birth energy, thermal width, Doppler shift, and velocity Doppler broadening.

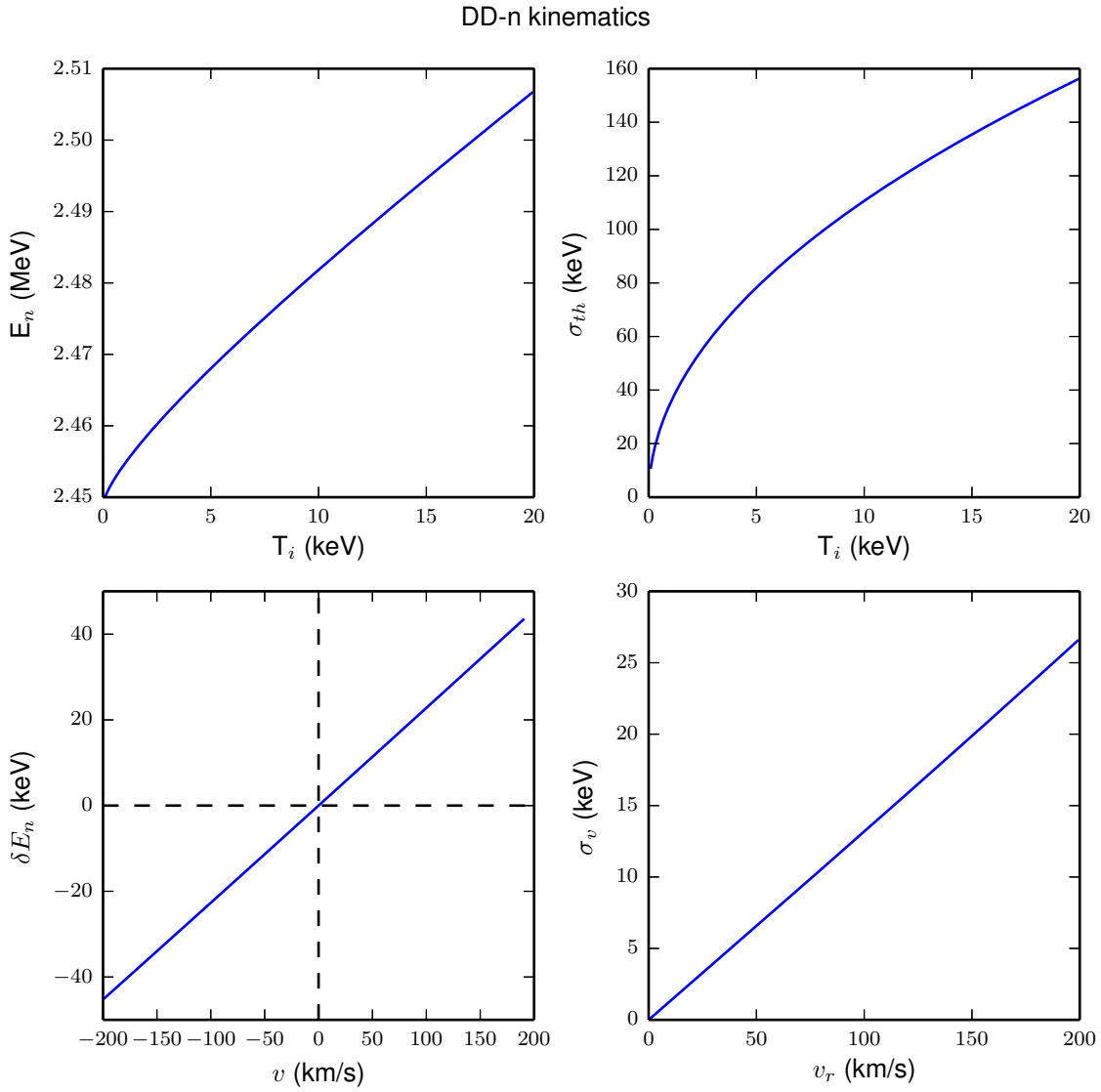

Figure K.5. DD-n kinematics: birth energy, thermal width, Doppler shift, and velocity Doppler broadening.

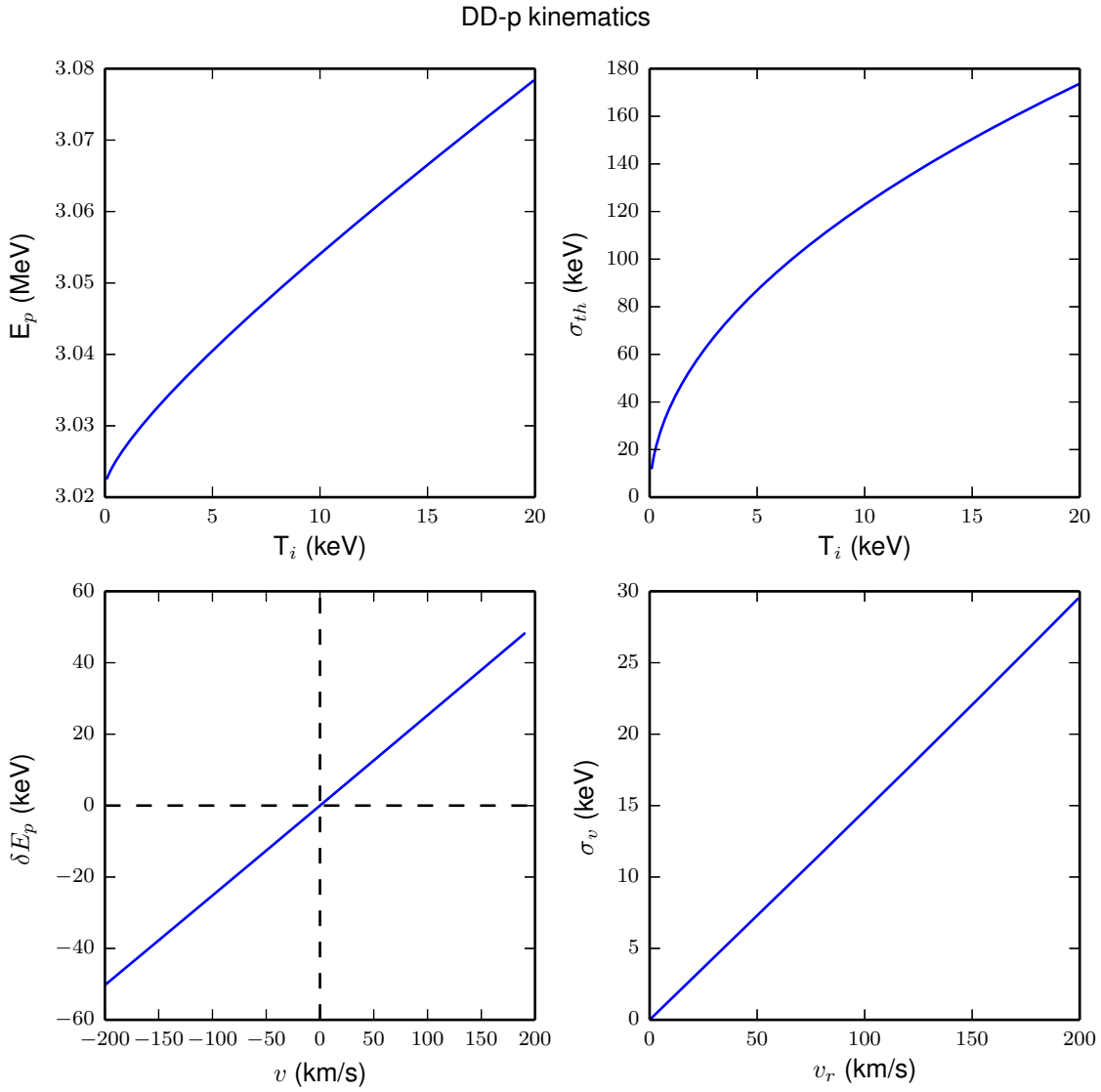

Figure K.6. DD-p kinematics: birth energy, thermal width, Doppler shift, and velocity Doppler broadening.

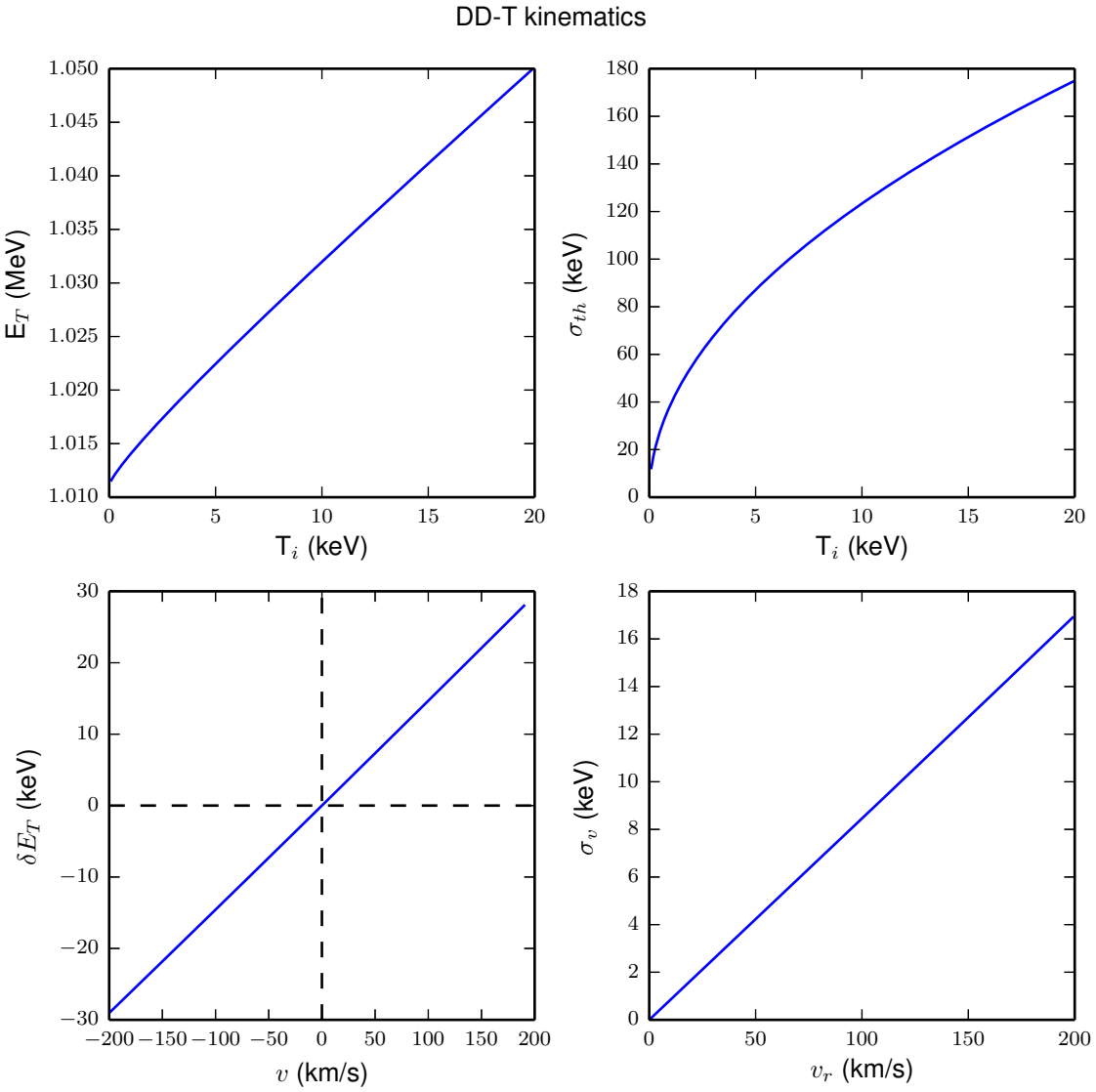

Figure K.7. DD-T kinematics: birth energy, thermal width, Doppler shift, and velocity Doppler broadening.

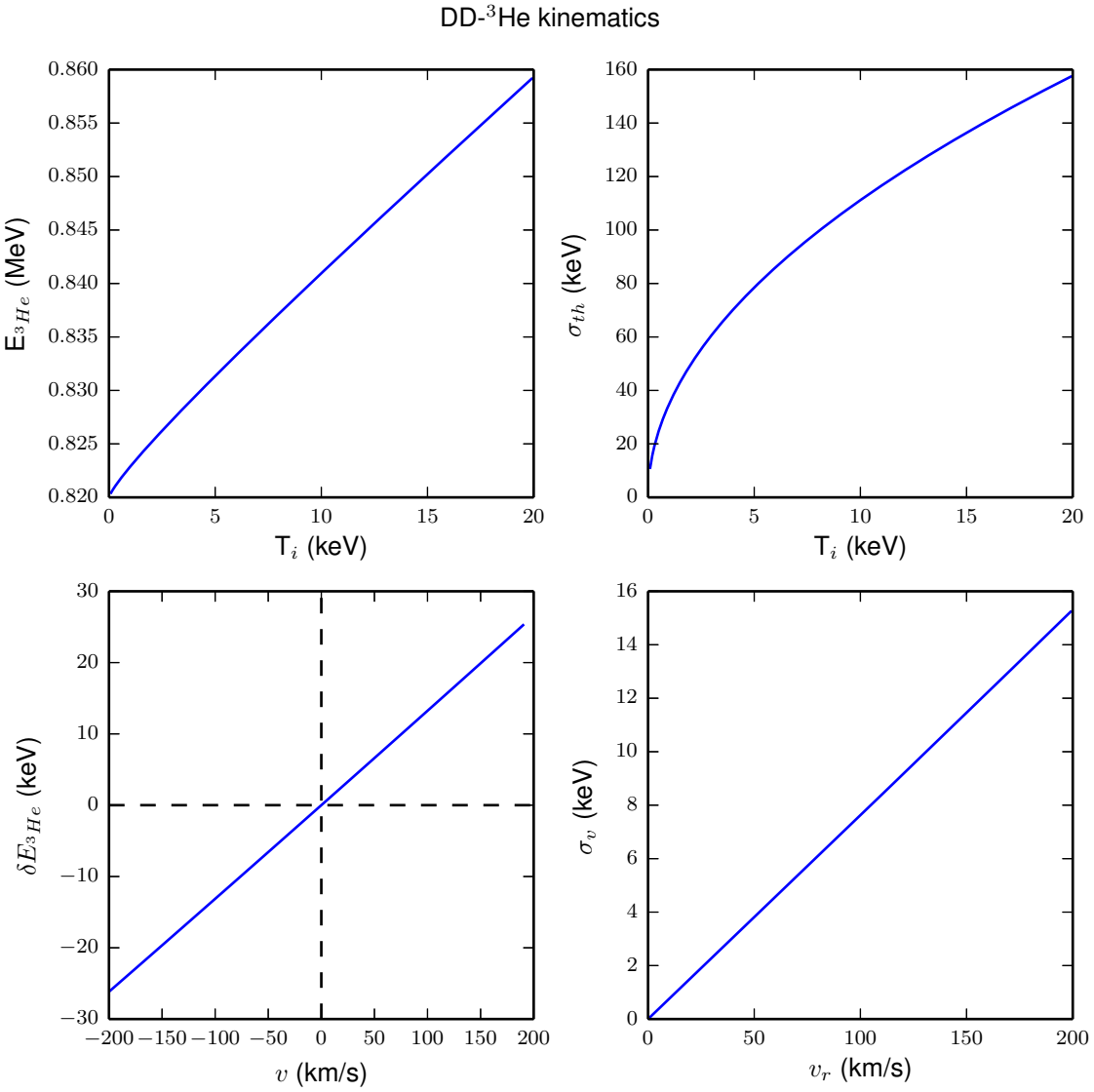

Figure K.8. DD-^{3}He kinematics: birth energy, thermal width, Doppler shift, and velocity Doppler broadening.